frontiers | Research Topics

The marine iodine cycle, past, present and future

Edited by
Rosie Chance, Dalton Hardisty, Anoop Sharad Mahajan, Maeve Carroll Lohan and Gregory A. Cutter

Published in
Frontiers in Marine Science

FRONTIERS EBOOK COPYRIGHT STATEMENT

The copyright in the text of individual articles in this ebook is the property of their respective authors or their respective institutions or funders. The copyright in graphics and images within each article may be subject to copyright of other parties. In both cases this is subject to a license granted to Frontiers.

The compilation of articles constituting this ebook is the property of Frontiers.

Each article within this ebook, and the ebook itself, are published under the most recent version of the Creative Commons CC-BY licence. The version current at the date of publication of this ebook is CC-BY 4.0. If the CC-BY licence is updated, the licence granted by Frontiers is automatically updated to the new version.

When exercising any right under the CC-BY licence, Frontiers must be attributed as the original publisher of the article or ebook, as applicable.

Authors have the responsibility of ensuring that any graphics or other materials which are the property of others may be included in the CC-BY licence, but this should be checked before relying on the CC-BY licence to reproduce those materials. Any copyright notices relating to those materials must be complied with.

Copyright and source acknowledgement notices may not be removed and must be displayed in any copy, derivative work or partial copy which includes the elements in question.

All copyright, and all rights therein, are protected by national and international copyright laws. The above represents a summary only. For further information please read Frontiers' Conditions for Website Use and Copyright Statement, and the applicable CC-BY licence.

ISSN 1664-8714
ISBN 978-2-8325-4916-2
DOI 10.3389/978-2-8325-4916-2

About Frontiers

Frontiers is more than just an open access publisher of scholarly articles: it is a pioneering approach to the world of academia, radically improving the way scholarly research is managed. The grand vision of Frontiers is a world where all people have an equal opportunity to seek, share and generate knowledge. Frontiers provides immediate and permanent online open access to all its publications, but this alone is not enough to realize our grand goals.

Frontiers journal series

The Frontiers journal series is a multi-tier and interdisciplinary set of open-access, online journals, promising a paradigm shift from the current review, selection and dissemination processes in academic publishing. All Frontiers journals are driven by researchers for researchers; therefore, they constitute a service to the scholarly community. At the same time, the *Frontiers journal series* operates on a revolutionary invention, the tiered publishing system, initially addressing specific communities of scholars, and gradually climbing up to broader public understanding, thus serving the interests of the lay society, too.

Dedication to quality

Each Frontiers article is a landmark of the highest quality, thanks to genuinely collaborative interactions between authors and review editors, who include some of the world's best academicians. Research must be certified by peers before entering a stream of knowledge that may eventually reach the public - and shape society; therefore, Frontiers only applies the most rigorous and unbiased reviews. Frontiers revolutionizes research publishing by freely delivering the most outstanding research, evaluated with no bias from both the academic and social point of view. By applying the most advanced information technologies, Frontiers is catapulting scholarly publishing into a new generation.

What are Frontiers Research Topics?

Frontiers Research Topics are very popular trademarks of the *Frontiers journals series*: they are collections of at least ten articles, all centered on a particular subject. With their unique mix of varied contributions from Original Research to Review Articles, Frontiers Research Topics unify the most influential researchers, the latest key findings and historical advances in a hot research area.

Find out more on how to host your own Frontiers Research Topic or contribute to one as an author by contacting the Frontiers editorial office: frontiersin.org/about/contact

The marine iodine cycle, past, present and future

Topic editors

Rosie Chance — University of York, United Kingdom
Dalton Hardisty — Michigan State University, United States
Anoop Sharad Mahajan — Indian Institute of Tropical Meteorology (IITM), India
Maeve Carroll Lohan — University of Southampton, United Kingdom
Gregory A. Cutter — Old Dominion University, United States

Citation

Chance, R., Hardisty, D., Mahajan, A. S., Lohan, M. C., Cutter, G. A., eds. (2024). *The marine iodine cycle, past, present and future*. Lausanne: Frontiers Media SA.
doi: 10.3389/978-2-8325-4916-2

Table of contents

04 Editorial: The marine iodine cycle, past, present and future
Rosie Chance, Gregory A. Cutter, Dalton S. Hardisty and Anoop S. Mahajan

07 Surface Inorganic Iodine Speciation in the Indian and Southern Oceans From 12°N to 70°S
Rosie Chance, Liselotte Tinel, Amit Sarkar, Alok K. Sinha, Anoop S. Mahajan, Racheal Chacko, P. Sabu, Rajdeep Roy, Tim D. Jickells, David P. Stevens, Martin Wadley and Lucy J. Carpenter

23 Soluble Iodine Speciation in Marine Aerosols Across the Indian and Pacific Ocean Basins
Elise S. Droste, Alex R. Baker, Chan Yodle, Andrew Smith and Laurens Ganzeveld

39 Devonian upper ocean redox trends across Laurussia: Testing potential influences of marine carbonate lithology on bulk rock I/Ca signals
Ruliang He, Maya Elrick, James Day, Wanyi Lu and Zunli Lu

51 Planktic foraminifera iodine/calcium ratios from plankton tows
Helge A. Winkelbauer, Babette A. A. Hoogakker, Rosie J. Chance, Catherine V. Davis, Christopher J. Anthony, Juliane Bischoff, Lucy J. Carpenter, Simon R. N. Chenery, Elliott M. Hamilton, Philip Holdship, Victoria L. Peck, Alex J. Poulton, Mark C. Stinchcombe and Karen F. Wishner

62 Review on the physical chemistry of iodine transformations in the oceans
George W. Luther III

78 Speciation of dissolved inorganic iodine in a coastal fjord: a time-series study from Bedford Basin, Nova Scotia, Canada
Qiang Shi, Jong Sung Kim and Douglas W. Wallace

93 Iodine-to-calcium ratios in deep-sea scleractinian and bamboo corals
Yun-Ju Sun, Laura F. Robinson, Ian J. Parkinson, Joseph A. Stewart, Wanyi Lu, Dalton S. Hardisty, Qian Liu, James Kershaw, Michèle LaVigne and Tristan J. Horner

105 Speciation and cycling of iodine in the subtropical North Pacific Ocean
Iulia-Mădălina Ştreangă, Daniel J. Repeta, Jerzy S. Blusztajn and Tristan J. Horner

120 Rates and pathways of iodine speciation transformations at the Bermuda Atlantic Time Series
Alexi A. Schnur, Kevin M. Sutherland, Colleen M. Hansel and Dalton S. Hardisty

134 Iodide, iodate & dissolved organic iodine in the temperate coastal ocean
Matthew R. Jones, Rosie Chance, Thomas Bell, Oban Jones, David C. Loades, Rebecca May, Liselotte Tinel, Katherine Weddell, Claire Widdicombe and Lucy J. Carpenter

frontiers | Frontiers in Marine Science

TYPE Editorial
PUBLISHED 09 May 2024
DOI 10.3389/fmars.2024.1417731

Check for updates

OPEN ACCESS

EDITED AND REVIEWED BY
Rob Middag,
Royal Netherlands Institute for Sea Research (NIOZ), Netherlands

*CORRESPONDENCE
Rosie Chance
rosie.chance@york.ac.uk

RECEIVED 15 April 2024
ACCEPTED 19 April 2024
PUBLISHED 09 May 2024

CITATION
Chance R, Cutter GA, Hardisty DS and Mahajan AS (2024) Editorial: The marine iodine cycle, past, present and future. *Front. Mar. Sci.* 11:1417731. doi: 10.3389/fmars.2024.1417731

COPYRIGHT
© 2024 Chance, Cutter, Hardisty and Mahajan. This is an open-access article distributed under the terms of the Creative Commons Attribution License (CC BY). The use, distribution or reproduction in other forums is permitted, provided the original author(s) and the copyright owner(s) are credited and that the original publication in this journal is cited, in accordance with accepted academic practice. No use, distribution or reproduction is permitted which does not comply with these terms.

Editorial: The marine iodine cycle, past, present and future

Rosie Chance[1]*, Gregory A. Cutter[2], Dalton S. Hardisty[3] and Anoop S. Mahajan[4]

[1]Wolfson Atmospheric Chemistry Laboratories, University of York, York, United Kingdom, [2]Department of Ocean & Earth Sciences, Old Dominion University, Norfolk, VA, United States, [3]Department of Earth and Environmental Sciences, Michigan State University, East Lansing, MI, United States, [4]Indian Institute of Tropical Meteorology, Ministry of Earth Sciences, Pune, India

KEYWORDS

iodide, iodate, iodine, seawater, paleoredox proxy

Editorial on the Research Topic
The marine iodine cycle, past, present and future

Iodine is a redox-active element that exists in multiple oxidation states and phases in the oceans, and is taken up and transformed by living organisms. The dominant forms in seawater are the dissolved anions iodide (I^-) and iodate (IO_3^-), along with smaller fractions of dissolved organic iodine (DOI), and particulate iodine (Chance et al., 2014). It plays an important role in atmospheric chemistry, impacting air quality and climate. Reaction with iodide-iodine at the ocean surface is a major sink for tropospheric ozone, a pollutant gas, and the main driver of the sea-air iodine flux. Understanding the distribution and drivers of marine iodine speciation is necessary to accurately quantify sea-air iodine fluxes and the marine ozone sink. Another key motivation for understanding the modern marine iodine cycle is the use of iodate-iodine abundance in ancient carbonate minerals as a proxy for oxygenation in the paleo-ocean (Lu et al., 2010). Refinement of this proxy to be more quantitative requires an improved understanding of the marine iodine cycle and how it responds to changes in redox conditions. Finally, iodine species, including anthropogenic radioisotopes, are also proposed as tracers of water masses and sedimentary inputs.

In this Research Topic, we bring together ten articles from the diverse research communities interested in the marine iodine cycle, including paleoceanographers, atmospheric chemists, and biogeochemists. The physical chemistry underpinning iodine's chemical speciation and transformations in the ocean is reviewed by Luther; this paper provides a theoretical basis for the field observations presented in this Research Topic.

Three observational papers report present-day iodine speciation in the Pacific, Atlantic and Indian Oceans. New profiles of iodide and iodate concentrations from the vicinity of station ALOHA (A Long-term Oligotrophic Habitat Assessment) in the subtropical North Pacific (Ştreangă et al., 2023) and station BATS (Bermuda Atlantic Time-series Study) in the Atlantic (Schnur et al., 2024) are in good agreement with observations made more than 30 years earlier (Campos et al., 1996), suggesting long term temporal stability in the distribution of iodine species. In addition, these two papers both use radiotracers as a powerful tool to probe iodine transformations. By incubating seawater spiked with ^{129}I, Ştreangă et al. find evidence for an intermediate iodine pool that is rapidly converted to iodate, and Schnur et al. are able to place an upper limit of <2.99 nM day^{-1} on the iodide

oxidation rate. Meanwhile, Chance et al. present sea surface iodide concentrations from ~12°N to ~70°S in the Indian Ocean and the Indian sector of the Southern Ocean, a historically undersampled ocean basin. The measurements confirm the trend of higher iodide at lower latitude seen elsewhere (Chance et al., 2014). Two extremely high iodide concentrations (~1000 nM) were encountered in the Bay of Bengal and are thought to be associated with sedimentary inputs under low oxygen conditions.

Shi et al. and Jones et al. each present time series observations of iodine speciation in coastal, temperate waters. Time series measurements of iodine speciation are scarce, so these data sets will be invaluable for incorporating seasonal variation into iodine parameterizations and models. Shi et al. present measurements made over 4.5 years in a fjord in Nova Scotia, Canada, and demonstrate that existing parameterizations for sea surface iodide are not accurate for this location. Jones et al. explore the drivers of seasonal changes in surface water iodine speciation in the English Channel. They find that while iodate reduction is associated with seasonal changes in biological productivity, an additional, possibly sedimentary, process affecting the total iodine budget may also be operating.

Speciation of iodine in the marine atmosphere is considered by Droste et al., who report iodine speciation in aerosol samples collected during four cruises in the East and West Pacific and Indian Oceans. Soluble organic iodine (SOI) was a relatively constant proportion of the total (~20%), while iodide and iodate were inversely related. Iodate reduction was attributed to aerosol acidity, which is greater in smaller particles and air masses influenced by anthropogenic emissions. Meanwhile, iodide and SOI were correlated, suggesting that SOI may be a source of aerosol iodide.

Carbonate-iodine abundance (as I/Ca ratios) has been used as a paleoredox proxy across essentially the entire geologic time scale (e.g., Hardisty et al., 2014; Lu et al., 2018; Hess et al., 2023). In this Research Topic, three studies have scrutinized the validity of various carbonate archives as records of marine iodate levels. Specifically, the archives studied were planktic foraminifera (Winkelbauer et al., 2023), deep-sea bamboo and scleractinian corals (Sun et al., 2023), and ancient bulk carbonate rocks (He et al., 2022). An important finding is that, while benthic and planktic foraminifera from core-tops are known to record iodate variations of the overlying water column (reviewed in Hoogakker et al., 2024), foraminifera from plankton tows demonstrated little-to-no iodine incorporation regardless of local iodate abundance (Winkelbauer et al., 2023). This finding highlights the need for future work to address at what stage — between living, post-mortem, and diagenesis — iodate is incorporated into foraminiferal tests. In contrast, Sun et al. are the first to demonstrate abundant iodate incorporation in deep-sea corals across a range of localities. Deep-sea corals may thus prove to be an important, relatively high-resolution record of recent oxygen minimum zone (OMZ) dynamics. Finally, He et al. address the influence of diagenetic processes on I/Ca in bulk carbonate samples by directly comparing I/Ca to lithology in Devonian-aged bulk carbonate. In addition to proxy calibration, this study provides evidence for potential paleoredox variations across this critical interval in environmental and biological evolution.

Several papers in this Research Topic showcase new analytical techniques. Both Shi et al. and Jones et al. use ion chromatography to measure iodine species, including DOI. These methods are less labour-intensive than the electrochemical and spectrophotometric techniques that have commonly been used in the past, and their development allows higher temporal and/or spatial resolution studies to be conducted. Ştreangă et al. used anion exchange chromatography coupled with isotope dilution inductively coupled plasma mass spectrometry, which offers improved precision over conventional methods.

In summary, this Research Topic demonstrates the broad range of activity in marine iodine research. Analytical advances are allowing more extensive and detailed observations of iodine speciation, including less abundant but potentially important intermediate forms such as DOI, and helping to constrain the rates of iodine transformations. The I/Ca paleoredox proxy continues to be refined and applied across a wide range of time scales and carbonate archives.

Author contributions

RC: Writing – original draft, Writing – review & editing. GC: Writing – original draft, Writing – review & editing. DH: Writing – original draft, Writing – review & editing. AM: Writing – original draft, Writing – review & editing.

Conflict of interest

The authors declare that the research was conducted in the absence of any commercial or financial relationships that could be construed as a potential conflict of interest.

Publisher's note

All claims expressed in this article are solely those of the authors and do not necessarily represent those of their affiliated organizations, or those of the publisher, the editors and the reviewers. Any product that may be evaluated in this article, or claim that may be made by its manufacturer, is not guaranteed or endorsed by the publisher.

References

Campos, M. L. A. M., Farrenkopf, A. M., Jickells, T. D., and Luther, G. W. (1996). A comparison of dissolved iodine cycling at the Bermuda Atlantic Time-Series station and Hawaii Ocean Time-Series Station. *Deep Sea Res. Part II Top. Stud. Oceanogr.* 43, 455–466. doi: 10.1016/0967-0645(95)00100-x

Chance, R., Baker, A. R., Carpenter, L., and Jickells, T. D. (2014). The distribution of iodide at the sea surface. *Environ. Sci. Process. Impacts* 16, 1841–1859. doi: 10.1039/c4em00139g

Hardisty, D. S., Lu, Z., Planavsky, N. J., Bekker, A., Philippot, P., Zhou, X., et al. (2014). An iodine record of Paleoproterozoic surface ocean oxygenation. *Geology* 42, 619–622. doi: 10.1130/G35439.1

Hess, A. V., Auderset, A., Rosenthal, Y., Miller, K. G., Zhou, X., Sigman, D. M., et al. (2023). A well-oxygenated eastern tropical Pacific during the warm Miocene. *Nature* 619, 521–525. doi: 10.1038/s41586-023-06104-6

Hoogakker, B., Davis, C., Wang, Y., Kusch, S., Nilsson-Kerr, K., Hardisty, D., et al. (2024). Reviews and syntheses: Review of proxies for low-oxygen paleoceanographic reconstructions. *EGUsphere* 2024, 1–154. doi: 10.5194/egusphere-2023-2981

Lu, Z., Jenkyns, H. C., and Rickaby, R. E. M. (2010). Iodine to calcium ratios in marine carbonate as a paleo-redox proxy during oceanic anoxic events. *Geology* 38, 1107–1110. doi: 10.1130/G31145.1

Lu, W., Ridgwell, A., Thomas, E., Hardisty, D. S., Luo, G., Algeo, T. J., et al. (2018). Late inception of a resiliently oxygenated upper ocean. *Science* 361, 174–177. doi: 10.1126/science.aar5372

frontiers in Marine Science

ORIGINAL RESEARCH
published: 31 August 2020
doi: 10.3389/fmars.2020.00621

Surface Inorganic Iodine Speciation in the Indian and Southern Oceans From 12°N to 70°S

Rosie Chance[1†], Liselotte Tinel[1†], Amit Sarkar[2‡], Alok K. Sinha[2], Anoop S. Mahajan[3], Racheal Chacko[2], P. Sabu[2], Rajdeep Roy[4], Tim D. Jickells[5], David P. Stevens[6], Martin Wadley[6] and Lucy J. Carpenter[1]*

[1] Wolfson Atmospheric Chemistry Laboratories, Department of Chemistry, University of York, York, United Kingdom, [2] National Centre for Polar and Ocean Research, Ministry of Earth Sciences, Goa, India, [3] Indian Institute of Tropical Meteorology, Ministry of Earth Sciences, Pune, India, [4] National Remote Sensing Centre, Indian Space Research Organisation, Hyderabad, India, [5] Centre for Ocean and Atmospheric Sciences, School of Environmental Sciences, University of East Anglia, Norwich, United Kingdom, [6] Centre for Ocean and Atmospheric Sciences, School of Mathematics, University of East Anglia, Norwich, United Kingdom

OPEN ACCESS

Edited by:
Mark James Hopwood,
GEOMAR Helmholtz Center for Ocean Research Kiel, Germany

Reviewed by:
Maxime M. Grand,
Moss Landing Marine Laboratories, United States
Maija Iris Heller,
Pontificia Universidad Católica de Valparaíso, Chile

***Correspondence:**
Rosie Chance
rosie.chance@york.ac.uk

[†] These authors have contributed equally to this work

[‡] **Present address:**
Amit Sarkar,
Ecosystem Based Management of Marine Resources Programme (EBMMR), Environment and Life Sciences Research Center, Kuwait Institute for Scientific Research, Salmiya, Kuwait

Specialty section:
This article was submitted to Marine Biogeochemistry, a section of the journal Frontiers in Marine Science

Received: 18 April 2020
Accepted: 07 July 2020
Published: 31 August 2020

Citation:
Chance R, Tinel L, Sarkar A, Sinha AK, Mahajan AS, Chacko R, Sabu P, Roy R, Jickells TD, Stevens DP, Wadley M and Carpenter LJ (2020) Surface Inorganic Iodine Speciation in the Indian and Southern Oceans From 12°N to 70°S. Front. Mar. Sci. 7:621. doi: 10.3389/fmars.2020.00621

Marine iodine speciation has emerged as a potential tracer of primary productivity, sedimentary inputs, and ocean oxygenation. The reaction of iodide with ozone at the sea surface has also been identified as the largest deposition sink for tropospheric ozone and the dominant source of iodine to the atmosphere. Accurate incorporation of these processes into atmospheric models requires improved understanding of iodide concentrations at the air-sea interface. Observations of sea surface iodide are relatively sparse and are particularly lacking in the Indian Ocean basin. Here we examine 127 new sea surface (≤10 m depth) iodide and iodate observations made during three cruises in the Indian Ocean and the Indian sector of the Southern Ocean. The observations span latitudes from ∼12°N to ∼70°S, and include three distinct hydrographic regimes: the South Indian subtropical gyre, the Southern Ocean and the northern Indian Ocean including the southern Bay of Bengal. Concentrations and spatial distribution of sea surface iodide follow the same general trends as in other ocean basins, with iodide concentrations tending to decrease with increasing latitude (and decreasing sea surface temperature). However, the gradient of this relationship was steeper in subtropical waters of the Indian Ocean than in the Atlantic or Pacific, suggesting that it might not be accurately represented by widely used parameterizations based on sea surface temperature. This difference in gradients between basins may arise from differences in phytoplankton community composition and/or iodide production rates. Iodide concentrations in the tropical northern Indian Ocean were higher and more variable than elsewhere. Two extremely high iodide concentrations (1241 and 949 nM) were encountered in the Bay of Bengal and are thought to be associated with sedimentary inputs under low oxygen conditions. Excluding these outliers, sea surface iodide concentrations ranged from 20 to 250 nM, with a median of 61 nM. Controls on sea surface iodide concentrations in the Indian Ocean were investigated using a

state-of-the-art iodine cycling model. Multiple interacting factors were found to drive the iodide distribution. Dilution via vertical mixing and mixed layer depth shoaling are key controls, and both also modulate the impact of biogeochemical iodide formation and loss processes.

Keywords: iodine, iodide, iodate, seawater, Indian Ocean, Southern Ocean

INTRODUCTION

Iodine is naturally present in the ocean, predominantly as the inorganic ions iodide (I^-) and iodate (IO_3^-). Iodine speciation is linked to many aspects of ocean biogeochemistry, and has been proposed as a tracer of primary productivity (Wong, 2001; Ducklow et al., 2018), sedimentary inputs and oxygen status (Lu et al., 2018; Moriyasu et al., 2020). In addition, the concentration of iodide at the sea surface has recently attracted renewed interest from atmospheric chemists because of its impact on atmospheric composition and air quality e.g., (Sherwen et al., 2017; Cuevas et al., 2018).

The heterogeneous reaction of iodide with ozone at the sea surface has been identified as the largest, but also most uncertain, deposition sink for tropospheric ozone (Hardacre et al., 2015), and the dominant source of volatile reactive iodine (as I_2 and HOI) to the lower atmosphere (Carpenter et al., 2013). Following emission from the ocean, reactive iodine species initiate catalytic ozone depletion cycles, and hence further influence the oxidative capacity of the atmosphere. Atmospheric iodine cycling results in the formation of iodide oxides, which have been implicated in the nucleation of particles in coastal marine areas (McFiggans et al., 2004; Allan et al., 2015). In remote marine locations, iodine chemistry may also indirectly contribute to the depletion of inorganic volatile species such as gaseous elemental mercury during the polar spring (Wang et al., 2014). The ozone-iodide reaction is now thought to be the dominant source of iodine to the atmosphere, with other sources (e.g., release of iodinated organic compounds by marine algae) contributing only around 20% of the total iodine flux to the atmosphere globally (Carpenter et al., 2013; Prados-Roman et al., 2015). To incorporate the sea surface ozone sink and/or iodine source into atmospheric models, iodide concentrations at the interface need to be predicted accurately. However, parameterizations for global sea surface iodide concentrations (Chance et al., 2014; MacDonald et al., 2014) have been limited by the relative scarcity of observations. This is particularly the case for the Indian Ocean basin, where only a few sea surface iodide observations have hitherto been reported (Chance et al., 2014), but atmospheric iodine chemistry has been investigated (e.g., Mahajan et al., 2019).

In ocean waters, total inorganic iodine concentrations (the sum of iodide and iodate) behave approximately conservatively, with a value of around 450–500 nM across most of the oceans e.g., (Elderfield and Truesdale, 1980; Truesdale et al., 2000). Iodate is thermodynamically the more stable form under oxygenated conditions, and hence is present at higher concentrations throughout most ocean depths. However, at the ocean surface iodide concentrations are elevated and iodate depleted, despite this being thermodynamically unfavorable. Sea surface iodide concentrations typically range from undetectable to ∼250 nM, with values higher than this only encountered as outliers (Chance et al., 2014). Iodide concentrations and the iodide to iodate ratio decline with depth below the euphotic zone, and iodide concentrations are generally very low (<20 nM) in oxygenated waters below ∼500 m e.g., (Nakayama et al., 1989; Waite et al., 2006; Bluhm et al., 2011). Under low oxygen conditions, iodide becomes the thermodynamically favorable form, and is found to dominate in sub-oxic and anoxic waters (e.g., Wong and Brewer, 1977; Rue et al., 1997; Cutter et al., 2018). In addition to the two inorganic forms, iodine also occurs in association with dissolved organic matter as so-called dissolved organic iodine [DOI; e.g., (Wong and Cheng, 1998)]. In the open ocean, levels of DOI are typically low (<5% of the total iodine), but higher levels (e.g., 22% of total iodine) have sometimes been encountered (Wong and Cheng, 1998). However, organic forms of iodine are abundant in estuarine environments, where they can represent up to 64% of the total iodine (Wong and Cheng, 1998; Schwehr and Santschi, 2003). Deposition of particulate iodine to the ocean floor is only a small sink for iodine, with most being remineralized in the water column (Wong et al., 1976). Meanwhile, redox cycling of iodine in sediments is thought to occur (e.g., Price and Calvert, 1977) and iodide-iodine may be released from reducing sediments (e.g., Farrenkopf and Luther, 2002; Cutter et al., 2018).

The ratio of iodide to iodate varies with location as well as depth. Sea surface iodide concentrations exhibit a pronounced latitudinal gradient, with highest surface iodide concentrations observed at low latitudes and in coastal waters (Chance et al., 2014). The distribution of iodine species in the oceans is thought to result from a combination of hydrodynamic and biogeochemical drivers, which are not yet fully understood (Chance et al., 2014). The formation of iodide from iodate in the euphotic zone is thought to be associated with primary productivity, but the exact mechanism by which this occurs is not yet known (Campos et al., 1996; Bluhm et al., 2010; Chance et al., 2010). Similarly, the route for iodide oxidation back to iodate has been elusive, although recent work has suggested it may be linked to bacterial nitrification (Zic et al., 2013; Hughes et al., under review). The lifetime of iodide with respect to oxidation is poorly constrained but thought to be relatively long, with estimates ranging from several months (Campos et al., 1996; Zic et al., 2013) or more (Hardisty et al., 2020), to as much as 40 years (Tsunogai, 1971; Edwards and Truesdale, 1997). Given the relatively long lifetime of iodide in seawater, its distribution is also strongly influenced by advection and vertical mixing (e.g., Campos et al., 1996; Truesdale et al., 2000). Seasonal variations in biological activity and ocean mixing may result in seasonality in iodine speciation in the mixed layer (e.g., Chance et al., 2010). The interplay of these driving factors results in global scale

correlations between sea-surface iodide concentrations and sea-surface temperature (SST), and nitrate (Chance et al., 2014), which have been used to predict sea-surface iodide fields (e.g., Ganzeveld et al., 2009; MacDonald et al., 2014; Sarwar et al., 2016). In particular, spatial variations in ocean mixed layer depth are likely to be the primary cause of the widely used relationship between sea surface iodide concentration and SST.

This manuscript explores an extensive new set of sea surface iodide and iodate observations from the Indian Ocean and the Indian sector of the Southern Ocean, spanning latitudes from ∼12°N to ∼70°S, regions which have been lacking in observations (Chance et al., 2014). To the best of our knowledge, only three studies have previously examined iodine speciation in the Indian Ocean, and all have been in the west of the basin [East African coastal area (Truesdale, 1978) and Arabian Sea (Farrenkopf et al., 1997; Farrenkopf and Luther, 2002)]. Of the data presented in these studies, there were only two sea surface iodide observations - both from the Arabian Sea (see **Figure 1**) - that could be included in Chance et al. (2014). The aim of this study was to substantially increase the number of observations in this region, in order to both improve understanding of large-scale gradients in ocean iodine speciation, and to increase global data coverage for model validation and the improvement of ocean iodide parameterizations. All of these will contribute to the creation of more accurate boundary conditions for atmospheric chemistry models.

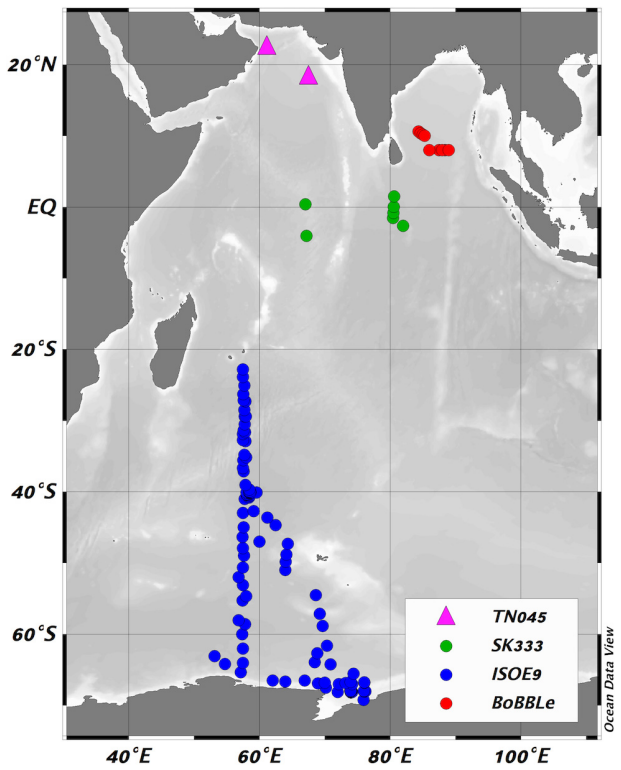

FIGURE 1 | Locations of new sea surface iodide observations made during this work, colored according to cruise (green – SK333, red – BoBBLe, blue – ISOE9) and previous observations from the region made by Farrenkopf and Luther (2002), and included in the compilation of Chance et al. (2014) (pink triangles). Figure produced using Ocean Data View (Schlitzer, 2014).

MATERIALS AND METHODS

Sample Collection

Samples were collected during three research cruises in the Indian Ocean and Indian sector of the Southern Ocean. Sampling locations for each cruise are shown in **Figure 1**. Samples were collected from the Bay of Bengal (BoB) during a zonal section cruise (Bay of Bengal Boundary Layer Experiment - BoBBLe) along 8°N, from 85.3°E to 89°E. The cruise took place between 24/6/2016 and 23/7/2016, on board the RV *Sindhu Sadhana*. In the Arabian Sea, samples were collected during the Rama mooring equatorial cruise IO1-16-SK (known as SK333 here), operated by Ministry of Earth Sciences, India (MoES) and National Oceanic and Atmospheric Administration, USA (NOAA), and taking place on the ORV *Sagar Kanya*. The cruise departed Chennai, India, on 23/08/2016 and returned to Sri Lanka on 23/09/2016. Samples were collected from the Southern Indian Ocean and Southern Ocean during the 9th Indian Southern Ocean Expedition (SOE9; Jan-March 2017), from Mauritius (22°S) to coastal waters of Prydz Bay, Antarctica (69°S) on board the MV *SA Agulhas*. Sampling included both (Antarctic) coastal and open ocean waters during this cruise.

During the BoBBLe and SOE9 cruises, surface water samples were obtained manually from the upper 30–70 cm of the sea surface using a metal bucket deployed over the windward side of the ship near the stern. Additional depth profile samples were obtained using a CTD (911 plus, Sea-Bird Electronics, United States) rosette equipped with 12 Niskin bottles. During the SOE9 cruise, depth profiles were taken at 17 CTD stations, and additional surface samples were taken (by bucket) at least twice a day along the entire cruise track (except when the ship was stationary for CTD stations). Sampling included two time-series, one at ∼40°S, and one in coastal Antarctic waters at ∼68°S (around the Polar Front), during which samples were collected at 4 or 6 h intervals for up to 72 h. During the SK333 cruise, samples were only collected using a CTD rosette. Sample dates, times and locations for all cruises are given in the online dataset available from the British Oceanographic Data Centre[1]. In this manuscript, both shallow CTD samples (depth ≤ 10 m) and "bucket" samples will be considered to be comparable, and representative of the ocean surface. This follows the approach taken in previous examinations of sea surface iodide concentrations (Chance et al., 2014). Note only surface samples are considered in this manuscript, although selected depth profiles are presented in the **Supplementary Material** to aid interpretation of surface concentrations.

Immediately following collection, samples were filtered (Whatman GF/F) under gentle vacuum, and transferred to 50 mL polypropylene screw cap tubes. Duplicate aliquots were prepared

[1]http://doi.org/czhx

for each sample. Aliquots were either stored at 4°C for on-board iodide determination within 24 h, or frozen at −20°C for transport back to our laboratories for analysis. The majority (91%) of frozen samples were analyzed within 12 months of collection, and all analyses were complete within 17 months of collection. Inorganic iodine speciation is preserved in frozen samples (≤−16°C) for at least one year (Campos, 1997). Repeat analyses of high and low concentration samples indicated that iodine speciation was preserved during the storage period. To avoid possible contamination, sample bottles for the iodine samples were kept strictly separated from the dissolved oxygen reagents containing iodine.

Iodide and Iodate Analysis

Iodide was determined by cathodic stripping square wave voltammetry (Luther et al., 1988; Campos, 1997) using a μAutolab III potentiostat connected to a 665VA stand (Metrohm) with a hanging mercury drop electrode, an Ag/AgCl reference electrode and a carbon or platinum auxiliary electrode. 12 (or 15) mL of the sample was introduced to a glass cell and 90 (or 112) μL of Triton X-100 (0.2%) was added. The sample was purged with N_2 (oxygen free grade) for 5 min before each measurement. The deposition potential was set at 0 V and deposition times were typically 60 s; scans ranged from 0 to −0.7 V, with a step of 2 mV, a 75 Hz frequency and a 0.02 V wave amplitude. Each scan was repeated 5–6 times, with scan repeatability equal or better than 5%. Calibration was by 2 or 3 standard additions of a KI solution ($\sim 10^{-5}$ or 10^{-6} M). Precision was estimated by repeat analysis (n = 6) of selected seawater samples over period of 10 days and was found to be lower than 7% relative standard deviation.

Iodate was measured using a spectrophotometer (UV-1800, Shimadzu; 4 decimal places) after reduction to iodonium (I_3^-) (Truesdale and Spencer, 1974; Jickells et al., 1988). 2.3 mL of the sample was introduced in the 1 cm UV quartz cell, 50 uL of sulfamic acid (1.5 M) was added, and the first absorbance value was obtained after 1 min. Then 150 μL of KI (0.6 M) was added and the second absorbance read after 2.5 min. Iodate concentrations were calculated from the difference between the two absorbances. Calibration was performed daily using a series of KIO_3 standard solutions. Samples were measured at least in triplicate with repeatability better than 5%; reported values are means. Reported errors are calculated by propagation of the standard deviation on the repeated measurements, the errors on the fit of the calibration and error on the volumes pipetted. Note that strictly, this method measures all inorganic iodine in oxidation states from 0 to +5, but as this fraction is dominated by iodate it is taken as a measure of iodate.

Supporting Measurements

Samples from CTD stations use the temperature, salinity and depth data directly obtained from the CTD. Precision of these measurements was as follows: temperature: ±0.001°C; conductivity: ±0.0001 S m^{-1}; depth: ±0.005% of the full scale. CTD salinity was calibrated using a high-precision salinometer (Guildline AUTOSAL). Temperature and salinity of manually collected "bucket" samples were determined using an outboard thermometer, and the salinometer, respectively.

Samples for nitrate (NO_3^-) analysis were collected in 250 mL narrow mouth polypropylene amber bottles (Nalgene). Each bottle was rinsed twice with the sample water prior to collection. Analysis was performed onboard as soon as possible after sample collection, using an SKALAR SAN+ segmented continuous flow AutoAnalyzer. Precision and accuracy of NO_3^- measurements were ±0.06 and ±0.07 μM, respectively.

Ocean Modeling

The ocean iodine cycling model described in Wadley et al. (2020) was used to evaluate which physical and biogeochemical processes drive the observed trends in iodide concentration in the Indian Ocean and Indian sector of the Southern Ocean. The model comprises a biogeochemical model of iodine cycling embedded in a three-dimensional global ocean circulation framework, and has been calibrated using the data from a recently available extended global sea surface iodide compilation (Chance et al., 2019) which includes the current data set, plus additional depth resolved iodide measurements [see (Wadley et al., 2020) for details]. In the model, iodide production is driven by primary production, and iodide loss (by oxidation) is linked to biological nitrification. A spatially variable I:C ratio is used to allow the model to better capture the observed iodide concentrations.

RESULTS AND DISCUSSION

Overview – Global Scale Trends

In total, 127 sea surface iodide observations and 130 sea surface iodate observations were made during the three cruises, including two time series. Measurements were made at 98 different sampling locations, spanning latitudes from ∼12°N to ∼70°S. This is a substantial increase in data coverage for the Indian Ocean and the Indian sector of the Southern Ocean region, which was previously particularly lacking in observations of sea surface iodine speciation (Chance et al., 2014). As noted in the introduction, only two sea surface iodide observations for the Indian Ocean were included in Chance et al. (2014), and both were from the Arabian Sea (see **Figure 1**).

The lowest iodide concentrations were observed at high latitudes, while the highest concentrations were encountered at the northern extent of the southern sub-tropical region and within the tropics (**Figure 2**). This latitudinal trend in sea surface iodide concentration broadly follows those observed in other ocean basins (**Figure 3**). In addition, a "dip" in sea surface iodide concentrations is seen around the equator and elevated concentrations are seen in coastal polar waters, as observed elsewhere (**Figures 2**, **3**; Chance et al., 2010, 2014). While these global scale trends are well documented in the Atlantic and Pacific basins e.g., (Tsunogai and Henmi, 1971; Campos et al., 1999; Truesdale et al., 2000; Bluhm et al., 2011), to the best of our knowledge this is the first time they have been confirmed in the Indian Ocean and the Indian section of the Southern Ocean.

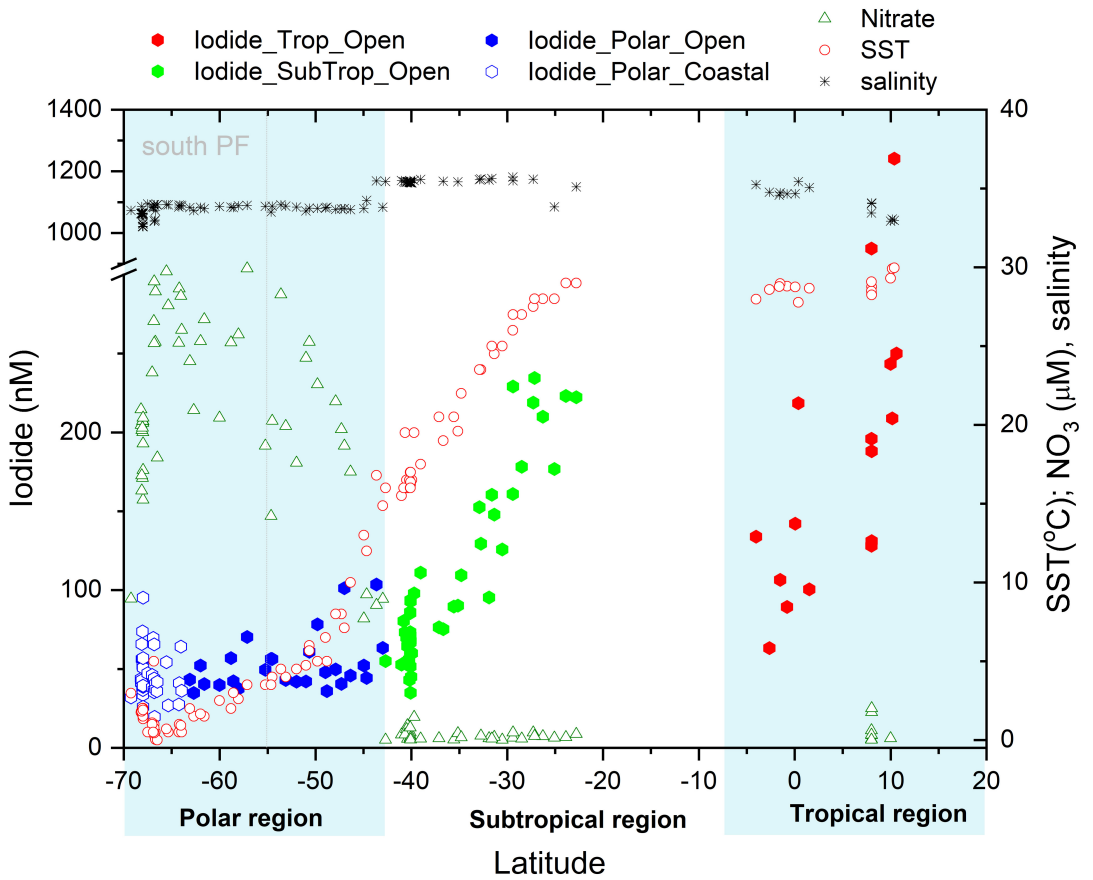

FIGURE 2 | Latitudinal variation of surface iodide concentrations in nM observed in the open Indian and Southern Ocean (•) and in the coastal Southern Ocean (○) compared to the observed sea surface temperature (°C), salinity and nitrate concentrations (µM). Boxes indicate the three different oceanographic regimes considered in the text. The dotted gray line indicates the position of the Polar Front (PF).

Considering the entire data set, sea surface iodide concentrations ranged from 20 to 1241 nM, with a median of 61 nM (**Figure 4**). The very large range in the data is primarily due to the presence of two very high outliers in the Bay of Bengal, which are discussed later. When these outliers are excluded, the upper limit of the data is reduced to 250 nM, bringing the range within the global range of marine iodide concentrations previously reported (Chance et al., 2014). The large range in the overall data set can mainly be ascribed to the large span of latitudes covered. The median value is somewhat lower than the global median value 77 nM; (Chance et al., 2014), reflecting the bias toward high latitude/low iodide samples in our data set.

Sea surface iodate concentrations ranged from 51 to 495 nM, with a median of 294 nM. Iodate concentrations broadly showed the opposite pattern to iodide concentrations, with highest median values in the Southern Ocean (median of 323 nM), intermediate values in the subtropical Indian Ocean (median of 294 nM) and lowest values in the tropical Indian Ocean (median 196 nM). However, there was only a very weak, inverse linear relationship between sea surface iodide and iodate concentrations ($R^2 = 0.16$, $p = 3 \times 10^{-6}$; **Figure 5**). Total iodine concentrations in seawater are typically ∼450–500 nM (Chance et al., 2014, and references therein), with the budget dominated by iodide and iodate. Here we find the sum of iodide and iodate was less than this at most sampling locations (**Figure 5**), with a median value of 380 nM (range 88 to 560 nM). Although somewhat unusual, comparable low total inorganic iodine concentrations have been reported elsewhere [e.g., North Sea (Hou et al., 2007), South East China Sea (Wong and Zhang, 2003)]. Depleted total inorganic iodine may be due to uptake of iodine to the particulate phase in the surface ocean, or the presence of a significant dissolved organic iodine reservoir. Although it could imply substantial loss of iodine from the surface ocean to the atmosphere, current knowledge suggests the magnitude of such fluxes (e.g., Carpenter et al., 2013) is too small to have such a large impact on the sea surface concentrations. No clear relationships were evident between total inorganic iodine and either latitude or nitrate concentration.

Our sampling area spanned a wide range of different hydrographic provinces and biogeochemical conditions (**Figure 2**). North of the equator, SST becomes a poor predictor of iodide concentration. To explore our data set further, we consider iodine speciation separately in each of three different hydrographic regimes (tropical, mid-latitudes, and polar).

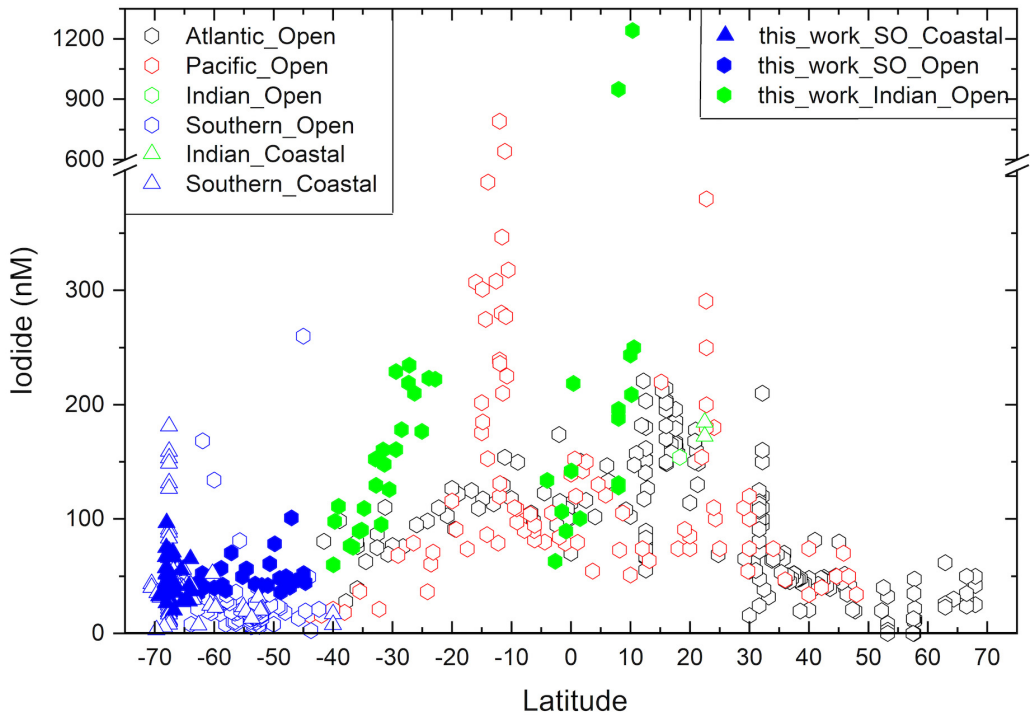

FIGURE 3 | Latitudinal variation of sea surface iodide concentrations in the Indian (green) and Indian sector of the Southern Ocean (SO; blue), compared to other ocean basins (Atlantic – black, Pacific – red). New observations made as part of this work are shown with filled symbols, while other values [see compilation of Chance et al. (2019)] are shown in hollow symbols. Division between ocean basins follows the borders proposed by the World Ocean Circulation Experiment (https://www.nodc.noaa.gov/woce/woce_v3/wocedata_1/woce-uot/summary/bound.htm), and (Orsi et al., 1995) for the Southern Ocean.

South Indian Subtropical Gyre (~23–42°S)

In the southern Indian Ocean, samples were collected along an approximate latitudinal transect at 57°E, from ~23 to 42°S. The open ocean transect spanned the Indian South subtropical gyre and the subtropical convergence zone. North of this region, at ~15°S, the Southern Equatorial Current (SEC; not sampled in this work) has been noted as a clear biogeochemical front, separating subtropical gyre waters from the lower oxygen northern Indian Ocean (Grand et al., 2015). The subtropical gyre waters are characterized by very low nitrate concentrations and relatively high salinity (**Figure 2**), with SST rising from ~15°C in the south to ~29°C in the north. Between these latitudes, iodide concentrations ranged from 35 to 235 nM and increased in step with decreasing latitude and increasing SST (**Figure 2**). In this region, iodide is strongly correlated with both latitude ($R^2 = 0.86$, $p = 3 \times 10^{-20}$) and SST ($R^2_{adj} = 0.89$, $p = 2 \times 10^{-22}$) (**Table 1**). These are stronger correlations than the global relationships reported in Chance et al., 2014, and also have steeper gradients than found in the Chance et al. (2014) data set (**Table 1**).

Nitrate concentrations have been used to predict sea-surface iodide concentrations (Ganzeveld et al., 2009), and significant relationships between iodide and nitrate in upper 100 m of the water column have been reported for the subtropical Atlantic (Campos et al., 1999). However, in our data set no relationship between nitrate and iodide was apparent ($R^2 = 0.0004$; **Table 1**), implying sea surface nitrate concentrations are a poor predictor of sea surface iodide in this hydrographic region. This likely reflects the fact we only consider surface concentrations, which exhibited low nitrate concentrations (86% of data points were below 0.5 μM), but substantial gradients for iodide.

Comparison of Latitudinal Sea Surface Iodide Gradients Between Subtropical Regions of Different Ocean Basins

Using the extended dataset of global sea surface iodide observations (Chance et al., 2019), sea surface iodide gradients in the subtropical regions of each of the ocean basins were compared (**Table 2**). Considering each of the major ocean gyres individually reveals that the latitudinal dependency of iodide is greater in the Indian Ocean than in the north Atlantic, north Pacific or south Atlantic (**Figure 3** and **Table 2**). Iodide in the south Pacific appears to also have a steep gradient if observations from the Peruvian upwelling region (Cutter et al., 2018) are included in the analysis. However, this dataset has an unusually large iodide concentration range (153 to 790 nM) within a small latitudinal band (~11 to 16°S), and does not exhibit a latitudinal trend in iodide as observed elsewhere. This distinct behavior may be due to the influence of sub-surface low oxygen waters. The remaining data from the south Pacific subtropical gyre is from a transect along the 170°W meridian from 12 to 38°S (Tsunogai and Henmi, 1971). If the Peruvian upwelling data is

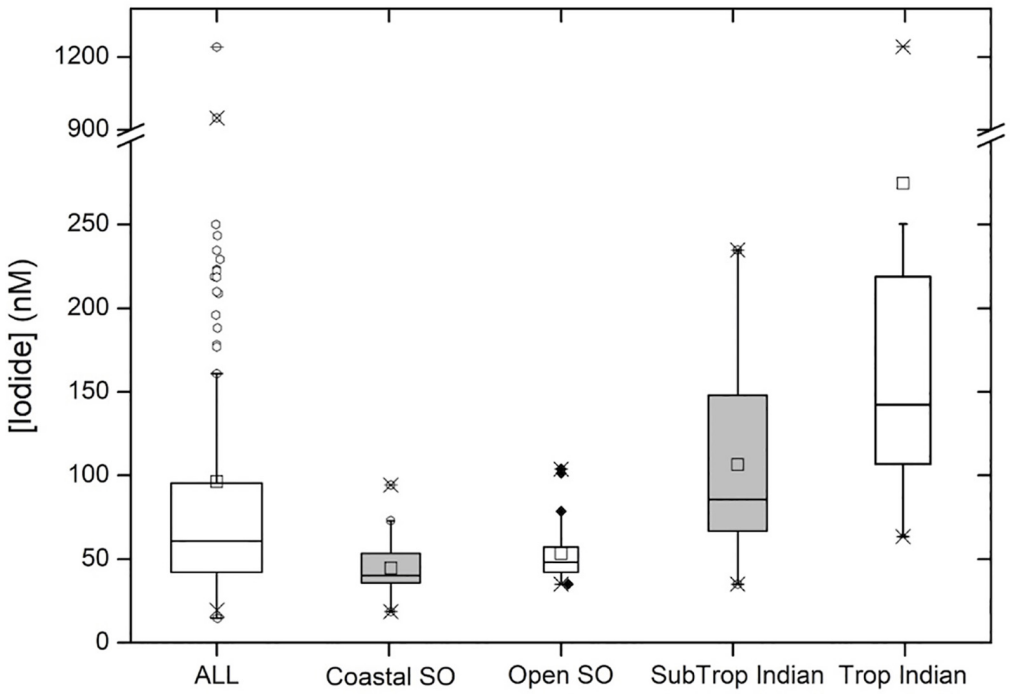

FIGURE 4 | Box and Whisker plot showing descriptive statistics for the entire data set ("ALL"; *n* = 127) and sub-divided into the following regions: polar coastal waters ("Coastal SO"; *n* = 38), open waters of the Southern Ocean ("Open SO"; *n* = 27), the Indian Ocean subtropical convergence zone and southern subtropical gyre ("SubTrop Indian"; *n* = 46 and the tropical Indian Ocean ("Trop Indian"; *n* = 16). See main text for more detailed descriptions of these categories. Center lines show the medians; squares are the means; box limits indicate the 25th and 75th percentiles; whiskers extend 1.5 times the interquartile range from the 25th and 75th percentiles, outliers are represented by dots; crosses represent 1st and 99th percentiles; width of the boxes is proportional to the square root of the sample size.

excluded from the gradient analysis, the remaining data for the south Pacific exhibits a comparable iodide gradient to the other ocean basins. The higher sea surface iodide gradient observed in the subtropical Indian Ocean is driven by concentrations at low latitudes (∼25°S) being approximately double those at comparable latitudes in the other ocean basins, rather than a difference between concentrations at the high latitude limits of the gyres (**Figure 3**).

The same trend is also evident in iodide vs. SST gradients, which are steeper in the Indian Ocean than in other basins (**Table 2**). This implies that the differences between basins cannot entirely be accounted for by differences in SST gradients. Examination of climatological data (World Ocean Atlas, see Chance et al., 2014 for details) for the locations and months of iodide observations does not demonstrate any clear differences in SST, nitrate or mixed layer depth (MLD; defined using potential temperature) between ocean basins that might account for the difference in iodide gradient. Although SST is not thought to directly impact iodine cycling itself, its correlation with iodide concentration is important as it is widely used to predict sea surface iodide fields for use in atmospheric models (e.g., Sarwar et al., 2016). The stronger latitudinal dependency of iodide in the Indian Ocean that we observe here is not replicated in sea surface iodide values predicted using commonly employed global scale parameterizations based on sea surface temperature (Chance et al., 2014; MacDonald et al., 2014). This is likely to introduce uncertainties specific to the Indian Ocean when using such parameterizations, for example in model calculations of iodine emissions from the sea surface.

The observational data is too limited to properly evaluate whether the pattern is the result of seasonal biases in sampling; of the data used in this comparison, all subtropical Indian Ocean observations were made during the southern hemisphere summer (January and February), while the modal months for observations in other basins were November (North Atlantic), October (South Atlantic) and March (North Pacific), see **Table 2**. In the South Pacific, if data from the Peruvian upwelling is excluded, at least 90% of observations used were made in January (Tsunogai and Henmi, 1971), i.e., in the same season as the Indian Ocean data. Despite this, they have a lower latitudinal gradient (slope = 2.8 compared to 9.5; **Table 2**), hinting that the difference between basins is not due to seasonal variation and/or sampling biases and may instead be due to differences in iodine cycling.

Although less pronounced, a relatively steep iodide vs. latitude gradient in the Indian Ocean is replicated in our model (**Table 2**), and hence a series of model sensitivity tests have been conducted to investigate which processes may be responsible for the apparent differences in the iodide gradient between ocean basins. Specifically, the model was run with each of the iodide forcing processes in the Indian Ocean and Indian sector of the Southern Ocean replaced by those from the Atlantic. **Figure 6** shows the forcing fields used for the two ocean basins, and the modeled

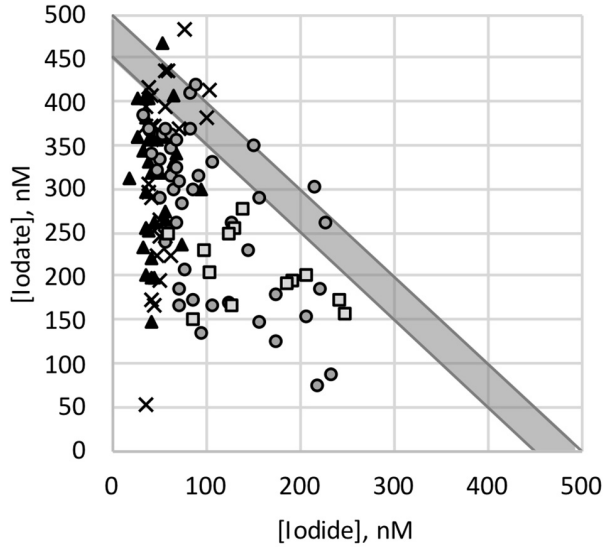

FIGURE 5 | Sea surface iodate concentrations plotted against iodide concentrations, for samples from polar coastal waters (▲), open waters of the Southern Ocean (×), the Indian Ocean subtropical convergence zone and southern subtropical gyre (○) and the tropical Indian Ocean (□). Gray line shows 1:1 relationship, assuming a total inorganic iodine concentration of 450 to 500 nM (Chance et al., 2014). Note for clarity two samples with very high iodide concentrations not shown.

TABLE 1 | Regression parameters for relationships between sea surface iodide (in nM) and latitude, SST and nitrate concentration, for iodide observations made in the Indian Ocean and Indian Ocean sector of the Southern Ocean during this work ("*All data*"), and hydrographic sub-divisions of this data-set.

Independent variable	R^2 / ρ_s	*Slope* –	*Intercept* –	*p* / *p*
Latitude				
All data	0.24	−3.4	251	**5×10^{-9}**
	−0.74	–	–	**0**
Sub-tropical	0.86	−9.5	449	**3×10^{-20}**
	−0.83	–	–	**1.1×10^{-12}**
Southern Ocean	0.10	−0.64	87	**0.01**
	−0.21	–	–	**9.6×10^{-3}**
*Tropical**	0.39	9.2	109	**0.02**
	0.59	–	–	**1.7×10^{-2}**
Chance et al., 2014	0.40	−2.7	200	**<0.05**
	−0.65	–	–	**<0.05**
SST (°C)				
All data	0.26	5.7	21	**1×10^{-9}**
	0.81	–	–	**0**
Sub-tropical	0.89	11.8	−130	**2×10^{-22}**
	0.87	–	–	**6.7×10^{-15}**
Southern Ocean	0.15	1.8	43	**0.002**
	0.35	–	–	**4.2×10^{-3}**
*Tropical**	0.14	37	901	0.2
	0.42	–	–	0.14
Chance et al., 2014	0.52	5.7	4	**<0.05**
	0.72	–	–	**<0.05**
[Nitrate], μM				
All data	0.17	−3.9	136	**3×10^{-5}**
	−0.58	–	–	**1.6×10^{-10}**
Sub-tropical	0.004	−13	118	0.7
	−0.02	–	–	0.93
Southern Ocean	0.03	−0.53	61	0.2
	−0.13	–	–	0.34
Tropical (*n* = 5)	0.21	−31	195	0.4
	−0.14	–	–	0.79
Chance et al., 2014	0.36	−5.2	125	**<0.05**
	−0.73	–	–	**<0.05**

*For comparison, the regression parameters presented in Chance et al., 2014, which were calculated using an earlier, global scale data set, are also shown ("Chance et al., 2014"). For each variable, top row gives results of Pearsons Product-Moment correlation (parametric) and bottom row gives results of Spearmans rank correlation (non-parametric). Statistically significant ($p < 5\%$) correlations are shown in bold. *Two extremely high iodide concentrations in tropical sub-set excluded from correlation analysis.*

iodide concentrations generated using these fields. The iodide vs. latitude gradient is significantly increased between 30°S and 20°S when the Indian Ocean productivity fields are replaced with those for the same latitudes in the Atlantic (**Figure 6c**). This is driven by a smaller decrease in productivity with decreasing latitude in the Indian Ocean than the Atlantic (**Figure 6b**). Thus productivity differences would act to decrease, rather than increase the iodide gradient. In the model oxidation of iodide in the mixed layer occurs as a function of nitrification, which is parameterized using the proportion of nitrate regenerated in the mixed layer (see Wadley et al., 2020). Differences in this ratio between the subtropical regions of the Indian and Atlantic oceans are small (**Figure 6d**), and have negligible impact on modeled iodide in the Indian Ocean (**Figure 6e**). At lower latitudes MLDs are similar in the two basins, but between ∼35 and 45°S, MLDs are significantly deeper in the Atlantic due to the greater northward extent of polar waters (**Figure 6f**). Since a deeper MLD dilutes iodide, modeled iodide concentrations are decreased between 45°S and 35°S when Atlantic MLDs are imposed in the Indian basin (**Figure 6g**). Again this further increases the latitudinal gradient of iodide, rather than decreasing it. Precipitation and evaporation act to dilute/concentrate iodide in the mixed layer, so changes in the net freshwater flux with latitude could influence the latitudinal iodide gradient. However, imposing the Atlantic surface freshwater flux in the Indian Basin had a negligible effect on modeled iodide (**Figure 6i**). Finally, the I:C ratio in the model determines the amount of iodide produced per unit carbon fixed by primary production. To fit model to the observed iodide in each basin, a higher I:C ratio is utilized in the Indian than in the Atlantic Ocean (**Figure 6j**; see Wadley et al., 2020). Replacing the I:C ratio in the Indian Ocean with that for the Atlantic Ocean results in lower modeled iodide concentrations in the Indian Ocean, but little overall change in the latitudinal iodide gradient (**Figure 6k**). Note the model currently underestimates the iodide gradient in the Indian Ocean (**Table 2**), and further refinement of the spatial variation in the I:C ratio is needed to improve the model fit to observations. This may show that the I:C ratio influences latitudinal gradients of iodide.

In summary, basin scale differences in four key forcing fields (productivity, nitrification, MLD and P-E) do not appear to explain the difference in latitudinal iodide gradient between the subtropical Indian and southern Atlantic oceans. In fact,

TABLE 2 | Gradients of sea surface iodide concentrations against latitude and sea surface temperature (SST) for open ocean subtropical waters (defined by province) of the global ocean basins.

Ocean basin	*n*	[I^-] vs. | Latitude|		[I^-] vs. SST		Modal month	% Frequency of modal month
		Slope	R^2	Slope	R^2		
North Atlantic	123	−3.5	0.40	12.2	0.47	November	39
South Atlantic	27	−2.2	0.60	6.3	0.60	October	70
North Pacific	24	−3.5	0.06	9.9	0.24	March	38
South Pacific-a	27	−14.3	0.40	6.6	0.01	November	37
South Pacific-b	10	−2.8	0.59	6.7	0.65	January	90
South Indian	46	−9.5	0.85	13.3	0.84	January	67
South Indian, modeled	–	−5.5	0.99	–	–	–	–

Iodide data from Chance et al. (2019) and sea surface temperatures from the World Ocean Atlas 2013 (Locarnini et al., 2013). Results shown for South Pacific data with (a) and without (b) observations from the Peruvian upwelling (Cutter et al., 2018), which do not exhibit a linear latitudinal trend.

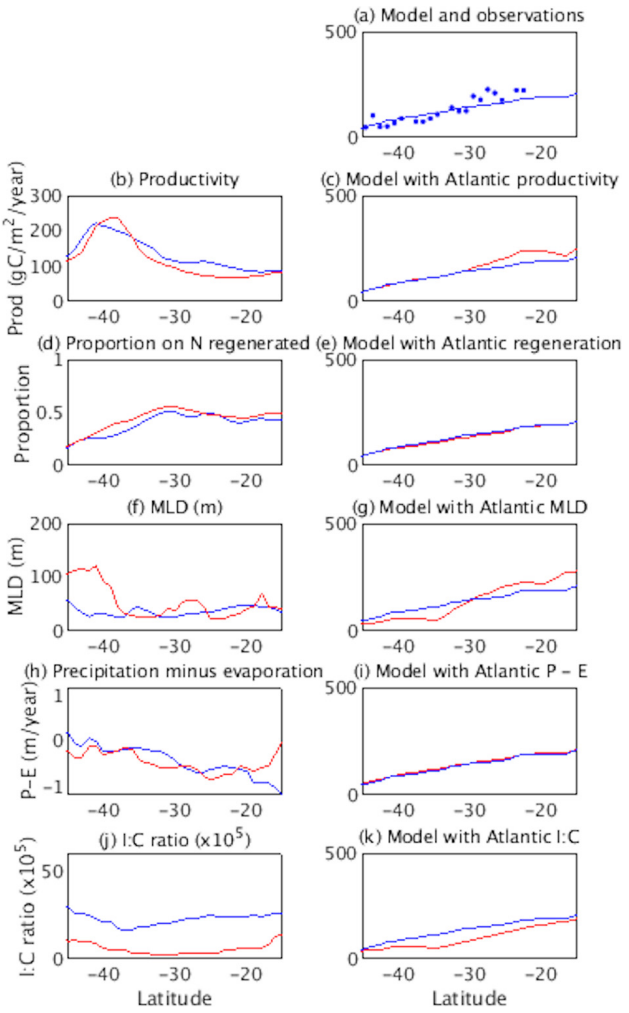

FIGURE 6 | Impact of imposing Atlantic forcings in the Indian Ocean basin in the iodine cycling model. Plots are annual mean iodide for 57°E in the Indian Ocean. **(a)** observed (dots) and modeled (line) iodide, in nM **(b,d,f,h,j)** latitudinal sections for each process-related quantity for the Indian (blue) and Atlantic (red) Oceans, **(c,e,g,i,k)** corresponding latitudinal sections of iodide for control (blue) and Atlantic forcing imposed over the Indian basin (red).

differences in productivity and MLD between the two basins appear to have the opposite effect, as Atlantic forcing fields resulting in an even steeper gradient than Indian Ocean forcing fields. Removal of advection in the model also results in an increase rather than a decrease in iodide at subtropical latitudes in the Indian Ocean (see later/**Figure 7**) and hence an even steeper latitudinal iodide gradient. This suggests the basin scale differences in iodide gradient are not due to advection in the Indian Ocean. Instead we suggest the difference may be the result of different phytoplankton types, with differing I:C iodide production ratios between basins. The need for a higher I:C ratio in the Indian Ocean/Indian sector of the Southern Ocean than the Atlantic (**Figure 6j**) implies there may be profound differences in microbiological community composition, and/or the cycling of iodine by such organisms between basins. *Synechococcus* dominates in the subtropical Indian Ocean, whereas Nanoeucaryotes and *Prochlorococcus* dominate in the subtropical Atlantic (Alvain et al., 2008). Recent work by our group indicates that the I:C ratio associated with iodide production varies between phytoplankton types, with *Synechococcus* having a higher I:C ratio than Nanoeucaryotes and *Prochlorococcus* types (Wadley et al., Manuscript in Preparation). Hence the higher relative abundance of *Synechococcus* in the subtropical Indian Ocean might account for the higher iodide concentrations observed at low latitudes, and the resulting steeper sea-surface iodide gradient. This also indicates that any change in microbiological community composition associated with climate change could significantly impact ocean iodide concentrations.

Southern Ocean Domain (~42°S–68°S)

At the subtropical front around 42°S, a decrease in salinity is accompanied by a sharp increase in nitrate concentration (**Figure 2**). This front marks the transition from the Indian Ocean to the Southern Ocean (Orsi et al., 1995). The colder, nutrient rich waters south of the subtropical front have much lower iodide content, with a median concentration of 43 nM and range of 20–104 nM (**Figure 4**). Relationships between iodide concentrations and latitude or SST in this region are much weaker than those observed further north (**Table 1**). This may be

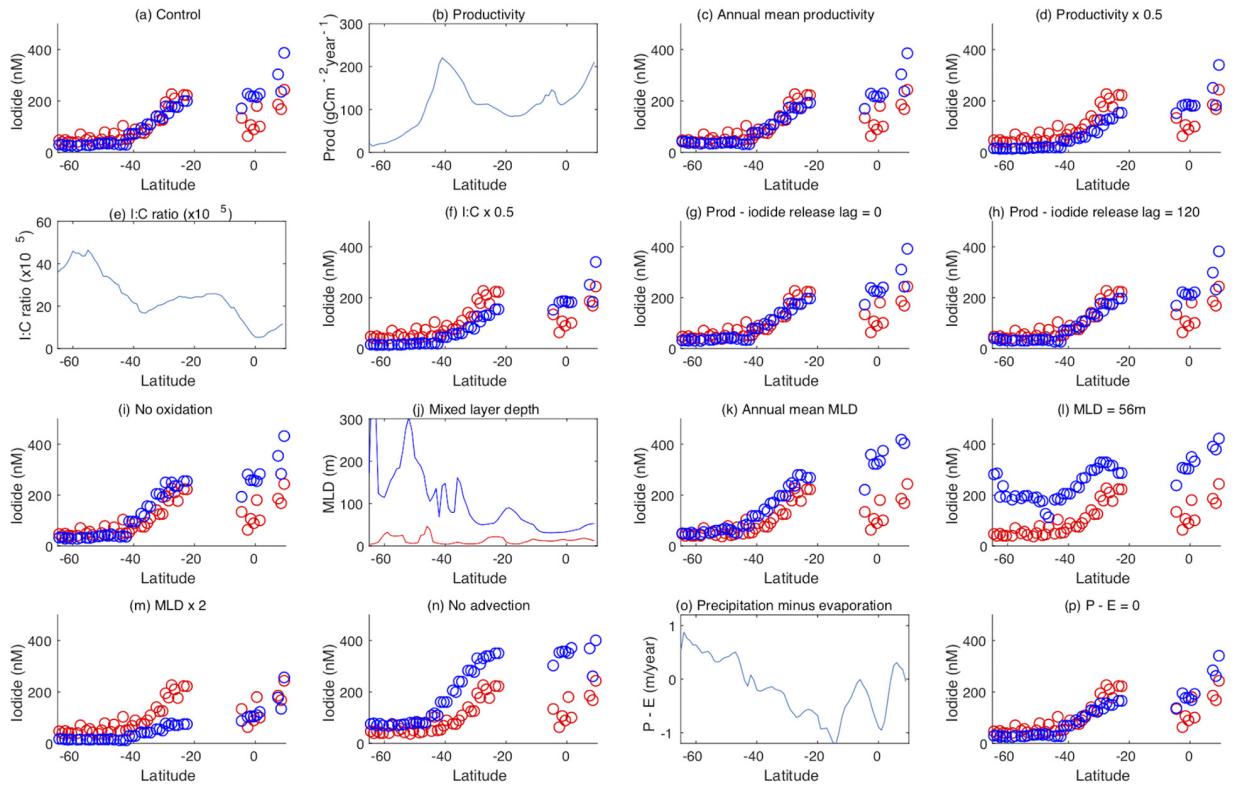

FIGURE 7 | Results from model process sensitivity experiments. **(a)** Observed (red) and model (blue) iodide concentrations as a function of latitude, in the Indian Ocean and the Indian sector of the Southern Ocean along a section at 60°E (note observed iodide over 500 nM have been excluded here) **(b)** observed primary productivity (Behrenfeld and Falkowski, 1997) as a function of latitude, **(c)** iodide with the seasonal cycle of productivity replaced with the annual mean, **(d)** iodide with seasonal productivity halved, **(e)** the model I:C ratio, **(f)** iodide with the model I:C ratio halved, **(g)** iodide with iodide release from plankton at the same time as carbon assimilation, **(h)** iodide with iodide release from plankton lagged 120 days from carbon assimilation, **(i)** no mixed layer oxidation of iodide, **(j)** maximum (blue) and minimum (red) mixed layer depth from the OCCAM model (Aksenov et al., 2010) as a function of latitude, **(k)** iodide with the seasonal cycle of mixed layer depth replaced with the annual mean, **(l)** iodide with the seasonal cycle of mixed layer depth replaced by the constant global mean of 56 m, **(m)** seasonal MLD doubled, **(n)** no vertical or horizontal advection, **(o)** P-E from the OCCAM model (Aksenov et al., 2010) as a function of latitude, **(p)** P-E set to zero.

due to disruption by strong, but variable, vertical mixing events, which are characteristic of the Southern Ocean. No significant relationship between sea surface iodide and nitrate was observed in the Southern Ocean samples (**Table 1**).

The Southern Ocean samples may be further subdivided into coastal (i.e., near the Antarctic continent) and open ocean samples. The former category was defined as samples falling within the Austral Polar biogeochemical province (Longhurst, 1998), while the latter category included samples from both the Antarctic and Sub-Antarctic provinces, and spanned the Polar Front. The range and distribution of concentrations seen in the coastal and open ocean subsets are very similar (**Figure 4**), despite the coastal samples spanning a much narrower latitudinal range (69–64°S, compared to 63–43°S). In the open ocean sub-set, iodide concentrations generally decrease moving south (R^2 = 0.16; p = 0.04), while in the coastal samples at the most southerly extreme of the data set, this relationship breaks down (R^2 = 0.02; **Figure 2**). A similar pattern is also reported in the global compilation of Chance et al. (2014), where Southern Ocean and Antarctic samples were predominantly from the Atlantic sector and the western Antarctic Peninsula. The range of concentrations observed in the Antarctic coastal samples (20 to 95 nM) is within that observed previously in coastal Antarctic waters during the austral summer (Chance et al., 2010). The magnitude of this variability is greater than can be accounted for by normalizing the iodide concentrations to salinity variations (e.g., due to ice melt water).

Northern Indian Ocean Including Southern Bay of Bengal (~4°S–11°N)

Samples were collected from open ocean locations in the Bay of Bengal and the Arabian Sea, between ~4°S and ~11°N. Sampling locations were all within the Indian Monsoon Gyre biogeochemical province (Longhurst, 1998), and shared high sea-surface temperatures, variable salinity and typically low nitrate concentrations. This sample sub-set showed the highest, and most variable iodide concentrations (range 63–1241 nM, median 165 nM; **Figure 4**). This was primarily due to the occurrence of two extremely high iodide concentrations (>900 nM) in the Bay of Bengal; excluding these values, the range in tropical open ocean iodide was still the largest of the three hydrographic regions surveyed, with a maximum of 250 nM being observed in the

Bay of Bengal (**Figure 4**). Such concentrations are comparable to measurements made at similar latitudes elsewhere (**Figure 3**).

All but one of the samples collected around the equator (∼5°S to ∼3°N) during the SK333 cruise had iodide concentrations in the range ∼80 to 120 nM. The exception to this was a station at 0°N where iodide concentrations reached ∼200 nM (**Figure 2**). As iodide concentrations were typically lower than in tropical waters further north and south (**Figure 2**), there was a positive rather than negative correlation between iodide and absolute latitude in this sample set (**Table 1**). A similar dip at very low latitudes is also seen in the Atlantic and Pacific (**Figure 3**; Chance et al., 2014). This feature is replicated in our model and is thought to be due to the advection and vertical mixing associated with the seasonally varying equatorial current system (see section).

As already noted, exceptionally high sea surface iodide concentrations of 1241 and 949 nM were observed at two stations in the Bay of Bengal (BS3 and BS8). Very high near-surface iodide concentrations were also observed at Station AR nearby (2039, 1546, and 479 nM at 10, 25, and 50 m, respectively, see **Supplementary Figure S1**). We believe these concentrations are real, and not the result of contamination or analytical error because: (i) repeat analyses gave the same results, (ii) very high concentration samples were also analyzed by ion chromatography, a completely independent method, and this yielded concentrations within 10% of those obtained by voltammetry (1277 and 960 nM for samples BS3 and BS8, respectively, and 1693 nM for Station AR at 25 m depth), (iii) results for Station AR show oceanographic consistency (see **Supplementary Figure S1**), (iv) no likely sources of iodine contamination were present during sampling. It is possible that the high, very localized, iodide concentrations could arise from the break-down of an iodine rich substrate, for instance a mass of brown macroalgae such as *Laminaria digitata*. However, nothing unusual of this nature was observed during sampling. These very high iodide levels result in total (dissolved) inorganic iodine concentrations more than double (2.2 and 2.6 times larger) the near universally observed value of ∼450–500 nM (Chance et al., 2014). This amount of iodide cannot be accounted for solely by the reduction of iodate in the water column (as this could only yield concentrations up to ∼500 nM). Instead it implies an exogenous source of iodine, which is either already in the form of iodide, or is reduced to iodide following introduction to the water column.

Samples with elevated iodide exhibited relatively low surface salinity (**Supplementary Figure S1**), possibly indicating an association with freshwater inputs. The Bay of Bengal is characterized by very heterogenous salinity - low salinity is caused by monsoon rainfall and high riverine inputs to the north, while high salinity water arrives from the Arabian Sea via the intense Southwest Monsoon Current (SMC). The BoBBLe cruise took place during the Asian summer monsoon season, during which the region experiences high rainfall. However, atmospheric wet deposition is thought unlikely to be the source of elevated iodide because meteoric water has a lower iodine content than seawater [20–124 nM (Sadasivan and Anand, 1979); 4.7–26.2 nM; (Gilfedder et al., 2007)]. Furthermore, observations of elevated sea surface iodide did not correspond to rainfall events encountered during the BoBBLe cruise itself. Similarly, riverine inputs are unlikely to be the iodide source, as total iodine concentrations in rivers, including the Ganges, are lower than or comparable to those in seawater [≤20 ug/L, ∼ 157 nM; (Moran et al., 2002; Ghose et al., 2003)], and the area surveyed was away from major outflows. While freshwater inputs are thus not thought to be the source of the excess iodide, stratification caused by rainwater dilution of surface layers could plausibly contribute to the persistence of high iodide concentrations at the ocean surface.

In addition to the SMC, the second main oceanographic feature in the BoBBLe study area is a wind driven upwelling feature called the Sri Lanka Dome (SLD), which manifests as a large cyclonic gyre in the south western part of the BoB to the east of Sri Lanka. Both the SLD and the SMC were well developed and distinct during the study period (Vinayachandran et al., 2018). Extreme iodide values were observed at stations north (AR, BS3) and east (BS8) of the SLD, but not in the stations that were inside the SLD (**Supplementary Figures S1, S2**; Vinayachandran et al., 2018). High iodide station AR exhibited high seawater pCO_2 (467–554 atm), low surface pH and low alkalinity, indicative of upwelled waters that are presumed to be associated with the SMC (Vinayachandran et al., 2018). Station BS3 was close in space and time, while station BS8 was also influenced by the SMC (Vinayachandran et al., 2018). We therefore speculate that the high iodide observed is in some way related to the SMC. However, the high salinity core of the SMC (i.e., Arabian Sea water), which was evident at depths of ∼25–150 m at stations east of the SLD, was not itself associated with elevated iodide (**Supplementary Figure S1**). This suggests the excess iodide was not in the main water mass carried by the SMC, and did not originate from the Arabian Sea. Instead we suggest its source could be coastal waters that are entrained in the periphery of the SMC and carried into the BoB with it.

Comparable high iodide concentrations have previously been observed in low oxygen sub-surface waters in the north western part of the Arabian Sea (Farrenkopf and Luther, 2002); these were attributed to advection from shelf sediments. More recently, plumes of very high iodide sub-surface concentrations (∼1000 nM) have also been reported in sub-oxic waters in the Eastern Tropical South Pacific (ETSP) (Cutter et al., 2018) and the Eastern Tropical North Pacific (ETNP) (Moriyasu et al., 2020). In both cases some outcropping of elevated iodide concentrations at the ocean surface was observed (Cutter et al., 2018; Moriyasu et al., 2020). In the ETSP, the plume followed an isopycnal and was associated with corresponding features in Fe(II) and nitrite, so was again thought to be due to a shelf sediment iodide source (Cutter et al., 2018). Elevated concentrations persisted more than 1000 km from the shelf break due to the relatively long iodide lifetime in seawater with respect to oxidation. Trace metal concentrations were not measured during the BoBBLe cruise, but sub-surface waters in the region have previously been reported to contain additional dissolved Fe from sedimentary inputs (Grand et al., 2015), suggesting it is plausible that stations on the edge of the SLD could be influenced by sedimentary interactions. Waters over the western Indian shelf experience severe hypoxia (Naqvi et al., 2000), and so could be subject

to significant sedimentary iodide inputs as implicated in other low oxygen regions (Farrenkopf and Luther, 2002; Cutter et al., 2018). During the Southwest Monsoon, the West Indian Coastal Current flows south along the west coast of India, and these waters are advected along the path of the SMC into the BoB. We speculate that such waters have potential to contain "excess" iodide levels as a result of sedimentary inputs, and that it is the remnants of these water masses that we may have sampled. Iodide has a long lifetime in oxygenated seawater (6 months to several years; Chance et al., 2014; Hardisty et al., 2020), and so a signal may be expected to persist where other indicators of sedimentary inputs are lost (Cutter et al., 2018), and could potentially reach the ocean surface via upwelling areas such as the south western BoB (**Supplementary Figure S2**).

In the northern Indian Ocean agreement between model and observations is poorer than elsewhere, but modeled concentrations fall within the range of the observations in the area. Furthermore, the model predicts unusually high iodide concentrations in the BoB, where extremely high iodide concentrations were observed. As the model does not currently include sedimentary processes, this suggests additional physical and biogeochemical processes may also contribute to elevated iodide levels in the BoB.

We believe this is the third reported observation of very elevated (>500 nM) iodide concentrations at the surface of the open ocean. The dataset reported by Cutter et al. (2018) contains two surface samples with iodide concentrations of 594 and 960 nM immediately off the coast of Peru, while transects in Moriyasu et al. (2020), show patches of high iodide outcropping at the surface. An extreme surface iodide concentration of ∼700 nM has also been reported for the brackish waters of the Skaggerrak (Truesdale et al., 2003), a shallow strait that is subject to hypoxia (Johannessen and Dahl, 1996). The paucity of previous observations suggests it is a rare phenomenon, but it may nonetheless be of local significance.

Atmospheric ozone deposition and iodine emission fluxes will proportionally increase where surface iodide concentrations are high. An increase in iodide from 150 to 2050 nM (×13.7) leads to a 5–6-fold increase in total iodine emissions, for a typical ambient ozone concentration of 25 ppb and a wind speed of 7 m s^{-1} (**Supplementary Figure S3**). This comprises a 4.5-fold increase in HOI emissions, which dominates the flux, and a 30-fold increase in I_2 emissions, which increase from 5.5% of the total flux at 150 nM iodide to 28% at 2050 nM iodide. It is assumed that the regional atmospheric impact of such "hot-spots" will be low, as they will only represent a small proportion of the relevant footprint area. However, the atmospheric impacts of such areas may become significant if either very localized processes are being considered, or their extent and/or frequency of occurrence increases. As areas of low oxygen waters in contact with shelf sediments become more extensive (Naqvi et al., 2000), the possibility that this could impact on surface iodide concentrations in coastal regions may need to be considered. Understanding the potential impact of low oxygen conditions and sedimentary inputs on surface iodide concentrations, and hence local atmospheric chemistry, requires both the sedimentary fluxes and the lifetime of iodide in oxygenated seawater to be better constrained. The atmospheric boundary layer above the northern Indian Ocean has high iodine oxide (IO) levels, with inputs dominated by the inorganic iodine flux from the ozone-iodide reaction (>90%), as a result of "ozone-related" pollution outflow (Prados-Roman et al., 2015). Hence atmospheric chemistry in the region may be particularly sensitive to changes in the surface iodide budget.

Exploring Physical and Biogeochemical Controls on Sea Surface Iodide in the Indian Ocean Using the Ocean Iodine Cycling Model

The trends in sea surface iodide concentrations observed across the south Indian subtropical gyre and Indian sector of the Southern Ocean are well replicated by the iodine cycling model of Wadley et al. (2020) (**Figure 7a**). We used the model to explore how physical (MLD, advection, net surface freshwater flux) and biogeochemical (productivity, iodide formation to carbon fixation ratio) factors influence iodine cycling in the study area.

Biological productivity drives iodide formation in the model, but has a different spatial distribution to iodide in the Indian Ocean basin (**Figures 7a,b**). Although both tend to increase moving north along the transect, the very strong peak in productivity centered on 40°S (**Figure 7b**) has no corresponding peak in either observed or simulated iodide concentrations. This indicates that other processes are also important in determining the iodide distribution. Imposing a constant level of productivity (set at the annual mean for each grid point) throughout the year had very little effect on modeled iodide concentrations, (**Figure 7c**), suggesting that the seasonal cycle of iodide production does not have a dominant effect on iodide concentrations. Halving the productivity in the model reduces simulated iodide concentrations by around a half south of 40°S (where iodide is very low, and iodate high), but only by around a quarter north of 40°S, and has almost no effect in the northern Indian Ocean where modeled iodide is highest (and thus modeled iodate lowest, at ≤300 nM). This may indicate that lower iodate concentrations to the north limit iodide production. The amount of iodide produced per unit primary productivity is specified in a spatially variable I:C ratio (**Figure 7e**; (Wadley et al., 2020). Halving this ratio is equivalent to halving primary production, and has identical consequences (**Figure 7f**).

As iodide is assumed to be evenly distributed throughout the mixed layer, surface concentrations are dependent on the MLD. Summer MLD minima are similar throughout the section, with typical values of a few tens of meters, whereas late winter MLD maxima increase with latitude (**Figure 7j**). Deepening of the MLD decreases iodide concentrations throughout the mixed layer as a result of dilution, while shoaling of the MLD decreases the total amount of iodide present integrated over the mixed layer, but does not change the concentration at any given depth within it. Removing the seasonal cycle of MLD in the model (by replacing with the annual mean MLD for each grid point) increases surface iodide concentrations, particularly at lower latitudes (**Figure 7k**), indicating that the removal of iodide through MLD shoaling is important. Removing

both seasonal and spatial variation in the MLD by setting it to a uniform 56 m results in substantial increases in surface iodide concentrations at higher latitudes (**Figure 7l**), due to elimination of both dilution and shoaling effects. In contrast, doubling the MLD decreases iodide concentrations, with the greatest effect seen where iodide concentrations are highest (**Figure 7m**). Interestingly, this brings modeled and observed iodide concentrations into good agreement around the equator. Inspection of SK333 CTD data indicates that at the time of sampling, actual MLDs in this region (between 50 and 100 m) were deeper than the climatological values used in the model (less than 40 m; **Figure 7j**), which may indicate that short term variations in MLD, for example due to weather events, affected iodide concentrations.

In the model, phytoplankton mediated iodide formation occurs 60 days after the uptake of carbon, and the interplay of this lag period with the MLD cycle could influence iodide concentrations. However, changing the duration of the lag to 0 and 120 days in the model has only a small impact on the iodide, and only at high latitudes (**Figures 7g,h**).

The seasonal MLD cycle imposes an annual timescale on the removal of iodide from the mixed layer where the seasonal cycle has a large amplitude, but vertical and horizontal advection also exchange water between the surface layer and ocean interior. Turning off the circulation in the model, so that vertical mixing is the only physical mechanism for iodide removal from the mixed layer also results in increased mixed layer iodide concentrations at almost all locations (**Figure 7n**).

In addition to removal by MLD shoaling, the model also allows for the removal of mixed layer iodide by oxidation to iodate, via a pathway linked to nitrification (Wadley et al., 2020; Hughes et al., under review). Eliminating this pathway has little impact on modeled iodide concentrations at high latitudes, but results in a significant increase in concentrations north of 40°S (**Figure 7i**). This is because the iodide oxidation timescale in the model is multi-annual, and hence its impact is modulated by the lifetime of iodide in the mixed layer with reference to vertical mixing. At high latitudes, large seasonal changes in the MLD result in low sensitivity to oxidation, whereas at lower latitudes there is less annual mixed layer exchange, resulting in a longer iodide residence time, and hence oxidation is a more important process for mixed layer iodide removal.

The net surface freshwater flux resulting from precipitation and evaporation (P-E) acts to, respectively, dilute or concentrate iodide in the mixed layer (**Figure 7o**). Setting the P-E flux to zero has a small impact on iodide, decreasing concentrations in the subtropical gyres where evaporation is strong. Thus at these latitudes evaporation results in a modest increase in iodide concentrations.

The model sensitivity tests described above confirm that sea surface iodide concentrations in the Indian and Southern Oceans are determined by a combination of factors which interact non-linearly. The dominant processes that determine iodide concentrations are the rate of iodide production, which is a function of productivity and the I:C ratio, and the MLD and its seasonal cycle, which acts to dilute and remove iodide from the surface layer. Loss by oxidation has the greatest impact at lower latitudes where physical removal mechanisms are weakest. As the climate changes over coming decades, changes in any of these factors are likely to result in changes in sea surface iodide concentrations. For example, the 100 to 300 m depth layer in the Indian Ocean has significantly warmed since 2003 as a result of heat distribution from the Pacific (Nieves et al., 2015) and this is likely to reduce stratification, and enhance vertical mixing, with an accompanying reduction in mixed layer iodide concentrations. Conversely, changes in nutrient inputs to the Indian Ocean and declining oxygen levels will act to reduce iodide oxidation, due to its association with nitrification (Hughes et al., under review), and hence may act to increase iodide concentrations. Any changes in productivity, and/or shifts to different phytoplankton types with different I:C ratios, will also potentially alter the rate of iodide production, although this has been found to predominantly impact on iodide concentrations at higher latitudes (Wadley et al., manuscript in preparation).

CONCLUDING REMARKS

The 127 sea surface iodide observations examined here represent a substantial (>10%) increase in the number of measurements that have been made across the global oceans (925 individual observations were included in Chance et al., 2014). They span nearly 80 degrees latitude in the Indian Ocean and Indian sector of the Southern Ocean, a region where very few (n = 2) surface observations were previously available. This increase in observations will facilitate better predictions of sea surface iodide concentrations, and consequent atmospheric chemistry, and the data has already been incorporated in a new global iodide database (Chance et al., 2019) and parameterization (Sherwen et al., 2019).

The large scale latitudinal trends observed in the Indian Ocean and Indian sector of the Southern Ocean are similar to those in other ocean basins (Chance et al., 2014). At subtropical latitudes, the latitudinal and temperature dependency of iodide is steeper than in other ocean basins. Therefore, using global scale relationships with SST [e.g., (MacDonald et al., 2014)] to predict regional scale iodide concentrations for the Indian Ocean will be subject to biases. Exploration of this basin scale difference using a state-of-the-art global iodine cycling model (Wadley et al., 2020) indicates that it may be driven by differences in biological iodide production. We have also used the model to explore the controls on the sea-surface iodide distribution in the Indian Ocean basin. Model sensitivity tests indicate that sea surface iodide is likely to be a function of vertical mixing and the seasonal cycle in MLD, the rate of iodide production, which is related to productivity and the I:C ratio, and – at lower latitudes – iodide oxidation in the mixed layer. These factors interact in a non-linear manner.

Exceptionally high iodide concentrations were observed at a small number of stations in the northern Indian Ocean. Such high concentrations are rare, but have been reported previously in low oxygen subsurface waters (Farrenkopf and Luther, 2002), and more recently, in surface waters above the Peruvian and Mexican oxygen deficient zones (Cutter et al., 2018; Moriyasu et al., 2020). In all cases, the excess iodide is suggested to be sedimentary in

origin, raising the possibility that processes at the sea floor could influence air-sea interactions, should that water reach the sea surface. Although such iodide "hot-spots" are unlikely to have significant impact on a global or regional scale, it is possible they may impact on local scale air-sea exchange processes involving iodine. Their existence also means care must be taken to ensure iodide concentrations used to generate parameterizations are representative of the entire study area.

Marine iodine cycling is anticipated to be affected by global change, with consequent impacts on atmospheric chemistry. The Indian Ocean basin is subject to a number of specific pressures with potential to affect iodine cycling. Despite the empirical relationship between SSI and SST, changes in vertical mixing as a result of the Indian Ocean warming may in fact reduce mixed layer iodide concentrations. Meanwhile, changes to biological processes as a result of anthropogenic nutrient inputs, ocean deoxygenation and changes in heat distribution are likely to impact iodide production and loss processes. Such changes will in turn impact ozone deposition and iodine emission from the sea surface.

DATA AVAILABILITY STATEMENT

Sea surface iodide concentration data described in this work is available from the British Oceanographic Data Centre, as part of a global compilation of observations doi: 10/czhx (Chance et al., 2019). Additional supporting datasets are available on request to the corresponding author.

AUTHOR CONTRIBUTIONS

LT, AS, AKS, and AM collected seawater samples during the three research cruises. LT and RoC analyzed the samples for iodine speciation. AS, AKS, and RR provided the supporting biogeochemical measurements. RaC and PS provided insight regarding physical oceanography in the study area. DS and MW performed the iodine modeling described in section "Concluding Remarks." RoC and LT interpreted the data and wrote the manuscript with input from TJ and MW, other authors also provided comments on the manuscript. LC, TJ, AM, and RoC conceived the study. All authors contributed to the article and approved the submitted version.

FUNDING

This work was funded by United Kingdom NERC grants NE/N009983/1 and NE/N01054X/1 awarded to RoC, LT, TJ, MW, DS, and LC. The research cruises were funded by the Ministry of Earth Sciences, India, and we thank the National Centre for Polar and Ocean Research for generously providing LT a berth on the SOE-09 expedition.

ACKNOWLEDGMENTS

We are grateful to the officers, crew and scientific parties onboard MV *SA Agulhas*, ORV *Sagar Kanya*, and RV *Sindhu Sadhana* for their essential support during the research cruises. We also thank Alex R. Baker (University of East Anglia) for loan of analytical equipment, and Matt Pickering (University of York) for help with ion chromatography analysis. The model simulations were undertaken on the High Performance Computing Cluster supported by the Research and Specialist Computing Support service at the University of East Anglia.

SUPPLEMENTARY MATERIAL

The Supplementary Material for this article can be found online at: https://www.frontiersin.org/articles/10.3389/fmars.2020.00621/full#supplementary-material

REFERENCES

Aksenov, Y., Bacon, S., Coward, A. C., and Nurser, A. J. G. (2010). The North Atlantic inflow to the Arctic Ocean: high-resolution model study. *J. Mar. Syst.* 79, 1–22. doi: 10.1016/j.jmarsys.2009.05.003

Allan, J. D., Williams, P. I., Najera, J., Whitehead, J. D., Flynn, M. J., Taylor, J. W., et al. (2015). Iodine observed in new particle formation events in the Arctic atmosphere during ACCACIA. *Atmos. Chem. Phys.* 15, 5599–5609. doi: 10.5194/acp-15-5599-2015

Alvain, S., Moulin, C., Dandonneau, Y., and Loisel, H. (2008). Seasonal distribution and succession of dominant phytoplankton groups in the global ocean: a satellite view. *Glob. Biogeochem. Cycles* 22:GB3001. doi: 10.1029/2007GB003154

Behrenfeld, M. J., and Falkowski, P. G. (1997). Photosynthetic rates derived from satellite-based chlorophyll concentration. *Limnol. Oceanogr.* 42, 1–20. doi: 10.4319/lo.1997.42.1.0001

Bluhm, K., Croot, P., Wuttig, K., and Lochte, K. (2010). Transformation of iodate to iodide in marine phytoplankton driven by cell senescence. *Aquat. Biol.* 11, 1–15. doi: 10.3354/ab00284

Bluhm, K., Croot, P. L., Huhn, O., Rohardt, G., and Lochte, K. (2011). Distribution of iodide and iodate in the Atlantic sector of the southern ocean during austral summer. *Deep Sea Res. Part II Top. Stud. Oceanogr.* 58, 2733–2748. doi: 10.1016/j.dsr2.2011.02.002

Campos, M. L. A. M. (1997). New approach to evaluating dissolved iodine speciation in natural waters using cathodic stripping voltammetry and a storage study for preserving iodine species. *Mar. Chem.* 57, 107–117. doi: 10.1016/s0304-4203(96)00093-x

Campos, M. L. A. M., Farrenkopf, A. M., Jickells, T. D., and Luther, G. W. (1996). A comparison of dissolved iodine cycling at the Bermuda Atlantic Time-Series station and Hawaii Ocean Time-Series Station. *Deep Sea Res. Part II Top. Stud. Oceanogr.* 43, 455–466. doi: 10.1016/0967-0645(95)00100-x

Campos, M. L. A. M., Sanders, R., and Jickells, T. (1999). The dissolved iodate and iodide distribution in the South Atlantic from the Weddell Sea to Brazil. *Mar. Chem.* 65, 167–175. doi: 10.1016/s0304-4203(98)00094-2

Carpenter, L. J., MacDonald, S. M., Shaw, M. D., Kumar, R., Saunders, R. W., Parthipan, R., et al. (2013). Atmospheric iodine levels influenced by sea surface emissions of inorganic iodine. *Nat. Geosci.* 6, 108–111. doi: 10.1038/ngeo1687

Chance, R., Baker, A. R., Carpenter, L., and Jickells, T. D. (2014). The distribution of iodide at the sea surface. *Environ. Sci. Process. Impacts* 16, 1841–1859. doi: 10.1039/c4em00139g

Chance, R., Weston, K., Baker, A. R., Hughes, C., Malin, G., Carpenter, L., et al. (2010). Seasonal and interannual variation of dissolved iodine speciation at a coastal Antarctic site. *Mar. Chem.* 118, 171–181. doi: 10.1016/j.marchem.2009.11.009

Chance, R. J., Tinel, L., Sherwen, T., Baker, A. R., Bell, T., Brindle, J., et al. (2019). Global sea-surface iodide observations, 1967-2018. *Sci. Data* 6:286.

Cuevas, C. A., Maffezzoli, N., Corella, J. P., Spolaor, A., Vallelonga, P., Kjaer, H. A., et al. (2018). Rapid increase in atmospheric iodine levels in the North Atlantic since the mid-20th century. *Nat. Commun.* 9:1452.

Cutter, G. A., Moffett, J. G., Nielsdottir, M. C., and Sanial, V. (2018). Multiple oxidation state trace elements in suboxic waters off Peru: *in situ* redox processes and advective/diffusive horizontal transport. *Mar. Chem.* 201, 77–89. doi: 10.1016/j.marchem.2018.01.003

Ducklow, H. W., Stukel, M. R., Eveleth, R., Doney, S. C., Jickells, T., Schofield, O., et al. (2018). Spring-summer net community production, new production, particle export and related water column biogeochemical processes in the marginal sea ice zone of the Western Antarctic Peninsula 2012-2014. *Philos. Trans. A Math. Phys. Eng. Sci.* 376:20170177. doi: 10.1098/rsta.2017.0177

Edwards, A., and Truesdale, V. W. (1997). Regeneration of inorganic iodine species in Loch Etive, a natural leaky incubator. *Estuar. Coast. Shelf Sci.* 45, 357–366. doi: 10.1006/ecss.1996.0185

Elderfield, H., and Truesdale, V. W. (1980). On the biophilic nature of iodine in seawater. *Earth Planet. Sci. Lett.* 50, 105–114. doi: 10.1016/0012-821x(80)90122-3

Farrenkopf, A. M., and Luther, G. W. (2002). Iodine chemistry reflects productivity and denitrification in the Arabian Sea: evidence for flux of dissolved species from sediments of western India into the OMZ. *Deep Sea Res. Part II Top. Stud. Oceanogr.* 49, 2303–2318. doi: 10.1016/s0967-0645(02)00038-3

Farrenkopf, A. M., Luther, G. W., Truesdale, V. W., and Van Der Weijden, C. H. (1997). Sub-surface iodide maxima: evidence for biologically catalyzed redox cycling in Arabian Sea OMZ during the SW intermonsoon. *Deep Sea Res. Part II Top. Stud. Oceanogr.* 44, 1391–1409. doi: 10.1016/s0967-0645(97)00013-1

Ganzeveld, L., Helmig, D., Fairall, C. W., Hare, J., and Pozzer, A. (2009). Atmosphere-ocean ozone exchange: a global modeling study of biogeochemical, atmospheric, and waterside turbulence dependencies. *Glob. Biogeochem. Cycles* 23:GB4021.

Ghose, N. C., Das, K., and Saha, D. (2003). Distribution of iodine in soil-water system in the Gandak basin, Bihar. *J. Geol. Soc. India* 62, 91–98.

Gilfedder, B. S., Petri, M., and Biester, H. (2007). Iodine speciation in rain and snow: Implications for the atmospheric iodine sink. *J. Geophys. Res. Atmos.* 112:D07301.

Grand, M. M., Measures, C. I., Hatta, M., Hiscock, W. T., Landing, W. M., Morton, P. L., et al. (2015). Dissolved Fe and Al in the upper 1000m of the eastern Indian Ocean: a high-resolution transect along 95°E from the Antarctic margin to the Bay of Bengal. *Glob. Biogeochem. Cycles* 29, 375–396. doi: 10.1002/2014gb004920

Hardacre, C., Wild, O., and Emberson, L. (2015). An evaluation of ozone dry deposition in global scale chemistry climate models. *Atmos. Chem. Phys.* 15, 6419–6436. doi: 10.5194/acp-15-6419-2015

Hardisty, D. S., Horner, T. J., Wankel, S. D., Blusztajn, J., and Nielsen, S. G. (2020). Experimental observations of marine iodide oxidation using a novel sparge-interface MC-ICP-MS technique. *Chem. Geol.* 532:119360. doi: 10.1016/j.chemgeo.2019.119360

Hou, X., Aldahan, A., Nielsen, S. P., Possnert, G., Nies, H., and Hedfors, J. (2007). Speciation of I-129 and I-127 in seawater and implications for sources and transport pathways in the North Sea. *Environ. Sci. Technol.* 41, 5993–5999. doi: 10.1021/es070575x

Jickells, T. D., Boyd, S. S., and Knap, A. H. (1988). Iodine cycling in the Sargasso Sea and the Bermuda Inshore waters. *Mar. Chem.* 24, 61–82. doi: 10.1016/0304-4203(88)90006-0

Johannessen, T., and Dahl, E. (1996). Declines in oxygen concentrations along the Norwegian Skagerrak coast, 1927-1993: a signal of ecosystem changes due to eutrophication? *Limnol. Oceanogr.* 41, 766–778. doi: 10.4319/lo.1996.41.4.0766

Locarnini, R. A., Mishonov, A. V., Antonov, J. I., Boyer, T. P., Garcia, H. E., Baranova, O. K., et al. (2013). *World Ocean Atlas 2013, Volume 1: Temperature*, eds S. Levitus, A. Mishonov. Silver Spring: NOAA Atlas NESDIS 73, 40.

Longhurst, A. R. (1998). *Ecological Geography of the Sea*. San Diego, CA: Academic Press.

Lu, W., Ridgwell, A., Thomas, E., Hardisty, D. S., Luo, G., Algeo, T. J., et al. (2018). Late inception of a resiliently oxygenated upper ocean. *Science* 361, 174–177.

Luther, G. W., Swartz, C. B., and Ullman, W. J. (1988). Direct determination of iodide in seawater by cathodic stripping square-wave voltammetry. *Anal. Chem.* 60, 1721–1724. doi: 10.1021/ac00168a017

MacDonald, S. M., Gómez Martín, J. C., Chance, R., Warriner, S., Saiz-Lopez, A., Carpenter, L. J., et al. (2014). A laboratory characterisation of inorganic iodine emissions from the sea surface: dependence on oceanic variables and parameterisation for global modelling. *Atmos. Chem. Phys.* 14, 5841–5852. doi: 10.5194/acp-14-5841-2014

Mahajan, A. S., Tinel, L., Hulswar, S., Cuevas, C. A., Wang, S., Ghude, S., et al. (2019). Observations of iodine oxide in the Indian Ocean marine boundary layer: a transect from the tropics to the high latitudes. *Atmos. Environ. X* 1:100016. doi: 10.1016/j.aeaoa.2019.100016

McFiggans, G., Coe, H., Burgess, R., Allan, J., Cubison, M., Alfarra, M. R., et al. (2004). Direct evidence for coastal iodine particles from Laminaria macroalgae - linkage to emissions of molecular iodine. *Atmos. Chem. Phys.* 4, 701–713. doi: 10.5194/acp-4-701-2004

Moran, J. E., Oktay, S. D., and Santschi, P. H. (2002). Sources of iodine and iodine 129 in rivers. *Water Resour. Res.* 38, 24-1–24-10.

Moriyasu, R., Evans, Z. C., Bolster, K. M., Hardisty, D. S., and Moffett, J. W. (2020). The distribution and redox speciation of iodine in the Eastern Tropical North Pacific Ocean. *Glob. Biogeochem. Cycles* 34:e2019GB006302.

Nakayama, E., Kimoto, T., Isshiki, K., Sohrin, Y., and Okazaki, S. (1989). Determination and distribution of iodide-iodine and total-iodine in the North Pacific Ocean by using a new automated electrochemical method. *Mar. Chem.* 27, 105–116. doi: 10.1016/0304-4203(89)90030-3

Naqvi, S. W. A., Jayakumar, D. A., Narvekar, P. V., Naik, H., Sarma, V. V. S. S., D'Souza, W., et al. (2000). Increased marine production of N2O due to intensifying anoxia on the Indian continental shelf. *Nature* 408, 346–349. doi: 10.1038/35042551

Nieves, V., Willis, J. K., and Patzert, W. C. (2015). Recent hiatus caused by decadal shift in indo-pacific heating. *Science* 349, 532–535. doi: 10.1126/science.aaa4521

Orsi, A. H., Whitworth, T., and Nowlin, W. D. (1995). On the meridional extent and fronts of the Antarctic Circumpolar Current. *Deep Sea Res. Part I Oceanogr. Res. Pap.* 42, 641–673. doi: 10.1016/0967-0637(95)00021-w

Prados-Roman, C., Cuevas, C. A., Hay, T., Fernandez, R. P., Mahajan, A. S., Royer, S. J., et al. (2015). Iodine oxide in the global marine boundary layer. *Atmos. Chem. Phys.* 15, 583–593. doi: 10.5194/acp-15-583-2015

Price, N. B., and Calvert, S. E. (1977). Contrasting geochemical behaviors of iodine and bromine in recent sediments from the Namibian shelf. *Geochim. Cosmochim. Acta* 41, 1769–1775. doi: 10.1016/0016-7037(77)90209-5

Rue, E. L., Smith, G. J., Cutter, G. A., and Bruland, K. W. (1997). The response of trace element redox couples to suboxic conditions in the water column. *Deep Sea Res. Part I Oceanogr. Res. Pap.* 44, 113–134. doi: 10.1016/s0967-0637(96)00088-x

Sadasivan, S., and Anand, S. J. S. (1979). Chlorine, bromine and iodine in monsoon rains in India. *Tellus* 31, 290–294. doi: 10.1111/j.2153-3490.1979.tb00907.x

Sarwar, G., Kang, D. W., Foley, K., Schwede, D., Gantt, B., and Mathur, R. (2016). Technical note: examining ozone deposition over seawater. *Atmos. Environ.* 141, 255–262. doi: 10.1016/j.atmosenv.2016.06.072

Schlitzer, R. (2014). *Ocean Data View*. Available online at: http://odv.awi.de (accessed January 21, 2017).

Schwehr, K. A., and Santschi, P. H. (2003). Sensitive determination of iodine species, including organo-iodine, for freshwater and seawater samples using high performance liquid chromatography and spectrophotometric detection. *Anal. Chim. Acta* 482, 59–71. doi: 10.1016/s0003-2670(03)00197-1

Sherwen, T., Chance, R. J., Tinel, L., Ellis, D., Evans, M. J., and Carpenter, L. J. (2019). A machine-learning-based global sea-surface iodide distribution. *Earth Syst. Sci. Data* 11, 1239–1262. doi: 10.5194/essd-11-1239-2019

Sherwen, T., Evans, M. J., Sommariva, R., Hollis, L. D. J., Ball, S. M., Monks, P. S., et al. (2017). Effects of halogens on European air-quality. *Faraday Discuss.* 200, 75–100. doi: 10.1039/c7fd00026j

Truesdale, V. W. (1978). Iodine in inshore and off-shore marine waters. *Mar. Chem.* 6, 1–13. doi: 10.1016/0304-4203(78)90002-6

Truesdale, V. W., Bale, A. J., and Woodward, E. M. S. (2000). The meridional distribution of dissolved iodine in near-surface waters of the Atlantic Ocean. *Prog. Oceanogr.* 45, 387–400. doi: 10.1016/s0079-6611(00)00009-4

Truesdale, V. W., Danielssen, D. S., and Waite, T. J. (2003). Summer and winter distributions of dissolved iodine in the Skagerrak. *Estuar. Coast. Shelf Sci.* 57, 701–713. doi: 10.1016/s0272-7714(02)00412-2

Truesdale, V. W., and Spencer, C. P. (1974). Studies on the determination of inorganic iodine in seawater. *Mar. Chem.* 2, 33–47. doi: 10.1016/0304-4203(74)90004-8

Tsunogai, S. (1971). Iodine in the deep water of the ocean. *Deep Sea Res. Oceanogr. Abstr.* 18, 913–919. doi: 10.1016/0011-7471(71)90065-9

Tsunogai, S., and Henmi, T. (1971). Iodine in the surface water of the Pacific Ocean. *J. Oceanogr. Soc. Jpn.* 27, 67–72.

Vinayachandran, P. N., Matthews, A. J., Kumar, K. V., Sanchez-Franks, A., Thushara, V., George, J., et al. (2018). BoBBLE: ocean–Atmosphere interaction and its impact on the South Asian Monsoon. *Bull. Am. Meteorol. Soc.* 99, 1569–1587. doi: 10.1175/bams-d-16-0230.1

Wadley, M. R., Stevens, D. P., Jickells, T. D., Hughes, C., Baker, A. R., Chance, R. J., et al. (2020). A global model for iodine speciation in the upper ocean. *Glob. Biogeochem. Cycles* 34:e2019GB006467. doi: 10.1029/2019GB006467

Waite, T. J., Truesdale, V. W., and Olafsson, J. (2006). The distribution of dissolved inorganic iodine in the seas around Iceland. *Mar. Chem.* 101, 54–67. doi: 10.1016/j.marchem.2006.01.003

Wang, F., Saiz-Lopez, A., Mahajan, A. S., Gómez Martín, J. C., Armstrong, D., Lemes, M., et al. (2014). Enhanced production of oxidised mercury over the tropical Pacific Ocean: a key missing oxidation pathway. *Atmos. Chem. Phys.* 14, 1323–1335. doi: 10.5194/acp-14-1323-2014

Wong, G. T. F. (2001). Coupling iodine speciation to primary, regenerated or "new" production: a re-evaluation. *Deep Sea Res. Part I Oceanogr. Res. Pap.* 48, 1459–1476. doi: 10.1016/s0967-0637(00)00097-2

Wong, G. T. F., and Brewer, P. G. (1977). Marine chemistry of iodine in anoxic basins. *Geochim. Cosmochim. Acta* 41, 151–159. doi: 10.1016/0016-7037(77)90195-8

Wong, G. T. F., Brewer, P. G., and Spencer, D. W. (1976). Distribution of particulate iodine in the Atlantic Ocean. *Earth Planet. Sci. Lett.* 32, 441–450. doi: 10.1016/0012-821x(76)90084-4

Wong, G. T. F., and Cheng, X. H. (1998). Dissolved organic iodine in marine waters: Determination, occurrence and analytical implications. *Mar. Chem.* 59, 271–281. doi: 10.1016/s0304-4203(97)00078-9

Wong, G. T. F., and Zhang, L. S. (2003). Geochemical dynamics of iodine in marginal seas: the southern East China Sea. *Deep Sea Res. Part II Top. Stud. Oceanogr.* 50, 1147–1162. doi: 10.1016/s0967-0645(03)00015-8

Zic, V., Caric, M., and Ciglenecki, I. (2013). The impact of natural water column mixing on iodine and nutrient speciation in a eutrophic anchialine pond (Rogoznica Lake, Croatia). *Estuar. Coast. Shelf Sci.* 133, 260–272. doi: 10.1016/j.ecss.2013.09.008

Conflict of Interest: The authors declare that the research was conducted in the absence of any commercial or financial relationships that could be construed as a potential conflict of interest.

Copyright © 2020 Chance, Tinel, Sarkar, Sinha, Mahajan, Chacko, Sabu, Roy, Jickells, Stevens, Wadley and Carpenter. This is an open-access article distributed under the terms of the Creative Commons Attribution License (CC BY). The use, distribution or reproduction in other forums is permitted, provided the original author(s) and the copyright owner(s) are credited and that the original publication in this journal is cited, in accordance with accepted academic practice. No use, distribution or reproduction is permitted which does not comply with these terms.

frontiers in Marine Science

ORIGINAL RESEARCH
published: 09 December 2021
doi: 10.3389/fmars.2021.788105

Soluble Iodine Speciation in Marine Aerosols Across the Indian and Pacific Ocean Basins

Elise S. Droste[1], Alex R. Baker[1], Chan Yodle[1†], Andrew Smith[1] and Laurens Ganzeveld[2]*

[1] Centre for Ocean and Atmospheric Sciences, School of Environmental Sciences, University of East Anglia, Norwich, United Kingdom, [2] Meteorology and Air Quality Section, Wageningen University, Wageningen, Netherlands

OPEN ACCESS

Edited by:
Anoop Sharad Mahajan, Indian Institute of Tropical Meteorology (IITM), India

Reviewed by:
Andrea Spolaor, National Research Council, Consiglio Nazionale delle Ricerche (CNR), Italy
Manuel Dall'Osto, Institute of Marine Sciences, Spanish National Research Council (CSIC), Spain

***Correspondence:**
Elise S. Droste
e.droste@uea.ac.uk

†Present address:
Chan Yodle, Department of Environmental Science, Faculty of Science and Technology, Chiang Mai Rajabhat University, Chiang Mai, Thailand

Specialty section:
This article was submitted to Marine Biogeochemistry, a section of the journal Frontiers in Marine Science

Received: *01 October 2021*
Accepted: *17 November 2021*
Published: *09 December 2021*

Citation:
Droste ES, Baker AR, Yodle C, Smith A and Ganzeveld L (2021) Soluble Iodine Speciation in Marine Aerosols Across the Indian and Pacific Ocean Basins. Front. Mar. Sci. 8:788105. doi: 10.3389/fmars.2021.788105

Iodine affects the radiative budget and the oxidative capacity of the atmosphere and is consequently involved in important climate feedbacks. A fraction of the iodine emitted by oceans ends up in aerosols, where complex halogen chemistry regulates the recycling of iodine to the gas-phase where it effectively destroys ozone. The iodine speciation and major ion composition of aerosol samples collected during four cruises in the East and West Pacific and Indian Oceans was studied to understand the influences on iodine's gas-aerosol phase recycling. A significant inverse relationship exists between iodide (I^-) and iodate (IO_3^-) proportions in both fine and coarse mode aerosols, with a relatively constant soluble organic iodine (SOI) fraction of 19.8% (median) for fine and coarse mode samples of all cruises combined. Consistent with previous work on the Atlantic Ocean, this work further provides observational support that IO_3^- reduction is attributed to aerosol acidity, which is associated to smaller aerosol particles and air masses that have been influenced by anthropogenic emissions. Significant correlations are found between SOI and I^-, which supports hypotheses that SOI may be a source for I^-. This data contributes to a growing observational dataset on aerosol iodine speciation and provides evidence for relatively constant proportions of iodine species in unpolluted marine aerosols. Future development in our understanding of iodine speciation depends on aerosol pH measurements and unravelling the complex composition of SOI in aerosols.

Keywords: iodine speciation, marine aerosols, Indian Ocean, Pacific Ocean, marine boundary layer (MBL)

INTRODUCTION

Iodine is ubiquitous in the troposphere where it plays an active role in atmospheric chemistry and important climate feedbacks (Prados-Roman et al., 2015a). Its volatile compounds contribute to aerosol particle formation mechanisms that affect the atmospheric radiative budget (O'Dowd et al., 2002; Read et al., 2008). It has furthermore been recognised to alter the oxidative capacity of the atmosphere by significantly destroying ozone (a pollutant) in the lower troposphere (Chameides and Davis, 1980; Chatfield and Crutzen, 1990; Davis et al., 1996; Mahajan et al., 2010). Biologically, iodine is a crucial element for mammalian metabolism (Whitehead, 1984), entering the food chain through atmospheric deposition on soil and crops.

The dominant source of iodine in the atmosphere is the surface ocean through biotic and abiotic processes (Mahajan et al., 2012). Volatile iodine compounds are released mostly in inorganic form, such as molecular iodine (I_2) and hypoiodous acid (HOI) (Carpenter et al., 2013; Prados-Roman et al., 2015b), but also as organic iodocarbons, such as CH_3I and CH_2I_2 (Klick and Abrahamsson, 1992; Moore and Tokarczyk, 1992; Schall et al., 1997; Martino et al., 2009; Jones et al., 2010). Rapid photolysis in the atmosphere releases the iodine atoms from these compounds, which subsequently participate in efficient ozone destruction cycles (Saiz-Lopez et al., 2012a,b).

Aerosols take up iodine, temporarily inhibiting its role in ozone destruction before recycling it back to the gas-phase. Aerosol composition, chemistry, and iodine speciation regulate the efficiency of iodine recycling and thus also the effect on ozone concentrations in the marine boundary layer (MBL) (Vogt et al., 1999; McFiggans et al., 2000; Hoffmann et al., 2001), and transport to continents where it may be deposited (Baker et al., 2001). Understanding aerosol iodine speciation in aerosols is therefore important to accurately reproduce ozone concentrations with atmospheric models, and to comprehend its effect on global radiation, climate, and feedbacks (Saiz-Lopez et al., 2012b).

Total soluble iodine (TSI) in aerosols in the MBL is characterised by geographical variability, being latitudinally and longitudinally dependent on global ocean temperature, seawater iodine content, and atmospheric ozone (Gómez Martín et al., 2021). TSI itself consists of iodide (I^-), iodate (IO_3^-), and soluble organic iodine (SOI). Other iodine species, such as HOI or I_2, are considered reactive or insoluble and therefore are not expected to be detectable in aerosols (Saiz-Lopez et al., 2012a).

Models have struggled to reproduce the variable iodine speciation, and thus also the MBL ozone levels, reported by observational studies (Gäbler and Heumann, 1993; Wimschneider and Heumann, 1995; Baker, 2004). Challenges in improving our understanding of the complex iodine chemistry in the MBL include sparsity of observational data and use of iodine speciation-altering extraction methods for samples (Xu S. Q. et al., 2010; Yodle and Baker, 2019).

We present aerosol iodine speciation data from three different major ocean basins: the West Pacific Ocean and, for the first time, the East Pacific Ocean and Indian Ocean. We investigate the consistency of the results with recent advancements in our understanding of aerosol iodine chemistry, including the role of SOI as a missing source for I^- (Baker, 2005; Pechtl et al., 2007) and possible explanations for the variability in the IO_3^- concentrations.

MATERIALS AND METHODS

Sample Collection

We present aerosol data obtained during four expeditions at sea between October 2009 and July 2017: TransBrom, SHIVA, OASIS, and M138 (**Figure 1** and **Table 1**). The aerosol speciation results for the SHIVA campaign have previously been published by Yodle and Baker (2019), for which data can be found here: Baker and Yodle (2018). Results for TransBrom (Baker and Yodle, 2021b), OASIS (Baker and Droste, 2021), and M138 (Baker, 2021) can be found in the PANGAEA® database.

Most aerosol samples were collected on stages 3 and 4 of Sierra-type cascade impactors, which together collected the aerosols > 1 μm, and a back-up non-slotted filter, which collected aerosols < 1 μm. SHIVA is the only campaign presented here for which aerosols were collected in bulk samples. Sample O10 collected during OASIS is the only sample for which all six stages of the cascade impactor were used. This allows us to analyse aerosol chemistry for seven different modal particle sizes in total (<0.1 to > 12 μm). Glass microfiber filters (GF) were used as aerosol collection substrates for all samples, except for the TransBrom samples, for which cellulose filters (CF) were used. GF substrates were washed twice with ultrapure (18.2 MΩ cm) water, dried, wrapped in aluminium foil and ashed at 450°C before use (Yodle and Baker, 2019). CF substrates were not treated before use. A wind sector controller linked an anemometer to the samplers and switched it off whenever the wind was coming from the direction of the ship's stacks to avoid contamination by the ship. Once collected, samples were wrapped in pre-combusted aluminium foil (GF substrates only), then frozen in separate sealed polyethylene bags until chemical analysis. More information on sample collection specifics can be found in **Table 1** and in the **Supplementary Material**.

Air Masses

Various air mass types sampled during the different campaigns were distinguished based on air mass back trajectories run for the duration of sample collection time with the Hybrid Single-Particle Lagrangian Integrated Trajectory (HYSPLIT) model from NOAA using NCEP/NCAR Reanalysis Project datasets (Stein et al., 2015). Back trajectories were run for 5 days prior to the sample collection time at 10, 500, and 1,000 m altitude to be able to consider the possibility of gravitational descent of particles from the free troposphere (longer range transport) into lower altitude MBL air masses.

Analytical Methodology

Ultrapure water was used to extract the aerosols from the filters. Samples were mechanically shaken on an orbital mixer for 30 min at room temperature and subsequently filtered (Minisart®, 0.20 μm), following the optimised extraction conditions described by Yodle and Baker (2019).

Ion chromatography (Dionex ICS-5000) was used to quantify the concentrations for Na^+, NH_4^+, Mg^{2+}, K^+, Ca^{2+}, Cl^-, NO_3^-, SO_4^{2-}, Br^-, $C_2O_4^{2-}$ (oxalate), and methanesulfonate (MSA). Cations and anions were analysed on CS12A and AS18 columns, respectively.

TSI, IO_3^-, and I^- content was determined following the methodology as described in Yodle and Baker (2019), using Inductively Coupled Plasma-Mass Spectrometry (ICP-MS, Thermo X-Series for TransBrom, SHIVA, and OASIS; iCAP TQ, Thermo Scientific for M138). TSI was measured directly with the ICP-MS, while I^- and IO_3^- were separated chromatographically using a Dionex AS16 exchange column. Blank values and detection limits are shown in **Table 2**.

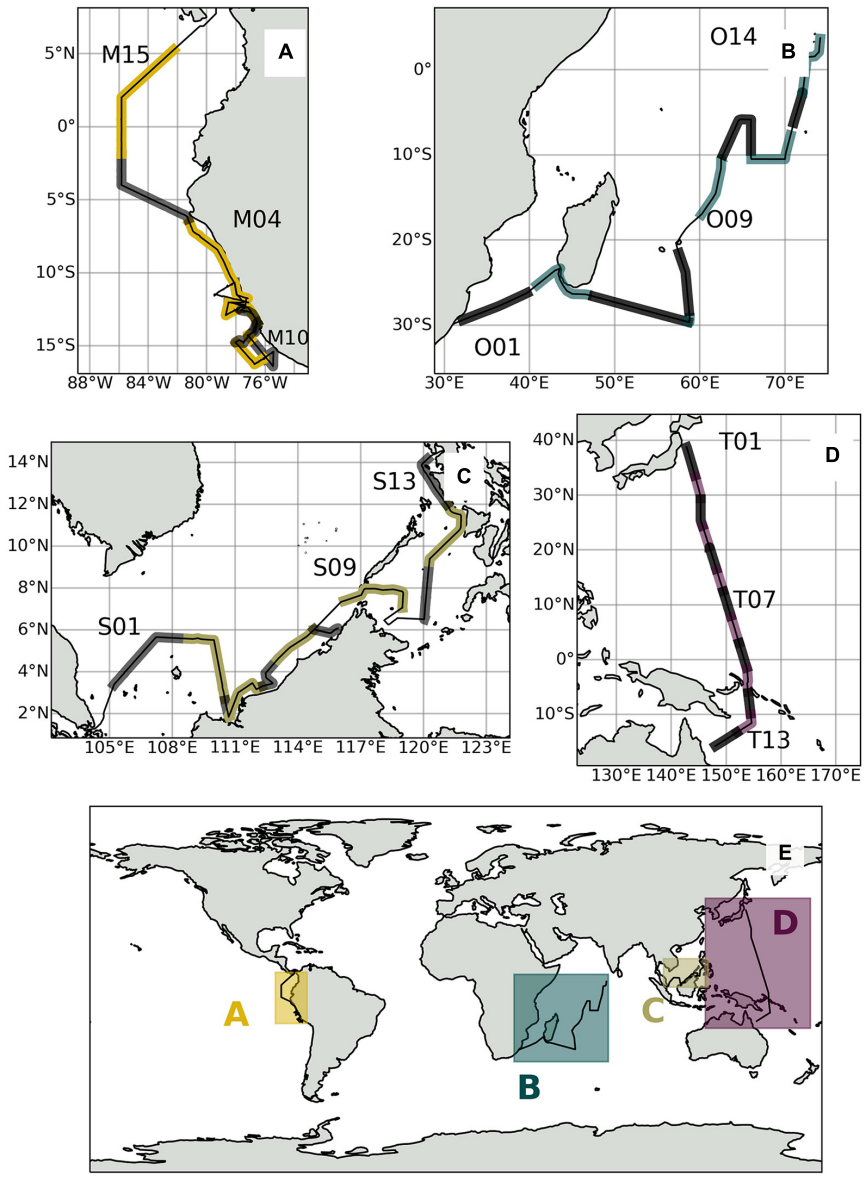

FIGURE 1 | (E) Global overview map of expedition tracks and sampling locations shown in alternating lighter and darker shades for **(A)** M138, **(B)** OASIS, **(C)** SHIVA, and **(D)** TransBrom.

TABLE 1 | Overview of sea-going expeditions presented in current work.

Expedition	Dates	Aerosol fractions collected	Aerosol Filters	Reference	Ship
TransBrom	09.10.2009–24.10.2009	Fine/coarse	Cellulose (Whatman 41)	Quack and Krüger, 2010; Martino et al., 2014	FS Sonne SO202
SHIVA	15.11.2011–29.11.2011	Bulk	Glass microfiber	Quack and Krüger, 2013	FS Sonne SO218
OASIS	08.07.2014–07.08.2014	Fine/coarse, 1 multi-size fractionated (O10)	Glass microfiber (Tisch filter TE-230-GF and Whatman Grade G653 GF)	Krüger et al., 2014a,b	FS Sonne SO234 1/2
M138	06.06.2017–01.07.2017	Fine/coarse	Glass microfiber (Tisch filter TE-230-GF and Whatman Grade G653 GF)	Bange et al., 2017	FS Meteor M138

TABLE 2 | Blank values (nmol/filter) and detection limits (pmol m^{-3}) for iodine species measured during each cruise.

Cruise		I^-		IO_3^-		TSI	
		<1 μm	>1 μm	<1 μm	>1 μm	<1 μm	>1 μm
TransBrom	Blank	0.19	0.16	< 0.21	<0.17	0.49	0.24
	Det. Limit [b]	0.18	0.30	0.15	0.12	0.50	0.21
SHIVA [a]	Blank	< 0.34	–	<0.35	–	1.2	–
	Det. Limit [b]	0.24	–	0.25	–	0.47	–
OASIS	Blank	0.23	0.19	< 0.18	<0.18	0.86	0.60
	Det. Limit [c]	0.13	0.07	0.07	0.07	0.29	0.21
M138	Blank	0.53	< 0.44	<0.72	< 0.72	<3.7	< 3.7
	Det. Limit [d]	0.50	0.21	0.34	0.34	1.8	1.8

[a] *Values given for SHIVA are for the single Whatman 41 filters used during that cruise.*
[b] *Detection limits representative of air volumes of 1,400 m^3.*
[c] *Detection limits representative of air volumes of 2,500 m^3.*
[d] *Detection limits representative of air volumes of 2,100 m^3.*

Following Baker (2005), SOI was determined based on the difference between TSI and the total inorganic iodine, i.e., I^- and IO_3^- (Eq. 1).

$$SOI = TSI - (I^- + IO_3^-) \quad (1)$$

The enrichment factor (EF) of TSI was calculated according to Eq. 2.

$$EF_{TSI} = \frac{[TSI]_{aerosol}/[Na^+]_{aerosol}}{[TSI]_{seawater}/[Na^+]_{seawater}} \quad (2)$$

The non-sea salt (nss) concentrations of various major ions are defined by the difference between what is measured in the aerosol and the concentration expected in the sea salt fraction (Eq. 3). The latter is based on the sodium content of the aerosol and the relevant ion's concentration in bulk seawater. Bulk seawater concentrations are taken from Stumm and Morgan (2012) for all ions except Br^- and iodine, which were taken from Wong (1991).

$$[nss - MI] = [MI]_{measured} - [Na^+]_{measured}\frac{[MI]_{seawater}}{[Na^+]_{seawater}} \quad (MI = major\ ion) \quad (3)$$

RESULTS

Air Mass Types

Table 3 gives an overview of the ten different air mass types that have been distinguished based on the air mass back trajectories run for each sample, and the abbreviations used below to identify these air mass types. Examples of air mass back trajectories representative of the air mass types are shown in **Figure 2**. Further details of the air mass classification process are given in section 1 of the **Supplementary Material**. We use these ten air mass classifications to better understand the aerosol composition and iodine speciation results in this dataset.

Major Ions Composition in Aerosols

The chemical composition of aerosols drives aqueous and heterogeneous reactions that are important to the iodine chemistry and speciation. Coarse mode aerosols (>1 μm) in the datasets presented here are dominated by sea salt aerosols, formed through primary aerosol production mechanisms, such as sea spray and bubble bursting (Smith et al., 1993). The nss-Ca^{2+} concentrations in the samples reported here were extremely low, i.e., 1–2 orders of magnitude lower than reported for aerosols containing Saharan dust over the Atlantic Ocean (Baker and Yodle, 2021a). Mineral dust therefore appears to be a minor component of the TransBrom, SHIVA, OASIS, and M138 aerosols. Secondary aerosol production mechanisms, such as the oxidation and subsequent condensation of gases, are often associated with fine mode aerosol particles (<1 μm; Blanchard and Woodcock, 1980). Ions such as nss-SO_4^{2-}, oxalate, and MSA are indeed predominantly found in the fine mode aerosol samples (**Figure 3**). NO_3^- has its highest concentrations in the coarse mode fractions, which is a result of nitric acid displacing Cl^- within sea salt aerosols (Robbins et al., 1959; Mamane and Gottlieb, 1992; Andreae and Crutzen, 1997).

Notable variability in major ion concentrations indicate the influence of different natural and anthropogenic emissions in the sampled air masses. Nss-SO_4^{2-}, NO_3^-, and oxalate are associated with fossil fuel and biomass combustion emissions. The concentrations of these ions in the aerosol samples are elevated in samples collected from air masses which have travelled over land at some point in the 5 days prior to sampling (types NEA, SCS, NCP, PER, and EPP). Similarly, NH_4^+, a tracer for agricultural emissions, has elevated concentrations in NEA, PER, and EPP air masses. For the SCS and NCP aerosols, NH_4^+ concentrations are relatively low, suggesting that these samples are primarily affected by fossil fuel combustion (Yodle and Baker, 2019). Nss-SO_4^{2-} and oxalate concentrations for SWP samples, as well as some for SEP samples, are also relatively high. Relatively high MSA concentrations in maritime southern hemisphere air masses (SWP and SEP) are indicative of a marine biogenic source of dimethyl sulfide, which likely also contributes to the nss-SO_4^{2-} observed in these air masses. The organic (oxalate) content of the

TABLE 3 | Description of air mass types for all expeditions.

Air mass type	Expedition	No. of samples	Sample IDs	Description
Northeast Asia (NEA)	TransBrom	3	T01-T03	Air masses have travelled over northern Japan and occasionally over northern China and Siberia with occasional wind directions from the north Pacific Ocean.
North West Pacific (NWP)	TransBrom	6	T04-T09	Air masses have travelled over the North West Pacific Ocean.
South West Pacific (SWP)	TransBrom	4	T10-T13	Air masses travelled over the South West Pacific Ocean east of Australia, occasionally with origins near Tasmania.
South China Sea (SCS)	SHIVA	5	S01-S05	Air masses travelled over South China Sea, or Sumatra, Borneo, and along the coast of Sarawak (Yodle and Baker, 2019)
North Central Pacific (NCP)	SHIVA	6	S06-S14	Air mass travelled over western Central Pacific Ocean and the Philippines (Yodle and Baker, 2019)
Remote Southern Ocean (RSO)	OASIS	5	O01-O05	Air masses travelled from the Southern Ocean, passing the southern tip of South Africa.
Remote Southern Indian (RSI)	OASIS	5	O09-O11, O13, O14	Air masses travelled over the southern Indian Ocean, predominantly from a westerly direction.
Southeast Pacific (SEP)	M138	6	M05, M09-M11, M14, M15	Air masses travelled over the southeast Pacific Ocean.
Peru (PER)	M138	2	M07, M13	Air masses travelled over Peru prior to sampling.
Mixed SEP/PER (EPP)	M138	4	M04, M06, M08, M12	Air masses sampled partly come from the southeast Pacific Ocean and partly from over Peru.

PER and EPP air masses may carry additional strong influences of the biologically productive Peruvian coastline, known to be an upwelling region (Kamykowski and Zentara, 1990; Ulloa and Pantoja, 2009), in addition to terrestrial anthropogenic and biogenic organic matter emissions. RSO, RSI, and NWP aerosols share a similar major ion profile. Their low concentrations of nss-SO_4^{2-}, NO_3^-, and oxalate suggest minor influence from land-based anthropogenic activities, which is consistent with their prevalent trajectories over open remote oceans. In this sense, these air masses are considered to be relatively "clean."

Iodine Concentration and Speciation

Gas-to-particle conversion processes are the dominant source of iodine in marine aerosols (Saiz-Lopez et al., 2012a), as is quantified by the enrichment factor (EF). The EF_{TSI} values for samples reported here range between 9 and 12,800 (**Tables 4**, **5**). Highest TSI concentrations are found for the East Pacific Ocean aerosol samples (**Figure 4** and **Supplementary Figure 5**), with medians ranging between 30.6 and 39.8 pmol m^{-3} (SEP, PER, and EPP types, fine and coarse modes combined; **Supplementary Table 2**). Their median EF_{TSI} values range between 360 and 640 (**Supplementary Table 2**).

The proportions of IO_3^-, I^-, and SOI are variable within and between air mass types. Conspicuous among all samples are the low or undetectable IO_3^- concentrations for many of the TransBrom aerosols (West Pacific Ocean). Exceptions are the coarse mode samples T06 and T11-T13 (the three southernmost samples), which have IO_3^- concentrations > 9.7 pmol m^{-3} (**Figure 4**). I^- and SOI are the dominant species in NEA and NWP samples, both accounting for around 50% of TSI. The coarse mode of samples T11-T13 are the only three TransBrom samples for which IO_3^- is the dominant species.

The bulk aerosols collected from the SCS and NCP air masses (SHIVA, West Pacific Ocean) have variable iodine species proportions where IO_3^- holds the highest fraction in eight of the 11 samples (Yodle and Baker, 2019). I^- concentrations are relatively constant along the SHIVA track at an average of 4.0 ± 1.1 pmol m^{-3}, although the SCS air masses seems to hold slightly less I^- compared to NCP air masses (Yodle and Baker, 2019). IO_3^- concentrations vary between 1.4 and 9.8 pmol m^{-3} and are not very different between the two air mass types.

Both the fine and coarse modes of the RSO and RSI aerosol samples (OASIS, Indian Ocean) have substantial amounts of IO_3^- (median of 4.1/5.3 pmol m^{-3} in fine/coarse mode of RSO and 2.7/7.8 in fine/coarse mode of RSI). IO_3^- is proportionally the dominant species in the coarse mode and most of the fine mode samples. The I^- concentrations in the fine mode of RSO aerosols are slightly higher (median 3.6 pmol m^{-3}) than their coarse mode counterparts, as well as compared to the fine and coarse modes of the RSI samples (medians ranging between 1.4–1.9 pmol m^{-3}; **Supplementary Table 2**).

Similarly to RSO and RSI, IO_3^- dominates the iodine speciation in the SEP air mass (**Figure 4** and **Supplementary Figure 5**), although the TSI concentration for SEP is substantially higher in the coarse mode (median 27.4 pmol m^{-3}) than in RSO and RSI (median 7.8 and 10.1 pmol m^{-3}, respectively; **Supplementary Table 2**). In contrast, I^- dominates the speciation for PER in both modes. EPP samples are those that are influenced by air masses of both marine and terrestrial origin, as indicated by their intermediate iodine speciation and species proportions, relative to SEP and PER (**Figure 5**).

Except for bulk aerosol samples S12 and S13 from NCP and coarse mode aerosols T06 and T09 from NWP, SOI is found in all samples: up to 4.7 pmol m^{-3} in the fine mode and 10.1 pmol m^{-3} in the coarse mode. Consistent with previous observations in the Atlantic Ocean (Baker, 2005; Baker and Yodle, 2021a), the SOI fraction in the fine mode samples is generally larger (median 29%) than in the coarse mode samples (median 19%). In many of the TransBrom samples, SOI has higher proportions than both I^- and IO_3^-, which has occasionally previously been observed in

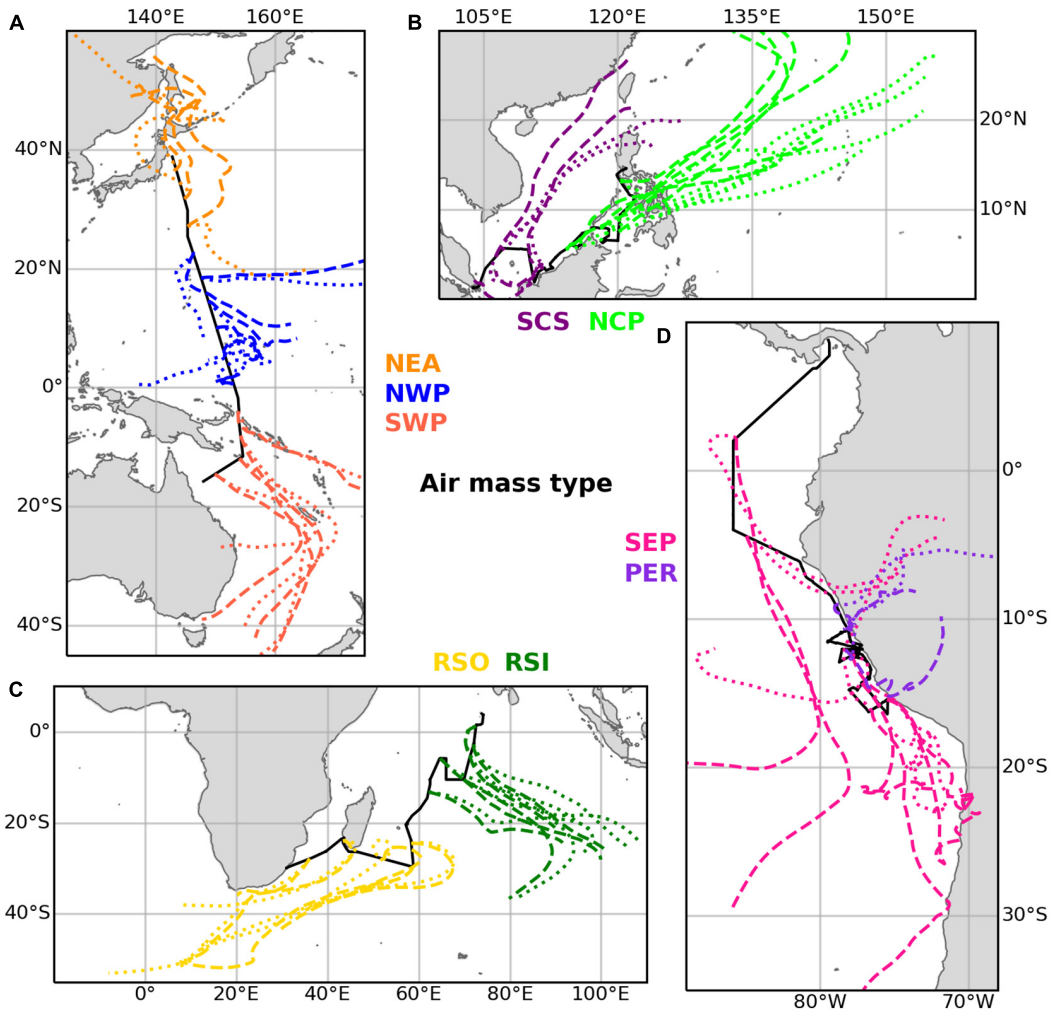

FIGURE 2 | Examples illustrating the trajectories of the main air mass types found in the datasets for **(A)** TransBrom, **(B)** SHIVA, **(C)** OASIS, and **(D)** M138. Dashed lines show trajectories for arrival heights of 10 m above the ships' positions. Dotted lines are for arrivals at 1,000 m. Examples of type EPP (M138) are not shown, as this classification was a mixture of the SEP and PER types.

coastal regions (Gilfedder et al., 2008) and in the southwestern Pacific Ocean (Lai et al., 2008).

The multi-size fractionated sample from OASIS (O10) has lowest TSI concentrations in modal size fractions 0.4 and >12 μm (**Figure 6**). SOI is found only in modal size fractions with sizes close to 1 or <0.1 μm. Among these, its concentration ranges between 0.49 and 0.60 pmol m^{-3}. The I^- to IO_3^- ratio is > 1 in the two smallest modal size fractions and <1 for larger aerosol particles. The distributions of Na^+, nss-SO_4^{2-}, and NO_3^- in sample O10 are shown in **Supplementary Figure 4**.

DISCUSSION

Influences on Iodine Concentration and Speciation

Table 6 shows the bulk/total TSI concentrations and EF_{TSI} values for the TransBrom, SHIVA, OASIS and M138 cruises, together with values reported for marine aerosols from other studies. Of the cruises reported here, TSI concentrations were highest in the M138 aerosols (particularly in the SEP samples collected off the coast of Peru; **Figure 4**). This may be due to stronger marine iodine sources in the eastern South Pacific. The median seawater I^- concentration in this region (396 nM) is over four times higher than the global median (89.0 nM; Chance et al., 2019a,b; **Supplementary Figure 7**). These high surface sea water I^- concentrations are probably sustained by a regional upwelling system which supplies both high I^- waters [due to reduction of IO_3^- in the sub-surface oxygen minimum zone associated with the upwelling (Cutter et al., 2018)] and nutrient-rich waters to the surface (Ulloa and Pantoja, 2009). Enhanced phytoplankton growth driven by this nutrient supply may also lead to further reduction of IO_3^- to I^- in surface waters (Bluhm et al., 2010). The unusually high surface I^- concentrations presumably enhance the flux of volatile iodine gases to the

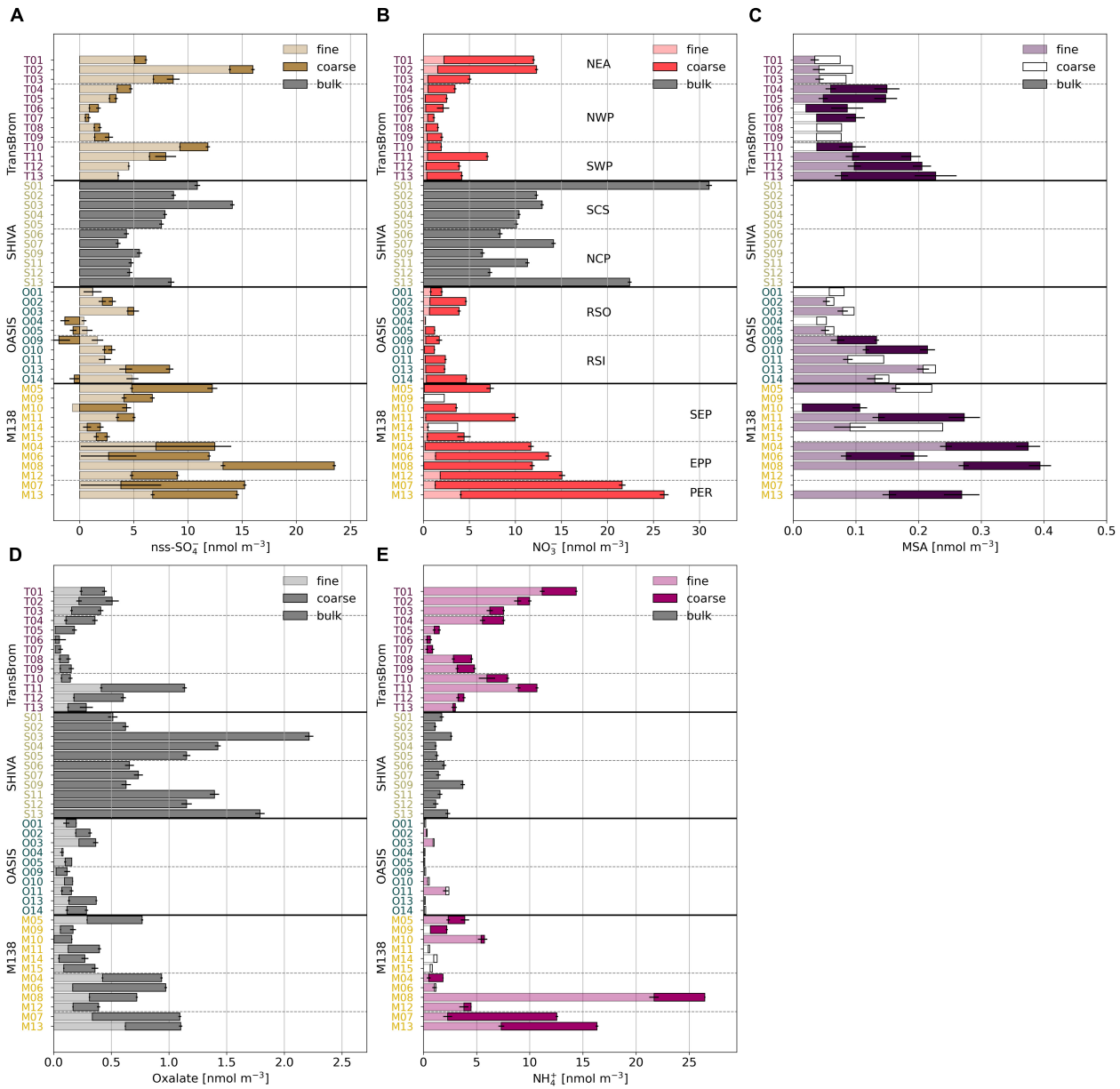

FIGURE 3 | Bar plots of **(A)** nss-SO_4^{2-}, **(B)** NO_3^-, **(C)** MSA, **(D)** oxalate, and **(E)** NH_4^+ in fine (light), coarse (dark), and bulk (grey) mode aerosol fractions for all samples of TransBrom (T01-T13), SHIVA (S01-S13), OASIS (O01-O14), and M138 (M04-M15). MSA was not measured in the SHIVA samples. Empty bars indicate concentrations below the detection limit. Nss-concentrations for which the error is larger than the parameter itself are omitted. Note that for M138 the sample order has been changed to allow the SEP, EPP, and PER air masses to be grouped together.

atmosphere following dry deposition of ozone (Ganzeveld et al., 2009) and subsequent reaction of I^- with ozone (Carpenter et al., 2013). Samples M14 and M15 are the most northern samples collected during the M138 campaign and are further removed from the coastal and upwelling region. This may explain the lower TSI concentrations compared to the other samples collected along the Peruvian coast. More generally, most of the results in **Table 6** (with the notable exception of those from TransBrom) indicate higher TSI concentrations in the northern hemisphere than in the south. As noted by Baker and Yodle (2021a), this pattern may be a consequence of higher sea-to-air fluxes of iodine in the northern hemisphere, driven by higher ozone concentrations, and thus dry ozone deposition, in the north.

TSI concentrations in the TransBrom samples (**Table 6**) are comparable to those presented for aerosols < 2.5 μm (PM2.5) collected along the transect of Lai et al. (2008), which covers a similar part of the West Pacific region. The unusually low (in the context of the SHIVA, OASIS, and M138 results) IO_3^- concentrations observed during TransBrom

TABLE 4 | Median and range of soluble iodine species concentrations (pmol m^{-3}) and enrichment factor (EF) of TSI in bulk aerosols for SHIVA and total (fine + coarse) for TransBrom, OASIS, and M138.

Cruise	TransBrom	SHIVA	OASIS	M138
Species	**Bulk**	**Bulk**	**Bulk**	**Bulk**
TSI	9.57 (3.08–32.0)	9.04 (7.0–15.9)	19.0 (12.4–30.6)	35.6 (6.41–65.4)
I^-	3.66 (1.08–18.7)	3.7 (2.25–6.09)	4.43 (1.65–7.51)	13.3 (1.0–33.9)
IO_3^-	0.71 (0.35–15.0)	4.19 (1.39–9.79)	11.1 (5.03–18.3)	14.7 (1.95–47.3)
SOI	4.0 (−1.11–12.6)	1.84 (−0.668–5.35)	4.21 (2.37–7.85)	6.4 (1.7–13.6)
EF_{TSI}	75 (16–440)	120 (35–310)	97 (57–280)	470 (61–760)

TABLE 5 | Median and range of soluble iodine species concentrations (pmol m^{-3}) and enrichment factor (EF) of TSI in fine and coarse mode aerosols the TransBrom, OASIS, and M138 expeditions.

Cruise	TransBrom		OASIS		M138	
Species	**Fine**	**Coarse**	**Fine**	**Coarse**	**Fine**	**Coarse**
TSI	2.86 (1.53–5.98)	6.89 (1.55–26.7)	8.52 (4.45–14.6)	10.1 (4.05–16.7)	9.59 (< 2.14–18.1)	23.7 (4.27–58.2)
I^-	1.2 (0.798–2.47)	2.27 (< 0.21–17.3)	2.61 (1.17–5.08)	1.44 (0.487–2.43)	6.91 (< 0.397–14.2)	5.55 (0.60–23.4)
IO_3^-	0.20 (< 0.18–0.35)	0.51 (0.13–14.8)	3.39 (1.47–8.0)	7.66 (2.6–11.6)	0.72 (< 0.18–11.4)	14.3 (1.73–45.4)
SOI	1.27 (0.53–4.42)	2.29 (−2.26–9.03)	2.72 (1.23–4.7)	1.54 (0.3–3.52)	1.6 (0.795–3.72)	3.92 (0.82–10.1)
EF_{TSI}	820 (180–3,040)	45 (9–380)	430 (350–1,130)	58 (21–160)	1,910 (440–12,800)	330 (43–580)

are similar to those reported by Lai et al. (2008). Cellulose filters were used for sampling during TransBrom and the Lai et al. study. Yodle and Baker (2019) reported low extraction recoveries of IO_3^- from cellulose filters, which raises the possibility that the low IO_3^- proportions reported for these two cruises in the West Pacific were due to artefacts introduced by the sampling/extraction procedures. However, such an artefact (if present at all) does not appear to have affected all of the TransBrom samples, because several exhibited both high concentrations and proportions of IO_3^- (**Figure 4C**). Despite the methodological differences of TransBrom and Lai et al.'s work compared to OASIS, SHIVA, and M138, it is not clear whether the iodine speciation for these two West Pacific cruises falls outside the natural variability in iodine speciation.

Iodine Species Proportions

Iodine speciation and proportions in the RSO, RSI, and SEP (and coarse mode SWP) samples are similar to one another (**Figure 5**) and are comparable to those of aerosols sampled from remote marine air masses in the northern and southern Atlantic Ocean [air masses RNA and RSA in Baker (2005) and Baker and Yodle (2021a)]. Common features of these marine air masses are the dominance of IO_3^- in the coarse mode and high percentages of IO_3^- in the fine mode. This suggests that the aerosol chemistry in remote air masses across different ocean basins is governed by similar processes. The NWP samples has a radically different speciation to the other remote air mass types. As discussed above, the reasons for this difference are unclear.

Iodine species proportions in air mass types with terrestrial origins (e.g., NEA, PER) are rather different to the clean marine samples (**Figure 5**), with substantially lower proportions of IO_3^- and higher proportions of I^- and SOI, especially in the fine mode. Indeed, there appears to be a gradient in the proportions of IO_3^- and I^- in samples from continentally/anthropogenically-influenced air masses (e.g., NEA, SCS, NCP, PER, EPP) and those of clean remote air masses (e.g., RSO, RSI, SEP, SWP) (**Figure 7**). This is consistent with data from the Atlantic Ocean, where IO_3^- proportions were lower and I^- and SOI proportions were higher in aerosols in air masses originating over Europe or southern Africa compared to those derived from the remote Atlantic Ocean (Baker and Yodle, 2021a).

With the exception of TransBrom results, the proportion of SOI among all fine and coarse mode samples is relatively constant regardless of I^- and IO_3^- proportions and air mass type. SOI proportions (excluding the TransBrom samples) range between 10% and 41% (median of 26 %) for fine mode samples and between 6% and 33% (median of 17%) for coarse mode samples. The higher enrichment of SOI in fine mode compared to coarse mode samples may be a result of sea spray production through bubble-bursting whereby proportionally more organic matter in the sea surface microlayer (SML) ends up in submicron film droplets rather than in the larger droplets (de Leeuw et al., 2011). If SOI is part of the composition of the organic matter, then this is a primary production mechanism. Alternatively, the organic matter may produce SOI within the aerosol through reactions with inorganic iodine compounds (Baker, 2005). In the coarse mode aerosols, SOI proportions seem lower in the remote ocean samples compared to the more continentally-influenced air masses, which could indicate primary sources of terrestrial organic matter, or primary sources of marine SOI through bubble-bursting within productive coastal regions (Seto and Duce, 1972; de Leeuw et al., 2011).

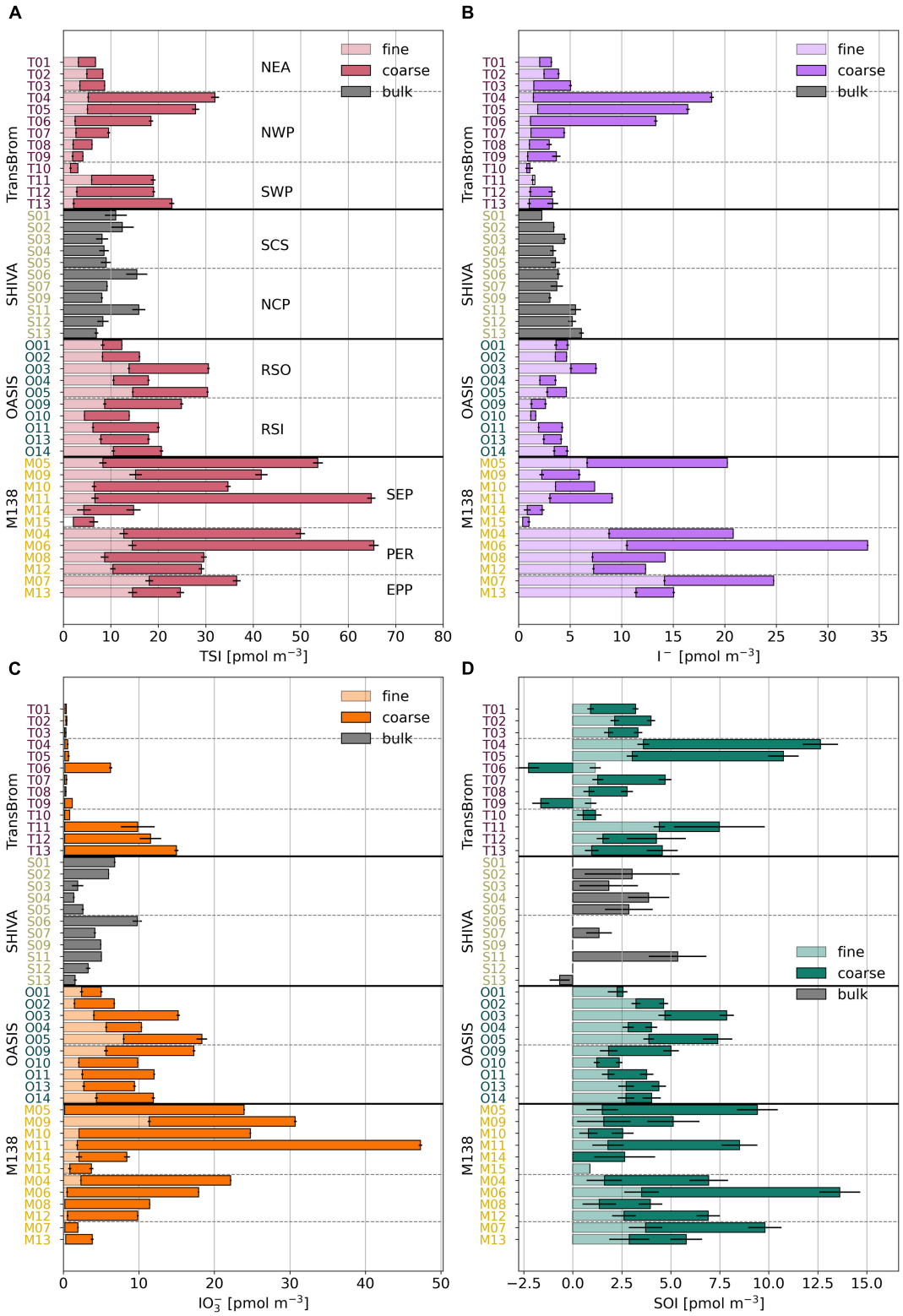

FIGURE 4 | Bar plots of TSI **(A)**, I^- **(B)**, IO_3^- **(C)**, and SOI **(D)** concentrations in fine (light), coarse (dark), and bulk (grey) mode for TransBrom, OASIS, M138, and SHIVA aerosol samples. Empty bars indicate concentrations below the detection limit. SOI concentrations for which the error is larger than the parameter itself are omitted. Details are as for **Figure 3**.

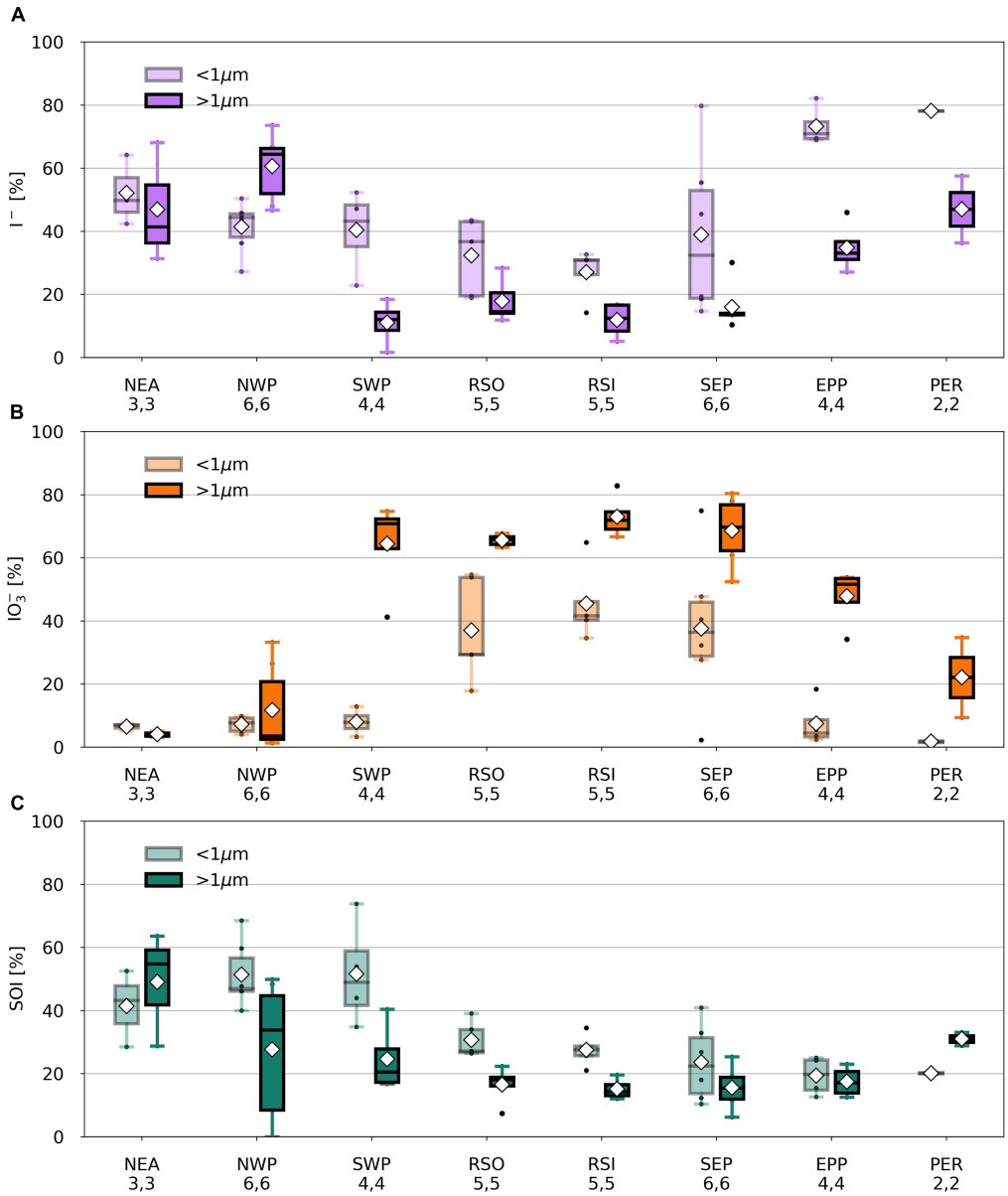

FIGURE 5 | Percentage I^- **(A)**, IO_3^- **(B)**, and SOI **(C)** of TSI in fine (light) and coarse (dark) mode aerosol samples per air mass type from TransBrom, OASIS, and M138. SOI concentrations for which the error is larger than the parameter itself are omitted. Black dots represent individual samples. White diamonds show the average value. Lower (upper) whisker extends to the sample that is within 1.5 × interquartile range lower (higher) beyond the first (third) quartile.

Interconversions Between Iodine Species

Baker and Yodle (2021a) recently examined the iodine speciation in aerosols collected from a variety of air mass types over the North and South Atlantic Oceans. They reported variations in speciation between these air mass types that were consistent with the controlling role of acidity on iodine species interconversions proposed by Pechtl et al. (2007). Specifically, Baker and Yodle (2021a) reported that IO_3^- was the dominant species in aerosols that were expected to be alkaline (i.e., unpolluted sea spray and mineral dust) and that IO_3^- was present in much lower proportions in aerosols that were expected to be acidic, such as in the fine mode in polluted terrestrial air masses. According to Pechtl et al. (2007), reduction of IO_3^- is promoted in acidic aerosols in the presence of I^- (Eq. 4). Furthermore, HOI can potentially react with dissolved organic matter (DOM; Truesdale and Luther, 1995), generating SOI, which then photo-dissociates, producing I^- (Baker, 2005; Eq. 5).

$$IO_3^- + I^- + 2H^+ \rightarrow HIO_2 + HOI \quad (4)$$

$$HOI + DOM \rightarrow SOI \rightarrow I^- + H^+ + DOM \quad (5)$$

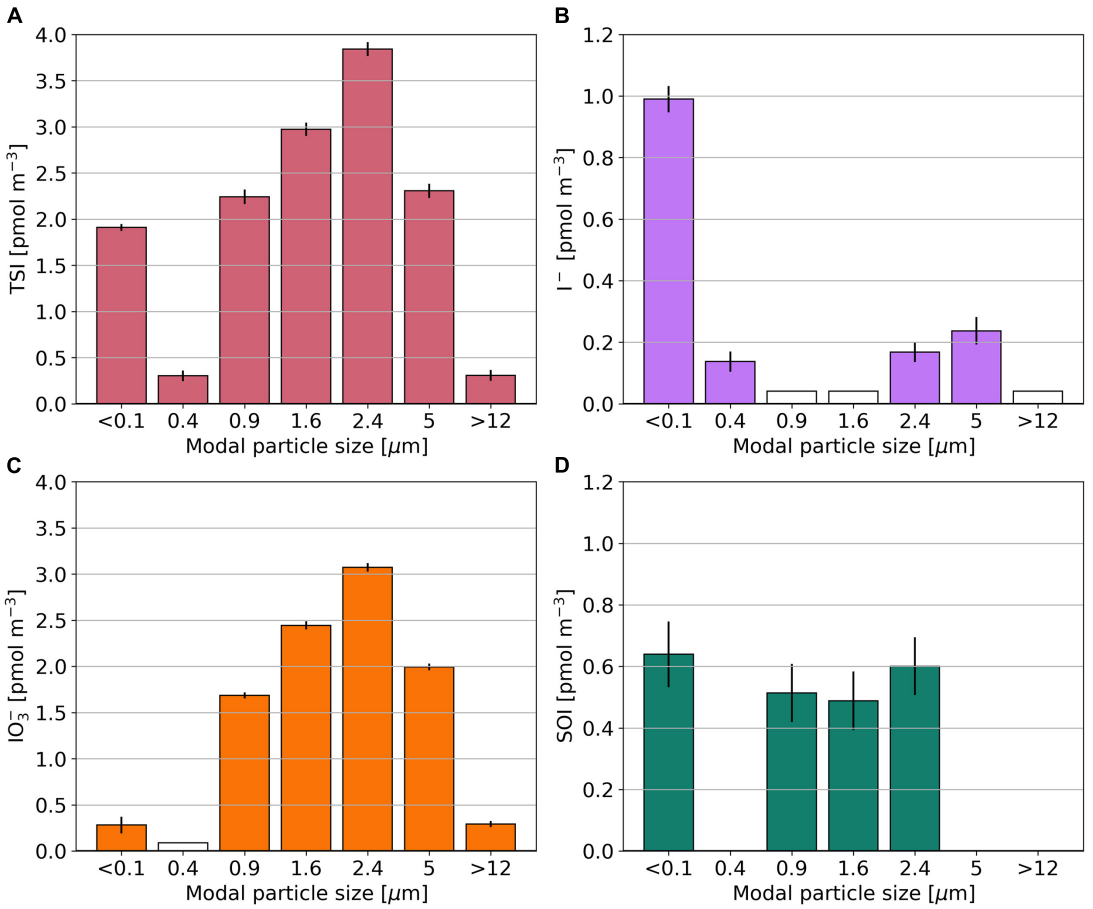

FIGURE 6 | Bar plots showing the TSI **(A)**, I^- **(B)**, IO_3^- **(C)**, and SOI **(D)** concentrations for the multi size segregated aerosol sample O10, collected during the OASIS expedition. Empty bars indicate concentrations below the detection limit. SOI concentrations for which the error is larger than the parameter itself are omitted.

The variations in iodine species proportions for the samples reported here are also broadly consistent with the results of the Pechtl et al. modelling study. Clean marine aerosols (RSO, RSI, SEP) are dominated by IO_3^-, even in the fine mode, while the fine mode aerosols of terrestrially-influenced air mass types (NEA, PER) contain very little IO_3^-. These terrestrial fine mode aerosols contain relatively high concentrations of acidic species (**Figure 3** and **Supplementary Figure 3**) and are likely to be strongly acidic (Keene et al., 2002; Pye et al., 2020). Note, however, that it was not possible to determine the pH of the samples collected during this study.

The sources and transformations of SOI in marine aerosols are still understood very poorly. In addition to the potential secondary formation of SOI (Eq. 5), it is also possible that SOI has a primary source through the direct incorporation of dissolved organic iodine (DOI) compounds into sea spray aerosols during bubble-bursting, especially for fine mode aerosols (Seto and Duce, 1972; de Leeuw et al., 2011). DOI distributions in the SML are not well known, but DOI concentrations have been reported to be higher in coastal waters than in the open ocean (Wong and Cheng, 1998). However, there does not appear to be any clear relationship between aerosol SOI concentrations or proportions and proximity of sampling locations to the coast which might indicate whether primary emissions of SOI are important.

Whether SOI has a primary or secondary source has important implications for iodine heterogeneous chemistry, because HOI also participates in other reactions, such as halogen activation that recycle I^- and other halogens back to the gas-phase (Eq. 6). Therefore, secondary formation of SOI (Eq. 5) might be expected to reduce halogen recycling through competition for HOI.

$$I^- + HOX + H^+ = IX + H_2O \; (X = I, Cl, Br) \qquad (6)$$

However it is produced, the photodissociation of SOI is very likely to be a source of I^- in aerosols. We found significant ($p < 0.01$) positive correlations between SOI and I^- for: fine and coarse mode aerosols from M138 (R^2 = 0.64, 0.77, respectively), fine mode aerosols from OASIS (R^2 = 0.64), and the coarse mode aerosols from TransBrom (R^2 = 0.92) (**Figure 8**). Positive correlations between SOI and I^- concentrations

TABLE 6 | Reported total soluble iodine (TSI) concentrations and enrichment factors of TSI with respect to sea spray in bulk/total aerosols collected over the oceans.

Ocean	TSI (pmol $m^{-}3$)	EF_{TSI}	References
Northern West Pacific	8.7 (4.1–32.0)	110 (16–440)	This work (TransBrom)
Southern West Pacific	19.0 (3.1–22.9)	56 (25–79)	This work (TransBrom)
Northern West Pacific	9.0 (7.0–15.9)	120 (35–310)	This work (SHIVA)
Southern Indian	19.0 (12.4–30.6)	97 (57–280)	This work (OASIS)
Southern East Pacific	35.6 (6.4–65.4)	470 (61–760)	This work (M138)
North Atlantic	27.3 (13.4–91.5)	277 (79–2,400)	Baker, 2005
South Atlantic	14.4 (8.4–32.9)	135 (40–520)	Baker, 2005
Western Pacific, Eastern Indian and Southern Ocean	9.4* (1.2–28.2) [a]		Lai et al., 2008
North Atlantic	37.5 (16.5–86.9)	150 (100–530)	Allan et al., 2009
West Pacific (30–65°N)	82* (19–243)		Xu S. et al., 2010
South Atlantic	5.8* (2.9–9.9) [a]		Lai et al., 2011
North Atlantic	34.6 (18.6–103)	300 (190–1,200)	Baker and Yodle, 2021a
South Atlantic	21.3 (12.4–41.7)	130 (59–620)	Baker and Yodle, 2021a

Values quoted are medians with ranges in parentheses, except where only means are available (*).
[a] PM2.5 samples were collected.

have also been found for Pacific samples in other datasets (Lai et al., 2008).

The relationships between SOI and I^- appear to vary between individual expeditions, especially in the fine mode (**Figure 8**). There are a number of factors that potentially influence these relationships, such as (a) the concentration and character of DOM and SOI in aerosols at each location which may be subject to location and seasonal variability, and (b) the acidity of the aerosol, which affects how fast I^- can be recycled to the gas-phase once formed by photodissociation of SOI, the removal of I^- and IO_3^- during reduction of IO_3^-, and potentially also the secondary formation of SOI (Truesdale and Luther, 1995).

Samples were collected in different seasons and years, during which iodine emissions and aerosol content have been shown to change (e.g., Xu S. et al., 2010; Cuevas et al., 2018). Changes in the magnitude and proportions of atmospheric pollutants over that time period could also have impacted aerosol iodine speciation. Even though samples in this work were collected between 2009 and 2017, we cannot assess the influence of long term or seasonal changes in our iodine speciation analysis or the observed variability. Aerosol samples are in themselves an integration of the time and space during which they were collected. Despite these contributing types of variability, the partitioning of aerosol samples into at least two size fractions and assessing the chemistry based on air mass types continues to give valuable information on the drivers of the aerosol iodine speciation.

Although the focus of this manuscript is on the speciation of iodine in the fine (<1 μm) and coarse (>1 μm) aerosol fractions, **Figure 6** [and similar distributions of I^-, IO_3^-, and SOI reported for a sample collected in the North Atlantic (Baker and Yodle, 2021a)] indicates that there is considerable heterogeneity of iodine speciation and the distribution of species that affect acidity (**Supplementary Figure 4**) within the fine and coarse fractions.

Wider Implications for Iodine Biogeochemistry

Paleoclimate research on Antarctic ice cores found detectable I^- throughout a record spanning the last 215 ky, but could only detect IO_3^- in ice from glacial time periods with high dust fluxes (Spolaor et al., 2013). This is consistent with the association between high IO_3^- concentrations and mineral dust in present-day marine aerosols (Baker and Yodle, 2021a) and suggests that dust alkalinity might account for the stability of IO_3^- in ice cores. Baker and Yodle (2021a) suggested that pH changes in fine and coarse mode aerosols in response to changing pollutant emissions since the Industrial Revolution (Baker et al., 2021) might affect iodine cycling (and ozone destruction rates) over time. Coastal mega cities are regions where aerosols have both high concentrations of sea spray and acidic species due to pollution. The results presented here suggest that acidification of sea spray aerosols potentially has an impact on iodine activation and thus on ozone destruction in those environments.

CONCLUSION

The data presented here for the West Pacific Ocean, East Pacific Ocean, and Indian Ocean contribute to a growing observational dataset on aerosol iodine speciation over the global ocean. While the results show appreciable variability among air masses and aerosol size fractions, they are broadly consistent with observations recently reported for the Atlantic Ocean (Baker and Yodle, 2021a). The use of uniform sampling and analytical methods between these two studies has allowed the general patterns in aerosol iodine speciation to be identified across all the major ocean basins for the first time. In alkaline aerosols, such as clean sea spray or mineral dust aerosols, IO_3^- is the dominant species. In aerosols with higher acidity and I^- availability, especially in polluted fine mode aerosols, IO_3^- is a minor species and I^- and SOI make up more significant fractions of the soluble iodine. Aerosol acidity is thought to be a major factor affecting the ratio of IO_3^- and I^- concentrations (Pechtl et al., 2007) and variations in acidity very likely contribute to the differences between iodine speciation in fine and coarse mode aerosols. SOI appears to be ubiquitous in marine aerosols. Its role in aerosol iodine cycling, and the wider impacts of iodine chemistry on tropospheric ozone, is dependent to some extent on the sources of SOI (primary or secondary, marine or terrestrial) and likely also on its composition, about which relatively little is known. Future progress in this area will require the measurement (Craig et al., 2018) or calculation

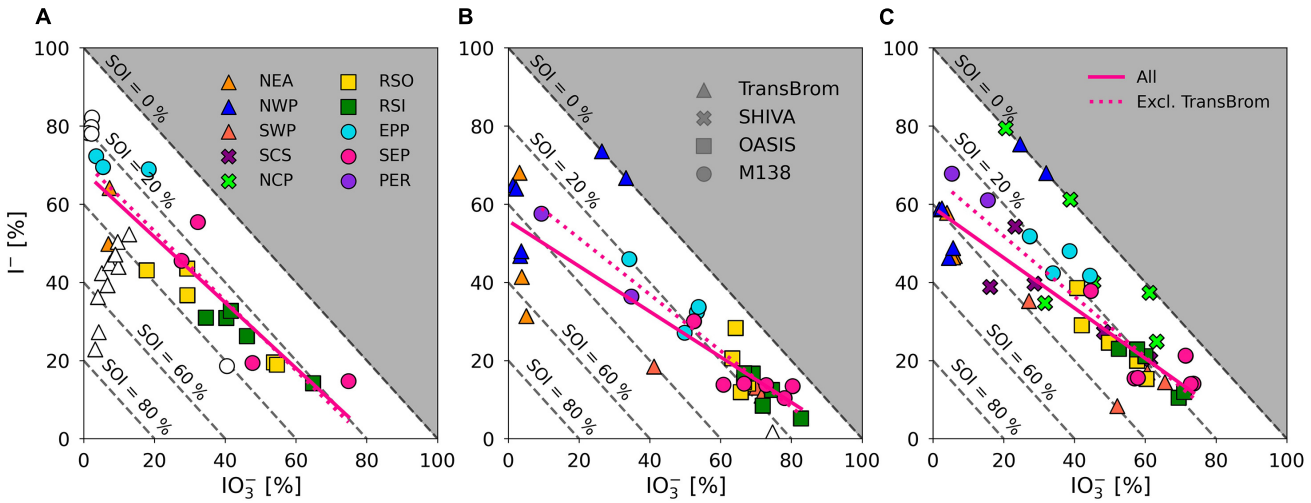

FIGURE 7 | Percentage I^- and IO_3^- of TSI plotted against each other for fine mode **(A)** and coarse mode **(B)**, aerosol samples on the TransBrom, OASIS, and M138 expeditions, and bulk/total **(C)** aerosol samples collected on the TransBrom (triangles), OASIS (squares), M138 (circles), and SHIVA (crosses) expeditions. Colour of markers corresponds to the air mass type associated to the sample (also see **Figure 2**). Empty markers indicate samples for which I^- or IO_3^- concentrations were below the detection limit. Linear regression lines are plotted for all fine, coarse, or bulk/total samples (solid) and all samples excluding those from the TransBrom expedition (dotted). Dashed diagonal lines indicate percentage of SOI of TSI. Samples for which concentrations were below the detection limit and samples where SOI < 0 are excluded from the linear regressions.

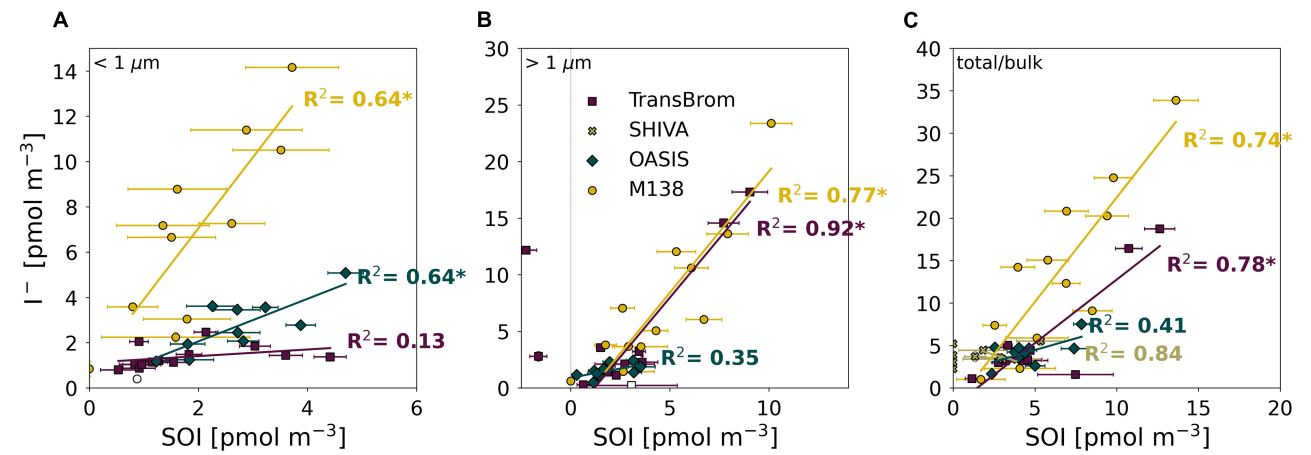

FIGURE 8 | SOI and I^- concentrations plotted against each other for the fine **(A)**, coarse **(B)**, and bulk/total mode **(C)** aerosol samples of TransBrom (purple), SHIVA (light green), OASIS (blue-green), and M138 (yellow). Empty markers indicate samples where the I^- concentration was below detection limit. The two coarse mode samples with negative SOI concentrations for TransBrom have been excluded from linear regressions. R-squared value of each regression line are shown in the plot. * indicates a significant linear relationship $p < 0.01$.

(Pye et al., 2020) of aerosol pH together with iodine speciation. Better understanding of the molecular character, sources, and reactivity of SOI will be necessary in order to incorporate the influence of this iodine fraction in numerical models of aerosol chemistry.

The robustness of the chemical drivers discussed in this work need to be tested alongside physical processes by process-based models, aiming to simulate representative aerosol iodine speciation in various environmental conditions, i.e., air mass types. The tight coupling between the aqueous-phase and gas-phase chemistry requires that gas-phase species concentrations be also validated, including the effect on atmospheric ozone levels and potential oceanic ozone deposition. Models can also address the combined effect of the aerosol iodine chemistry on marine ozone deposition and possible feedback processes through oceanic iodine emission and subsequent ozone destruction pathways. The globally consistent observational datasets presented here and by Baker and Yodle (2021a), together with the global sea surface I^- observations (Chance et al., 2019a), provide a significant benchmark to support those process modelling studies.

DATA AVAILABILITY STATEMENT

The datasets presented in this study can be found in the PANGAEA online repository at the following links: https://doi.org/10.1594/PANGAEA.935937 (TransBrom), https://doi.org/10.1594/PANGAEA.891321 (SHIVA), https://doi.org/10.1594/PANGAEA.935883 (OASIS), and https://doi.org/10.1594/PANGAEA.936483 (M138).

AUTHOR CONTRIBUTIONS

ED led the writing process of the manuscript, and analysed, processed, and interpreted the OASIS iodine species results. AB developed the concept for the study and contributed to the writing of the manuscript. CY analysed, processed, and interpreted the major ion and iodine species results for TransBrom and SHIVA. AS analysed, processed, and interpreted the major ion and iodine species concentrations for M138. LG co-guided the process of the study on the OASIS aerosol samples. All authors commented on the manuscript.

FUNDING

We would like to thank the Royal Thai Government for providing a studentship for CY and the United Kingdom Natural Environment Research Council (Grant NE/H00548X/1) and the University of East Anglia for supporting analysis costs. We would also like to thank the German Federal Ministry of Education and Research (BMBF) for providing the funding for the TransBrom (Grant No. 03G0731A), SHIVA (Grant No. 03G218A), and OASIS (Grant No. 03G0235A) expeditions. M138 was funded by the German Science Foundation (DFG) *via* the Collaborative Research Centre (Sonderforschungsbereich) 754 at Kiel University/GEOMAR, Kiel, Germany (www.sfb754.de).

ACKNOWLEDGMENTS

We would like to thank the Peruvian authorities for their generous permission to work in their territorial waters. We would also like to thank Yuanxin Tian for measuring the major ion composition in the OASIS samples, and Graham Chilvers for assistance with the IC-ICP-MS analyses. We would also further like to thank the following people for aerosol sample collection: Christian Müller, Sebastian Wache and Arne Lanatowitz (TransBrom), Anke Schneider (SHIVA), Birgit Quack (SHIVA and OASIS), and Hermann Bange (M138). We would additionally like to thank Birgit Quack for the coordination of the sample collection on the TransBrom, SHIVA, and OASIS expeditions. We would also like to thank two reviewers for their time and valuable comments, which helped us improve the quality of the manuscript.

SUPPLEMENTARY MATERIAL

The Supplementary Material for this article can be found online at: https://www.frontiersin.org/articles/10.3389/fmars.2021.788105/full#supplementary-material

REFERENCES

Allan, J. D., Topping, D. O., Good, N., Irwin, M., Flynn, M., Williams, P. I., et al. (2009). Composition and properties of atmospheric particles in the eastern Atlantic and impacts on gas phase uptake rates. *Atmos. Chem. Phys.* 9, 9299–9314. doi: 10.5194/acp-9-9299-2009

Andreae, M. O., and Crutzen, P. J. (1997). Atmospheric aerosols: biogeochemical sources and role in atmospheric chemistry. *Science* 276, 1052–1058. doi: 10.1126/science.276.5315.1052

Baker, A. R. (2004). Inorganic iodine speciation in tropical Atlantic aerosol. *Geophys. Res. Lett.* 31:L23S02. doi: 10.1029/2004GL020144

Baker, A. R. (2005). Marine aerosol iodine chemistry: the importance of soluble organic iodine. *Environ. Chem.* 2, 295–298. doi: 10.1071/EN05070

Baker, A. R. (2021). Aerosol Chemical Composition (Major Ions and Iodine Species) in Samples Collected During the M138 Cruise in the Eastern Pacific Ocean, June 2017. PANGAEA. doi: 10.1594/PANGAEA.936483

Baker, A. R., and Droste, E. (2021). *Aerosol Soluble Chemical Composition for OASIS Cruise (SO234/2 & SO235), Indian Ocean, July-August 2014, Determined By Ion Chromatography and Inductively Coupled Plasma - Mass Spectrometry*. PANGAEA. doi: 10.1594/PANGAEA.935883

Baker, A. R., Kanakidou, M., Nenes, A., Myriokefalitakis, S., Croot, P. L., Duce, R. A., et al. (2021). Changing atmospheric acidity as a modulator of nutrient deposition and ocean biogeochemistry. *Sci. Adv.* 7:eabd8800. doi: 10.1126/sciadv.abd8800

Baker, A. R., Tunnicliffe, C., and Jickells, T. D. (2001). Iodine speciation and deposition fluxes from the marine atmosphere. *J. Geophys. Res. Atmos.* 106, 28743–28749. doi: 10.1029/2000JD000004

Baker, A. R., and Yodle, C. (2018). *Aerosol Major Ions and Iodine Speciation Over South China and Sulu Seas collected daily during SONNE Cruise SO218*. PANGAEA. doi: 10.1594/PANGAEA.891321

Baker, A. R., and Yodle, C. (2021b). *Aerosol Chemical Composition (Major Ions and Iodine Speciation) During the TransBrom Cruise in the Western Pacific Ocean, October 2009*. PANGAEA. doi: 10.1594/PANGAEA.935937

Baker, A. R., and Yodle, C. (2021a). Measurement report: indirect evidence for the controlling influence of acidity on the speciation of iodine in Atlantic aerosols. *Atmos. Chem. Phys.* 21, 13067–13076. doi: 10.5194/acp-21-13067-2021

Bange, H., Arevalo-Martinez, D. L., Baker, A. R., Bristow, L., Burmeister, K., Cisternas-Novoa, C., et al. (2017). *Organic Matter Fluxes and Biogeochemical Processes in the OMZ Off Peru, Cruise No. M138, 01 June-03 July 2017, Callao (Peru)-Bahia Las Minas (Panama), Open Access . Meteor-Berichte, 138*. Bonn: Gutachterpanel Forschungsschiffe, 69. doi: 10.2312/cr_m138

Blanchard, D. C., and Woodcock, A. H. (1980). The production, concentration, and vertical distribution of the sea-salt aerosol. *Ann. N. Y. Acad. Sci.* 338, 330–347. doi: 10.1111/j.1749-6632.1980.tb17130.x

Bluhm, K., Croot, P., Wuttig, K., and Lochte, K. (2010). Transformation of iodate to iodide in marine phytoplankton driven by cell senescence. *Aquat. Biol.* 11, 1–15. doi: 10.3354/ab00284

Carpenter, L. J., MacDonald, S. M., Shaw, M. D., Kumar, R., Saunders, R. W., Parthipan, R., et al. (2013). Atmospheric iodine levels influenced by sea surface emissions of inorganic iodine. *Nat. Geosci.* 6, 108–111. doi: 10.1038/ngeo1687

Chameides, W. L., and Davis, D. D. (1980). Iodine: its possible role in tropospheric photochemistry. *J. Geophys. Res. Oceans* 85, 7383–7398. doi: 10.1029/JC085iC12p07383

Chance, R., Tinel, L., Sherwen, T., Baker, A., Bell, T., Brindle, J., et al. (2019a). Global sea-surface iodide observations, 1967–2018. *Sci. Data* 6:286. doi: 10.1038/s41597-019-0288-y

Chance, R., Tinel, L., Sherwen, T., Baker, A., Bell, T., Brindle, J., et al. (2019b). *Global Sea-Surface Iodide Observations, 1967-2018*. Swindon: Natural Environment Research Council.

Chatfield, R. B., and Crutzen, P. J. (1990). Are there interactions of iodine and sulfur species in marine air photochemistry? *J. Geophys. Res. Atmos.* 95, 22319–22341. doi: 10.1029/JD095iD13p22319

Craig, R. L., Peterson, P. K., Nandy, L., Lei, Z., Hossain, M. A., Camarena, S., et al. (2018). Direct determination of aerosol pH: size-resolved measurements of submicrometer and supermicrometer aqueous particles. *Anal. Chem.* 90, 11232–11239. doi: 10.1021/acs.analchem.8b00586

Cuevas, C. A., Maffezzoli, N., Corella, J. P., Spolaor, A., Vallelonga, P., Kjær, H. A., et al. (2018). Rapid increase in atmospheric iodine levels in the North Atlantic since the mid-20th century. *Nat. Commun.* 9:1452. doi: 10.1038/s41467-018-03756-1

Cutter, G. A., Moffett, J. G., Nielsdottir, M. C., and Sanial, V. (2018). Multiple oxidation state trace elements in suboxic waters off Peru: in situ redox processes and advective/diffusive horizontal transport. *Mar. Chem.* 201, 77–89. doi: 10.1016/j.marchem.2018.01.003

Davis, D., Crawford, J., Liu, S., McKeen, S., Bandy, A., Thornton, D., et al. (1996). Potential impact of iodine on tropospheric levels of ozone and other critical oxidants. *J. Geophys. Res. Atmos.* 101, 2135–2147. doi: 10.1029/95JD02727

de Leeuw, G., Andreas, E. L., Anguelova, M. D., Fairall, C. W., Lewis, E. R., O'Dowd, C., et al. (2011). Production flux of sea spray aerosol. *Rev. Geophys.* 49:RG2001. doi: 10.1029/2010RG000349

Gäbler, H. E., and Heumann, K. G. (1993). Determination of atmospheric iodine species using a system of specifically prepared filters and IDMS. *Fresenius J. Anal. Chem.* 345, 53–59. doi: 10.1007/BF00323326

Ganzeveld, L., Helmig, D., Fairall, C. W., Hare, J., and Pozzer, A. (2009). Atmosphere-ocean ozone exchange: a global modeling study of biogeochemical, atmospheric, and waterside turbulence dependencies. *Glob. Biogeochem. Cycles* 23:GB4021. doi: 10.1029/2008GB003301

Gilfedder, B. S., Lai, S. C., Petri, M., Biester, H., and Hoffmann, T. (2008). Iodine speciation in rain, snow and aerosols. *Atmos. Chem. Phys.* 8, 6069–6084. doi: 10.5194/acp-8-6069-2008

Gómez Martín, J. C., Saiz-Lopez, A., Cuevas, C. A., Fernandez, R. P., Gilfedder, B., Weller, R., et al. (2021). Spatial and temporal variability of iodine in aerosol. *J. Geophys. Res. Atmos.* 126:e2020JD034410. doi: 10.1029/2020JD034410

Hoffmann, T., O'Dowd, C. D., and Seinfeld, J. H. (2001). Iodine oxide homogeneous nucleation: an explanation for coastal new particle production. *Geophys. Res. Lett.* 28, 1949–1952. doi: 10.1029/2000GL012399

Jones, C. E., Hornsby, K. E., Sommariva, R., Dunk, R. M., Von Glasow, R., McFiggans, G., et al. (2010). Quantifying the contribution of marine organic gases to atmospheric iodine. *Geophys. Res. Lett.* 37:L18804. doi: 10.1029/2010GL043990

Kamykowski, D., and Zentara, S. J. (1990). Hypoxia in the world ocean as recorded in the historical data set. *Deep Sea Res. Part A Oceanogr. Res. Papers* 37, 1861–1874. doi: 10.1016/0198-0149(90)90082-7

Keene, W. C., Pszenny, A. A., Maben, J. R., and Sander, R. (2002). Variation of marine aerosol acidity with particle size. *Geophys. Res. Lett.* 29:1101. doi: 10.1029/2001GL013881

Klick, S., and Abrahamsson, K. (1992). Biogenic volatile iodated hydrocarbons in the ocean. *J. Geophys. Res. Oceans* 97, 12683–12687. doi: 10.1029/92JC00948

Krüger, K., Quack, B., and Marandino, C. (2014a). *RV SONNEFahrtbericht /Cruise Report SO234-2, 08-20.07.2014, Durban,South Africa-PortLouis, Mauritius - SPACES OASIS Indian Ocean, GEOMAR Report, N.Ser.020*. Kiel: GEOMAR, 87.

Krüger, K., Quack, B., and Marandino, C. (2014b). *RV SONNEFahrtbericht /Cruise Report SO235, 23.07-07.08.2014, PortLouis, Mauritius to Malé, Maldives, GEOMAR Report, N.Ser.021*. Kiel: GEOMAR, 65.

Lai, S. C., Hoffmann, T., and Xie, Z. Q. (2008). Iodine speciation in marine aerosols along a 30,000 km round-trip cruise path from Shanghai, China to Prydz Bay, Antarctica. *Geophys. Res. Lett.* 35, L21803. doi: 10.1029/2008GL035492

Lai, S. C., Williams, J., Arnold, S. R., Atlas, E. L., Gebhardt, S., and Hoffmann, T. (2011). Iodine containing species in the remote marine boundary layer: a link to oceanic phytoplankton. *Geophys. Res. Lett.* 38:L20801. doi: 10.1029/2011GL049035

Mahajan, A., Gómez Martín, J., Hay, T., Royer, S.-J., Yvon-Lewis, S., Liu, Y., et al. (2012). Latitudinal distribution of reactive iodine in the Eastern Pacific and its link to open ocean sources. *Atmos. Chem. Phys.* 12, 11609–11617. doi: 10.5194/acp-12-11609-2012

Mahajan, A., Plane, J., Oetjen, H., Mendes, L., Saunders, R., Saiz-Lopez, A., et al. (2010). Measurement and modelling of tropospheric reactive halogen species over the tropical Atlantic Ocean. *Atmos. Chem. Phys.* 10, 4611–4624. doi: 10.5194/acp-10-4611-2010

Mamane, Y., and Gottlieb, J. (1992). Nitrate formation on sea-salt and mineral particles - a single particle approach. *Atmos. Environ. Part A Gen. Top.* 26, 1763–1769. doi: 10.1016/0960-1686(92)90073-T

Martino, M., Hamilton, D., Baker, A. R., Jickells, T. D., Bromley, T., Nojiri, Y., et al. (2014). Western Pacific atmospheric nutrient deposition fluxes, their impact on surface ocean productivity. *Glob. Biogeochem. Cycles* 28, 712–728. doi: 10.1002/2013GB004794

Martino, M., Mills, G. P., Woeltjen, J., and Liss, P. S. (2009). A new source of volatile organoiodine compounds in surface seawater. *Geophys. Res. Lett.* 36:L01609. doi: 10.1029/2008GL036334

McFiggans, G., Plane, J. M., Allan, B. J., Carpenter, L. J., Coe, H., and O'Dowd, C. (2000). A modeling study of iodine chemistry in the marine boundary layer. *J. Geophys. Res. Atmos.* 105, 14371–14385. doi: 10.1029/1999JD901187

Moore, R. M., and Tokarczyk, R. (1992). Chloro-iodomethane in N. Atlantic waters: a potentially significant source of atmospheric iodine. *Geophys. Res. Lett.* 19, 1779–1782. doi: 10.1029/92GL01796

O'Dowd, C. D., Jimenez, J. L., Bahreini, R., Flagan, R. C., Seinfeld, J. H., Hämeri, K., et al. (2002). Marine aerosol formation from biogenic iodine emissions. *Nature* 417, 632–636. doi: 10.1038/nature00775

Pechtl, S., Schmitz, G., and Glasow, R. V. (2007). Modelling iodide–iodate speciation in atmospheric aerosol: contributions of inorganic and organic iodine chemistry. *Atmos. Chem. Phys.* 7, 1381–1393. doi: 10.5194/acp-7-1381-2007

Prados-Roman, C., Cuevas, C. A., Fernandez, R. P., Kinnison, D. E., Lamarque, J. F., and Saiz-Lopez, A. (2015a). A negative feedback between anthropogenic ozone pollution and enhanced ocean emissions of iodine. *Atmos. Chem. Phys.* 15, 2215–2224. doi: 10.5194/acp-15-2215-2015

Prados-Roman, C., Cuevas, C. A., Hay, T., Fernandez, R. P., Mahajan, A. S., Royer, S. J., et al. (2015b). Iodine oxide in the global marine boundary layer. *Atmos. Chem. Phys.* 15, 583–593. doi: 10.5194/acp-15-583-2015

Pye, H. O. T., Nenes, A., Alexander, B., Ault, A. P., Barth, M. C., Clegg, S. L., et al. (2020). The acidity of atmospheric particles and clouds. *Atmos. Chem. Phys.* 20, 4809–4888. doi: 10.5194/acp-20-4809-2020

Quack, B., and Krüger, K. (2010). *FS SONNE Fahrtbericht/Cruise Report: TransBrom SONNE, Tomakomai, Japan-Townsville, Australia, 09.10.-24.10.2009 [SO202-TRANSIT]*. Kiel: IFM-GEOMAR.

Quack, B., and Krüger, K. (2013). RV SONNE Fahrtbericht/Cruise Report SO218 SHIVA 15-29.11. 2011 Singapore-Manila, Philippines stratospheric ozone: halogens in a varying atmosphere part 1: SO218-SHIVA summary report (in German) part 2: SO218-SHIVA english reports of participating groups. *GEOMAR Rep. (N. Ser.)* 12:112.

Read, K. A., Mahajan, A. S., Carpenter, L. J., Evans, M. J., Faria, B. V., Heard, D. E., et al. (2008). Extensive halogen-mediated ozone destruction over the tropical Atlantic Ocean. *Nature* 453, 1232–1235. doi: 10.1038/nature07035

Robbins, R. C., Cadle, R. D., and Eckhardt, D. L. (1959). The conversion of sodium chloride to hydrogen chloride in the atmosphe. *J. Atmos. Sci.* 16, 53–56. doi: 10.1175/1520-04691959016<0053:TCOSCT<2.0.CO;2

Saiz-Lopez, A., Lamarque, J. F., Kinnison, D. E., Tilmes, S., Ordóñez, C., Orlando, J. J., et al. (2012b). Estimating the climate significance of halogen-driven ozone loss in the tropical marine troposphere. *Atmos. Chem. Phys.* 12, 3939–3949. doi: 10.5194/acp-12-3939-2012

Saiz-Lopez, A., Plane, J. M., Baker, A. R., Carpenter, L. J., von Glasow, R., Gómez Martín, J. C., et al. (2012a). Atmospheric chemistry of iodine. *Chem. Rev.* 112, 1773–1804. doi: 10.1021/cr200029u

Schall, C., Heumann, K. G., and Kirst, G. O. (1997). Biogenic volatile organoiodine and organobromine hydrocarbons in the Atlantic ocean from 42 N to 72 S. *Fresenius J. Anal. Chem.* 359, 298–305. doi: 10.1007/s002160050577

Seto, F. Y., and Duce, R. A. (1972). A laboratory study of iodine enrichment on atmospheric sea-salt particles produced by bubbles. *J. Geophys. Res.* 77, 5339–5349. doi: 10.1029/JC077i027p05339

Smith, M. H., Park, P. M., and Consterdine, I. E. (1993). Marine aerosol concentrations and estimated fluxes over the sea. *Q. J. R. Meteorol. Soc.* 119, 809–824. doi: 10.1002/qj.49711951211

Spolaor, A., Vallelonga, P., Plane, J. M. C., Kehrwald, N., Gabrieli, J., and Varin, C. (2013). Halogen species record Antarctic sea ice extent over glacial–interglacial periods. *Atmos. Chem. Phys.* 13, 6623–6635. doi: 10.5194/acp-13-6623-2013

Stein, A. F., Draxler, R. R., Rolph, G. D., Stunder, B. J., Cohen, M. D., and Ngan, F. (2015). NOAA's HYSPLIT atmospheric transport and dispersion modeling system. *Bull. Am. Meteorol. Soc.* 96, 2059–2077. doi: 10.1175/BAMS-D-14-00110.1

Stumm, W., and Morgan, J. J. (2012). *Aquatic Chemistry: Chemical Equilibria and Rates in Natural Waters*, Vol. 126. Hoboken, NJ: John Wiley & Sons.

Truesdale, V. W., and Luther, G. W. (1995). Molecular iodine reduction by natural and model organic substances in seawater. *Aquat. Geochem.* 1, 89–104. doi: 10.1007/BF01025232

Ulloa, O., and Pantoja, S. (2009). The oxygen minimum zone of the eastern South Pacific. *Deep Sea Res. Part II Top. Stud. Oceanogr.* 56, 987–991. doi: 10.1016/j.dsr2.2008.12.004

Vogt, R., Sander, R., Von Glasow, R., and Crutzen, P. J. (1999). Iodine chemistry and its role in halogen activation and ozone loss in the marine boundary layer: a model study. *J. Atmos. Chem.* 32, 375–395. doi: 10.1023/A:1006179901037

Whitehead, D. C. (1984). The distribution and transformations of iodine in the environment. *Environ. Int.* 10, 321–339. doi: 10.1016/0160-4120(84)90139-9

Wimschneider, A., and Heumann, K. G. (1995). Iodine speciation in size fractionated atmospheric particles by isotope dilution mass spectrometry. *Fresenius J. Anal. Chem.* 353, 191–196. doi: 10.1007/s00216535030191

Wong, G. T. (1991). The marine geochemistry of iodine. *Rev. Aquat. Sci.* 4, 45–73.

Wong, G. T., and Cheng, X. H. (1998). Dissolved organic iodine in marine waters: determination, occurrence and analytical implications. *Mar. Chem.* 59, 271–281. doi: 10.1016/S0304-4203(97)00078-9

Xu, S., Xie, Z., Li, B., Liu, W., Sun, L., Kang, H., et al. (2010). Iodine speciation in marine aerosols along a 15 000-km round-trip cruise path from Shanghai, China, to the Arctic Ocean. *Environ. Chem.* 7, 406–412. doi: 10.1071/EN10048

Xu, S.-Q., Xie, Z.-Q., Liu, W., Yang, H.-X., and Li, B. (2010). Extraction and determination of total bromine, iodine, and their species in atmospheric aerosol. *Chin. J. Anal. Chem.* 38, 219–224. doi: 10.1016/S1872-2040(09)60026-8

Yodle, C., and Baker, A. R. (2019). Influence of collection substrate and extraction method on the speciation of soluble iodine in atmospheric aerosols. *Atmos. Environ. X* 1:100009. doi: 10.1016/j.aeaoa.2019.100009

Conflict of Interest: The authors declare that the research was conducted in the absence of any commercial or financial relationships that could be construed as a potential conflict of interest.

Publisher's Note: All claims expressed in this article are solely those of the authors and do not necessarily represent those of their affiliated organizations, or those of the publisher, the editors and the reviewers. Any product that may be evaluated in this article, or claim that may be made by its manufacturer, is not guaranteed or endorsed by the publisher.

Copyright © 2021 Droste, Baker, Yodle, Smith and Ganzeveld. This is an open-access article distributed under the terms of the Creative Commons Attribution License (CC BY). The use, distribution or reproduction in other forums is permitted, provided the original author(s) and the copyright owner(s) are credited and that the original publication in this journal is cited, in accordance with accepted academic practice. No use, distribution or reproduction is permitted which does not comply with these terms.

frontiers | Frontiers in Marine Science

TYPE Original Research
PUBLISHED 11 October 2022
DOI 10.3389/fmars.2022.874759

Check for updates

OPEN ACCESS

EDITED BY
Dalton Hardisty,
Michigan State University,
United States

REVIEWED BY
Chelsie N. Bowman,
Georgia Southern University,
United States
Charles Diamond,
University of California, Riverside,
United States

*CORRESPONDENCE
Zunli Lu
zunlilu@syr.edu

SPECIALTY SECTION
This article was submitted to Marine Biogeochemistry, a section of the journal Frontiers in Marine Science

RECEIVED 12 February 2022
ACCEPTED 30 August 2022
PUBLISHED 11 October 2022

CITATION
He R, Elrick M, Day J, Lu W and Lu Z (2022) Devonian upper ocean redox trends across Laurussia: Testing potential influences of marine carbonate lithology on bulk rock I/Ca signals.
Front. Mar. Sci. 9:874759.
doi: 10.3389/fmars.2022.874759

COPYRIGHT
© 2022 He, Elrick, Day, Lu and Lu. This is an open-access article distributed under the terms of the Creative Commons Attribution License (CC BY). The use, distribution or reproduction in other forums is permitted, provided the original author(s) and the copyright owner(s) are credited and that the original publication in this journal is cited, in accordance with accepted academic practice. No use, distribution or reproduction is permitted which does not comply with these terms.

Devonian upper ocean redox trends across Laurussia: Testing potential influences of marine carbonate lithology on bulk rock I/Ca signals

Ruliang He[1,2], Maya Elrick[3], James Day[4], Wanyi Lu[2] and Zunli Lu[2]*

[1]State Key Laboratory of Continental Dynamics, Shaanxi Key Laboratory of Early Life and Environments, Department of Geology, Northwest University, Xi'an, China, [2]Department of Earth and Environmental Sciences, Syracuse University, Syracuse, NY, United States, [3]Earth and Planetary Sciences, University of New Mexico, Albuquerque, NM, United States, [4]Department of Geography-Geology, Illinois State University, Normal, IL, United States

The Devonian is characterized by major changes in ocean-atmosphere O_2 concentrations, colonialization of continents by plants and animals, and widespread marine anoxic events associated with rapid $\delta^{13}C$ excursions and biotic crises. However, the long-term upper ocean redox trend for the Devonian is still not well understood. This study presents new I/Ca data from well-dated Lower Devonian through Upper Devonian limestone sections from the Great Basin (western Laurussia) and the Illinois Basin (central Laurussia). In addition, to better address potential influences of lithology and stratigraphy on I/Ca redox signals, I/Ca data are reported here as carbonate lithology-specific. Results indicate that lithologic changes do not exert a dominant control on bulk carbonate I/Ca trends, but the effects of some diagenetic overprints cannot be ruled out. For the Illinois Basin, low I/Ca values (more reducing) are recorded during the Pragian to Emsian and increased but fluctuating values are recorded during the Eifelian to Givetian. The Great Basin I/Ca trends suggest local upper oceans were more reducing in the Lochkovian, more oxic in the Pragian-Emsian, return to more reducing in the Eifelian, then to increasingly more oxic, but fluctuating in the Givetian-Frasnian. The local I/Ca variations at Great Basin likely share more similarity with global upper ocean condition (compared to the Illinois Basin) based on its position adjacent to the Panthalassic Ocean and its temporal co-variation with global environmental volatility trends. The overall reducing and variable redox conditions of local upper ocean (if not a diagenetic signal) during the Middle and Late Devonian of Great Basin coincide with evidence of increased global environmental volatility suggesting seawater redox may have been an important part of environmental instability at this time.

KEYWORDS

Devonian, Great Basin, Illinois Basin, I/Ca, seawater redox

1 Introduction

1.1 Devonian environmental changes and ocean redox conditions

The Earth system went through profound changes during the Devonian (419.2 to 358.9 Ma). Atmospheric pO_2 increased to near-modern levels, as suggested by multiple lines of geochemical (Dahl et al., 2010; Wallace et al., 2017; Lu et al., 2018; Elrick et al., 2022) and modeling evidence (Lenton et al., 2016; Krause et al., 2018). At the same time, vascular plants diversified (Gensel and Andrews, 1987; Elick et al., 1998; Meyer-Berthaud et al., 1999; Stein et al., 2007; Kenrick and Strullu-Derrien, 2014; Dahl and Arens, 2020) and may have driven increased pO_2 level by increasing organic carbon burial (Kump, 1988; Lenton et al., 2016). In the Mid-Late Devonian, the development in size and root depths of vascular plants are hypothesized to have enhanced continental weathering rates and nutrient load to oceans, resulting in episodes of elevated marine primary productivity, marine anoxia and widespread deposition of black shales (Algeo and Scheckler, 1998).

The significant increase in atmospheric and oceanic oxygen levels did not apparently result in long-term environmental stability. Instead, Brett et al. (2020) suggested that biologic and environmental responses show a range of volatility (e.g., fluctuations of surface seawater temperatures (SST), $\delta^{13}C$, eustasy, and hypoxic or anoxia-induced biotic turnovers/extinctions). For example, the Early Devonian is characterized by infrequent but large global carbon isotope fluctuations and fewer bio-crises (Brett et al., 2020) (e.g., Klonk event). In contrast, during the Middle and Late Devonian, frequent marine bio-crises occurred, such as the Hangenberg, Kellwasser, Taghanic, Kačak and Chotěc events, coinciding with the accumulation of widespread organic-rich marine facies and positive carbon isotope excursions (House, 2002; Becker et al., 2016; Becker et al., 2020).

Marine redox conditions may have played an important role. Lithological and geochemical evidence suggests that most of Late Devonian bio-events are associated with short-lived (Myr-scale) anoxic conditions in bottom waters (e.g., Murphy et al., 2000; Werne et al., 2002; Sageman et al., 2003; Rimmer, 2004; Lash and Blood, 2014; White et al., 2018). However, these intervals of black shale deposition and coeval bio-crises provide only brief snapshots of redox conditions for Late Devonian. The newly published U isotope data from marine limestones provides the first long-term redox constraint for the Devonian global ocean (Elrick et al., 2022). Additional local redox data, from the Devonian shallow oceans where most paleoenvironmental and paleontological signals are preserved, will be helpful for untangling the relationship among environmental volatility, changes in the biosphere, and ocean redox conditions during the Devonian.

In this study, we 1) evaluate upper ocean redox patterns from the interval spanning the Early to Late Devonian (Lochkovian-Frasnian) using carbonate lithology-specific I/Ca trends from the Great Basin and Illinois Basin, 2) compare these results to existing I/Ca trends from the Middle Devonian of the Appalachian Basin, and 3) discuss the combined Laurussia-wide upper ocean redox trends with previously identified global paleoenvironmental volatility patterns (Brett et al., 2020).

1.2 Carbonate lithology-specific approach

As marine carbonate rocks usually have heterogenous compositions with various biogenic and non-biogenic components precipitated in different water depths, including porewater, I/Ca records measured from bulk carbonate rocks may represent a mixed signal. For example, I/Ca signals can vary among different foraminifera species and associated coarse bulk fraction within the same Cenozoic core (e.g., Zhou et al., 2014; Zhou et al., 2016). Indeed, the influence from lithologic changes is an unavoidable issue for all bulk carbonate geochemical proxies, especially for long-term reconstructions that contain different depositional facies, including I/Ca used here. For research focusing on deep-time samples, it is challenging to generate long-term, continuous I/Ca profiles for a specific carbonate component. In this study, we attempt a new approach, namely a carbonate lithology-specific I/Ca investigation, on Devonian limestones from the Great Basin and Illinois Basin, by identifying facies for each sample and assessing influences they might have on I/Ca values.

1.3 Iodine as a redox proxy

Iodine is an important element for biogeochemical and redox reactions (Küpper et al., 2011). In the modern seawater, iodine has a residence time of ~ 300 kyr and a uniform concentration of ~ 0.45 μmol/L (Elderfield and Truesdale, 1980) and its concentration can be an order of magnitude lower in freshwater (Fehn, 2012). For two thermodynamically stable iodine species, iodate (IO_3^-) is the major species in well-oxygenated waters (Truesdale and Bailey, 2000), while iodide (I^-) dominates at depth in anoxic waters (Wong and Brewer, 1977) and in anoxic porewaters (Kennedy and Elderfield, 1987a, b).

Iodate is the only species that can be incorporated into the carbonate crystal lattice (Lu et al., 2010) by substituting of CO_3^{2-} with IO_3^- (Podder et al., 2017; Feng and Redfern, 2018). Therefore, high I/Ca ratios found in bulk carbonate rocks indicate precipitation from more oxic upper ocean waters where iodate is present, although the oxidation rate can be very slow (Hardisty et al., 2020). Low I/Ca values may represent

the development of O_2-depleted conditions in or near the upper ocean or the influence from diagenetic process which is only known to reduce original values (Hardisty et al., 2017). The proxy has been widely applied to bulk carbonate samples to study the relationships among local ocean redox changes, major climate changes, and bio-crises from the Proterozoic and Phanerozoic (e.g., Zhou et al., 2015; Lu et al., 2017; Liu et al., 2019; Shang et al., 2019; He et al., 2020a; He et al., 2020b). More details about the I/Ca proxy are discussed in the recent review by Lu et al. (2020b).

2 Geological background

The Devonian Great Basin succession in Nevada accumulated in the southern subtropics along the westward-deepening epicontinental seaway of western Laurussia (Morrow and Sandberg, 2008) (Figures 1, S1). The western margin of Laurussia accumulated passive-margin deposits from the late Proterozoic through Middle Devonian followed by foreland basin deposits (associated with the Antler orogeny) in the Late Devonian through Early Mississippian (Morrow and Sandberg, 2008). The Great Basin composite section (~800 m) spans the middle Early Devonian through early Late Devonian (middle Lochkovian to middle Frasnian). Two central Nevada locations were sampled, including Coal Canyon (Simpson Park Range) and the northern Antelope Range (Figure S1). For each section, we used previously reported conodont biostratigraphy to determine zone-level age control and to correlate sections (section 1 in supplementary discussion). The Coal Canyon (Lochkovian) section represents deposition seaward of the shelf edge in basinal environments (Johnson and Murphy, 1984). The northern Antelope section (Pragian to Frasnian) represents basinal, slope, shelf edge, and middle shelf environments depending on the position of eustatic sea level (Johnson et al., 1996; Morrow and Sandberg, 2008). Parts of the Emsian, Givetian, and Frasnian were deposited in basinal environments in the northern Antelopes.

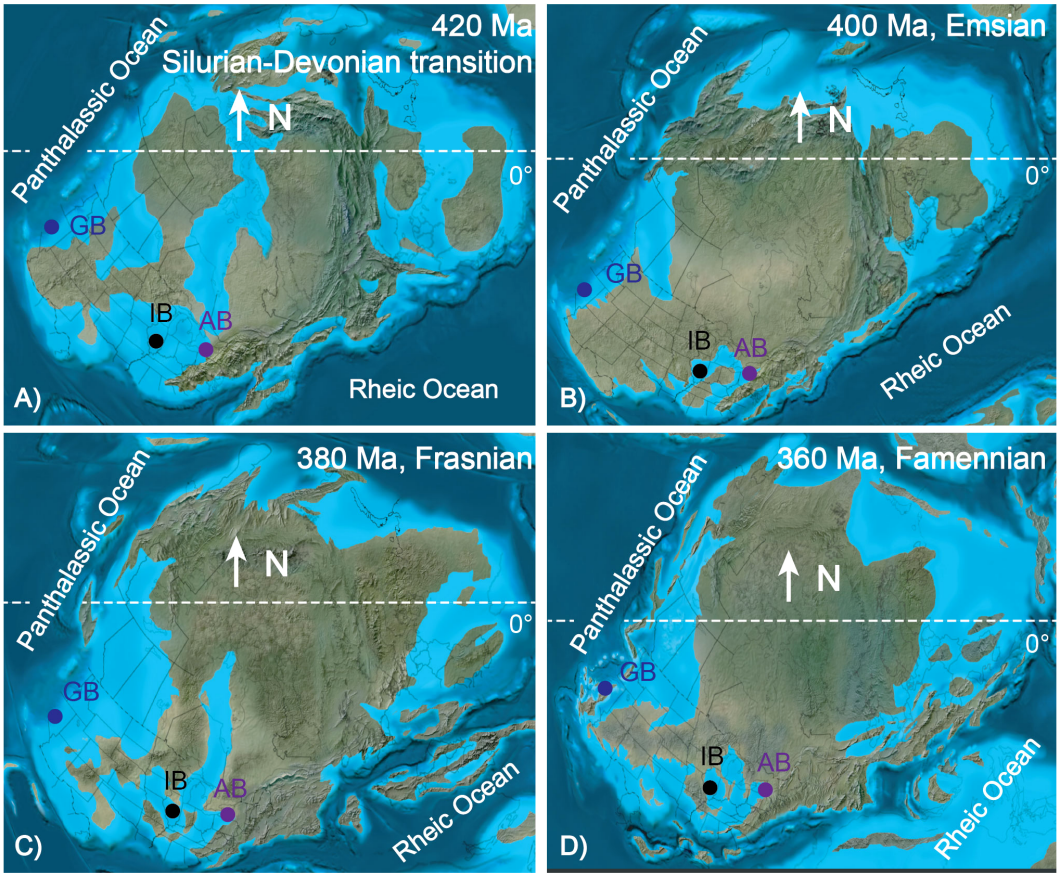

FIGURE 1
Paleogeographic maps of Laurussia during different stages **(A–D)** of Devonian. Maps are based on Blakey (2018). Dashed white lines represent the paleo-equator. GB represents the location of Great Basin composite section. IB represents the location of Illinois State Geological Survey White County Core of Illinois Basin. AB represents the location of the Middle Devonian core from the Appalachian Basin (He et al., 2020b).

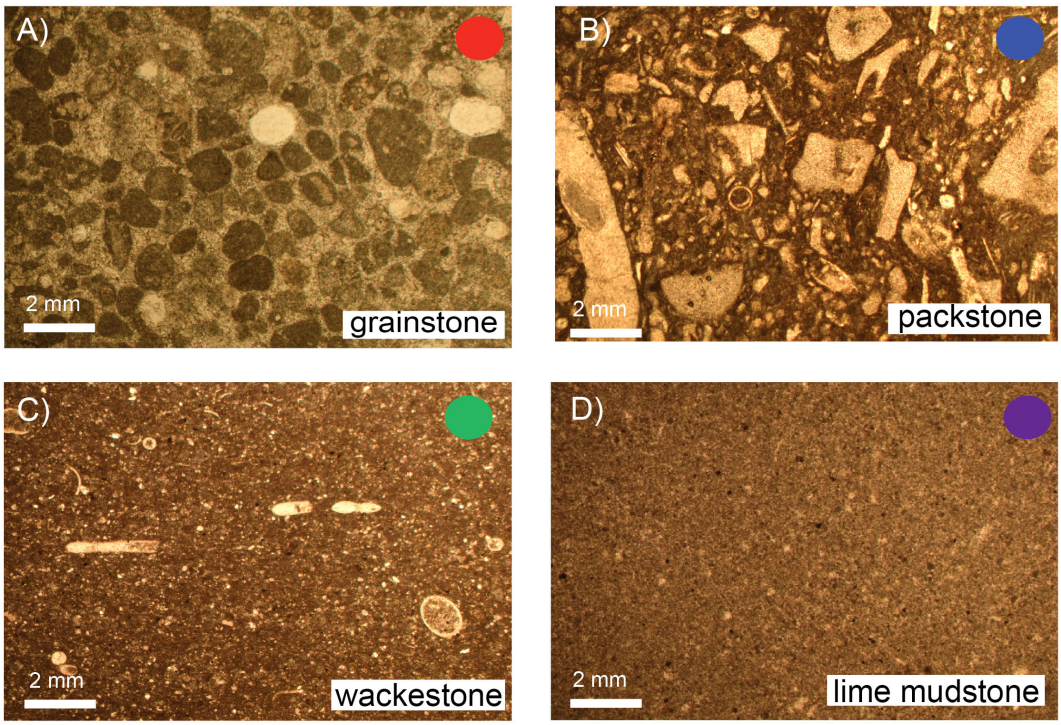

FIGURE 2
Thin section photographs of the main four lithologic groups identified in the composite Great Basin section of Nevada. Photos were taken under plane-polarized light. The colored solid circles are consistent with the colors shown in Figures 3–6 and S2. From **(A–D)**, lithologic transitions are from coarse grained to fine grained and depositional environments transition from upper shoreface to offshore environments. Note abundant early marine cements in the grainstone of **(A)**.

The Illinois Basin is one of the major interior cratonic basins of Laurussia, and accumulated up to 4.5 km of Cambrian through Pennsylvanian marine carbonate and siliciclastic deposits (Buschbach and Kolata, 1990; Kolata and Nelson, 1990). I/Ca data of Illinois Basin are measured from samples of the Illinois Geological Survey White County Core (~110 m thick; Figure 1) that spans the Pragian to early Givetian. The succession accumulated in shallow-water epicontinental sea carbonate settings in the southern subtropics of central Laurussia (Figure 1). The connection to the adjacent Rheic Ocean was restricted during Early Devonian eustatic lowstands, but became more open as eustatic sea level rose in the Middle and Late Devonian (Johnson et al., 1985) (Figure 1). Relative age control comes from conodont biostratigraphy (Day et al., 2012).

3 Samples and methods

3.1 Sample preparation

Samples for I/Ca and trace element analysis for the Great Basin section were collected at ~5-10 m intervals and at ~1-5 m intervals for C isotopes. To establish a carbonate lithology-specific I/Ca profile, the sections were described on a bed-by-bed basis using traditional field- and petrographic-based observations of grain size, sedimentary structures, color, fossil types/abundance, and facies associations. For the Illinois Basin core, samples were collected at ~1-3 m intervals for I/Ca analysis and carbonate lithologies were interpreted from core observations. Samples for elemental analyses were collected at ~5-10 m intervals for Great Basin and ~1 m intervals for Illinois Basin, and were chipped into small, non-weathered fragments, and were powdered in a Spex shatterbox with an alumina puck pulverizer. It should be noted that all the powdered samples are from rock fragments, rather than from micro-drilled carbonate powders.

3.2 I/Ca measurements

A total of 129 samples for Great Basin section and 77 samples for Illinois Basin core were selected for iodine analysis. Around 2-5 mg powdered samples were weighed and then rinsed with deionized (DI) water to remove any iodine that is attached on the surface of sample. To extract iodine from the

carbonate fraction, diluted HNO_3 (3% by volume) was added to clean powders in microcentrifuge tubes and the solution was separated from the residuals immediately after samples stopped reacting. The dissolved fraction was then diluted to solutions of ~ 50 ppm Ca and mixed with a matrix solution containing internal standards (Cs and In) and buffered with tertiary amine. Measurements of iodine, calcium and magnesium concentrations were performed on a quadrupole inductively coupled plasma mass spectrometer (ICP-MS, Bruker M90) at Syracuse University. The precisions are typically better than 1% for ^{127}I and the detection limit is usually better than 0.1 μmol/mol. The long-term accuracy is guaranteed by frequently repeated measurements of the standard reference material JCp-1 (Lu et al., 2020b).

3.3 C isotope, major and trace elements measurements

Carbonate C isotope measurements were performed at the University of New Mexico Center for Stable Isotopes. Isotope values were analyzed using continuous flow Isotope Ratio Mass Spectrometry with a Gasbench device coupled to a Thermo Fisher Scientific Delta V Plus Isotope Mass Spectrometer. The reproducibility was better than 0.1‰ for $\delta^{13}C$ based on repeats of laboratory standard (Carrara Marble) and the laboratory standards were calibrated versus NBS 19.

For elemental analyses, rock powders were dissolved in 1 M HNO_3, and solutions were centrifuged to remove insoluble residue. A solution split was diluted to ~200 ppm Ca with 2% HNO_3 and analyzed for a full suite of major, trace, and rare-earth element abundances on a Thermo Scientific ICAP-Q inductively coupled plasma mass spectrometer (ICP-MS) at Arizona State University. The analytical precision for all elements of interest was <5%.

4 Results

4.1 Great Basin

The I/Ca trends are divided into four stratigraphic intervals (Figures 3, 5). The Lochkovian consistently records low I/Ca with most of values lower than 1 μmol/mol, followed by an abrupt increase to 1 to 3 μmol/mol during the Pragian and Emsian. Near the Emsian-Eifelian unconformable boundary, I/Ca shifts back to nearly 0 μmol/mol and remains near detection limit through the Eifelian, except for a short-term I/Ca excursion of up to ~ 1.5

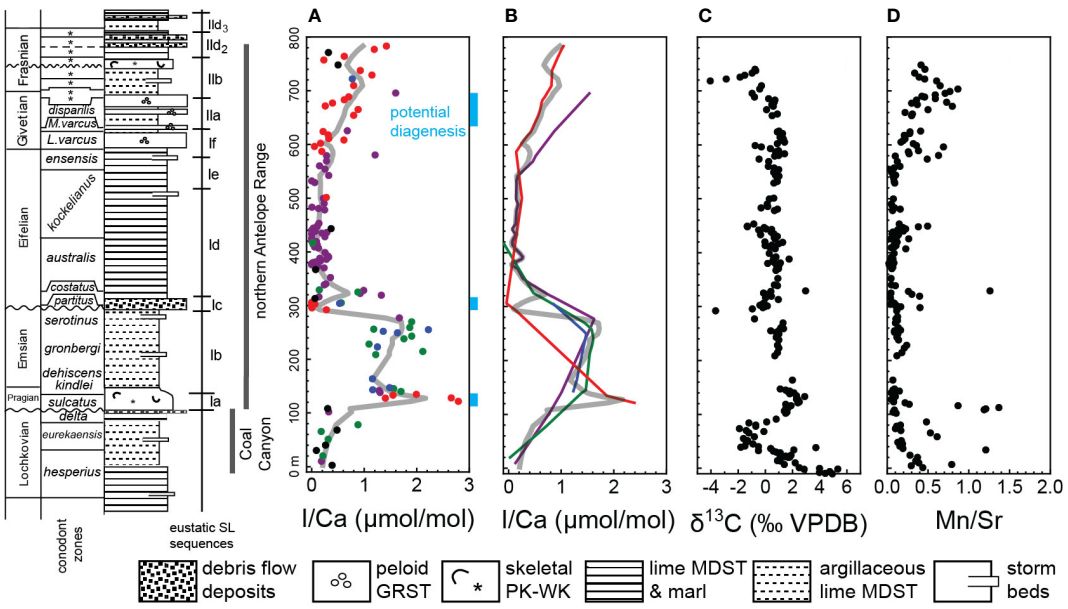

FIGURE 3
Geochemical measurements of the Great Basin composite section: **(A)** carbonate lithology-specific I/Ca ratio, **(B)** LOWESS smoothing trends for four lithologic facies, **(C)** bulk carbonate carbon isotopes, **(D)** Mn/Sr ratios. Color code for lithological groups: grainstone (red), packstone (blue), wackestone (green), lime mudstone (purple), unassigned (black). The thicker gray lines in **(A, B)** show the LOWESS smoothing results of all the samples, while other colored lines represent the LOWESS smoothing for each lithological group (with the same color code as the dots). GRST, grainstone; PK, packstone, WK, wackestone; MDST, mudstone, SL, sea level. Blue lines in **(A)** represent intervals that may record potential diagenetic alteration. *Conodont zones not labelled are (in ascending order): *norrisi, MN 1-2, MN 3, MN 6, hassi-jamieae, l. rhenana, u. rhenana, linguiformis*.

μmol/mol. From the Givetian to Frasnian, I/Ca gradually increases to ~ 2 μmol/mol, but shifts back to near zero values episodically and fluctuates in the range of 0 to 2 μmol/mol. Nevertheless, the overall I/Ca average of Givetian-Frasnian interval is lower than that of the Pragian-Emsian (Figure 5).

4.2 Illinois Basin

I/Ca values are consistently low (< 0.5 μmol/mol) in the Pragian and Emsian (Figure 4A). In the early Eifelian, values increase slightly to ~0.5 μmol/mol until the late Eifelian with a brief peak to ~1 μmol/mol, followed by an increase to fluctuating values (up to ~ 3 μmol/mol) in the late Eifelian through Givetian (Figure 4A). The timing of the major I/Ca increase and fluctuating values during the Givetian is coeval to that observed in the Great Basin section (Figure 3A).

5 Discussion

5.1 Carbonate lithology-specific I/Ca record

Geochemical measurements conducted on bulk carbonate rock samples are potentially influenced by lithologic variability and diagenesis. To avoid effects of lithologic influences, measurements can be performed on specific biologic components, such as individual brachiopod calcite or conodont apatite (van Geldern et al., 2006; Joachimski et al., 2009), but then the sample resolution is limited by available facies containing appropriate fossil types and abundances. On the other hand, some studies compare stratigraphic trends of redox proxies to sedimentologic and petrographic characteristics and fossil assemblages to investigate the nature of geochemical signals (e.g., Bowman et al., 2020). We take a similar approach for this study and compare I/Ca values and trends to specific carbonate rock types and sequence stratigraphy (Figures 3, 4).

For the Great Basin, the sampled carbonate rocks span the entire scheme of Dunham's classification, from grainstone to lime mudstone (Dunham, 1962). Using field and petrographic observations, the stratigraphy was subdivided into four major depositional groups including: upper shoreface (composed of skeletal/peloid grainstones-packstones), lower shoreface (skeletal packstones-wackestones), and moderately to poorly oxygenated offshore (bioturbated skeletal lime mudstones-wackestones and lime mudstones) (Figure 2). The lime mudstone that represents a low-energy environment is a dominant part of the Eifelian (~ 300 - 600 m; Figure 3). Tentaculinids are found in mudstones of the lower *australis* zone of the Eifelian (325 - 370 m). Skeletal wackestone and

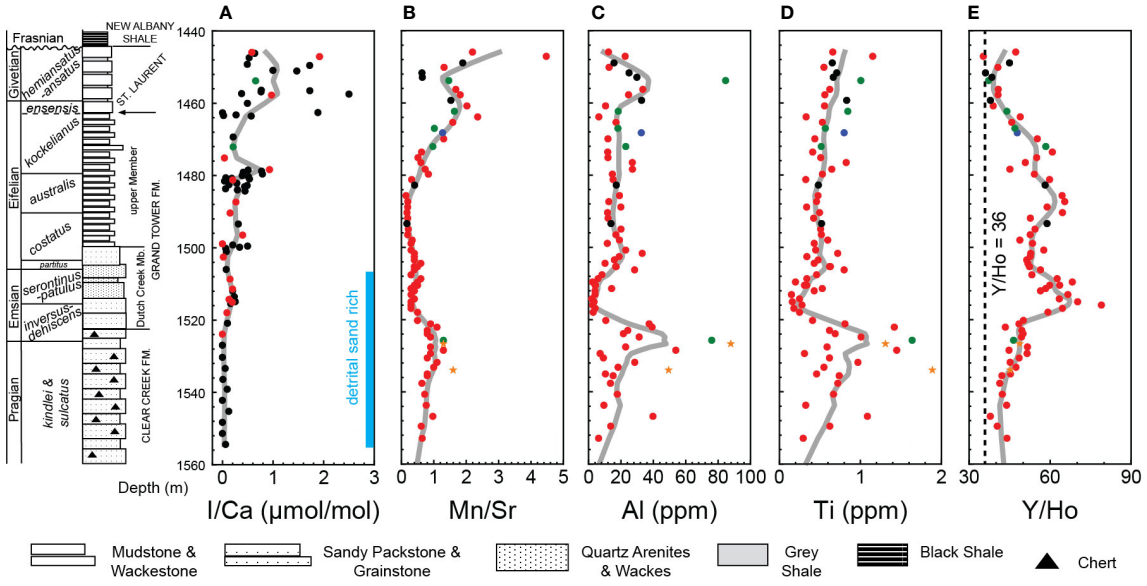

FIGURE 4
Geochemical measurements from the Illinois Basin core. **(A)** Carbonate lithology-specific I/Ca ratios, **(B)** Mn/Sr ratios, **(C)** Al concentration, **(D)** Ti concentration, **(E)** Y/Ho ratios. The gray curves show the results of LOWESS smoothing. The black dashed line in **(E)** shows Y/Ho = 36. Values higher than 36 indicate primary marine REEs signals [e.g., Ling et al. (2013)]. Note all the results were measured from the carbonate fraction. The Pragian-Emsian portion is rich in quartz sands (blue vertical line). Samples of **(A)** and samples of **(B–E)** are from the same core but not measured from same depth. Color code for lithological groups: grainstone (red), packstone (blue), wackestone (green), lime mudstone (purple), unassigned (black). Brown stars in Pragian of **(B–E)** represent quartz sandstones with calcite cements.

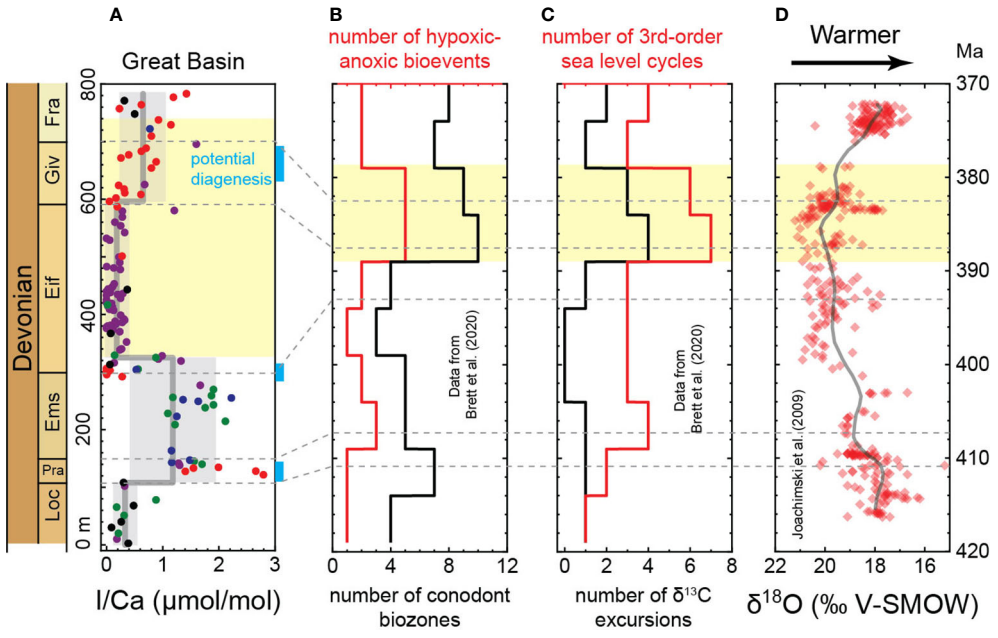

FIGURE 5
I/Ca ratios of the Great Basin section and compiled Devonian environmental and biotic parameters. **(A)** Stratigraphic trends of I/Ca are subdivided into four intervals; the straight gray lines represent averages of I/Ca within each interval, and the gray boxes show the ranges of one standard deviation. **(B, C)** Numbers of conodont biozones, hypoxic/anoxic-related bioevents, carbon isotope excursions, global sea level changes within Devonian time bins of 5 Myr durations. Data are modified from Tables 2 and 4 of Brett et al. (2020) and we used the subdivided zonation for conodont zones here. **(D)** Global records of oxygen isotopes of conodont apatite (Joachimski et al., 2009). The gray curve in **(D)** represents locfit regression of Joachimski et al. (2009). The gray dashed lines correlate the Great Basin stage boundaries to those of the compiled datasets. The yellow boxes highlight the intervals of highest volatility identified by Brett et al. (2020). Color code for lithological groups: grainstone (red), packstone (blue), wackestone (green), lime mudstone (purple), unassigned (black).

packstone compose most of the Lower Devonian (Figure 3). Skeletal grainstones are observed in the Pragian and the grainstones with crinoid can be found in the bottom of the Eifelian. Last, the Givetian and Frasnian contain abundant peloid grainstones. Therefore, the four facies are unevenly distributed throughout the composite section (Figure 3). The stratigraphic I/Ca trends of each facies are plotted individually (Figure 3B) to investigate the influence of carbonate facies on I/Ca values. We found I/Ca ratios of each facies consistently show similar stratigraphic trends as the overall trend that combines all the facies, except the succession of Emsian grainstones due to the absence of samples (Figures 3A, B). Moreover, all four facies have a wide range of I/Ca values (Figure 3). For example, relatively low Lochkovian and Eifelian I/Ca values occur in all four facies and the same is true of the higher I/Ca values that occur in the Emsian, late Givetian and early Frasnian (Figure 3B). In addition, I/Ca trends show no systematic variations across eustatically generated, Myr-scale, sequence boundaries, except for relatively abrupt I/Ca changes near the two Lower Devonian unconformities (Figure 3). Therefore, the lithological variation across the composite section does not have a major influence on stratigraphic I/Ca trends.

The majority of the Illinois Basin samples are composed of shallow-water crinoidal grainstones with minor calcite-cemented quartz sandstone in the Pragian and skeletal wackestone and packstone in the upper Eifelian to Givetian. The predominance of grainstone limits robust evaluation of relationships between the full range carbonate facies types and I/Ca values (Figure 4A). The Pragian to Emsian grainstones contain abundant quartz sands and the rock type records lower I/Ca ratios (Figure 4). The detrital quartz component is likely related to fluvial input during long-term eustatic sea level lowstand. The influx of fluvial waters with lower iodine concentrations may explain the lower I/Ca values in this interval.

This approach of reporting detailed carbonate lithology along with bulk rock I/Ca measurements may have important potential in assisting the interpretations of bulk carbonate I/Ca analyses. It is a logic similar to utilizing species-specific foraminiferal records during the Cenozoic (e.g., Zachos et al., 2001). We suggest this approach be adopted in future deep-time I/Ca carbonate studies.

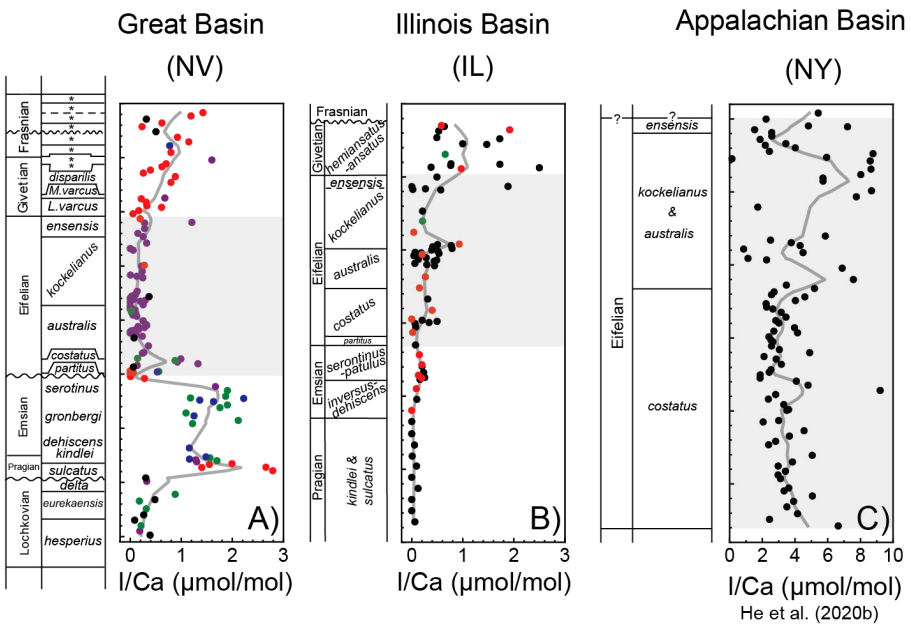

FIGURE 6
I/Ca comparisons among the three basins: **(A)** Great Basin, **(B)** Illinois Basin, **(C)** Appalachian Basin (He et al., 2020b). Gray shadings identify the Eifelian interval overlapping between all three basins for comparison. A closer comparison for the Eifelian stage is in Supplementary Figure S2. Color code for lithological groups: grainstone (red), packstone (blue), wackestone (green), lime mudstone (purple), unassigned (black). *Conodont zones not labelled are (in ascending order): *norrisi, MN 1-2, MN 3, MN 6, hassi-jamieae, l. rhenana, u. rhenana, linguiformis*.

5.2 Diagenetic influences

A detailed study of Neogene-Quaternary Bahamian carbonates evaluated I/Ca values of diagenetically altered samples and documented that diagenesis (including dolomitization) reduced rather than increased original I/Ca values in all cases (Hardisty et al., 2017).

In the Great Basin, thin section observation indicates that grainstones contain abundant early marine cements, especially in the Pragian, Eifelian, Givetian, and Frasnian (labeled in Figure 3A). Thus, it suggests the grainstones may have experienced some level of diagenetic iodate loss. Therefore, the occurrence of grainstones throughout the Great Basin section and the potential for diagenetic iodate loss may explain some of the observed I/Ca trends. For example, fluctuating Givetian-Frasnian I/Ca values may represent the effects of intermittent diagenetic iodate loss rather than original fluctuating redox conditions (Figure 3A). Mn/Sr values also aid in evaluating the effects of diagenesis. Due to the difference in mobility of Sr and Mn, higher Mn/Sr ratios are usually generated after stronger rock-fluid reactions with reducing fluids and can be used to evaluate the overprint from diagenesis (Lohmann, 1988). Relatively low Mn/Sr (<2) ratios throughout the section suggest the interaction with Mn-rich anoxic porewater was limited. Low Mg/Ca ratios (with most ratios <0.1 mol/mol) suggest dolomitization was minor (Supplementary Table 1).

In the Illinois Basin, limestone samples of Pragian to Emsian contain abundant detrital quartz sands with calcite cements (Figure 4). This calls into question the primary nature of the I/Ca signal in this interval and the influences due to diagenesis. Future work that details the I/Ca values from specific components of heterogenous limestones or additional samples from better preserved sections are required to interpret whether the observed signal records primary or altered redox trends. Mn/Sr values are lower than 2 for most of the samples, except for the uppermost Eifelian to lower Givetian where Mn/Sr values reach up to 4.5 (Figure 4B). If this part of the section with higher Mn/Sr values reflects a more diagenetically altered interval, original I/Ca ratios could have been higher due to diagenetic iodate loss (Figure 4). Last, the overall low Mg/Ca (most ratios < 0.1 mol/mol) also suggests limited dolomitization (Supplementary Table 3).

5.3 Local redox conditions of Great Basin and Illinois Basin

5.3.1 Great Basin

Although some grainstone samples of the Great Basin section may have been influenced by the diagenetic iodine loss (Figure 3A), I/Ca values of grainstones are not consistently low (especially the Pragian and Frasnian) and they still follow the stratigraphic trend of other facies (Figure 3B), suggesting

diagenesis may not totally erase the original signals. Therefore, combining with data from other facies, it is possible that our I/Ca data captures general trends in local primary seawater redox. If correct, relatively higher I/Ca values of the Pragian-Emsian suggest the local seawater may have been more oxic during Early Devonian, except the Lochkovian. On the other hand, a relatively lower I/Ca background during the Eifelian may be related to more anoxic conditions; in addition, more oxic conditions may have developed locally in the Givetian and Frasnian, indicated by higher I/Ca values. It should be noted that the low I/Ca values may reflect carbonate precipitation from waters close to the OMZ or oxycline, rather than directly within anoxic waters, because recent studies suggested that the I/Ca sometimes is more related to a mixing of regional marine redox environments rather than *in situ* processes (Lu et al., 2020a; Hardisty et al., 2021).

5.3.2 Illinois Basin

Illinois I/Ca trends do not match the Great Basin, especially during the Pragian-Emsian, with consistently low I/Ca ratios close to 0 μmol/mol (Figure 4A). If diagenesis did not uniformly reset I/Ca ratios of these samples to nearly 0 μmol/mol during the Eifelian, the relatively low I/Ca background of the Eifelian is consistent with the anoxic conditions recorded in the Great Basin. From the late Eifelian to early Givetian, the overall increased I/Ca values indicate increased local oxygenation (Figure 4A). The fluctuating I/Ca signal during this interval may be related to a frequently shifting redox conditions or simply reflect diagenetic iodate loss considering the higher Mn/Sr ratios found at this interval (Figure 4).

5.4 Inter-basinal comparison: influence of paleogeography

Paleogeography can influence I/Ca as a local redox proxy, since iodine chemistry in the water column can be influenced by local hydrography, local redox, and also major changes in global ocean conditions (e.g., Zhou et al., 2015). Based on the paleogeographic reconstructions (Figure 1 and Morrow and Sandberg, 2008), the Great Basin section was located along the western margin of Laurussia and connected directly to the Panthalassic Ocean during the Devonian. Development of an OMZ is very common in western continental margins in the tropics and subtropics (Hay, 1995), such as the modern eastern tropical Pacific where the upwelling-driven productivity and poor ventilation result in a large OMZ. Although the Devonian Great Basin was a shallow epeiric sea, its redox condition can still be influenced by OMZ that may have developed along the west margin of Laurussia. In contrast, the Illinois and Appalachian basins were isolated epeiric sea basins situated in central and eastern margin of Laurussia continent at higher latitudes (~ 30°S; Figure 1). The I/Ca range found in the Great Basin is lower than that of the Appalachian Basin (e.g., during the Eifelian; Figures 6 and S2). During the Late Ordovician, a western Laurentia continental margin site closer to the upwelling and OMZ also had a relatively lower range of I/Ca than the section from eastern Laurentia (Pohl et al., 2021), suggesting similar paleogeographical redox patterns.

The different stratigraphic I/Ca trends and ranges in Appalachian and Illinois Basins may also be related to the variable restriction to the Panthalassic Ocean. The paleoceanographic conditions of Devonian epeiric seas (i.e., Illinois and Appalachian basins) are not well-constrained. The difference between the Eifelian I/Ca trends in the Illinois Basin and Appalachian Basin is likely due to the >1500 km distance between the locations, physical separation by exposed arches and sills during lower eustatic sea levels of the Early-Middle Devonian. This interpretation of lateral redox and salinity changes in the Middle Devonian epeiric seaway is consistent with the super-estuarine circulation model in which the lateral advection of deeper water from open ocean controls the redox condition of epeiric seas (Algeo et al., 2008) and spatially heterogenous Fe speciation and trace metals within Late Devonian Appalachian Basin (Gilleaudeau et al., 2021). The uniformly low I/Ca background (nearly 0 μmol/mol) of Pragian-Emsian Illinois Basin strata may also be related to mixing with fresh water from fluvial discharge during lower eustatic sea levels. Although the modern seawater-like Y/Ho ratios (>36) suggest a deposition in a marine environment, terrestrial sand content and elevated Al and Ti concentration indicate the contribution from terrestrial processes cannot be excluded (Figure 4 and the section 2 of Supplementary Discussion).

5.5 Devonian seawater redox conditions

Both proxy (Mo isotope, U isotope, I/Ca ratio, Ce anomaly and charcoal abundance) and model (COPSE and GEOCARBSULF) results suggest atmospheric pO_2 levels increased during the Devonian (Dahl et al., 2010; Glasspool and Scott, 2010; Lenton et al., 2016; Wallace et al., 2017; Krause et al., 2018; Lu et al., 2018; Elrick et al., 2022). The increase in I/Ca ratios from Lochkovian to Emsian in the Great Basin section (Figure 3A) could be related to the rise of atmospheric oxygen levels impacting the upper ocean. Since I/Ca itself is a local marine redox proxy and not a direct proxy for atmospheric oxygen levels, I/Ca data from multiple locations in addition to Laurussia or additional evidence from independent global redox proxies will be required to pin down the timing of Devonian pO_2 rise.

5.6 Devonian environmental volatility

As the publications of high-resolution radiometric ages for the Devonian accumulate, Brett et al. (2020) are able to

investigate the environmental volatility based on the frequency of fluctuations in environmental and biotic parameters, including SST, $\delta^{13}C$, eustasy, and hypoxic or anoxia-induced biotic turnovers/extinctions (Figure 5). A higher environmental volatility is usually considered as more frequent occurrences of environmental and biotic events over a given interval of time (e.g., number of events per million years). Brett et al. (2020) suggests a relatively less volatile interval from the Lochkovian to middle Eifelian, followed by peak environmental volatility during the late Eifelian through early Frasnian with more frequent occurrences of biozone turnover, hypoxic-anoxic events, C isotope excursions and sea level changes (Figures 5B, C). The mechanism behind the increased environmental volatility is not well understood; however, this time interval coincides with lower SST (Joachimski et al., 2009), orbital-scale glacio-eustasy (Elrick and Witzke, 2016), more frequent Myr-scale sea-level changes, and increased continental weathering (van Geldern et al., 2006) (Figure 5).

Here, we compare the Devonian environmental volatility with I/Ca ratios from Great Basin under the assumption that it may record the most primary seawater redox trends. The more oxygenated upper ocean conditions during the Pragian-Emsian of the Great Basin, suggested by the higher I/Ca ratios, are consistent with the notion of relatively stable Early Devonian biotic environments (Figure 5). The onset of high-volatility environments starts at the late Eifelian (Brett et al., 2020). Due to an unconformity along the Emsian-Eifelian boundary (missing *partitus* and parts of *serotinus* and *patulus* zones) and low sedimentation rates (especially for the *costatus* zone), the lower Eifelian is very thin in the Great Basin section (Figure 3). Therefore, the boundary between the *costatus* and *australis* zones of upper Eifelian at ~ 325 m is equivalent to the onset of high volatility (Figures 3, 5). I/Ca trends in the Great Basin suggest an expansion of OMZ from the early into the late Eifelian, followed by OMZ fluctuations during Givetian-Frasnian, so the I/Ca data largely echoes the reconstructed environmental volatility (though not strictly with a one-to-one match). Even though I/Ca data from a single location records local redox conditions, the redox changes can still mimic the global ocean redox evolution (Lu et al., 2020b). It is not unreasonable to suggest that the local Great Basin water column captured some fundamental changes in global redox trends, considering the coincidence between I/Ca ratios and environmental volatility and the proximity and connectedness to the Panthalassic Ocean.

Previous studies interpret that many Devonian bio-events, for example Taghanic, Kellwasser, Hangenberg and other less significant events that are classified by Becker et al. (2016) as extinctions at lower taxonomic level (such as genera and species) with fewer groups, were the result of expanded anoxia (e.g., Zambito et al., 2012; Formolo et al., 2014; White et al., 2018; Liu et al., 2019; Zhang et al., 2020). In this study, although the frequent occurrences of biozone turnovers and bio-events in the late Eifelian to early Frasnian correlate with overall more reducing conditions in the Great Basin, we do not find a one-for-one co-variation between upper ocean redox conditions in our Great Basin section and those less significant bio-events. It indicates that ocean deoxygenation may not be the sole trigger for all the later Devonian bio-events.

6 Conclusion

Carbonate lithology-specific I/Ca data from Early to Late Devonian (Lochkovian to Frasnian) limestones accumulating in the Great Basin and Illinois Basin of Laurussia indicates that the overall I/Ca trends are not systematically influenced by lithology or eustatic sea-level changes. Upper ocean redox trends in the Great Basin are characterized by higher I/Ca values (more oxic conditions) in the Pragian-Emsian, a shift to lower values (more reducing conditions) in the Eifelian, followed by slightly higher and fluctuating I/Ca trends in the Givetian and Frasnian. The more reducing and fluctuating redox conditions in the Middle and Late Devonian are coincident with previously interpreted intervals of high environmental volatility. Illinois Basin I/Ca trends record low values (reducing conditions) in the Pragian-Emsian followed by increasing and fluctuating values in the Eifelian-Givetian. The different I/Ca signals between the two basins are likely related to variations in local upper ocean redox, hydrographic conditions associated with varying paleogeography and eustasy, and/or diagenesis. To further evaluate global versus local redox evolution of Devonian oceans, other I/Ca records and independent redox proxies from other locations are required along with additional indicators of diagenesis.

Data availability statement

The original contributions presented in the study are included in the article/Supplementary Material. Further inquiries can be directed to the corresponding author.

Author contributions

RH and ZL designed the study. RH wrote the draft with input from all coauthors. RH and WL carried out the I/Ca analyses. ME and JD collected samples. ME carried out lithologic analyses. All authors contributed to the article and approved the submitted version.

Funding

Partial funding for this study was provided by the National Science Foundation (OCE-1232620 and EAR-2121445 to ZL; EAR-1733991 to ME).

Acknowledgments

We would like to thank Charles Diamond, a reviewer, the guest editor Dalton Hardisty and two reviewers of an earlier submission for their constructive comments and suggestions. RH thanks the support from the Research Excellence Doctoral Funding (REDF) Fellowships of Syracuse University.

Conflict of interest

The authors declare that the research was conducted in the absence of any commercial or financial relationships that could be construed as a potential conflict of interest.

Publisher's note

All claims expressed in this article are solely those of the authors and do not necessarily represent those of their affiliated organizations, or those of the publisher, the editors and the reviewers. Any product that may be evaluated in this article, or claim that may be made by its manufacturer, is not guaranteed or endorsed by the publisher.

Supplementary material

The Supplementary Material for this article can be found online at: https://www.frontiersin.org/articles/10.3389/fmars.2022.874759/full#supplementary-material

References

Algeo, T. J., Heckel, P. H., Maynard, J. B., Blakey, R., Rowe, H., Pratt, B., et al. (2008). "Modern and ancient epeiric seas and the super-estuarine circulation model of marine anoxia," in *Dynamics of epeiric seas: sedimentological, paleontological and geochemical perspectives*, vol. 48. (St. John's, Canada: Geological Association of Canada, Special Publication), 7–38.

Algeo, T. J., and Scheckler, S. E. (1998). Terrestrial-marine teleconnections in the Devonian: links between the evolution of land plants, weathering processes, and marine anoxic events. *Philos. Trans. R. Soc. London. Ser. B.: Biol. Sci.* 353, 113–130. doi: 10.1098/rstb.1998.0195

Becker, R. T., Königshof, P., and Brett, C. E. (2016). Devonian Climate, sea level and evolutionary events: an introduction. *Geologic. Soc. London. Special. Publications.* 423, 1–10. doi: 10.1144/SP423.15

Becker, R. T., Marshall, J. E. A., Da Silva, A. C., Agterberg, F. P., Gradstein, F. M., and Ogg, J. G. (2020). The Devonian period. *Geologic. Time. Scale.*, 733–810. doi: 10.1016/B978-0-12-824360-2.00022-X

Blakey, R. (2018) *Paleogeography and geologic evolution of north America*. Available at: https://deeptimemaps.com/ (Accessed March 2018).

Bowman, C. N., Lindskog, A., Kozik, N. P., Richbourg, C. G., Owens, J. D., and Young, S. A. (2020). Integrated sedimentary, biotic, and paleoredox dynamics from multiple localities in southern laurentia during the late Silurian (Ludfordian) extinction event. *Palaeogeogr. Palaeoclimatol. Palaeoecol.* 553, 109799. doi: 10.1016/j.palaeo.2020.109799

Brett, C. E., Zambito, J. J., McLaughlin, P. I., and Emsbo, P. (2020). Revised perspectives on Devonian biozonation and environmental volatility in the wake of recent time-scale revisions. *Palaeogeogr. Palaeoclimatol. Palaeoecol.* 549, 733–810. doi: 10.1016/j.palaeo.2018.06.037

Buschbach, T. C., and Kolata, D. R. (1990). *Regional setting of Illinois basin: chapter 1: part i. Illinois basin: regional setting*. AAPG MEMOIR.

Dahl, T. W., and Arens, S. K. M. (2020). The impacts of land plant evolution on earth's climate and oxygenation state – an interdisciplinary review. *Chem. Geology.* 547, 119665. doi: 10.1016/j.chemgeo.2020.119665

Dahl, T. W., Hammarlund, E. U., Anbar, A. D., Bond, D. P., Gill, B. C., Gordon, G. W., et al. (2010). Devonian Rise in atmospheric oxygen correlated to the radiations of terrestrial plants and large predatory fish. *Proc. Natl. Acad. Sci.* 107, 17911–17915. doi: 10.1073/pnas.1011287107

Day, J. E., Gouwy, S., and MacLeod, K. G. (2012). *Lower-middle Devonian (Pragian-lower givetian) conodont biostratigraphy, middle Devonian sea level record and estimated conodont apatite $\delta^{18}O$ sea surface temperature changes in the southern Illinois basin, USA*. GSA Annual Meeting, Charlotte, North Carolina, USA

Dunham, R. J. (1962). *Classification of carbonate rocks according to depositional textures*.

Elderfield, H., and Truesdale, V. W. (1980). On the biophilic nature of iodine in seawater. *Earth Planetary. Sci. Lett.* 50, 105–114. doi: 10.1016/0012-821X(80)90122-3

Elick, J. M., Driese, S. G., and Mora, C. I. (1998). Very large plant and root traces from the early to middle Devonian: Implications for early terrestrial ecosystems and atmospheric p(CO2). *Geology* 26:143–146. doi: 10.1130/0091-7613(1998)026<0143:VLPART>2.3.CO;2

Elrick, M., Gilleaudeau, G. J., Romaniello, S. J., Algeo, T. J., Morford, J. L., Sabbatino, M., et al. (2022). Major early-middle Devonian oceanic oxygenation linked to early land plant evolution detected using high-resolution U isotopes of marine limestones. *Earth Planetary. Sci. Lett.* 581:117410. doi: 10.1016/j.epsl.2022.117410

Elrick, M., and Witzke, B. (2016). Orbital-scale glacio-eustasy in the middle Devonian detected using oxygen isotopes of conodont apatite: Implications for long-term greenhouse–icehouse climatic transitions. *Palaeogeogr. Palaeoclimatol. Palaeoecol.* 445, 50–59. doi: 10.1016/j.palaeo.2015.12.019

Fehn, U. (2012). Tracing crustal fluids: Applications of natural 129I and 36Cl. *Annu. Rev. Earth Planetary. Sci.* 40, 45–67. doi: 10.1146/annurev-earth-042711-105528

Feng, X., and Redfern, S. A. T. (2018). Iodate in calcite, aragonite and vaterite CaCO3: Insights from first-principles calculations and implications for the I/Ca geochemical proxy. *Geochimica. Cosmochim. Acta* 236, 351–360. doi: 10.1016/j.gca.2018.02.017

Formolo, M. J., Riedinger, N., and Gill, B. C. (2014). Geochemical evidence for euxinia during the late Devonian extinction events in the Michigan basin (U.S.A.). *Palaeogeogr. Palaeoclimatol. Palaeoecol.* 414, 146–154. doi: 10.1016/j.palaeo.2014.08.024

Gensel, P. G., and Andrews, H. N. (1987). The evolution of early land plants. *Am. Scientist.* 75, 478–489. Available at: https://www.jstor.org/stable/27854789

Gilleaudeau, G. J., Algeo, T. J., Lyons, T. W., Bates, S., and Anbar, A. D. (2021). Novel watermass reconstruction in the early Mississippian Appalachian seaway based on integrated proxy records of redox and salinity. *Earth Planetary. Sci. Lett.* 558:116746. doi: 10.1016/j.epsl.2021.116746

Glasspool, I. J., and Scott, A. C. (2010). Phanerozoic concentrations of atmospheric oxygen reconstructed from sedimentary charcoal. *Nat. Geosci.* 3, 627. doi: 10.1038/ngeo923

Hardisty, D. S., Horner, T. J., Evans, N., Moriyasu, R., Babbin, A. R., Wankel, S. D., et al. (2021). Limited iodate reduction in shipboard seawater incubations from the Eastern tropical north pacific oxygen deficient zone. *Earth Planetary. Sci. Lett.* 554:116676. doi: 10.1016/j.epsl.2020.116676

Hardisty, D., Horner, T., Wankel, S., Blusztajn, J., and Nielsen, S. (2020). Experimental observations of marine iodide oxidation using a novel sparge-interface MC-ICP-MS technique. *Chem. Geol.* 532, 119360. doi: 10.1016/j.chemgeo.2019.119360

Hardisty, D. S., Lu, Z., Bekker, A., Diamond, C. W., Gill, B. C., Jiang, G., et al. (2017). Perspectives on proterozoic surface ocean redox from iodine contents in ancient and recent carbonate. *Earth Planetary. Sci. Lett.* 463, 159–170. doi: 10.1016/j.epsl.2017.01.032

Hay, W. W. (1995). Paleoceanography of marine organic-carbon-rich sediments: A. Y. Huc (ed.), Paleogeography, Paleoclimate and Source Rocks, American Association of Petroleum Geologists Memoir 40, 21–59. doi: 10.1306/St40595C2

He, R., Jiang, G., Lu, W., and Lu, Z. (2020a). Iodine records from the ediacaran doushantuo cap carbonates of the Yangtze block, south China. *Precambrian. Res.* 347:105843. doi: 10.1016/j.precamres.2020.105843

He, R., Lu, W., Junium, C. K., Ver Straeten, C. A., and Lu, Z. (2020b). Paleo-redox context of the mid-Devonian Appalachian basin and its relevance to biocrises. *Geochimica. Cosmochim. Acta* 287, 328–340. doi: 10.1016/j.gca.2019.12.019

House, M. R. (2002). Strength, timing, setting and cause of mid-Palaeozoic extinctions. *Palaeogeogr. Palaeoclimatol. Palaeoecol.* 181, 5–25. doi: 10.1016/S0031-0182(01)00471-0

Joachimski, M. M., Breisig, S., Buggisch, W., Talent, J. A., Mawson, R., Gereke, M., et al. (2009). Devonian Climate and reef evolution: Insights from oxygen isotopes in apatite. *Earth Planetary. Sci. Lett.* 284, 599–609. doi: 10.1016/j.epsl.2009.05.028

Johnson, J., Klapper, G., and Elrick, M. (1996). Devonian Transgressive-regressive cycles and biostratigraphy, northern antelope range, Nevada: establishment of reference horizons for global cycles. *Palaios* 11(1):3–14. doi: 10.2307/3515112

Johnson, J., Klapper, G., and Sandberg, C. A. (1985). Devonian Eustatic fluctuations in euramerica. *Geologic. Soc. America Bull.* 96, 567–587. doi: 10.1130/0016-7606(1985)96<567:DEFIE>2.0.CO;2

Johnson, J., and Murphy, M. (1984). Time-rock model for siluro-Devonian continental shelf, western united states. *Geologic. Soc. America Bull.* 95, 1349–1359. doi: 10.1130/0016-7606(1984)95<1349:TMFSCS>2.0.CO;2

Kennedy, H., and Elderfield, H. (1987a). Iodine diagenesis in non-pelagic deep-sea sediments. *Geochimica. Cosmochim. Acta* 51, 2505–2514. doi: 10.1016/0016-7037(87)90301-2

Kennedy, H., and Elderfield, H. (1987b). Iodine diagenesis in pelagic deep-sea sediments. *Geochimica. Cosmochim. Acta* 51, 2489–2504. doi: 10.1016/0016-7037(87)90300-0

Kenrick, P., and Strullu-Derrien, C. (2014). The origin and early evolution of roots. *Plant Physiol.* 166, 570–580. doi: 10.1104/pp.114.244517

Kolata, D. R., and Nelson, W. J. (1990). *Tectonic history of the Illinois basin: Chapter 18: Part i. Illinois basin: Evolution.*

Krause, A. J., Mills, B. J., Zhang, S., Planavsky, N. J., Lenton, T. M., and Poulton, S. W. (2018). Stepwise oxygenation of the Paleozoic atmosphere. *Nat. Commun.* 9, 4081. doi: 10.1038/s41467-018-06383-y

Kump, L. (1988). Terrestrial feedback in atmospheric oxygen regulation by fire and phosphorus. *Nature* 335, 152. doi: 10.1038/335152a0

Küpper, F. C., Feiters, M. C., Olofsson, B., Kaiho, T., Yanagida, S., Zimmermann, M. B., et al. (2011). Commemorating two centuries of iodine research: an interdisciplinary overview of current research. *Angewandte. Chemie. Int. Edition.* 50, 11598–11620. doi: 10.1002/anie.201100028

Lash, G. G., and Blood, D. R. (2014). Organic matter accumulation, redox, and diagenetic history of the Marcellus formation, southwestern Pennsylvania, Appalachian basin. *Mar. Petroleum. Geology.* 57, 244–263. doi: 10.1016/j.marpetgeo.2014.06.001

Lenton, T. M., Dahl, T. W., Daines, S. J., Mills, B. J., Ozaki, K., Saltzman, M. R., et al. (2016). Earliest land plants created modern levels of atmospheric oxygen. *Proc. Natl. Acad. Sci.* 113, 9704–9709. doi: 10.1073/pnas.1604787113

Ling, H.-F., Chen, X., Li, D., Wang, D., Shields-Zhou, G. A., and Zhu, M. (2013). Cerium anomaly variations in ediacaran–earliest Cambrian carbonates from the Yangtze gorges area, south China: Implications for oxygenation of coeval shallow seawater. *Precambrian. Res.* 225, 110–127. doi: 10.1016/j.precamres.2011.10.011

Liu, J., Luo, G., Lu, Z., Lu, W., Qie, W., Zhang, F., et al. (2019). Intensified ocean deoxygenation during the end Devonian mass extinction. *Geochem. Geophys. Geosyst.* 20, 6187–6198. doi: 10.1029/2019GC008614

Lohmann, K. C. (1988). *Geochemical patterns of meteoric diagenetic systems and their application to studies of paleokarst, paleokarst* (Springer), 58–80. Springer, New York, NY.

Lu, W., Dickson, A. J., Thomas, E., Rickaby, R. E. M., Chapman, P., and Lu, Z. (2020a). Refining the planktic foraminiferal I/Ca proxy: Results from the southeast Atlantic ocean. *Geochimica. Cosmochim. Acta* 287, 318–327. doi: 10.1016/j.gca.2019.10.025

Lu, Z., Jenkyns, H. C., and Rickaby, R. E. M. (2010). Iodine to calcium ratios in marine carbonate as a paleo-redox proxy during oceanic anoxic events. *Geology* 38, 1107–1110. doi: 10.1130/G31145.1

Lu, Z., Lu, W., Rickaby, R. E., and Thomas, E. (2020b). Earth History of Oxygen and the iprOxy (Elements in Geochemical Tracers in Earth System Science). Cambridge: Cambridge University Press. doi: 10.1017/9781108688604

Lu, W., Ridgwell, A., Thomas, E., Hardisty, D. S., Luo, G., Algeo, T. J., et al. (2018). Late inception of a resiliently oxygenated upper ocean. *Science* 361, 174–177. doi: 10.1126/science.aar5372

Lu, W., Wörndle, S., Halverson, G., Zhou, X., Bekker, A., Rainbird, R., et al. (2017). Iodine proxy evidence for increased ocean oxygenation during the bitter springs anomaly. *Geochem. Perspect. Lett.* 5, 53–57. doi: 10.7185/geochemlet.1746

Meyer-Berthaud, B., Scheckler, S. E., and Wendt, J. (1999). Archaeopteris is the earliest known modern tree. *Nature* 398, 700–701. doi: 10.1038/19516

Morrow, J. R., and Sandberg, C. A. (2008). Evolution of Devonian carbonate-shelf margin, Nevada. *Geosphere* 4:445–458. doi: 10.1130/GES00134.1

Murphy, A. E., Sageman, B. B., Hollander, D. J., Lyons, T. W., and Brett, C. E. (2000). Black shale deposition and faunal overturn in the Devonian Appalachian basin: Clastic starvation, seasonal water-column mixing, and efficient biolimiting nutrient recycling. *Paleoceanography* 15, 280–291. doi: 10.1029/1999PA000445

Podder, J., Lin, J., Sun, W., Botis, S. M., Tse, J., Chen, N., et al. (2017). Iodate in calcite and vaterite: Insights from synchrotron X-ray absorption spectroscopy and first-principles calculations. *Geochimica. Cosmochim. Acta* 198, 218–228. doi: 10.1016/j.gca.2016.11.032

Pohl, A., Lu, Z., Lu, W., Stockey, R. G., Elrick, M., Li, M., et al. (2021). Vertical decoupling in late Ordovician anoxia due to reorganization of ocean circulation. *Nat. Geosci.* 14, 868–873. doi: 10.1038/s41561-021-00843-9

Rimmer, S. M. (2004). Geochemical paleoredox indicators in Devonian–Mississippian black shales, central Appalachian basin (USA). *Chem. Geology.* 206, 373–391. doi: 10.1016/j.chemgeo.2003.12.029

Sageman, B. B., Murphy, A. E., Werne, J. P., Ver Straeten, C. A., Hollander, D. J., and Lyons, T. W. (2003). A tale of shales: the relative roles of production, decomposition, and dilution in the accumulation of organic-rich strata, middle–upper Devonian, Appalachian basin. *Chem. Geology.* 195, 229–273. doi: 10.1016/S0009-2541(02)00397-2

Shang, M., Tang, D., Shi, X., Zhou, L., Zhou, X., Song, H., et al. (2019). A pulse of oxygen increase in the early mesoproterozoic ocean at ca. 1.57–1.56 Ga. *Earth Planetary. Sci. Lett.* 527, 115797. doi: 10.1016/j.epsl.2019.115797

Stein, W. E., Mannolini, F., Hernick, L. V., Landing, E., and Berry, C. M. (2007). Giant cladoxylopsid trees resolve the enigma of the earth's earliest forest stumps at gilboa. *Nature* 446, 904–907. doi: 10.1038/nature05705

Truesdale, V. W., and Bailey, G. W. (2000). Dissolved iodate and total iodine during an extreme hypoxic event in the southern benguela system. *Estuar. Coast. Shelf. Sci.* 50, 751–760. doi: 10.1006/ecss.2000.0609

van Geldern, R., Joachimski, M. M., Day, J., Jansen, U., Alvarez, F., Yolkin, E. A., et al. (2006). Carbon, oxygen and strontium isotope records of Devonian brachiopod shell calcite. *Palaeogeogr. Palaeoclimatol. Palaeoecol.* 240, 47–67. doi: 10.1016/j.palaeo.2006.03.045

Wallace, M. W., Shuster, A., Greig, A., Planavsky, N. J., and Reed, C. P. (2017). Oxygenation history of the neoproterozoic to early phanerozoic and the rise of land plants. *Earth Planetary. Sci. Lett.* 466, 12–19. doi: 10.1016/j.epsl.2017.02.046

Werne, J. P., Sageman, B. B., Lyons, T. W., and Hollander, D. J. (2002). An integrated assessment of a "type euxinic" deposit: evidence for multiple controls on black shale deposition in the middle Devonian oatka creek formation. *Am. J. Sci.* 302, 110–143. doi: 10.2475/ajs.302.2.110

White, D. A., Elrick, M., Romaniello, S., and Zhang, F. (2018). Global seawater redox trends during the late Devonian mass extinction detected using U isotopes of marine limestones. *Earth Planetary. Sci. Lett.* 503, 68–77. doi: 10.1016/j.epsl.2018.09.020

Wong, G. T., and Brewer, P. G. (1977). The marine chemistry of iodine in anoxic basins. *Geochimica et Cosmochimica Acta.* 41, 151–159. doi: 10.1016/0016-7037(77)90195-8

Zachos, J., Pagani, M., Sloan, L., Thomas, E., and Billups, K. (2001). Trends, rhythms, and aberrations in global climate 65 ma to present. *science* 292, 686–693.doi: 10.1126/science.1059412

Zambito, J. J., Brett, C. E., and Baird, G. C. (2012). The late middle Devonian (Givetian) global taghanic biocrisis in its type area (Northern Appalachian basin): Geologically rapid faunal transitions driven by global and local environmental changes. *Earth Life*, 677–703.doi: 10.1007/978-90-481-3428-1_22

Zhang, F., Dahl, T. W., Lenton, T. M., Luo, G., Shen, S.-Z., Algeo, T. J., et al. (2020). Extensive marine anoxia associated with the late Devonian hangenberg crisis. *Earth Planetary. Sci. Lett.* 533:115976. . doi: 10.1016/j.epsl.2019.115976

Zhou, X., Jenkyns, H. C., Owens, J. D., Junium, C. K., Zheng, X.-Y., Sageman, B. B., et al. (2015). Upper ocean oxygenation dynamics from I/Ca ratios during the cenomanian-turonian OAE 2. *Paleoceanography* 30, 510–526.doi: 10.1002/2014PA002741

Zhou, X., Thomas, E., Rickaby, R. E. M., Winguth, A. M. E., and Lu, Z. (2014). I/Ca evidence for upper ocean deoxygenation during the PETM. *Paleoceanography* 29, 964–975.doi: 10.1002/2014PA002702

Zhou, X., Thomas, E., Winguth, A. M. E., Ridgwell, A., Scher, H., Hoogakker, B. A. A., et al. (2016). Expanded oxygen minimum zones during the late Paleocene-early Eocene: Hints from multiproxy comparison and ocean modeling. *Paleoceanography* 31, 1532–1546. doi: 10.1002/2016PA003020

frontiers | Frontiers in Marine Science

TYPE Original Research
PUBLISHED 02 February 2023
DOI 10.3389/fmars.2023.1095570

Check for updates

OPEN ACCESS

EDITED BY
Khan M. G. Mostofa,
Tianjin University, China

REVIEWED BY
Ralf Schiebel,
Max Planck Society, Germany
Franck Bassinot,
UMR8212 Laboratoire des Sciences du Climat et de l'Environnement (LSCE), France

*CORRESPONDENCE
Helge A. Winkelbauer
helge.winkelbauer@gmail.com
Babette A. A. Hoogakker
b.hoogakker@hw.ac.uk

SPECIALTY SECTION
This article was submitted to Marine Biogeochemistry, a section of the journal Frontiers in Marine Science

RECEIVED 11 November 2022
ACCEPTED 23 January 2023
PUBLISHED 02 February 2023

CITATION
Winkelbauer HA, Hoogakker BAA, Chance RJ, Davis CV, Anthony CJ, Bischoff J, Carpenter LJ, Chenery SRN, Hamilton EM, Holdship P, Peck VL, Poulton AJ, Stinchcombe MC and Wishner KF (2023) Planktic foraminifera iodine/calcium ratios from plankton tows. *Front. Mar. Sci.* 10:1095570. doi: 10.3389/fmars.2023.1095570

COPYRIGHT
© 2023 Winkelbauer, Hoogakker, Chance, Davis, Anthony, Bischoff, Carpenter, Chenery, Hamilton, Holdship, Peck, Poulton, Stinchcombe and Wishner. This is an open-access article distributed under the terms of the Creative Commons Attribution License (CC BY). The use, distribution or reproduction in other forums is permitted, provided the original author(s) and the copyright owner(s) are credited and that the original publication in this journal is cited, in accordance with accepted academic practice. No use, distribution or reproduction is permitted which does not comply with these terms.

Planktic foraminifera iodine/calcium ratios from plankton tows

Helge A. Winkelbauer[1]*, Babette A. A. Hoogakker[1]*, Rosie J. Chance[2], Catherine V. Davis[3], Christopher J. Anthony[2], Juliane Bischoff[1], Lucy J. Carpenter[2], Simon R. N. Chenery[4], Elliott M. Hamilton[4], Philip Holdship[5], Victoria L. Peck[6], Alex J. Poulton[1], Mark C. Stinchcombe[7] and Karen F. Wishner[8]

[1]Lyell Centre for Earth and Marine Science and Technology, Heriot-Watt University, Edinburgh, United Kingdom, [2]Wolfson Atmospheric Chemistry Laboratories, Department of Chemistry, University of York, York, United Kingdom, [3]Department of Marine, Earth, and Atmospheric Sciences, North Carolina State University, Raleigh, NC, United States, [4]Inorganic Geochemistry, Centre for Environmental Geochemistry, British Geological Survey, Environmental Science Centre, Nottingham, United Kingdom, [5]Department of Earth Sciences, University of Oxford, Oxford, United Kingdom, [6]BAS-Arctic Working Group, British Antarctic Survey, Cambridge, United Kingdom, [7]National Oceanography Centre, Ocean BioGeosciences, Southampton, United Kingdom, [8]Graduate School of Oceanography, University of Rhode Island, Narragansett, RI, United States

Planktic foraminifera test iodine to calcium ratios represent an emerging proxy method to assess subsurface seawater oxygenation states. Several core-top studies show lower planktic foraminifera I/Ca in locations with oxygen depleted subsurface waters compared to well oxygenated environments. The reasoning behind this trend is that only the oxidized species of iodine, iodate, is incorporated in foraminiferal calcite. The I/Ca of foraminiferal calcite is thought to reflect iodate contents in seawater. To test this hypothesis, we compare planktic foraminifera I/Ca ratios, obtained from plankton tows, with published and new seawater iodate concentrations from 1) the Eastern North Pacific with extensive oxygen depletion, 2) the Benguela Current System with moderately depleted oxygen concentrations, and 3) the well oxygenated North and South Atlantic. We find the lowest I/Ca ratios (0.07 µmol/mol) in planktic foraminifera retrieved from the Eastern North Pacific, and higher values for samples (up to 0.72 µmol/mol) obtained from the Benguela Current System and North and South Atlantic. The I/Ca ratios of plankton tow foraminifera from environments with well oxygenated subsurface waters, however, are an order of magnitude lower compared to core-tops from similarly well-oxygenated regions. This would suggest that planktic foraminifera gain iodine post-mortem, either when sinking through the water column, or during burial.

KEYWORDS

I/Ca, planktic foraminifera, plankton nets, oxygen concentration, oxygen proxy

Introduction

Ocean deoxygenation caused by global warming poses a major threat to the sustainability of fisheries and marine ecosystems, as well as key global biogeochemical cycles (Breitburg et al., 2018). Oxygen minimum zones (OMZs) are predicted to expand dramatically by 2100 (Oschlies et al., 2008). Being able to trace the existence of past OMZs, using sedimentary proxies, is crucial to understand OMZ dynamics and improve future predictions.

The chemical speciation of redox active elements such as iodine often reflects seawater oxygen levels – iodine in the oceans exists predominantly as iodide (I^-) and iodate (IO^{3-}), with the former being dominant in anoxic environments (Wong and Brewer, 1977; Wong et al., 1985; Rue et al., 1997; Truesdale and Bailey, 2000). Planktic foraminifera are ubiquitous microorganisms that incorporate iodate into their calcite shells (Lu et al., 2016b). Due to the broad dependency of iodine speciation on seawater oxygen levels, iodine to calcium ratios (I/Ca) in planktic foraminifera may be a promising tool to assess the oxygenation state of the seawater that they calcified in. Use of I/Ca in carbonates as a paleo tracer for ocean oxygen levels primarily depends on the iodate concentration in seawater; abiotic calcite synthesis experiments suggest that iodate is the preferred iodine species taken up into calcite, and that the amount incorporated reflects concentrations in seawater (Lu et al., 2010; Zhang et al., 2013). Synchrotron X-ray absorption spectroscopy and first-principles calculations confirm that iodate ions substitute for carbonate ions in the calcite crystal lattice (Podder et al., 2017; Feng and Redfern, 2018). However, this needs to be further tested in the natural marine environment on living foraminifera.

Limited observations from oxygen-depleted environments such as the Eastern Tropical South Pacific or Gulf of Mexico do not show a clear trend when comparing surface water iodate concentrations from areas with suboxia (O_2 <10 µmol/kg) to those from similar latitudes lacking suboxia (Figure 1). Planktic foraminifera from sediment core-tops (< 5,000 years) from areas with extensive suboxia have very low I/Ca ratios (<1 µmol/mol), compared with those from well-oxygenated regions (I/Ca ratios > 4 µmol/mol) (Lu et al., 2016a), which is thought to coincide with lower seawater iodate concentrations. Recent applications of proxy I/Ca ratios have shed new light on glacial subsurface water oxygen concentrations, suggesting that the Pacific sector of the Southern Ocean was oxygen depleted during glacial times (Lu et al., 2016a), with tandem downward expansion of the Eastern Tropical North Pacific (ETNP) OMZ (Hoogakker et al., 2018). Currently the planktic foraminifera I/Ca proxy can only be applied qualitatively, as we do not have a clear mechanistic understanding of iodine incorporation into the calcite.

Until now I/Ca calibration studies have focused on recent (< 5000 years) sediment core-tops, but not on fresh foraminifera from plankton nets. We do not know what seawater iodate concentrations core-top foraminifera calcified in. This leaves uncertainties as to what extent shell I/Ca is directly proportionate to seawater iodate. Core-top measurements from areas with an

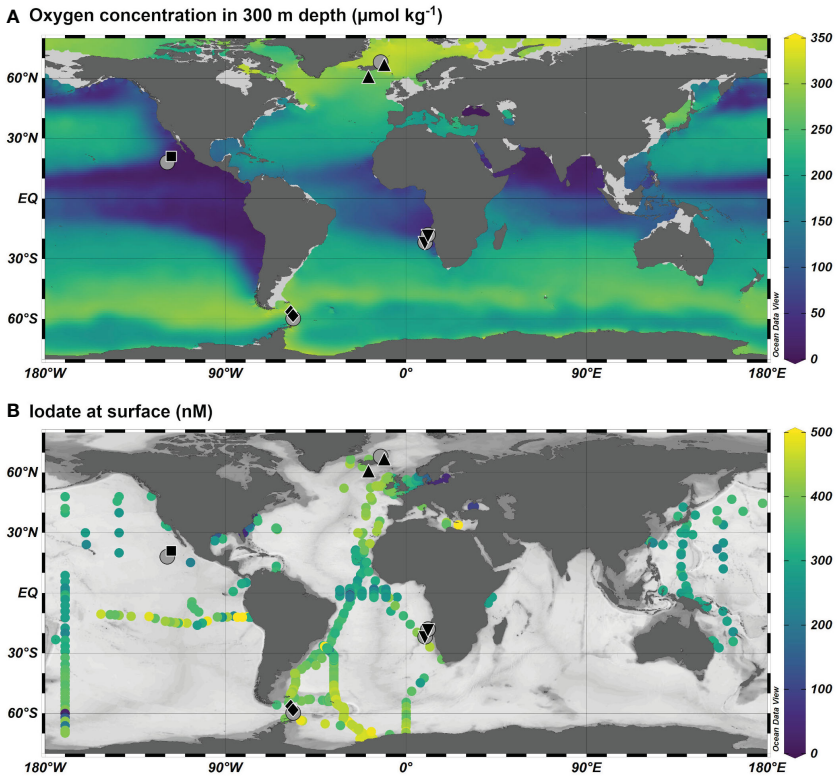

FIGURE 1
Station map for plankton tows (black, see Table 1) and iodate profiles (grey circles) from Moriyasu et al. (2020) in the Pacific, Bluhm et al. (2011) in the Southern Ocean, Waite et al. (2006) in the North Atlantic and from this study in the Benguela Upwelling System. **(A)** Average oxygen concentration at 300 m from the World Ocean Atlas 2018 (Garcia et al., 2019). **(B)** Iodate concentration at the surface (< 15 m) from the compilation described in Chance et al. (2014), plus Cutter et al. (2018) and Moriyasu et al. (2020) (dataset available: https://www.bco-dmo.org/dataset/776552). Plotted using Ocean Data View (Schlitzer, 2022).

extensive OMZ show consistently low I/Ca <2.5 µmol/mol for both mixed layer species and deeper dwellers (Lu et al., 2016a; Hoogakker et al., 2018; Lu et al., 2020). Observations show that the well-oxygenated mixed layer above the OMZ contains iodate, whilst the deeper anoxic waters generally do not (Rue et al., 1997; Cutter et al., 2018; Moriyasu et al., 2020). This leaves the conundrum of why in certain locations mixed layer planktic foraminifera species show low I/Ca ratios as do the deeper dwelling species.

To assess the extent to which seawater iodate is incorporated in planktic foraminifera shells we present I/Ca measured from the shells of foraminifera caught in plankton tows. This includes samples from the tropical Northeast Pacific, with an intense OMZ, samples from the Benguela area, with a weakly developed OMZ, and samples from the North and South Atlantic with a well-oxygenated water column. We compare these planktic foraminifera I/Ca ratios with published (Pacific, North and South Atlantic) and novel (Benguela) water column iodate and dissolved oxygen measurements.

Locations

Eastern Tropical North Pacific OMZ

The Eastern Tropical North Pacific has one of the worlds' largest OMZs, and contains very depleted O_2 levels (minimum between 2 and 10 µmol/kg at ~430 m water depth; Wishner et al., 2018). Coastal upwelling causes high productivity and high sinking fluxes of organic matter to depth. Accumulation of nitrite in subsurface waters is indicative of nitrate reduction (Garfield et al., 1983; Buchwald et al., 2015; Medina Faull et al., 2020). The sample area is located offshore, away from the upwelling and high productivity, though nevertheless it is characterized by low oxygen as a result of low oxygen waters moving away from the coast and poorly ventilated intermediate waters in the ETNP (Table 1). Within the core of the OMZ, oxygen levels reach 2 µmol/kg. The depth of the upper boundary of the OMZ in the area varies between ~ 100 and 130 m. Like its South Pacific counterpart, it is thought that there is lateral input of excess iodide-iodine from the sedimentary margins (Cutter et al., 2018; Moriyasu et al., 2020).

Benguela current

The Benguela Current is an eastern boundary current, which flows north along the coast of South Africa and Namibia until it meets warm southward flowing equatorial surface currents between 15.5° S and 17° S (Veitch et al., 2006). The location of the Angola-Benguela front that separates northward and southward flowing waters changes seasonally. Upwelling along the coast introduces nutrients to the

TABLE 1 Sample details, locations and I/Ca values of plankton net samples.

Location	Name/Event	Latitude	Longitude	Species	Water depth (m)	I/Ca (µmol/mol)
Eastern North Pacific OMZ	SKQ2017_721_6+7+8+9	21.55°N	117.80°W	*T. sacculifer*	125 to surface	*
Eastern North Pacific OMZ	SKQ2017_726_4+7	21.55°N	117.80°W	*T. sacculifer*	~ 430 ± 5	0.09
Eastern North Pacific OMZ	SKQ2017_726_6	21.55°N	117.80°W	*O. universa*	~ 430 ± 5	0.07
Eastern North Pacific OMZ	SKQ2017_726_6+8	21.55°N	117.80°W	*Globigerinella siphonifera*	~ 430 ± 5	0.17
Eastern North Pacific OMZ	SKQ2017_726_7	21.55°N	117.80°W	*O. universa*	~ 430 ± 5	0.07
Eastern North Pacific OMZ	SKQ2017_726_8	21.55°N	117.80°W	*O. universa*	~ 430 ± 5	0.07
Benguela Current SB	DY090 #07/ E96	21.56°S	9.47°E	*G. menardii*	120 to surface	0.33
Benguela Current NB	DY090 #13/ E189	18.02°S	11.01°E	*G. menardii*	120 to surface	0.33
Benguela Current NB	DY090 #14/ E190	18.02°S	11.01°E	*G. inflata*	750 to 500	0.53
Benguela Current NB	DY090 #17/ E190	18.02°S	11.01°E	*G. inflata*	120 to surface	0.72
Benguela Current NB	DY090 #17/ E190	18.02°S	11.01°E	*G. inflata*	120 to surface	0.48
Benguela Current NB	DY090 #18/ E214	18.03°S	11.01°E	*G. inflata*	120 to surface	0.55
North Atlantic	JR271 B5	60°N	18.67°W	*G. bulloides*	200 to surface	0.34
North Atlantic	JR271 B6	65.98°N	10.72°W	*N. pachyderma*	200 to surface	0.38
S Atlantic	JR274 B1	56.47°S	57.43°W	*G. bulloides*	200 to surface	0.65
S Atlantic	JR274 B1	56.47°S	57.43°W	*G. bulloides*	200 to surface	0.19
S Atlantic	JR274 B3	58.37°S	56.25°W	*N. pachyderma*	200 to surface	0.3

*Below detection limit.
SB, South Benguela; NB, North Benguela.

photic zone, causing high primary productivity. Decomposition of this organic material results in modest depletion of sub-surface oxygen levels.

Both sampling locations (Table 1) are in the northern half of the Benguela system, but south of the Angola-Benguela Front. The mixed layer depth during the sampling (MLD) at the offshore site South Benguela (SB) was 50 m with a surface water temperature of 20.6°C (Figure 1). The surface water at the site North Benguela (NB) was 2.8°C colder with a variable MLD between 15 m and 45 m during the sampling period. Oxygen values were slightly lower at NB than SB with a minimum of 25 µmol/kg at 300 m (compared to 41 µmol kg-1 at SB at 420 m). The main difference between sites was the much shallower onset of oxygen-depleted waters just below the surface mixed layer at NB, as opposed to at a depth of ~120 m in SB. South Benguela displayed a typical low-nutrient tropical open ocean chlorophyll-a profile with a subsurface maximum of 0.4 mg/m^3 at 70 m depth. In contrast, NB had a surface chlorophyll-a maximum with an average of 1 mg/m^3.

North and South Atlantic Ocean

The North and South Atlantic samples represent well-oxygenated water masses which do not have dissolved oxygen concentrations below 235 µmol/kg in the upper 1000 m. The North Atlantic samples came from two sites to the south and to the east of Iceland with average SST of ca. 9°C (Table 1). Deep-water production in the Greenland and Norwegian seas causes a particularly well-ventilated water column with oxygen concentrations of 265–330 µmol/kg (WOA18, Boyer et al., 2018).

The South Atlantic samples were from the Drake Passage through which the Antarctic Circumpolar Current flows along with its strong associated fronts (Orsi et al., 1995). The two samples are two degrees of latitude apart from each other (see Table 1 for coordinates) with SSTs of 1.7°C and 5.4°C and high oxygen concentrations in the water column of 260–330 µmol/kg (WOA18, Boyer et al., 2018). These waters are well ventilated with Antarctic intermediate waters due to Southern Ocean overturning circulation.

Methods

Collection of samples during the cruises

Planktic foraminifera samples for the ETNP were collected using a horizontally towed 1 m^2 MOCNESS (Multiple Opening/Closing Net and Environmental Sensing System, 222 µm mesh size) at ~425 m for station 726 and a vertical haul from 125 m to the surface for station 721 during R/V Sikuliaq cruise SKQ201701S in Jan-Feb 2017 (Wishner et al., 2018). At sea, the samples were stored in sodium-borate-buffered seawater and formalin. Several months later they were picked and stored in dry slides.

Planktic foraminifera samples from the Benguela Current were collected during research cruise DY090 aboard the RRS Discovery in May to June 2018 using vertical hauls of Bongo nets and a MultiNet® Mammoth with 100 µm mesh size. Most nets sampled the upper 120 m of the water column, but one sample was from a depth of 750 m to 500 m. Samples were washed from the net into a bucket with surface seawater. Following gravitational settling, planktic foraminifera were collected from the bottom of the bucket using a hand pipette. Foraminifera were washed over a 100 µm mesh with pH-adjusted Milli-Q (ammonia solution, pH > 8), and oven dried (40 to 50°C, 8–12 h) before storage.

Samples from two stations in the well-oxygenated high latitude North Atlantic (Greenland and Norwegian Seas) and two stations in the South Atlantic (Drake Passage) were collected during two research cruises (JR271 in 2012 and JR274 in 2013) as part of the UK Ocean Acidification Research Program (www.oceanacidification.org.uk). Plankton samples from vertical Bongo net hauls (200 m to surface, 100 µm mesh size) were collected, rinsed, dried, and stored in the same way as the samples from the Benguela Current.

Seawater: oxygen concentrations

For the Pacific cruise SKQ2017, oxygen data was derived from two sources: a Sea-Bird SB911 plus CTD including a SBE43 dissolved oxygen sensor attached to the MOCNESS, and a CTD with an Aanderaa 4831F oxygen sensor was attached to a Wire Flyer (towed deep oscillating profiler) (Wishner et al., 2018). The Wire Flyer and MOCNESS oxygen sensors were cross-calibrated during the cruise and by post-cruise analyses. For the Benguela cruise DY090, *in situ* oxygen data came from a Sea-Bird SBE43 dissolved oxygen sensor attached to a SBE 9plus CDT calibrated against discrete Winkler titrations using a Metrohm 716 DMS Titrino (cruise report: https://www.bodc.ac.uk/resources/inventories/cruise_inventory/reports/dy090.pdf).

Seawater iodate

During the Benguela cruise DY090 seawater samples for iodine analyses were taken from the upper 1000 m (except two CTD casts to >3500 m depth), at the same depths as discrete oxygen samples. Following collection, the samples were filtered (0.2 µm, polycarbonate Whatman Nucleopore™ filter) under gentle vacuum, and transferred to 50 mL polypropylene screw cap tubes. Duplicate aliquots were prepared for each sample, one for iodate and the other for iodide analysis. Aliquots were frozen at −20°C for transport back to the University of York for analysis. The majority (65%) of frozen samples were analyzed within 12 months of collection, and all analyses were complete within 32 months of collection. Campos (1997) has shown that inorganic iodine speciation is preserved in filtered frozen samples (≤−16°C) for at least one year and Schwehr and Santschi (2003) found no significant change after three years. Iodate was determined using a spectrophotometer (UV-1800, Shimadzu) after reduction to iodonium (Truesdale and Spencer, 1974; Jickells et al., 1988), with calibration using external KIO3 standards. Around half the samples were analyzed singly, and the other half in triplicate, due to a change in laboratory protocol. Where samples were analyzed singly, precision was estimated by propagation of error from the calibration curve. Where samples were analyzed in triplicate, precision was estimated from the standard deviation of the replicates. The precision of these measurements varied, and is shown as individual error bars on each

data point (Figure 2 and Supplementary information). Fifty percent of samples had a percentage relative standard deviation (%RSD) of less than or equal to 4%, and 92% had a %RSD below 15%. The limit of detection was approximately 50 nM. The iodate measurements from the North and South Atlantic (Waite et al., 2006; Bluhm et al., 2011) were made using the same iodometric method as our own measurements.

Planktic foraminifera I/Ca ratios

Towed planktic foraminifera I/Ca ratios were measured using a magnetic-sector ICP-MS (Thermo Finnigan Element 2 at the Department of Earth Sciences, University of Oxford) and an Agilent Technologies 8900 ICP-QQQ (British Geological Survey Keyworth). On average we used 90 specimens per analysis. As reference material we used the carbonate standard JCP-1 which is not certified as an I/Ca standard but is often used in I/Ca studies. It is a ground coral, which we measured at 4.27 ± 0.10 µmol/mol in Oxford (n=13) and 4.82 ± 0.06 µmol/mol in Keyworth (n=6). Previously published I/Ca ratios for the JCP-1 coral are 4.33 ± 0.16 µmol/mol (Chai and Muramatsu, 2007), 4.27 ± 0.06 µmol/mol (Lu et al., 2010) and 3.82 ± 0.08 µmol/mol (Glock et al., 2014). For the Pacific samples, only dead (empty) planktic foraminifera specimens were selected, which contrasts to samples from the North and South Atlantic and the two stations in the Benguela Current System where most foraminifera were alive, with their cytoplasm present.

Prior to all analyses, samples were rinsed with ultra-pure (18.2 MΩ cm) water and treated to remove organic material. Glock et al. (2016) showed that organic material in benthic foraminifera could be a significant source of iodine. We carried out a set of experiments on core-top samples (ODP Site 1088, 0-1 cm, 41.14°S, 13.56°E, 2082 m below sea level) to assess which method may remove organic material/iodine contamination most effectively, using A) 1% buffered H_2O_2 x 6, following Winkelbauer et al. (2021), B) 50% (v/v) buffered H_2O_2 for 30 minutes (Anand et al., 2003), C) soaking in bleach, and D) combustion at 450 °C. Before measuring I/Ca ratios in planktic foraminifera each sample was initially rinsed in ultra-pure de-ionized water. We assume that the cleaning method resulting in the lowest planktic foraminifera I/Ca ratios, was the most adequate at removing organic material within and adhered to the foraminifera tests. Overall, the method of Winkelbauer et al. (2021), using 1% (v/v) buffered H_2O_2 acquires the lowest I/Ca result, whereas the method using bleach showed the highest value (Table 2). We therefore used the method of Winkelbauer et al. (2021) to remove organic material, which involved six repetitions of soaking the crushed samples in buffered 1% (v/v) H_2O_2 at boiling point for ten minutes. The same sample from ODP 1088, 0-1 cm was also used to measure planktic foraminifera with different preservation states, i.e., semi-transparent tests and fully opaque encrusted tests.

Results

Figure 2 shows a generalized overview of seawater dissolved oxygen and iodate concentrations for the different locations. For the Eastern Tropical North Pacific, we show water column data from station F19 (Falkor cruise FK 180624) obtained by Moriyasu et al. (2020), which is 400 km away from our plankton tow location. At this location dissolved oxygen concentrations (~200 µmol/kg) were uniform in the top 80 m and then decrease to almost 0 µmol/kg at 140 m water depth and deeper in the water column (Figure 2D). Between 0 and 110 m water depth iodate concentrations at this location vary between ~250 and 330 nmol/l, decreasing to < 50 nmol/l until ~ 210 m after which they increased to >400 nmol/l (Figure 2A).

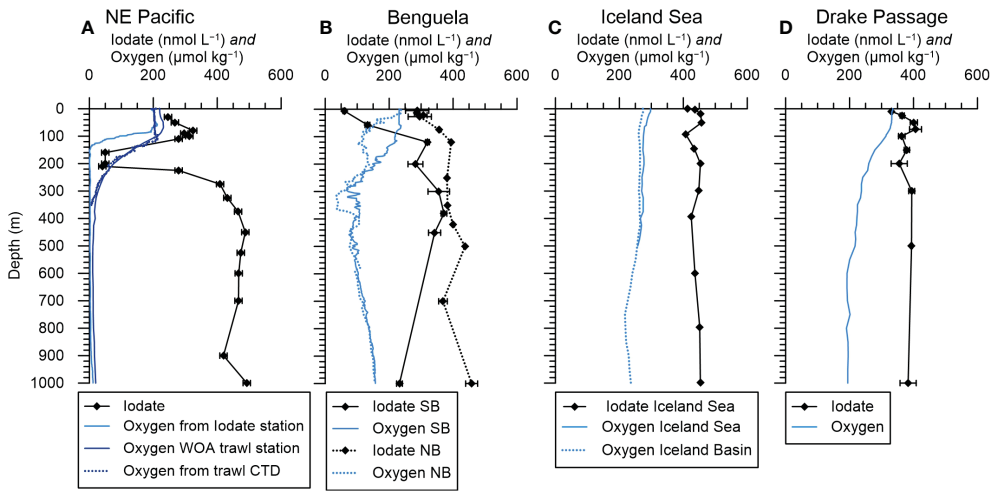

FIGURE 2
Representative profiles of oxygen and iodate concentrations from selected stations for comparison with foraminifera I/Ca ratios. **(A)** Station F19 in the NE Pacific. Oxygen from Evans et al. (2020) and iodate from Moriyasu et al. (2020). The plankton net sample for the North-East Pacific is 400 km away from the iodate profile station and an oxygen profile from the plankton trawl station (Wishner et al., 2018) is shown along the closest WOA18 grid point profile. **(B)** South Benguela (SB, continuous lines, CTD cast 7) and North Benguela (NB, dotted lines, CTD cast 18). **(C)** Iceland Basin iodate profile from Waite et al. (2006) and oxygen from WOA18 (Garcia et al., 2019). **(D)** Drake Passage iodate profile (PS71/232-1) from Bluhm et al. (2011) and oxygen from WOA18 (Garcia et al., 2019).

TABLE 2 Effect of different organic material removal techniques on core-top sample from ODP 1088 (0-1 cm, > 300 µm *Globigerina bulloides*).

Sample	Organic carbon removal treatment	I/Ca in µmol/mol
A1	Buffered 1% H_2O_2	4.2
A2*	Buffered 1% H_2O_2	3.9
B1	Buffered 50 % H_2O_2	4.0
B2	Buffered 50 % H_2O_2	5.0
C1	Soaking in bleach (4 hours)	5.9
C2	Soaking in bleach (4 hours)	5.3
D1	Combustion at 450 °C	4.7
D2	Combustion at 450 °C	4.4

*Was stabilized using tetramethylammonium hydroxide but cleaned using the same method. For a comparison of stabilization techniques please refer to Winkelbauer et al. (2021).

At the Benguela location, the SB station had a mixed layer with oxygen concentrations of 232–218 µmol/kg between 0 and 120 m (Figure 2B). At the North Benguela station there is a two-step decrease in dissolved oxygen from the surface with 237 µmol/kg to 310 m where the lowest dissolved oxygen concentrations of ~ 35 µmol/kg occurred (Figure 2B).

Iodate concentrations were variable over time at both stations in the Benguela Current System, and the closest CTD casts to the net hauls are shown in Figure 2B. At SB, the CTD and bottle sampling was ca. 40 hours before the net hauls and at NB all net samples were taken within 32 h before or after the CTD and bottle sampling. At both stations the iodate concentration increased from the surface to 120 m depth, though the water samples from SB had lower concentrations going from 60 nmol/l to 320 nmol/l while NB had concentrations from 226 nmol/l to 400 nmol/l (Figure 2B). Water samples from four days earlier (CTD 1) at SB had higher iodate concentrations in the top 120 m, ranging from 230 to 300 nmol/l. Comparable depletions of iodate in low latitude surface waters have been observed elsewhere in the Atlantic, and are attributed to a combination of biological activity and stratification (e.g., Campos et al., 1996; Truesdale et al., 2000). The extent of the depletion seen in CTD 7 is particularly large, and the change over four days rapid given the relatively slow rates of iodine transformations (see e.g., Chance et al., 2014). We suggest this could be due to advection of a localized area of particularly high biological activity near the station. The two CTDs 1 and 7 are also ca. 40 km apart from each other and therefore reflect local variation in surface iodate distribution (see Supplementary Table 1 for exact locations and times of the CTDs). In the deeper water, below 120 m, the iodate concentrations were also always lower at SB than at NB despite oxygen concentrations being similar. This may result from the slow iodine oxidation kinetics and highlights that iodate concentrations are not solely a function of oxygen level. All iodate and oxygen profiles are shown in supplementary Figures 1-3.

There are two plankton tow sites in the North Atlantic, one in the Iceland Sea northeast of Iceland (JR271 B6, Table 1) and the other in the Iceland Basin southeast of Iceland (JR271 B5). The closest iodate profiles are from Waite et al. (2006) and we use the North-East station, which was ca. 240 km northwest of our station JR271 B6. In Figure 2C the August 2000 profile from Waite et al. (2006) is shown, as this season matches best with the plankton samples that were taken in June 2012. Both oxygen and iodate profiles show little vertical variation, with mean iodate values of 410 nmol/l in the upper 150 m and a slight surface reduction to 390 nmol/l. The climatological oxygen concentrations were 200 to 300 µmol/mol (WOA18, Garcia et al., 2019) for both plankton net stations around Iceland.

Water column measurements from Drake Passage were ~150 km and ~370 km distance away from the plankton tow sites. At this location (59.5°S, 56.5°W) dissolved oxygen concentrations decrease gradually from ~330 µmol/kg at the surface to 200 µmol/kg at 1000 m (Figure 2D, WOA18, Garcia et al., 2019). The closest iodate profile is at station PS71/232-1 from Bluhm et al. (2011) and shows slightly lower sea surface iodate concentrations of 330 nmol/l, but uniform further below (350 to 400 nmol/l). Both oxygen and iodate concentrations have similar high values across the whole Drake Passage (Bluhm et al., 2011; Garcia et al., 2019).

Tow-derived planktic foraminifera I/Ca ratios vary between the detection limit of the method (average 0.1 µmol/mol) and 0.72 µmol/mol, with the lowest values reported for the Northeastern tropical Pacific Site (between detection limit and 0.17 µmol/mol), whereas at the Benguela and North and South Atlantic stations they varied between 0.19 µmol/mol and 0.72 µmol/mol (Table 1).

In addition, three species of planktic foraminifera from the South Atlantic ODP core 1088 (0-1 cm, 41.14°S, 13.56°E) were analyzed. They were displaying either semi-transparent tests (fresh) or encrusted white tests (gametogenic and diagenetic overprint). The semi-transparent samples are on average 0.89 ± 0.65 µmol/mol lower than the white specimens at an average I/Ca of 2.89 µmol/mol (Table 3).

Discussion

Seawater oxygen and net haul planktic foraminifera I/Ca ratios

In Figure 3 we compare tow-derived planktic foraminifera I/Ca ratios with *in situ* (i.e., the plankton net depth range) and water column minimum oxygen concentrations to assess whether planktic foraminifera I/Ca ratios reflect redox conditions. There is no relationship between fresh planktic foraminifera I/Ca ratios and *in situ* oxygen concentrations. We note that none of the species analyzed

TABLE 3 I/Ca results of foraminifera with semi-transparent and cloudy appearances from ODP core 1088 (0 to 1 cm).

Species	Semi-transparent specimen I/Ca (µmol/mol)	White specimens I/Ca (µmol/mol)
Globigerina bulloides	2.42	3.07
Globorotalia truncatulinoides	3.13	4.49 4.66
Globorotalia inflata	3.13	4.12 3.03

have a habitat in the OMZ, as shallower-dwelling species have historically been used for I/Ca reconstructions (Lu et al., 2016b; Hoogakker et al., 2018). However, when we compare planktic foraminifera I/Ca ratios with minimum oxygen concentrations (following Lu et al., 2016a and Lu et al., 2020), then we observe that the lowest I/Ca ratios of ≤ 0.17 µmol/mol correspond to the lowest oxygen concentration of < 10 µmol/kg, while the other samples are still widely spread (Figure 3). This threshold is much lower than previously observed for core top I/Ca ratios that are generally below 2.5 µmol/mol when minimum oxygen concentration is below 50 to 100 µmol/kg (Lu et al., 2016a; Lu et al., 2020). The lack of a relationship between planktic foraminifera I/Ca and *in situ* oxygen concentrations could be reflective of the relatively long time of months to years it takes for iodide to be oxidized back to iodate within the oxygenated surface waters overlying oxygen depleted waters (Hardisty et al., 2020 and references therein). At higher oxygen concentrations, between 40 and 300 µmol/kg, planktic foraminifera I/Ca varies between 0.19 and 0.72 µmol/mol.

Seawater oxygen, iodate and tow planktic foraminifera I/Ca ratios

This is the first study to compare modern planktic foraminifera I/Ca ratios versus dissolved oxygen and iodate concentrations. It is important to note that we only have *in situ* oxygen and iodate profiles from the same location as the plankton-tows for the Benguela locations. For the other three locations we used the nearest profiles available from other studies, which were not only sampled during a different year but also at a distance from the tows. As can be seen from Figure 1, the global database for ocean iodine speciation is still very limited in coverage (Chance et al., 2019). Despite relatively sparse observations, large scale latitudinal and depth gradients in iodate abundance are well described (see e.g., Chance et al., 2014), and the profiles we have selected for comparison are consistent with these trends. We compare our North Atlantic plankton tow samples with the iodate and oxygen profiles of station "NE" from Waite et al. (2006), ca. 240 km northwest of our station JR271 B6. Waite et al. (2006) found iodine speciation in this region to be spatially and temporally stable – iodate profiles were very similar (> 400 nmol/L throughout the top 1000 m) to the NE station at additional stations four degrees further south ("SW") and 15 degrees further west ("NW"), and showed very little variation between November, February, and August. For the NE Pacific, iodate and supporting oxygen profiles are from a location to the south of the plankton tow (distance 400 km). However, with iodate in subsurface and mixed layer water being quite variable in the Pacific (Rue et al., 1997; Cutter et al., 2018; Moriyasu et al., 2020), we are constrained in our comparison of seawater iodate concentrations with planktic foraminifera I/Ca ratios. Below ~ 300 m, all four locations show uniform 400 nmol/l, whilst oxygen concentrations vary considerably (Figure 2). In the top 300 m there are some notable differences, with

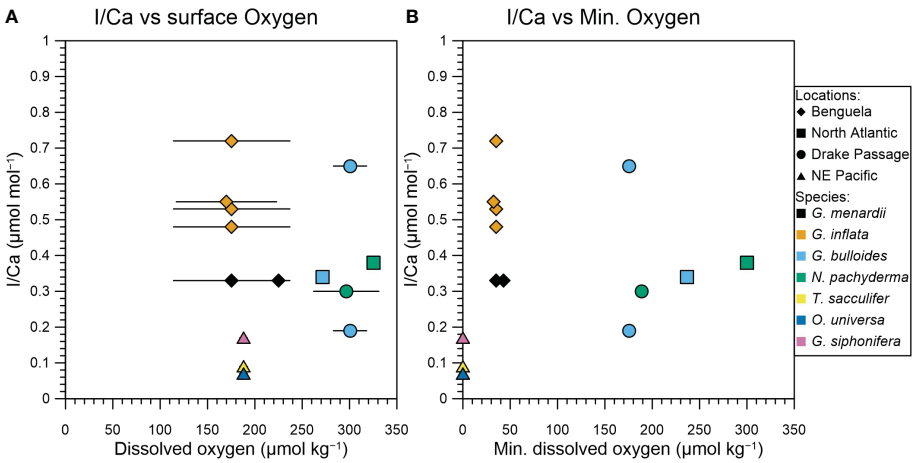

FIGURE 3
I/Ca values of planktic foraminifera compared to seawater oxygen concentrations. **(A)** planktic foraminifera I/Ca from net hauls *vs.* mean oxygen concentrations from the upper 120 m from nearby CTD casts. The range shows the maximum and minimum oxygen concentrations in the upper 120 m. **(B)** planktic foraminifera I/Ca *vs.* the minimum water column oxygen concentration, generally deeper down in the water column.

the NE Pacific showing a large reduction in iodate when oxygen levels fall below 5 µmol/kg.

In surface waters oxygen concentrations are influenced by primary production, temperature, remineralization of organic material, and mixing with other water masses. The distribution of iodide and iodate in the oxygenated ocean is thought to arise from the interplay of the biologically mediated transformations, and physical mixing and advection processes (Campos et al., 1996; Truesdale and Bailey, 2000; Chance et al., 2014). In areas where oxygen is severely depleted, such as subsurface oxygen minimum zones, iodide becomes the dominant form of iodine (e.g., Wong and Brewer, 1977; Wong et al., 1985; Rue et al., 1997; Truesdale and Bailey, 2000). It appears that iodate becomes depleted, and iodide the dominant iodine species when oxygen concentrations fall below 7 ± 2 µmol/kg (Rue et al., 1997; Cutter et al., 2018; Moriyasu et al., 2020). It is only in the NE Pacific that oxygen reaches such low levels (Figure 2).

Comparison of our planktic foraminifera I/Ca ratios with seawater dissolved iodate does not show a very clear relationship (Figure 4). We use the depth range of the nets to calculate a vertically weighted mean iodate concentration. In the top 120 m of the well-oxygenated North and South Atlantic the mean iodate concentrations are slightly elevated (310-360 nmol/l) compared to the Benguela and NE Pacific (210-340 nmol/l). While the iodate profiles in the top 120 m at Benguela and the NE Pacific look similar, the planktic foraminifera from the NE Pacific have lower I/Ca values compared with those from the Benguela sites (Figure 4). Unless *in situ* seawater iodate values at the NE Pacific sites are lower than measured for station 19 ~400 km away from the site, these results suggest that the relationship between planktic foraminifera I/Ca and seawater iodate concentration may not be straightforward. More contemporary data containing planktic foraminifera I/Ca and seawater iodate concentrations are needed to improve our understanding of the use of planktic foraminifera I/Ca as a potential subsurface redox proxy.

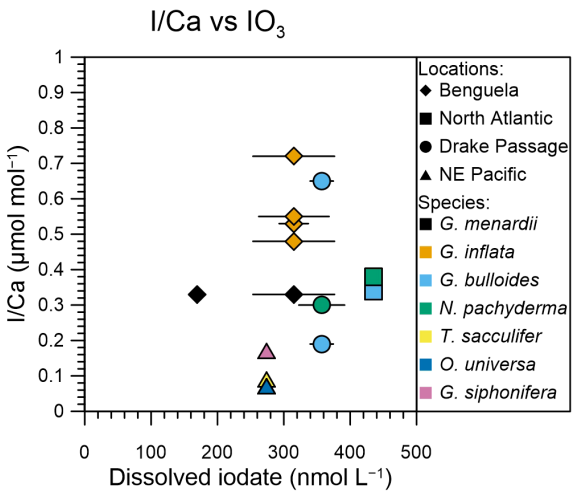

FIGURE 4
I/Ca of planktic foraminifera relative to dissolved mean iodate from the upper 120 m of the water column, representing the habitat of the analyzed species. Iodate values are from representative profiles up to 400 km away from the foraminifer sampling site as detailed in section 4.

Comparison of plankton tow derived planktic foraminifera I/Ca with core-tops

There are various proxies that have been used to capture low oxygen waters of OMZs: presence/absence of sedimentary laminations, benthic foraminifera assemblages and morphology, redox sensitive metals, and nitrogen isotopes (Moffitt et al., 2015; Rathburn et al., 2018; Erdem et al., 2020; Studer et al., 2021). Application of most of these proxies are however limited to sediment cores that are immersed in low oxygen waters (Winkelbauer et al., 2021), limiting the areal extent of assessments of past OMZs to the upper continental slope. Iodine/calcium ratios, measured in planktic foraminifera that calcified in close proximity of the OMZ (e.g., in seawater directly within or above it) have the potential to expand research on seawater redox conditions to the open ocean (Winkelbauer et al., 2021), as do planktic-foraminifera shell-bound nitrogen isotopes (Smart et al., 2020; Studer et al., 2021). Any downcore application of such proxies needs calibration whether quantitative or qualitative.

Core-top planktic foraminifera I/Ca data can be divided into two groups: those with I/Ca ratios of > 4 µmol/mol, which appear to be characteristic of areas where minimum dissolved oxygen concentrations are between 100 and 280 µmol/mol; and those with I/Ca < 2.5 µmol/mol, which appear to be characteristic of areas where minimum subsurface oxygen concentrations are below 90 µmol/mol (Figure 5, Lu et al., 2016a; Lu et al., 2020). These authors compared their planktic foraminifera I/Ca data with the lowest oxygen concentrations in the water column, which does not generally represent the water depth that the foraminifera calcify at. For example, for the North-East Pacific, Davis et al. (2021) show that only a few planktic foraminifera species, like *Globorotaloides hexagonus*, are found in very low oxygen environments, whereas most species are found in the well-oxygenated mixed layer. Lu et al. (2020) argue that minimum water column oxygen concentrations need to be used as the oxygen content must drop below a certain threshold to trigger iodate reduction, which then gets recorded as low foraminiferal I/Ca (Lu et al., 2016a). Seawater iodate generally starts to reduce under suboxic conditions (O_2 <10 µmol/kg), so a low I/Ca ratio < 1 µmol/mol in our planktic foraminifera samples cannot be explained by iodate reduction when the minimum oxygen concentration is > 100 µmol/kg (Figure 5).

Another important question is how signals from the OMZ/oxygen depleted waters are communicated to planktic foraminifera living in the generally shallower and better oxygenated mixed layer. Potentially, this could be related to the time it takes for iodide to oxidize to iodate, where in settings with suboxia in subsurface waters the iodate concentration of the mixed layer above is decreased as a result of vertical exchange compared to settings with a mildly hypoxic or well oxygenated water column. More research is needed to explore this.

It is striking that across the spectrum of dissolved oxygen concentrations planktic foraminifera I/Ca ratios from core-tops are significantly higher than tow-derived samples (Figure 5). In OMZ environments, core-top samples show considerable variation, with I/Ca ratios between the detection limit and 2.5 µmol/mol; whereas plankton tow samples are limited to 0.17 µmol/mol. Furthermore, core-top planktic foraminifera I/Ca ratios from

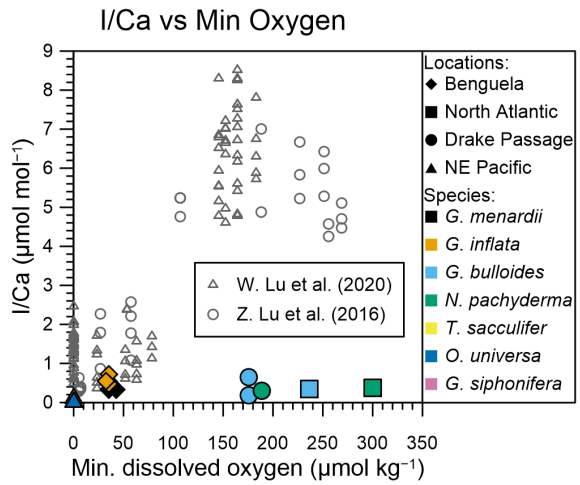

FIGURE 5
Same as Figure 3, but with added planktic foraminifera core-top samples (grey) from Lu et al. (2016b) and Lu et al. (2020). The colors and symbols of plankton-tow samples are as in Figure 3. Note the change in scale for the x-axis needed to include the core-top samples.

better oxygenated environments (>100 µmol/kg) show values between 4 and 9 µmol/mol; plankton tows only reach 0.72 µmol/mol (Figure 5).

Our observations of an order of magnitude lower I/Ca ratios in planktic foraminifera from plankton tows compared with core-tops would suggest that planktic foraminifera gain iodine post-mortem. This could be *via* abiotic incorporation shortly after gametogenesis, or when sinking through the water column, or following burial because the bottom waters were better ventilated with high iodate concentrations. Post depositional crust formation has been observed in planktic foraminifera with the potential to affect paleoproxy records of Mg/Ca and Sr/Ca (Branson et al., 2015). Diagenetic processes could also influence the I/Ca ratio of foraminifera tests, depending on the iodate concentration of the pore water. Throughout their lifecycle, planktic foraminifera migrate vertically through the water column. At the end of their lifecycle, prior to or during gametogenesis, various species form a calcite crust, which can potentially account for most of the total shell mass. Gametogenic crusts can dominate the element signature of the shell (Steinhardt et al., 2015). Steinhardt et al. (2015) show that planktic foraminifera Mg/Ca ratios of *N. dutertrei* and *G. scitula* are significantly lower (50%) in the crust compared with ontogenic calcite. Incorporation of iodate seems to be higher in abiotic calcification (Lu et al., 2010) compared to biotic calcification of foraminifera (Figure 5), therefore, abiotic crust growth in the sediments can increase the overall I/Ca of foraminifera after deposition. If crust also plays a role in planktic foraminifera I/Ca ratios, then the results shown here (Figure 5) would suggest that crust addition in well-oxygenated settings causes a 5 to 11 times *increase* in I/Ca ratios, whereas in lower oxygenated settings this is reduced (in case of suboxic water column) or is *negligible* (in case of mild hypoxia in the water column). However, we do not univocally observe a greater I/Ca enrichment in species that form a thicker crust, like *N. dutertrei* or *N. pachyderma* (Lu et al., 2016a; Hoogakker et al., 2018; Lu et al., 2020).

To further assess the potential effect of crusts on planktic foraminifera I/Ca ratios, we measured I/Ca ratios for *G. bulloides*, *G. truncatulinoides* and *G. inflata* samples from ODP Site 1088 (0-1 cm), comparing heavily encrusted samples with those that were transparent to semi-transparent (i.e., limited encrustation). *Globigerina bulloides* does not form a crust to the degree that *G. truncatulinoides* and *G. inflata* do in the water column such that most overgrowth in this species should happen after sedimentation at the seafloor. While the transparent samples did not show similar values as the plankton tows (e.g., below 1 µmol/mol) their I/Ca ratios were lower compared to those that showed considerable encrustation (Table 3). This supports our hypothesis that in higher oxygenated settings crusts are associated with increased I/Ca ratios of core-top planktic foraminifera.

Conclusions

Here we compared planktic foraminifera I/Ca ratios, obtained from plankton tows, with published and new measurements of seawater iodate and oxygen concentrations from 1) the Eastern North Pacific with extensive oxygen depletion, 2) the Benguela Current System with moderately depleted oxygen concentrations, and 3) the well oxygenated North and South Atlantic. While we do not observe a clear relationship between seawater iodate concentration in the upper 120 m and planktic foraminifera I/Ca, we do find that the lower planktic foraminifera I/Ca ratios are found in areas characterized by depleted oxygen concentrations in subsurface waters at 430 m. The observed trend is similar to that of core-top studies, however, plankton-tow derived samples from well-oxygenated regions have I/Ca ratios that are an order of magnitude lower than their core-top counterparts. We suggest that planktic foraminifera may gain iodine prior to or following gametogenesis or post-mortem, at least in well-oxygenated areas, either when falling through the water column, or through burial.

Data availability statement

The original contributions presented in the study are included in the article/Supplementary Material. Further inquiries can be directed to the corresponding authors.

Author contributions

HW and BH have created the concept and design of the study. HW, BH, EH, SC, and PH have conducted the I/Ca analysis. HW has prepared figures and managed the data. BH and HW have contributed to writing the first draft of the manuscript. RC, CD, LC, SC, PH, AP, and KW have commented on the first draft of the manuscript. RC, LC, and CA have organized and conducted the analysis of seawater iodate concentrations in York. RC has curated the global iodate data. KW has collected the plankton samples on cruise SKQ2017 and CD picked them. JB contributed to the sample preparation in the Lyell Centre. VP collected plankton samples on cruises JR271 and JR274. HW and AP contributed to sampling iodate

water samples and plankton samples on cruise DY090. MS analyzed oxygen samples on cruise DY090. KW has taken plankton samples and provided sensor data on cruise SKQ2017. All authors contributed to the article and approved the submitted version.

Funding

This work was supported by a James Watt Scholarship awarded to HW. BH acknowledges support from UKRI Future Leaders Grant MR/S034293/1 and UK Natural Environment Research Council (NERC) grant NE/I020563/1. RC and LC profited from NERC grant NE/N009983/1 (Iodide in the ocean:distribution and impact on iodine flux and ozone loss) and NE/W00027X/1 (Iodine sea-air emissions and atmospheric impacts in a changing world (I-SEA)). Collection of the foraminifera specimens (by the MOCNESS net) in the Eastern Tropical Pacific OMZ during two research cruises was funded by National Science Foundation grant OCE-1459243 (PIs were Seibel, Wishner, and Roman). United States National Science Foundation OCE-1851589 to CD was used to support the isolation of foraminifera from MOCNESS tows in the Eastern Tropical North Pacific. The Benguela Cruise "COMICS" was funded by NERC with the codes NE/M020835/1 and NE/M020835/2. VP benefited from the UK Ocean Acidification research programme which was funded by the Department for Environment, Food and Rural Affairs, the NERC and the Department of Energy and Climate Change (NE/H017267/1, NE/H017097/1).

Acknowledgments

The authors thank the crews and scientific team of the *R/V Sikuliaq* SKQ201701S, *RRS Discovery* DY090 and *James Clark Ross* JR271 and JR274 cruises for help with the sample acquisition. Joe Install and Rhianna Evans are thanked for their contributions to iodate water sample analysis.

Conflict of interest

The authors declare that the research was conducted in the absence of any commercial or financial relationships that could be construed as a potential conflict of interest.

Publisher's note

All claims expressed in this article are solely those of the authors and do not necessarily represent those of their affiliated organizations, or those of the publisher, the editors and the reviewers. Any product that may be evaluated in this article, or claim that may be made by its manufacturer, is not guaranteed or endorsed by the publisher.

Supplementary material

The Supplementary Material for this article can be found online at: https://www.frontiersin.org/articles/10.3389/fmars.2023.1095570/full#supplementary-material

SUPPLEMENTARY FIGURE 1
CTD bottle profiles of iodate (circles) and dissolved oxygen (diamonds) concentrations from the station South Benguela.

SUPPLEMENTARY FIGURE 2
CTD bottle profiles of iodate (circles) and dissolved oxygen (diamonds) concentrations from the station North Benguela.

SUPPLEMENTARY FIGURE 3
More CTD bottle profiles of iodate (circles) and dissolved oxygen (diamonds) concentrations from the station North Benguela.

References

Anand, P., Elderfield, H., and Conte, M. H. (2003). Calibration of Mg/Ca thermometry in planktonic foraminifera from a sediment trap time series. *Paleoceanography* 18 (2):1050. doi: 10.1029/2002PA000846

Bluhm, K., Croot, P. L., Huhn, O., Rohardt, G., and Lochte, K. (2011). Distribution of iodide and iodate in the Atlantic sector of the southern ocean during austral summer. *Deep Sea Res. Part II: Topical Stud. Oceanogr.* 58 (25-26), 2733–2748. doi: 10.1016/j.dsr2.2011.02.002

Boyer, T. P., Garcia, H., Locarnini, R., Zweng, M., Mishonov, A., Reagan, J., et al. (2018). *World ocean atlas 2018 [temperature, oxygen and nitrate subsets]* (NOAA National Centers for Environmental Information). https://www.ncei.noaa.gov/archive/accession/NCEI-WOA18

Branson, O., Read, E., Redfern, S. A., Rau, C., and Elderfield, H. (2015). Revisiting diagenesis on the ontong Java plateau: Evidence for authigenic crust precipitation in globorotalia tumida. *Paleoceanography* 30 (11), 1490–1502. doi: 10.1002/2014PA002759

Breitburg, D., Levin, L. A., Oschlies, A., Grégoire, M., Chavez, F. P., Conley, D. J., et al. (2018). Declining oxygen in the global ocean and coastal waters. *Sci. (New York N.Y.)* 359 (6371):eaam7240. doi: 10.1126/science.aam7240

Buchwald, C., Santoro, A. E., Stanley, R. H. R., and Casciotti, K. L. (2015). Nitrogen cycling in the secondary nitrite maximum of the eastern tropical north pacific off Costa Rica. *Global Biogeochem. Cycles* 29 (12), 2061–2081. doi: 10.1002/2015GB005187

Campos, M. L. A. M. (1997). New approach to evaluating dissolved iodine speciation in natural waters using cathodic stripping voltammetry and a storage study for preserving iodine species. *Mar. Chem.* 57 (1-2), 107–117. doi: 10.1016/S0304-4203(96)00093-X

Campos, M. L. A. M., Farrenkopf, A. M., Jickells, T. D., and Luther, G. W.III (1996). A comparison of dissolved iodine cycling at the Bermuda Atlantic time-series station and Hawaii ocean time-series station. *Deep Sea Res. Part II: Topical Stud. Oceanogr.* 43 (2-3), 455–466. doi: 10.1016/0967-0645(95)00100-X

Chai, J. Y., and Muramatsu, Y. (2007). Determination of bromine and iodine in twenty-three geochemical reference materials by ICP-MS. *Geostandards Geoanalytical Res.* 31 (2), 143–150. doi: 10.1111/j.1751-908X.2007.00856.x

Chance, R., Baker, A. R., Carpenter, L. J., and Jickells, T. D. (2014). The distribution of iodide at the sea surface. *Environ. Sci.: Processes Impacts* 16 (8), 1841–1859. doi: 10.1039/C4EM00139G

Chance, R., Tinel, L., Sherwen, T., Baker, A. R., Bell, T., Brindle, J., et al. (2019). Metadata record for: Global sea-surface iodide observations *ScientificData* 6 1967–2018. doi: 10.6084/M9.FIGSHARE.10130129

Cutter, G. A., Moffett, J. W., Nielsdóttir, M. C., and Sanial, V. (2018). Multiple oxidation state trace elements in suboxic waters off Peru: *In situ* redox processes and advective/diffusive horizontal transport. *Mar. Chem.* 201, 77–89. doi: 10.1016/j.marchem.2018.01.003

Davis, C. V., Wishner, K., Renema, W., and Hull, P. M. (2021). Vertical distribution of planktic foraminifera through an oxygen minimum zone: how assemblages and test morphology reflect oxygen concentrations. *Biogeosciences* 18 (3), 977–992. doi: 10.5194/bg-18-977-2021

Erdem, Z., Schönfeld, J., Rathburn, A. E., Pérez, M.–E., Cardich, J., and Glock, N. (2020). Bottom-water deoxygenation at the Peruvian margin during the last deglaciation recorded by benthic foraminifera. *Biogeosciences* 17 (12), 3165–3182. doi: 10.5194/bg-17-3165-2020

Evans, N., Boles, E., Kwiecinski, J. V., Mullen, S., Wolf, M., Devol, A. H., et al. (2020). The role of water masses in shaping the distribution of redox active compounds in the

Eastern tropical north pacific oxygen deficient zone and influencing low oxygen concentrations in the eastern pacific ocean. *Limnol. Oceanogr.* 65 (8), 1688–1705. doi: 10.1002/lno.11412

Feng, X., and Redfern, S. A. T. (2018). Iodate in calcite, aragonite and vaterite CaCO 3 : Insights from first-principles calculations and implications for the I/Ca geochemical proxy. *Geochimica Et Cosmochimica Acta* 236, 351–360. doi: 10.1016/j.gca.2018.02.017

Garcia, H. E., Weathers, K. W., Paver, C. R., Smolyar, I., Boyer, T. P., Locarnini, M. M., et al. (2019). "World ocean atlas 2018," in *Dissolved oxygen, apparent oxygen utilization, and dissolved oxygen saturation* NOAA Atlas NESDIS 3,83 38. https://archimer.ifremer.fr/doc/00651/76337

Garfield, P. C., Packard, T. T., Friederich, G. E., and Codispoti, L. A. (1983). A subsurface particle maximum layer and enhanced microbial activity in the secondary nitrite maximum of the northeastern tropical pacific ocean. *J. Mar. Res.* 41 (4), 747–768. doi: 10.1357/002224083788520496

Glock, N., Liebetrau, V., and Eisenhauer, A. (2014). I/Ca ratios in benthic foraminifera from the Peruvian oxygen minimum zone: analytical methodology and evaluation as a proxy for redox conditions. *Biogeosciences* 11 (23), 7077–7095. doi: 10.5194/bg-11-7077-2014

Glock, N., Liebetrau, V., Eisenhauer, A., and Rocholl, A. (2016). High resolution I/Ca ratios of benthic foraminifera from the Peruvian oxygen-minimum-zone: A SIMS derived assessment of a potential redox proxy. *Chem. Geology* 447, 40–53. doi: 10.1016/j.chemgeo.2016.10.025

Hardisty, D. S., Horner, T. J., Wankel, S. D., Blusztajn, J., and Nielsen, S. G. (2020). Experimental observations of marine iodide oxidation using a novel sparge-interface MC-ICP-MS technique. *Chem. Geology* 532, 119360. doi: 10.1016/j.chemgeo.2019.119360

Hoogakker, B. A. A., Lu, Z., Umling, N., Jones, L., Zhou, X., Rickaby, R. E. M., et al. (2018). Glacial expansion of oxygen-depleted seawater in the eastern tropical pacific. *Nature* 562 (7727), 410–413. doi: 10.1038/s41586-018-0589-x

Jickells, T. D., Boyd, S. S., and Knap, A. H. (1988). Iodine cycling in the Sargasso Sea and the Bermuda inshore waters. *Mar. Chem.* 24 (1), 61–82. doi: 10.1016/0304-4203(88)90006-0

Lu, W., Dickson, A. J., Thomas, E., Rickaby, R. E., Chapman, P., and Lu, Z. (2020). Refining the planktic foraminiferal I/Ca proxy: Results from the southeast Atlantic ocean. *Geochimica Cosmochimica Acta* 287, 318–327. doi: 10.1016/j.gca.2019.10.025

Lu, Z., Hoogakker, B. A. A., Hillenbrand, C.–D., Zhou, X., Thomas, E., Gutchess, K. M., et al. (2016a). Oxygen depletion recorded in upper waters of the glacial southern ocean. *Nat. Commun.* 7, 11146. doi: 10.1038/ncomms11146

Lu, Z., Hoogakker, B. A. A., Hillenbrand, C.-D., Zhou, X., Thomas, E., Gutchess, K. M., et al. (2016b). "Oxygen depletion recorded in upper waters of the glacial southern ocean," in *(Table S1) I/Ca ratios of surface sediments* (PANGAEA). doi: 10.1594/PANGAEA.869449

Lu, Z., Jenkyns, H. C., and Rickaby, R. E. M. (2010). Iodine to calcium ratios in marine carbonate as a paleo-redox proxy during oceanic anoxic events. *Geology* 38 (12), 1107–1110. doi: 10.1130/G31145.1

Medina Faull, L., Mara, P., Taylor, G. T., and Edgcomb, V. P. (2020). Imprint of trace dissolved oxygen on prokaryoplankton community structure in an oxygen minimum zone. *Front. Mar. Sci.* 7 (360). doi: 10.3389/fmars.2020.00360

Moffitt, S. E., Moffitt, R. A., Sauthoff, W., Davis, C. V., Hewett, K., and Hill, T. M. (2015). Paleoceanographic insights on recent oxygen minimum zone expansion: Lessons for modern oceanography. *PloS One* 10 (1), e0115246. doi: 10.1371/journal.pone.0115246

Moriyasu, R., Evans, Z. C., Bolster, K. M., Hardisty, D. S., and Moffett, J. W. (2020). The distribution and redox speciation of iodine in the Eastern tropical north pacific ocean. *Global Biogeochem. Cycles* 34 (2):e2019GB00630. doi: 10.1029/2019GB006302

Orsi, A. H., Whitworth, III, T., and Nowlin, J. W.D. (1995). On the meridional extent and fronts of the Antarctic circumpolar current. *Deep Sea Res. Part I: Oceanographic Res. Papers* 42 (5), 641–673. doi: 10.1016/0967-0637(95)00021-W

Oschlies, A., Schulz, K. G., Riebesell, U., and Schmittner, A. (2008). Simulated 21st century's increase in oceanic suboxia by CO 2 -enhanced biotic carbon export. *Global Biogeochem. Cycles* 22 (4):467–473. doi: 10.1029/2007GB003147

Podder, J., Lin, J., Sun, W., Botis, S. M., Tse, J., Chen, N., et al. (2017). Iodate in calcite and vaterite: Insights from synchrotron X-ray absorption spectroscopy and first-principles calculations. *Geochimica Et Cosmochimica Acta* 198, 218–228. doi: 10.1016/j.gca.2016.11.032

Rathburn, A. E., Willingham, J., Ziebis, W., Burkett, A. M., and Corliss, B. H. (2018). A new biological proxy for deep-sea paleo-oxygen: Pores of epifaunal benthic foraminifera. *Sci. Rep.* 8 (1), 9456. doi: 10.1038/s41598-018-27793-4

Rue, E. L., Smith, G. J., Cutter, G. A., and Bruland, K. W. (1997). The response of trace element redox couples to suboxic conditions in the water column. *Deep Sea Res. Part I: Oceanographic Res. Papers* 44 (1), 113–134. doi: 10.1016/S0967-0637(96)00088-X

Schlitzer, R. (2022) *Ocean data view*. Available at: https://odv.awi.de.

Schwehr, K. A., and Santschi, P. H. (2003). Sensitive determination of iodine species, including organo-iodine, for freshwater and seawater samples using high performance liquid chromatography and spectrophotometric detection. *Analytica Chimica Acta* 482 (1), 59–71. doi: 10.1016/S0003-2670(03)00197-1

Smart, S. M., Fawcett, S. E., Ren, H., Schiebel, R., Tompkins, E. M., Martínez-García, A., et al. (2020). The nitrogen isotopic composition of tissue and shell-bound organic matter of planktic foraminifera in southern ocean surface waters. *Geochem. Geophysics Geosystems* 21 (2):e2019GC008440. doi: 10.1029/2019GC008440

Steinhardt, J., de Nooijer, L. J., Brummer, G.–J.A., and Reichart, G.–J. (2015). Profiling planktonic foraminiferal crust formation. *Geochem. Geophysics Geosystems* 16 (7), 2409–2430. doi: 10.1002/2015GC005752

Studer, A. S., Mekik, F., Ren, H., Hain, M. P., Oleynik, S., Martínez-García, A., et al. (2021). Ice Age-Holocene similarity of Foraminifera-Bound nitrogen isotope ratios in the Eastern equatorial pacific. *Paleoceanogr. Paleoclimatol.* 36 (5):e2020PA004063. doi: 10.1029/2020PA004063

Truesdale, V. W., and Bailey, G. W. (2000). Dissolved iodate and total iodine during an extreme hypoxic event in the southern benguela system. *Estuarine Coast. Shelf Sci.* 50 (6), 751–760. doi: 10.1006/ecss.2000.0609

Truesdale, V. W., Bale, A., and Woodward, E. (2000). The meridional distribution of dissolved iodine in near-surface waters of the Atlantic ocean. *Prog. Oceanogr.* 45 (3-4), 387–400. doi: 10.1016/S0079-6611(00)00009-4

Truesdale, V. W., and Spencer, C. P. (1974). Studies on the determination of inorganic iodine in seawater. *Mar. Chem.* 2 (1), 33–47. doi: 10.1016/0304-4203(74)90004-8

Veitch, J. A., Florenchie, P., and Shillington, F. A. (2006). Seasonal and interannual fluctuations of the Angola–benguela frontal zone (ABFZ) using 4.5 km resolution satellite imagery from 1982 to 1999. *Int. J. Remote Sens.* 27 (5), 987–998. doi: 10.1080/01431160500127914

Waite, T. J., Truesdale, V. W., and Olafsson, J. (2006). The distribution of dissolved inorganic iodine in the seas around Iceland. *Mar. Chem.* 101 (1-2), 54–67. doi: 10.1016/j.marchem.2006.01.003

Winkelbauer, H., Cordova-Rodriguez, K., Reyes-Macaya, D., Scott, J., Glock, N., Lu, Z., et al. (2021). Foraminifera iodine to calcium ratios: approach and cleaning. *Geochem. Geophysics Geosystems* 22, 1–11. doi: 10.1029/2021GC009811

Wishner, K. F., Seibel, B. A., Roman, C., Deutsch, C., Outram, D., Shaw, C. T., et al. (2018). Ocean deoxygenation and zooplankton: Very small oxygen differences matter. *Sci. Adv.* 4 (12), eaau5180. doi: 10.1126/sciadv.aau5180

Wong, G. T., and Brewer, P. G. (1977). The marine chemistry of iodine in anoxic basins. *Geochimica Et Cosmochimica Acta* 41 (1), 151–159. doi: 10.1016/0016-7037(77)90195-8

Wong, G. T., Takayanagi, K., and Todd, J. F. (1985). Dissolved iodine in waters overlying and in the orca basin, gulf of Mexico. *Mar. Chem.* 17 (2), 177–183. doi: 10.1016/0304-4203(85)90072-6

Zhang, S., Xu, C., Creeley, D., Ho, Y.–F., Li, H.–P., Grandbois, R., et al. (2013). Iodine-129 and iodine-127 speciation in groundwater at the hanford site, US: Iodate incorporation into calcite. *Environ. Sci. Technol.* 47 (17), 9635–9642. doi: 10.1021/es401816e

frontiers | Frontiers in Marine Science

TYPE Review
PUBLISHED 15 February 2023
DOI 10.3389/fmars.2023.1085618

Check for updates

OPEN ACCESS

EDITED BY
Rosie Chance,
University of York, United Kingdom

REVIEWED BY
Lucy J. Carpenter,
University of York, United Kingdom
Alex Baker,
University of East Anglia, United Kingdom

*CORRESPONDENCE
George W. Luther III
luther@udel.edu

SPECIALTY SECTION
This article was submitted to Marine Biogeochemistry, a section of the journal Frontiers in Marine Science

RECEIVED 31 October 2022
ACCEPTED 03 January 2023
PUBLISHED 15 February 2023

CITATION
Luther GW III (2023) Review on the physical chemistry of iodine transformations in the oceans. *Front. Mar. Sci.* 10:1085618. doi: 10.3389/fmars.2023.1085618

COPYRIGHT
© 2023 Luther. This is an open-access article distributed under the terms of the Creative Commons Attribution License (CC BY). The use, distribution or reproduction in other forums is permitted, provided the original author(s) and the copyright owner(s) are credited and that the original publication in this journal is cited, in accordance with accepted academic practice. No use, distribution or reproduction is permitted which does not comply with these terms.

Review on the physical chemistry of iodine transformations in the oceans

George W. Luther III*

School of Marine Science and Policy, University of Delaware, Lewes, DE, United States

The transformation between iodate (IO_3^-), the thermodynamically stable form of iodine, and iodide (I^-), the kinetically stable form of iodine, has received much attention because these species are often dependent on the oxygen concentration, which ranges from saturation to non-detectable in the ocean. As suboxic conditions in the ocean's major oxygen minimum zones indicate that IO_3^- is minimal or non-detectable, the incorporation of IO_3^- into carbonate minerals has been used as a redox proxy to determine the O_2 state of the ocean. Here, I look at the one and two electron transfers between iodine species with a variety of oxidants and reductants to show thermodynamics of these transformations. The IO_3^- to IO_2^- conversion is shown to be the controlling step in the reduction reaction sequence due to thermodynamic considerations. As IO_3^- reduction to IO_2^- is more favorable than NO_3^- reduction to NO_2^- at oceanic pH values, there is no need for nitrate reductase for IO_3^- reduction as other reductants (e.g. Fe^{2+}, Mn^{2+}) and dissimilatory IO_3^- reduction by microbes during organic matter decomposition can affect the transformation. Unfortunately, there is a dearth of information on the kinetics of reductants with IO_3^-; thus, the thermodynamic calculations suggest avenues for research. Conversely, there is significant information on the kinetics of I^- oxidation with various oxygen species. In the environment, I^- oxidation is the controlling step for oxidation. The oxidants that can lead to IO_3^- are reactive oxygen species with O_3 and •OH being the most potent as well as sedimentary oxidized Mn, which occurs at lower pH than ocean waters. Recent work has shown that iodide oxidizing bacteria can also form IO_3^-. I^- oxidation is more facile at the sea surface microlayer and in the atmosphere due to O_3.

KEYWORDS

iodate, iodide, iodine intermediates, thermodynamics, oxidation, reduction

1 Introduction

The thermodynamically favorable form of iodine in seawater is iodate (IO_3^-). However, iodide (I^-) is present in oxic, suboxic and anoxic waters. The one electron transfer reaction of I^- with molecular oxygen, $^3O_2$, to form the iodine atom (I•) and superoxide (O_2^-) is thermodynamically unfavorable as is the reaction of two I^- with $^3O_2$ to form I_2 and H_2O_2 (Luther et al., 1995; Luther, 2011). Thus, other oxidants are required to initiate abiotic iodide oxidation, and I^- is a known sink for O_3. Biotic iodide oxidation has received much interest

with one report showing conversion of iodide to iodate (Hughes et al., 2021). Iodate reduction can occur with common reductants (e.g., sulfide, Fe^{2+}), and various organisms that decompose organic matter using iodate as the electron acceptor. Nitrate reductase and dimethyl sulfoxide reductase enzymes from these and planktonic microbes are considered important mediators for biotic iodate reduction (e.g., Hung et al., 2005; Amachi, 2008). Thus, there has been extensive interest in the chemistry of these two iodine species and the possible intermediates that form during their 6-electron redox interconversion ever since the element, iodine, was first discovered as I_2 during the study of brown kelp algae of the Laminariales (kelps/seaweeds) by Courtois in the early 1800s (Wong, 1991; Küpper et al., 2008; Küpper et al., 2011).

Possible chemical species that form during the $IO_3^- \leftrightarrow I^-$ interconversion are given in eqn. (1a, b). The loss of an O atom is equivalent to a two-electron transfer resulting in the reduction of the iodine from +5 in IO_3^- to +3 for IO_2^- (HOIO) to +1 for HOI (IO^-) and to -1 for I^-. The acid-base species in parentheses are minor species at seawater pH as the pK_a values for HOI and HOIO are 10.7 (K_a = 2 x 10^{-11}) and 4.49 (K_a = 3.2 x 10^{-5}), respectively.

$$IO_3^- \leftrightarrow IO_2^-(HOIO) \leftrightarrow HOI(IO^-) \leftrightarrow I^- \quad (1a)$$

Equation 1b shows the interconversion between HOI and I^- as HOI undergoes one-electron transfer to I_2 followed by another one-electron reduction per I atom to I^-.

$$HOI(IO^-) \leftrightarrow I_2 \leftrightarrow I^- \quad (1b)$$

This work considers the thermodynamics of these transformations during the reduction of IO_3^-, which occurs in anoxic systems, during organic matter decomposition and by phytoplankton, as well as the oxidation of I^-, which occurs by the direct oxidation of iodide by iodide oxidizing bacteria, oxidized metals and reactive oxygen species (ROS) that are produced by certain microbes, (macro)algae and abiotic processes including photochemistry. In a previous work (Luther, 2011), the chemistry and thermodynamics of chloride, bromide and iodide oxidation were compared; however, I(+3) species (HOIO, iodous acid, and IO_2^-, iodite) and stepwise iodate reduction were not considered. Here, stepwise reactions of the iodine species in equations 1a and 1b with environmentally important reactants (including transient ROS species) are considered for both the oxidation of I^- and the reduction of IO_3^- to affect their interconversion. The kinetics of these stepwise reactions are also considered. Kinetic data for the first step(s) in iodide oxidation are available, but less kinetic information is available for iodate reduction.

2 Methods

2.1 Calculations of aqueous redox potentials from half-reactions

Table 1 gives several equations for redox half-reactions that include the pH dependence for the reaction considered. These are pε(pH) relationships based on the balanced chemical equations and the thermodynamics of each chemical species. The basic mathematical approach has been fully developed in standard textbooks (Stumm and Morgan, 1996; Luther, 2016) and used in previous publications (Luther, 2010; Luther, 2011). Aqueous thermodynamic data to calculate the pε(pH) or logK(pH) relationships in Table 1 (at 25°C and 1 atm) are from Stumm and Morgan (1996) and other sources (Bard et al., 1985; Stanbury, 1989). The value used for the Gibbs free energy for Fe^{2+} (-90.53 kJ/mole) is that discussed in Rickard and Luther (2007). Values of the free energy for HOIO and IO_2^- are from Schmitz (2008).

The calculated pε value from each half-reaction is given as a function of pH as in the examples in Table 1, and these half reactions can be used for simple calculations of the pE values of full reactions (see next section). When H^+ or OH^- is not in a balanced equation for a half-reaction, there is no pH dependence on the half-reaction. The pε calculated is termed pε(pH) which provides a log K for each half-reaction at a given pH. Concentration dependence for the other reactants are not considered in the calculation; thus, these are considered standard state calculations. When concentration dependence is considered, the calculated pε value can vary as in the following example for the O_2/H_2O couple (O1 in Table 1).

Using the balanced half reaction and the Gibbs free energy of formation of each species at 25°C, the Gibbs free energy of the reaction and the equilibrium constant are calculated.

$$\begin{array}{cccccc} O_{2(aq)} + & 4\ H^+ + & 4e^- \rightarrow & 2H_2O & & \\ 16.32 & 0 & 0 & 2(-237.18) & \Delta G^\circ_{formation}\ (kJ/mol) & \end{array}$$

The standard state ΔG° for the reaction = - 490.68 kJ/2 moles H_2O or 4 moles of electrons. The equilibrium constant (K_4^0) is given in eqn. 2a where {} indicates activity for each chemical species and the activity of H_2O is defined as 1.

$$K_4^0 = \frac{\{H_2O\}^2}{\{O_2\}\ \{H^+\}^4\ \{e^-\}^4} \quad (2a)$$

On expanding, eqn. 2b results.

$$\log K_4^0 = -\log\{O_{2(aq)}\} - \log\{H^+\}^4 - \log\{e^-\}^4 = \frac{\Delta G^0_{reaction}}{2.303\ RT} = 86.00 \quad (2b)$$

$\log K_4^0$ is for 4 mole of electrons or 21.50 for 1 mole of electrons. For a one-electron half-reaction, we have

$$^1/_4O_{2(aq)} + H^+ + e^- \rightarrow {}^1/_2H_2O$$

And equation 2b becomes equation 2c

$$\frac{1}{4}\log K_4^0 = -\frac{1}{4}\log\{O_{2(aq)}\} - \log\{H^+\} - \log\{e^-\} \quad (2c)$$

or

$$\frac{1}{4}\log K_4^0 = -\frac{1}{4}\log\{O_{2(aq)}\} + pH + p\varepsilon \quad and\ \ on\ \ rearranging$$

$$p\varepsilon = \frac{1}{4}\log K_4^0 + \frac{1}{4}\log\{O_{2(aq)}\} - pH$$

From the Nernst Equation, $p\varepsilon^o = 1/4 \log K_4^0 = 21.50$ (the standard state value), which on substitution gives equation O1 (see Table 1) where concentration is used for $O_{2(aq)}$.

TABLE 1 Reduction half-reactions for relevant species of oxygen, nitrogen, sulfur, manganese, iron and iodine normalized to one electron.

OXYGEN REACTIONS		
four electron reaction normalized to one electron		
$¼\ O_{2(aq)} + H^+ + e^- \rightarrow ½H_2O$	$pε = 21.50 - pH + ¼ \log [O_{2(aq)}]$	(O1)
	$pε = pε° - pH = 21.50 - pH$	(O1a)
two electron reactions normalized to one electron		
$½O_{2(aq)} + H^+ + e^- \rightarrow ½H_2O_2$	$pε = pε° - pH = 13.18 - pH$	(O2)
$½H_2O_2 + H^+ + e^- \rightarrow H_2O$	$pε = pε° - pH = 29.82 - pH$	(O3)
$½O_3 + H^+ + e^- \rightarrow ½O_{2(aq)} + ½H_2O$	$pε = pε° - pH = 34.64 - pH$	(O4)
$½{}^1O_{2(aq)} + H^+ + e^- \rightarrow ½H_2O_2$	$pε = pε° - pH = 21.57 - pH$	(O5)
One electron transfer reactions only		
$O_{2(aq)} + e^- \rightarrow O^-_{2(aq)}$	$pε = pε° = -2.72$	(O6)
$O^-_{2(aq)} + 2H^+ + e^- \rightarrow H_2O_2$	$pε = pε° - 2\ pH = 29.08 - 2pH$	(O7)
$H_2O_2 + H^+ + e^- \rightarrow H_2O + OH•$	$pε = pε° - pH = 16.71 - pH$	(O8)
$OH• + e^- \rightarrow OH^-$	$pε = pε° = 28.92 + pOH$	(O9a)
$OH• + H^+ + e^- \rightarrow H_2O$	$pε = pε° = 42.92 - pH$	(O9b)
$^1O_{2(aq)} + e^- \rightarrow O^-_{2(aq)}$	$pε = pε° = 14.04$	(O10)
$O_3 + e^- \rightarrow O_3^-$	$pε = pε° = 17.08$	(O11)
NITROGEN REACTIONS		
two electron reactions (per N) normalized to one electron		
$½NO_3^- + H^+ + e^- \rightarrow ½NO_2^- + ½H_2O$	$pε = pε° - pH = 14.28 - pH$	(N1)
$½N_2O + H^+ + e^- \rightarrow ½N_2 + ½H_2O$	$pε = pε° - pH = 29.91 - pH$	(N2)
$½N_2H_5^+ + 1.5H^+ + e^- \rightarrow NH_4^+$	$pε = pε° - 1.5\ pH = 21.56 - 1.5\ pH$	(N3a)
$½N_2H_4 + 2H^+ + e^- \rightarrow NH_4^+$	$pε = pε° - 2\ pH = 25.51 - 2\ pH$	(N3b)
$½NH_3OH^+ + H^+ + e^- \rightarrow NH_4^+ + ½H_2O$	$pε = pε° - pH = 22.83 - pH$	(N4a)
$½NH_2OH + 1.5H^+ + e^- \rightarrow ½NH_4^+ + ½H_2O$	$pε = pε° - 1.5\ pH = 29.77 - 1.5\ pH$	(N4b)
$¼N_2 + 1.25H^+ + e^- \rightarrow ¼N_2H_5^+$	$pε = pε° - 1.25pH = -3.89 - 1.25pH$	(N5)
$½N_2 + H_2O + H^+ + e^- \rightarrow NH_2OH$	$pε = pε° - pH = -22.82 - pH$	(N6)
One electron (per N) transfer reactions only		
$NO_3^- + 2H^+ + e^- \rightarrow NO_2 + H_2O$	$pε = pε° - 2\ pH = 13.07 - 2\ pH$	(N7)
$NO_2 + e^- \rightarrow NO_2^-$	$pε = pε° = 15.6$	(N8)
$NO_2 + H^+ + e^- \rightarrow HNO_2$	$pε = pε° - pH = 16.51 - pH$	(N8a)
SULFUR REACTIONS		
Two-electron reactions normalized to one electron		
$½S + H^+ + e^- \rightarrow ½H_2S$	$pε = pε° - pH = 2.44 - pH$	(S1)
$½S + ½H^+ + e^- \rightarrow ½HS^-$	$pε = pε° - 0.5\ pH = -1.06 - 0.5\ pH$	(S2)
$½(CH_3)_2SO + H^+ + e^- \rightarrow ½(CH_3)_2S + ½H_2O$	$pε = pε° - 0.5\ pH = 11.56 - pH$	(S3)
One-electron transfer reactions only		
$HS• + e^- \rightarrow HS^-$	$pε = pε° = 18.26$	(S4)
$HS• + H^+ + e^- \rightarrow H_2S$	$pε = pε° - pH = 25.21 - pH$	(S5)
$S + H^+ + e^- \rightarrow HS•$	$pε = pε° - pH = -20.33 - pH$	(S6)

(Continued)

TABLE 1 Continued

MANGANESE REACTIONS		
two electron reactions normalized to one electron		
$½MnO_2 + 2H^+ + e^- \rightarrow ½Mn^{2+} + H_2O$	$pε = pε° - 2\ pH = 20.80 - 2\ pH$	(Mn1)
$½Mn_3O_4 + 4H^+ + e^- \rightarrow 3/2Mn^{2+} + 2H_2O$	$pε = pε° - 4\ pH = 30.82 - 4\ pH$	(Mn2)
One electron transfer reaction only		
$MnOOH + 3\ H^+ + e^- \rightarrow Mn^{2+} + 2\ H_2O$	$pε = pε° - 3\ pH = 25.35 - 3\ pH$	(Mn3)
IRON REACTIONS		
two electron reaction normalized to one electron		
$½Fe_3O_4 + 4H^+ + e^- \rightarrow 3/2Fe^{2+} + 2H_2O$	$pε = pε° - 4\ pH = 18.20 - 4\ pH$	(Fe1)
One electron transfer reactions only		
$FeOOH + 3\ H^+ + e^- \rightarrow Fe^{2+} + 2\ H_2O$	$pε = pε° - 3\ pH = 13.37 - 3\ pH$	(Fe2)
$Fe(OH)_3 + 3\ H^+ + e^- \rightarrow Fe^{2+} + 3\ H_2O$	$pε = pε° - 3\ pH = 18.03 - 3\ pH$	(Fe3)
IODINE REACTIONS		
One electron transfer reaction only		
$½\ I_2 + e^- \rightarrow I^-$	$pε = pε° = 10.50$	(Io1)
two electron reactions normalized to one electron		
$½\ HOI + ½\ H^+ + e^- \rightarrow ½\ I^- + ½\ H_2O$	$pε = pε° - 0.5\ pH = 16.66 - 0.5\ pH$	(Io2)
$HOI + H^+ + e^- \rightarrow ½\ I_2 + H_2O$	$pε = pε° - pH = 22.91 - pH$	(Io3)
$½\ HOIO + H^+ + e^- \rightarrow ½\ HOI + ½\ H_2O$	$pε = pε° - pH = 21.10 - pH$	(Io4a)
$½IO_2^- + 1.5H^+ + e^- \rightarrow ½HOI + ½H_2O$	$pε = pε° - 1.5\ pH = 24.06 - 1.5\ pH$	(Io4b)
$½IO_3^- + 1.5H^+ + e^- \rightarrow ½HOIO + ½H_2O$	$pε = pε° - 1.5\ pH = 17.89 - 1.5\ pH$	(Io5a)
$½IO_3^- + H^+ + e^- \rightarrow ½IO_2^- + ½H_2O$	$pε = pε° - pH = 14.91 - pH$	(Io5b)
six electron reaction normalized to one electron		
$1/6\ IO_3^- + H^+ + e^- \rightarrow 1/6\ I^- + ½H_2O$	$pε = pε° - pH = 18.55 - pH$	(Io6)
	$pε = 18.55 - pH - \frac{1}{6}\ log\frac{[I^-]}{[IO_3^-]}$	

Activities of all reactants other than H^+ are at unity.

$$pε = pε^o + {}^1/_4 log[O_{2(aq)}] - pH = 21.50 + {}^1/_4 log\{O_{2(aq)}\} - pH \quad (O1)$$

At ocean surface conditions of 211 μM O_2 (211 x 10^{-6} M; 100% saturation at 25°C and salinity of 35), this expression becomes

$$pε = 21.50 + {}^1/_4\ log[211 \times 10^{-6}M] - pH = 20.58 - pH$$

and at a pH of 8, pε = 12.58.

At 1μM O_2 (10^{-6} M) which occurs in oxygen minimum zones, this expression becomes

$$pε = 21.50 + {}^1/_4 log[10^{-6}M] - pH \quad = 20.00 - pH$$

and at a pH of 7.5, pε = 12.50.

At unit activity for all reagents including H^+, pε = pε°. At unit activity of all reagents other than the H^+, equation O1a results, which is used for many calculations in this paper.

$$pε = pε^o - pH = 21.50 - pH \quad (O1a)$$

Note that the above equations show a 1.50 log unit change for an O_2 concentration range from 1 μM to unity activity (O1a) so the calculations could vary an order of magnitude or more in either direction when concentration dependence is included. However, comparisons can be more easily made when combining different half-reactions at a given pH. This permits an assessment of which combined half-reactions are thermodynamically favorable and thus more likely to occur in a given environmental setting.

2.2 Coupling half-reactions

As an example of coupling two half reactions to determine whether a reaction is favorable, I use the data in Table 1 for the reduction of IO_3^- (Io5b) by NO_2^- (N1) in equation 3.

$$NO_2^- + IO_3^- \rightarrow NO_3^- + IO_2^- \quad (3)$$

Equation 4 is used to calculate a complete reaction's pε or $\Delta\log K_{reaction}$ value. All values of $\Delta\log K_{reaction} > 0$ indicate a favorable reaction and all values of $\Delta\log K_{reaction} < 0$ indicate an unfavorable reaction.

$$p\varepsilon_{reaction} = p\varepsilon_{red} + p\varepsilon_{oxid} = \Delta\log K_{reaction} \quad (4)$$

At a pH of 7, the $p\varepsilon_{red}$ values for IO_3^- and NO_3^- are 7.91 and 7.28, respectively. As NO_2^- is the reductant, it is oxidized; thus, the sign for $p\varepsilon_{red}$ (7.28) is reversed to become $p\varepsilon_{oxid}$ (-7.28).

$$\Delta\log K_{reaction} = p\varepsilon_{red}(IO_3^-) + p\varepsilon_{oxid}(NO_3^-) = 7.91 + (-7.28) = 0.63$$

For reaction 3, there is no pH dependence as the pH dependence of each half-reaction is similar so cancels.

For this work, Table 1 lists the pε(pH) values for Mn, Fe, oxygen, nitrogen, sulfur and iodine species for the relevant iodine redox reactions considered. Dissolved Fe(II) and Mn(II) are primarily hexaaquo species until the pH is > 7, where hydroxo complexes start to become important. As most reactions occur *via* one and two-electron transfers, the calculations will permit assessment of a thermodynamically unfavorable step along a reaction coordinate of six-electrons as in the reduction of iodate to iodide and the oxidation of iodide to iodate. From surface waters to decomposition zones, seawater pH values range from 8 down to 7; thus, the following discussion will emphasize this pH range.

3 Results and discussion: Iodate reduction

3.1 Iodate and iodide speciation at different seawater oxygen conditions

In the oxic environment, the oxidizing condition of the environment or pε is set by the 4-electron transfer reaction of the $O_{2(aq)}/H_2O$ couple [reaction O1 in Table 1]. At a pH of 8, temperature 25^{0}C and a salinity of 35, 100% $O_{2(aq)}$ saturation is 211 µM, which gives a pε of 12.58 (Figure 1). As the IO_3^-/I^- couple has a pε of 10.56 at pH = 8, IO_3^- is the thermodynamically favored iodine species.

Entering the pε value for a given $[O_{2(aq)}]$ into equation Io6 allows the determination of the iodide to iodate ratio and the actual concentration of each assuming a total iodine concentration of 450-470 nM (Elderfield and Truesdale, 1980). Figure 1 shows the iodate and iodide concentrations are equivalent at a pε of 10.56. The vertical lines indicate the environmental pε for $[O_{2(aq)}]$ of 1, 10, 100 nM, and 1, 50 and 211 µM. As oxygen minimum zones (OMZ) of the Arabian Sea and the equatorial Pacific Ocean have $[O_{2(aq)}]$ concentrations in the 1-100 nM range (Revsbech et al., 2009; Lehner et al., 2015), calculations show that IO_3^- is the thermodynamically preferred iodine species even at 1 nM $O_{2(aq)}$, which gives a pε of 11.25 for the $O_{2(aq)}/H_2O$ couple. However, I^- is the dominant iodine species detected in OMZ waters (Wong and Brewer, 1977; Luther and Campbell, 1991; Rue et al., 1997; Farrenkopf and Luther, 2002; Cutter et al., 2018). At $[O_{2(aq)}]$ concentrations ≤ 1 µM, IO_3^-, NO_3^- and Mn^{2+} concentrations are now similar or higher in concentration and should determine the pε of the water.

As most reactions occur by 1- or 2-electron transfers, Figure 2 shows the redox sequence for two electron transfer redox couples

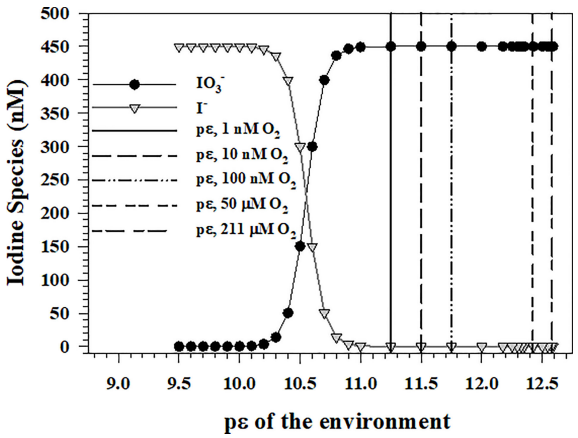

FIGURE 1
IO_3^- and I^- concentrations for a total iodine concentration of 450 nM at different environmental pε values assuming that $O_{2(aq)}$ reduction to H_2O sets the pε value of ocean waters.

NO_3^-/NO_2^-(N1), MnO_2/Mn^{2+} (Mn1) and the one-electron redox couple $Fe(OH)_3/Fe^{2+}$ (Fe3) over a wide range of pH. The redox sequence at pH = 8 is as expected for the N, Mn and Fe systems. As NO_2^- (up to 12 µM) and Mn^{2+} (up to 8 µM) are formed at OMZ oxic-anoxic transition zones (e.g., Arabian Sea, Black Sea, Equatiorial Pacific, see Lewis and Luther, 2000; Trouwborst et al., 2006; Cutter et al., 2018, respectively) and are in higher concentration than $O_{2(aq)}$, the $NO_3^- \rightarrow NO_2^-$(N1) and $MnO_2 \rightarrow Mn^{2+}$ (Mn1) couples can be chosen to set the environmental pε. At pH = 8, the NO_3^- to NO_2^- pε is 6.15 and the MnO_2 to Mn^{2+} pε is 4.80. At pH = 7, the NO_3^- to NO_2^- pε is 7.28 and the MnO_2 to Mn^{2+} pε is 6.80. At these pε values, $O_{2(aq)}$ is below 1 nM, and I^- is now the thermodynamically favored iodine species when comparing these data with the IO_3^-/I^- couple (pε of 10.56 at pH = 8).

Figure 2 also shows that the IO_3^-/IO_2^- couple (Io5b) should be the first step in the reaction sequence of iodate to iodide (eqn. 1a). As the pε of the IO_3^-/IO_2^- couple has a more positive pε value than the N, Mn and Fe couples in Figure 2, IO_3^- reduction is more favorable than these couples even though it is very close to the NO_3^-/NO_2^- couple. Thus, IO_3^- is predicted to reduce before NO_3^-, and biological activity (e.g., nitrate reductase activity) is not necessary to reduce IO_3^- (see section

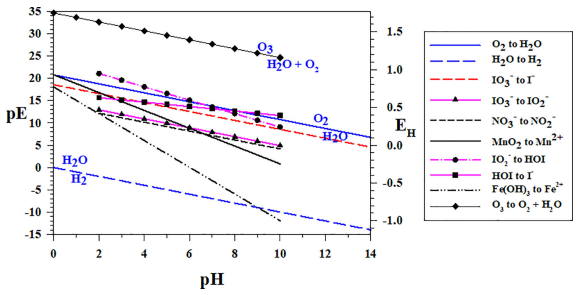

FIGURE 2
Two electron transfer redox couples for O_3 (O4), N (N1), Mn (Mn1) and I (Io2a, Io4b, Io5b), and one electron transfer redox couple for Fe (Fe3). The oxidized species is always above the line and the reduced below the line as in the O_2/H_2O and the H_2O/H_2 couples, which dictate the water stability field.

3.2). Because of the strong pH dependence for the Mn and Fe couples, they cross the IO_3^-/IO_2^- and NO_3^-/NO_2^- couples at lower pH, which have similar slopes. Thus, NO_2^- is predicted to reduce IO_3^- to IO_2^- (eqn. 3). Interestingly, Mn^{2+} and Fe^{2+} should be poorer reductants than NO_2^- for conversion of IO_3^- to IO_2^- at a pH< 6 and pH< 1, respectively, but are more favorable to reduce IO_3^- than NO_2^- above those pH values (see sections 3.2 and 3.3).

Although the IO_3^- to I^- conversion occurs at higher pε, it is a 6-electron transfer (IO6), which is not a facile process. Thus, the intermediates (IO_2^- and HOI) will dictate the reactivity sequence *via* a combination of thermodynamic and kinetic considerations.

As shown in Figure 2, IO_2^- reduction to HOI and HOI reduction to I^- are also more favorable at higher pε values than the IO_3^- to I^- couple. At a pH = 8, the IO_2^- to HOI couple has a pε value of 12.06 corresponding to 2 µM O_2 (see Figure 1). Similarly, the HOI to I^- couple has a pε value of 12.66 corresponding to 250 µM O_2. At a pH of 7, both couples have pε values greater than 13 indicating that, even at O_2 saturation, I^- is the dominant species predicted when these intermediates form. At a pH = 7.5 (that is found in many OMZ waters), both IO_2^- to HOI and HOI to I^- couples have pε values greater than 12.6; also indicating that at O_2 saturation, I^- is the dominant species predicted. Thus, the intermediates IO_2^- and HOI are not predicted to be stable in marine waters; thus, the conversion of IO_3^- to IO_2^- is a key step. Interestingly, Hardisty et al. (2021) found *in situ* IO_3^- reduction in the oxycline where $[O_{2(aq)}]$ was 11 µM, but not at $[O_{2(aq)}]$< 2 µM. Lastly, the O_3 to $O_2 + H_2O$ couple is highly oxidizing indicating that all iodine couples should lead to IO_3^- formation. O_3 reactions will be discussed in more detail below (sections 4.2, 4.7).

In the next sections (3.2 – 3.5), the thermodynamics for the conversion of iodate to iodide *via* the intermediates outlined in equations 1a and 1b by environmental reductants are considered to show what step, if any, in the reduction of iodate to iodide may be unfavorable over a wide range of pH. Iodate reduction is well known in the marine environment (e.g., Wong and Brewer, 1977; Wong et al., 1985; Luther and Campbell, 1991; Rue et al., 1997; Farrenkopf and Luther, 2002; Cutter et al., 2018) and occurs *via* chemical reductants like sulfide (Zhang and Whitfield, 1986) and *via* microbes like *Shewanella putrfaciens* (Farrenkopf et al., 1997) and *Shewanella oneidensis* (Mok et al., 2018) during dissimilatory reduction coupled with decomposition (oxidation) of organic matter as well as phytoplankton mediated processes (e.g., Chance et al., 2007).

3.2 Iodate reduction by NO_2^-

Although NO_2^- has not yet been shown to be a reductant for IO_3^- in aqueous lab studies (eqn. 3), HNO_2 is a reductant for MnO_2 (Luther and Popp, 2002) and Mn(III)-pyrophosphate (Luther et al., 2021). Figure 3A shows the thermodynamic calculations for the stepwise conversion of IO_3^- to I^- by NO_2^- reduction (NO_2^- oxidizes to NO_3^-). All 2-electron transfer reactions, which involve O atom loss for iodine, are favorable over the pH range. For seawater pH (7-8), the least favorable reaction is the IO_3^- to IO_2^- reaction whereas the IO_2^- to HOI and HOI to I^- reactions are more favorable. Thus, the IO_3^- to IO_2^- conversion appears to be the controlling step in the reaction sequence. The 1-electron transfer reaction of HOI to I_2 is the most favorable, but the second 1-electron transfer reaction of I_2 to I^- is only favorable at pH > 4. Thus, reduction of IO_3^- to I^- by NO_2^- is predicted *via* 1-electron or 2-electron transfer reactions at seawater pH values. The data plotted in Figure 2 indicate that once IO_2^- forms there is no thermodynamic barrier to I^- formation.

The IO_3^- reaction with NO_2^- has been reported to produce I_2 in ice by Kim et al. (2019), but not in solution. The pH in the ice was 3 where HNO_2 and H_2ONO^+ exist and are the likely reductants. Thus, polar areas may be locales for IO_3^- reduction. At seawater pH, the reaction seems to be hindered by kinetics in the transition state as each reactant (IO_3^- and NO_2^-) is an anion, which will repel each other.

3.3 Biological iodate reduction

The marine literature has many reports on the uptake of IO_3^- (with or without NO_3^-) by phytoplankton with the iodine released as I^- (e.g., Elderfield and Truesdale, 1980; Wong, 2001; Wong et al., 2002; Chance et al., 2007; Bluhm et al., 2010). As a result of this iodate uptake, NO_3^- reductase was presumed by some researchers to be a key process for IO_3^- reduction to I^-. Also, Bluhm et al. (2010) and Carrano et al. (2020) showed that algal senescence enhanced I^- release, and Hepach et al. (2020) showed that there is a considerable lag between IO_3^- uptake and I^- release due to senescence.

NO_3^- reductase appears to reduce IO_3^- in some phytoplankton (Hung et al., 2005). However, de la Cuesta and Manley (2009) showed that I^- can be up taken by phytoplankton, and that different phytoplankton uptake I^- whereas other phytoplankton uptake IO_3^-. Thus, there is no need for nitrate reductase for IO_3^- reduction as I^- can be up taken by some phytoplankton rather than form from IO_3^- reduction. Moreover, Waite and Truesdale (2003) showed that nitrate reductase was not important for IO_3^- reduction by *Isochrysis galbana*. The latter study is consistent with the thermodynamics of the reduction IO_3^- to IO_2^- being more favorable than the reduction NO_3^- to NO_2^-.

Furthermore, under anaerobic conditions, dissimilatory IO_3^- reduction occurs without nitrate reductase for the denitrifying bacterium, *Pseudomonas stutzeri*, (Amachi et al., 2007; Amachi, 2008). Reyes-Umana et al. (2022) and Yamazaki et al. (2020) showed that iodate reductase is in the periplasmic space of *Pseudomonas sp* SCT. Also, Mok et al. (2018) showed that dissimilatory IO_3^- reduction by *Shewanella oneidensis* does not involve nitrate reductase. Recently, Shin et al. (2022) showed that *Shewanella oneidensis* requires extracellular dimethylsulfoxide (DMSO) reductase involving a molybdenum enzyme center for IO_3^- reduction. Guo et al. (2022) studied bacterial genomes in a variety of environments and documented that *Shewanella oneidensis* are ubiquitous in all fresh and marine waters; they concluded that IO_3^- reduction is a major biogeochemical process. Thus, nitrate reductase (also an O atom transfer reaction) is not a requirement for bacterial IO_3^- reduction to I^-.

The interconversion of dimethylsulfoxide with dimethylsulfide during dissimilatory IO_3^- reduction is another 2-electron O-atom transfer reaction. Moreover, the reactions of DMS to reduce HOI, IO_2^- and IO_3^- are thermodynamically favorable (Figure 3B, DMSO reduction is in S3, Table 1 and occurs at a lower pε than NO_3^- and IO_3^- reduction). The reaction of DMS with HOI has been suggested by

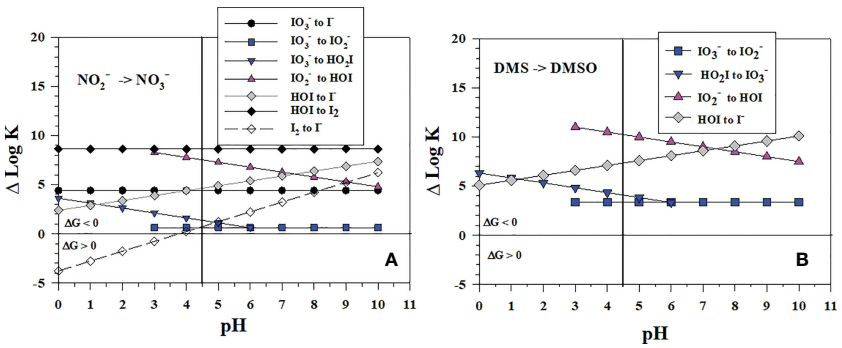

FIGURE 3
Thermodynamics for **(A)** the 1-electron and 2-electron reductions of IO_3^- (Io5a, Io5b, Io6), IO_2^- (Io4b), HOI (Io2, Io3), and I_2 (Io1) by NO_2^- (N1) and **(B)** 2-electron reductions of IO_3^- (Io5b), IO_2^- (Io4a, Io4b), HOI (Io2) by DMS (S3). The vertical line represents the pK_a value of 4.49 for HO_2I. Data above the horizontal line at $\Delta logK$ ($\Delta logK_{reaction}$) = 0 indicate a favorable reaction and data below the horizontal line indicate an unfavorable reaction.

Müller et al. (2021) to be a sink for DMS based on the rapid reaction of DMS with HOBr.

3.4 Iodate reduction by Mn^{2+} and Fe^{2+}

Figure 4 shows the thermodynamics for the stepwise conversion of IO_3^- to I^- by reduction with Mn^{2+} and Fe^{2+}. Concentrations of Mn^{2+} and Fe^{2+} range from several nM to µM in OMZs (e.g., Trouwborst et al., 2006; Moffett and German, 2020) and in suboxic porewaters (e.g., Oldham et al., 2019; Owings et al., 2021) to mM in waters emanating from hydrothermal vents (e.g., Estes et al., 2022); in these cases, Mn^{2+} and Fe^{2+} are normally higher in concentration than the total iodine concentration. For the 2-electron transfer reactions with Mn^{2+}, only the IO_2^- to HOI reaction is favorable over the entire pH range. The IO_3^- to IO_2^- reaction is favorable only at pH > 6 whereas the other reactions are favorable at pH > 3. Thus, the IO_3^- to IO_2^- conversion is the controlling step in the reaction sequence when Mn^{2+} is the reductant. Using high resolution porewater profiles of I^- and Mn^{2+} obtained by voltammetric microelectrodes, Anschutz et al. (2000) showed that a I^- maximum occurred at the depth where upward diffusing Mn(II) was being removed and proposed that I^- formed by the reaction of IO_3^- with Mn^{2+} under suboxic conditions. The reaction has not been investigated in laboratory studies.

For the reaction sequence with Fe^{2+}, all iodine species reductions are favorable over the entire pH range except for the I_2 to I^- reaction, which is favorable at pH > 2.5. Thus, there is no thermodynamic inhibition to IO_3^- reduction to I^- by Fe^{2+}, and this abiotic reaction at a pH of 7 was reported to be 92% complete after 2 hours using initial concentrations of 2 mM Fe^{2+} and 0.1 mM IO_3^- (Councell et al., 1997). Because the $Fe(OH)_3$ to Fe^{2+} couple is a 1-electron transfer, two Fe^{2+} are required in each step of the sequence. Again, the IO_3^- to IO_2^- conversion is the least favorable and likely controlling step in this reaction sequence.

Comparing Figures 3, 4 indicates that the Mn^{2+} and NO_2^- reactions with iodine species have a similar range of $\Delta logK_{reaction}$ values whereas the Fe^{2+} reactions with iodine species are more favorable (higher $\Delta logK_{reaction}$ values).

3.5 Iodate reduction by sulfide

In sulfidic waters and porewaters, IO_3^- does not exist as sulfide reacts readily with it (Zhang and Whitfield, 1986), and S(0) forms as the initial sulfur product. Figure 5 shows the thermodynamics for the stepwise conversion of IO_3^- to IO_2^- and to HOI by sulfide where S(0) forms as an intermediate leading to S_8. As the Gibbs free energy of formation for HSOH is unknown, HSOH could not be evaluated as an

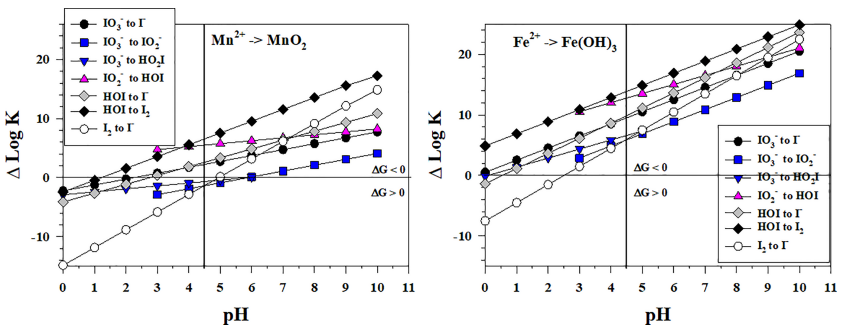

FIGURE 4
Thermodynamics for the reduction of IO_3^- (Io5a, Io5b, Io6), IO_2^- (Io4b), HOI (Io2, Io3), and I_2 (Io1) by Mn^{2+} (Mn1) and Fe^{2+} (Fe3). The vertical line represents the pK_a value of 4.49 for HO_2I. Data above the horizontal line at $\Delta logK$ ($\Delta logK_{reaction}$) = 0 indicate a favorable reaction and data below the horizontal line indicate an unfavorable reaction.

intermediate, which on continued oxidation would form SO_4^{2-}. The reaction of sulfide with I_2 and HOI is well known as the iodometric titration, so calculations were not performed. The only unfavorable iodine reduction reactions are the 1-electron reductions that lead to the formation of the HS radical (HS• or HS rad). The conversion of IO_2^- to HOI is more favorable as it has the larger $\Delta logK_{reaction}$ values. Again, the IO_3^- to IO_2^- conversion is the least favorable and likely controlling step in this reaction sequence.

3.6 Iodate reduction by NH_4^+

Figure 6 shows the thermodynamics for the stepwise conversion of IO_3^- to IO_2^- by NH_4^+ where hydrazine (N_2H_4) and hydroxylamine (NH_2OH) as well as their protonated forms could form as the first N intermediates. The thermodynamic calculations for these 2 electron transfers indicate that these reactions are not favorable. However, the reaction of the intermediates, if they could form by other processes, with IO_3^- to form N_2 is very favorable. Thus, the IO_3^- to IO_2^- conversion is the controlling step in the reaction sequence with NH_4^+.

4 Results and discussion: Iodide oxidation

4.1 Iodide oxidation by NO_3^-, MnO_2 and $Fe(OH)_3$

Figures 3–6 showed the reduction of IO_3^- with reductants. All values of $\Delta logK_{reaction} > 0$ indicate a favorable reaction and all values of $\Delta logK_{reaction} < 0$ indicate an unfavorable reaction. These figures can be used to discuss the reverse reaction of I^- oxidation with oxidants. For reverse reactions, when a $\Delta logK_{reaction} < 0$, then I^- oxidation is favorable, but when $\Delta logK_{reaction} > 0$, I^- oxidation is unfavorable.

In Figure 3, NO_3^- is not an oxidant for I^- (reverse of the NO_2^- and I_2 reaction) except for the formation of I_2 at a pH< 4.

In Figure 4, MnO_2 oxidizes I^- to HOI (reverse of the Mn^{2+} and HOI reaction) at a pH< 3 and I^- to I_2 (reverse of the Mn^{2+} and I_2 reaction) at a pH< 5. A couple of laboratory studies showed I^- oxidation with synthetic birnessite (δ-MnO_2). First, Fox et al. (2009) showed that I_2 was produced over the pH range 4.50 – 6.25, and that IO_3^- formed in smaller amounts. The kinetics of the reaction were slower at higher pH by 1.5 log units (> 30-fold) and were slower when smaller amounts of MnO_2 were added (Table 2). Allard et al. (2009) investigated the same reactants to a pH of 7.5 and found I_2 and IO_3^- as products; above pH = 7 the reaction is very slow. Iodate was found mainly in lower pH waters. Both I_2 and IO_3^- adsorb to the birnessite surface. Similar results have been found over the pH range 4-6 for Mn(III) solids (Szlamkowicz et al., 2022). These MnO_x reactions with I^- are much slower that the reactions with reactive oxygen species (Table 2). Nevertheless, these are important as Kennedy and Elderfield (1987a, 1987b) showed that the conversion of iodide to iodate occurred in marine sediments.

Figure 4 also shows that I^- oxidation by $Fe(OH)_3$ to I_2 (reverse of the Fe^{2+} and I_2 reaction) should occur only at a pH< 2.5. The I^- to HOI conversion (reverse of the Fe^{2+} and HOI reaction) is favorable at pH ≤ 0.5.

4.2 Iodide oxidation by oxygen species

Figure 7 shows the thermodynamics of I^- oxidation to I_2 by oxygen species. Figure 7A shows that the one-electron process for I^- oxidation with $^3O_2$ is thermodynamically unfavorable over all pH whereas Figure 7B shows that the two-electron process is favorable at a pH< 3. Figure 7A shows that the successive 1-electron oxidations of I^- where superoxide (O_2^-) is reduced to hydrogen peroxide (H_2O_2), which is reduced to hydroxyl radical (•OH). Only •OH is thermodynamically favorable over the pH range considered. O_2^- and H_2O_2 show favorable reactions at pH< 9 and pH< 6, respectively.

By contrast, Figure 7B shows that the reactions of I^- with the 2-electron oxidants H_2O_2, $^1O_2$ and O_3 are all thermodynamically favorable. The likely reaction pathway is the loss of 2-electrons to produce I^+, which then reacts with I^- to form I_2. Note that H_2O_2 reacts to form H_2O not •OH in Figure 7B. The 2-electron reaction with O_3 (Figure 7B) is more favorable than the 1-electron reaction (Figure 7A).

Wong and Zhang (2008) showed that H_2O_2 oxidizes I^- in artificial seawater from pH 7-9, which is consistent with Figure 7B. However, I^- oxidation does not lead to iodate. In fact, I^- reforms. They proposed that I_2 formed and was reduced back to I^-, but they did not provide a mechanism. The reverse reaction of I_2 with •OH ($\Delta logK_{reaction} < 0$ in

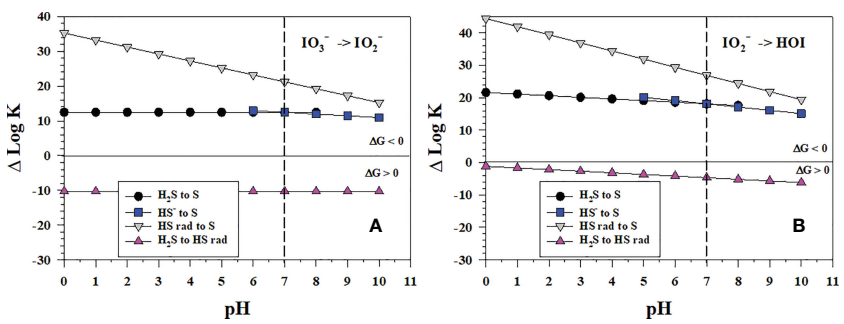

FIGURE 5
Thermodynamics for the 2-electron transfer reductions of **(A)** IO_3^- (Io5b) and **(B)** IO_2^- (Io4b) by sulfide species (S1, S2, S4, S5). The vertical line represents the pK_{a1} value for H_2S. Data above the horizontal line at ΔlogK ($\Delta logK_{reaction}$) = 0 indicate a favorable reaction and data below the horizontal line indicate an unfavorable reaction.

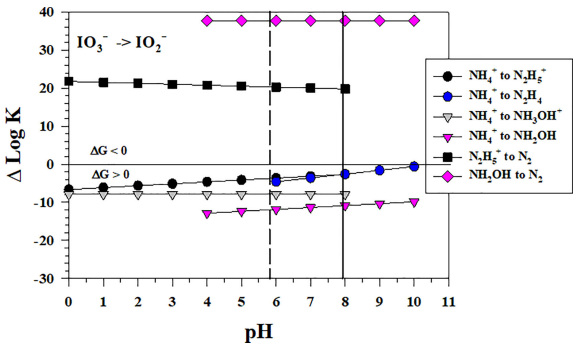

FIGURE 6
Thermodynamics for the reduction of IO_3^- to IO_2^- (IO5b) by NH_4^+ to hydrazine species (N3a, N3b), hydroxylamine species (N4a, N4b) and by $N_2H_5^+$ (N5) and NH_2OH (N6). The vertical lines represent the pK_a values for NH_3OH^+ (5.82) and $N_2H_5^+$ (7.93), respectively. Data above the horizontal line at ΔlogK ($\Delta logK_{reaction}$) = 0 indicate a favorable reaction and data below the horizontal line indicate an unfavorable reaction.

the plot) is favorable to reform H_2O_2 and I^- at pH > 6 whereas the reverse reaction of H_2O_2 with I_2 to reform O_2^- and I^- is favorable at a pH > 9 ($\Delta logK_{reaction} < 0$ in the plot). These thermodynamic data indicate that H_2O_2 can form I_2 in a 2-electron transfer (Figure 7B) and then reduce I_2 to I^- in a 1-electron transfer (Figure 7A).

At seawater pH, superoxide, O_2^-, can oxidize I^- to I_2 and the reaction occurs with a rate constant of 10^8 $M^{-1}s^{-1}$ (Bielski et al., 1985; Table 2). Because I_2 is a good electron acceptor, the subsequent reaction of O_2^- with I_2 leads to I_2^- (Schwarz and Bielski, 1986). As to be discussed in section 4.3, I_2 reacts with organic matter to form organo-iodine compounds. Extracellular O_2^- is generated by *Roseobacter* sp. AzwK-3b (Li et al., 2014) and results in the oxidation of Mn^{2+} to Mn (III,IV) oxides. However, Li et al. (2014) found that O_2^- also oxidized I^-. Considering that extracellular O_2^- formation is a widespread phenomenon among marine and terrestrial bacteria, this could represent an important first step in the pathway for iodide oxidation in some environments. The Mn oxides formed by *Roseobacter* sp. AzwK-3b are not the oxidant as MnO_2 kinetics is slower (Table 2).

To obtain IO_3^-, further oxidation of I_2 to HOI must occur, and •OH is one candidate with a rate constant of 1.2 x 10^{10} (Buxton et al., 1988; Table 2). Also, O_3 has a rate constant of 1.2 x 10^9 (Liu et al., 2001).

I_2 is a prominent intermediate in I^- oxidation yet HOI is needed to form IO_3^-. HOI can form directly from I^- and I_2 oxidation or from hydrolysis of I_2 (reverse of eqn. 5), which is fast at basic pH (Wong, 1991). Figure 8A shows that of the successive 1-electron oxidants (starting from O_2) for I_2 oxidation, only •OH is thermodynamically favorable over all pH to form HOI whereas O_3 is favorable at pH > 6, and O_2^- is favorable at pH< 6. H_2O_2 as a 1-electron oxidant cannot oxidize I_2 to form HOI, but H_2O_2 can reduce HOI to I_2 (reverse of the O_2^- and I_2 reaction). Figure 8B indicates that, as 2-electron oxidants, H_2O_2 and O_3 oxidation can lead to HOI formation. Comparing Δlog K values in Figures 7, 8 indicates that oxidation of I_2 to HOI is less favorable than the oxidation of I^- to I_2.

These data also indicate why the comproportionation reaction of HOI with I^- to form I_2 can occur (eqn. 5, Carpenter et al., 2013).

$$H^+ + HOI + I^- \leftrightarrow I_2 + H_2O \quad (5)$$

Although disproportionation of HOI to IO_3^- and I^- (eqn. 6) is fast in strongly basic solution, it is not detectable at seawater pH (Wong, 1991).

$$3HOI + 3OH^- \leftrightarrow IO_3^- + 2I^- + 3H_2O \quad (6)$$

Figure 9 shows the successive 2-electron oxidation reactions of I^-, HOI and IO_2^- with $^3O_2$, $^1O_2$, H_2O_2 and O_3. $^3O_2$ cannot affect the oxidation at any pH. Figure 9 shows that O_3 oxidation reactions with I^-, HOI and IO_2^- are favorable; thus, O_3 can affect the complete oxidation of I^- to IO_3^-. Also, the H_2O_2 oxidation reactions of I^-, HOI and IO_2^- are favorable and can lead to IO_3^- formation; however, the kinetics of H_2O_2 oxidation can be slow. Haloperoxidase enzymes from organisms enhance the kinetics (Butler and Sandy, 2009) as does the reaction of H_2O_2 with carboxylic acids secreted by microbes to form peroxy carboxylic acids, which in turn oxidize I^- to I_2 (Li et al., 2012). The reactive oxygen species $^1O_2$ can oxidize I^- at pH< 10, oxidize HOI at pH > 5, and IO_2^- over all pH. Thus, $^1O_2$ can be an oxidant of I^- to IO_3^- at seawater pH. These data indicate that HOI oxidation leads to IO_3^- formation.

Interestingly, ΔlogK values in Figure 9A show that the thermodynamics of I^- oxidation by the 2-electron oxidants O_3 and H_2O_2 to form HOI is slightly less favorable than I_2 formation

TABLE 2 Kinetic rate constants for the reaction of oxidants with Iodide and I_2.

I^- with oxidant	k_{12} (M^{-1} s^{-1})	reference
O_3	1.2 x 10^9	Liu et al. (2001)
$^1O_2$	8.7 x 10^5 - 8.7 x 10^6	Wilkinson et al. (1995), p. 896, pH ~ 7
•OH	1.2 x 10^{10}	Buxton et al. (1988) p. 527, 684
O_2^-/HO_2	1 x 10^8	Bielski et al. (1985), p. 1063
H_2O_2	0.69	Mohammed and Liebhafsky (1934)
MnO_2	3 x 10^3 (M^{-2} s^{-1})	Fox et al. (2009) includes pH dependence
I_2 with oxidant		
HO_2	1.8 x 10^7	Schwarz and Bielski (1986)

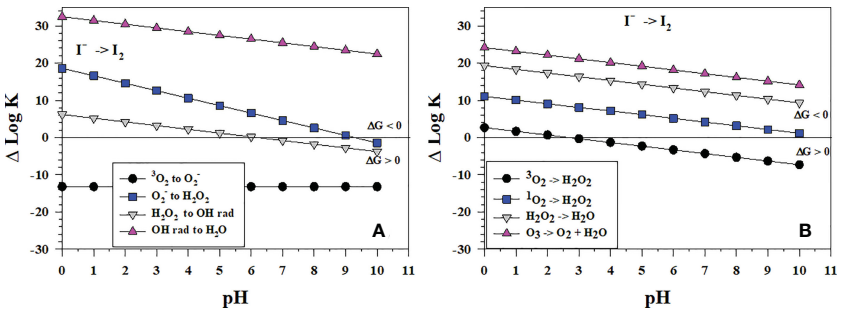

FIGURE 7
Thermodynamics for I_2 formation *via* the oxidation of I^- (Io1) with **(A)** the successive 1-electron oxidants $^3O_2$ (O6), O_2^- (O7), H_2O_2 (O8) and •OH (O9b); **(B)** the 2-electron oxidants $^3O_2$ (O2), $^1O_2$ (O5), H_2O_2 (O3), and O_3 (O4). Data above the horizontal line at ΔlogK ($\Delta logK_{reaction}$) = 0 indicate a favorable reaction and data below the horizontal line indicate an unfavorable reaction.

(Figure 7B). Conversely, thermodynamics of I^- oxidation by H_2O_2 as a 2-electron oxidant to form HOI (Figure 9A) is more favorable than I_2 formation (Figure 7A).

As shown in Figure 10, a potentially potent oxidant for I^- is N_2O, which is an O atom transfer oxidant like O_3. However, the N_2O concentration in seawater is minor, but the largest reported values are 90 and 250 nmol kg^{-1} for the OMZs of the Arabian Sea (Freing et al., 2012) and the Eastern Tropical North Pacific (Damgaard et al., 2020), respectively. These values are smaller than the total iodine concentration in seawater. The N_2O concentration in the atmosphere is 335 ppbv (August 2022, https://www.n2olevels.org), which is equivalent to 0.0331 Pa or 7.8 nM dissolved in surface seawater (salinity of 35) at 20 ^{0}C using the solubility data from Weiss and Price (1980).

4.3 ROS in seawater

Reactive oxygen species exist in marine waters, but at low concentrations. O_3 penetrates a few micrometers through the water-air interface at surface iodide concentrations (Carpenter et al., 2013). Powers and Miller (2014) showed that solar-induced processes with organic matter in freshwater and seawater are a major source of ROS (as O_2^-, H_2O_2, and •OH) with the inventory and production rates for H_2O_2 in surface seawater being highest of the ROS. Also, Sutherland et al. (2020) report that dark, extracellular O_2^- production is prolific among marine heterotrophic bacteria, cyanobacteria, and eukaryotes. In surface ocean waters, the concentration of H_2O_2 ranges from 20 - 80 nM (Yuan and Shiller, 2001), biological O_2^- production gives a total concentration of ~ 0.07 to 0.30 nM (Sutherland et al., 2020), •OH concentration is ~10^{-18} M (Mopper and Zhou, 1990), and $^1O_2$ concentration ranges from 10^{-13} to 10^{-14} M (Sunday et al., 2020). However, these ROS concentrations are typically smaller than I^- concentrations, which range from 10 to 200 nM (Chance et al., 2019). Thus, I^- oxidation in seawater samples should be difficult to observe experimentally. Hardisty et al. (2020) tracked the addition of stable isotopes of iodide in sample incubations and report the rate of I^- oxidation to be 118–189 nM yr^{-1}, which is similar to rates reported by mass balance approaches (Campos et al., 1996a; Truesdale et al., 2001; Žic and Branica, 2006; Žic et al., 2008). Hardisty et al. (2020) report that the product is likely HOI that results in the formation of organic-iodine compounds (see section 4.6) which on decomposition can release I^-.

As the surface concentrations of ROS are smaller than the I^- concentration, the question is how does I^- get oxidized to IO_3^- in seawater? Microbial processes and the oxidation of I species in the atmosphere by ROS are likely candidates. These are now discussed.

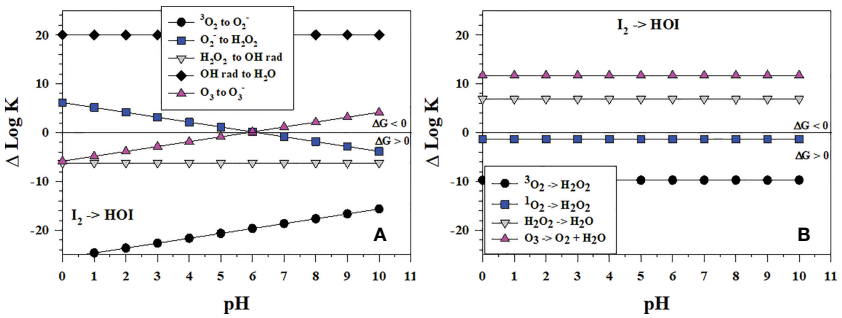

FIGURE 8
Thermodynamics for the formation of HOI *via* the oxidation of I_2 (Io3) with **(A)** the successive 1-electron oxidants $^3O_2$ (O6), O_2^- (O7), H_2O_2 (O8), •OH (O9b) and O_3 (O11); **(B)** the 2-electron oxidants $^3O_2$ (O2), $^1O_2$ (O5), H_2O_2 (O3), and O_3 (O4). Data above the horizontal line at ΔlogK ($\Delta logK_{reaction}$) = 0 indicate a favorable reaction and data below the horizontal line indicate an unfavorable reaction.

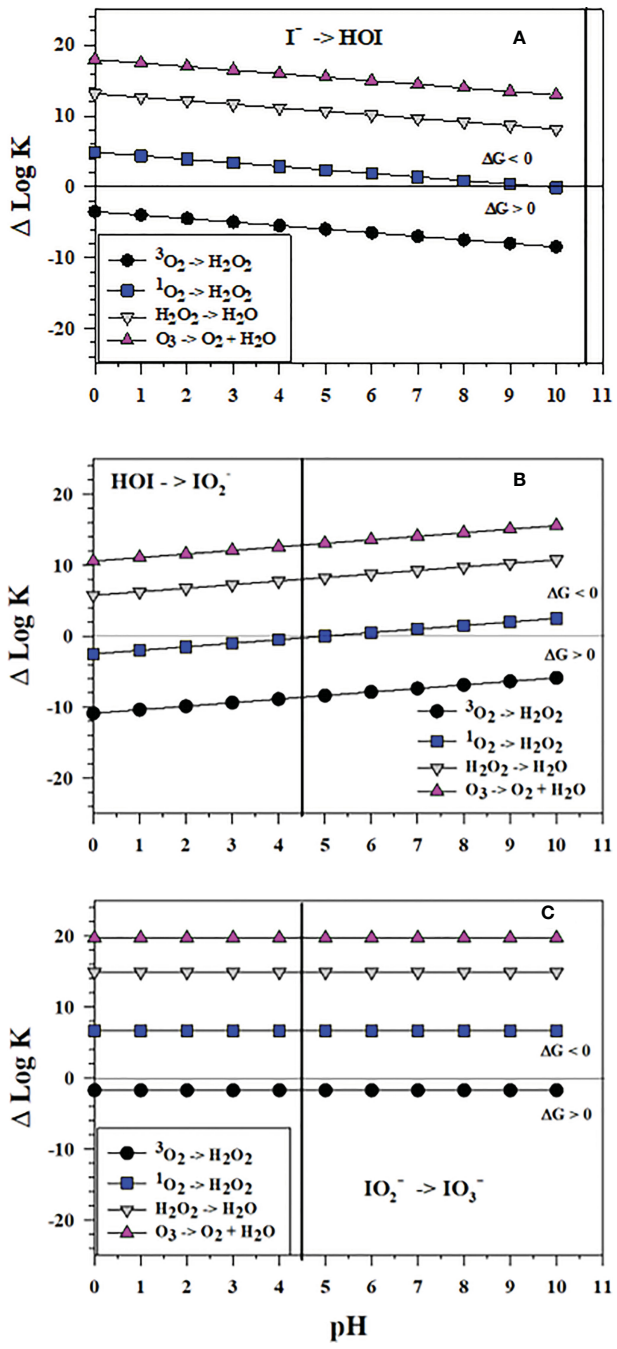

FIGURE 9
Thermodynamics for the reaction of $^3O_2$ (O2), $^1O_2$ (O5), H_2O_2 (O3), and O_3 (O4) as 2-electron oxidants with **(A)** I^- to form HOI (Io2), **(B)** HOI to form IO_2^- (Io4b) and **(C)** IO_2^- to form IO_3^- (Io5b). The vertical lines represent the pK_a value of 4.49 for HO_2I dissociation to IO_2^-. Data above the horizontal line at ΔlogK ($\Delta logK_{reaction}$) = 0 indicate a favorable reaction and data below the horizontal line indicate an unfavorable reaction.

4.4 Iodide oxidation in brown kelp

Brown kelp are the strongest accumulators of iodine as I^- among living organisms (up to 100 mM, Küpper et al., 2008). The element iodine was discovered by the formation of I_2 during exposure of brown kelp to concentrated sulfuric acid, which oxidized I^- to I_2. Kelp

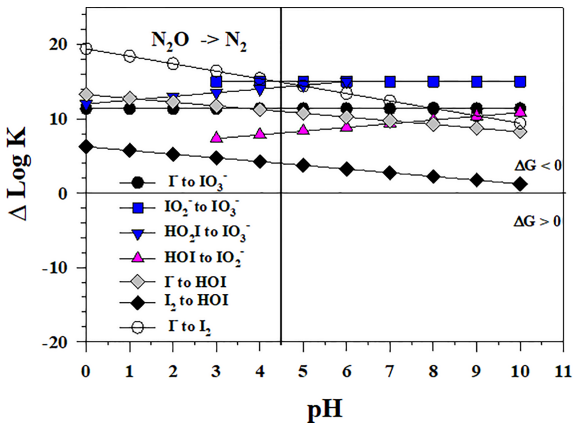

FIGURE 10
Thermodynamics for the 1- and 2- electron reductions of IO_3^- (Io5a, Io5b, Io6), IO_2^- (Io4b), HOI (Io2, Io3), and I_2 (Io1) by N_2O (N2). Data above the horizontal line at ΔlogK ($\Delta logK_{reaction}$) = 0 indicate a favorable reaction and data below the horizontal line indicate an unfavorable reaction.

releases I^- on the thallus surface and in the apoplast when undergoing oxidative stress during the partial emersion of the brown kelp forest at low tide; e.g., by exposure to high irradiance, desiccation, and atmospheric O_3. Kelp contain vanadium haloperoxidases (Colin et al., 2003; Küpper et al., 2008) that enhance I^- oxidation by H_2O_2. Whereas the nonenzymatic reaction of I^- with H_2O_2 is slow, the reactions with O_3, O_2^-, $^1O_2$, and •OH are very fast (> 10^8 $M^{-1}s^{-1}$, Table 2); they are also faster than MnO_2 oxidation of I^-. Küpper et al. (2008) consider I^- as the simplest antioxidant known.

4.5 Iodide oxidation by microbes

Hughes et al. (2021) report that IO_3^- production occurs in cultures of the ammonia-oxidizing bacteria *Nitrosomonas* sp. and *Nitrosococcus oceani* supplied with I^-, but not in cultures of three different nitrite oxidizing bacteria. Information on the enzymes mediating the oxidation were not studied. Nevertheless, NH_4^+ oxidation *via* nitrification occurs *via* NH_2OH formation which is a 2-electron reaction. Further reaction of NH_2OH *via* metalloenzymes (e.g., Mo and W oxidases that transfer O atoms) leads to NO_2^- (a 4-electron transfer) and NO_3^-. I^- likely goes through the intermediates IO_2^- and HOI to form IO_3^-, but these intermediates are reactive and not detectable by present analytical methods unlike NO_2^-.

Consistent with the Hughes et al. (2021) report, Kennedy and Elderfield (1987a, 1987b) showed that the conversion of iodide to iodate occurred in marine sediments. Microbial intervention is likely, but reaction of I^- with oxidized Mn is possible depending on the pH.

Amachi and Iino (2022) reviewed the genus *Iodidimonas*, which was originally found in brines, but was also cultured from seawater enriched with I^-. I_2 is the first oxidation product. *Iodidimonas* contains the iodide oxidizing enzyme (IOX), which is an extracellular protein that contains multicopper oxidases. *Iodidimonas* requires O_2, not H_2O_2, as the electron acceptor. Other oxidants are required to oxidize I_2 to IO_3^- with O_3 and •OH being the most effective.

4.6 HOI and I_2 formation leads to organic iodine

Competing with the inorganic interconversion between iodide and iodate is the formation of organic iodine compounds. Formation of C-I bonds can occur during the reduction of IO_3^- and oxidation of I^-. Complete reduction of IO_3^- to I^- does not need to occur intercellularly and can lead to HOI and I_2 formation as in Figure 4. The first step in I^- oxidation also leads to I_2 and HOI. I_2 is neutral and adds to organic compounds such as olefins, which are not very reactive in seawater, whereas I^+ in HOI reacts with α-keto compounds and peptides through keto-enol isomerization (Truesdale and Luther, 1995). Both I_2 and HOI lead to volatile and nonvolatile organic-iodine (R-I) compounds with C-I or N-I bonds, and Harvey (1980) showed that N-iodo amides were the main organic iodine components in marine sediments. On decay of organic compounds, the C(N)-I bond breaks leading to I^- release, which mimics the senescence pathway outlined by Bluhm et al. (2010) and Hepach et al. (2020). Recently, Ooki et al. (2022) showed that CH_3I and CH_3CH_2I formed in sediments from polar and subpolar seas and was related to increased phytodetritus at the seafloor after the spring bloom.

Allard and Gallard (2013) showed that the oxidation of I^- by birnessite in the presence of organic matter also led to CH_3I over the pH range 4-5.

As total iodine in surface ocean waters is lower by a few percent compared to deep waters (Wong, 1991), the decomposition of organic-iodine leads to some I^- release, which may be oxidized to IO_3^- by ammonia-oxidizing bacteria (Hughes et al., 2021). This is similar to release and oxidation of NH_4^+ to NO_3^- from particulate organic matter in deep waters that results in an increase of NO_3^- concentration with depth (recycled element profile). Deep waters contain mainly IO_3^-, so not much I^- is released to the deep-water column by *in situ* water column processes, and most organic-iodine gets to the sediments where it is released as I^- (Kennedy and Elderfield, 1987a, Kennedy and Elderfields 1987b; Luther et al., 1995). Kennedy and Elderfield (1987a, 1987b) and Shimmield and Pedersen (1990) report that the molar I/C ratio in planktonic organisms is 10^{-4} whereas it is typically $>10^{-3}$ in sediments. Decomposition of sedimentary organic-I releases I^- to porewaters and the overlying water column where it can be transported hundreds of kilometers offshore along isopycnal surfaces in OMZs (Farrenkopf and Luther, 2002; Cutter et al., 2018).

4.7 Surface seawater and atmospheric formation of IO_3^-, and iodine speciation in the atmosphere

There is significant literature showing that coastal and oceanic regions are sources of iodine emissions to the atmosphere, and I note some important aspects of this air-sea connection. I^- reacts with O_3 to form IO^-, which at seawater pH forms HOI. Carpenter et al. (2013) showed that this reaction occurs in the first few micrometers below the air-water interface and that HOI is ten-fold greater than I_2 above the sea surface. HOI contributes 75% of the observed iodine oxide aerosol levels over the tropical Atlantic Ocean, and these iodine emissions to the atmosphere have increased 3-fold over the last century due to the increase in anthropogenic O_3 (Carpenter et al., 2021). O_3 reacts stepwise with this gaseous HOI (IO^-) and gaseous IO_2^- to form IO_3^-, which can attach to aerosols.

Formation and release of gaseous I_2 from seawater to air permits photochemical breaking of the I-I bond to form gaseous I atoms, •I, which are reactive radicals. Similarly, release of volatile organic-iodine compounds leads to the homolytic cleavage of the C-I bond to form I•. O_3 reacts readily with I• to form gaseous IO• in the marine boundary layer (Whalley et al., 2010). Further stepwise oxidation of gaseous IO•/HOI leads to IO_3^-. In laboratory experiments using mass spectrometry detection, Teiwes et al. (2019) showed that hydrated iodide, $I(H_2O)^-$, reacts with gaseous O_3 to form IO_2^- directly without formation of gaseous HOI or IO^-; thus, HIO_3/IO_3^- can form in a two-step reaction sequence in the atmosphere.

Using mass spectrometry to evaluate atmospheric I_xO_y cluster and (nano)particle formation above seabed macroalgae, Sipilä et al. (2016) showed the stepwise formation of HIO_3 *via* HOI and IO•, which leads to $(I_2O_5)_x$ clusters (x=2-5) containing HIO_3 that result in iodine rich aerosol particles. These data on the formation of I_2O_5 aerosols agree with the exothermic $\Delta H_{reaction}$ values of iodine oxide species reacting with O_3 and each other calculated using quantum mechanics (Kaltsoyannis and Plane, 2008). Sipilä et al. (2016) also showed that cluster formation increased as a burst at low tide indicating significant I_2 release from the macroalgae (and subsequent oxidation) as found by Küpper et al. (2008). Hydration of I_2O_5 leads to two IO_3^-. In mass spectrometry laboratory studies, Martín et al. (2022) showed that new iodine containing (nano) particles and IO_3^- also form in the presence of NO_3^- and provide $\Delta H_{reaction}$ data for the gas phase reactions involved. Experiments using the CERN CLOUD (Cosmics Leaving Outdoor Droplets) chamber documented the formation of HIO_3 *via* iodooxy hypoiodite, IOIO, as an intermediate (Finkenzeller et al., 2022) and the fast growth of HIO_3 as (nano)particles (He et al., 2021).

In recent atmospheric campaigns, Koenig et al. (2020) showed that IO_3^- is the main iodine reservoir as it forms on aerosols in the stratosphere with iodine being responsible for 32% of the halogen induced O_3 loss. Cuevas et al. (2022) also showed that iodine can dominate (~73%) the halogen-mediated lower stratospheric ozone loss during summer and early fall, when the heterogeneous reactivation of inorganic chlorine and bromine reservoirs is reduced.

The information in the preceding paragraphs along with the thermodynamic data from Martín et al. (2022), Figure 2 (the half reaction for O_3 to O_2 and H_2O) and Figure 9 predict that IO_3^- should be the dominant species in the atmosphere. Although reduction of IO_3^- is not predicted in an oxidizing atmosphere, analyses of rainwater (Campos et al., 1996b; Truesdale and Jones, 1996; Baker et al., 2001; Hou et al., 2009), aerosols (Gilfedder et al., 2008; Droste et al., 2021) and snow (Gilfedder et al., 2008) in the marine boundary layer indicate that aqueous iodide and iodate coexist. Hou et al. (2009) reviewed wet iodine speciation data and reported that IO_3^- predominates over I^- from marine sources/air masses whereas I^- predominates from continental air masses.

There are several ways that I^- (or reduced I) can form in rainwater and aerosols. The interconversion between IO_3^- and I^- at the pH of wet deposition also leads to HOI and I_2, which can react with organic material forming C-I bonds that can release I^- (section 4.6). This material has been given the term soluble organically bound iodine and can be larger than the sum of the concentrations of IO_3^- and I^- in

aerosols (Gilfedder et al., 2008; Droste et al., 2021). Soluble organically bound iodine can form from release of natural organic iodine from land and sea (a primary source) or from the reaction of natural organic material with HOI or I_2 in the atmosphere (a secondary source). On photolysis of C-I, I• forms and reacts with O_3, and on C-I reaction with nucleophiles, I^- forms. During a study on the formation of cloud condensation nuclei, Huang et al. (2022) also showed that natural gaseous organic material in the marine boundary layer reacts with IO_3^- in aerosols resulting in gaseous I_2, which can be reoxidized to IO_3^- (catalysis) or react to form organic-I compounds. Lastly, Cuevas et al. (2022) reported that photolysis of IO_3^- particles in the stratosphere at a wavelength of about 260 nm can lead to gaseous I• and O_2 during transport from the tropics to the Antarctic region. Thus, there are several pathways for reduction of IO_3^- in the atmosphere.

5 Conclusions

The reduction of IO_3^- to I^- in solution is a facile process by biotic and abiotic reactions. The intermediates IO_2^- and HOI dictate the reactivity sequence *via* a combination of thermodynamic and kinetic considerations. The IO_3^- to IO_2^- conversion is the least favorable and likely controlling step in this reaction sequence, but there is no need for nitrate reductase for IO_3^- reduction based on numerous studies. The data from this study indicate that once IO_2^- forms there is no thermodynamic barrier to I^- formation. Chemical reduction of all iodine species (not iodide) by sulfide, Fe^{2+} and Mn^{2+} are favorable at seawater and sedimentary pH values, but only sulfide has been studied in the laboratory at oceanic pH values. Dissimilatory IO_3^- reduction during organic matter decomposition seems to be a key process as the IO_3^-/IO_2^- couple is more favorable than the NO_3^-/NO_2^- couple.

However, the oxidation of I^- back to IO_3^- *via* $^3O_2$ has a major thermodynamic barrier in solution, and the disproportionation of HOI at seawater pH values is not measurable. Thus, ROS, oxidized Mn and microbes are important for I^- oxidation to IO_3^- due to favorable thermodynamics and kinetics (Table 2). Recent reports of microbial oxidation have not documented the entire six-electron oxidation in a stepwise manner so further work on this topic is necessary. Oxidation of I^- by oxidized Mn is a pH dependent reaction and less likely at seawater pH values but could occur in sedimentary environments. The reactions of O_3 and •OH with iodine species (not IO_3^-) are thermodynamically favorable over all pH. However, ROS are not normally in significant concentration in seawater to influence IO_3^- formation. Notable exceptions are for (1) sea surface microlayer, which adsorbs atmospheric O_3, and (2) the reaction of Fe^{2+} with O_2 that leads to Fenton chemistry with •OH production. Systems where Fenton chemistry can occur are at/near hydrothermal vents (Shaw et al., 2021), submarine groundwaters (Burns et al., 2010), and sediments or water columns where O_2 and Fe^{2+} concentration profiles overlap including ancient earth (Chan et al., 2016).

I^- is a major sink for O_3 in the sea surface microlayer and the atmosphere. IO_3^- formation in the atmosphere and IO_3^- redeposition to surface seawater may be major iodine processes with the latter being similar to the deposition of trace metals from wet and dry deposition to the surface ocean (e.g., Chance et al., 2015; Meskhidze et al., 2019). Most atmospheric iodine originates from marine sources where I^- oxidation to I_2 and homolytic cleavage of C-I bonds occurs; thus, gaseous iodine emissions from the ocean are reduced. IO_3^- forms from these sources during oxidation by O_3 in the atmosphere. An estimate of atmospheric deposition of IO_3^- to the ocean surface could be made by using the amount of IO_3^- in rainwater and aerosols that would be returned to the ocean surface, but more information on iodine speciation in rainwater and aerosols is needed as global spatial coverage appears limited. Despite major advances in iodine geochemistry over the last two decades, significant research is still needed on the processes that affect I^- oxidation to IO_3^- in the atmosphere, seawater and ocean sediments.

Author contributions

The author confirms being the sole contributor of this work and has approved it for publication.

Acknowledgments

The author thanks NSF for funding his group's research on iodine marine chemistry over his career, and Thomas Church and Timothy Ferdelman for suggesting the author's initial foray into iodine chemistry. The author thanks the reviewers and guest editor, Rosie Chance, for their comments and constructive suggestions to improve the manuscript.

Conflict of interest

The author declares that the research was conducted in the absence of any commercial or financial relationships that could be construed as a potential conflict of interest.

Publisher's note

All claims expressed in this article are solely those of the authors and do not necessarily represent those of their affiliated organizations, or those of the publisher, the editors and the reviewers. Any product that may be evaluated in this article, or claim that may be made by its manufacturer, is not guaranteed or endorsed by the publisher.

References

Allard, S., and Gallard, H. (2013). Abiotic formation of methyl iodide on synthetic birnessite: A mechanistic study. *Sci. Total Environ.* 463–464, 169–175. doi: 10.1016/j.scitotenv.2013.05.079

Allard, S., von Gunten, U., Sahli, E., Nicolau, R., and Gallard, H. (2009). Oxidation of iodide and iodine on birnessite (δ-MnO2) in the pH range 4–8. *Water Res.* 43, 3417–3426. doi: 10.1016/j.watres.2009.05.018

Amachi, S. (2008). Microbial contribution to global iodine cycling: volatilization, accumulation, reduction, oxidation, and sorption of iodine. *Microbes Environ.* 23 (4), 269–276. doi: 10.1264/jsme2.me08548

Amachi, S., and Iino, T. (2022). The genus *Iodidimonas*: From its discovery to potential applications. *Microorganisms* 10, 1661. doi: 10.3390/microorganisms10081661

Amachi, S., Kawaguchi, N., Muramatsu, Y., Tsuchiya, S., Watanabe, Y., Shinoyama, H., et al. (2007). Dissimilatory iodate reduction by marine pseudomonas sp. strain SCT. *Appl. Environ. Microbiol.* 73, 5725–5730. doi: 10.1128/AEM.00241-07

Anschutz, P., Sundby, B., Lefrançois, L., Luther, III, G. W., and Mucci, A. (2000). Interactions between metal oxides and species of nitrogen and iodine in bioturbated marine sediments, geochim. *Cosmochim. Acta* 64, 2751–2763. doi: 10.1016/S0016-7037(00)00400-2

Baker, A. R., Tunnicliffe, C., and Jickells, T. D. (2001). Iodine speciation and deposition fluxes from the marine atmosphere. *J. Geophys. Res.* 106, 28743–28749. doi: 10.1029/2000JD000004

Bard, A. J., Parsons, R., and Jordan, J. (1985). *Standard potentials in aqueous solution. 1st ed* (New York: M. Dekker), 834.

Bielski, B. H. J., Cabelli, D. E., Arudi, R. L., and Ross, A. B. (1985). Reactivity of HO_2/O_2^- radicals in aqueous solution. *J. Phys. Chem. Ref. Data* 14, 1041–1100. doi: 10.1063/1.555739

Bluhm, K., Croot, P., Wuttig, K., and Lochte, K. (2010). Transformation of iodate to iodide in marine phytoplankton driven by cell senescence. *Aquat. Biol.* 11, 1–15. doi: 10.3354/ab00284

Burns, J. M., Craig, P. S., Shaw, T. J., and Ferry, J. L. (2010). Multivariate examination of Fe(II)/Fe(III) cycling and consequent hydroxyl radical generation. *Environ. Sci. Technol.* 44, 7226–7231. doi: 10.1021/es903519m

Butler, A., and Sandy, M. (2009). Mechanistic considerations of halogenating enzymes. *Nature* 460, 848–854. doi: 10.1038/nature08303

Buxton, G. V., Greenstock, C. L., Helman, W. P., and Ross, A. B. (1988). Critical review of rate constants for reactions of hydrated electrons, hydrogen atoms and hydroxyl radicals in aqueous solution. *J. Phys. Chem. Ref. Data* 17, 513–886. doi: 10.1063/1.555805

Campos, M., Farrenkopf, A., Jickells, T., and Luther, G. (1996). A comparison of dissolved iodine cycling at the Bermuda Atlantic time-series station and Hawaii ocean time-series station. *Deep-Sea Res. II Top. Stud. Oceanogr.* 43 (2), 455–466. doi: 10.1016/0967-0645(95)00100-X

Campos, M. L. A. M., Nightingale, P. D., and Jickells, T. D. (1996). A comparison of methyl iodide emissions from seawater and wet depositional fluxes of iodine over the southern north Sea. *Tellus* 48, 106–114. doi: 10.3402/tellusb.v48i1.15830

Carpenter, L. J., Chance, R. J., Sherwen, T., Adams, T. J., Ball, S. M., Evans, M. J., et al. (2021). Marine iodine emissions in a changing world. *Proc. R. Soc A* 477, 20200824. doi: 10.1098/rspa.2020.0824

Carpenter, L., MacDonald, S., Shaw, M., Kumar, R., Saunders, R. W., Parthipan, R., et al. (2013). Atmospheric iodine levels influenced by sea surface emissions of inorganic iodine. *Nat. Geosci.* 6, 108–111. doi: 10.1038/ngeo1687

Carrano, M. W., Yarimizu, K., Gonzales, J. L., Cruz-López, R., Edwards, M. S., Tymon, T. M., et al. (2020). The influence of marine algae on iodine speciation in the coastal ocean. *Algae* 35 (2), 167–176. doi: 10.4490/algae.2020.35.5.25

Chance, R. J., Jickells, T. D., and Baker, A. R. (2015). Atmospheric trace metal concentrations, solubility and deposition fluxes in remote marine air over the south-east Atlantic. *Mar. Chem.* 177, 45–56. doi: 10.1016/j.marchem.2015.06.028

Chance, R., Malin, G., Jickells, T., and Baker, A. R. (2007). Reduction of iodate to iodide by cold water diatom cultures. *Mar. Chem.* 105, 169–180. doi: 10.1016/j.marchem.2006.06.008

Chance, R. J., Tinel, L., Sherwen, T., Baker, A. R., Bell, T., Brindle, J., et al. (2019). Global sea-surface iodide observations 1967–2018. *Sci. Data* 6, 286. doi: 10.1038/s41597-019-0288-y

Chan, C. S., Emerson, D., and Luther, G. (2016). The role of microaerophilic fe-oxidizing micro-organisms in producing banded iron formations. *Geobiology* 14, 509–528. doi: 10.1111/gbi.12192

Colin, C., Leblanc, C., Wagner, E., Delage, L., Leize-Wagner, E., van Dorsselaer, A., et al. (2003). The brown algal kelp laminaria digitata features distinct bromoperoxidase and iodoperoxidase activities. *J. Biol. Chem.* 278, 23545–23552. doi: 10.1074/jbc.M300247200

Councell, T. B., Landa, E. R., and Lovely, D. R. (1997). Microbial reduction of iodate. *Water Air Soil pollut.* 100, 99–106. doi: 10.1023/A:1018370423790

Cuevas, C. A., Fernandez, R. P., Kinnison, D. E., Li, Q., Lamarques, J.-F., Trabelsi, T., et al. (2022). The influence of iodine on the Antarctic stratospheric ozone hole. *Proc. Natl. Acad. Sci. U.S.A.* 119, No. 7, e2110864119. doi: 10.1073/pnas.2110864119

Cutter, G. A., Moffett, J. G., Nielsdottir, M. C., and Sanial, V. (2018). Multiple oxidation state trace elements in suboxic waters off Peru: *in situ* redox processes and advective/diffusive horizontal transport. *Mar. Chem.* 201, 77–89. doi: 10.1016/j.marchem.2018.01.003

Damgaard, L. R., Jelly, C., Casciotti, K., Ward, B. B., and Revsbech, N. P. (2020). Amperometric sensor for nanomolar nitrous oxide analysis. *Anal. Chim. Acta* 1101, 135–140. doi: 10.1016/j.aca.2019.12.019

de la Cuesta, J. L., and Manley, S. L. (2009). Iodine assimilation by marine diatoms and other phytoplankton in nitrate-replete conditions. *Limnology Oceanogr.* 54, 1653–1664. doi: 10.4319/lo.2009.54.5.1653

Droste, E. S., Baker, A. R., Yodle, C., Smith, A., and Ganzeveld, L. (2021). Soluble iodine speciation in marine aerosols across the Indian and pacific ocean basins. *Front. Mar. Sci.* 8, 788105. doi: 10.3389/fmars.2021.788105

Elderfield, H., and Truesdale, V. W. (1980). On the biophilic nature of iodine in seawater. *Earth Planet. Sci. Lett.* 50, 105–114. doi: 10.1016/0012-821X(80)90122-3

Estes, E. R., Berti, D., Findlay, A. J., Hochella, M. F.Jr., Shaw, T. J., Yücel, M., et al. (2022). Differential behavior of metal sulfides in hydrothermal plumes and diffuse flows. *ACS Earth Space Chem.* 6, 1429–1442. doi: 10.1021/acsearthspacechem.1c00377

Farrenkopf, A. M., Dollhopf, M. E., Chadhain, S. N., Luther, G. W., and Nealson, K. H. (1997). Reduction of iodate in seawater during Arabian Sea shipboard incubations and in laboratory cultures of the marine bacterium *Shewanella putrefaciens* strain MR-4. *Mar. Chem.* 57 (3), 347–354. doi: 10.1016/S0304-4203(97)00039-X

Farrenkopf, A. M., and Luther, G. W. (2002). Iodine chemistry reflects productivity and denitrification in the Arabian Sea: Evidence for flux of dissolved species from sediments of western India into the OMZ. *Deep-Sea Res. II Top. Stud. Oceanogr* 49 (12), 2303–2318. doi: 10.1016/S0967-0645(02)00038-3

Finkenzeller, H., Iyer, S., He, X. C., Simon, M., Koenig, T. K., Lee, C. F., et al. (2022). The gas-phase formation mechanism of iodic acid as an atmospheric aerosol source. *Nat. Chem* 15, 129-135. doi: 10.1038/s41557-022-01067-z

Fox, P. M., Davis, J. A., and Luther, III, G. W. (2009). The kinetics of iodide oxidation by the manganese oxide mineral birnessite. *Geochim. Cosmochim. Acta* 73, 2850–2861. doi: 10.1016/j.gca.2009.02.016

Freing, A., Wallace, D. W. R., and Bange, H. W. (2012). Global oceanic production of nitrous oxide. *Phil. Trans. R. Soc B* 367, 1245–1255. doi: 10.1098/rstb.2011.0360

Gilfedder, B. S., Lai, S. C., Petri, M., Biester, H., and Hoffmann, T. (2008). Iodine speciation in rain, snow and aerosols. *Atmos. Chem. Phys.* 8, 6069–6084. doi: 10.5194/acp-8-6069-2008

Guo, J., Jiang, J., Peng, Z., Zhong, Y., Jiang, Y., Jiang, Z., et al. (2022). Global occurrence of the bacteria with capability for extracellular reduction of iodate. *Front. Microbiol.* 13. doi: 10.3389/fmicb.2022.1070601

Hardisty, D. H., Horner, T. J., Evans, Z. C., Moriyasu, R., Babbin, A. R., Wankel, S. D., et al. (2021). Limited in situ iodate reduction within the Eastern tropical north pacific oxygen deficient zone. *Earth Planetary Sci. Lett.* 554, 116676. doi: 10.1016/j.chemgeo.2019.119360

Hardisty, D. H., Horner, T. J., Wankel, S. D., Blusztajn, J., and Nielsen, S. G. (2020). Experimental observations of marine iodide oxidation using a novel sparge interface MC-ICP-MS technique. *Chem. Geol.* 532, 119360. doi: 10.1016/j.chemgeo.2019.119360

Harvey, G. R. (1980). A study of the chemistry of iodine and bromine in marine sediments. *Mar. Chem.* 8, 327–332. doi: 10.1016/0304-4203(80)90021-3

He, X.-C., Tham, Y. J., Dada, L., Wang, M., Finkenzeller, H., Stolzenberg, D., et al. (2021). Role of iodine oxoacids in atmospheric aerosol nucleation. *Science* 371, 589–595. doi: 10.1126/science.abe0298

Hepach, H., Hughes, C., Hogg, K., Collings, S., and Chance, R. (2020). Senescence as the main driver of iodide release from a diverse range of marine phytoplankton. *Biogeosciences* 17, 2453–2471. doi: 10.5194/bg-17-2453-2020

Hou, X. L., Aldahan, A., Nielsen, S. P., and Possnert, G. (2009). Time series of I-129 and I-127 speciation in precipitation from Denmark. *Environ. Sci. Technol.* 43, 6522–6528. doi: 10.1021/es9012678

Huang, R.-J., Hoffmann, T., Ovadnevaite, J., Laaksonen, A., Kokkola, H., Xu, W., et al. (2022). Heterogeneous iodine-organic chemistry fast-tracks marine new particle formation. *Proc. Natl. Acad. Sci. U.S.A.* 119, e2201729119. doi: 10.1073/pnas.2201729119

Hughes, C., Barton, E., Hepach, H., Chance, R., Pickering, M. D., Hogg, K., et al. (2021). Oxidation of iodide to iodate by cultures of marine ammonia-oxidising bacteria. *Mar. Chem.* 234, 104000. doi: 10.1016/j.marchem.2021.104000

Hung, C.-C., Wong, G. T. F., and Dunstan, W. M. (2005). Iodate reduction activity in nitrate reductase extracts from marine phytoplankton. *Bul. Mar. Sci.* 76, 61–72.

Kaltsoyannis, N., and Plane, J. M. C. (2008). Quantum chemical calculations on a selection of iodine-containing species (IO, OIO, INO_3, $(IO)_2$, $I2O_3$, $I2O_4$ and $I2O_5$) of importance in the atmosphere. *Phys. Chem. Chem. Phys.* 10, 1723–1733. doi: 10.1039/b715687c

Kennedy, H. A., and Elderfield, H. (1987a). Iodine diagenesis in pelagic deep-sea sediments. *Geochim. Cosmchim. Acta* 51, 2489–2504. doi: 10.1016/0016-7037(87)90300-0

Kennedy, H. A., and Elderfield, H. (1987b). Iodine diagenesis in non-pelagic deep-sea sediments. *Geochim. Cosmchim. Acta* 51, 2505–2514. doi: 10.1016/0016-7037(87)90301-2

Kim, K., Ju, J., Kim, B., Chung, H. Y., Vetráková, L., Heger, D., et al. (2019). Nitrite-induced activation of iodate into molecular iodine in frozen solution. *Environ. Sci. Technol.* 53, 4892–4900. doi: 10.1021/acs.est.8b06638

Koenig, T. K., Baidar, S., Campuzano-Jost, P., Cuevas, C. A., Dix, B., Fernandez, R. P., et al. (2020). Quantitative detection of iodine in the stratosphere. *Proc. Natl. Acad. Sci. U.S.A.* 117, 1860–1866. doi: 10.1073/pnas.1916828117

Küpper, F. C., Carpenter, L. J., McFiggans, G. B., Palmer, C. J., Waite, T. J., Boneberg, E.-M., et al. (2008). Iodide accumulation provides kelp with an inorganic antioxidant impacting atmospheric chemistry. *Proc. Natl. Acad. Sci. U. S. A.* 105, 6954–6958. doi: 10.1073/pnas.0709959105

Küpper, F. C., Feiters, M. C., Olofsson, B., Kaiho, T., Yanagida, S., Zimmermann, M. B., et al. (2011). Commemorating two centuries of iodine research: An interdisciplinary overview of current research. *Angewandte Chemie Int. Editions* 50, 11598–11620. doi: 10.1002/anie.201100028

Lehner, P., Larndorfer, C., Garcia-Robledo, E., Larsen, M., Borisov, S. M., Revsbech, N.-P., et al. (2015). LUMOS - a sensitive and reliable optode system for measuring dissolved oxygen in the nanomolar range. *PloS One* 10 (6), e0128125. doi: 10.1371/journal.pone.0128125

Lewis, B. L., and Luther, III, G. W. (2000). Processes controlling the distribution and cycling of manganese in the oxygen minimum zone of the Arabian Sea. *Deep Sea Res.* 47, 1541–1561. doi: 10.1016/S0967-0645(99)00153-8

Li, H.-P., Daniel, B., Creeley, D., Grandbois, R., Zhang, S., Xu, C., et al. (2014). Superoxide production by a manganese-oxidizing bacterium facilitates iodide oxidation. *Appl. Environ. Microbio* 80, 2693–2699. doi: 10.1128/AEM.00400-14

Liu, Q., Schurter, L. M., Muller, C. E., Aloisio, S., Francisco, J. S., and Margerum, D. W. (2001). Kinetics and mechanisms of aqueous ozone reactions with bromide, sulfite, hydrogen sulfite, iodide, and nitrite ions. *Inorg. Chem.* 40, 4436–4442. doi: 10.1021/ic000919j

Li, H.-P., Yeager, C. M., Brinkmeyer, R., Zhang, S., Ho, Y.-F., Xu, C., et al. (2012). Bacterial production of organic acids enhances H_2O_2-dependent iodide oxidation. *Environ. Sci. Technol.* 46, 4837–4844. doi: 10.1021/es203683v

Luther, III, G. W. (2010). The role of one and two electron transfer reactions in forming thermodynamically unstable intermediates as barriers in multi-electron redox reactions. *Aquat. Geochem.* 16, 395–420. doi: 10.1007/s10498-009-9082-3

Luther, III, G. W. (2011). Thermodynamic redox calculations for one and two electron transfer steps: Implications for halide oxidation and halogen environmental cycling. In *Aquatic Redox Chemistry* editors, P. G. Tratnyek, T. J. Grundl and S. B. Haderlein (Washington, D.C.: American Chemical Society) 15–35. doi: 10.1021/.bk-2011-1071.ch002

Luther, III, G. W. (2016). *Inorganic chemistry for geochemistry and environmental sciences: Fundamentals and applications*. (Chichester, West Sussex: John Wiley & Sons Ltd.) 456.

Luther, G. W., and Campbell, T. (1991). Iodine speciation in the water column of the black Sea. *Deep Sea Res. Part A. Oceanographic Res. Papers* 38, S875–S882. doi: 10.1007/978-94-011-2608-3_11

Luther, G. W.III, Karolewski, J. S., Sutherland, K. M., Hansel, C. M., and Wankel, S. D. (2021). The abiotic nitrite oxidation by ligand-bound manganese (III): the chemical mechanism. *Aquat. Geochem.* 27, 207–220. doi: 10.1007/s10498-021-09396-0

Luther, III, G. W., and Popp, J. I. (2002). Kinetics of the abiotic reduction of polymeric manganese dioxide by nitrite: An anaerobic nitrification reaction. *Aquat. Geochem.* 8, 15–36. doi: 10.1023/A:1020325604920

Luther, III, G. W., Wu, J., and Cullen, J. (1995). "Redox chemistry of iodine in seawater: frontier molecular orbital theory considerations," in *Aquatic chemistry: Interfacial and interspecies processes*, vol. 244 . Eds. C. P. Huang, C. R. O'Melia and J. J. Morgan (Washington, DC: American Chemical Society), 135–155. doi: 10.1021/ba-1995-0244.ch006

Martín, J. C. G., Lewis, T. R., James, A. D., Saiz-Lopez, A., and Plane, J. M. C. (2022). Insights into the chemistry of iodine new particle formation: The role of iodine oxides and the source of iodic acid. *J. Am. Chem. Soc* 144, 9240–9253. doi: 10.1021/jacs.1c12957

Meskhidze, N., Völker, C., Al-Abadleh, H. A., Barbeau, K., Bressac, M., Buck, C., et al. (2019). Perspective on identifying and characterizing the processes controlling iron speciation and residence time at the atmosphere-ocean interface mar. *Chem.* 217, 103704. doi: 10.1016/j.marchem.2019.103704

Moffett, J. W., and German, C. R. (2020). Distribution of iron in the Western Indian ocean and the Eastern tropical south pacific: An inter-basin comparison. *Chem. Geol.* 532, 119334. doi: 10.1016/j.chemgeo.2019.119334

Mohammed, A., and Liebhafsky, H. A. (1934). The kinetics of the reduction of hydrogen peroxide by the halides. *J. Amer. Chem. Soc* 56, 1680–1685. doi: 10.1021/ja01323a009

Mok, J. K., Toporek, Y. L., Hyun-Dong, S., Lee, B. D., Lee, M. H., and DiChristina, T. J. (2018). Iodate reduction by shewanella oneidensis does not involve nitrate reductase. *Geomicrobiol. J* 35, 570-579. doi: 10.1080/01490451.2018.1430189

Mopper, K., and Zhou, X. (1990). Hydroxyl radical photoproduction in the sea and its potential impact on marine processes. *Science* 250, 661–664. doi: 10.1126/science.250.4981.661

Müller, E., von Gunten, U., Bouchet, S., Droz, B., and Winkel, L. H. E. (2021). Reaction of DMS and HOBr as a sink for marine DMS and an inhibitor of bromoform formation. *Environ. Sci. Technol.* 55, 5547–5558. doi: 10.1021/acs.est.0c08189

Oldham, V. E., Jones, M. R., Siebecker, M., Mucci, A., Tebo, B. M., and Luther, III, G. W. (2019). The speciation and mobility of Mn and fe in estuarine sediments. *Aquat. Geochemistry* 25, 3–26. doi: 10.1007/s10498-019-09351-0

Ooki, A., Minamikawa, K., Meng, F., Miyashita, N., Hirawake, T., Ueno, H., et al. (2022). Marine sediment as a likely source of methyl and ethyl iodides in subpolar and polar seas. *Commun. Earth Environ.* 3, 180. doi: 10.1038/s43247-022-00513-7

Owings, S. M., Laurie Bréthous, L., Eitel, E. M., Fields, B. P., Boever, A., Beckler, J. S., et al. (2021). Differential manganese and iron recycling and transport in continental margin sediments of the northern gulf of Mexico. *Mar. Chem.* 229, 103908. doi: 10.1016/j.marchem.2020.103908

Powers, L. C., and Miller, W. L. (2014). Blending remote sensing data products to estimate photochemical production of hydrogen peroxide and superoxide in the surface ocean. *Environ. Sci. Process. Impacts* 16, 792–806. doi: 10.1039/C3EM00617D

Revsbech, N. P., Larsen, L. H., Gundersen, J., Dalsgaard, T., Ulloa, O., and Thamdrup, B. (2009). Determination of ultra-low oxygen concentrations in oxygen minimum zones by the STOX sensor. *Limnol. Oceanogr. Methods* 7, 371–381. doi: 10.4319/lom.2009.7.371

Reyes-Umana, V., Henning, Z., Lee, K., Barnum, T. P., and Coates, J. D. (2022). Genetic and phylogenetic analysis of dissimilatory iodate-reducing bacteria identifies potential niches across the world's oceans. *ISME J.* 16, 38–49. doi: 10.1038/s41396-021-01034-5

Rickard, D., and Luther, III, G. W. (2007). Chemistry of iron sulfides. *Chem. Rev.* 107, 514–562. doi: 10.1021/cr0503658

Rue, E. L., Smith, G. J., Cutter, G. A., and Bruland, K. W. (1997). The response of trace element redox couples to suboxic conditions in the water column. deep-Sea res. *I Oceanogr. Res. Pap.* 44 (1), 113–134. doi: 10.1016/S0967-0637(96)00088-X

Schmitz, G. (2008). Inorganic reactions of Iodine(III) in acidic solutions and free energy of iodous acid formation. *Int. J. Chem. Kinet.* 40, 647–652. doi: 10.1002/kin.20344

Schwarz, H. A., and Bielski, B. H. J. (1986). Reactions of HO_2 and $O2^-$ with iodine and bromine and the I_2^- and I atom reduction potentials. *J. Phys. Chem.* 90, 1445–1448. doi: 10.1021/j100398a045

Shaw, T. J., Luther, G. W.III, Rosas, R., Oldham, V. E., Coffey, N. R., Ferry, J. L., et al. (2021). Fe-catalyzed sulfide oxidation in hydrothermal plumes is a source of reactive oxygen species to the ocean. *Proc. Natl. Acad. Sci. U.S.A.* 118 (40), e2026654118. doi: 10.1073/pnas.2026654118

Shimmield, G. B., and Pedersen, T. F. (1990). The geochemistry of reactive trace metals and halogens in hemipelagic continental margin sediments. *Rev. Aquat. Sci.* 3, 255–279.

Shin, H.-D., Toporek, Y., Mok, J. K., Maekawa, R., Lee, B. D., Howard, M. H., et al. (2022). Iodate reduction by *Shewanella oneidensis* requires genes encoding an extracellular dimethylsulfoxide reductase. *Front. Microbiol.* 13. doi: 10.3389/fmicb.2022.852942

Sipilä, M., Sarnela, N., Jokinen, T., Henschel, H., Junninen, H, Kontkanen, J., et al. (2016). Molecular-scale evidence of aerosol particle formation *via* sequential addition of HIO_3. *Nature* 537, 532–534. doi: 10.1038/nature19314

Stanbury, D. (1989). "Reduction potentials involving inorganic free radicals in aqueous solution," in *Advances in inorganic chemistry*, vol. 33 . Ed. A. G. Sykes (New York: Academic Press), 69–138.

Stumm, W., and Morgan, J. J. (1996). *Aquatic chemistry. 3rd edition* (New York: John Wiley), 1022.

Sunday, M. O., Takeda, K., and Sakugawa, H. (2020). Singlet oxygen photogeneration in coastal seawater: Prospect of Large-scale modeling in seawater surface and its environmental significance. *Environ. Sci. Technol.* 54, 6125–6133. doi: 10.1021/acs.est.0c00463

Sutherland, K. M., Wankel, S. D., and Hansel, C. M. (2020). Dark biological superoxide production as a significant flux and sink of marine dissolved oxygen. *Proc. Natl. Acad. Sci. U.S.A.* 117, 3433–3439. doi: 10.1073/pnas.1912313117

Szlamkowicz, I. B., Fentress, A. J., Longen, L. F., Stanberry, J. S., and Anagnostopoulos, V. A. (2022). Transformations and speciation of iodine in the environment as a result of oxidation by manganese minerals. *ACS Earth Space Chem.* 6, 1948–1956. doi: 10.1021/acsearthspacechem.1c00372

Teiwes, R., Elm, J., Bilde, M., and Pedersen, H. B. (2019). The reaction of hydrated iodide $I(H_2O)^-$ with ozone: A new route to IO_2^- products. *Phys. Chem. Chem. Phys.* 21, 17546–17554. doi: 10.1039/C9CP01734H

Trouwborst, R. E., Clement, B. G., Tebo, B. M., Glazer, B. T., and Luther, G. W.III (2006). Soluble Mn(III) in suboxic zones. *Science* 313, 1955–1957. doi: 10.1126/science.1132876

Truesdale, V. W., and Jones, S. D. (1996). The variation of iodate and total iodine in some UK rainwaters during 1980-1981. *J. Hydrology* 179, 67–86. doi: 10.1016/0022-1694(95)02873-0

Truesdale, V. W., and Luther, III, G. W. (1995). Molecular iodine reduction by natural and model organic substances in seawater. *Aquat. Geochem.* 1, 89–104. doi: 10.1007/BF01025232

Truesdale, V. W., Watts, S. F., and Rendell, A. (2001). On the possibility of iodide oxidation in the near-surface of the black Sea and its implications to iodine in the general ocean. *Deep-Sea Res. I Oceanogr. Res. Pap* 48 (11), 2397–2412. doi: 10.1016/S0967-0637(01)00021-8

Waite, T. J., and Truesdale, V. W. (2003). Iodate reduction by *Isochrysis galbana* is relatively insensitive to de-activation of nitrate reductase activity–are phytoplankton really responsible for iodate reduction in seawater? *Mar. Chem.* 81, 137–148.

Weiss, R. F., and Price, B. A. (1980). Nitrous oxide solubility in water and seawater. *Mar Chem.* 8, 347–359. doi: 10.1016/0304-4203(80)90024-9

Whalley, L. K., Furneaux, K. L., Goddard, A., Lee, J. D., Mahajan, A., Oetjen, H., et al. (2010). The chemistry of OH and HO_2 radicals in the boundary layer over the tropical Atlantic ocean. *Atmos. Chem. Phys.* 10, 1555–1576. doi: 10.5194/acp-10-1555-2010

Wilkinson, F., Helman, W. P., and Ross, A. B. (1995). Rate constants for the decay and reactions of the lowest electronically excited singlet state of molecular oxygen in solution. *expanded revised compilation. J. Phys. Chem. Ref. Data* 24, 663–1021. doi: 10.1063/1.555965

Wong, G. T. F. (1991). The marine geochemistry of iodine. *Rev. Aquat. Sci.* 4, 45–73.

Wong, G. T. F. (2001). Coupling iodine speciation to primary, regenerated or "new" production: A re-evaluation. *Deep Sea Res. Part I Oceanographic Res. Papers* 48, 1459–1476. doi: 10.1016/S0967-0637(00)00097-2

Wong, G. T., and Brewer, P. G. (1977). The marine chemistry of iodine in anoxic basins. *Geochim. Cosmochim. Acta* 41 (1), 151–159. doi: 10.1016/0016-7037(77)90195-8

Wong, G. T. F., Piumsomboon, A. U., and Dunstan, W. M. (2002). The transformation of iodate to iodide in marine phytoplankton cultures. *Mar. Ecol. Prog. Ser.* 237, 27–39. doi: 10.3354/meps237027

Wong, G. T., Takayanagi, K., and Todd, J. T. (1985). Dissolved iodine in waters overlying and in the orca basin, gulf of Mexico. *Mar. Chem.* 17, 177–183. doi: 10.1016/0304-4203(85)90072-6

Wong, G. T., and Zhang, L.-S. (2008). The kinetics of the reactions between iodide and hydrogen peroxide in seawater. *Mar. Chem.* 111, 22–29. doi: 10.1016/j.marchem.2007.04.007

Yamazaki, C., Kashiwa, S., Horiuchi, A., Kasahara, Y., Yamamura, S., and Amachi, S. A. (2020). Novel dimethylsulfoxide reductase family of molybdenum enzyme. *Environ. Microbiol.* 22, 2196–2212. doi: 10.1111/1462-2920.14988

Yuan, J., and Shiller, A. M. (2001). The distribution of hydrogen peroxide in the southern and central Atlantic ocean. *Deep Sea Res. Part II Top. Stud. Oceanogr* 48, 2947–2970. doi: 10.1016/S0967-0645(01)00026-1

Zhang, J.-Z., and Whitfield, M. (1986). Kinetics of inorganic reactions in seawater. 1. the reduction of iodate by bisulphide. *Mar. Chem.* 19, 121–137. doi: 10.1016/0304-4203(86)90044-7

Žic, V., and Branica, M. (2006). The distributions of iodate and iodide in rogoznica lake (East Adriatic coast). *Estuar. Coast. Shelf Sci.* 66 (1), 55–66. doi: 10.1016/j.ecss.2005.07.022

Žic, V., Truesdale, V. W., and Cukrov, N. (2008). The distribution of iodide and iodate in anchialine cave waters–evidence for sustained localised oxidation of iodide to iodate in marine water. *Mar. Chem.* 112 (3–4), 168–178. doi: 10.1016/j.marchem.2008.09.001

frontiers | Frontiers in Marine Science

TYPE Original Research
PUBLISHED 29 June 2023
DOI 10.3389/fmars.2023.1171999

Check for updates

OPEN ACCESS

EDITED BY
Dalton Hardisty,
Michigan State University, United States

REVIEWED BY
Peng Lin,
University of Georgia, United States
Natalya Evans,
University of California Santa Barbara, United States

*CORRESPONDENCE
Qiang Shi
qshi@dal.ca
Douglas W. Wallace
Douglas.Wallace@Dal.Ca

RECEIVED 22 February 2023
ACCEPTED 09 June 2023
PUBLISHED 29 June 2023

CITATION
Shi Q, Kim JS and Wallace DW (2023) Speciation of dissolved inorganic iodine in a coastal fjord: a time-series study from Bedford Basin, Nova Scotia, Canada. *Front. Mar. Sci.* 10:1171999. doi: 10.3389/fmars.2023.1171999

COPYRIGHT
© 2023 Shi, Kim and Wallace. This is an open-access article distributed under the terms of the Creative Commons Attribution License (CC BY). The use, distribution or reproduction in other forums is permitted, provided the original author(s) and the copyright owner(s) are credited and that the original publication in this journal is cited, in accordance with accepted academic practice. No use, distribution or reproduction is permitted which does not comply with these terms.

Speciation of dissolved inorganic iodine in a coastal fjord: a time-series study from Bedford Basin, Nova Scotia, Canada

Qiang Shi[1*], Jong Sung Kim[2,3] and Douglas W. Wallace[1*]

[1]Department Oceanography, Dalhousie University, Halifax, NS, Canada, [2]Department of Community Health and Epidemiology, Dalhousie University, Halifax, NS, Canada, [3]Department of Occupational and Environmental Health, The University of Iowa, Iowa City, IA, United States

We report a long-term (4.5 year) time-series with weekly resolution of iodide and iodate measurements made at 4 depths within the Bedford Basin: a 70 m deep, seasonally stratified, coastal fjord located near Halifax, Nova Scotia, Canada. The subsurface data (60 m) reveal strong inverse correlations of both iodide and total dissolved iodine (TDI) with dissolved oxygen and indicate that there is *in-situ* reduction of iodate in subsurface waters (in the presence of oxygen) as well as an additional external source of iodide from the remineralization of sinking organic matter, a flux from sediments, or both. Surface water (<10 m) iodide concentrations increase gradually from spring (70 nmol L^{-1}) through fall (120-150 nmol L^{-1}) and are not well represented by the current empirical parameterizations used to predict surface water iodide levels globally. The vertical gradient of iodide between subsurface and surface waters increases over the summer as a result of subsurface processes and, together with diapycnal mixing, may contribute to the seasonal accumulation of iodide in surface water. Examination of a global surface water iodide data compilation reveals an inverse relationship with subsurface oxygen concentrations which suggests that subsurface remineralization and sediment-water fluxes coupled with vertical mixing may also contribute to surface water iodide variability on a global scale.

KEYWORDS

ocean time series, iodide, iodate, biogeochemistry, fjord, total dissolved iodine

1 Introduction

Iodine (I) is a bioactive element which is subject to complex biogeochemical reactions in the ocean including redox-related transformations between inorganic species (e.g., iodide and iodate), acid-base chemistry (e.g., of HOI), occurrence of numerous volatile gaseous forms, both organic (e.g., CH_3I) and inorganic (e.g., I_2), and nutrient-like behavior involving uptake by organisms into particles, particulate transport and remineralization at depth and in sediments. The ocean is the major reservoir of iodine at the earth's surface, and most iodine within the atmosphere or in food (Hatch-mcchesney and Lieberman, 2022) is derived,

directly or indirectly, from the oceanic reservoir. Hence, interest in the oceanic distribution and speciation of iodine arises from of a variety of considerations including: a) the important role that iodine plays for tropospheric (Davis et al., 1996; McFiggans et al., 2000; Carpenter et al., 2013) and, in some cases, stratospheric chemistry (Tegtmeier et al., 2013) including ozone destruction (Saiz-Lopez and Von Glasow, 2012); b) significance as a pathway for radiological hazards (e.g., via ^{131}I (Kawamura et al., 2011)); c) its essential role for human and animal health, including for synthesis of thyroid hormones in humans and other organisms including fish and fish larvae used for aquaculture (Witt et al., 2009); d) the potential of iodine-containing species or isotopes as tracers, for example as a proxy of paleo-redox conditions (e.g. (Raisbeck and Yiou, 1999)) or for tracking ocean circulation (use of ^{129}I; Casacuberta et al., 2018; A. M. Wefing et al., 2019; Anne Marie Wefing et al., 2021).

In a recent review, Carpenter et al. (2021) noted that the cycling of iodine, including its release to the atmosphere and effect on atmospheric chemistry and ozone, is likely to be changing as a consequence of climate change. Yet, despite its broad importance, and several decades of research (Carpenter et al., 2021), understanding of the processes that control transformations of iodine within the ocean, or exchanges with the atmosphere or sediments, remains incomplete. For example, there remains incomplete understanding of the processes that control concentrations of iodide in surface seawater (Carpenter et al., 2021; R. Chance et al., 2014) and the processes by which iodide is re-oxidized to iodate (iodine's thermodynamically stable state in oxic seawater). Several empirical parameterizations of surface iodide concentrations have been developed but do not necessarily correspond well with the distribution of iodine monoxide (IO) in the atmosphere (Carpenter et al., 2021). Even the iodine to carbon ratio involved in transport of iodine between surface and deep ocean waters via particles, appears uncertain (Elderfield and Truesdale, 1980; Carpenter et al., 2021). Carpenter et al. (2021) notes that the gaps in understanding include that we have little or no characterizations of the seasonal variation of iodine species, even of sea-surface iodide concentrations, anywhere in the ocean.

Haas et al. (2021) pointed out that multi-disciplinary time-series can be key to elucidation of biogeochemical processes, such as nitrification in coastal waters, that often involve complex interactions between the physical environment with microbial populations. Shi and Wallace (2018) made the same point, specifically with respect to cycling of iodine. They argued that understanding of iodine cycling could best be advanced through the combination and co-location of: a) comprehensive measurement of various iodine species with high temporal resolution; b) repeated experimentation in the context of the time-series (Shi et al., 2014) and c) biogeochemical modelling. A barrier to this comprehensive approach is the logistical effort required to sustain the three components, over the long term. Hence most iodine-related research remains opportunistic and typically takes advantage of occasional research cruises and other opportunities for sampling, as they arise.

We present here the results of time-series measurement of iodine speciation (mainly iodide and iodate) which were made in the context of a broader time-series of biogeochemical, microbial and physical properties, in Bedford Basin (BB), Nova Scotia, Canada. The time-series data are used to shed light on potential mechanisms of iodine cycling and to develop hypotheses that can be addressed by further targeted experimentation and modelling.

2 Methods and sampling

2.1 Collection of samples

Time-series observations of physical, chemical and biological parameters have been carried out in the Bedford Basin (44.69°N, -63.63°E) near Halifax, Canada since 1992 (Li, 1998). Additional information about the sampling has been reported by Shi and Wallace (2018) and Haas et al. (2021). Samples for inorganic iodine analysis were collected weekly with 10-L Niskin bottles attached to a rosette sampler at 1, 5, 10 and 60 m, in the center of the Bedford Basin.

Each bottle was rinsed twice with the sample water prior to collection. After filtration through a 0.45 µm membrane nylon filter (on board), all samples (50ml in high-density polyethylene (HDPE) bottles) were stored at 4 °C in a refrigerator prior to analysis.

We have divided the inorganic iodine time-series into two periods: a) pre-pandemic (May 2018 to March 2020) and b) post-pandemic (July 2021 to December 2022). Some samples from the pre-pandemic period were stored for more than half a year before analysis, due to work being conducted, simultaneously, on the improvement of analytical methods and precision. Methods were settled during the pandemic and during the post-pandemic period, samples were stored for a maximum of 3 weeks and benefitted from improved precision.

2.2 Analytical method for iodine analysis

The concentration of iodide (I^-) was determined by high pressure ion chromatography (HPIC, Dionex ICS-5000, Thermo Fisher Seicentific) using the method of Sanz Rodriguez et al., 2016. The concentration of iodate (IO_3^-) was determined with the same method, by difference, after quantitative reduction to iodide using ascorbic acid in the presence of hydrochloric acid (HCl) (Campos, 1997; Brandao, 2001). Here we note that dissolved organic iodine (DOI) can also be transformed to iodide with this treatment. Hence our reported concentrations of total dissolved iodine (TDI) represent $[I^-] + [IO_3^-] + [DOI]$. However, DOI concentrations in seawater are generally much lower than iodate, and typically range from 10 to 40 nmol L^{-1} (Wong and Cheng, 1998; Truesdale et al., 2001). We checked the DOI levels in samples collected at three depths in Bedford Basin in both November 2022 and April 2023, using the three-step procedure of Jones et al. (2023) which involves addition of $Ca(ClO)_2$, Na_2SO_3 and NH_2OH–HCl. These samples covered seasons with both high (April 2023) and low (November 2022) oxygen concentrations. The tests confirmed that our reduction with ascorbic acid does convert DOI to iodide, however the measured DOI levels were in the range expected (37 ± 12 nmol

L^{-1}) and did not vary significantly between the two sampling periods.

The HCl (37%, Fisher Chemical) was diluted using Milli-Q water (MQW) to prepare a 6 M HCl solution. L-ascorbic acid (>99%, ACROS Organics) was used to prepare the required 0.2 M aqueous solution. Both were stored in glass bottles at 4 °C.

For calibration, stock solutions of iodide and iodate (0.45 M and 0.05 M, respectively) were prepared by dissolving potassium iodide (99.5%, Sigma) and sodium iodate (99.5%, Sigma) in MQW. They were stored in HDPE containers at 4 °C and newly prepared every three months. Working standard solutions of 9.04 µmol L^{-1} iodide and 5.31µmol L^{-1} iodate were freshly prepared by diluting 10 µL and 50 µL of each of these stock solutions, respectively, with 500 ml MQW. Calibration standards between 0.03 and 0.64 µmol L^{-1} (5-point calibration curve) were prepared by dilution of the working standard solutions in artificial seawater (2019-2020) or Milli-Q water (2018, 2021-2022). The artificial seawater was prepared according to the recipe of Strickland and Parsons (1972). The calibration solutions were prepared every two days.

For samples and standards alike, the procedure before injection involved adding 25 µl of 6M HCl solution and 15 µl of 0.2 M L-ascorbic acid solution to 4960 µl of seawater sample followed by mixing by vortex for more than 1 minute (Sanz Rodriguez et al., 2016). Aliquots of either 25 µl (2019-2020) or 125 ul (2021-2022) were injected via a Dionex AS Autosampler (Thermo Fisher Scientific) into a Dionex ICS-3000 IC system coupled with a UV detector (VWD-variable wavelength detector, Thermo Fisher Scientific). The initial sample aliquot size of 25 µl, was increased to 125 µl for samples analyzed since 2020. The instrument was equipped with an EGG-KOH cartridge, a column heater a guard column (Dionex IonPac AG20,50×4.0 mm ID, particle size 11 µm), and a separator column (Dionex IonPac AS 20, 250×4.0 mm ID, particle size 7.5 µm). The UV detector was operated at 226 nm. The 25 or 125 µl samples were injected onto the column and KOH was used as the eluent at a flow rate of 1.0 ml/min with a gradient program starting from 13 nmol L^{-1} (hold 1 min) to 35 nmol L^{-1} at 2 min then to 70 nmol L^{-1} at 14 min (hold 2 min) before returning to 13 nmol L^{-1}. The total run time was 26 min, and the analysis were carried out at 30 °C. Every sample was analysed in triplicate. The standard deviation (SD) of triplicate measurements (integrated peak area) was<10%. Blanks of Milli-Q water were run between all sample analyses. Due to salt buildup, the separation column needed to be cleaned at least every three months. Dirty columns caused peak shifts and peak shape changes and reduced precision. In this study, each data point for iodine shown in the graphs represents the results of the average of three replicate measurements.

2.3 Measurement of open ocean profiles

In order to test this method's comparability with other methods used historically, we analyzed samples from offshore profiles collected on the Scotian Shelf and over the continental slope of the NW Atlantic (the HUD2020063 Fall AZMP Mission (Atlantic Zone Monitoring Program)). The two locations are shown on the map (Figure 1). These profiles (Figure S1) were highly consistent with results from prior open ocean work. For example, total dissolved iodine (TDI) in deep water averaged 479.1 nmol L^{-1} (± 13.4 nmol L^{-1}), consistent with values measured elsewhere in the North Atlantic Ocean (Campos et al., 1996). Surface iodide was ca. 60-80 nmol L^{-1}, which is also comparable to values measured previously at similar latitudes and depths (Chance et al., 2014; Chance et al., 2019; Carpenter et al., 2021).

3 Results

3.1 Environmental variables in the bedford basin

The time-series of temperature, salinity, dissolved oxygen, fluorescence/Chl *a* and total dissolved inorganic nitrogen (DIN = [NH4+] + [NO2-] + [NO3-]) at 4 depths are presented in Figures 2, 3. Near-surface temperatures start to rise above winter values of 3 °C, and stratified conditions develop, around early April with temperatures reaching ca. 21 °C by the end of August

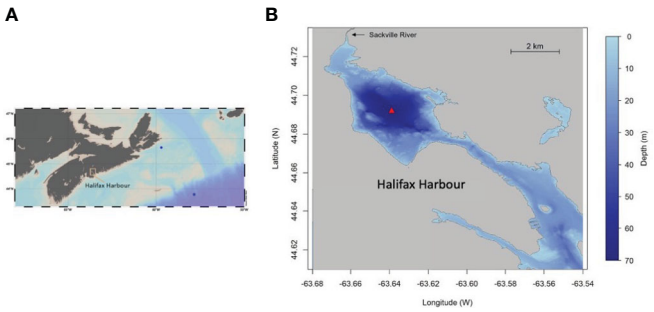

FIGURE 1
(A) Map of Nova Scotia, Canada and the Scotian Shelf, showing two locations (blue circles) where samples were collected over the continental shelf and slope for quality assurance (Supplemental Materials 1.1); **(B)** Bathymetric map of Bedford Basin and Halifax Harbour showing location (red triangle) of the time-series measurements; the map is adapted from that shown in Rakshit et al., 2023).

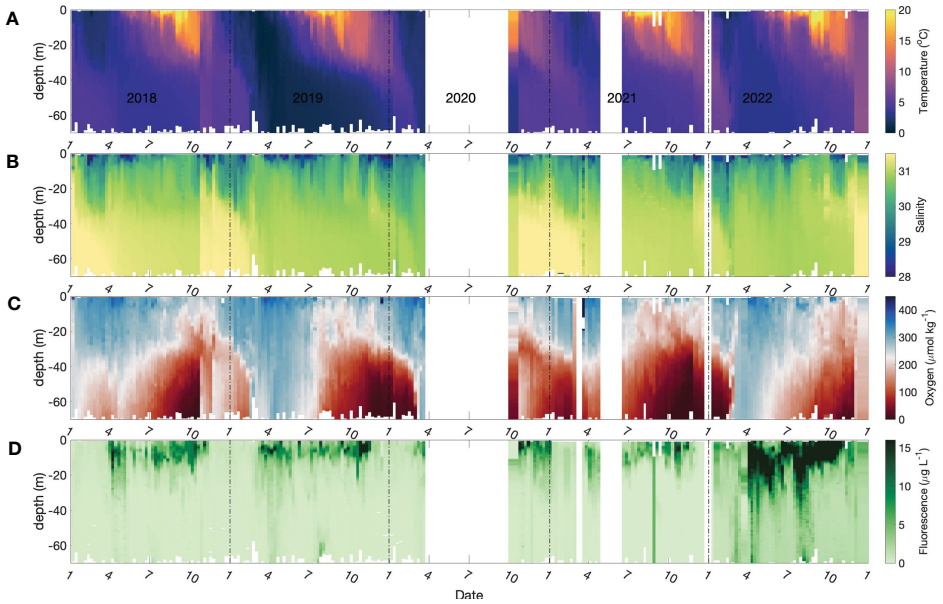

FIGURE 2
Seasonal patterns of environmental and biological variables in Bedford Basin from January 2018 to Dec 2021. **(A)** temperature; **(B)** salinity **(C)** dissolved oxygen; **(D)** chlorophyll fluorescence. The data gap in 2020 was the result of cessation of the time-series due to COVID-19 restrictions.

(Figures 2A and 3A). Salinity ranges from 26 to 31 through the entire water column, with the lowest salinities occurring very close to the surface (Figures 2B and 3B blue line). The near-surface stratification varies seasonally, primarily due to summertime heating.

The dissolved oxygen time-series (Figures 2C and 3C) shows the effect of temperature-dependent solubility variations in surface waters as well as intrusions and late-winter vertical mixing in deeper water (Rakshit et al., 2023). For instance, in October 2018 the salinity of bottom water increased from 31.2 to 31.6 (Figure 3G), and oxygen concentration increased from 25 µmol kg^{-1} to 210 µmol kg^{-1} (Figure 3I), reflecting the arrival of an "intrusion" of shelf water. In surface waters, the highest O_2 concentrations occurred between March and April in association with the lowest seawater

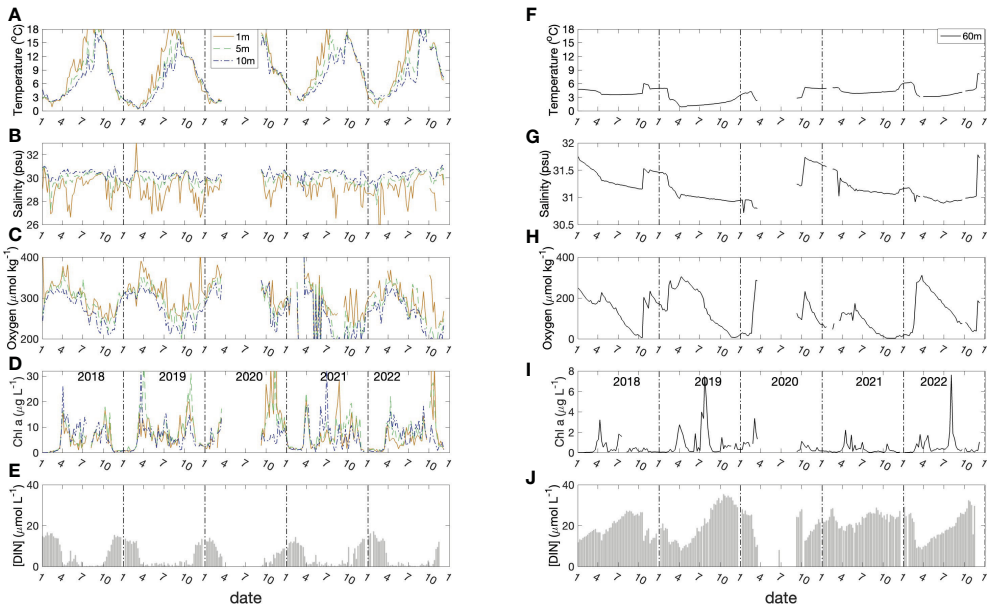

FIGURE 3
Seasonal variation of physical and biological parameters at 1, 5,10 meters (left panel; **A–E**) and 60 meters (right panel; **F–J**). The data gap in 2020 was the result of cessation of the time-series due to COVID-19 restrictions.

temperatures. The vertical gradient of O_2 concentration was, generally, smallest towards the end of April as a result of vertical mixing. Sub-surface O_2 concentrations (>30 m) decreased in summer due to respiration unless interrupted by an intrusion. In most winters, intense vertical mixing coupled with gas exchange replenished bottom water oxygen levels to near-saturation levels (300 µmol kg^{-1}). However, winter mixing was weaker than normal in 2020/2021 compared with previous years, so that oxygen levels did not get fully replenished and did not exceed 150 µmol kg^{-1} at the end of winter. This led to an unusual 5-month period of near anoxic conditions late in 2021 (Figure 3H) compared with more typical ca. 2-to-3-month hypoxic periods during the previous decade. During this unusual 5-month hypoxic period, iodide concentration reached the highest value (496.9 nmol L^{-1}) measured during the entire observation period.

Two blooms (spring and autumn) were observed typically, each year, in the time-series of chlorophyll *a* concentration in surface water (Figures 2D and 3D). The seasonal variation of dissolved inorganic nitrogen (sum of [NH_4^+], [NO_2^-], [NO_3^-]) in surface water is plotted in Figure 3E. In winter, when chlorophyll *a* levels are low due to light limitation, DIN concentrations reach ca. 18 µmol L^{-1} but are drawn down to low levels (< 1 µmol L^{-1}) after the spring bloom (Figure 3E). Summertime chlorophyll *a* levels are moderate but variable (3 to 15 µg L^{-1}), likely reflecting continuing nutrient input (e.g. from runoff and/or sewage treatment plants). In the bottom water, DIN concentrations (mean: 20 µmol L^{-1}) were higher than the concentrations in surface water (Figure 3J) throughout most of the year. The DIN composition in bottom water showed a clear progression due to nitrification from ammonium to nitrate, with occasional accumulation of low levels (< 0.5 µmol L^{-1}) of nitrite. The timing of the onset of nitrification is variable from year to year in response to variations in the intensity and duration of winter mixing which dilutes the population of nitrifiers in bottom water to variable extents (Haas et al., 2021).

3.2 Variation of iodine concentration in bedford basin

Figure 4 shows that although Bedford Basin receives considerable freshwater input, there was no significant relationship observed between TDI and salinity, likely because the salinity range was too restricted in the centre of the Basin (usually from 28.5 to 31). Our measurements of the Sackville River, the major freshwater source to Bedford Basin, confirmed that the freshwater endmember concentration was very low (TDI: 40.1 ± 4.5 nmol L^{-1}; n=3). The average total dissolved iodine concentration (TDI) when "rationalized" to a standard salinity of 35 (Truesdale, 1994; Truesdale, 1995; Truesdale et al., 2001) was 428 ± 76 nmol L^{-1} (n = 478) for near-surface water samples. However, from now on, because the correlation with salinity is not significant at the time-series location, we discuss measured concentrations, without rationalization.

The long-term, temporal variations of iodide, iodate, and total dissolved iodine are shown in Figure 5. Iodide in surface water (1, 5 and 10 m) ranged between 10 to 200 nmol L^{-1} over the entire time-series (mean: 83 ± 34 nmol L^{-1}, except for a few samples with >200 nmol L^{-1}) whereas iodate varied from 100 to 600 nmol L^{-1} (mean: 283± 65 nmol L^{-1}). The TDI concentration was 366 ± 67 nmol L^{-1} for near-surface samples. However, variability was considerably smaller during Period 2 of the time-series when analytical precision was better (see methods). The means and other summary statistics for iodide, iodate and TDI in the upper 10 m and at 60 m are given for the two time periods in Table 1.

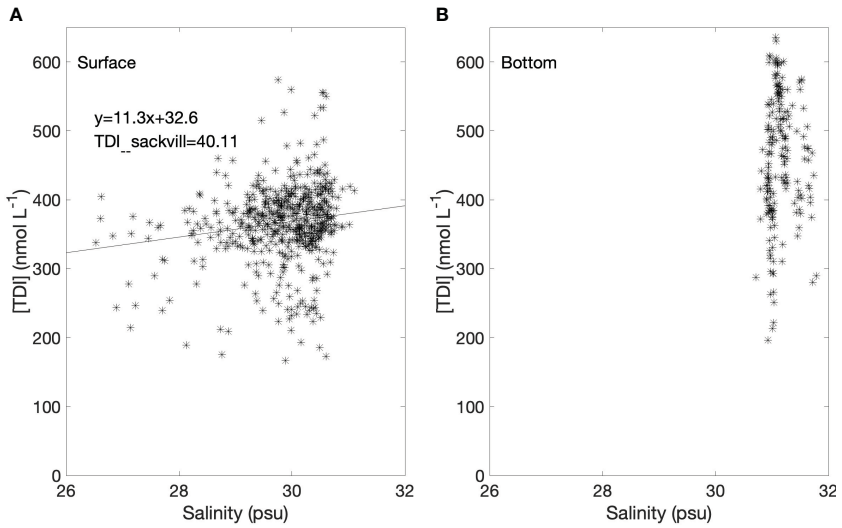

FIGURE 4
(A) Total dissolved iodine (TDI) in surface water (1, 5 and 10 m) versus salinity. The linear regression line is also shown (slope: 11.3, intercept: 32.6, R^2: 0.21). **(B)** TDI in subsurface (60 m) versus salinity.

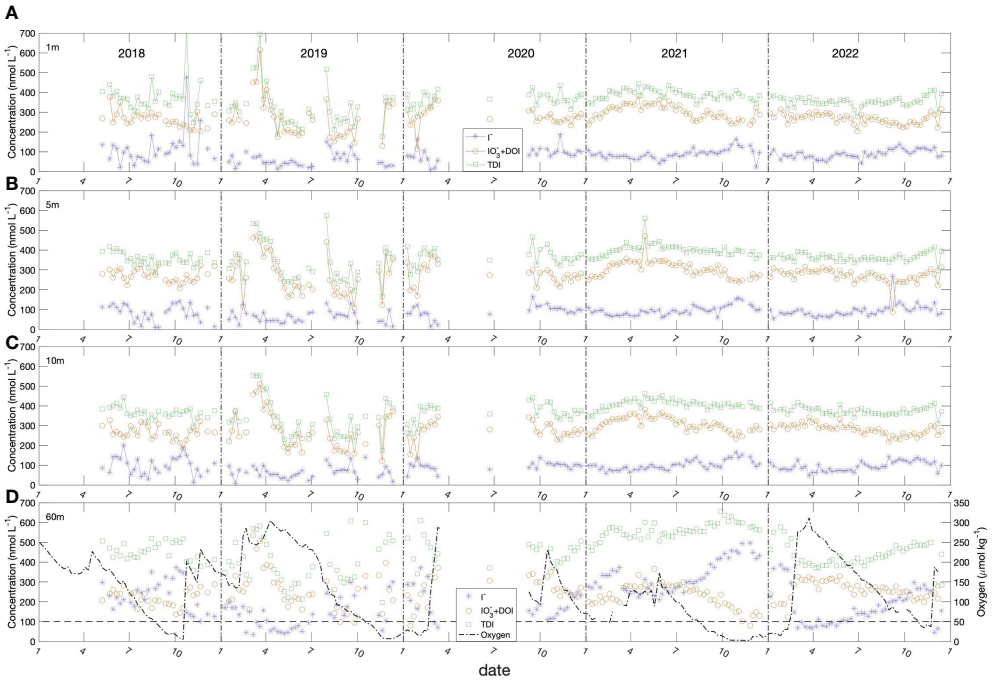

FIGURE 5
Seasonal variation of iodide (blue stars), iodate + DOI (dark yellow circles, DOI levels were in the range of 37 ± 12 nmol L^{-1}), TDI (green diamonds) in the Bedford Basin at **(A)** 1 m, **(B)** 5 m, **(C)** 10 m and **(D)** 60 m. Also shown in panel **(D)** is the oxygen concentration. The average standard deviations (SD) of triplicate measurements were I^- of ± 9 nmol L^{-1}; TDI of ± 14 nmol L^{-1} and IO_3^- + DOI of ± 22 nmol L^{-1}.

The data from Period 2 reveal gradual accumulation of iodide in surface water (1, 5, 10 m) over spring and summer, from lowest values of ca. 70 nmol L^{-1} in spring (March, April, May) to maximum concentrations of ca. 120 to 150 nmol L^{-1} in fall (October, November). The noisier data from Period 1 show similar trends, with a decline from maximum concentrations in fall 2018 to minimum values in spring 2019 (ca. 30-50 nmol L^{-1}), followed by an apparent increase over the subsequent summer.

Iodide behaved very differently at 60 m, with generally higher concentrations (ca. 3 times higher) and much larger amplitude variability (50 to 550 nmol L^{-1}). Iodide at 60 m also showed a strong inverse correlation with oxygen, so that it increased from the onset of stratification in April to when the water column convectively overturned in February/March unless interrupted by a shelf water intrusion, which reset values to ca. 50 nmol L^{-1}.

Total dissolved iodine (TDI: iodide + iodate + DOI) in surface waters had levels averaging 367.8 ± 64.2 nmol L^{-1} over the entire time period and 387.5 ± 30.9 nmol L^{-1} during the better characterized Period 2. However, TDI increased systematically over the year in deep (60 m) water, following the onset of stratification and, again, had an inverse correlation with oxygen. The mean TDI concentration (511 ± 72.4 nmol L^{-1}; n=83) (Figure 5D) was significantly higher than the surface water concentration at the 95% confidence interval. Unless interrupted by shelf water intrusions, TDI increased from minimum values of 371 nmol L^{-1} in late winter to maxima of 657 nmol L^{-1} in the fall or early winter and were anti-correlated with dissolved oxygen.

Overall, iodate concentrations were always higher than iodide concentrations in near-surface waters. However, this picture was reversed in the bottom water, where iodide concentrations were

TABLE 1 Overall statistics for iodide, iodate and TDI in the upper 10m (s: surface water) and at 60 m (ss: subsurface water) during the two sampling periods referred to in the text.

	Iodide (nM)				Iodate (nM)				TDI (nM)			
Period	Mean	SD	n	Skew	Mean	SD	n	Skew	Mean	SD	n	Skew
P1 (s)	77.2	48.4	261	2.8	269.8	77.0	261	0.8	346.8	82.0	261	0.8
P2 (s)	94.4	25.1	342	1.4	285.6	37.2	342	0.2	379.9	31.6	342	0.5
All (s)	87.4	37.3	603	2.3	279.2	57.2	603	0.5	366.6	59.8	603	0.3
P1 (ss)	179.7	92.2	94	0.3	242.8	85.8	94	1.0	422.4	95.8	94	-0.2
P2 (ss)	239.2	112.6	115	0.3	250.1	53.8	115	-0.6	489.4	78.7	115	-0.2
All (ss)	214.7	108.7	209	0.4	247.1	68.9	209	0.6	461.6	92.3	209	-0.4

generally, higher than iodate concentrations, especially when oxygen concentrations dropped below 130-140 µmol kg^{-1} (Figure 5D, horizontal dash line).

4 Discussion

Time-series have the potential to reveal underlying mechanisms and controls of complex biogeochemical transformations. Here we discuss the observations from Bedford Basin in connection with inorganic iodine transformations that have been discussed, inconclusively to-date, in the literature.

4.1 Magnitude and controls of surface iodide concentrations

As noted by Carpenter et al. (2021) and Wadley et al. (2020), the potential for iodide to impact atmospheric chemistry on global scales, and for its impact to change as a result of global environmental change, necessitates mechanistic understanding (and a model) of iodide formation in near-surface water. However to date, models used in atmospheric chemistry rely mainly on empirical relationships to represent spatial and temporal variations of sea surface iodide. There is no certainty that the selected, correlated parameters are related mechanistically to iodide production, or that the correlations will remain invariant in the future (e.g. in the context of climate change).

In Figures 6A, B we compare iodide levels predicted by three published empirical and statistical relationships, with concentrations observed in the upper 10 m during the Bedford Basin time-series. The observed levels are notably higher than predicted by all of the empirical relationships. In the case of the temperature-dependent relationships of Chance et al. (2014) and Macdonald et al. (2014) by factors of 2-4 and 5-15, respectively. The nitrate-based parameterizations derived from Campos et al. (1999) bracket the average observed concentrations (in summer), especially during Period 2 (Figure 5B) but do not capture the seasonal accumulation. A random-forest regression approach (Sherwen et al., 2019) predicts global average values comparable to those of Chance et al. (2014). Based on Figure 6 in Sherwen et al. (2019), their prediction of annual average concentrations for NW Atlantic coastal waters appears to be in the range 60-100 nmol L^{-1}, which is consistent with our observations.

There appears to be consensus in the literature that a biologically-mediated reduction process operating within the surface layer is responsible for the presence of iodide in surface water. Campos et al. (1996) proposed that iodide reduction was proportional to primary production, however data collected subsequently from the South Atlantic and Weddell Sea (Campos et al., 1999) appeared inconsistent with this hypothesis. The mechanisms responsible for production of iodide in surface waters remain unresolved. Two distinct mechanisms for iodate reduction in the surface layer have been proposed: a) through the action of nitrate reductase (Hung et al., 2005); b) by reaction with reduced metabolites, such as reduced sulfur compounds, that are released from phytoplankton cells upon senescence (Bluhm et al., 2010). Campos et al. (1999) noted a general increase of iodide as nitrate concentrations decreased along a N-S transect in the South Atlantic. They postulated reduced iodide production in the presence of high nitrate as a result of "chemical competition", under the assumption that nitrate reductase was responsible. They reported a

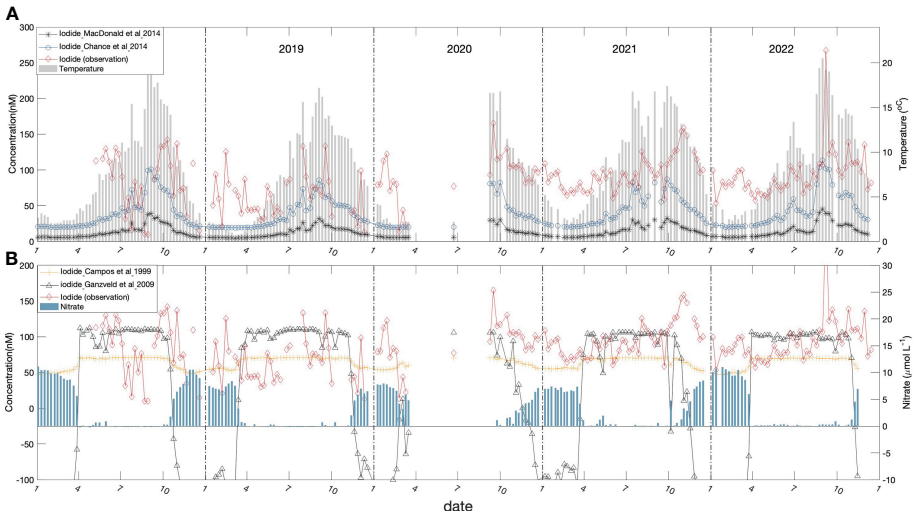

FIGURE 6
Sea-surface iodide predicted from empirical parameterizations (for 5 m in Bedford Basin) plotted against the observed concentrations (red line): **(A)** iodide predicted based on the empirical relationships with sea surface temperature of Macdonald et al. (2014) (black closed circles and line) and Chance et al. (2014) (blue open circles and line); also plotted is sea surface temperature (grey bar). **(B)** predictions of iodide (nmol L^{-1}) at 5 m depth from empirical relationships with nitrate for regions inside ($[I^-] = 106 - 29 \times [NO_3^-]$; black line) and outside ($[I^-] = 70.4 - 2.12 \times [NO_3^-]$; green line) the South Atlantic sub-tropical gyre as derived by Ganzevald et al., 2009 from the relationships reported by Campos et al. (1999). Also shown are the variation of nitrate (blue bars).

range of empirical inverse correlations with surface nitrate which have been summarized and applied by Ganzeveld et al. (2009) (see Figure 6B). Macdonald et al. (2014) proposed empirical correlations with sea surface temperature on the basis that increased temperature and, hence, stratification allows iodate to be reduced to iodide in the surface layer by either blocking of iodate replenishment from below or by facilitating reduction through the prolonged isolation of surface water.

The temporal variability of surface iodide may provide clues about underlying processes and controls. For example, the trends shown in Figure 6 do not appear consistent with the temperature-only parameterizations, because concentrations continue to rise in the fall, even as temperature is dropping. As noted earlier, the overall pattern appears to be of gradual accumulation, starting in April/May and changing sign in October/November. This period of accumulation coincides with the period when nitrate is depleted in surface waters (Figure 6B) and is therefore consistent with either, or both of the proposed biological mechanisms for *in-situ* iodate-reduction. Nitrate depletion could promote cell senescence and increase the potential for leakage of reduced species that can react with iodate (Bluhm et al., 2010). Alternatively, iodide could be produced by nitrate reductase as noted above, especially when competition from ambient nitrate for active sites is reduced (Campos et al., 1999; Hung et al., 2005). However, the empirical correlations with nitrate taken from the open ocean do not represent the gradual build-up of iodide over the summer through fall (Figure 6B) and either under-predict concentrations in summer or in winter, depending on the relationship used.

It is not possible to choose between alternative biological production mechanisms based on our time-series data alone. Manipulative experiments conducted in the context of the time-series (e.g., using manipulation of, for example, nitrate reductase activity (Waite and Truesdale, 2003)) might allow elucidation of specific hypothesised mechanisms and controlling factors.

4.2 Iodide accumulation in the bottom water

During stratified periods, the bottom water of Bedford Basin was relatively isolated from near-surface waters and hence from exchange with the atmosphere, and was marked by steady declines of oxygen. During these periods, iodide increased monotonically and iodate decreased, unless interrupted by intrusions (such as at the end of October 2018) or by wintertime vertical mixing (typically in late February/March) both of which caused oxygen to increase. In Figure 7, the periods with different oxygen trends (decreasing, increasing and stable) are denoted with shading. The rates of iodide accumulation and iodate decrease calculated for the periods with decreasing oxygen are presented in Table 2.

The average accumulation rate of iodide in subsurface water (60 m) for the period with decreasing oxygen was 1.26 nmol day^{-1}. This is 4 times higher than the accumulation observed in surface waters over the summer (ca. 60 nmol L^{-1} over 7 months) and also 3-5 times higher than net rates of iodide accumulation (and iodate depletion) of 0.27 to 0.55 nmol day^{-1} observed in the surface ocean over 78 days by Chance et al. (2010). Further, because the rate of iodide increase is consistently higher than the corresponding rate of iodate decrease (typically by a factor of 2), our data show that accumulation of iodide in BB bottom water is not only from *in-situ* reduction of iodate, but also involves a source of iodine that is external to the bottom water itself.

Both iodide and TDI had strong, inverse correlations with oxygen at 60 m as shown in Figure 8, whereas there were no significant correlations in near surface waters. Oxygen at 60 m can vary due to a) biogeochemical processes (including respiration/oxidation of organic material within the water-column or loss to underlying sediments via sediment-water exchange) and b) physical transport (mixing with surface waters or shelf-water intrusions). In addition to physical processes, the biogeochemical processes affecting inorganic iodine speciation include the "internal" or *in-*

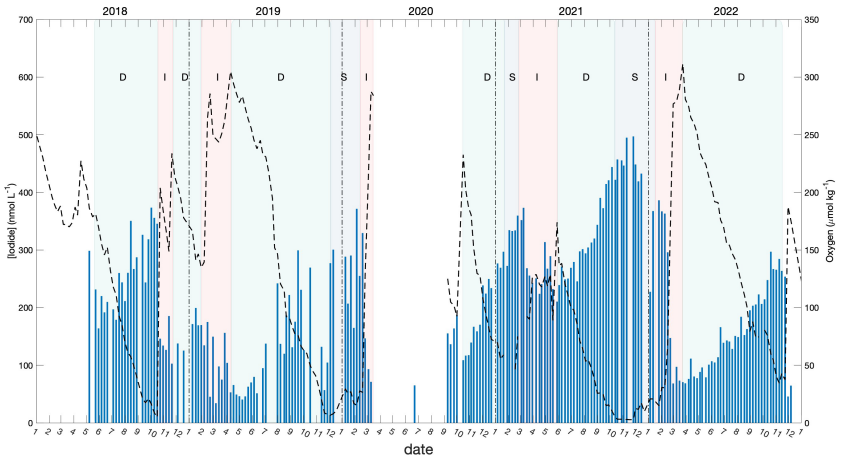

FIGURE 7
Seasonal variation of iodide in the bottom water (blue bars) with the variation of oxygen (dashed lines). Light green shading denotes periods when the oxygen concentration was decreasing in the bottom water ("D"), red shading denotes period when the oxygen concentration was increasing ("I"), and grey shading represents period when the oxygen concentration was stable (varied between 0 to 25 µmol kg^{-1}).

TABLE 2 Rates (nmol day^{-1}) of iodine accumulation in Bedford Basin bottom water during periods of decreasing oxygen concentrations.

Rate (nM day^{-1})	2018	2019	2020	2021	2022	Mean
I^-	1.27	0.75	1.89	1.57	0.84	1.26
IO_3^-	-0.75	-0.04	-0.77	-0.87	-0.39	-0.56
TDI	0.52	0.71	1.12	0.69	0.45	0.70

(Note that IO_3^- is calculated from measurements of I^- and TDI, so that the three parameters are not fully independent of each other). The rates are calculated using linear regression of the observed concentration of each species with time.

situ reduction of dissolved iodate to iodide within the water column (increases iodide but leaves TDI unchanged) and "external" supply from/to sediments and via remineralization from sinking organic material, both of which change both iodide and TDI. External supply processes are most likely to alter iodine concentrations significantly when bottom waters are isolated, and both mixing and intrusions would drive a linear relationship between iodide and oxygen during periods of increasing oxygen concentration. On the other hand, reduction of iodate to iodide, remineralization of sinking organic material, or fluxes of iodine from the sediments, would also result in correlations with oxygen, in this case during periods of decreasing oxygen. The latter could even be non-linear if the process was dependent on oxygen concentrations (Lu et al., 2010).

We therefore examined correlations of oxygen separately for periods of decreasing and increasing oxygen (i.e., between the "D" and "I" periods in Figure 7). Figures 8A, B shows that the regression slopes for $[I^-]$:$[O_2]$ are statistically indistinguishable between periods when oxygen was increasing or decreasing, whereas the TDI vs O_2 correlation was steeper during periods of decreasing oxygen, reflecting the accumulation of iodine from external sources during periods when the bottom water was isolated. Overall, the slopes of the $[I^-]$:$[O_2]$ regressions were steeper than those for [TDI]:$[O_2]$ which must be due to *in-situ* reduction of iodate. We also examined patterns of residuals but could detect no patterns suggestive of non-linear relationships with oxygen.

Here we assume that the observed increase of iodide at 60 m ($\Delta[I^-]_{Obs}$) has a source from *in-situ* reduction of iodate (Reyes-Umana et al., 2022), $\Delta[I^-]_{redn,}$ and an external source ($\Delta[I^-]_{ext}$) that could represent either release from sinking particulate material and/or from sediments:

$$\Delta[I^-]_{Obs} = \Delta[I^-]_{redn} + \Delta[I^-]_{ext} \quad (1)$$

As noted, *in-situ* reduction of iodate does not increase [TDI] so that

$$\Delta[TDI] = \Delta[I^-]_{ext} \quad (2)$$

and:

$$\Delta[I^-]_{redn} = \Delta[I^-]_{Obs} - \Delta[TDI] \quad (3)$$

If $\Delta[I^-]_{ext}$ is assumed to be due to release during remineralization of sinking particles ($\Delta[I^-]_{part}$) it can also be related to the sinking carbon flux and consumption of oxygen via the respiratory quotient (RQ = $\Delta C/-\Delta[O_2]$) for marine organic material and the I:C ratio in marine particulate matter:

$$\Delta[I^-]_{part} = \Delta[TDI] = (I/C)_{part} \times \Delta[O_2] \times RQ \quad (4)$$

Where estimates of RQ range widely (see (Robinson, 2019) for review). Using a median value for RQ of 0.88 from field studies, the $(I/C)_{part}$ can be estimated from:

$$(I/C)_{part} = (\Delta[TDI]/\Delta[O_2]) \times 0.88 \quad (5)$$

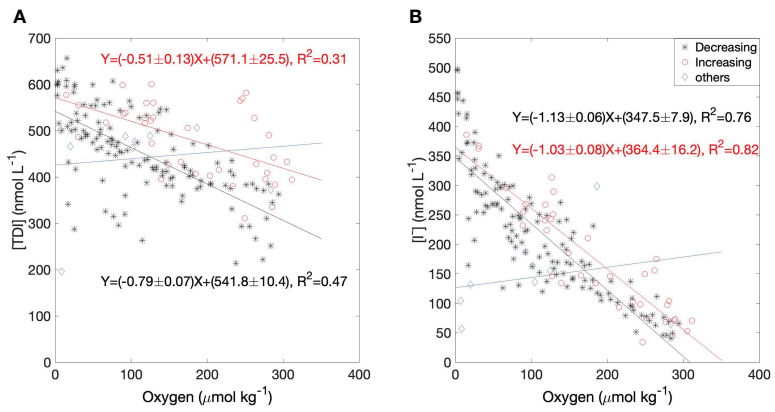

FIGURE 8
Linear regressions of **(A)** TDI and **(B)** iodide against dissolved oxygen in bottom water of Bedford Basin (60 m). Black stars represent data from periods when the oxygen concentration was decreasing in the bottom water and both iodide and TDI were accumulating; red circles represent data from periods when the oxygen concentration was increasing due to physical processes such as vertical mixing and/or intrusions; blue diamonds represent other periods (mainly when oxygen concentrations were not changing).

Our regression results give $\Delta[TDI]/\Delta[O_2]$ of 5.8 x 10^{-4} which implies an I:C ratio of 5 x 10^{-4}. This value is of the same order of magnitude but higher than several estimates in the literature: for example, Elderfield and Truesdale (1980) estimated I:C to be 1.4 x 10^{-4}, and Farrenkopf et al. (1997) also suggested a value of 1 x10^{-4}. Wadley et al. (2020) chose a base value of 3 x 10^{-4} for use in their global model of iodine cycling, based on a literature survey.

Our I:C estimate, together with those cited above, is much higher than some other estimates based on studies of iodine uptake by phytoplankton which inferred I:C ratios as low as 10^{-8} to 10^{-6} (Moriyasu et al., 2020). On the other hand, the I:C ratios in oxic sediments are even higher, of order 10^{-3} (Moriyasu et al., 2020). Wadley et al. (2020) assumed a base value of 3 x 10^{-4} in their model but experimented with ratios ranging from 4.7 x 10^{-6} to 1.2 x 10^{-3} which they noted covered the range of literature estimates. Allowing the I:C ratio to vary regionally helped to improve the fit of their model to surface water iodide observations at the global scale.

On the other hand, the external supply of iodide to BB deep water might involve release from reducing sediments. Our sampling depth at 60 m is approximately 10 m above the seafloor. From Figure 3C, we can see that the layer of low oxygen concentration extends to about 40m depth in summer. Ullman and Aller (1980) reported fluxes of iodide from coastal sediments ranging from ca. 5 to 41 µmol m^{-2} day^{-1} under anoxic conditions. If we assume that this iodide flux is added to a 30 m thick bottom layer (40 m to 70 m), the iodide accumulation rate would be between 0.2 to 1.4 nmol day^{-1}. This represents either a small fraction or all of the observed accumulation rate of 1.25 nmol day^{-1}. The nature of the external source of iodide to BB bottom waters therefore requires further resolution. This might best be achieved using pore-water profiles and/or benthic chamber studies. A very preliminary, limited study with core incubations of BB sediment (see Supplementary Material S1.3) gave estimates of the flux of iodide from sediment ranging from ca. 19.2 to 43.8 µmol m^{-2} day^{-1} in November (2 weeks after an intrusion), and -2.7 to 8.2 µmol m^{-2} day^{-1} in May. The associated iodide accumulation rates for a 30 m thick bottom layer would be -0.1 to 1.5 nmol day^{-1}. These preliminary flux estimates are therefore consistent with the flux rates of iodide reported by Ullman and Aller (1980). Here we should note that the core incubations shortly after an intrusion of shelf water may have been impacted by altered redox conditions, so that rates may not be representative of long-term averages.

Based on the accumulation rates of TDI and the loss rates of iodate summarized in Table 1, it can be concluded that the observed iodide accumulation is supported to approximately equal extent by *in-situ* reduction of iodate and external inputs. Some of the external input is likely due to shallow remineralization of sinking organic matter within the water column, as suggested based on open ocean time-series measurements made off Bermuda by Campos et al. (1996). However, the relative importance of the remineralization source vs. a sediment source in Bedford Basin requires further definition.

4.3 Fate of subsurface iodide

The time-series data show that high-levels of iodide accumulate in shallow (< 60 m), subsurface waters, even in the presence of significant quantities of oxygen. The accumulated iodide is "reset" to levels more typical of surface waters as a result of displacement of bottom water by intrusions of saltier shelf waters in summer and by convective mixing in winter. Given that iodide oxidation is known to be very slow (Luther et al., 1995), both mechanisms imply an upward transport of accumulated iodide which could, potentially, contribute to elevation of surface levels of iodide over the year. The effect of specific mixing events or intrusions on surface levels is not typically visible in our time-series, however, likely because the weekly sampling frequency misses the signature of such episodic, sudden events. Clearly, even with weekly sampling, key processes affecting near-surface iodide are not resolved.

While episodic upward transport of iodide due to convection and/or intrusions was not captured, the more rapid accumulation of iodide in subsurface waters raises the possibility that the gradual accumulation of iodide in surface waters over the summer and fall is a consequence of vertical (diapycnal) mixing acting on a steadily increasing vertical gradient of iodide.

Based on the observed iodide vs oxygen correlation at 60 m (Figure 8B) and assuming this applies to the vertical concentration profile of iodide, we have used continuous CTD profiles of oxygen to reconstruct vertical iodide profiles over the stratified period (not shown). Based on this, we estimate that the vertical gradient of iodide (below the sill depth of 20 m) increased from ca. 1 nmol L^{-1} m^{-1} in early summer (April) to ca. 4 nmol L^{-1} m^{-1} in Fall (October). Assuming a constant vertical eddy diffusivity, this implies that the upward flux of iodide into the surface layer increases by a factor of 4 over the summer and fall. It is therefore possible that the gradual, seasonal accumulation of iodide in surface waters over the summer and fall is not due only to *in-situ* formation within the surface layer as commonly assumed, but rather reflects a steadily increasing upward flux associated with more rapid iodide accumulation in subsurface waters due to shallow remineralization.

Further modelling of iodide distributions, including the effect of tidal exchanges with shelf waters through "the Narrows", would be required to evaluate this contribution to the surface water iodide budget more quantitatively. However, the conceptual picture of iodine cycling emerging from the time-series in a high productivity, coastal basin, has some differences from the generally assumed view which generally considers mixing with subsurface waters as a sink for iodide produced in the surface layer. For example, based on this perspective, the computational scheme used in the first global-scale model of iodine cycling (Wadley et al., 2020) has iodide produced exclusively in the euphotic zone in connection with primary productivity, with convective mixing in winter representing a loss for surface-produced iodide. No account is taken of the potential for iodate reduction in subsurface waters with less oxygen, and where remineralization of organic matter takes place. Significantly, the model invokes a loss for iodide due to oxidation via nitrification (ammonium oxidation) that controls iodide levels in the surface layer.

Our results, on the other hand, show that iodide accumulates in surface waters when nutrient concentrations are low, but that iodide is produced to a much greater extent in waters immediately beneath the euphotic zone, including via reduction of iodate at oxygen levels that are well above zero. The accumulation of iodide in the

subsurface, dark waters was also contributed to by external inputs such as release of iodide from sinking organic matter or from sediments. In Bedford Basin, deepening of the mixed-layer therefore represents a source of iodide to the surface layer rather than a sink, as assumed in the model formulation of Wadley et al. (2020).

While we are not claiming that the processes involved in cycling of iodine in Bedford Basin are the same as those affecting broad regions of the open ocean, we suggest that given the paucity of time-series, globally, additional mechanisms should be considered and evaluated. We therefore examine the global relation of surface iodide to subsurface oxygen in section (4.4) below.

A further key uncertainty relates to the processes and timescales of iodide oxidation. Chemical oxidation kinetics are slow (Luther et al., 1995), so oxidation and loss of iodide via a biologically-mediated mechanism has been suggested as a sink for iodide. One suggestion is that the oxidation of iodide is connected with ammonium oxidation during nitrification. Hughes et al. (2021) demonstrated that ammonium oxidising bacteria can mediate iodide oxidation to iodate during culture incubations with added excess iodide. Wadley et al. (2020) built this process into their global model of iodine cycling where surface layer nitrification played a key role as a "fast" sink for iodide, especially in sub-tropical waters. They noted, however, that there were trade-offs between their choice of I:C ratios and oxidation timescales and/or mechanisms, in terms of goodness of fit of modelled and observed iodide concentrations in surface waters at the global scale.

Bedford Basin has notably high and variable rates of nitrification in subsurface waters as seen in the accumulation of nitrate shown in Figure 9. Haas et al. (2021) has shown that the activity and growth of ammonia oxidisers is significant but varies interannually depending on the intensity of wintertime mixing. Nevertheless, very large concentrations of ammonium are oxidised seasonally as evidenced by the seasonal appearance of nitrate (see Figure 9B).

In our time-series data (Figure 9 and Supplementary Material Figure S2), nitrification is correlated with the reduction of iodate rather the oxidation of iodide, which appears to contradict the finding from studies with microbial cultures that ammonia oxidation is a sink for iodide (Hughes et al., 2021). However, despite the correlation, our results should not be taken to imply that nitrification is responsible for the increase of iodide. It is possible that both iodate reduction and iodide oxidation can be mediated by ammonia oxidizers or that the effect of oxidation via nitrification is masked by even stronger reduction of iodate that occurs simultaneously in the subsurface waters of Bedford Basin.

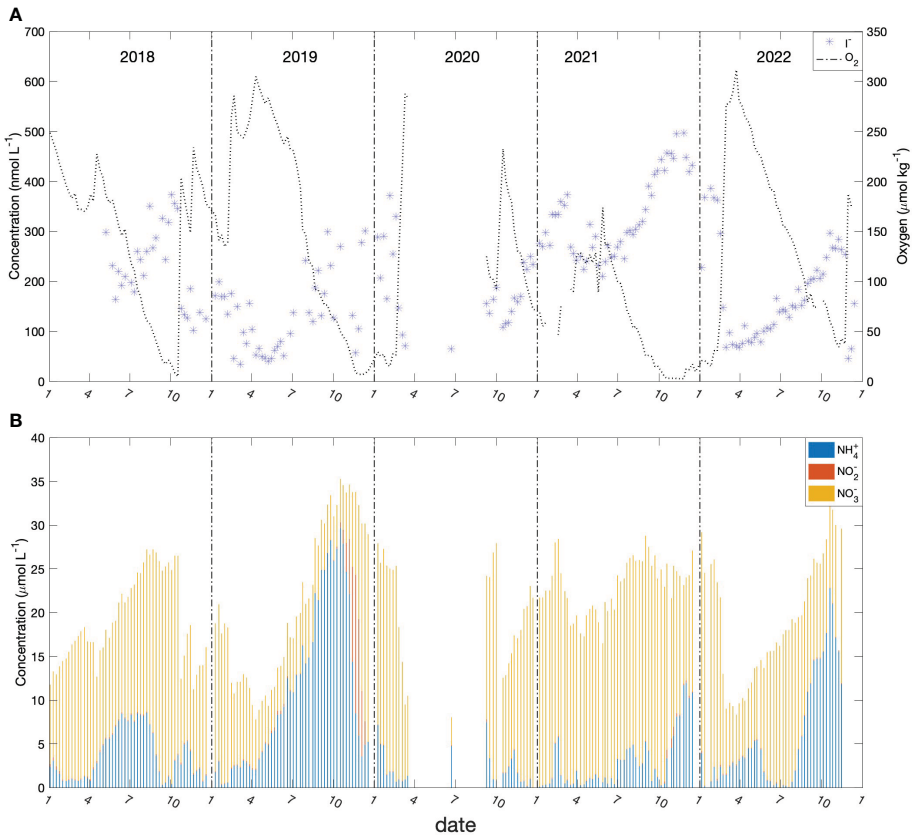

FIGURE 9
Time series of biogeochemical observations at 60m depth in BB from 2018 to 2022. **(A)** iodide (blue stars) and oxygen (dash line); **(B)** NH_4^+ (blue bar); NO_2^- (red bar) and NO_3^- (yellow bar).

4.4 Empirical parameterizations of surface iodide: role of subsurface oxygen

We showed in section 4.1 that the current empirical relationships used to predict surface iodide concentrations do not capture the levels and variability of iodide observed in surface waters of Bedford Basin. The Bedford Basin data point to a strong source of iodide immediately below the euphotic zone that might impact surface water levels via upward vertical/diapycnal mixing. Given this, we examined the global database of surface iodide levels from the open ocean (as compiled by Chance et al., 2019) and compared near surface iodide concentrations with subsurface concentrations of oxygen at 100 m depth (referred to here as [O_2]@100m) that were extracted for the same locations as the iodide data from the World Ocean Atlas (https://www.ncei.noaa.gov/access/world-ocean-atlas-2018f/bin/woa18oxnuf.pl?parameter=o). The relationship is shown in Figures 10A, B. The overall data set is noisy, and data density is variable, both geographically and in relation to subsurface oxygen concentrations. We therefore smoothed the relationship using a LOESS fit (Figure 10A) to illustrate the general relationship and binned the data into 25 µmol kg^{-1} intervals for the box-whisker plot shown in Figure 10B.

Although the choice of parameters for the LOESS fit is subjective, it is notable that all very high surface iodide concentrations in the dataset are from regions where [O_2]@100m<25 µmol kg^{-1} and the lowest surface iodide concentrations are found where [O_2]@100m is high. A regression between surface iodide and [O_2]@100m is highly significant for the subset of data with O_2@100m< 100 µmol kg^{-1}. However there is notable scatter in the relationship in the range 160< [O_2]@100 m< 240. Much of these data are from the eastern tropical Pacific (coloured symbols) and were excluded when calculating the LOESS fit. These data were collected from a cruise which focussed on sampling upper ocean waters that are strongly impacted by the "shelf to basin shuttle" of reduced species (Severmann et al., 2008; Evans et al., 2020). These waters have been advected offshore from continental shelves with very low oxygen concentrations which are also impacted by sediment-water exchange of reduced species. These surface waters have been shown to have chemical characteristics (e.g., distributions of longer-lived, reduced species) that reflect their low-oxygen origins even if gas exchange has subsequently replenished the oxygen levels. In other words, in some regions, the concentrations of long-lived reduced species such as iodide are under kinetic control, allowing for advection far from the locations and conditions where they are formed (Hawco et al., 2016; Cutter et al., 2018).

The formulation of a new empirical parameterization for surface iodide is well beyond the scope of this paper; however, the overall relationship with subsurface oxygen shown in Figure 10 suggests that subsurface oxygen levels and/or the oxygen history of surface water might be a useful predictor of near-surface iodide, both temporally (as in Bedford Basin) and globally. In general, our results are consistent with the use of iodine-to-calcium ratios (I/Ca) in shallow carbonates as a proxy of seawater redox conditions throughout Earth history (Lu et al., 2010; Hardisty et al., 2014). The underlying mechanistic bases for an empirical relationship with oxygen exist, however, the non-local role of the "shelf-to-basin shuttle" will need to be considered explicitly in some regions. Further quantitative studies, including measurements made deliberately across gradients of subsurface oxygen, and including use of biogeochemical modelling, will be required to develop this hypothesis further.

5 Conclusions and next steps

We have presented a description of an unusually long (4.5 year), highly-resolved (weekly) time-series of inorganic iodine speciation from a seasonally hypoxic coastal fjord. The data revealed strong inverse correlations of both iodide (I^-) and total dissolved iodine (TDI= [I^-]+ [IO_3^-]+[DOI]) with dissolved oxygen in subsurface waters of the fjord (i.e., at 60 m). Our limited characterization of DOI is that its concentration remained relatively low (mean of 37 nmol L^{-1}) and did not vary greatly over the year. The observed relationships suggest that there is a seasonal cycle of subsurface TDI driven by external sources such as remineralization of sinking

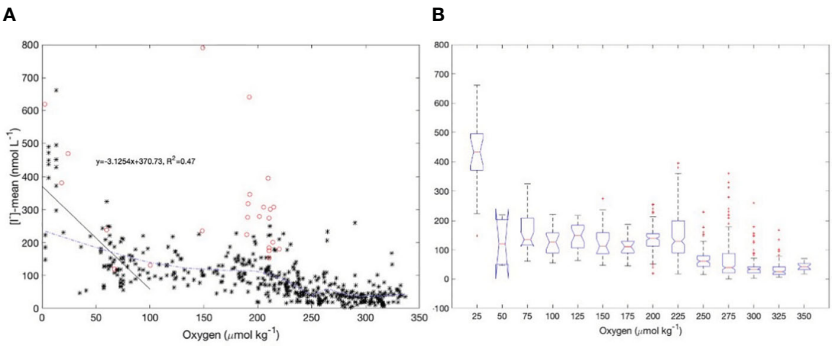

FIGURE 10
(A) LOESS fit (blue dashed line) of the global database of surface iodide levels (Chance et al., 2019) from the open ocean and subsurface oxygen concentrations (at 100 m depth) that were extracted for the same locations from the World Ocean Atlas. Data reported by Cutter et al. (2018) from the eastern Pacific (red circles) were excluded from the fit. A linear regression (black solid line) was calculated for data where the subsurface oxygen concentrations were less than 100 µmol kg^{-1}; **(B)** box-whisker plot between surface iodide levels and subsurface oxygen concentrations using the same data set. The bin size is 25 µmol kg^{-1} in oxygen concentration.

organic particles and/or releases from the sediment. There is also clear seasonality of subsurface iodide, with roughly 50% of the iodide increase originating from *in-situ* reduction of iodate in the water column (apparently at all oxygen levels) and the remainder added via external sources such as from sinking particles and/or sediment-water exchange.

The near-surface iodide concentrations were relatively low throughout the year but showed a weak build-up (from 70 nmol L^{-1} to 150 nmol L^{-1}) over summer and through late fall. The magnitude and temporal variability of the iodide concentration in surface waters was not well-predicted by current empirical parameterizations that have been developed on the basis of surface iodide measurements on a global scale.

The key features observed in the time-series data are also not, necessarily, consistent with mechanisms, parameterizations and assumptions that form the basis of an initial mechanistic model used to predict surface iodide on a global scale. Notably, the subsurface ocean appears to act as a source rather than a sink for surface iodide, and nitrification in subsurface waters was positively correlated with the reduction of iodate to iodide, even though studies with microbial cultures have shown that nitrification (ammonia oxidation) acts as a sink for iodide.

Based on qualitative examination of the time-series, we hypothesis that the seasonal build-up of iodide in surface waters is at least partly a consequence of seasonal production of iodide in sub-surface waters, coupled with vertical mixing. Examination of the global surface ocean data set for iodide, suggests there is an overall relationship between oxygen concentrations underlying the surface layer and iodide concentrations in surface water which may be consistent with this process and might contribute to future parameterizations and/or model representations of iodine cycling.

Overall, the time-series study in Bedford Basin shows again the power and potential of multi-disciplinary time-series for revealing complex mechanisms and testing hypotheses concerning the physical-biogeochemical interactions responsible for element speciation in the ocean. Next steps are to conduct experimental studies and manipulations to test hypothesised mechanisms of iodine cycling (including better characterization of sediment-water exchange) in the context of the time-series and to examine iodine cycling, quantitatively, using models.

Data availability statement

The original contributions presented in the study are included in the article/Supplementary Material. Further inquiries can be directed to the corresponding authors.

Author contributions

QS and DW conceptualized the study. QS analyzed the samples with guidance of JK. QS and DW wrote the manuscript. DW and JK contributed to detailed discussions. All authors contributed to the article and approved the submitted version.

Acknowledgments

This work was funded by the Canada Excellence Research Chair in Ocean Science and Technology at Dalhousie University, a Seed Fund of the Ocean Frontier Institute, and the MEOPAR Network of Centres of Excellence. Sampling of the Bedford Basin time-series was supported by MEOPAR's Observation Core, Bedford Basin Monitoring Program (BBMP) and Department of Fisheries and Ocean, Canada (DFO). The authors thank Richard Davies, Magdalena Walclawik and the crew of the Sigma-T for assistance with sampling and logistics. The assistance and guidance in the laboratory from Claire Normandeau, Anadiuska Rondon Vivas and Erin Keltie is also acknowledged. We thank Subhadeep Rakshit for conducting the core incubations and for discussions.

Conflict of interest

The authors declare that the research was conducted in the absence of any commercial or financial relationships that could be construed as a potential conflict of interest.

Publisher's note

All claims expressed in this article are solely those of the authors and do not necessarily represent those of their affiliated organizations, or those of the publisher, the editors and the reviewers. Any product that may be evaluated in this article, or claim that may be made by its manufacturer, is not guaranteed or endorsed by the publisher.

Supplementary material

The Supplementary Material for this article can be found online at: https://www.frontiersin.org/articles/10.3389/fmars.2023.1171999/full#supplementary-material

References

Bluhm, K., Croot, P., Wuttig, K., and Lochte, K. (2010). Transformation of iodate to iodide in marine phytoplankton driven by cell senescence. *Aquat. Biol.* 11 (1), 1–15. doi: 10.3354/ab00284

Brandao, A. C. (2001). *Iodine Distribution in the Australian Sector of the Southern Ocean and Its Relation to New Production and Water Masses* (Thesis, University of Tasmania).

Campos, M. (1997). New approach to evaluating dissolved iodine speciation in natural waters using cathodic stripping voltammetry and a storage study for preserving iodine species. *Mar. Chem.* 57 (1–2), 107–117. doi: 10.1016/S0304-4203(96)00093-X

Campos, M., Farrenkopf, A. M., Jickells, T. D., and Luther, G. W. (1996). A comparison of dissolved iodine cycling at the Bermuda Atlantic time-series station

and Hawaii ocean time-series station. *Deep Sea Res. Part II: Topical Stud. Oceanogr.* 43 (2–3), 455–466. doi: 10.1016/0967-0645(95)00100-X

Campos, M. L. A. M., Sanders, R., and Jickells, T. (1999). The Dissolved Iodate and Iodide Distribution in the South Atlantic from the Weddell Sea to Brazil. *Mar. Chem.* (65), 167–175. doi: 10.1016/S0304-4203(98)00094-2

Carpenter, L. J., Chance, R. J., Sherwen, T., Adams, T. J., Ball, S. M., Evans, M. J., et al. (2021). Marine iodine emissions in a changing world, proceedings of the royal society a: mathematical. *Phys. Eng. Sci.* A 477 (20200824). doi: 10.1098/rspa.2020.0824

Carpenter, L. J., MacDonald, S. M., Shaw, M. D., Kumar, R., Saunders, R. W., Parthipan, R., et al. (2013). Atmospheric iodine levels influenced by sea surface emissions of inorganic iodine. *Nat. Geosci.* 6 (2), 108–111. doi: 10.1038/ngeo1687

Casacuberta, N., Christl, M., Vockenhuber, C., Wefing, A. M., Wacker, L., Masqué, P., et al. (2018). Tracing the three Atlantic branches entering the Arctic ocean with 129I and 236U. *J. Geophys. Res.: Oceans* 123 (9), 6909–6921. doi: 10.1029/2018JC014168

Chance, R., Baker, A. R., Carpenter, L., and Jickells, T. D. (2014). The distribution of iodide at the sea surface. *Environ. Sci.: Processes Impacts* 16 (8), 1841–1859. doi: 10.1039/c4em00139g

Chance, R. J., Tinel, L., Sherwen, T., Baker, A. R., Bell, T., Brindle, J., et al. (2019). Global sea-surface iodide observations 1967-2018. *Sci. Data* 6 (1), 286. doi: 10.1038/s41597-019-0288-y

Chance, R., Weston, K., Baker, A. R., Hughes, C., Malin, G., Carpenter, L., et al. (2010). Seasonal and interannual variation of dissolved iodine speciation at a coastal Antarctic site. *Mar. Chem.* 118 (3–4), 171–181. doi: 10.1016/j.marchem.2009.11.009

Cutter, G. A., Moffett, J. G., Nielsdóttir, M. C., and Sanial, V. (2018). Multiple oxidation state trace elements in suboxic waters off Peru: *In situ* redox processes and advective/diffusive horizontal transport. *Mar. Chem.* 201 (March 2017), 77–89. doi: 10.1016/j.marchem.2018.01.003

Davis, D., Crawford, J., Liu, S., McKeen, S., Bandy, A., Thornton, D., et al. (1996). Potential impact of iodine on tropospheric levels of ozone and other critical oxidants. *J. Geophys. Res.: Atmospheres* 101 (D1), 2135–2147. doi: 10.1029/95JD02727

Elderfield, H., and Truesdale, V. W. (1980). On the biophilic nature of iodine in seawater. *Earth Planet. Sci. Lett.* 50 (1), 105–114. doi: 10.1016/0012-821X(80)90122-3

Evans, N., Boles, E., Kwiecinski, J. V., Mullen, S., Wolf, M., Devol, A. H., et al. (2020). The role of water masses in shaping the distribution of redox active compounds in the Eastern tropical north pacific oxygen deficient zone and influencing low oxygen concentrations in the eastern pacific ocean. *Limnol. Oceanogr.* 65 (8), 1688–1705. doi: 10.1002/lno.11412

Farrenkopf, A. M., Luther, G. W., Truesdale, V. W., and van der Weijden, C. H. (1997). Sub-Surface iodide maxima: evidence for biologically catalyzed redox cycling in Arabian Sea OMZ during the SW intermonsoon. *Deep Sea Res. Part II: Topical Stud. Oceanogr.* 44 (6–7), 1391–1409. doi: 10.1016/S0967-0645(97)00013-1

Ganzeveld, L., Helmig, D., Fairall, C. W., Hare, J., and Pozzer, A. (2009). Atmosphere-ocean ozone exchange: a global modeling study of biogeochemical, atmospheric, and waterside turbulence dependencies. *Global Biogeochem. Cycles* 23 (4), 1–16. doi: 10.1029/2008GB003301

Haas, S., Robicheau, B. M., Rakshit, S., Tolman, J., Algar, C. K., LaRoche, J., et al. (2021). Physical mixing controls and decouples nitrification via biomass dilution. *Proc. Natl. Acad. Sci.* 118 (18), e2004877118 doi: 10.1073/pnas.2004877118

Hardisty, D. S., Lu, Z., Planavsky, N. J, Bekker, A., Philippot, P., and Zhou, X. (2014). An Iodine Record of Paleoproterozoic Surface Ocean Oxygenation. *Geology* 42 (7), 619–22.

Hatch-mcchesney, A., and Lieberman, H. R. (2022).). iodine and iodine Deficiency: a comprehensive review of a re-emerging issue. *Nutrients* 14 (17). doi: 10.3390/nu14173474

Hawco, N. J., Ohnemus, D. C., Resing, J. A., Twining, B. S., and Saito, M. A. (2016). A dissolved cobalt plume in the oxygen minimum zone of the eastern tropical south pacific. *Biogeosciences* 13 (20), 5697–5717. doi: 10.5194/bg-13-5697-2016

Hughes, C., Barton, E., Hepach, H., Chance, R., Pickering, M. D., Hogg, K., et al. (2021). Oxidation of iodide to iodate by cultures of marine ammonia-oxidising bacteria. *Mar. Chem.* 234 (June). doi: 10.1016/j.marchem.2021.104000

Hung, C. C., Wong, G. T. F., and Dunstan, W. M. (2005). Iodate reduction activity in nitrate reductase extracts from marine phytoplankton. *Bull. Mar. Sci.* 76 (1), 61–72.

Jones, M. R., Chance, R., Dadic, R., Hannula, H. R., May, R., Ward, M., et al. (2023). Environmental iodine speciation quantification in seawater and snow using ion exchange chromatography and UV spectrophotometric detection. *Anal. Chimica Acta* 1239 (November 2022), 340700. doi: 10.1016/j.aca.2022.340700

Kawamura, H., Kobayashi, T., Furuno, A., In, T., Ishikawa, Y., Nakayama, T., et al. (2011). Preliminary numerical experiments on oceanic dispersion of 131 I and 137 Cs discharged into the ocean because of the fukushima daiichi nuclear power plant disaster. *J. Nucl. Sci. Technol.* 48 (11), 1349–1356. doi: 10.1080/18811248.2011.9711826

Li, W. K. W. (1998). Annual average abundance of heterotrophic bacteria and *Synechococcus* in surface ocean waters. *Limnol. Oceanogr.* 43 (7), 1746–1753. doi: 10.4319/lo.1998.43.7.1746

Lu, Z., Jenkyns, H. C., and Rickaby, R. E. M. (2010). Iodine to calcium ratios in marine carbonate as a paleo-redox proxy during oceanic anoxic events. *Geology* 38 (12), 1107–1110. doi: 10.1130/G31145.1

Luther, G. W., Wu, J., and Cullen, J. B. (1995). Redox chemistry of iodine in seawater: frontier molecular orbital theory considerations. *Aquat. Chem.* 135–155. doi: 10.1021/ba-1995-0244.ch006

Macdonald, S. M., Gómez Martín, J. C., Chance, R., Warriner, S., Saiz-Lopez, A., Carpenter, L. J., et al. (2014). A laboratory characterisation of inorganic iodine emissions from the sea surface: dependence on oceanic variables and parameterisation for global modelling. *Atmospheric. Chem. Phys.* 14 (11), 5841–5852. doi: 10.5194/acp-14-5841-2014

McFiggans, G., Plane, J., Allan, B. J., Carpenter, L. J., Coe, H., and O'Dowd, C. (2000). A modeling study of iodine chemistry in the marine boundary layer. *J. Geophys. Res.: Atmospheres* 105 (D11), 14371–14385. doi: 10.1029/1999JD901187

Moriyasu, R., Evans, Z. C., Bolster, K. M., Hardisty, D. S., and Moffett, J. W. (2020). The distribution and redox speciation of iodine in the Eastern tropical north pacific ocean. *Global Biogeochem. Cycles* 34 (2), 1–23. doi: 10.1029/2019gb006302

Raisbeck, G. M., and Yiou, F. (1999). 129I in the oceans: origins and applications. *Sci. Total Environ.* 237–238, 31–41. doi: 10.1016/S0048-9697(99)00122-9

Rakshit, S., Dale, A. W., Wallace, D. W., and Algar, C. K. (2023). Sources and sinks of bottom water oxygen in a seasonally hypoxic fjord. *Front. Mar. Sci.* 10, 1148091. doi: 10.3389/fmars.2023.1148091

Reyes-Umana, V., Henning, Z., Lee, K., Barnum, T. P., and Coates, J. D. (2022). Genetic and phylogenetic analysis of dissimilatory iodate-reducing bacteria identifies potential niches across the world's oceans. *ISME J.* 16 (1), 38–49. doi: 10.1038/s41396-021-01034-5

Robinson, C. (2019). Microbial respiration, the engine of ocean deoxygenation. *Front. Mar. Sci.* 5 (JAN). doi: 10.3389/fmars.2018.00533

Saiz-Lopez, A., and Von Glasow, R. (2012). Reactive halogen chemistry in the troposphere. *Chem. Soc. Rev.* 41 (19), 6448. doi: 10.1039/c2cs35208g

Sanz Rodriguez, E., Setiawan, A. N., Pope, S., Haddad, P. R., Nesterenko, P. N., and Paull, B. (2016). A simple and sensitive method for the determination of iodide and iodate in raw, ultraviolet- and ozone-treated aquacultural seawater samples using ion chromatography coupled to an ultraviolet detector. *Anal. Methods* 8 (28), 5587–5595. doi: 10.1039/c6ay01381c

Severmann, S., Lyons, T. W., Anbar, A., McManus, J., and Gordon, G. (2008). Modern iron isotope perspective on the benthic iron shuttle and the redox evolution of ancient oceans. *Geology* 36 (6), 487–490. doi: 10.1130/G24670A.1

Sherwen, T., Chance, R. J., Tinel, L., Ellis, D., Evans, M. J., and Carpenter, L. J. (2019). A machine-learning-based global sea-surface iodide distribution. *Earth Syst. Sci. Data* 11 (3), 1239–1262. doi: 10.5194/essd-11-1239-2019

Shi, Q., Petrick, G., Quack, B., Marandino, C., and Wallace, D. W. R. (2014). A time series of incubation experiments to examine the production and loss of CH3I in surface seawater. *J. Geophys. Res. Oceans* 2, 1022–1037. doi: 10.1002/2013JC009415

Shi, Q., and Wallace, D. (2018). A 3-year time series of volatile organic iodocarbons in Bedford basin, Nova Scotia: a northwestern Atlantic fjord. *Ocean Sci.* 14 (6), 1385–1403. doi: 10.5194/os-14-1385-2018

Strickland, J. D. H., and Parsons, T. R. (1972). *The journal of higher education: A practical handbook of seawater analysis*. Canada:Fisheries research board of Canada Ottawa.

Tegtmeier, S., Krüger, K., Quack, B., Atlas, E., Blake, D. R., Boenisch, H., et al. (2013). The contribution of oceanic methyl iodide to stratospheric iodine. *Atmospheric Chem. Phys.* 13 (23), 11869–11886. doi: 10.5194/acp-13-11869-2013

Truesdale, V. W. (1994). Distribution of dissolved iodine in the Irish Sea, a temperate shelf Sea, estuarine. *Coast. Shelf Sci.* 38 (5), 435–446. doi: 10.1006/ecss.1994.1030

Truesdale, V. W. (1995). The distribution of dissolved iodine in hebridean waters during mid-winter. *Mar. Environ. Res.* 40 (3), 277–288. doi: 10.1016/0141-1136(94)00147-H

Truesdale, V. W., Nausch, G., and Baker, A. (2001).). the distribution of iodine in the Baltic Sea during summer. *Mar. Chem.* 74 (2–3), 87–98. doi: 10.1016/S0304-4203(00)00115-8

Ullman, W. J., and Aller, R. C. (1980). Dissolved iodine flux from estuarine sediments and implications for the enrichment of iodine at the sediment water interface. *Geochimica Cosmochimica Acta* 44 (8), 1177–1184. doi: 10.1016/0016-7037(80)90071-X

Wadley, M. R., Stevens, D. P., Jickells, T. D., Hughes, C., Chance, R., Hepach, H., et al. (2020). A global model for iodine speciation in the upper ocean. *Global Biogeochem. Cycles* 34 (9). doi: 10.1029/2019GB006467

Waite, T. J., and Truesdale, V. W. (2003). Iodate reduction by isochrysis galbana is relatively insensitive to de-activation of nitrate reductase activity - are phytoplankton really responsible for iodate reduction in seawater? *Mar. Chem.* 81 (3–4), 137–148. doi: 10.1016/S0304-4203(03)00013-6

Wefing, A. M., Casacuberta, N., Christl, M., Gruber, N., and Smith, J. N. (2021). Circulation timescales of Atlantic water in the Arctic ocean determined from anthropogenic radionuclides. *Ocean Sci.* 17 (1), 111–129. doi: 10.5194/os-17-111-2021

Wefing, A. M., Christl, M., Vockenhuber, C., Rutgers van der Loeff, M., and Casacuberta, N. (2019). Tracing Atlantic waters using 129 I and 236 U in the fram

strait in 2016. *J. Geophys. Res.: Oceans* 124 (2), 882–896. doi: 10.1029/2018JC014399

Witt, E. M., Laidley, C. W., Liu, K. K. M., Hirano, T., and Grau, E. G. (2009). Correlation between environmental iodide concentrations and larval growth, survival, and whole body concentrations of thyroid hormones and cortisol in pacific threadfin (Polydactylus sexfilis). *Aquaculture* 289 (3–4), 357–364. doi: 10.1016/j.aquaculture.2009.01.024

Wong, G. T. F., and Cheng, X. H. (1998). Dissolved organic iodine in marine waters: determination, occurrence and analytical implications. *Mar. Chem.* 59 (3–4), 271–281. doi: 10.1016/S0304-4203(97)00078-9

frontiers | Frontiers in Marine Science

TYPE Original Research
PUBLISHED 07 November 2023
DOI 10.3389/fmars.2023.1264380

Check for updates

OPEN ACCESS

EDITED BY
Alex J. Poulton,
Heriot-Watt University, United Kingdom

REVIEWED BY
Zunli Lu,
Syracuse University, United States
George W. Luther,
University of Delaware, United States

*CORRESPONDENCE
Yun-Ju Sun
yj.sun@bristol.ac.uk

RECEIVED 20 July 2023
ACCEPTED 18 October 2023
PUBLISHED 07 November 2023

CITATION
Sun Y-J, Robinson LF, Parkinson IJ, Stewart JA, Lu W, Hardisty DS, Liu Q, Kershaw J, LaVigne M and Horner TJ (2023) Iodine-to-calcium ratios in deep-sea scleractinian and bamboo corals. *Front. Mar. Sci.* 10:1264380. doi: 10.3389/fmars.2023.1264380

COPYRIGHT
© 2023 Sun, Robinson, Parkinson, Stewart, Lu, Hardisty, Liu, Kershaw, LaVigne and Horner. This is an open-access article distributed under the terms of the Creative Commons Attribution License (CC BY). The use, distribution or reproduction in other forums is permitted, provided the original author(s) and the copyright owner(s) are credited and that the original publication in this journal is cited, in accordance with accepted academic practice. No use, distribution or reproduction is permitted which does not comply with these terms.

Iodine-to-calcium ratios in deep-sea scleractinian and bamboo corals

Yun-Ju Sun[1*], Laura F. Robinson[1,2], Ian J. Parkinson[1], Joseph A. Stewart[1], Wanyi Lu[3], Dalton S. Hardisty[4], Qian Liu[1], James Kershaw[1], Michèle LaVigne[5] and Tristan J. Horner[6]

[1]School of Earth Sciences, University of Bristol, Bristol, United Kingdom, [2]Department of Environment and Geography, University of York, York, United Kingdom, [3]Department of Geology and Geophysics, Woods Hole Oceanographic Institution, Woods Hole, MA, United States, [4]Department of Earth and Environmental Sciences, Michigan State University, East Lansing, MI, United States, [5]Department of Earth and Oceanographic Science, Bowdoin College, Brunswick, ME, United States, [6]Department of Marine Chemistry and Geochemistry, Woods Hole Oceanographic Institution, Woods Hole, MA, United States

The distribution of dissolved iodine in seawater is sensitive to multiple biogeochemical cycles, including those of nitrogen and oxygen. The iodine-to-calcium ratio (I/Ca) of marine carbonates, such as bulk carbonate or foraminifera, has emerged as a potential proxy for changes in past seawater oxygenation. However, the utility of the I/Ca proxy in deep-sea corals, natural archives of seawater chemistry with wide spatial coverage and radiometric dating potential, remains unexplored. Here, we present the first I/Ca data obtained from modern deep-sea corals, specifically scleractinian and bamboo corals, collected from the Atlantic, Eastern Pacific, and Southern Oceans, encompassing a wide range of seawater oxygen concentrations (10–280 μmol/kg). In contrast to thermodynamic predictions, we observe higher I/Ca ratios in aragonitic corals (scleractinian) compared to calcitic corals (bamboo). This observation suggests a strong biological control during iodate incorporation into deep-sea coral skeletons. For the majority of scleractinian corals, I/Ca exhibits a covariation with local seawater iodate concentrations, which is closely related to seawater oxygen content. Scleractinian corals also exhibit notably lower I/Ca below a seawater oxygen threshold of approximately 160 μmol/kg. In contrast, no significant differences in I/Ca are found among bamboo corals across the range of oxygen concentrations encountered (15–240 μmol/kg). In the North Atlantic, several hydrographic factors, such as temperature and/or salinity, may additionally affect coral I/Ca. Our results highlight the potential of I/Ca ratios in deep-sea scleractinian corals to serve as an indicator of past seawater iodate concentrations, providing valuable insights into historical seawater oxygen levels.

KEYWORDS

biogenic carbonate, iodate incorporation, seawater oxygenation proxy, dissolved oxygen, marine redox state

1 Introduction

Iodine, a biophilic element, circulates between the hydrosphere, atmosphere, and biosphere and plays important roles in Earth's biogeochemical cycles (Carpenter et al., 2021). For example, the ocean is the dominant source of iodine to the atmosphere and the predominant sink for the tropospheric ozone (Carpenter et al., 2013). Because iodine is a redox-sensitive element, its speciation and distribution in the ocean has been linked to primary productivity (Farrenkopf and Luther, 2002), benthic processes (Cutter et al., 2018; Moriyasu et al., 2020), and ocean oxygenation (Lu et al., 2020c). Therefore, understanding the behavior of marine iodine provides insights into both biogeochemical processes and ocean circulation.

In the ocean, iodine has two stable inorganic species, iodate (IO_3^-, the oxidized form) and iodide (I^-, the reduced form). The reduction of the iodate to iodide is related to dissolved oxygen content and has a similar redox potential and Gibbs free energy to that of the nitrate–nitrite redox couple (Figure 1; Farrenkopf et al., 1997; Rue et al., 1997; Luther, 2023). The concentration of total inorganic iodine in the ocean is generally conservative (450 to 500 nM; Chance et al., 2014) with a long residence time (~300 thousand years; Broecker and Peng, 1982). Seawater iodine speciation is primarily controlled by two processes: *in situ* redox reactions (Rue et al., 1997) and regional water-mass mixing (Evans et al., 2020; Hardisty et al., 2021). *In situ* transformation refers to the processes of iodate reduction to iodide in anoxic conditions and iodide re-oxidation to iodate in oxic waters. Under oxic conditions, iodate is the dominant species in the water column (Truesdale et al., 2000). Elevated iodide and low iodate are observed in low oxygen regions, such as oxygen minimum zones (OMZs) and deep anoxic basins (Wong and Brewer, 1977; Cutter et al., 2018; Rapp et al., 2020). The asymmetric reaction rates of iodide oxidation and iodate reduction complicate the relationship between iodine and oxygen, decoupling the relative concentrations in the subsurface ocean (Hardisty et al., 2021). In addition, mixing of water masses with different iodate concentrations from adjacent regions influences the seawater iodate concentration. For example, relatively slow reduction rates and elevated offshore I^- concentrations are found in areas like the Eastern Tropical North Pacific (Hardisty et al., 2021), and excess I^- concentrations can also come from sedimentary inputs (Farrenkopf and Luther, 2002; Cutter et al., 2018; Moriyasu et al., 2020; Moriyasu et al., 2023).

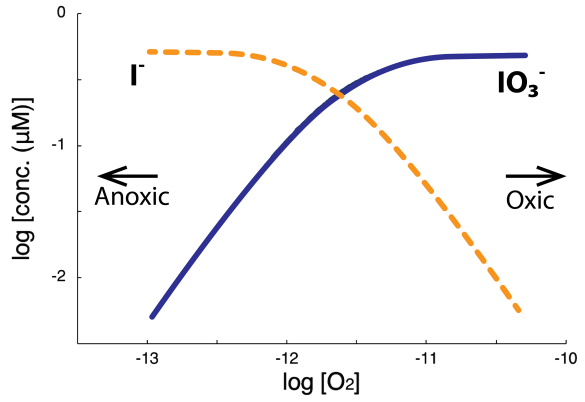

FIGURE 1
Iodine speciation against oxygen concentration constrained by the reaction $IO_3^- \leftrightarrow I^- + \frac{3}{2}O_{2\,(aq)}$ with standard hydrogen electrode potential E^0 = -0.144V at 1 atm and 298 K (Haynes, 2014) with Henry's law constant = 1.3×10^{-3} (mole/L/atm). This calculation assumes ideal solution behaviour and a total iodine concentration of 0.5 μM. The equilibrium constant (K) of the above reaction can be equated with concentration through $K = \frac{[I^-][O_2]^{3/2}}{[IO_3^-]} = e^{\frac{-\Delta G}{RT}}$, where $[I^-]$, $[IO_3^-]$, and $[O_2]$ represents the dissolved concentration of iodide, iodate, and oxygen, respectively. ΔG is the Gibbs free energy of the above reaction and is equated with the standard electrode potential via $\Delta G = -zFE^0$, where z is the number of electrons transferred (z = 6 in this case) and F is the Faraday constant.

Building on field observations, the iodine-to-calcium ratio (I/Ca) in marine carbonates can potentially record the redox state in seawater, with higher carbonate I/Ca assumed to record higher IO_3^- and therefore higher oxygen concentrations in seawater. This potential is based on the premise that iodate is the only species of iodine incorporated into carbonate (Lu et al., 2010); indeed, computational simulations have confirmed that iodate substitutes for the carbonate ion in the lattice (Podder et al., 2017; Kerisit et al., 2018). The theory that iodate is the sole species of iodine incorporated into carbonates has also been demonstrated experimentally for calcite (Zhou et al., 2014) and dolomite (Hashim et al., 2022). Hence, both marine carbonates have been applied to study oxygenation across different timescales throughout Earth's history (Lu et al., 2020c). Moreover, as iodate reduction does not occur before the dissolved oxygen is depleted to a threshold of ~11 μmol/kg (Hardisty et al., 2021), the I/Ca proxy can serve as a semi-quantitative proxy that puts qualitative constraints on oxygen concentration. Based on globally distributed core-top planktic foraminiferal samples, a threshold I/Ca value (~2.5 μmol/mol) was proposed to indicate hypoxic O_2 conditions (~70 to 100 μmol/kg) in the upper water column (Lu et al., 2020b; Lu et al., 2016). Furthermore, data from benthic (epifaunal) foraminifera suggested that low benthic I/Ca value (<3 μmol/mol) indicated low bottom water oxygen (<50 μmol/kg) (Lu et al., 2020b). However, applying foraminiferal I/Ca as an oxygenation proxy has its limitations: planktic foraminifera migrate vertically during their living cycles thus complicating the reconstruction of *in situ* oxygen level (Lu et al., 2020a), the change of benthic microhabitat (e.g., migration to deeper sediments where a sharp oxygen gradient within the pore water occurs), and subsequent diagenetic processes (e.g., aragonite recrystallisation) could potentially influence benthic foraminiferal I/Ca values (Glock et al., 2014).

Deep-sea corals (DSCs) are valuable palaeoceanographic archives of intermediate- and deep-ocean conditions. They can be accurately and precisely dated by radiometric methods (Cheng et al., 2000), which allows for studying the leads and lags of the climate system on millennial timescales (e.g., Chen et al., 2023). Moreover, DSCs thrive across a wide geographic and bathymetric distribution range (Roberts et al., 2006) and have even been found within the hypoxic zone in Southeast Atlantic (Hebbeln et al., 2020; Orejas et al., 2021) and Northeast Pacific (Ross et al., 2020). Numerous elemental and isotopic ratios have already been developed as environmental proxies in DSCs (e.g., Li/Mg ratio,

radiocarbon, neodymium isotopes; Robinson et al., 2014) and thus DSCs are an appealing archive of iodine geochemistry. Despite this potential, there have been no systematic investigations of I/Ca in DSCs. In this study, we investigate iodine geochemistry in two modern DSC taxa: Scleractinia (aragonite-structured) and bamboo corals (calcite-structured) from across the global ocean (Atlantic Ocean, Eastern Pacific, and Southern Ocean). We examine the mechanisms of iodate incorporation into DSCs, explore the relationship between I/Ca in DSCs and ambient seawater properties, and assess the potential of I/Ca in DSCs as an oxygenation proxy.

2 Samples and methods

2.1 Deep-sea coral sample collection

We analyzed deep-sea scleractinian coral skeletons (n=63) and bamboo coral skeletons (n=13) collected from the Labrador Sea (RRS *Discovery* DY081), the Rockall Bank in the Northeast Atlantic (RRS *James Cook* JC136), the tropical North Atlantic (RRS *James Cook* JC094), the southwest Atlantic (collection from National Historical Museum, Brazil), the Drake Passage region of the Southern Ocean (R/V *Nathaniel B. Palmer* 1103), the northeast Pacific (R/V *Western Flyer* in the year 2004 and 2007), the Marquesas Islands in the central equatorial Pacific (R/V *Alis* MUSORSTOM 9; collection from National Museum of Natural History, France), and the Galápagos Archipelago (R/V *Melville* MV1007; *Alucia* AL1508; E/V *Nautilus* NA064) (Figure 2). Sample depths ranged from 60 to 2800 m. The majority of deep-sea corals in this study were collected alive with organic tissue attached using a Remotely Operated Vehicle (ROV). If live samples were not available, selected sub-fossil specimens preserved in pristine condition with radiometric ages < 50 years were used (Galápagos samples, n=3; Northeast Atlantic samples, n=4; Equatorial Atlantic samples, n=6), which can be treated as "modern" corals (dating method taken from Chen et al., 2015). The ages of the California margin's bamboo corals are adapted from radiocarbon analyses (Frenkel et al., 2017). All the corals were paired with available hydrographic data from seawater observational data (see below). Coral samples in this study are subgrouped by location, and the dominant water masses are listed in Table 1.

We grouped DSC by taxonomic order and their distinct mineralogy for further comparison. First, scleractinian coral samples include solitary genera *Balanophyllia, Caryophyllia, Desmophyllum*, and the colonial genus *Enallopsammia*. The skeletal mineralogy of these scleractinian corals is aragonite. Second, bamboo corals belong to the *Isidella* and *Keratoisis* subfamilies with high-Mg calcitic mineralogy. The full coral sample metadata are included in Supplementary Table 1.

2.2 Hydrographic data

Concentrations of seawater iodate and iodide data were taken from published sources (Wong and Brewer, 1977; Elderfield and Truesdale, 1980; Bluhm et al., 2011; Cutter et al., 2018; Moriyasu et al., 2020; Rapp et al., 2020). Station sites were selected in the closest proximity to the coral site, and the representative value was interpolated from the two closest available measurement depths. Measured seawater iodate/iodide data for the modern ocean, especially depth profiles, remain limited. As a result, some locations and deeper depths lack paired seawater values (e.g., Vayda Seamount in the Equatorial Atlantic). The time-series seawater iodine records have supported the use of single-point sources of seawater data (Campos et al., 1996). The largest published analytical precision for seawater data was 1% (RSD) (Rue et al., 1997). The uncertainty for each seawater iodate/iodide value was estimated from vertical variation between the three most proximal measurements at each coral location (± 2 SD).

The paired dissolved oxygen and hydrographic data (temperature, salinity, $[CO_3^{2-}]$, pH, concentrations of nitrate, phosphate, and silicate) for coral samples were taken from

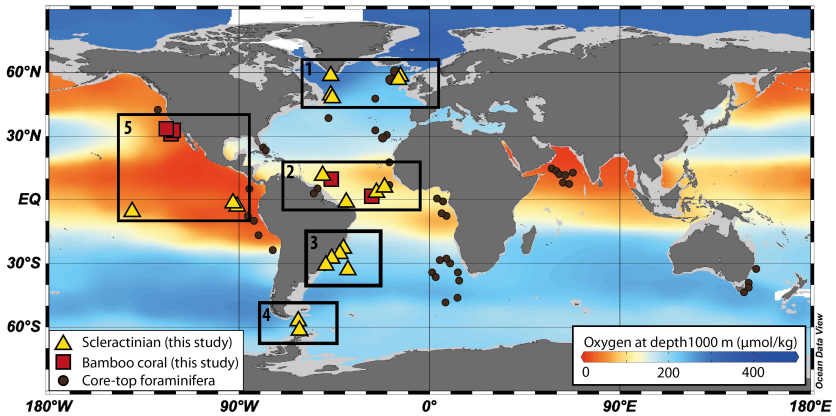

FIGURE 2
Base map illustrating the global mean distribution of oxygen concentrations from GLODAP2 database at 1000 m water depth (Lauvset et al., 2022). The deep-sea coral sample locations are marked as triangles (scleractinian corals) and squares (bamboo corals), including the North Atlantic (location 1), Tropical North Atlantic (location 2), Southwest Atlantic (location 3), Southern Ocean (Atlantic sector; location 4), Eastern Pacific (location 5). The locations of benthic foraminifera data (black dots) are from published studies (Glock et al., 2014; Lu et al., 2020b; Lu et al., 2022).

TABLE 1 Location and depth range of deep-sea coral samples in this study, along with the dominant water mass.

Location	Site	Latitude, Longitude	Coral depth range	Dominant water mass
North Atlantic	Labrador Sea	50.1°N, 45.4°W	1055-2700 m	Labrador Sea Water (LSW)[a]
	North Rockall Bank	58.9°N, 13.4°W	580-1165 m	subpolar Mode Water (SPMW)[a]
Tropical North Atlantic	Carter Seamount	9.2°N, 21.3°W	300-1080 m	Antarctic Intermediate Water (AAIW)[b]
			1260-2400 m	North Atlantic Deep Water (NADW)[b]
	Knipovich Seamount	5.6°N, 26.9°W	300-1080 m	Antarctic Intermediate Water (AAIW)[b]
			1260-2400 m	North Atlantic Deep Water (NADW)[b]
	Vayda Seamount	14.9°N, 48.2°W	1455 m	North Atlantic Deep Water (NADW)[b]
Southwest Atlantic	Rio Grande Rise	30.2°S, 36.9°W	240-950 m	Antarctic Intermediate Water (AAIW)[c]
			1050-1510 m	upper Circumpolar Deep Water (uCDW)[c]
	Brazilian continental margin	20.5-27.0°S, 38.0-47.0°W	240-950 m	Antarctic Intermediate Water (AAIW)[c]
			1050-1510 m	upper Circumpolar Deep Water (uCDW)[c]
	West Equatorial Atlantic	2.3°S, 38.3°W	240-950 m	Antarctic Intermediate Water (AAIW)[c]
			1050-1510 m	upper Circumpolar Deep Water (uCDW)[c]
Southern Ocean (Atlantic sector)	Drake Passage	54.5°S, 62.2°W	315 m	Subantarctic Mode Waters (SAMW)[d]
			1400-1900 m	Antarctic Intermediate Water (AAIW)[d]
Eastern Pacific	California Margin	33.2-37.4°N, 120.9-123.4°W	870-1500 m	Antarctic Intermediate Water (AAIW)[e]
			2055 m	Pacific Deep Water (PDW)[e]
	Marquesas Islands (Central Pacific)	7.9°S, 140.7°W	160-285 m	South Pacific Central Water (SPCW)[e]
	Galápagos Archipelago	0.4-1.2°N, 90.6-91.3°W	250-300 m	13°C water mass (13CW)[f]
			450-500 m	Antarctic Intermediate Water (AAIW)[f]

The map view is shown in Figure 2. References from García-Ibáñez et al. (2018)[a], Liu and Tanhua (2021)[b], Sumida et al. (2020)[c], Hartin et al. (2011)[d], Peters et al. (2018)[e], Evans et al. (2020)[f]. The hydrographic properties of paired water masses are listed in Supplementary Table 2.

sensor-mounted CTD/ROV measurements or extracted from the GLODAP2 bottle database (Lauvset et al., 2022). The uncertainty on dissolved oxygen estimates is based on the three most proximal measurements. The oxygen content of the Galápagos site is from the nearest published site (Salinas-de-León et al., 2020). These measurements were all within 300 km and 100 m water depth of coral sampling sites. The seawater [CO_3^{2-}] was obtained using the CO2sys.xls program (Pelletier et al., 2007). The input parameters were alkalinity and dissolved inorganic carbon from the GLODAP2 bottle database with dissociation constants taken from Dickson and Millero (1987). All paired seawater data are reported in Supplementary Table 1.

2.3 Sample preparation

Coral samples were treated in bleaching solution (30% v/v sodium hypochlorite solution (reagent grade, Fisher Scientific) in water; ~5% active Cl) after collection and air-dried before physical scraping to remove attached organic matter. A diamond-coated rotary blade was used to cut pieces of each coral for analysis. We applied coral sampling criteria as described by Stewart et al. (2020): Only coral theca walls were sampled to avoid microstructural bias, such as from highly contrasting trace metal chemistry in centers of calcification (Gagnon et al., 2007). Coral fragments (~1 g) were then finely crushed using a pestle and mortar to provide a homogeneous powder. Most coral samples were prepared at the University of Bristol, and the bamboo coral samples from the California margin were prepared at the University of California, Davis.

The I/Ca coral sample preparations were modified from Lu et al. (2022). Approximately 5 mg of the coral powder was taken for each sample. The cleaning procedure only involved MQ water cleaning for potential clay contamination. This cleaning step is critical in I/Ca measurements of foraminifera (Winkelbauer et al., 2021) and we included it for completeness; however, we note for coral samples clay contamination is generally negligible. Neither oxidative nor reductive cleaning steps were applied to best preserve volatile iodine from loss during sample preparation. Reductive cleaning was considered unnecessary as Fe-Mn coatings contain a limited iodine (Zhou et al., 2014). Organic matter in DSCs was removed

in previous steps via physical scraping and treatment in dilute sodium hypochlorite solution.

For most samples, Mg/Ca measurements were conducted alongside iodine measurements. However, for those samples that required separate analysis due to the use of a different instrument (see below), trace element analysis (e.g., Mg/Ca, Mn/Ca) was performed using separate sample aliquots. Those samples were prepared following methods by Barker et al. (2003) and Stewart et al. (2020). Briefly, samples (~5 mg) underwent reductive cleaning (warm bath in 80˚C, 3.5% hydrous hydrazine buffered in citric acid/ammonia), oxidative cleaning (warm bath in 80˚C, 1% H_2O_2 buffered in ammonia), and weak acid polish (0.0005 M HNO_3). The samples were then dissolved in 0.5 M HNO_3, with a final diluted aliquot containing 4 mM [Ca] taken for analysis. The Mg/Ca of the California Margin bamboo corals were taken from Geyman et al. (2019).

2.4 Analytical techniques

To prepare the samples for iodine measurement, cleaned coral samples were dissolved in 3% HNO_3 buffered by 2% tetramethylammonium hydroxide (TMAH) to stabilize the iodine. Dissolved samples were then stored at 4°C. Iodine concentrations were measured the next day in diluted solutions containing ~50 ppm Ca, 5 ppb internal standards (Sc, In, Cs), 0.5% TMAH, and 0.5% nitric acid. The pH of the solution was controlled (pH = ~2) to minimize iodine volatilization (Cook et al., 2022). DSC I/Ca analyses were carried out on a Thermo Scientific iCAP Q reverse quadrupole inductively coupled plasma mass spectrometer (ICP-MS) at Woods Hole Oceanographic Institution and a Thermo Scientific iCAP triple quadrupole (TQ) ICP-MS at Michigan State University, employing similar techniques. For the latter, Ca, I, and Mg were each measured in both single-quadrupole and triple-quadrupole modes. Freshly made iodine calibration solutions (iodide solution, I.V. Labs, Inc., with 50 ppm [Ca]), calcium calibration solutions standards and blank solutions containing 0.5% TMAH and 0.5% nitric acid were analysed routinely to monitor contributions from processing blanks and instrument memory, which were all matrix-matched with all the samples. ICP-MS standards (Cs, In, Sc) were added to each sample and calibration solution as internal standards and used to normalize the target analytes. A calibration line was produced every 5 to 8 blocks to correct instrumental drift, and data were corrected using the slope of the drift monitors over time. Reference material in-house standard (*Porites* coral; aragonite) and international standard JCp-1 (*Porites* coral; aragonite) were measured after every 5 to 8 samples.

In-house coral standard (*Porites* coral; aragonite) showed consistency within the run, and the I/Ca value yielded 3.58 ± 0.36 µmol/mol (1 σ, n = 24). To compare data between labs, the I/Ca value of JCp-1 for all batches measured at WHOI is 3.91 ± 0.36 µmol/mol (1 σ, n = 34), and at Michigan State University is 4.09 ± 0.34 µmol/mol (1 σ, n = 7). Both results are within the uncertainty of published I/Ca values, where 3.70 ± 0.27 µmol/mol (1 σ, n = 2280) in Lu et al. (2020c) and 4.12 ± 0.26 µmol/mol (1 σ, n = 41) in Zhou et al. (2022). These standard data are shown in Supplementary Table 3.

For I/Ca data generated using the iCAP RQ ICP-MS, paired Mg/Ca data were separately measured on a Thermo Scientific Element2 ICP-MS at the University of Bristol. An aliquot of the dissolved sample (separate powder from I/Ca data) was analysed using well-characterized, matrix-matched, synthetic standard solutions to yield Mg/Ca ratios. Both NIST RM 8301-coral (simulated coral solution) and JCp-1 (uncleaned) carbonate reference materials were measured repeatedly and yielded a long-term analytical precision of < ± 2% (1 σ).

3 Results

For scleractinian corals at all sites (n = 49), I/Ca varied from 4.81 to 13.64 µmol/mol across seawater oxygen contents of 12 to 281 µmol/kg (Figure 3; Supplementary Table 1). A key observation is that the I/Ca data can be separated into two groups at seawater O_2 concentration above and below 160 µmol/kg. Samples with O_2 concentration < 160 µmol/kg exhibit a mean I/Ca of 7.53 ± 1.02 (RSD = 14%, n = 19), whereas the samples from O_2 concentration > 160 exhibit a mean I/Ca of 9.30 ± 1.75 (RSD = 19%; n = 30). Though there is a slight overlap in the I/Ca of the two groups, they are nonetheless statistically significantly different (unequal variances t-test, $t(46.78) = -4.47$, p = 5.02e-05).

Bamboo corals are composed of high-Mg calcite; therefore, to compare results with scleractinian (aragonite) I/Ca data, we discuss the results in these samples regarding I/(Ca+Mg). The I/(Ca+Mg) of bamboo corals are in the range of 1.91 to 2.84 µmol/mol within oxygen content of 20 to 240 µmol/kg from Eastern North Pacific (n = 4) and Tropical North Atlantic (n = 9) (Figure 3; Supplementary Table 1). There is one exception for an outlier with an I/(Ca+Mg) value of 8.63 µmol/mol in O_2 concentration = 215 µmol/kg. This outlier value is not included in further discussion. The bamboo coral I/(Ca+Mg) varied from 1.57 to 2.22 µmol/mol. There are no significant differences across the oxygen concentrations range but a slight increase of I/(Ca+Mg) at O_2 concentration >160 µmol/kg (Supplementary Figure 3).

4 Discussion

I/Ca in marine carbonates , such as foraminifera, has shown the potential to record redox changes (Lu et al., 2020c). To explore this potential and iodine systematics in DSCs, we: (1) discuss the I/Ca ratios in different carbonate morphologies- aragonite and calcite, from two coral taxa; (2) discuss iodate incorporation mechanisms using seawater iodate concentration data and our coral I/Ca measurements; and (3) evaluate the potential of applying DSC I/Ca as a seawater oxygenation proxy.

4.1 Iodine concentration in aragonite versus calcite

Incorporating iodine species in calcium carbonate strongly depends on the mineral structure. Previous studies determined

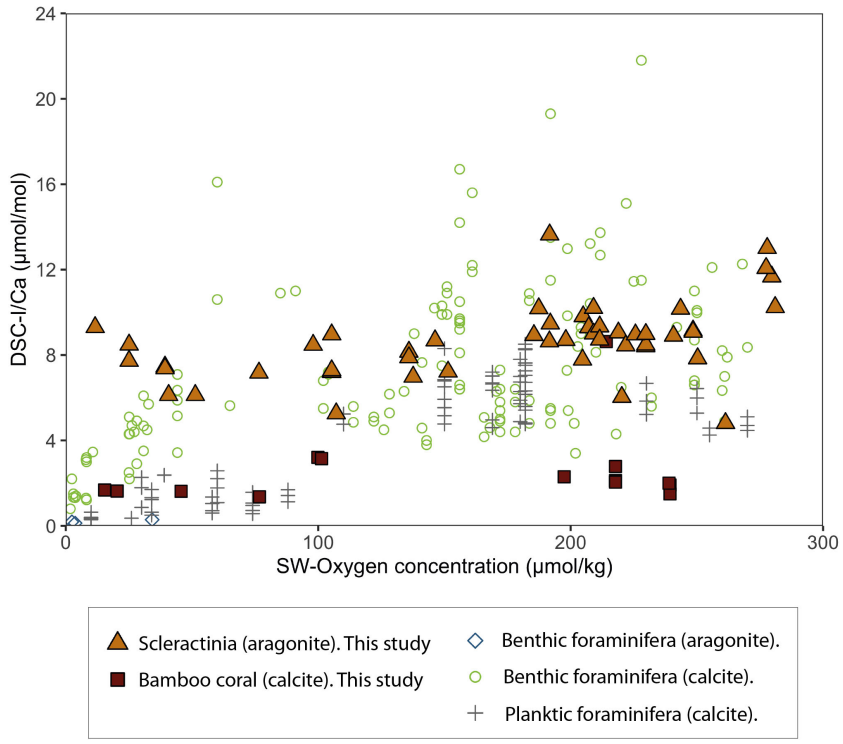

FIGURE 3
Modern deep-sea coral I/Ca and adjacent seawater oxygen concentration, with published core-top foraminifera dataset. The filled symbols denote the deep-sea coral data from this study, and the opened symbols are from published studies (Glock et al., 2014; Lu et al., 2020b; Lu et al., 2022). The bamboo corals (high-Mg calcite, red squares) are plotted using I/(Ca+Mg) for the *y*-axis for direct comparison to aragonites. Seawater oxygen data is taken from nearby sites in the GLODAP2 database (Lauvset et al., 2022), and dissolved oxygen measurements at the Galápagos site (Salinas-de-León et al., 2020).

the site location of iodine within carbonates. In contrast to most of the major/trace cations that exchange with Ca^{2+} in the carbonate structure, negatively charged iodine (as an iodate ion) has been confirmed to substitute for the carbonate ion in calcium carbonate (Podder et al., 2017). Results from computational simulations show that the iodate substitution into calcite involves a lower energy penalty than substitution into aragonite, meaning that iodate is preferentially partitioned into calcite over aragonite (Feng and Redfern, 2018). While incorporating iodate ion, the calcite lattice of the iodine-bearing structure remains the same (rhombohedral), but for iodine-bearing aragonite, the original orthorhombic cell reduces in symmetry to monoclinic. This leads to a large partitioning difference between calcite to aragonite.

Surprisingly, our results show that the iodine concentration is higher in aragonitic scleractinian corals (mean I/Ca = 8.5 µmol/mol) compared to calcitic bamboo corals (mean I/Ca = 2.4 µmol/mol; Figure 3). This contradicts the results from computational simulations that predict a higher iodine relative abundance in calcite than in aragonite (Feng and Redfern, 2018). We emphasize that this comparison is done between I/Ca in scleractinian corals and I/(Ca+Mg) in bamboo corals, but since the iodate is substituting for the carbonate ion, the effect of higher Mg content in bamboo corals is minimal (Supplementary Figure 2). Additionally, the computational simulations were based on a concentrated iodate system with I/Ca ≈40 mmol/mol, almost 5,000 times higher than mean scleractinian DSC I/Ca. Despite these substantial concentration differences, the results of iodate incorporation from our DSCs do not align with the enthalpic penalties and local distortion effects predicted by theoretical simulations. Previous studies noted inconsistencies between thermodynamic calculations and synthesis experiments in iodine-bearing carbonate systems. For example, if thermodynamics are the only influence of iodate incorporation, increased temperature is expected to favor iodate incorporation due to the entropic advantage. However, the synthetic calcite experiment showed lower partition coefficients for iodate at higher temperatures (Zhou et al., 2014). In addition, the energetic penalty for iodate incorporation is less significant in vaterite than in calcite (Feng and Redfern, 2018), but synthesis experiments suggest that iodine is preferentially incorporated into calcite over vaterite (Podder et al., 2017). Moreover, simulation studies in calcite suggest a mechanism of surface segregation. From an entropy point of view, iodate could be more prone to substitute for CO_3^{2-} in aragonite than calcite, as aragonite is more soluble than calcite (Mucci, 1983). These discrepancies, however, are largely unexplained and potential mechanisms remain a subject of speculation. These mechanisms include temperature-dependence of iodine speciation in aqueous solutions (Burns et al., 1990), and/or kinetic effects associated with carbonate dissolution and reprecipitation reactions.

Biological or 'vital' effects are another plausible control on iodine partitioning in DSCs. During coral calcification,

scleractinian coral increases the Ca concentration and pH of their calcifying fluid through the activity of the Ca/proton-pumps (Cohen and McConnaughey, 2003). This leads to a higher carbonate saturation, which favors aragonite precipitation. By contrast, bamboo corals experience a more complex anion exchange (bicarbonate), which includes a combination of Ca/proton pumping and bicarbonate active transport, the latter of which has been proposed for sulfate incorporation (Flöter et al., 2022). Bicarbonate active transport delivers bicarbonate to the calcifying fluid to keep the calcite saturation at a high level and increases carbonate ion concentration by shifting the calcifying fluid pH. This process leads to a decrease in the calcifying fluid sulphur:carbonate ratio and thus a decrease in bamboo coral skeletal S:Ca ratio. This is also supported by a calcifying fluid study and boron isotope measurements that suggested bamboo corals undergo a minimal modification of their internal pH compared to scleractinian corals (Farmer et al., 2015). As sulfate also replaces the carbonate ion in the carbonate lattice, an analogous mechanism may be involved in iodate incorporation. The additional bicarbonate active transport in bamboo corals may be responsible for their lower I/Ca values compared to scleractinian corals. We thus argue that the biological control on iodate partitioning between different DSC families represents a more robust control than mineralogical differences.

Further studies are required to better understand iodine incorporation, including the divergent results from the thermodynamic calculation and experimental measurements, the factors controlling over iodine incorporation (e.g., pH, temperature), the growth rate effects of biogenic carbonate during calcification, and DSC culture experiments of iodine uptake. This also highlights the need for biogenic carbonate studies to consider a group-specific classification, such as family, genus, or species when developing proxy applications (e.g., Kershaw et al., 2023).

4.2 Scleractinian coral I/Ca and its incorporation

With the large difference in iodine concentration in DSCs due to their carbonate structures reported here, we first focus on scleractinian coral (aragonite) and investigate the potential controlling factors of I/Ca. Scleractinian coral I/Ca increases with seawater iodate concentration, except for samples from high latitudes (Figure 4B). A similar relationship has been reported in synthesis experiments for calcite, with a significant linear correlation between calcite I/Ca and ambient water iodate concentration (Lu et al., 2010; Zhou et al., 2014). Aragonitic coral I/Ca is overall higher than synthetic calcite I/Ca for a given water/seawater iodate concentration (Figure 4B). With the exception of high latitude samples (North Atlantic and Southern Ocean), the slope of the linear regression line for the scleractinian corals is strikingly similar to that of the synthetic calcite (Figure 4B; Lu et al., 2010). This relationship suggests similar modes of incorporation of iodate into coral aragonite and synthetic calcite structures. Still, a few uncertainties may raise concerns about the findings. The calcite synthesis experiments were conducted in deionized water rather than seawater, which may affect the incorporation of iodate. Also, this process was found to be temperature dependent, with greater incorporation at low temperatures and less at higher temperatures (Zhou et al., 2014). Nevertheless, the consistency between iodate incorporation into coral aragonite and synthetic calcite suggests that iodine in marine carbonate is incorporated mainly from surrounding seawater and in turn that the iodate concentration of ambient seawater could be a controlling factor for coral I/Ca.

In contrast, corals from high latitudes, specifically the North Atlantic and Southern Oceans, exhibit I/Ca ratios that deviate from values expected based on their nearby seawater iodate concentrations (450 to 500 nM; Figure 5). To further investigate this effect, we explore the secondary environmental controls on these samples. The I/Ca values do not correlate with seawater pH, $[CO_3^{2-}]$, dissolved phosphate concentrations, or dissolved nitrate concentrations at all sites (Supplementary Figure 1). However, on a regional scale, corals from the North Atlantic show that I/Ca and temperature have a negative correlation (Figure 5C). Also, I/Ca is negatively correlated with salinity (Figure 5D) due to the fact that seawater temperature and salinity are highly correlated at these sites. A similar negative correlation between I/Ca and temperature has also been reported in synthetic calcite experiments (Zhou et al., 2014) and core-top benthic foraminifera from the Little Bahama Bank region where oxygen concentrations are high (150 to 200 µmol/kg) (Lu et al., 2022). We speculate that, similar to benthic foraminifera, corals may naturally incorporate more iodate into their carbonate structure at lower temperatures. Another possible influencing factor is seasonal seawater iodate changes at high latitudes. Seawater iodate concentration at coastal Antarctic sites varies from 250 to 400 nM, with an interannual variability of around 160 nM (three observation years at 15 m depth) related to iodate reduction by biological productivity (Chance et al., 2010). Due to the limited longer-term seawater data, it is difficult to explore further the impact of temperature and seasonal iodate variation on coral I/Ca. Thus, further investigation of iodine incorporation into DSCs from high-latitude regions is needed.

The concentration of seawater iodate varies with oxygen content, and coral I/Ca ratios reflect these iodate concentrations; hence, this allows coral I/Ca to be used as a proxy for seawater oxygen content. Our results show that the coral I/Ca-O_2 relationship undergoes an apparent "step change" at O_2 concentration ≈ 160 µmol/kg, whereafter coral I/Ca remains elevated at high oxygen levels (Figure 4C). This significant step change is also present in both benthic and planktic foraminifera (Figure 3; Glock et al., 2014; Lu et al., 2020b; Lu et al., 2022), where a low O_2 threshold for planktics occurs at around 100 µmol/kg (I/Ca < 2.5 µmol/mol), and for benthics at about 50 µmol/kg (I/Ca < 3 µmol/mol). Although the semi-quantitative I/Ca-O_2 relationships remain empirical, the oxygen thresholds in DSC I/Ca could correspond to their metabolic limits. Laboratory studies of *Lophelia pertusa* (scleractinian) have shown it maintains respiratory independence at high oxygen concentrations, but that respiration rate declines rapidly below a critical oxygen level of ~140 µmol/kg (Dodds et al., 2007). These results also agree with field-based population distributions in the North Atlantic, which indicate that DSCs are absent at the local oxygen minimum of around 150

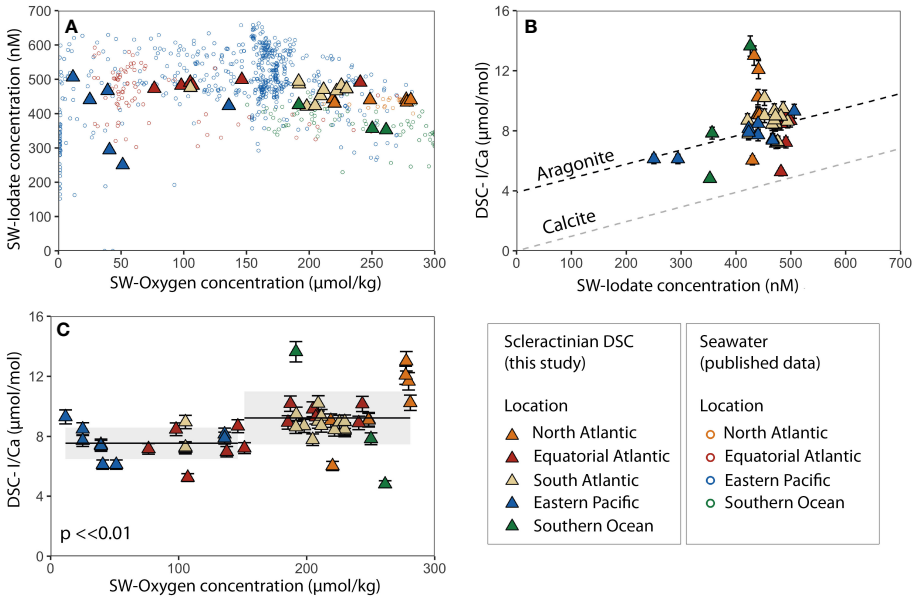

FIGURE 4
Cross-plots for scleractinian deep-sea coral (DSC) I/Ca and ambient seawater oxygen concentration. **(A)** Dissolved oxygen concentration versus dissolved iodate concentration in seawater. Proximal seawater iodate/iodide data were taken from published sources (Wong and Brewer, 1977; Elderfield and Truesdale, 1980; Bluhm et al., 2011; Cutter et al., 2018; Rapp et al., 2020). DSCs are in filled triangles and seawater data are in circles. The colours represent locations: North Atlantic (orange), Equatorial Atlantic (red), Southwest Atlantic (beige), Eastern Pacific (blue) and Southern Ocean (green). **(B)** Ambient seawater iodate concentration versus coral I/Ca. The black dashed line is a linear regression line of scleractinian DSC I/Ca (aragonite) without samples from the North Atlantic and Southern Ocean (y = 0.00937x + 3.90). The grey dashed line is the iodine incorporation results from calcite synthesis (y = 0.00974x; Lu et al., 2010). **(C)** Dissolved oxygen concentration versus I/Ca in deep-sea coral. The grey areas represent 1 SD. Error bar I/Ca in coral: 1 σ = 5%.

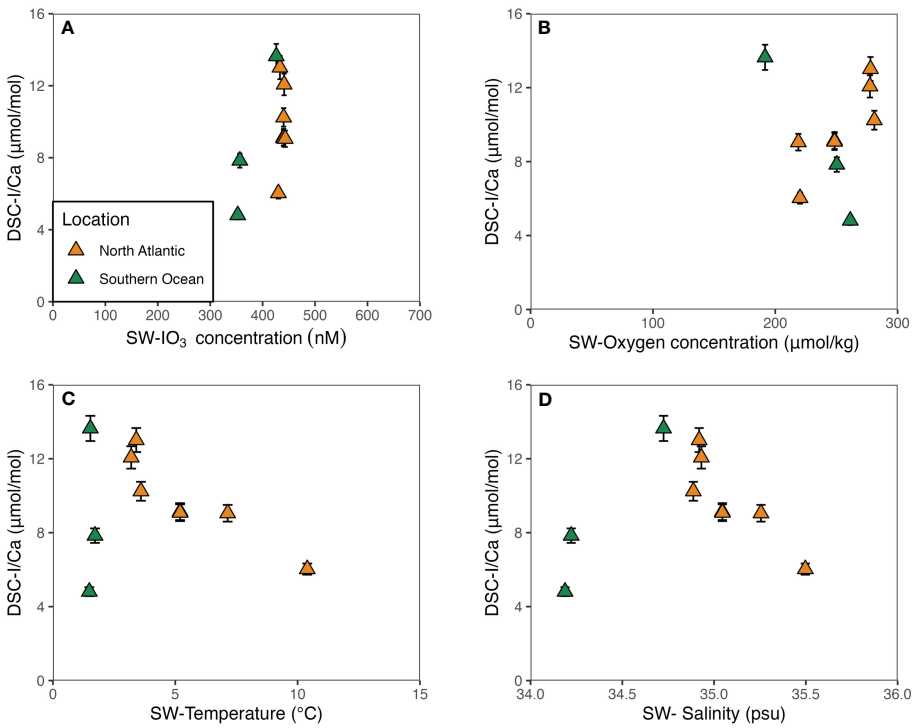

FIGURE 5
Deep-sea scleractinian coral (DSC) I/Ca values from high-latitude regions (North Atlantic and Southern Ocean) and ambient seawater parameters: **(A)** iodate concentration, **(B)** oxygen, **(C)** temperature, and **(D)** salinity. Paired seawater data are published iodate data (Elderfield and Truesdale, 1980; Bluhm et al., 2011), and the GLODAP 2 bottle database (Lauvset et al., 2022). Seawater temperature is positively correlated with salinity in the North Atlantic (R^2 = 0.97). The symbols used are identical to those in Figure 4. Error bar I/Ca in coral: 1 σ = 5%.

µmol/kg (Thiagarajan et al., 2013). Further paleohabitat studies in the Southern Ocean also suggest that corals were less prevalent in the deep Polar Front (~1200 m depth) during the Antarctic Cold Reversal (14.7-13 ka), when seawater oxygen levels fell below this threshold. (Stewart et al., 2021). Together, these studies suggest DSCs have a change in biological function around an O_2 threshold at ~160 µmol/kg, which could correspond to a potential change in iodate incorporation.

We next compare the I/Ca in aragonitic foraminifera versus aragonitic corals. The only I/Ca dataset from modern/recent aragonitic benthic foraminifera is *Hoeglundina elegans* from OMZs off the Peru margin, which suggests no significant correlation between I/Ca and bottom water oxygen concentration (Glock et al., 2014). These authors concluded that this might be due to the dissolution and recrystallisation of metastable aragonite that can happen at the early stage of diagenesis, thus altering I/Ca ratios. However, their study only focused on extremely low dissolved oxygen content (< 10 µmol/kg), meaning iodate reduction had occurred and making iodide the prevalent iodine species in this setting. The I/Ca data only varies in a relatively small range (~0.1 to 0.3 µmol/mol), which makes it difficult to detect significant variations. Our results for DSCs argue against this finding and suggest that I/Ca in aragonite could reflect seawater oxygen content. The low aragonitic *H. elegans* I/Ca versus higher I/Ca in scleractinian corals at locations with O_2 concentrations < ~50 µmol/kgare possibly due to the difference in seawater iodate concentrations and/or regional water mass mixing processes related to their locations (i.e., *H. elegans* were collected at OMZs off Peruvian margin; scleractinian corals were collected at OMZ closer to the equator), or the difference between foraminifera and DSC calcification processes.

Lastly, we find no significant oxygen threshold in our bamboo coral I/Ca results, but a hint of a slight increase of I/Ca values at O_2 concentration < ~160 umol/kg (Supplementary Figure 3). This could be explained by reduced vital effects in bamboo corals (Section 4.1) and/or sampling biases given the limited available data. Additional calibration studies of bamboo corals are required before they can be used to study paleo-oxygenation. Due to these limitations, we focus on the potential use of scleractinian corals for future proxy applications.

4.3 Implications for the DSC I/Ca paleo-oxygenation proxy

Here, we propose that iodate incorporation in deep-sea corals is linked to seawater oxygen content. Scleractinian corals exhibit a "step-change" in I/Ca at an O_2 concentration ≈ 160 µmol/kg, which may be further utilized as an indicator to reconstruct marine oxygen content similarly to I/Ca measurements in foraminifera (e.g., Lu et al., 2020c).

Decreasing marine dissolved oxygen content as a result of global warming is predicted to accelerate in the near future (Oschlies et al., 2018). Due to the probable threat to marine ecosystems, understanding the linkages between the carbon and oxygen cycles is vital. Scleractinian DSCs offer a promising, well-dated archive of past oceanic environments, and by applying an I/Ca-oxygenation proxy, the reconstructed oxygenation records could shed new light on key paleoclimate events. For example. during the last ice age, the deep Pacific is thought to have stored more respired carbon when oxygen-depleted deep waters were expanded in the eastern tropical Pacific (Hoogakker et al., 2018). However, redox proxies commonly used to tackle this issue, such as authigenic uranium, benthic foraminifera carbon isotope gradients and biomarker preservation, sometimes yield different oxygen-level reconstructions due to the limitations of each proxy (Jacobel et al., 2020). The DSC I/Ca proxy has the advantage of recording variations in intermediate water masses, providing an independent proxy perspective on oxygen reconstructions. For example, glacial to modern seawater O_2 concentration in the South Indian Ocean is suggested to have increased from ~100 to ~220 µmol/kg (Gottschalk et al., 2020). This range covers our coral I/Ca-O_2 threshold and provides an alternative archive to study deep-ocean oxygenation, focusing on abrupt events during the last millennium owing to the absolute radiometric dating potential of DSCs.

One potential obstacle to utilizing the I/Ca proxy in scleractinian coral is the biological behavior under low oxygen conditions (e.g., Hughes et al., 2020). Recent studies have shown that DSCs are able to thrive under hypoxic environments (e.g., Hebbeln et al., 2020; Salinas-de-León et al., 2020), but the question remains whether DSCs would modify their calcification to adopt to extreme conditions. For example, *Lophelia pertusa* would exhibit high mortality to maintain respiratory competence under low O_2 concentration by utilizing polyp expansion to increase tissue surface area and facilitate a diffusive gas exchange (Dodds et al., 2007). However, whether these processes would affect iodate incorporation during coral skeleton formation is unknown. Culture studies are therefore required to further explore the I/Ca ratio in DSCs as an oxygenation proxy. Nevertheless, DSCs serve as a potential archive that will allow us to indicate marine oxygen concentration above or below a specific level in the past.

5 Conclusions

Our study provides insight into the incorporation mechanisms of iodine into deep-sea corals (DSCs) and its potential as a proxy for seawater oxygenation. Contrary to computational simulations suggesting that iodate preferentially partitions into calcite over aragonite, our findings show that scleractinian corals (aragonitic) generally exhibit higher I/Ca than bamboo corals (calcitic). This suggests that biological processes exert a stronger control over iodine incorporation into DSC skelektons than mineralogical differences. For scleractinian corals, the potential main controlling factor on coral I/Ca is the iodate concentration of ambient seawater, except for a few high-latitude samples that potentially exhibit a strong secondary temperature/salinity influence. The I/Ca of bamboo corals does not appear to be sensitive to ambient iodate—and, by extension, oxygen—concentrations, which may relate to biological influences on calcification.

Overall, our data suggest that scleractinian DSCs have the potential to track water mass dissolved O_2 content at a certain level, as evidenced by a significant I/Ca "step change" occurring at oxygen concentrations around 160 µmol/kg. This relationship can provide an independent perspective on seawater O_2 concentration reconstructions that may help resolve discrepancies between

existing oxygenation proxies. Our study provides a first-order empirical understanding of the I/Ca systematics of natural corals and their relationship with the ambient seawater characteristics. This reveals the potential of DSC I/Ca to reconstruct past changes in oxygen levels of water masses and improve our understanding of Earth's biogeochemical history.

Data availability statement

The original contributions presented in the study are included in the article/Supplementary Material. Further inquiries can be directed to the corresponding author.

Author contributions

YS: Conceptualization, Data curation, Funding acquisition, Investigation, Writing – original draft. LR: Conceptualization, Funding acquisition, Resources, Supervision, Writing – original draft, Writing – review & editing. IP: Supervision, Writing – original draft, Writing – review & editing. JS: Supervision, Writing – original draft, Writing – review & editing. WL: Investigation, Methodology, Writing – review & editing. DH: Investigation, Resources, Writing – review & editing. QL: Resources, Writing – review & editing. JK: Resources, Writing – review & editing. ML: Resources, Writing – review & editing. TH: Conceptualization, Investigation, Resources, Writing – original draft, Writing – review & editing.

Funding

The author(s) declare financial support was received for the research, authorship, and/or publication of this article. Funding for this work was provided by a bursary from Antarctic Science Ltd. and a *Government Scholarship Program for overseas study* from the Ministry of Education, Taiwan awarded to Y-J.S, and NERC grants awarded to LR (NE/S001743/1; NE/R005117/1; NE/N003861/1; NE/X00127X/1). Cruise DY081 was funded by the *European Research Council starting grant* ICY-LAB (Grant Agreement 678371). TH acknowledges support from the Woods Hole Oceanographic Institution's *President's Innovation Fund* and *The Breene M. Kerr Early Career Scientist Endowment Fund*. DH thanks NSF CO award # 1829406.

Acknowledgments

We acknowledge the crew and researchers on board the research vessels that obtained the samples for this study. We thank the Charles Darwin Foundation, Galápagos National Park, and INOCAR for Galápagos sampling. AL0508 was supported by The Dalio Explore Fund. We also acknowledge the Galápagos National Park directorate for permission to map and collect submarine rock and biological samples (PC-44-15) and the Charles Darwin Foundation for facilitating scientific collaboration in the Galápagos. Access to specimens from the Muséum National d'Histoire Naturelle (MNHN, Paris) was facilitated by Magalie Castelin (Cnidaria curator) and Jonathan Blettery (SYNTHESYS+, a grant awarded to James Kershaw). MNHN specimens were obtained during expedition MUSORSTOM 9, organised by the MNHN and the Institut de Recherche pour le Développement as part of the Tropical Deep-Sea Benthos program (previously MUSORSTOM). The authors are grateful to the cruise leader, Bertrand Richer de Forges, and to Helmut Zibrowius who identified the specimens. We acknowledge the support from Konrad Hughen providing international and in-house coral standards for iodine measurement. We thank Keyi Cheng, Maureen Auro, Jerzy S Blusztajn, Christopher D Coath, Jamie Lewis, Carolyn Taylor, Maria Luiza De Carvalho Ferreira, Yingchu Shen and Maoyu Wang for their help with laboratory work. We thank Jui-Yen Lin and Kuan-Yu Lin for the discussions on iodine speciation thermodynamics. We thank Zunli Lu and George W Luther as well as the Editor Alex J Poulton for their constructive comments that greatly improved the manuscript.

Conflict of interest

The authors declare that the research was conducted in the absence of any commercial or financial relationships that could be construed as a potential conflict of interest.

The reviewer ZL declared a past co-authorship with the author WL to the handling Editor.

Publisher's note

All claims expressed in this article are solely those of the authors and do not necessarily represent those of their affiliated organizations, or those of the publisher, the editors and the reviewers. Any product that may be evaluated in this article, or claim that may be made by its manufacturer, is not guaranteed or endorsed by the publisher.

Supplementary material

The Supplementary Material for this article can be found online at: https://www.frontiersin.org/articles/10.3389/fmars.2023.1264380/full#supplementary-material

References

Barker, S., Greaves, M., and Elderfield, H. (2003). A study of cleaning procedures used for foraminiferal Mg/Ca paleothermometry: MG/CA PALEOTHERMOMETRY. *Geochem. Geophys. Geosyst.* 4, n/a–n/a. doi: 10.1029/2003GC000559

Bluhm, K., Croot, P. L., Huhn, O., Rohardt, G., and Lochte, K. (2011). Distribution of iodide and iodate in the Atlantic sector of the southern ocean during austral summer. *Deep Sea Res. Part II: Topical Stud. Oceanography* 58, 2733–2748. doi: 10.1016/j.dsr2.2011.02.002

Broecker, W. S., and Peng, T. H. (1982). *Tracers in the Sea* (Palisades, New York: Lamont-Doherty Geological Observatory, Columbia University).

Burns, W. G., Matsuda, M., and Sims, H. E. (1990). Temperature dependence of the equilibrium constant for iodine hydrolysis at temperatures between 25 and 120 °C. *J. Chem. Soc. Faraday Trans.* 86, 1443–1447. doi: 10.1039/FT9908601443

Campos, M. L. A. M., Farrenkopf, A. M., Jickells, T. D., and Luther, G. W. (1996). A comparison of dissolved iodine cycling at the Bermuda Atlantic Time-series Station and Hawaii Ocean Time-series Station. *Deep Sea Res. Part II: Topical Stud. Oceanography* 43, 455–466. doi: 10.1016/0967-0645(95)00100-X

Carpenter, L. J., Chance, R. J., Sherwen, T., Adams, T. J., Ball, S. M., Evans, M. J., et al. (2021). Marine iodine emissions in a changing world. *Proc. R. Soc A.* 477, 20200824. doi: 10.1098/rspa.2020.0824

Carpenter, L. J., MacDonald, S. M., Shaw, M. D., Kumar, R., Saunders, R. W., Parthipan, R., et al. (2013). Atmospheric iodine levels influenced by sea surface emissions of inorganic iodine. *Nat. Geosci* 6, 108–111. doi: 10.1038/ngeo1687

Chance, R., Baker, A. R., Carpenter, L., and Jickells, T. D. (2014). The distribution of iodide at the sea surface. *Environ. Sci.: Processes Impacts* 16, 1841–1859. doi: 10.1039/C4EM00139G

Chance, R., Weston, K., Baker, A. R., Hughes, C., Malin, G., Carpenter, L., et al. (2010). Seasonal and interannual variation of dissolved iodine speciation at a coastal Antarctic site. *Mar. Chem.* 118, 171–181. doi: 10.1016/j.marchem.2009.11.009

Chen, T., Robinson, L. F., Burke, A., Southon, J., Spooner, P., Morris, P. J., et al. (2015). Synchronous centennial abrupt events in the ocean and atmosphere during the last deglaciation. *Science* 349, 1537–1541. doi: 10.1126/science.aac6159

Chen, T., Robinson, L. F., Li, T., Burke, A., Zhang, X., Stewart, J. A., et al. (2023). Radiocarbon evidence for the stability of polar ocean overturning during the Holocene. *Nat. Geosci.* 16, 631–636. doi: 10.1038/s41561-023-01214-2

Cheng, H., Adkins, J., Edwards, R. L., and Boyle, E. A. (2000). U-Th dating of deep-sea corals. *Geochimica Cosmochimica Acta* 64, 2401–2416. doi: 10.1016/S0016-7037(99)00422-6

Cohen, A. L., and McConnaughey, T. A. (2003). Geochemical perspectives on coral mineralization. *Rev. Mineralogy Geochemistry* 54, 151–187. doi: 10.2113/0540151

Cook, M. K., Dial, A. R., and Hendy, I. L. (2022). Iodine stability as a function of pH and its implications for simultaneous multi-element ICP-MS analysis of marine carbonates for paleoenvironmental reconstructions. *Mar. Chem.* 245, 104148. doi: 10.1016/j.marchem.2022.104148

Cutter, G. A., Moffett, J. W., Nielsdóttir, M. C., and Sanial, V. (2018). Multiple oxidation state trace elements in suboxic waters off Peru: *In situ* redox processes and advective/diffusive horizontal transport. *Mar. Chem.* 201, 77–89. doi: 10.1016/j.marchem.2018.01.003

Dickson, A. G., and Millero, F. J. (1987). A comparison of the equilibrium constants for the dissociation of carbonic acid in seawater media. *Deep Sea Res. Part A. Oceanographic Res. Papers* 34, 1733–1743. doi: 10.1016/0198-0149(87)90021-5

Dodds, L. A., Roberts, J. M., Taylor, A. C., and Marubini, F. (2007). Metabolic tolerance of the cold-water coral Lophelia pertusa (Scleractinia) to temperature and dissolved oxygen change. *J. Exp. Mar. Biol. Ecol.* 349, 205–214. doi: 10.1016/j.jembe.2007.05.013

Elderfield, H., and Truesdale, V. W. (1980). On the biophilic nature of iodine in seawater. *Earth Planetary Sci. Lett.* 50, 105–114. doi: 10.1016/0012-821X(80)90122-3

Evans, N., Boles, E., Kwiecinski, J. V., Mullen, S., Wolf, M., Devol, A. H., et al. (2020). The role of water masses in shaping the distribution of redox active compounds in the Eastern Tropical North Pacific oxygen deficient zone and influencing low oxygen concentrations in the eastern Pacific Ocean. *Limnol Oceanogr* 65, 1688–1705. doi: 10.1002/lno.11412

Farmer, J. R., Hönisch, B., Robinson, L. F., and Hill, T. M. (2015). Effects of seawater-pH and biomineralization on the boron isotopic composition of deep-sea bamboo corals. *Geochimica Cosmochimica Acta* 155, 86–106. doi: 10.1016/j.gca.2015.01.018

Farrenkopf, A. M., Dollhopf, M. E., Chadhain, S. N., Luther, G. W., and Nealson, K. H. (1997). Reduction of iodate in seawater during Arabian Sea shipboard incubations and in laboratory cultures of the marine bacterium Shewanella putrefaciens strain MR-4. *Mar. Chem.* 57, 347–354. doi: 10.1016/S0304-4203(97)00039-X

Farrenkopf, A. M., and Luther, G. W. (2002). Iodine chemistry reflects productivity and denitrification in the Arabian Sea: evidence for flux of dissolved species from sediments of western India into the OMZ. *Deep Sea Res. Part II: Topical Stud. Oceanography* 49, 2303–2318. doi: 10.1016/S0967-0645(02)00038-3

Feng, X., and Redfern, S. A. T. (2018). Iodate in calcite, aragonite and vaterite CaCO3: Insights from first-principles calculations and implications for the I/Ca geochemical proxy. *Geochimica Cosmochimica Acta* 236, 351–360. doi: 10.1016/j.gca.2018.02.017

Flöter, S., Fietzke, J., Gutjahr, M., Nehrke, G., and Eisenhauer, A. (2022). Incorporation of Na and S in bamboo coral skeletons. *Chem. Geology* 597, 120795. doi: 10.1016/j.chemgeo.2022.120795

Frenkel, M. M., LaVigne, M., Miller, H. R., Hill, T. M., McNichol, A., and Gaylord, M. L. (2017). Quantifying bamboo coral growth rate nonlinearity with the radiocarbon bomb spike: A new model for paleoceanographic chronology development. *Deep Sea Res. Part I: Oceanographic Res. Papers* 125, 26–39. doi: 10.1016/j.dsr.2017.04.006

Gagnon, A. C., Adkins, J. F., Fernandez, D. P., and Robinson, L. F. (2007). Sr/Ca and Mg/Ca vital effects correlated with skeletal architecture in a scleractinian deep-sea coral and the role of Rayleigh fractionation. *Earth Planetary Sci. Lett.* 261, 280–295. doi: 10.1016/j.epsl.2007.07.013

García-Ibáñez, M. I., Pérez, F. F., Lherminier, P., Zunino, P., Mercier, H., and Tréguer, P. (2018). Water mass distributions and transports for the 2014 GEOVIDE cruise in the North Atlantic. *Biogeosciences* 15, 2075–2090. doi: 10.5194/bg-15-2075-2018

Geyman, B. M., Ptacek, J. L., LaVigne, M., and Horner, T. J. (2019). Barium in deep-sea bamboo corals: Phase associations, barium stable isotopes, & prospects for paleoceanography. *Earth Planetary Sci. Lett.* 525, 115751. doi: 10.1016/j.epsl.2019.115751

Glock, N., Liebetrau, V., and Eisenhauer, A. (2014). I/Ca ratios in benthic foraminifera from the Peruvian oxygen minimum zone: analytical methodology and evaluation as a proxy for redox conditions. *Biogeosciences* 11, 7077–7095. doi: 10.5194/bg-11-7077-2014

Gottschalk, J., Michel, E., Thöle, L. M., Studer, A. S., Hasenfratz, A. P., Schmid, N., et al. (2020). Glacial heterogeneity in Southern Ocean carbon storage abated by fast South Indian deglacial carbon release. *Nat. Commun.* 11, 6192. doi: 10.1038/s41467-020-20034-1

Hardisty, D. S., Horner, T. J., Evans, N., Moriyasu, R., Babbin, A. R., Wankel, S. D., et al. (2021). Limited iodate reduction in shipboard seawater incubations from the Eastern Tropical North Pacific oxygen deficient zone. *Earth Planetary Sci. Lett.* 554, 116676. doi: 10.1016/j.epsl.2020.116676

Hartin, C. A., Fine, R. A., Sloyan, B. M., Talley, L. D., Chereskin, T. K., and Happell, J. (2011). Formation rates of Subantarctic mode water and Antarctic intermediate water within the South Pacific. *Deep Sea Res. Part I: Oceanographic Res. Papers* 58, 524–534. doi: 10.1016/j.dsr.2011.02.010

Hashim, M. S., Burke, J. E., Hardisty, D. S., and Kaczmarek, S. E. (2022). Iodine incorporation into dolomite: Experimental constraints and implications for the iodine redox proxy and Proterozoic Ocean. *Geochimica Cosmochimica Acta* 338, 365–381. doi: 10.1016/j.gca.2022.10.027

Haynes, W. M. (Ed.). (2014). *CRC Handbook of Chemistry and Physics* (Boca Raton, FL, USA: CRC Press). doi: 10.1201/b17118

Hebbeln, D., Wienberg, C., Dullo, W.-C., Freiwald, A., Mienis, F., Orejas, C., et al. (2020). Cold-water coral reefs thriving under hypoxia. *Coral Reefs* 39, 853–859. doi: 10.1007/s00338-020-01934-6

Hoogakker, B. A. A., Lu, Z., Umling, N., Jones, L., Zhou, X., Rickaby, R. E. M., et al. (2018). Glacial expansion of oxygen-depleted seawater in the eastern tropical Pacific. *Nature* 562, 410–413. doi: 10.1038/s41586-018-0589-x

Hughes, D. J., Alderdice, R., Cooney, C., Kühl, M., Pernice, M., Voolstra, C. R., et al. (2020). Coral reef survival under accelerating ocean deoxygenation. *Nat. Clim. Change* 10, 296–307. doi: 10.1038/s41558-020-0737-9

Jacobel, A. W., Anderson, R. F., Jaccard, S. L., McManus, J. F., Pavia, F. J., and Winckler, G. (2020). Deep Pacific storage of respired carbon during the last ice age: Perspectives from bottom water oxygen reconstructions. *Quaternary Sci. Rev.* 230, 106065. doi: 10.1016/j.quascirev.2019.106065

Kerisit, S. N., Smith, F. N., Saslow, S. A., Hoover, M. E., Lawter, A. R., and Qafoku, N. P. (2018). Incorporation modes of iodate in calcite. *Environ. Sci. Technol.* 52, 5902–5910. doi: 10.1021/acs.est.8b00339

Kershaw, J., Stewart, J. A., Strawson, I., de Carvalho Ferreira, M. L., Robinson, L. F., Hendry, K. R., et al. (2023). Ba/Ca of stylasterid coral skeletons records dissolved seawater barium concentrations. *Chem. Geology* 622, 121355. doi: 10.1016/j.chemgeo.2023.121355

Lauvset, S. K., Lange, N., Tanhua, T., Bittig, H. C., Olsen, A., Kozyr, A., et al. (2022). GLODAPv2.2022: the latest version of the global interior ocean biogeochemical data product. *Earth Syst. Sci. Data* 14, 5543–5572. doi: 10.5194/essd-14-5543-2022

Liu, M., and Tanhua, T. (2021). Water masses in the Atlantic Ocean: characteristics and distributions. *Ocean Sci.* 17, 463–486. doi: 10.5194/os-17-463-2021

Lu, W., Dickson, A. J., Thomas, E., Rickaby, R. E. M., Chapman, P., and Lu, Z. (2020a). Refining the planktic foraminiferal I/Ca proxy: Results from the Southeast Atlantic Ocean. *Geochimica Cosmochimica Acta* 287, 318–327. doi: 10.1016/j.gca.2019.10.025

Lu, W., Rickaby, R. E. M., Hoogakker, B. A. A., Rathburn, A. E., Burkett, A. M., Dickson, A. J., et al. (2020b). I/Ca in epifaunal benthic foraminifera: A semi-quantitative proxy for bottom water oxygen in a multi-proxy compilation for glacial ocean deoxygenation. *Earth Planetary Sci. Lett.* 533, 116055. doi: 10.1016/j.epsl.2019.116055

Lu, W., Wang, Y., Oppo, D. W., Nielsen, S. G., and Costa, K. M. (2022). Comparing paleo-oxygenation proxies (benthic foraminiferal surface porosity, I/Ca, authigenic uranium) on modern sediments and the glacial Arabian Sea. *Geochimica Cosmochimica Acta* 331, 69–85. doi: 10.1016/j.gca.2022.06.001

Lu, Z., Jenkyns, H. C., and Rickaby, R. E. M. (2010). Iodine to calcium ratios in marine carbonate as a paleo-redox proxy during oceanic anoxic events. *Geology* 38, 1107–1110. doi: 10.1130/G31145.1

Lu, Z., Lu, W., Rickaby, R. E. M., and Thomas, E. (2020c). *Earth History of Oxygen and the iprOxy (Elements in Geochemical Tracers in Earth System Science)*. (Cambridge: Cambridge University Press). doi: 10.1017/9781108688604

Lu, Z., Hoogakker, B. A. A., Hillenbrand, C.-D., Zhou, X., Thomas, E., Gutchess, K. G., et al. (2016). Oxygen depletion recorded in upper waters of the glacial Southern Ocean. *Nat. Commun.* 7, 11146. doi: 10.1038/ncomms11146

Luther, G. W. (2023). Review on the physical chemistry of iodine transformations in the oceans. *Front. Mar. Sci.* 10. doi: 10.3389/fmars.2023.1085618

Moriyasu, R., Bolster, K. M., Hardisty, D. S., Kadko, D. C., Stephens, M. P., and Moffett, J. W. (2023). Meridional survey of the central pacific reveals iodide accumulation in equatorial surface waters and benthic sources in the abyssal plain. *Global Biogeochemical Cycles* 37, e2021GB007300. doi: 10.1029/2021GB007300

Moriyasu, R., Evans, N., Bolster, K. M., Hardisty, D. S., and Moffett, J. W. (2020). The distribution and redox speciation of iodine in the Eastern Tropical North Pacific Ocean. *Global Biogeochem. Cycles* 34. doi: 10.1029/2019GB006302

Mucci, A. (1983). The solubility of calcite and aragonite in seawater at various salinities, temperatures, and one atmosphere total pressure. *Am. J. Sci.* 283, 780–799. doi: 10.2475/ajs.283.7.780

Orejas, C., Wienberg, C., Titschack, J., Tamborrino, L., Freiwald, A., and Hebbeln, D. (2021). Madrepora oculata forms large frameworks in hypoxic waters off Angola (SE Atlantic). *Sci. Rep.* 11, 15170. doi: 10.1038/s41598-021-94579-6

Oschlies, A., Brandt, P., Stramma, L., and Schmidtko, S. (2018). Drivers and mechanisms of ocean deoxygenation. *Nat. Geosci* 11, 467–473. doi: 10.1038/s41561-018-0152-2

Pelletier, G. J., Lewis, E., and Wallace, D. (2007). CO2SYS. XLS: A calculator for the CO2 system in seawater for Microsoft Excel/VBA. (Olympia, WA/Upton, NY, USA: Washington State Department of Ecology/Brookhaven National Laboratory).

Peters, B. D., Jenkins, W. J., Swift, J. H., German, C. R., Moffett, J. W., Cutter, G. A., et al. (2018). Water mass analysis of the 2013 US GEOTRACES eastern Pacific zonal transect (GP16). *Mar. Chem.* 201, 6–19. doi: 10.1016/j.marchem.2017.09.007

Podder, J., Lin, J., Sun, W., Botis, S. M., Tse, J., Chen, N., et al. (2017). Iodate in calcite and vaterite: Insights from synchrotron X-ray absorption spectroscopy and first-principles calculations. *Geochimica Cosmochimica Acta* 198, 218–228. doi: 10.1016/j.gca.2016.11.032

Rapp, I., Schlosser, C., Browning, T. J., Wolf, F., Le Moigne, F. A. C., Gledhill, M., et al. (2020). El Niño-driven oxygenation impacts Peruvian shelf iron supply to the South Pacific Ocean. *Geophys. Res. Lett.* 47. doi: 10.1029/2019GL086631

Roberts, J. M., Wheeler, A. J., and Freiwald, A. (2006). Reefs of the deep: The biology and geology of cold-water coral ecosystems. *Science* 312, 543–547. doi: 10.1126/science.1119861

Robinson, L. F., Adkins, J. F., Frank, N., Gagnon, A. C., Prouty, N. G., Brendan Roark, E., et al. (2014). The geochemistry of deep-sea coral skeletons: A review of vital effects and applications for palaeoceanography. *Deep Sea Res. Part II: Topical Stud. Oceanography* 99, 184–198. doi: 10.1016/j.dsr2.2013.06.005

Ross, T., Du Preez, C., and Ianson, D. (2020). Rapid deep ocean deoxygenation and acidification threaten life on Northeast Pacific seamounts. *Global Change Biol.* 26, 6424–6444. doi: 10.1111/gcb.15307

Rue, E. L., Smith, G. J., Cutter, G. A., and Bruland, K. W. (1997). The response of trace element redox couples to suboxic conditions in the water column. *Deep Sea Res. Part I: Oceanographic Res. Papers* 44, 113–134. doi: 10.1016/S0967-0637(96)00088-X

Salinas-de-León, P., Martí-Puig, P., Buglass, S., Arnés-Urgellés, C., Rastoin-Laplane, E., Creemers, M., et al. (2020). Characterization of deep-sea benthic invertebrate megafauna of the Galapagos Islands. *Sci. Rep.* 10, 13894. doi: 10.1038/s41598-020-70744-1

Stewart, J. A., Li, T., Spooner, P. T., Burke, A., Chen, T., Roberts, J., et al. (2021). Productivity and dissolved oxygen controls on the Southern Ocean Deep-Sea Benthos during the antarctic cold reversal. *Paleoceanog Paleoclimatol* 36, e2021PA004288. doi: 10.1029/2021PA004288

Stewart, J. A., Robinson, L. F., Day, R. D., Strawson, I., Burke, A., Rae, J. W. B., et al. (2020). Refining trace metal temperature proxies in cold-water scleractinian and stylasterid corals. *Earth Planetary Sci. Lett.* 545, 116412. doi: 10.1016/j.epsl.2020.116412

Sumida, P. Y. G., Bernardino, A. F., and De Léo, F. C. (2020). *Brazilian Deep-Sea Biodiversity*. (Cham: Springer International Publishing). doi: 10.1007/978-3-030-53222-2

Thiagarajan, N., Gerlach, D., Roberts, M. L., Burke, A., McNichol, A., Jenkins, W. J., et al. (2013). Movement of deep-sea coral populations on climatic timescales: CORAL POPULATIONS AND CLIMATE. *Paleoceanography* 28, 227–236. doi: 10.1002/palo.20023

Truesdale, V. W., Bale, A. J., and Woodward, E. M. S. (2000). The meridional distribution of dissolved iodine in near-surface waters of the Atlantic Ocean. *Prog. Oceanography* 45, 387–400. doi: 10.1016/S0079-6611(00)00009-4

Winkelbauer, H., Cordova-Rodriguez, K., Reyes-Macaya, D., Scott, J., Glock, N., Lu, Z., et al. (2021). Foraminifera iodine to calcium ratios: approach and cleaning. *Geochem Geophys Geosyst* 22. doi: 10.1029/2021GC009811

Wong, G. T. F., and Brewer, P. G. (1977). The marine chemistry of iodine in anoxic basins. *Geochimica Cosmochimica Acta* 41, 151–159. doi: 10.1016/0016-7037(77)90195-8

Zhou, X., Hess, A. V., Bu, K., Sagawa, T., and Rosenthal, Y. (2022). Simultaneous determination of I/ca and other elemental ratios in foraminifera: comparing results from acidic and basic solutions. *Geochem Geophys Geosyst* 23. doi: 10.1029/2022GC010660

Zhou, X., Thomas, E., Rickaby, R. E. M., Winguth, A. M. E., and Lu, Z. (2014). I/Ca evidence for upper ocean deoxygenation during the PETM. *Paleoceanography* 29, 964–975. doi: 10.1002/2014PA002702

frontiers | Frontiers in Marine Science

TYPE Original Research
PUBLISHED 08 January 2024
DOI 10.3389/fmars.2023.1272968

Check for updates

OPEN ACCESS

EDITED BY
Gregory A. Cutter,
Old Dominion University, United States

REVIEWED BY
Martha Gledhill,
Helmholtz Association of German Research Centres (HZ), Germany
Maija Iris Heller,
University of Galway, Ireland

*CORRESPONDENCE
Iulia-Mădălina Ştreangă
iuliams@mit.edu

RECEIVED 04 August 2023
ACCEPTED 13 December 2023
PUBLISHED 08 January 2024

CITATION
Ştreangă I-M, Repeta DJ, Blusztajn JS and Horner TJ (2024) Speciation and cycling of iodine in the subtropical North Pacific Ocean. *Front. Mar. Sci.* 10:1272968. doi: 10.3389/fmars.2023.1272968

COPYRIGHT
© 2024 Ştreangă, Repeta, Blusztajn and Horner. This is an open-access article distributed under the terms of the Creative Commons Attribution License (CC BY). The use, distribution or reproduction in other forums is permitted, provided the original author(s) and the copyright owner(s) are credited and that the original publication in this journal is cited, in accordance with accepted academic practice. No use, distribution or reproduction is permitted which does not comply with these terms.

Speciation and cycling of iodine in the subtropical North Pacific Ocean

Iulia-Mădălina Ştreangă[1,2,3]*, Daniel J. Repeta[1], Jerzy S. Blusztajn[3,4] and Tristan J. Horner[1,3]

[1]Department of Marine Chemistry and Geochemistry, Woods Hole Oceanographic Institution, Woods Hole, MA, United States, [2]Department of Earth, Atmospheric and Planetary Sciences, Massachusetts Institute of Technology, Cambridge, MA, United States, [3]NIRVANA Labs, Woods Hole Oceanographic Institution, Woods Hole, MA, United States, [4]Department of Geology and Geophysics, Woods Hole Oceanographic Institution, Woods Hole, MA, United States

Iodine intersects with the marine biogeochemical cycles of several major elements and can influence air quality through reactions with tropospheric ozone. Iodine is also an element of interest in paleoclimatology, whereby iodine-to-calcium ratios in marine carbonates are widely used as a proxy for past ocean redox state. While inorganic iodine in seawater is found predominantly in its reduced and oxidized anionic forms, iodide (I^-) and iodate (IO_3^-), the rates, mechanisms and intermediate species by which iodine cycles between these inorganic pools are poorly understood. Here, we address these issues by characterizing the speciation, composition and cycling of iodine in the upper 1,000 m of the water column at Station ALOHA in the subtropical North Pacific Ocean. We first obtained high-precision profiles of iodine speciation using isotope dilution and anion exchange chromatography, with measurements performed using inductively coupled plasma mass spectrometry (ICP-MS). These profiles indicate an apparent iodine deficit in surface waters approaching 8% of the predicted total, which we ascribe partly to the existence of dissolved organic iodine that is not resolved during chromatography. To test this, we passed large volumes of seawater through solid phase extraction columns and analyzed the eluent using high-performance liquid chromatography ICP-MS. These analyses reveal a significant pool of dissolved organic iodine in open ocean seawater, the concentration and complexity of which diminish with increasing water depth. Finally, we analyzed the rates of IO_3^- formation using shipboard incubations of surface seawater amended with $^{129}I^-$. These experiments suggest that intermediate iodine species oxidize to IO_3^- much faster than I^- does, and that rates of IO_3^- formation are dependent on the presence of particles, but not light levels. Our study documents the dynamics of iodine cycling in the subtropical ocean, highlighting the critical role of intermediates in mediating redox transformations between the major inorganic iodine species.

KEYWORDS

Station ALOHA, iodate formation, organic iodine, iodine intermediates, oxidation mechanisms

10.3389/fmars.2023.1272968

1 Introduction

Understanding marine iodine geochemistry is imperative due to its integral role in numerous environmental processes. The ocean is the major source of iodine to the atmosphere via both biological and non-biological pathways (Fuge and Johnson, 2015). Once released, photochemically active iodocarbons have tropospheric lifetimes ranging from a few minutes to a few days (Solomon et al., 1994; Carpenter et al., 2021). Upon photolysis and oxidation, these organic halogens form IO radicals, a major source of particles that can act as cloud condensation nuclei and influence cloud properties (Bluhm et al., 2010). Furthermore, dissolved iodide reacts with tropospheric ozone at the surface ocean, fueling a catalytic pathway (Chance et al., 2014) that accounts for approximately 15% tropospheric ozone loss globally (Sherwen et al., 2016a; Sherwen et al., 2016b). Iodine is also an element of interest in paleoclimatology, with iodine-to-calcium ratios in marine carbonates being widely interpreted as proxies for the oxygenation state of the ocean through geological time (e.g. Lu et al., 2018; Lu et al., 2020; Sun et al., 2023). In seawater, iodine is primarily found in its reduced and oxidized anionic forms, iodide (I^-) and iodate (IO_3^-), respectively. Measurements of total iodine concentrations across the world's oceans reveal relatively constant values between 450–500 nM. Despite being thermodynamically unstable in oxygenated waters, I^- can be the dominant iodine species in coastal and low latitude regions, with concentrations as high as 300 nM (e.g., Chance et al., 2014; Sherwen et al., 2019). At latitudes above 40° north and south and deeper in the water column, IO_3^- is the dominant species (Chance et al., 2014; Chance et al., 2020). Unraveling the underlying reasons for this distinctive speciation pattern, particularly in the surface ocean, necessitates a deeper understanding of the processes governing iodine transformations.

One of the central challenges to understanding iodine biogeochemistry lies in elucidating the rates, mechanisms and intermediates involved in the transformation of iodine between its reduced and oxidized forms. It is generally thought that I^- oxidation to IO_3^- is much slower than the reverse transformation at both high and low oxygen concentrations (Hardisty et al., 2021); however, I^- oxidation is a highly uncertain process (Carpenter et al., 2021). Previous studies have reported I^- oxidation rates ranging between 1.5–8.2 nM yr^{-1} (He et al., 2013) and 560 nM yr^{-1} in oxic waters (Campos et al., 1996), mostly determined by mass balance approaches. Abiotic I^- oxidation is thought to be too slow to account for the more rapid I^- oxidation rates reported to date. Instead, I– oxidation is thought to be mediated by particles, such as reactive Mn oxides, by reactive oxygen species produced photochemically, or via direct or indirect biological processes (e.g., Amachi, 2008; Bluhm et al., 2010; Carpenter et al., 2021; Luther, 2023). Given that there is a six-electron transfer between I^- and IO_3^-, it is unlikely that I^- oxidation leads directly to IO_3^- production. Instead, several intermediate iodine species likely mediate this transformation, such as molecular iodine (I_2), hypoiodous acid (HOI) and iodite (IO_2^-; Luther, 2023; Figure 1). Both HOI and I_2 can react with organic matter to form iodine-bearing organic compounds (Luther, 2023), which have yet to be chemically characterized. The existence of these compounds has been documented in coastal areas (Luther et al., 1991), but they are widely considered to be negligible in the open ocean (Edwards and Truesdale, 1997; Wadley et al., 2020). A mismatch observed between the amounts of IO_3^- reduced and I^- produced during incubation studies has led to the suggestion that dissolved organic iodine (DOI) can be synthesized by a wide range of microalgae and cyanobacteria (Chance et al., 2007; van Bergeijk et al., 2016; Hepach et al., 2020).

Conventional methods lack the precision required to discern subtle variations in iodine speciation during an experiment, which can be particularly significant in the case of slow processes, such as I^- oxidation. The most common method used for measuring I^- concentrations is cathodic stripping square wave voltammetry (Luther et al., 1988a; Chance et al., 2014; Moriyasu et al., 2020; Moriyasu et al., 2023), while IO_3^- is usually quantified using differential pulse polarography (Herring and Liss, 1974) and spectrophotometric methods (Wong and Brewer, 1974; Rue et al., 1997). In most studies, only I^- or IO_3^- is measured, alongside total inorganic iodine, and the difference between the two is used to calculate the abundance of the other species (Liss et al., 1973; Takayanagi and Wong, 1986; Jickells et al., 1988; Truesdale and Jones, 2000). These conventional approaches for measuring iodine speciation achieve a typical precision of between 5 and 10% (Campos et al., 1996), which are unlikely to resolve the small changes in iodine speciation that are believed to occur over short timescales. Thus, incubation experiments are particularly suitable for studying iodine cycling over short timescales. While a new method using ion exchange chromatography coupled to spectrophotometric iodine detection can achieve a precision as good as 2–4% (Jones et al., 2023), any concentration-based approach to studying iodine redox transformations is fundamentally limited by the difficulty in constraining the specific reaction pathway involved in the formation of a given iodine species (Figure 1).

To address these challenges, we leveraged a recently developed method using ^{129}I, a long-lived radioactive isotope of iodine (half-life of 15.7 Myr), as a tracer to study iodine redox transformations in seawater. In the context of our experiments, the natural abundance of ^{129}I in the open ocean is negligible, with $^{129}I/^{127}I$ ratios varying between 10^{-11} and 10^{-6} (Qi et al., 2023). By coupling isotope dilution to chromatographic separation of iodine measurement by ICP-MS, this method, adapted from Hardisty et al. (2020), offers unprecedented precision for measuring iodine speciation and transformation rates. Short incubation experiments can be conducted to study the rates and mechanisms of these reactions, on timescales relevant to biological processes occurring in the ocean. Likewise, recent developments in high-pressure liquid chromatography ICP-MS (HPLC-ICP-MS) and electrospray ionization MS have enabled the isolation and quantification of low-abundance organic ligands in seawater (Boiteau et al., 2013; Boiteau and Repeta, 2015; Li et al., 2021). These methods can be used to test for the existence of DOI.

In this study, we investigated the rates, mechanisms and intermediates governing iodine redox transformations in the subtropical North Pacific Ocean near Station ALOHA. We

10.3389/fmars.2023.1272968

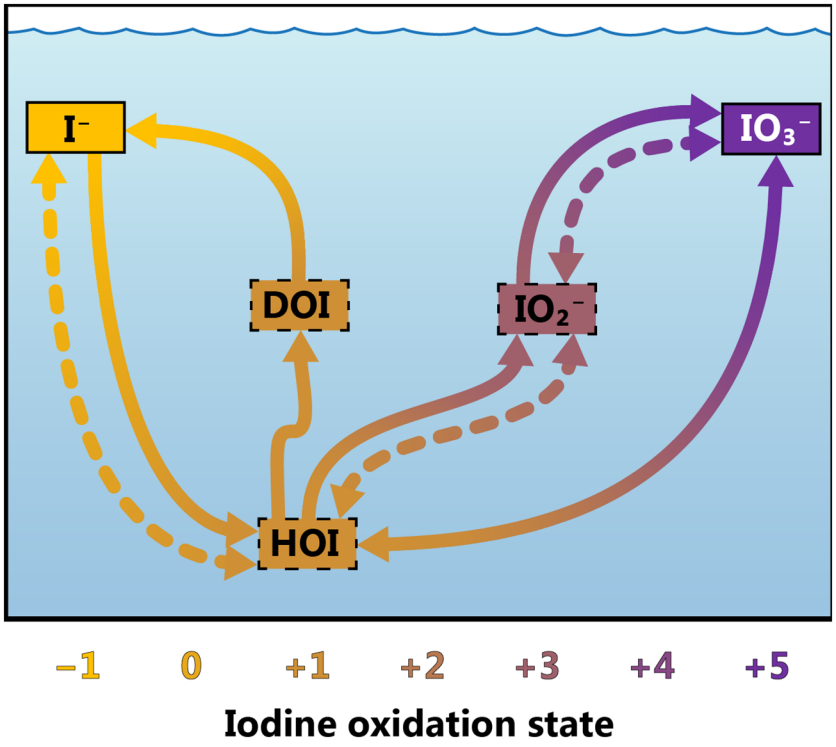

FIGURE 1
Conceptual model of iodine cycling at Station ALOHA. Arrows represent transformations between various iodine species. Abiotic processes are represented as dotted lines and biotic or biologically mediated processes with solid lines. The solid bounding boxes around iodide and iodate indicate that these species are resolved by our ion-exchange chemistry, while the dotted bounding boxes around the other species imply that they are not resolved by our method. Iodide (I^-), iodate (IO_3^-), iodite (IO_2^-), hypoiodous acid (HOI) and dissolved organic iodine (DOI) have been included, while molecular iodine, I_2 (oxidation state 0), has been omitted. Dissolved organic iodine has been assigned an oxidation state of +1, although its precise composition is unknown.

tackled these issues in four steps. First, we report profiles of iodine speciation measured using isotope dilution ICP-MS and compare our results with the pioneering work of Campos et al. (1996). Second, we apply a novel HPLC-ICP-MS method to investigate the existence of DOI in open ocean seawater samples. Third, we conduct short-term ^{129}I-amended incubation experiments to constrain rates of IO_3^- formation. Finally, we use the same series of experiments to investigate the roles of particles and light on the formation of IO_3^-. This research advances our understanding of iodine cycling in seawater and the role of particles and organics in sustaining it.

2 Methods

2.1 Sample collection

Samples were collected onboard the R/V *Kilo Moana* between 22 July and 5 August 2021 (Cruise ID KM2112). Sampling occurred at and around Station ALOHA (Figure 2), as part of the Simons Collaboration on Ocean Processes and Ecology (SCOPE) Particles and Growth in the Oceanic Nutricline (PARAGON) cruise. The profile samples were collected in 60 mL high density polyethylene (HDPE) bottles that were cleaned in several steps. First, bottles were soaked in a 1% Citranox© solution for one week, before rinsing five times with deionized water. Second, bottles were soaked in a 10% (by volume) solution of hydrochloric acid (HCl) for one week, then rinsed three times with 18.2 MΩ cm^{-2}-grade water from a Milli-Q system (MilliporeSigma©). For all profile samples, 60 mL of seawater were filtered directly from the Go-Flo bottle using a 0.2 µm Pall© Acropak-200 Supor filter. Information about the time and location at which the three CTD profiles were collected is summarized in Table 1. Profile 2 was collected with a conventional rosette, whereas Profiles 1 and 3 were collected with a trace-metal–clean rosette. The samples were refrigerated immediately after collection. Spiking and chromatographic separation of iodine was performed within 14 months of collection using 20 mL of seawater from each profile sample. Iodine speciation in filtered seawater is stable for at least a year if samples are stored refrigerated and sealed (Campos, 1997).

The shipboard incubations were conducted in triplicate over a 60-hour period, with surface water collected with a conventional rosette from a fourth CTD deployment (Table 1; Figure 2). All 60 mL incubation samples were collected into polycarbonate bottles cleaned using the same protocol as for HDPE bottles. Polycarbonate bottles were placed in an on-deck incubator that was continuously flushed with surface seawater to maintain *in situ* temperature. Four different conditions were tested (Table 1). Prior to the start of the

10.3389/fmars.2023.1272968

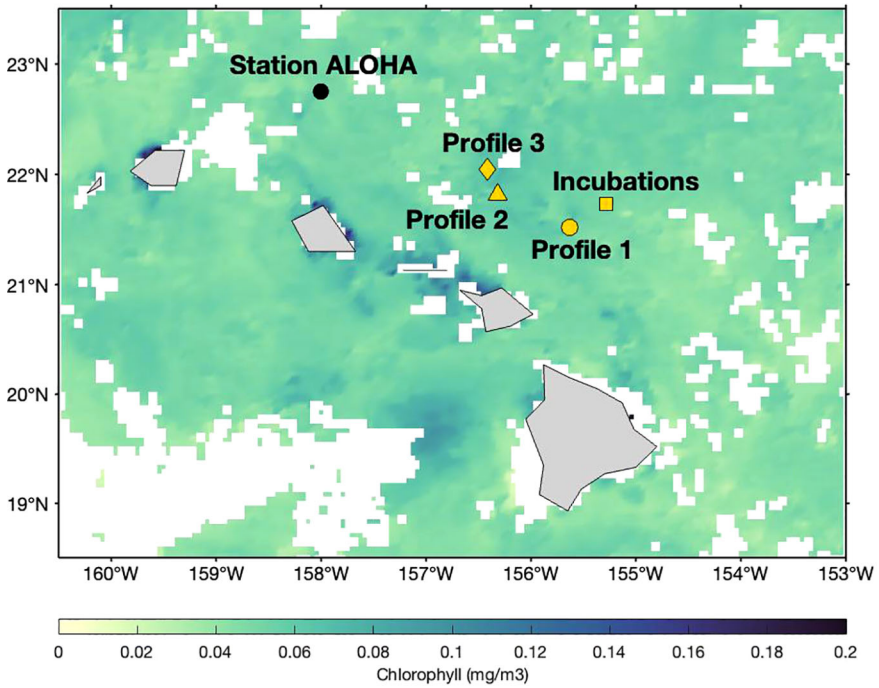

FIGURE 2
Locations of deployments relative to Station ALOHA: Profile 1 (filled circle), Profile 2 (filled triangle), Profile 3 (filled diamond) and location corresponding to the collection of incubation samples (filled square). The surface chlorophyll data is the 8-day composite of Stage Level 3 NASA Aqua-MODIS Ocean Color data product between 28 July–4 August 2021.

incubation period, each 60 mL sample was individually spiked with 45 µL of a ^{129}I working solution. At each of the six sampling timepoints, an entire sample volume was sacrificed for all corresponding triplicates under the four conditions. The added spike amount was ≈ 45 nM ^{129}I, approximately 10% of the previously determined *in situ* total ^{127}I concentrations. The working solution was prepared by adding 1.366 mL of an Eckert & Ziegler© stock spike solution, with a total activity of 18,500 Bq (0.5 µCi) ^{129}I in the form of sodium iodide, to 48.634 mL of 18.2 MΩ H_2O. Triplicates were incubated and processed every 12 hours. At each sampling point, the unfiltered samples were filtered through a 0.2 µm filter, collected and stored at 4°C. The filtered samples were not filtered again prior to refrigeration. Laboratory analysis on these samples was conducted between 14–18 months after collection.

2.2 Determination of stock spike solution composition and speciation

In order to accurately use ^{129}I for isotope dilution ICP-MS, the ^{129}I/^{127}I ratio and total iodine concentration of the spike solution needed to be determined. This was achieved by preparing a set of 10 standards with spike-to-standard volumetric mixing ratios between 0.03 and 1. These were prepared by mixing a SPEX CertiPrep© 1,000 µg mL^{-1} ^{127} I^- standard solution, the stock spike solution and 18.2 MΩ H_2O in various known proportions, and measuring using a quadrupole ICP-MS (Thermo Scientific© iCap-Q) at the Woods Hole Oceanographic Institution (WHOI) Plasma Facility. The theoretical ^{129}I/^{127}I ratio of each mixture was calculated using Equation 1:

TABLE 1 Summary of deployment information for the profile and incubation samples.

Deployment	Event ID	Location	Type of sample	Date (GMT)	Time points
Profile 1	TM5	21°31'N 155°38'W	Profile	2021-07-27	N/A
Profile 2	CTD 27	21°49'N 156°19'W		2021-07-30	
Profile 3	TM 13	22°03'N 156°25'W		2021-07-31	
Exp. 1 (light, unfiltered)	CTD 6	21°44'N 155°17'W	Incubation	2021-07-25	0, 12, 24, 36, 48, 60 hours
Exp. 2 (dark, unfiltered)					
Exp. 3 (light, filtered)					
Exp. 4 (dark, filtered)					

10.3389/fmars.2023.1272968

$$\frac{129}{127}I_{theoretical} = \frac{(1 - f_{127-std}) * \frac{129}{127}I_{spike} * [I]_{spike}}{f_{127-std} * [I]_{127-std} + (1 - f_{127-std}) * [I]_{spike}} \quad (1)$$

where $f_{127-std}$ is the volumetric fraction of the certified ^{127}I standard solution in the prepared standard solution; $\frac{129}{127}I_{spike}$ is the iodine isotopic ratio of the stock spike solution; $[I]_{spike}$ is the total iodine concentration of the spike solution in nmol mL^{-1} and $[I]_{127-std}$ is the total iodine concentration of the certified ^{127}I standard solution. We then calculated the $^{129}I/^{127}I$ of the spike by finding the composition that minimized the root-mean-square error between theoretical and measured $^{129}I/^{127}I$ for the 10 mixtures. This exercise revealed that the best-fit spike composition was $\frac{129}{127}I_{spike}$= 3.76 and $[I]_{spike}$= 626 nmol mL^{-1}. The spike composition was also determined using MC-ICP-MS, yielding a $^{129}I/^{127}I$ of 3.58, which is ≈ 5% lower than that determined using ICP-MS. The MC-ICP-MS value was obtained without standard addition, via a direct analysis of the spike itself using the wet-sparge sample introduction method (Section 2.5.). The slight difference in spike composition between the two measurement approaches likely derives from differences in the sample introduction method (liquid versus wet sparge) and from instrument-specific considerations (e.g., collision cell, plasma conditions, lens stack). For consistency between approaches, a spike composition of 3.76 was assumed for all samples measured using the ICP-MS and a value of 3.58 for those measured using MC-ICP-MS.

2.3 Calculation of spike amounts to be added to profile samples

Optimal spiking for isotope dilution is achieved when the $^{129}I/^{127}I$ ratio of the target mixture is close to the geometric mean of the natural and spike compositions (Stracke et al., 2014). This raises two issues for iodine. First, in most natural seawater, ^{129}I is essentially absent compared to ^{127}I (e.g., 0.03 fM in the subtropical Pacific Ocean; Qi et al., 2023). This means that the optimal $^{129}I/^{127}I$ ratio would be so low as to be unamenable to analysis by ICP-MS. Second, the concentration of different inorganic iodine species varies with depth. Thus, optimal spiking requires prior knowledge of the iodine distribution. To work around these issues, we estimated likely *in situ* $[IO_3^-]$ and $[I^-]$ from literature data and aimed for a target $^{129}I/^{127}I$ ratio of between 0.5–1.0 for both iodine fractions. This wider target ensured that there was sufficient ^{129}I for analysis in each sample, and likewise reduced the relative magnitude of the interference from isobaric xenon-129 on *m/z* 129.

Iodine species separation was achieved in two steps: first by eluting I^-, followed by separating IO_3^- after reducing it to I^- and similarly eluting it. Therefore, each 20 mL seawater sample was spiked twice, before and after the isolation of the I^- fraction. Table 2 summarizes the targeted concentrations and the amounts of ^{129}I working solution which were added to the profile samples collected from various depths. The approximate I^- and IO_3^- *in situ* concentrations were estimated from the results reported in Campos et al. (1996) for Station ALOHA during the summer. Procedural blanks were monitored by processing 20 mL aliquots of 18.2 MΩ H_2O alongside profile samples. Blanks were spiked with the same amount of ^{129}I as seawater samples below 500 m depth. No procedural blanks were processed alongside the incubation experiment samples, since this correction would affect all samples equally and would not change the overall trends.

2.4 Chromatographic separation of reduced and oxidized iodine species

Sample processing took place within Class 100 laminar flow workbenches situated in the NIRVANA Labs (Non-traditional Isotope Research on Various Advanced Novel Applications). We used a two-step chromatographic protocol to separate and isolate the major inorganic forms of iodine in seawater. This protocol was based on the method described by Hardisty et al. (2020). Briefly, separation was performed by packing acid-cleaned 5 mm (inner diameter) quartz-glass columns with 0.5 mL of AG-1X8 anion-exchange resin (BioRad©). The resin was batch cleaned with 6 M reagent-grade HCl (Fischer Scientific© ACS plus) and thoroughly rinsed with 18.2 MΩ H_2O prior to loading onto the columns. Due to initially very high iodine concentrations in our procedural blanks, we introduced a cleaning protocol which followed the first step of the chromatographic procedure, substituting seawater sample with 18.2 MΩ H_2O.

TABLE 2 Determination of optimal volume of working solution to be added to profile samples in the first and the second steps, based on approximate I^- and IO_3^- *in situ* concentrations at each depth.

Depth (m) of seawater sample	Approx. $[I^-]$ (nM) in seawater sample	Approx. $[IO_3^-]$ (nM) in seawater sample	Optimal $[^{129}I]$ (nM) for first spiking event (prior to I^- separation)	First step (µl of working solution added)	Optimal $[^{129}I]$ (nM) for second spiking event (after I^- separation)	Second step (µl of working solution added)
500 -1000	0	450	0.06	10	270	399.6
300 - 400	50	400	30	44.4	240	355.2
200, 250	100	350	60	88.8	210	310.8
100 - 150	150	300	90	133.2	180	266.4
5 - 75	200	250	120	177.6	150	222
Blank	0	0	0.06	10	0.06	10

After rinsing the resin and loading 20 mL seawater sample, the oxidized iodine fraction was collected, spiked, refrigerated overnight and further processed the following day. Simultaneous with the spike addition, 500 µL of 1.2 M HCl and 80 µL of 0.3 M sodium bisulfite ($NaHSO_3$, Acros© ACS-grade) were added to the IO_3^- fraction to completely reduce it to I^-. The final I^- fraction was eluted following the addition of 15 mL of a mixed 2 M nitric acid (HNO_3; Fisher Scientific© certified ACS plus) and 18% tetramethylammonium hydroxide solution (TMAH, Alfa Aesar© 25% w/w aq. Solution Electronic Grade) and refrigerated. The role of TMAH was to keep iodine stable in solution and prevent its volatilization (Hardisty et al., 2020). The second step of the separation involved rinsing the loaded resin again and loading the oxidized fraction (containing the reduced IO_3^-) onto the columns. The final IO_3^- fraction was then eluted (as I^-) with 15 mL of the 2 M HNO_3 and 18% TMAH solution, collected and refrigerated. The processed samples were analyzed via mass spectrometry within weeks of separation.

The chromatographic separation of the profile samples differed slightly from that of the incubation samples. Since the incubation samples had already been amended with $^{129}I^-$, they were not spiked again in the laboratory prior to the separation of reduced and oxidized iodine. The entire volume (60 mL) of the incubation experiments was loaded onto the columns to maximize the quantity of ^{129}I for measurement via MC-ICP-MS. This difference in processed sample volumes necessitated an increase in the amounts of HCl and $NaHSO_3$ added to the incubation samples prior to the second step in the separation (1 mL HCl and 160 µL $NaHSO_3$, respectively).

2.5 Instrumental analyses and data reduction

All spiked seawater samples were analyzed at the WHOI Plasma Facility. Seawater profile samples were analyzed using a quadrupole ICP-MS operated in Kinetic Energy Discrimination mode with helium as the collision cell gas. Solutions were prepared in 2 mL polypropylene vials soaked in a 50% (by volume) solution of concentrated reagent-grade HCl. The vials contained 100 µL of the collected final fraction (in 2 M HNO_3 and 18% TMAH), 20 µL of a 10 µg mL^{-1} Tellurium (Te, Assurance© 1000 mg L^{-1} Te) standard solution (internal standard) and 1.88 mL 18.2 MΩ H_2O. To account for instrument memory, a solution containing only 2 M HNO_3, 18% TMAH and Te was analyzed between each sample. Likewise, the wash solution used between samples contained 2 M HNO_3 and 18% TMAH, but no Te.

Data processing comprised several steps, namely: removing xenon (Xe) interferences on m/z 129, noting that Xe is present in trace amounts in the argon carrier gas; correcting for instrumental mass fractionation; isolating memory effects; and quantifying procedural blanks. The process started by assigning an initial value for the instrumental mass bias correction factor, f (in this case, 6). This value was used together with raw $^{131}Xe/^{126}Te$ to calculate true (solar) fractionation-corrected $^{131}Xe/^{126}Te$ ratios, which were then used to determine the contribution of ^{126}Te to the m/z 126 ion beam for each sample and blank. This allowed us to calculate raw Xe-corrected $^{126}Te/^{125}Te$ ratios, which could then be used to re-assess f according to Equation 2. The process was iterated three times to ensure convergence of the final f value. The next step involved correcting for the contribution of ^{129}Xe to the 129 ion beam in a similar fashion, in order to obtain ^{129}Xe-corrected ^{129}I counts. The preceding blank in the instrumental run sequence was subtracted from every sample to correct for instrument memory. The resultant $^{129}I/^{127}I$ ratios were then corrected for instrumental mass fractionation. These corrected values were then used, together with the stock spike solution isotopic composition and the known volumes of added working solution, to calculate each sample's initial ^{127}I concentration in nM.

$$\frac{M_{126Te^f}}{M_{125Te}} = \frac{\frac{126Te}{125Te_{raw}}}{\frac{126Te}{125Te_{solar}}} \quad (2)$$

The incubation experiments were analyzed using a ThermoFinnigan© Neptune MC-ICP-MS, also situated in the WHOI Plasma Facility, according to the gas-based sparge approach described in Hardisty et al. (2020). This method involves introducing iodine into the instrument as a gas, by reacting it with a strong oxidizing agent, in this case concentrated HNO_3. For all measurements, 4 mL of sample (in 2 M HNO_3 and 18% TMAH) were combined with 2 mL of 18.2 MΩ H_2O, and 4 mL of concentrated HNO_3 were injected through a syringe to volatilize the iodine to I_2 gas (Hardisty et al., 2020). To minimize the risk of extinguishing the plasma, the tubing connecting the sparge vial with the sample to the Neptune was disconnected upon HNO_3 addition and reconnected after the first few seconds of reaction.

Corrections similar to those described above for the profile samples were applied in MATLAB (Mathworks©) to account for background iodine contributions, Xe interference and instrumental mass fractionation. Final values for $^{129}I/^{127}I$ ratios were weighted using an integration-by-integration approach based on the intensities of the 129- and 127-iodine beams (Hardisty et al., 2020).

2.6 Separation and analysis of DOI

Polycarbonate bottles, cleaned following the protocol described above, were used to collect 4L samples at various depths from the CTD27 cast (using the conventional rosette; Table 1; Figure 2). These samples were first filtered through 0.2 µm Pall Acropak-200 Supor filters before being extracted on Bond-Elut ENV (1 g, 6 mL, Agilent©) solid phase extraction (SPE) columns, by pumping each sample at a rate of 20 mL min^{-1}. Before sample collection, the SPE columns were conditioned with three column volumes of methanol, followed by three column volumes of 18.2 MΩ H_2O. The SPE columns were frozen at −20°C after extraction and shipped frozen to WHOI at the end of the cruise. Approximately one year after the cruise, the SPE columns were thawed, rinsed with 6 mL of 18.2 MΩ H_2O to remove salts, and eluted with 6 mL of distilled methanol (Optima, Fischer Scientific©). To concentrate the DOI compounds in a final volume of 500 µL, the methanol extracts were placed in a vacuum centrifuge (SpeedVac, Thermo Scientific©) for 3.5 hours at 35°C.

The samples were analyzed via HPLC-ICP-MS, which allows the separation of iodine-bearing organic compounds in each sample based on the compounds' polarity. A 20 µL sample aliquot was combined with 5 µL of a cobalamin solution (used as internal standard) and 25 µL of 18.2 MΩ H_2O. A 10 µL aliquot of this solution was loaded onto a C18 column (0.5 x 150 mm, 3.5 µm particle size, Agilent©) connected to a Dionex Ultimate 3000 LC system (Thermo Scientific©). The LC system flow was directed into an iCAP Q (Thermo Scientific©) quadrupole MS at a rate of 20 µL min^{-1} using the instrument's loading pump module. After a 10 minute initial hold at 95/5% A/B (A = 5mM ammonium formate solution in 18.2 MΩ H_2O, B = 5mM ammonium formate solution in distilled methanol), the DOI compounds were separated using a 30-minute gradient to 5/95% A/B, followed by a 10-minute isocratic hold at 5/95% A/B. Helium was used as the collision gas and oxygen was introduced at 25 mL min^{-1} throughout the analysis, to prevent carbon deposits from forming on the ICP-MS interface. The intensity of the ^{127}I ion beam was monitored in Kinetic Energy Discrimination mode using an integration time of 0.01 seconds.

3 Results

3.1 *In situ* measurements

3.1.1 Inorganic speciation

The concentrations of reduced, oxidized, total, and salinity-predicted iodine for the three vertical profiles are shown in Figure 3. All associated data are provided in Supplementary Table 1. Iodide and IO_3^- concentrations were determined using isotope dilution ICP-MS. Total iodine concentrations were calculated as the sum of I^- and IO_3^-. The salinity-predicted iodine concentrations were estimated assuming a total iodine:salinity ratio of 15., which is the arithmetic mean of the seven samples measured at or below 500 m. *In situ* salinity was then used to predict total iodine at each depth, and any excess (or deficit) in iodine was quantified by comparing the salinity-predicted value to the measured total.

In addition to the samples, the I^- and IO_3^- concentrations for two 18.2 MΩ H_2O blanks and one 800 m sample (from Profile 2), which was analyzed twice, were processed to quantify contamination during processing. The 800 m sample was assumed to have negligible I^- concentration, as expected of deep-water samples. The average of the two I^- concentrations measured in this sample (4.5 nM) was used to calculate sample processing blanks and was subtracted from all I^- measurements. Negative values obtained for all but one 18.2 MΩ H_2O I^- and IO_3^- blanks could not be used to determine process blanks. The limit of detection, calculated as 3 standard deviations of all I^- and IO_3 process blanks (excluding IO_3^- concentrations measured in the 800 m sample), was determined as 10.5 nM 3 SD, (n = 6). All I^- concentrations below this value were considered below detection and assigned a value of zero.

Iodide concentrations are highest in the first 150 m of the water column, remaining relatively constant at 206 ± 11 nM (± 2 SD, n = 13). Below that, I^- concentrations decrease rapidly to negligible values deeper than 300 m. The distribution of IO_3^- shows the opposite pattern, with lower concentrations of 284 ± 12 nM (± 2 SD, n = 13) in the first 150 m, followed by an increase to concentrations around 482 ± 60 nM (± 2 SD, n = 19) below this depth. As previously mentioned, it is expected for IO_3^- to dominate iodine speciation deeper in the water column, due to its thermodynamic stability under oxygenated conditions. These

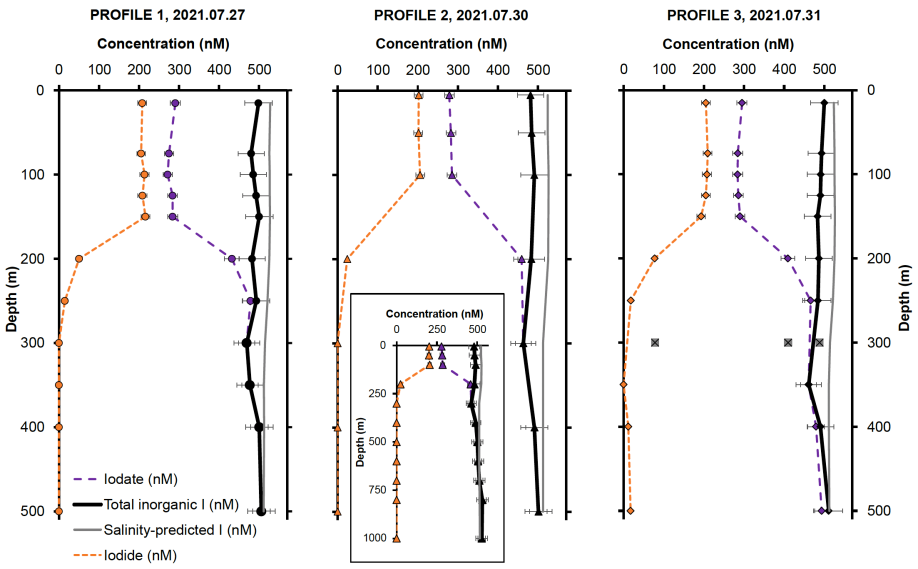

FIGURE 3
Inorganic iodine speciation and concentrations for Profile 1, Profile 2 and Profile 3, collected on July 27, 30 and 31, respectively. The outliers at 300 m in Profile 3 are most probably due to contamination during shipboard sampling or from bottles triggering at a different depth. Error bars represent two relative standard deviations from the arithmetic mean of all measurements for a particular iodine species (I^-, IO_3^-) in the first 150 m of the water column. The inset in the Profile 2 panel shows iodine speciation concentrations in nM over the whole depth profile (1000 m). The symbols in each panel match the profile collection sites shown in Figure 2.

inorganic iodine concentration patterns agree well with previously reported measurements at Station ALOHA, which show high surface I^- and corresponding low surface IO_3^- concentrations at low latitudes, characteristic of the Atlantic (Truesdale et al., 2000; Campos et al., 1999), Pacific (Tsunogai and Henmi, 1971) and Indian oceans (Chance et al., 2020) tropical waters. There is good agreement between the I^- and IO_3^- distributions in all three CTD profiles, as shown in Figure 3.

We estimate the precision of our iodine speciation measurements using the profile data. To do so, we assumed that I^- and IO_3^- were invariant over the top 150 m, and calculated the RSD of all I^- and IO_3^- measurements in this depth range. Using this method, our measurement precision is estimated as ±4.3% for IO_3^-, ± 5.3% for I^-, and ±6.8% (2 RSD) for total iodine concentrations.

A comparison of total iodine with salinity-predicted iodine reveals resolvable apparent iodine deficits near the sea surface. This deficit may signify a potential loss of iodine from surface waters, either to the atmosphere or deeper ocean, or it might denote an 'apparent deficit,' whereby certain iodine species are unresolved by our chromatographic methods. We discuss possible explanations in more detail in Section 4.3. Regardless of the cause, this apparent iodine deficit is lowest for Profile 3 (24 ± 0.5 nM in surface waters; ± 2 SD, $n = 7$) and highest for Profile 2 (43 ± 0.5 nM at the surface; ± 2 SD, $n = 7$). The apparent deficit constitutes 6% and 7% of salinity-predicted total iodine in the top 100 m for Profile 3 and Profile 1 respectively, and 8% for Profile 2.

3.1.2 Dissolved organic iodine

The chromatograms shown in Figure 4 correspond to samples collected at multiple depths. Each of the well-defined peaks represents one or several discrete DOI compounds, which elute at different times during the HPLC-ICP-MS analysis as a function of their polarities. More polar compounds elute early, while non-polar compounds elute toward the end of the analysis. Several such peaks of different intensities are observed in the 5 m sample. Fewer discrete peaks are present as depth increases, with three large peaks seen in the 200 m sample, but only one dominant peak in the 500 m and 1000 m samples. A major feature of the 5 m chromatogram is the presence of a large unresolved complex mixture, which appears as a rise in the baseline in Figure 4 and decreases in abundance deeper in the water column, as seen in the other chromatograms. The unresolved complex mixture represents DOI compounds that are present in seawater, but are not well resolved by the chromatographic methods used here. More unresolved compounds are present in the upper 200 m of the water column than at depth.

3.2 Rate experiments

We observe significant and systematic changes in $(^{129}I/^{127}I)_{iodate}$ during our 60-hour incubation experiments (Figure 5). Since some IO_3^- is present in the $^{129}I^-$ spike (Hardisty et al., 2020), all experiments start with $(^{129}I/^{127}I)_{iodate} \approx 0.04$. This value represents a mixture between IO_3^- added in the spike ($^{129}I/^{127}I \approx 3.6$; Section 2.2.) and background IO_3^- present in seawater ($^{129}I/^{127}I \approx 0$). Additionally, incubation samples were not homogenized prior to the start of the experiments, as each of the 60 mL bottles was filled and spiked separately. Therefore, the $^{129}I/^{127}I$ ratios at t=0 varied between individual samples, and this variation is a source of uncertainty between triplicates analyses. To calculate the precision of individual $(^{129}I/^{127}I)_{iodate}$ values, we performed a bootstrapped uncertainty estimation. Here we randomly selected three of the t_0 samples and calculated their mean $^{129}I/^{127}I$ ratio, repeating the

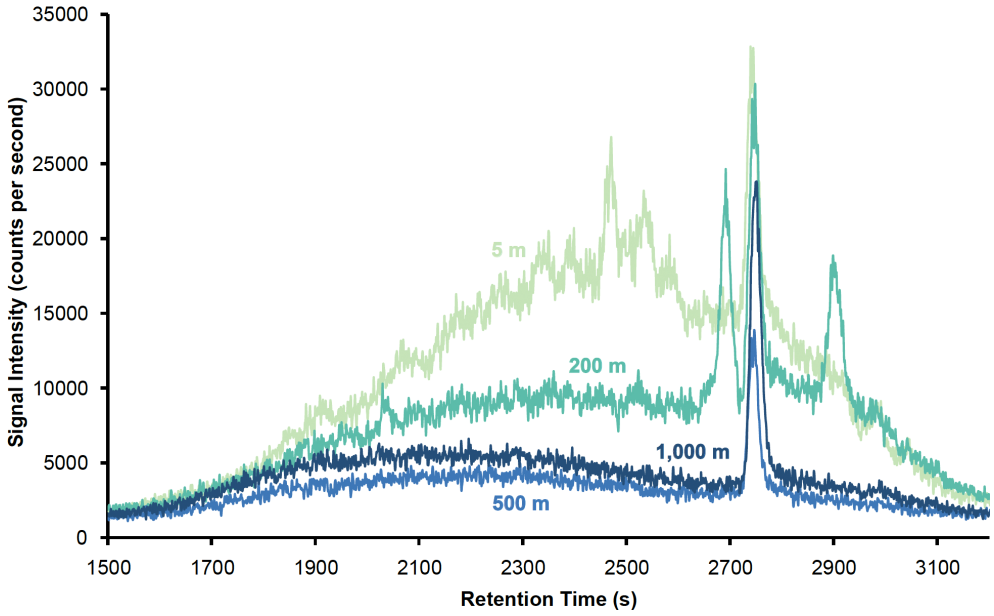

FIGURE 4
^{127}I HPLC-ICP-MS chromatograms of samples collected from the CTD27 cast at 5, 200, 500 and 1000 m.

random selection 100,000 times. The initial IO_3^- isotopic ratio for all four experiments, $(^{129}I/^{127}I)_{iodate}$ = 0.0360, was assumed to be the mean ratio from the 100,000 iterations (dotted lines in Figure 5). The measurement uncertainty was calculated as two standard deviations of the bootstrapped means (± 0.00302; 2 SD; gray shaded areas in Figure 5), equivalent to an uncertainty of 8.3% (2 RSD). The $^{129}I/^{127}I$ ratio in the I^- fraction for the rate experiments was also measured. If we apply the same uncertainty (8.3%) to the measured $(^{129}I/^{127}I)_{iodide}$, no significant changes in the I^- isotopic ratios are observed in any of the experiments (data shown in Supplementary Table 2). Therefore, our discussion is focused on investigating trends in $(^{129}I/^{127}I)_{iodate}$.

Variations in $(^{129}I/^{127}I)_{iodate}$ across the four experiments ranged from 0.0280 to 0.0365, equivalent to relative changes from the initial value of 0.0360 of -22.3 and +1.3%, respectively (Figure 5; Table 3). Of the 60 time course measurements, 51 fall below the initial $(^{129}I/^{127}I)_{iodate}$, although only the two unfiltered experiments remain outside the initial value during the 60-hour interval. Both unfiltered experiments have mean $(^{129}I/^{127}I)_{iodate}$=0.030 between t=12 hours and t=60 hours, which is 16-17% lower than $(^{129}I/^{127}I)_{iodate}$ at t=0. In contrast, the filtered–dark experiment has a decrease of only 8% to $^{129}I/^{127}I$=0.033, while the filtered–light experiment decreases by 6% to $^{129}I/^{127}I$=0.034 over the last 48 hours. These smaller changes for the filtered experiments are within measurement uncertainty of the initial value. Beyond 48 hours, both unfiltered experiments show a slight increase in $(^{129}I/^{127}I)_{iodate}$, with the final samples at 60 hours back to within uncertainty of the initial composition.

4 Discussion

4.1 Comparison with historical data

The concentration profiles chosen for comparison with our dataset are the June 1994 measurements reported in the seasonal study that Campos et al. (1996) conducted at the Hawaii Ocean Time series (HOT), centered around Station ALOHA. These profiles were selected because they were also sampled during summer, and they covered a depth range similar to the one used for our measurements. In their study, concentrations of I^-, IO_3^- and total iodine were determined in the upper 500 m of the water column using voltammetry and differential pulse polarography (Takayanagi and Wong, 1986; Luther et al., 1988a), with higher measurement resolution in the top 250 m compared to the rest of

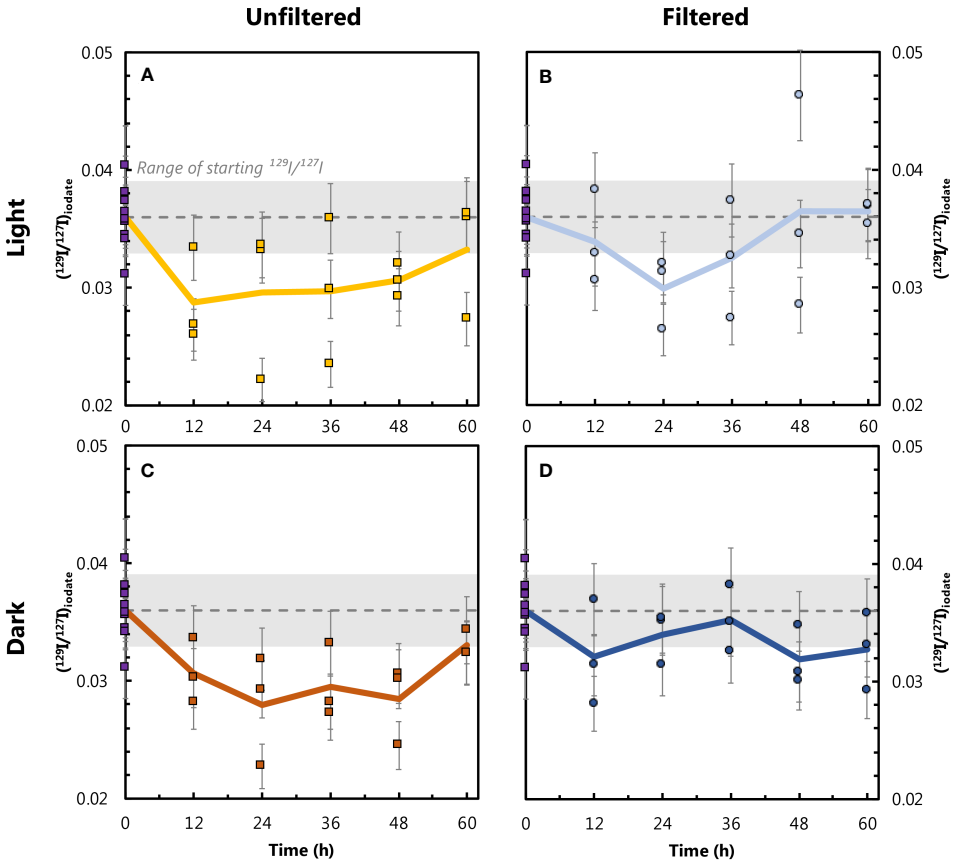

FIGURE 5
Changes in $(^{129}I/^{127}I)_{iodate}$ over the course of the incubation experiments for the unfiltered–light **(A)**, filtered–light **(B)**, unfiltered–dark **(C)** and filtered–dark **(D)** conditions. The dotted lines correspond to the average isotopic ratio at t=0 (0.036), generated via bootstrapping as described in the main text. The gray shaded areas correspond to two standard deviations resulting from the bootstrapping analysis. Error bars for triplicate data points represent 8.3% measurement precision uncertainty. The thick lines represent arithmetic means of triplicate measurements throughout the experiments.

10.3389/fmars.2023.1272968

TABLE 3 Replicate measurements of iodate $^{129}I/^{127}I$ at each time point and arithmetic means of replicates for the four incubation experiments.

Timepoint	Replicate	Unfiltered–light	Filtered–light	Unfiltered–dark	Filtered–dark
t=0	a	0.034	0.034	0.036	0.036
	b	0.038	0.034	0.031	0.034
	c	0.040	0.036	0.040	0.037
	Triplicate mean	*0.038*	*0.035*	*0.036*	*0.036*
t=12 hours	a	0.027	0.031	0.034	0.031
	b	0.033	0.033	0.030	0.028
	c	0.026	0.038	0.028	0.037
	Triplicate mean	*0.029*	*0.034*	*0.031*	*0.032*
t=24 hours	a	0.022	0.026	0.029	0.031
	b	0.033	0.032	0.032	0.035
	c	0.034	0.031	0.023	0.035
	Triplicate mean	*0.030*	*0.030*	*0.028*	*0.034*
t=36 hours	a	0.023	0.027	0.033	0.033
	b	0.036	0.033	0.028	0.038
	c	0.030	0.037	0.027	0.035
	Triplicate mean	*0.030*	*0.032*	*0.030*	*0.035*
t=48 hours	a	0.032	0.046	0.031	0.031
	b	0.029	0.028	0.025	0.030
	c	0.031	0.035	0.030	0.035
	Triplicate mean	*0.031*	*0.036*	*0.028*	*0.032*
t=60 hours	a	0.027	0.037	0.032	0.029
	b	0.036	0.037	0.032	0.036
	c	0.036	0.035	0.034	0.033
	Triplicate mean	*0.033*	*0.036*	*0.033*	*0.033*

All uncertainties are estimated as ± 8.3 % (2 SD). See Section 3.2. for details.

the profiles (Figure 6A). For a more direct comparison between our study and that of Campos et al. (1996), a composite upper 500 m profile was created by averaging iodine concentrations from Profiles 1, 2 and 3 from this study at each depth (Figure 6B). Profile 2 values were used at depths 5 and 50 m.

The general shape of the profiles reported by Campos et al. (1996) for summer 1994 is similar to the results reported here, showing the characteristic decrease in I^- and increase in IO_3^- with increasing water depth. However, one difference between the two studies is the rate of change in iodine concentrations between surface and deeper waters. Our results indicate a rapid change in iodine concentrations between 150 and 200 m depth, whereas Campos et al. (1996) record a more gradual decline in I^- and increase in IO_3^- from the surface down to 250 m depth. Their results also show greater variability in iodine speciation in the upper 200 m, with IO_3^- concentrations changing by up to 140 nM between 25 and 40 m, for instance. The lack of variability in surface iodine concentrations reported in this study can mostly be attributed to the increased precision of our isotope dilution method compared to the conventional methods used by Campos et al. (1996). We believe that the smaller variations in the upper water column are indicative of our newer measurements being more oceanographically consistent.

Despite these differences in precision, however, there is good agreement between iodine concentrations measured almost 30 years apart at Station ALOHA. For instance, I^- concentrations in the upper 100 m average 215 ± 52 nM in 1994 and 206 ± 11 nM for the three profiles analyzed in this study. This overall similarity increases our confidence in affirming that the results we report here are representative of general conditions around Station ALOHA. The long residence time of surface water at Station ALOHA (approximately 10 years) led Campos et al. (1996) to conclude that IO_3^- reduction by phytoplankton is the main source of I^- to the euphotic zone. Thus, they invoked a correspondingly rapid rate of I^- oxidation (560 nM/year) to explain why I^- concentrations remain constant and do not approach total iodine concentrations over the residence time of the water.

It is also noteworthy that Campos et al. (1996) did not detect any evidence for iodine depletion at the time of their measurements.

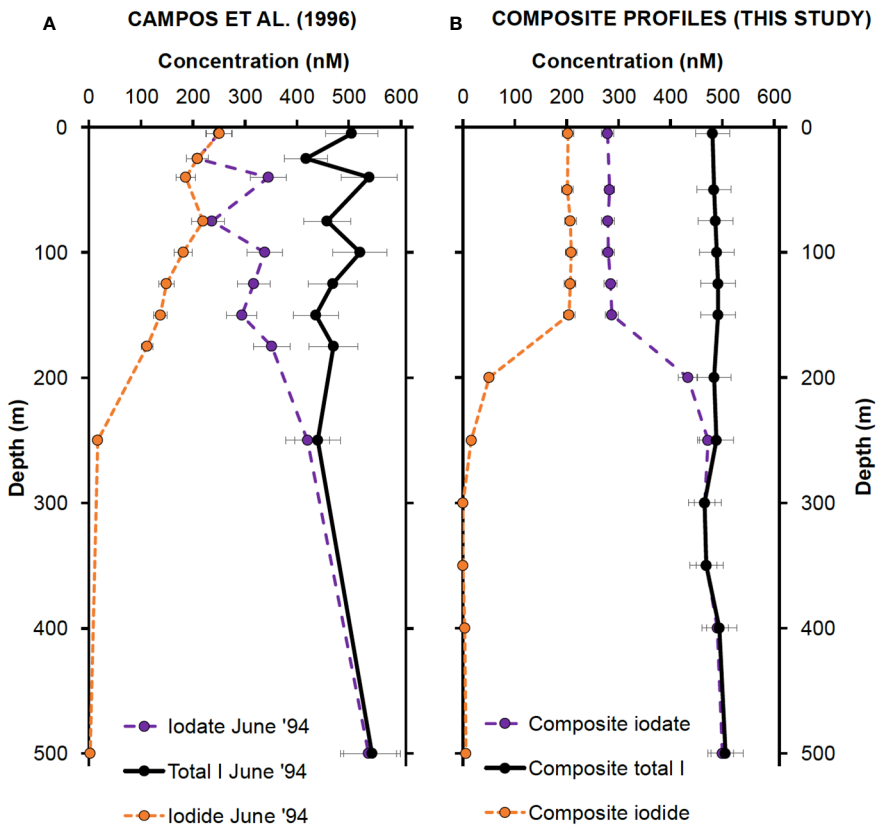

FIGURE 6
(A) Inorganic iodine speciation measurements made in June 1994 by Campos et al., 1996. The data were extracted graphically using the WebPlotDigitizer software (https://automeris.io/WebPlotDigitizer/). Error bars represent 10% uncertainty estimates. **(B)** Composite upper 500 m profiles created by averaging iodine concentrations from Profiles 1, 2 and 3 (this study) at each depth. Profile 2 values were used at depths 5 and 50 m. Error bars correspond to precision previously estimated for iodide, iodate and total iodine (5.3%, 4.3% and 6.8%, respectively).

In contrast, we observe deficits in the top 100 m that constitute up to 8% of salinity-predicted total iodine. Our observations are consistent with data reported by Elderfield and Truesdale (1980), who noted that total iodine depletions of up to 13% are common in stratified tropical waters. To discern whether these deficits indicate actual losses of iodine to the atmosphere or deeper water, or if they represent apparent deficits due to organic iodine species that are unresolved during chromatography, we performed a direct examination of the characteristics of DOI, discussed next.

4.2 Identification of significant open-ocean DOI

In order to gain a more complete understanding of iodine cycling at Station ALOHA, we collected samples for DOI analysis. These samples provide insight into a less studied dimension of iodine cycling in the region, but also more generally in the open ocean, where it is widely believed that DOI does not constitute a significant component of the iodine pool (Luther et al., 1991; Wadley et al., 2020).

The dominant peak observed at all depths in Figure 4 is a common feature of all four chromatograms, indicating that the DOI compound(s) it corresponds to are found throughout the upper 1000 m of the water column at Station ALOHA, at higher concentration compared to the other DOI compounds resolved by this chromatographic separation. The overall decrease in the amount of unresolvable complex DOI compounds with increasing water depth suggests that the DOI fraction at Station ALOHA is more abundant and increasingly complex closer to the surface.

These results confirm the presence of a DOI fraction in the euphotic zone at Station ALOHA. Although identification of the individual compounds that comprise this fraction will have to await further processing, this analysis is the first step toward the characterization of DOI in this region. While it is challenging to provide absolute concentrations with the method as implemented here, a semi-quantitative analysis indicates that the most abundant discrete peaks correspond to compounds found in concentrations on the order of pM in seawater. However, only a fraction of the dissolved organic matter present in seawater might be retained by the SPE column, therefore these estimates are a lower bound on DOI concentrations.

4.3 Iodate formation rates during the incubation experiments

The results from the incubation experiments can be used to provide insight into the factors which determine the rate of IO_3^- formation in surface waters at Station ALOHA. Campos et al.

(1996) assumed that horizontal advection processes in the region do not play an important role in iodine cycling, although they considered mixing out of the euphotic zone as a sink for I^-. Assuming I^- oxidation is a first-order reaction, the authors calculated the rate constant of this reaction to be 5.15 $year^{-1}$. In this and the next sections, we use the results from the incubation experiments to revisit the magnitude of the contribution of *in situ* I^- oxidation to the total sink of I^- at Station ALOHA.

The goal of the incubation experiments was to observe and quantify the rate of IO_3^- formation. This was achieved by labeling the I^- pool, as this is believed to be the primary substrate for IO_3^- formation. Were we to observe IO_3^- formation from I^- oxidation over the course of the experiments, we would expect to see an increase in $(^{129}I/^{127}I)_{iodate}$. Our experimental approach is analogous to how oxidation kinetics for other elements have been investigated in the past (for instance, Moffett, 1994).

We observe systematic differences in $(^{129}I/^{127}I)_{iodate}$ over the course of the experiments. Moreover, inter-experiment variations indicate that certain treatments affected IO_3^- formation rates. In the case of the filtered–light and filtered–dark experiments, the arithmetic means of the triplicates of most time points are within (or very close to) uncertainty of the starting composition, indicating no significant change in $(^{129}I/^{127}I)_{iodate}$ over the course of these incubations. However, the arithmetic means of the triplicates from the unfiltered experiments dip below the initial value after t=0. The largest decline in $(^{129}I/^{127}I)_{iodate}$ occurs in the first 12 hours of the unfiltered–light and unfiltered–dark incubations. For the unfiltered–light experiment, average $(^{129}I/^{127}I)_{iodate}$ at t=12 hours is 0.029, which is 19% lower than $(^{129}I/^{127}I)_{iodate}$ at t=0 (0.036). For the unfiltered–dark experiment, average $(^{129}I/^{127}I)_{iodate}$ decreases by 14% between t=0 and t=12 hours, from 0.036 to 0.031. This initial fast decline is followed by a period between t=12 hours and t=48 hours, during which $(^{129}I/^{127}I)_{iodate}$ shows little variation for both unfiltered experiments, remaining well below the initial isotopic composition. The unfiltered experiments show a slight increase in $(^{129}I/^{127}I)_{iodate}$ at t=60 hours, with the triplicates from both experiments averaging 0.033 (8% below the initial value). While it is not clear whether this trend would have continued beyond the final time point, it is plausible that this slight increase in $(^{129}I/^{127}I)_{iodate}$ reflects the oxidation of some spike-derived $^{129}I^-$ through to $^{129}IO_3^-$.

Iodate $^{129}I/^{127}I$ shows the most significant changes in experiments where particles were present. These particles are most likely a mixture of abiotic and biotic components, and they can have multiple roles in the formation of IO_3^-. For instance, abiotic particles containing iodine might dissolve during the experiments, adding ^{127}I to the dissolved IO_3^- pool and causing the $(^{129}I/^{127}I)_{iodate}$ to decrease. Likewise, ^{127}I could be added to the IO_3^- fraction through biotic particles, such as from cell lysis. We deem both possibilities unlikely. First, we are not aware of any abiotic particles that contain significant amounts of iodine. Second, seawater at Station ALOHA typically contains< 2 µg L^{-1} of organic carbon in living biomass (Karl and Church, 2014). If considering an iodine:carbon ratio of 10^{-4} for organic matter (Elderfield and Truesdale, 1980), complete oxidation of this material would add less than 17 pM to the IO_3^- pool. Microorganisms such as ammonia-oxidizing bacteria have been shown to have a catalytic role in IO_3^- formation, promoting I^- oxidation to IO_3^- (Hughes et al., 2021). However, substantial ammonium oxidation rates have only been detected in the lower euphotic zone at Station ALOHA, below the primary nitrite maximum (Dore and Karl, 1996). This suggests that ammonia-oxidizing bacteria do not play a significant role in I^- oxidation in surface waters at Station ALOHA. Due to a lack of culture-based studies focused on I^- oxidation, it is unclear which other microbial groups are able to oxidize significant amounts of I^- to IO_3^- in the ocean, although partial I^- oxidation to small molecular weight organics has been previously documented for various classes of phytoplankton (Manley and de la Cuesta, 1997). Given that there are no obvious differences between the unfiltered–dark and unfiltered–light experiments, it is reasonable to infer that photoautotrophs do not contribute significantly to IO_3^- formation, at least over the course of our experiments.

The decrease in $(^{129}I/^{127}I)_{iodate}$ observed at the beginning of the unfiltered incubations indicates a small but rapid gain of ^{127}I in the IO_3^- pool. The gain of ^{127}I must originate from a pool of iodine that does not contain spike-derived ^{129}I and is not resolved by anion-exchange chromatography. This pool likely contains iodine with oxidation states intermediate between that of I^- (-1) and IO_3^- (+5; Figure 1). As noted in Section 1, several intermediate species are known to mediate I^- oxidation to IO_3^- and would have existed in our incubation samples at the time of spiking. Our analyses do not allow us to confidently identify these intermediates, but we suspect that DOI and HOI are major components of this pool. Indeed, our results in Section 3.1.2. confirm the existence of a significant pool of DOI at Station ALOHA. Thus, for $(^{129}I/^{127}I)_{iodate}$ to initially decline in the unfiltered experiments, the transformation between intermediates and IO_3^- must be much faster than the net oxidation of I^- to IO_3^-. Similarly, intermediates oxidation must be faster than the oxidation of I^- into intermediates, assuming that I^- must first pass through intermediates before being oxidized to IO_3^-.

In this context, it is reasonable to assume that the apparent iodine deficits inferred from our total iodine calculations can be accounted for by this pool of intermediates. The variability in apparent iodine deficits implied by our measurements suggests that changes in the speciation and distribution of intermediate iodine compounds can occur on small spatial and temporal scales, indicating a higher reactivity of this pool compared to I^- and IO_3^-. As mentioned above, the largest changes in $(^{129}I/^{127}I)_{iodate}$ are recorded between t=0 and t=12 hours. Over this interval, the rapid decline in $(^{129}I/^{127}I)_{iodate}$ can be attributed to the transformation of intermediates into IO_3^-, and the measured isotopic ratios at the two initial time points can be used to estimate rate constants for this reaction.

Several studies have documented that the oxidized fraction separated during the second step of the chromatography (Section 2.4.) includes some DOI (Hou et al., 1999; Hardisty et al., 2020). At Station ALOHA, dissolved organic carbon concentrations average 56 µM in the first 1000 m of the water column (Zigah et al., 2017). Considering our sample size of 20 mL (for the profile samples) and an iodine:carbon ratio of 10^{-4} as before, this would correspond to approximately 5.6 nM added DOI, which is below our detection limit of 10.5 nM (Section 3.1.1.). Moreover, were the DOI and IO_3^-

10.3389/fmars.2023.1272968

pools to be analyzed together, our results would not imply apparent iodine deficits in the surface, nor would they show a change in $(^{129}I/^{127}I)_{iodate}$ during the incubation experiments. Therefore, we believe that no significant amounts of DOI were resolved by our inorganic chromatographic separation.

4.4 Calculation of oxidation rates

The surface seawater used for the incubation experiments was collected from a fourth CTD cast (Table 1; Figure 2). Nevertheless, Profile 1 was the most proximal to this fourth cast, both chronologically and geographically. Therefore, for the purpose of estimating the rate of intermediates oxidation to IO_3^-, we considered the seawater $^{127}IO_3^-$ concentration prior to spiking equal to that measured at 15 m depth in the TM5 profile (291 nM). The $(^{129}I/^{127}I)_{iodate}$ at t=0 was set to 0.036, as calculated from the bootstrapping analysis detailed in Section 3.2. Using this initial isotopic ratio, concentrations of $^{127}IO_3^-$ and $^{129}IO_3^-$ immediately after spike addition were determined. The $(^{129}I/^{127}I)_{iodate}$ values at t=12 hours were set to 0.029 and 0.031 for the unfiltered–light and unfiltered–dark experiments respectively (average of triplicates, Table 3). These calculations assume that the pool of intermediates is initially free of ^{129}I and that there is no formation of $^{129}IO_3^-$ during the first 12 hours. Given the uncertainty regarding the nature of the oxidation reactions, we calculated rate constants assuming zero, first and second order kinetics.

The reaction rate constants for the oxidation of intermediates to IO_3^- in the unfiltered experiments are summarized in Table 4. These rate constants were calculated as a function of the product (IO_3^-) and represent minimum gross rates at which IO_3^- is being generated from the oxidation of spike-free intermediates in surface waters. Our calculations do not account for possible concomitant reduction of IO_3^- to DOI, so these numbers represent net, rather than gross, oxidation rates over the first 12 hours. These rates correspond to a consumption of around 70 nM of intermediates during the initial 12 hours, which is around two times larger than our estimates for the apparent iodine deficits in any of the CTD profiles discussed in this study (the largest being 43 ± 0.5 nM at the surface for Profile 2). Considering zero-order kinetics, we estimate that between 34,000 (for the unfiltered–dark conditions) and 50,000 (for the unfiltered–light experiment) nM of intermediates oxidize to IO_3^- every year. For such high oxidation rates to be sustained, the pool of intermediates in seawater must be rapidly replenished, but these experiments do not shed light on this process.

Our calculated rates of intermediates oxidation at Station ALOHA are extremely rapid relative to rates of I^- oxidation to IO_3^-. Since $(^{129}I/^{127}I)_{iodate}$ ratios decrease systematically during the experiments, but do not increase significantly until t=60 hours, we infer that net I^- to IO_3^- oxidation rates at Station ALOHA are slower than the rate of oxidation of intermediates to IO_3^-. Unfortunately, given the large uncertainty in reaction kinetics and the lack of constraints on the abundance and isotopic evolution of the intermediates, it is not possible to obtain more precise estimates at this time. The first order rate constant reported by Campos et al. (1996) of 5.15 $year^{-1}$ is orders of magnitude smaller than our first order estimates for the oxidation of intermediates. However, the overall reaction rates also depend on the concentrations of the reactants. The I^- pool is much larger than the pool of intermediates in seawater; in the absence of more information about the *in situ* formation of intermediate iodine species, we would therefore expect I^- oxidation to be the dominant source of IO_3^- over longer time scales, as opposed to oxidation of intermediates, due to the fast exhaustion of this latter pool.

The slight increase in $(^{129}I/^{127}I)_{iodate}$ in the last 12 hours of the unfiltered experiments may be evidence of some $^{129}I^-$ being completely oxidized to IO_3^-. The trend can be seen in both light and dark unfiltered treatments; however, this trend remains tentative and longer-term incubation studies will be required to assess whether oxidation continues beyond this time.

We propose a conceptual model of iodine cycling in the oligotrophic ocean, schematically represented in Figure 1. Although we can estimate the contribution of only one of these arrows to total iodine cycling, this model could be referred to for future work aimed at disentangling the complex interactions between the numerous iodine species co-existing in the ocean. More information about the abundance and identity of DOI and iodine intermediates are needed in order to better constrain the variables included in this model and to confidently determine rates of I^- oxidation in the surface ocean.

TABLE 4 Reaction rate constants for the oxidation of iodine intermediates into iodate, determined as a function of iodate concentrations and isotopic ratios in the unfiltered experiments for various reaction kinetics.

	0 order: k ($nM/year^{-1}$)	1st order: k ($year^{-1}$)	2nd order: k (nM^{-1} $year^{-1}$)
Unfiltered–light	5.16E+04	1.57E+02	4.81E-01
Unfiltered–dark	3.44E+04	1.09E+02	3.43E-01

5 Conclusions

The results reported in this study offer an updated perspective on iodine speciation and cycling at Station ALOHA. Our methodological approaches include the application of isotope dilution and mass spectrometry to measure concentrations and isotopic ratios of various iodine pools with increased precision compared to historical speciation measurements. Inorganic iodine distributions at Station ALOHA are in agreement with global patterns showing increased surface I^- concentrations in tropical waters and a shift toward IO_3^--dominated waters below the euphotic zone. In general, there is good agreement between concentrations reported almost thirty years ago and measurements made in this study. Salinity-predicted iodine concentrations reveal the existence of an apparent iodine deficit in surface waters, which we suspect is composed of iodine species of intermediate oxidation state, such as HOI and DOI. Indeed, we

collected and analyzed large volumes of seawater and obtained a profile of DOI, a component of the dissolved iodine pool which has previously been considered negligible in the open ocean. Although total iodine abundances are dominated by the inorganic forms, our results document the existence of DOI at Station ALOHA, showing systematic decreases in abundance and complexity with increasing water depth. While additional analyses will be needed to identify the organic compounds that comprise the DOI pool, our results demonstrate its complex nature. Short-term incubation experiments further reveal a fast gain of ^{127}I in the IO_3^- pool that we attribute to rapid oxidation of to ^{127}I -bearing intermediate species, such as DOI and HOI. Net I^- oxidation to IO_3^- occurs slower than the oxidation of intermediates to IO_3^-; however, assignment of reaction rate constants depends heavily on reaction order, which remains unknown. The presence of particles accelerates IO_3^- formation, although light levels have no effect. Overall I^- oxidation must be a slow process, as confirmed by a lack of significant increase in $(^{129}I/^{127}I)_{iodate}$ over the course of 60-hour incubations.

Data availability statement

The original contributions presented in the study are included in the article/Supplementary Material. Further inquiries can be directed to the corresponding author.

Author contributions

I-MŞ: Formal Analysis, Investigation, Writing – original draft, Writing – review & editing, Methodology. TH: Conceptualization, Formal Analysis, Funding acquisition, Supervision, Visualization, Writing – review & editing, Methodology. DR: Conceptualization, Funding acquisition, Supervision, Writing – review & editing, Methodology. JB: Formal Analysis, Investigation, Writing – review & editing, Methodology.

Funding

The author(s) declare financial support was received for the research, authorship, and/or publication of this article. This work was supported by grants from the Simons Foundation (Simons Collaboration on Ocean Ecology [SCOPE] Award 329108 to DR), the U.S. National Science Foundation (to TH) and by the *Breene M. Kerr Early Career Scientist Endowment Fund* (OCE-2023456 to TH).

Acknowledgments

We thank the crew of *R/V Kilo Moana* for their help in collecting the samples and Maureen Auro for assisting with the chromatographic separation of inorganic iodine. We are grateful to Lydia Babcock-Adams, Jay Li and Matthew McIlvin for their assistance with running the HPLC and ICP-MS; Gretchen Swarr for help in the WHOI Plasma Facility; Dalton Hardisty for his valuable comments on the manuscript; Alexi Schnur for sharing helpful insights about the laboratory protocols; and Michael Dotzel for expertise with exploring multiple modeling approaches.

Conflict of interest

The authors declare that the research was conducted in the absence of any commercial or financial relationships that could be construed as a potential conflict of interest.

Publisher's note

All claims expressed in this article are solely those of the authors and do not necessarily represent those of their affiliated organizations, or those of the publisher, the editors and the reviewers. Any product that may be evaluated in this article, or claim that may be made by its manufacturer, is not guaranteed or endorsed by the publisher.

Supplementary material

The Supplementary Material for this article can be found online at: https://www.frontiersin.org/articles/10.3389/fmars.2023.1272968/full#supplementary-material

References

Amachi, S. (2008). Microbial contribution to global iodine cycling: volatilization, accumulation, reduction, oxidation and sorption of iodine. *Microbes Environ.* 23, 269–276. doi: 10.1264/jsme2.ME08548

Bluhm, K., Croot, P., Wuttig, K., and Lochte, K. (2010). Transformation of iodate to iodide in marine phytoplankton driven by cell senescence. *Aquat. Biol.* 11 (1), 1–15. doi: 10.3354/ab00284

Boiteau, R. M., Fitzsimmons, J. N., Repeta, D. J., and Boyle, E. A. (2013). Detection of iron ligands in seawater and marine cyanobacteria cultures by high-performance liquid chromatography – inductively coupled plasma-mass spectroscopy. *Analytical Chem.* 85, 4357–4362. doi: 10.1021/ac3034568

Boiteau, R. M., and Repeta, D. J. (2015). An extended siderophore suite from Synechococcus sp. PCC 7002 revealed by LC-ICPMS-ESIMS. *Metallomics* 7, 877–884. doi: 10.1039/C5MT00005J

Campos, M. L. A. M. (1997). New approach to evaluating dissolved iodine speciation in natural waters using cathodic stripping voltammetry and a storage study for preserving iodine species. *Mar. Chem.* 57, 107–117. doi: 10.1016/S0304-4203(96)00093-X

Campos, M. L. A. M., Farrenkopf, A. M., Jickells, T. D., and Luther, G. W.III (1996). A comparison of dissolved iodine cycling at the Bermuda Atlantic Time-series Station

and Hawaii Ocean Time-series Station. *Deep Sea Res. II* 43 (2-3), 455–466. doi: 10.1016/0967-0645(95)00100-X

Campos, M. L. A. M., Sanders, R., and Jickells, T. (1999). The dissolved iodate and iodide distribution in the South Atlantic from the Weddell Sea to Brazil. *Mar. Chem.* 65, 167–175. doi: 10.1016/S0304-4203(98)00094-2

Carpenter, L. J., Chance, R. J., Sherwen, T., Adams, T. J., Ball, S. M., Evans, M. J., et al. (2021). Marine iodine emissions in a changing world. *Proc. to R. Soc. A* 477, 20200824. doi: 10.1098/rspa.2020.0824

Chance, R., Baker, A., Carpenter, L., and Jickells, T. (2014). The distribution of iodide at the sea surface. *Environ. Sciences: Processes Impacts* 16 (8), 1841–1859. doi: 10.1039/C4EM00139G

Chance, R., Malin, G., Jickells, T., and Baker, A. (2007). Reduction of iodate to iodide by cold water diatom cultures. *Mar. Chem.* 105 (1-2), 169–180. doi: 10.1016/j.marchem.2006.06.008

Chance, R., Tinel, L., Sarkar, A., Sinha, A., Mahajan, A., Chacko, R., et al. (2020). Surface inorganic iodine speciation in the Indian and southern oceans from 12°N to 70° S. *Front. Mar. Sci.* 7. doi: 10.3389/fmars.2020.00621

Dore, J. E., and Karl, D. M. (1996). Nitrification in the euphotic zone as a source for nitrite, nitrate and nitrous oxide at Station ALOHA. *Limnology Oceanography* 41, 1619–1628. doi: 10.4319/lo.1996.41.8.1619

Edwards, A., and Truesdale, V. W. (1997). Regeneration of inorganic iodine species in Loch Etive, a natural leaky incubator. *Estuarine Coast. Shelf Sci.* 45, 357–366. doi: 10.1006/ecss.1996.0185

Elderfield, H., and Truesdale, V. W. (1980). On the biophilic nature of iodine in seawater. *Earth Planetary Sci. Lett.* 50, 105–114. doi: 10.1016/0012-821X(80)90122-3

Fuge, R., and Johnson, C. C. (2015). Iodine and human health, the role of environmental geochemistry and diet, a review. *Appl. Geochemistry* 63, 282–302. doi: 10.1016/j.apgeochem.2015.09.013

Hardisty, D., Horner, T., Evans, N., Moriyasu, R., Babbin, A., Wankel, S., et al. (2021). Limited iodate reduction in shipboard seawater incubations from the Eastern Tropical North Pacific oxygen deficient zone. *Earth Planetary Sci. Lett.* 554, 116676. doi: 10.1016/j.epsl.2020.116676

Hardisty, D. S., Horner, T. J., Wankel, S. D., Blusztajn, J., and Nielsen, S. G. (2020). Experimental observations of marine iodide oxidation using a novel sparge-interface MC-ICP-MS technique. *Chem. Geology* 532, 119360. doi: 10.1016/j.chemgeo.2019.119360

He, P., Hou, X., Aldahan, A., Possnert, G., and Yi, P. (2013). Iodine isotopes species finger-printing environmental conditions in surface water along the northeastern Atlantic Ocean. *Sci. Rep.* 3, 2685. doi: 10.1038/srep02685

Hepach, H., Hughes, C., Hogg, K., Collings, S., and Chance, R. (2020). Senescence as the main driver of iodide release from a diverse range of marine phytoplankton. *Biogeosciences* 17, 2453–2471. doi: 10.5194/bg-17-2453-2020. 2020.

Herring, J. R., and Liss, P. S. (1974). A new method for the determination of iodine species in seawater. *Deep Sea Res.* 21, 777–783. doi: 10.1016/0011-7471(74)90085-0

Hou, X., Dahlgaard, H., Rietz, B., Jacobsen, U., Nielsen, S. P., and Aarkrog, A. (1999). Determination of chemical species of iodine in seawater by radiochemical neutron activation analysis combined with ion-exchange preseparation. *Analytical Chem.* 71 (14), 2745–2750. doi: 10.1021/ac9813639

Hughes, C., Barton, E., Hepach, H., Chance, R., Pickering, M., Hogg, K., et al. (2021). Oxidation of iodide to iodate by cultures of marine ammonia-oxidising bacteria. *Mar. Chem.* 234, 104000. doi: 10.1016/j.marchem.2021.104000

Jickells, T. D., Boyd, S. S., and Knap, A. H. (1988). Iodine cycling in the Sargasso Sea and the Bermuda inshore waters. *Mar. Chem.* 24, 61–82. doi: 10.1016/0304-4203(88)90006-0

Jones, M. R., Chance, R., Dadic, R., Hannula, H.-R., May, R., Ward, M., et al. (2023). Environmental iodine speciation quantification in seawater and snow using ion exchange chromatography and UV spectrophotometric detection. *Analytica Chimica Acta* 1239, 340700. doi: 10.1016/j.aca.2022.340700

Karl, D. M., and Church, M. J. (2014). Microbial oceanography at the Hawaii Ocean Time-series programme. *Nat. Reviwes* 12, 699–713. doi: 10.1038/nrmicro3333

Li, J., Boiteau, R. M., Babcock-Adams, L., Acker, M., Song, Z., McIlvin, M. R., et al. (2021). Element-selective targeting of nutrient metabolites in environmental samples by inductively coupled plasma mass spectrometry and electrospray ionization mass spectrometry. *Front. Mar. Sci.* 8, 630494. doi: 10.3389/fmars.2021.630494

Liss, P. S., Herring, J. R., and Goldberg, E. D. (1973). The iodide/iodate system in seawater as a possible measure of redox potential. *Nat. Phys. Sci.* 242, 108–109. doi: 10.1038/physci242108a0

Lu, W., Ridgwell, A., Thomas, E., Hardisty, D., Luo, G., Algeo, T., et al. (2018). Late inception of a resiliently oxygenated upper ocean. *Science* 361, 174–177. doi: 10.1126/science.aar5372

Lu, Z., Lu, W., Rickaby, R., and Thomas, E. (2020). *Earth History of Oxygen and the iprOxy (Elements in Geochemical Tracers in Earth System Science)* (Cambridge: Cambridge University Press). doi: 10.1017/9781108688604

Luther, G. W.III (2023). Review on the physical chemistry of iodine transformations in the oceans. *Front. Mar. Sci.* 10. doi: 10.3389/fmars.2023.1085618

Luther, G. W. III, Branson-Swartz, C., and Ullman, W. J. (1988a). Direct determination of iodide in seawater by cathodic stripping square wave voltammetry. *Analytical Chem.* 60, 1721–1724. doi: 10.1021/ac00168a017

Luther, G. W. III, Ferdelman, T., Culberson, C. H., Kostka, J., and Wu, J. F. (1991). Iodine chemistry in the water column of the Chesapeake Bay: Evidence for organic iodine forms. *Estuarine Coast. Shelf Sci.* 32 (3), 267–279. doi: 10.1016/0272-7714(91)90020-C

Manley, S. L., and de la Cuesta, J. L. (1997). Methyl iodide production from marine phytoplankton cultures. *Limnology oceanography* 42 (1), 142–147. doi: 10.4319/lo.1997.42.1.0142

Moffett, J. W. (1994). A radiotracer study of cerium and manganese uptake onto suspended particles in Chesapeake Bay. *Geochimica Cosmochimica Acta* 58 (2), 695–703. doi: 10.1016/0016-7037(94)90499-5

Moriyasu, R., Bolster, K. M., Hardisty, D. S., Kadko, D. C., Stephens, M. P., and Moffett, J. W. (2023). Meridional survey of the central Pacific reveals iodide accumulation in equatorial surface waters and benthic sources in abyssal plain. *Global Biogeochemical Cycles* 37, e2021GB007300. doi: 10.1029/2021GB007300

Moriyasu, R., Evans, N., Bolster, K. M., Hardisty, D. S., and Moffett, J. W. (2020). The distribution and redox speciation of iodine in the Eastern Tropical North Pacific Ocean. *Global Biogeochemical Cycles* 34, e2019GB006302. doi: 10.1029/2019GB006302

Qi, Y., Matsuzaki, H., Yamagata, T., and Nagai, H. (2023). Iodine cycling in the subarctic Pacific Ocean: insights from ^{129}I. *Geochimica Cosmochimica Acta* 344, 12–23. doi: 10.1016/j.gca.2023.01.006

Rue, E. L., Smith, G. J., Cutter, G. A., and Bruland, K. W. (1997). The response of trace element redox couples to suboxic conditions in the water column. *Deep Sea Res. Part I: Oceanographic Res. Papers* 44 (1), 113–134. doi: 10.1016/S0967-0637(96)00088-X

Sherwen, T., Chance, R. J., Tinel, L., Ellis, D., Evans, M. J., and Carpenter, L. J. (2019). A machine-learning-based global sea-surface iodide distribution. *Earth System Sci. Data* 11, 1239–1262. doi: 10.5194/essd-11-1239-2019

Sherwen, T. M., Evans, M. J., Spracklen, D. V., Carpenter, L. J., Chance, R., Baker, A. R., et al. (2016a). Global modeling of tropospheric iodine aerosol. *Geophysical Res. Lett.* 43, 10,012–10,019. doi: 10.1002/2016GL070062

Sherwen, T. M., Schmidt, J. A., Evans, M. J., Carpenter, L. J., Großmann, K., Eastham, S. D., et al. (2016b). Global impacts of tropospheric halogens (Cl, Br, I) on oxidants and composition in GEOS-Chem. *Atmospheric Chem. Phys.* 16, 12,239–12,271. doi: 10.5194/acp-16-12239-2016

Solomon, S., Garcia, R. R., and Ravishankara, A. R. (1994). On the role of iodine in ozone depletion. *J. Geophysical Res.* 99 (D10), 20,491–20,499. doi: 10.1029/94JD02028

Stracke, A., Scherer, E. E., and Reynolds, B. C. (2014). Application of isotope dilution in geochemistry. *Treatise geochemistry second edition* 15, 71–86. doi: 10.1016/B978-0-08-095975-7.01404-2

Sun, Y.-J., Robinson, L.F., Parkinson, I.J., Stewart, J.A., Lu, W., Hardisty, D. S., Liu, Q., Kershaw, J., LaVigne, M., et al. (2023). Iodine-to-calcium ratios in deepsea scleractinian and bamboo corals. *EFront. Mar. Sci.* 10, 1264380. doi: 10.3389/fmars.2023.1264380

Takayanagi, K., and Wong, G. T. F. (1986). The oxidation of iodide to iodate for the polarographic determination of total iodine in natural waters. *Talanta* 33, 451–454. doi: 10.1016/0039-9140(86)80115-1

Truesdale, V. W., Bale, A. J., and Woodward, E. M. S. (2000). The meridional distribution of dissolved iodine in near-surface waters of the Atlantic Ocean. *Prog. Oceanography* 45, 387–400. doi: 10.1016/S0079-6611(00)00009-4

Truesdale, V. W., and Jones, K. (2000). Steady-state mixing of iodine in shelf seas off the British Isles. *Continental shelf Res.* 20, 1889–1905. doi: 10.1016/S0278-4343(00)00050-9

Tsunogai, S., and Henmi, T. (1971). Iodine in the surface water of the Pacific Ocean. *J. Oceanographical Soc. Japan* 27, 67–72. doi: 10.1007/BF02109332

van Bergeijk, S., Hernández, L., Zubía, E., and Cañavate, J. (2016). Iodine balance, growth and biochemical composition of three marine microalgae cultured under various inorganic iodine concentrations. *Mar. Biol.* 163 (5). doi: 10.1007/s00227-016-2884-0

Wadley, M. R., Stevens, D. P., Jickells, T. D., Hughes, C., Chance, R., Hepach, H., et al. (2020). A global model for iodine speciation in the upper ocean. *Global Biogeochemical Cycles* 34, e2019GB006467. doi: 10.1029/2019GB006467

Wong, G. T. F., and Brewer, P. G. (1974). The determination and distribution of iodate in South Atlantic waters. *J. Mar. Res.* 32, 25–36.

Zigah, P. K., McNichol, A. P., Xu, L., Johnson, C., Santinelli, C., Karl, D. M., et al. (2017). Allochthonous sources and dynamic cycling of ocean dissolved organic carbon revealed by carbon isotopes. *Geophysical Res. Lett.* 44 (5), 2407–2415. doi: 10.1002/2016GL071348

frontiers | Frontiers in Marine Science

TYPE Original Research
PUBLISHED 09 January 2024
DOI 10.3389/fmars.2023.1272870

Check for updates

OPEN ACCESS

EDITED BY
John Lee Ferry,
University of South Carolina, United States

REVIEWED BY
Rosie Chance,
University of York, United Kingdom
Peter Leslie Croot,
University of Galway, Ireland

*CORRESPONDENCE
Alexi A. Schnur
schnural@msu.edu

RECEIVED 04 August 2023
ACCEPTED 07 December 2023
PUBLISHED 09 January 2024

CITATION
Schnur AA, Sutherland KM, Hansel CM and Hardisty DS (2024) Rates and pathways of iodine speciation transformations at the Bermuda Atlantic Time Series. *Front. Mar. Sci.* 10:1272870. doi: 10.3389/fmars.2023.1272870

COPYRIGHT
© 2024 Schnur, Sutherland, Hansel and Hardisty. This is an open-access article distributed under the terms of the Creative Commons Attribution License (CC BY). The use, distribution or reproduction in other forums is permitted, provided the original author(s) and the copyright owner(s) are credited and that the original publication in this journal is cited, in accordance with accepted academic practice. No use, distribution or reproduction is permitted which does not comply with these terms.

Rates and pathways of iodine speciation transformations at the Bermuda Atlantic Time Series

Alexi A. Schnur[1]*, Kevin M. Sutherland[2], Colleen M. Hansel[3] and Dalton S. Hardisty[1]

[1]Department of Earth and Environmental Sciences, Michigan State University, East Lansing, MI, United States, [2]Department of Earth and Planetary Sciences, Harvard University, Cambridge, MA, United States, [3]Department of Marine Chemistry and Geochemistry, Woods Hole Oceanographic Institution, Woods Hole, MA, United States

The distribution of iodine in the surface ocean – of which iodide-iodine is a large destructor of tropospheric ozone (O_3) – can be attributed to both *in situ* (i.e., biological) and *ex situ* (i.e., mixing) drivers. Currently, uncertainty regarding the rates and mechanisms of iodide (I^-) oxidation render it difficult to distinguish the importance of *in situ* reactions vs *ex situ* mixing in driving iodine's distribution, thus leading to uncertainty in climatological ozone atmospheric models. It has been hypothesized that reactive oxygen species (ROS), such as superoxide ($O_2^{\bullet-}$) or hydrogen peroxide (H_2O_2), may be needed for I^- oxidation to occur at the sea surface, but this has yet to be demonstrated in natural marine waters. To test the role of ROS in iodine redox transformations, shipboard isotope tracer incubations were conducted as part of the Bermuda Atlantic Time Series (BATS) in the Sargasso Sea in September of 2018. Incubation trials evaluated the effects of ROS ($O_2^{\bullet-}$, H_2O_2) on iodine redox transformations over time and at euphotic and sub-photic depths. Rates of I^- oxidation were assessed using a $^{129}I^-$ tracer ($t_{1/2}$ ~15.7 Myr) added to all incubations, and $^{129}I/^{127}I$ ratios of individual iodine species (I^-, IO_3^-). Our results show a lack of I^- oxidation to IO_3^- within the resolution of our tracer approach – i.e., <2.99 nM/day, or <1091.4 nM/yr. In addition, we present new ROS data from BATS and compare our iodine speciation profiles to that from two previous studies conducted at BATS, which demonstrate long-term iodine stability. These results indicate that *ex situ* processes, such as vertical mixing, may play an important role in broader iodine species' distribution in this and similar regions.

KEYWORDS

iodine, redox transformations, superoxide & hydrogen peroxide, isotope tracer, incubations, oxidation, iodide, iodate

1 Introduction

Iodine is a redox-sensitive element that is found ubiquitously in the surface ocean at an average concentration of about 450 nM (Elderfield and Truesdale, 1980; Chance et al., 2014; Moriyasu et al., 2023). Knowledge of the distribution of iodine's two major redox species – iodide (I^-) and iodate (IO_3^-) – at the sea surface is important for our understanding of iodine's role in atmospheric cycles through the destruction of ozone (O_3) by I^-, a significant O_3 sink (Carpenter et al., 2013; Chance et al., 2014; Luhar et al., 2017). The destruction of O_3 by $I^\bullet$ releases hypoiodous acid (HOI) and I_2 to the atmosphere, which photolyzes to I atoms and continues to break down atmospheric O_3 (Carpenter et al., 2013). An understanding of the rates and mechanisms that contribute to the distribution of I^- and IO_3^- at the sea surface can aid in our understanding of tropospheric O_3 destruction and its importance in the cycles of global climate change and impact on air quality.

In well-oxygenated portions of the open ocean, IO_3^- is found at levels exceeding 250 nM at the surface, increasing in concentration with depth in sub-photic waters (>350 nM). In much of the open ocean water column, I^- concentrations are found to be inversely correlated with $[IO_3^-]$; however, I^- is consistently found to be present in larger amounts (up to 250 nM) than would be expected if O_2 were the direct oxidant of I^- in fully oxygenated surface waters (Chance et al., 2014). Indeed, O_2 is not thermodynamically favored to fully oxidize I^- to IO_3^- and the oxidant responsible for the reaction is unknown (Luther et al., 1995; Luther, 2023). Given multiple known pathways of IO_3^- reduction, it is clear however that I^- oxidation is occurring within marine waters but is likely sluggish (1.5-560 nM/yr) (Campos et al., 1996; Edwards and Truesdale, 1997; Truesdale et al., 2001b; Žic and Branica, 2006; He et al., 2013; Hardisty et al., 2020; Hughes et al., 2021). For example, *in situ* reduction of IO_3^- to I^- by phytoplankton and bacteria is known to be a major pathway through which I^- accumulates in areas of generally high primary productivity, such as upwelling zones and along coasts (Bluhm et al., 2010). Some iodine may be assimilated and later released during cell senescence (Hepach et al., 2020) and may account for "missing iodine" that is found in mass balance calculations of these areas.

The extracellular production of reactive oxygen species (ROS) by oxygenic photo- and heterotrophic bacteria promotes a variety of cell functions (Hansel and Diaz, 2021) and may also aid in the oxidation of I^- in surface waters. Extracellular $O_2^{\bullet-}$ production by these bacteria varies as a function of species, where it ranges from 0.1-3.7 amol cell^{-1} h^{-1} (heterotrophs) to 4.3-13,400 amol cell^{-1} h^{-1} (oxygenic phototrophs) (Diaz et al., 2013; Sutherland et al., 2020). Similarly, bacteria and phytoplankton are also sources of H_2O_2 to the marine environment, both through the secretion of intracellular pools and extracellular production. Extracellular $O_2^{\bullet-}$ production by *Roseobacter* sp. AzwK-3b – 15-20% of coastal bacterial communities (Bond et al., 2020) – was shown in cell cultures to promote I^- oxidation in the absence of Mn^{2+}, which is preferentially oxidized (Li et al., 2014; Hansel et al., 2019) (Figure 1). Oxidation is thought to be completed extracellularly through the aid of these

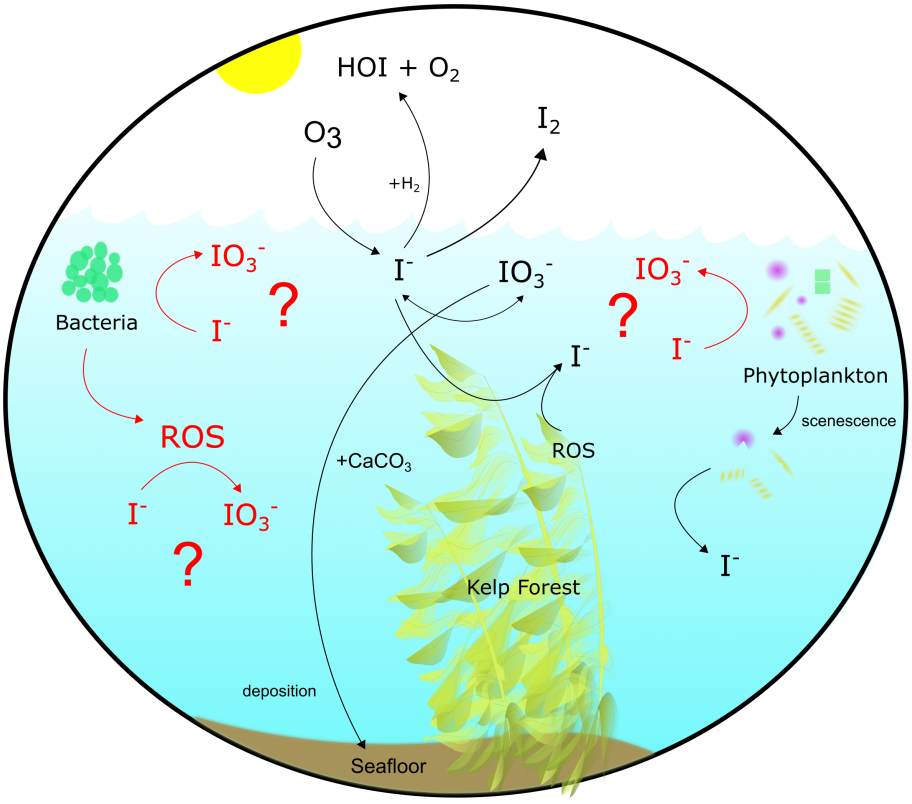

FIGURE 1
Iodine cycling in the modern surface ocean. Processes highlighted in red were examined in this study.

ROS (Li et al., 2014). This mechanism has yet to be tested under ambient marine conditions.

Here, we performed shipboard ^{129}I radiotracer incubations under ambient seawater conditions to investigate the role of ROS in I^- oxidation processes at the Bermuda Atlantic Time Series (BATS) in September 2018. ^{129}I has a half-life of ~15.7 Ma and is therefore useful as a tracer on timescales of decades or less (Hardisty et al., 2020; Hardisty et al., 2021). To build on previous studies, the ROS H_2O_2 and $O_2^{\bullet-}$ were added to experiments at levels analogous to natural seawater concentrations to investigate their effect on oxidation of I^- to IO_3^-, or vice versa. In addition, we have measured iodine speciation and $O_2^{\bullet-}$ in depth profiles from the BATS and the adjacent Hydrostation S. Our iodine speciation is compared to previous measurements from 1993 to 1994 and 1984 to 1985 (Jickells et al., 1988; Campos et al., 1996), thus providing the first long-term intercomparison for marine iodine.

2 Methods

2.1 Sample collection

Seawater was collected from the Bermuda Atlantic Time Series (BATS) and Hydrostation S sites in the Sargasso Sea in September 2018. Depth profile investigations at BATS were taken at 32.343°N 64.594°W at 21 separate depths between 1 m and 4500 m. Hydrostation S samples were taken at 32.165°N 64.501°W at 10 depths between 1 m and 500 m. Incubation water was taken from two depths (1 m and 240 m) and collected into four carboys (two euphotic (1 m) and two subphotic (240 m)) between 20:30 and 22:30 ADT. One carboy from each depth was filtered using a 0.2 µm filter to remove bacteria and other biology and particles while another was left unfiltered. ^{129}I ($t_{1/2} \cong 15.7$ My) (Eckert and Ziegler Isotope Products ©) (Hardisty et al., 2020; Hardisty et al., 2021), was added directly to each of the carboys at a targeted concentration of ~70 nM $^{129}I^-$ for investigating iodine redox reactions in natural seawater over time. $^{129}I^-$ was added before aliquoting the carboy water for individual incubations to ensure homogenous $^{129}I^-$ concentrations at t_0 for all incubations. 200 ml from each carboy were fractionated into separated incubation containers. Samples for t_0 were immediately subsampled from spiked incubation containers, with this and subsequent (t_1, t_2, t_f) subsamples being ~50 ml. All subsamples were immediately filtered at 0.2 µm to end interaction with biology after sampling. Subsamples were refrigerated and stored at 4°C until they returned to Michigan State University and were frozen for storage. Campos (1997) showed that seawater samples stored refrigerated (4°C) or frozen (-20°C) did not show signs of degradation in total iodine measurements over a one-to-three-year period – well over the eight-month timeframe in which measurement of these samples began after collection.

2.2 Incubation setup

Five incubation factors were used to create 20 incubation trials using a ship-deck light-filtering incubator to mimic at-depth light filtration, cooled with a continuous resupply of ambient surface seawater and stored in translucent and amber high-density polyethylene (HDPE) Nalgene bottles for dark incubations: each done in triplicate (Table 1). Factors included: 1) filtering of samples through a 0.2 µm syringe filter, meant as a control to screen filtered seawater of bacteria and macro-organisms and particles, kept in either the light or the dark depending on incubation, (Campos et al., 1996; Farrenkopf et al., 1997; Hardisty et al., 2020); 2) addition of $O_2^{\bullet-}$ dismutase (SOD) to incubations both filtered and unfiltered, but all left in the dark, intended as a control to remove ambient $O_2^{\bullet-}$ in seawater (Li et al., 2012; Diaz et al., 2013; Sutherland et al., 2020); 3) addition of superoxide thermal source (SOTS) or hydrogen peroxide (H_2O_2) to filtered samples kept in the dark in separate experiments, both suspected of being able to aid in oxidation of I^- to IO_3^- in seawater; 4) unfiltered water in the dark to determine the role, if any, of photochemical reactions that may cause the reduction of IO_3^- to I^- in the presence of organic matter (Spokes and Liss, 1996; Chance et al., 2014); 5) additions of $MnCl_2$ to iterations of the above in order to consider the potential of preferential Mn^{2+} oxidation relative to I^-. Note that controls 2 and 5 were only relevant if I^- oxidation was detected in the other controls.

Superoxide thermal source was kept frozen (-80°C) until it was added daily by pipette to incubations 11 and 19 (Table 1) as a combination of 1 ml dimethyl sulfoxide (DMSO) + 1 mg SOTS (3028 µM SOTS) (Cayman Chemicals, CAS number 223507-96-8)

TABLE 1 Factor setup and inclusion for all 20 incubation trials and controls.

Depth Zone (1 m or 240 m)	Photic	Photic	Photic	Photic	Subphotic	Subphotic
Light Condition (Light/Dark)	Light	Dark	Light	Dark	Dark	Dark
Treatment (Filtered/Unfiltered)	Unfiltered	Unfiltered	Filtered	Filtered	Unfiltered	Filtered
Control	#1	**#3**	**#6**	**#8**	**#13**	**#16**
+Superoxide Dismutase (SOD)		#4		#9	#14	#17
+Manganese Chloride ($MnCl_2$)	#2	#5	#7	#10	#15	#18
+Superoxide Thermal Source (SOTS)				**#11**		**#19**
+Hydrogen Peroxide (H_2O_2)				**#12**		**#20**

Photic samples are from 1 m depth, while subphotic samples are from 240 m depth. Filtered samples were filtered through a 0.2 µm filter for removal of bacteria and macroorganisms. Each incubation number consists of 12 samples; four timepoints sampled in triplicate. Bolded sample numbers in table indicate data for those incubations illustrated in this publication.

and diluted to 15 µM SOTS within seawater samples, which provides ≥25 nM $O_2^{\bullet-}$ at the surface water temperatures at BATS and Hydrostation S (Heller and Croot, 2010). This was made fresh daily immediately before adding to samples and added daily to account for natural decay. The $O_2^{\bullet-}$ concentration of the SOTS stock was not analyzed but $O_2^{\bullet-}$ concentration was analyzed in one experiment a few hours post-SOTS addition – to allow to reach steady state concentrations – to confirm $O_2^{\bullet-}$ accumulation. Hydrogen peroxide (30%) was added at a volume targeting 50 nM H_2O_2 in each solution. SOD was added by pipette daily – thus accounting for decay and titration via potentially newly formed $O_2^{\bullet-}$ within the incubations – from a stock concentration of 4 kU/ml to incubations to produce samples with SOD concentration of 0.32 kU/ml. Given potential long oxidation timescales of I^-, all incubations were performed over a 140-hour time period, with subsamples collected for iodine species measurement at t_0, ~t_{40}, ~t_{88}, and ~t_{140} hours.

2.3 Analytical methods

2.3.1 Superoxide

The steady-state concentration of $O_2^{\bullet-}$ was determined as previously described with some minor modifications (Sutherland et al., 2020). Water samples were collected using 12 L Ocean Test Equipment bottles on a 24-position Sea-Bird CTD rosette. Samples were transferred into dark, acid washed bottles and measured between 30 minutes and six hours of the collection time. Thirty minutes was chosen as a sample delay period because it is greater than 10 half-lives of $O_2^{\bullet-}$ in typical marine waters, meaning that any $O_2^{\bullet-}$ remaining is the result of light-independent $O_2^{\bullet-}$ production by microbial communities in the bottles (Roe et al., 2016). Samples collected above the thermocline were incubated on deck with continuously flowing surface water (28.2°C and 29.2°C at Hydrostation S and BATS, respectively) and samples below the thermocline were incubated at 4°C.

Superoxide concentrations were measured using an FeLume Mini (Waterville Analytical) and the $O_2^{\bullet-}$-specific chemiluminescent probe methyl cypridina luciferin analog (MCLA, Santa Cruz Biotechnology, Rose et al., 2008) stored at 4°C. Recent work using these methods has demonstrated that filtration of natural seawater can produce additional $O_2^{\bullet-}$ (Roe et al., 2016). To avoid introducing this bias into sample measurements, we used the following equation:

$$[O_2^{\bullet-}]_{sample} = [O_2^{\bullet-}]_{USW} - [O_2^{\bullet-}]_{AFSW}$$

where $[O_2^{\bullet-}]_{USW}$ represents the measured concentration of $O_2^{\bullet-}$ in unfiltered seawater (USW) and $[O_2^{\bullet-}]_{AFSW}$ represents the concentration of $O_2^{\bullet-}$ in aged (>24 hours) filtered (0.2 µm Sterivex filter) seawater (AFSW) amended with 75 µM diethylene-triaminepentaacetic acid (DTPA) to complex any metals present in the sample. Each measurement consisted of running a 25 mL USW sample through the FeLume system (3 mL/min) for several minutes until a steady signal was recorded. After a steady signal was recorded, 2 µL superoxide dismutase (SOD; Superoxide Dismutase from bovine erythrocytes >3,000 U/mg, Sigma, stock prepared in DI water to 4,000 U/mL) was added to the sample to quench all $O_2^{\bullet-}$ in the sample. The same procedure was followed for the AFSW samples. The reported $O_2^{\bullet-}$ concentrations represent the difference between the USW and the AFSW concentrations, the latter allowing us to eliminate the portion of the measured signal due to MCLA auto-oxidation in each particular sample matrix. Calibration curves were generated daily from three or more paired observations of time-zero $O_2^{\bullet-}$ concentration (dependent variable) and chemiluminescence (independent variable) using linear regression. Separate calibration curves were used for each of the two storage temperatures. Because chemiluminescence values were baseline-corrected, regression lines were forced through the origin. Calibrations yielded highly linear curves (typically R^2 >0.9), with a typical sensitivity of one chemiluminescence unit per pM $O_2^{\bullet-}$.

2.3.2 Spectrophotometry

Iodate was measured using the spectrophotometric method outlined in Jickells et al. (1988), using 10% potassium iodide (KI) solution and 1.5 M sulfamic acid (H_3NSO_3). 10% KI was made fresh daily. Samples were measured using a VWR UV-Vis Scanning 3100 PC spectrophotometer and accompanying UV-Vis Analyst software using VWR® Two-Sided Disposable Plastic Cuvettes for measurements within the visible range (300-900 nm), path length 10 mm. Fisherbrand® Semi-Micro Quartz Cuvettes (Cat. No. 14-958-126) for wavelengths 200-2500 nm, were used for repeated measurements of samples 3.5 years after the initial IO_3^- measurements, with similar results obtained.

Jickells' (1988) method of IO_3^- reaction with excess I^- in acidic conditions yields triiodide (I_3^-) and is specific to IO_3^- (Jickells et al., 1988; Moriyasu et al., 2020; Moriyasu et al., 2023). Triiodide in reacted samples was measured at a ~320 nm trough, with the lowest point being found between 300 and 350 nm, peak at 350 nm, and secondary trough at 400 nm ($A(IO_3^-)_x$). The concentrations of IO_3^- ($nM_{IO_3^-}$) were calculated from these values using the equation:

$$nM_{IO_3^-} = (A(IO_3^-)_{350} - (A(IO_3^-)_{\sim 320} + A(IO_3^-)_{400})/2) * m_{standard\ curve}$$

where $m_{standard\ curve}$ is the value of the slope of the standard curve created with potassium iodate (KIO_3^-), calculated between zero and 500 nM KIO_3^- and calibrated using standard additions of KIO_3^- to seawater.

2.3.3 Ion chromatography

We used a previously established ion-exchange chromatography method (Wong and Brewer, 1977; Hou et al., 1999; Hou et al., 2001; Hou et al., 2007; Hou et al., 2009; Hardisty et al., 2020; Hardisty et al., 2021; Moriyasu et al., 2023) to separate I^-, IO_3^-, and DOI from natural seawater samples. Iodide fractions were measured via ICP-MS for I^- concentrations (see section 2.3.4) since yields are known to reach ~100% (Hardisty et al., 2020), and then subsequently measured for $^{129}I/^{127}I$ ratios via MC-ICP-MS (see section 2.3.5). Previous IO_3^- yields have been found to commonly be between 90-95% (Hou et al., 1999; Hou et al., 2001; Hou et al., 2007; Hou et al., 2009), thus, IO_3^- and DOI fractions were only measured for $^{129}I/^{127}I$ ratios and not used to quantify concentrations from ICP-MS. Spot-checks on IO_3^- fractions

were completed on ICP-MS to test reproducibility between spectrophotometric and ICP-MS measurements, with 82 to >100% agreement between methods for [IO_3^-] measured (Table 2). Glass columns used for iodine redox species separation were packed with PYREX glass wool and 1 ml (volumetric) AG1-X8 resin that was cleaned of any residual iodine after packing using one full ion-exchange chromatography "cleaning" procedure (substituting sample for 18.2 MΩ-cm water) before samples were run through columns for collection of iodine redox species using the same chromatography procedure. About 10 ml of each sample – which was quantified gravimetrically before addition – were used during each procedure.

The ion chromatography procedure specifically elutes I^- from the seawater matrix. Iodate and DOI were independently separated prior to the I^- elution step. The DOI and IO_3^- fractions were then reduced to I^- using concentrated hydrochloric acid (HCl) and 0.3 M sodium bisulfite ($NaHSO_3$) at pH <2 (Hou et al., 1999; Hou et al., 2009; Reifenhaüser and Heumann, 1990; Hardisty et al., 2020). Samples were left overnight and then run through ion exchange chromatography columns the next day, using the same I^- elution procedure described above in an eluent of 18% TMAH/2 M HNO_3. Like the samples, the eluent mass was determined gravimetrically, which together were used for determining concentrations, when relevant. The eluent was then directly diluted for measurement via ICP-MS and/or MC-ICP-MS.

For quality control, a 200 ppb I^- solution diluted from a 1000 ± 4 ug/ml I^- solution in 1% tetraethyl ammonium (TEA) (I^-, DOI) or KIO_3^- (IO_3^-) standard was run alongside samples through columns as a monitor of iodine elution efficiency from columns to estimate yields. At least two 18.2 MΩ-cm water blanks were also run as monitors of contamination with sample sets. At least one sample replicate was also included in each column set for assessment of reproducibility between column runs.

2.3.4 ICP-MS

[$^{127}I^-$] was measured by a Thermoscientific iCap triple-quad inductively coupled plasma mass spectrometer (ICP-MS-TQ) using Qtegra software version 2.10.3324.131 in both single-quad (SQ) and triple-quad (TQ) mode with O_2 reaction cell gas. A Teledyne ASX 520 autosampler was used to deliver liquid solution to the ICP-MS. Samples analyzed by ICP-MS were diluted 1:20 or 1:40 in a 0.9% tetramethyl ammonium hydroxide (TMAH)/0.1 M nitric acid (HNO_3) or 0.45% TMAH/0.05 M HNO_3 solution, respectively. The same dilutions were used for ICP-MS rinse solutions. Data was corrected relative to the internal standards In, Rh, and Cs. Internal standards used were from Inorganic Ventures© – In was a 1001 ± 3 ug/ml solution in 2% HNO_3; Rh was a 999 ± 5 ug/ml solution in 15% HCl; and Cs was a 1000 ± 4 ug/ml solution in 0.1% HNO – to create a 5 ppb internal standard solution that was spiked into each measured sample directly or using an inline mixing chamber. The ^{127}I standard used for creating standard curves and column standard samples was a 1000 ± 4 ug/ml I^- solution in 1% tetraethylammonium (TEA).

2.3.5 MC-ICP-MS ratios ($^{129}I/^{127}I$)

Iodine isotope ratios ($^{129}I/^{127}I$) were measured at Woods Hole Oceanographic Institution (WHOI) via a ThermoFinnegan Neptune MC-ICP-MS according to Hardisty et al. (2020). Specific ion beams mass/charge (m/z) were monitored for Te (126, 128, 130) and Xe (126, 128, 129, 130, 131, 132) isotopes, as well as ^{132}Ba and ^{127}I and ^{129}I in faraday cups L3-L1 and H1-H3 with m/z 129 in the center position. Tuning was completed before running samples each morning to optimize beam intensity. A 500 ppb Te solution (Inorganic Ventures©) was used to account for mass bias corrections. Corrections needed for isobaric interferences were tracked via ^{131}Xe.

We utilized a gas-based "sparge" method for iodine sample introduction and desolvation with a 300 uL/min quartz nebulizer for Ar carrier gas Te solution introduction, using a regular sample cone and x-type skimmer cone (Hardisty et al., 2020; Hardisty et al., 2021). 30 ml Teflon vials, outfitted with pre-formed "sparge caps" that allowed for Ar gas flow through the sample, held ≤6 ml sample (solution containing fractions representing I^-, DOI, or IO_3^-). Teflon vials used for running samples were cleaned before use with each sample in 50% nitric acid for >3 hours at 90°C, then rinsed with 18.2 MΩ-cm water and allowed to air dry in hood until next use. Teflon tubing connecting samples to the Neptune intake were changed regularly to inhibit cross-contamination between sample runs. Before connection to the torch, Ar gas flow rate was decreased to ~0.1 L min^{-1} and Ar was run through the connected sample for one minute to purge air out of the sample container before connecting to the torch. After the sample was connected to the torch, the gas rate was increased to ~1.2 L min^{-1}. Te signal was monitored for

TABLE 2 IO_3^- and DOI spot-check measurements compared via spectrophotometry and ICP-MS.

Incubation	Sample Set	Redox	Timepoint	Spectrophotometry (nM)	ICP-MS (nM)
8	162 (single)	IO_3^-	t0	319 (n=1)	274 ± 42 (n=2)
11	196-198 (average)	IO_3^-	t0	309 ± 32 (n=3)	252 ± 51 (n=3)
11	205-207 (average)	IO_3^-	t_f (142.5 h)	249 ± 8 (n=3)	252 ± 100 (n=3)
12	210 (single)	IO_3^-	t0	255 (n=1)	229 ± 20 (n=2)
12	208-210 (average)	IO_3^-	t0	255 ± 11 (n=3)	229 ± 35 (n=3)
12	217-218, 315 (average)	IO_3^-	t_f (143.25 h)	209 ± 18 (n=3)	233 ± 5 (n=3)
8	162 (single)	DOI	t_0	–	46 ± 3 (n=2)
12	210 (single)	DOI	t_0	–	38 ± 7 (n=2)

stabilization, increasing to a value of 3-7 V. The sample run was started after Te signal stabilized, and then 4 ml concentrated 70% HNO_3 was added upstream of the sample vial to induce volatilization of iodine samples. The sum of nitric and iodine eluent was kept <10 ml to allow for headspace to prevent bubbling over, which can inadvertently introduce liquid upstream of the sample vial, preventing sample measurement. Data were corrected as described in Hardisty et al. (2020), for a final $^{129}I/^{127}I$ ratio and standard deviation output.

3 Results

3.1 Iodine speciation and superoxide in depth profiles

Depth profiles of I^- and IO_3^- (nM), $O_2^{\bullet-}$ (pM), temperature (°C), and dissolved oxygen (µM) at BATS and Hydrostation S are detailed in Figure 2 and show predictable changes throughout depth of IO_3^- and I^-. The dark, particle-associated superoxide steady-state concentration at BATS and Hydrostation S span 4-720 pM through the water column between 1 m and 4553 m at BATS and Hydrostation S sampling sites. Superoxide concentrations were highest between the surface and 1000 meters and fall within the range of previously reported water column values (Hansard et al., 2010; Rusak et al., 2011; Roe et al., 2016). Temperature and dissolved oxygen values are available from cruise CTD data at http://batsftp.bios.edu/. Depth profiles of I^- and IO_3^- mirror that of previous studies of iodine in an oxygenated seawater, with I^- accumulation in the surface elevated at the expense of IO_3^- and with iodine below the euphotic zone being almost completely IO_3^- except for the bottom water sample at 4500 m which has relatively elevated I^-. We also show I^- and IO_3^- reported from previous studies at BATS which were limited to shallower depths (2500 m) than that studied here (4500 m).

It is notable that there appears to be elevated superoxide concentrations at some intermediate water sample depths (e.g., 500 m). This is somewhat at odds with the expectation that light-independent superoxide production will scale with cell abundance and activity. While we did not measure additional biological parameters that might allow us to interpret these concentrations, it is apparent that elevated superoxide concentration do coincide with significant dissolved oxygen gradients. It is possible that elevated superoxide is either a direct or indirect result of remineralization processes occurring at these depths.

3.2 Iodine measurements from incubations

In incubation samples, initial $[IO_3^-]$ values measured spectrophotometrically were found to be within the range of 209 nM to 452 nM, while I^- separated from incubation samples via ion-exchange chromatography was found to be in the range of 92 nM to 235 nM from ICP-MS measurements (Table 2, Figures 3–5). Iodate values were spot-checked via exchange chromatography and ICP-MS and were found to be consistent with spectrophotometric measurements but showed a larger standard deviation in most cases, consistent with potential variability in yields (Table 2). It is interesting to note that, in some cases, filtered conditions have a lower measured $[IO_3^-]$ than unfiltered conditions (Figure 3A, subphotic depth).

Measured $[I^-]$ shows no change over time in any of the incubations investigated (Figures 4–6). This is also true for $[IO_3^-]$ for most incubation trials; however, IO_3^- values in incubations that included sequential additions of $O_2^{\bullet-}$ (10 nM/24 hrs) and H_2O_2 (50 nM/48 hrs) showed a decrease in $[IO_3^-]$ over time, from 309 nM to 249 nM and 255 nM to 204 nM, respectively. Given an interference causing a baseline shift in these incubations (discussed in Supplementary Information), these samples were corrected for by selecting the minimum trough value between 300 nm and 350 nm for spectrophotometer concentration calculations (section 2.3.2) instead of the exact 320 nm value, which was impacted and artificially increased by the interference shift. With correction, a

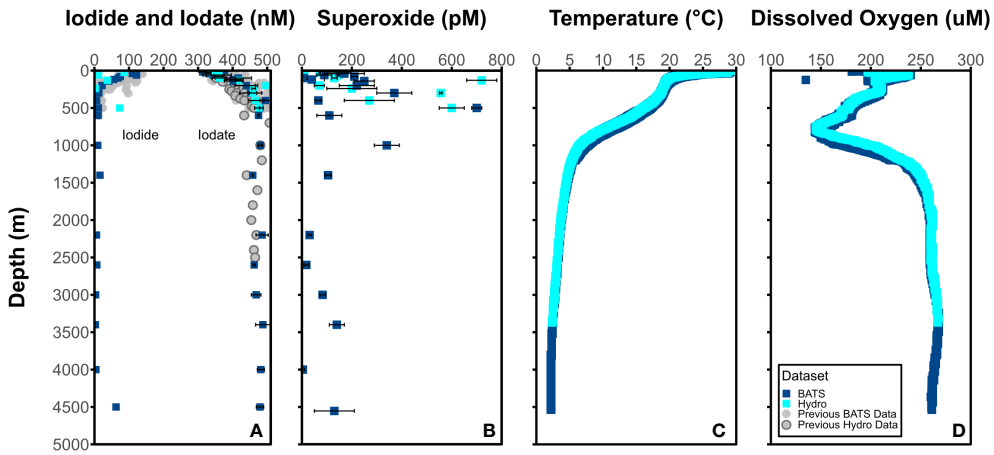

FIGURE 2
Concentrations of **(A)** I^- (left) and IO_3^- (right) (nM) and **(B)** $O_2^{\bullet-}$ (pM) at BATS (blue square) and Hydrostation S (cyan square) stations. Average **(C)** temperature (°C) and **(D)** dissolved oxygen (µM) from BATS and Hydrostation S stations also included.

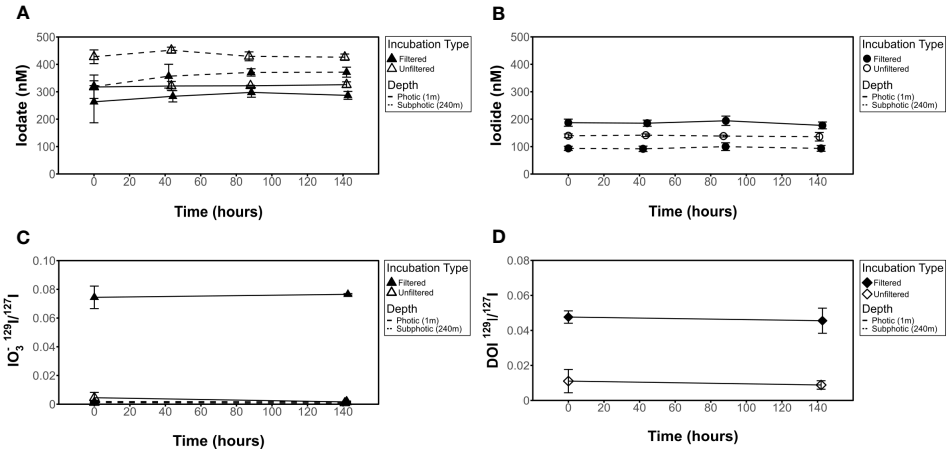

FIGURE 3
Influence of 0.2 µm filter on [IO_3^-], [I^-], IO_3^- $^{129}I/^{127}I$ ratios, and DOI $^{129}I/^{127}I$ ratios for dark incubations. No change seen in **(A)** [IO_3^-], **(B)** [I^-], **(C)** $^{129}I/^{127}I$ IO_3^- isotope ratio, or **(D)** $^{129}I/^{127}I$ DOI isotope ratio results in filtered (incubations 8 and 16) or unfiltered (incubations 3 and 13) experiments.

decrease in IO_3^- concentration was still observed. Since there was no corresponding increase in [I^-] or decrease in $^{129}I^-/^{127}I^-$, which would be anticipated for $^{127}IO_3^-$ reduction to I^-, this could indicate reduction of IO_3^- to an iodine intermediate not identified in this study. That said, it more likely reflects interferences from SOTS degradation products which have an overlapping absorbance range with I_3 near 320 nm. Specifically, 4-Formyl Benzoic acid is a degradation product of SOTS-1 (Ingold et al., 1997; Konya et al., 2000; Heller and Croot, 2010) and ROS-induced oxidation products of CDOM have overlapping absorption peaks. Notably, the SOTS degradation products do not account for the same observations made for the same trend observed in H_2O_2 observations. Importantly, we acknowledge that the spectrophotometric IO_3^- measurement is highly prone to interferences (Truesdale, 1978; Luther et al., 1988). Seawater background measurements at 350 nm have the potential to correct these interferences (Hepach et al., 2020; Jones et al., 2023).

Note that the controls with addition of SOD and $MnCl_2$ (meant to test the potential to stop I^- oxidation via scrubbing of superoxide or added preferred electron donor) were only relevant if I^- oxidation was observed in other controls, so are not considered further. These data are available in Supplementary Table 1.

DOI was not a focus of this study but was quantified in some instances for concentration (Table 2) as well as for $^{129}I/^{127}I$ ratios in incubations (described in the next section). We note that DOI concentrations in measured incubations (~7.5-9.5% of total dissolved iodine) were larger than we anticipated for open ocean areas where DOI is commonly negligible or uncharacterized (Wong and Cheng, 1998). DOI has previously been found to account for up to 10% of the total iodine pool in coastal areas (Chance et al., 2014).

3.3 $^{129}I/^{127}I$ isotope ratios

While all incubations were measured for [IO_3^-], we did not measure $^{129}I/^{127}I$ ratios for all incubations. This is because of the lack of variation observed in $^{129}I/^{127}I$ for the targeted ROS and other incubations. Measured $^{129}I/^{127}I$ ratios measured from chosen incubation experiments show no change over time beyond error bars in any of the incubations investigated (Figures 3–5). This includes IO_3^-, I^-, and DOI. This also includes the $^{129}I/^{127}I$ of I^- in the ROS-based incubations where a decrease in spectrophotometrically quantified [IO_3^-] was observed.

Initial $^{129}I/^{127}I$ ratios were consistent for measured I^- samples, which was expected given that the spike was added to a larger stock volume of seawater that was then aliquoted for the incubations. Average $^{129}I/^{127}I$ ratios for I^- at t_0 ranged from 0.29 ± 0.004 to 0.32 ± 0.002 at the surface. Initial isotope ratios for IO_3^- range from 0.0016 ± 0.0006 to 0.088 ± 0.0005 and 0.0008 ± 0.0001 to 0.002 ± 0.0002 for 1 m (photic) and 240 m (subphotic) depths, respectively, with incubation 8 (photic, dark, filtered) being a slight outlier at 0.07 ± 0.00024. It is notable that ^{129}I was observed in both the DOI and IO_3^- fractions, though it was added as I^-. Initial IO_3^- and DOI values were still predictably quite low, as Hardisty et al. (2020) demonstrated the spike is mostly $^{129}I^-$ with only minor $^{129}IO_3^-$, with the same being expected for DOI. Initial DOI values ranged between 0.005 ± 0.002 and 0.01 ± 0.003, with incubation 8 again being a slight outlier at 0.05 ± 0.004 (Figure 4).

3.4 Calculating I^- oxidation rates and constraining uncertainty

While oxidation was not observed, we quantified the maximum possible rates that would maintain our time series for $^{129}I/^{127}I$ of IO_3^- within the error (1 s.d.). Maximum daily gross rates of I^- oxidation determined by incubation conditions were calculated using isotope mass balance equations outlined in Hardisty et al. (2020). Average and standard deviation of triplicate initial and final incubation timepoint spectrophotometer measurements of ^{127}[IO_3^-], ICP-MS measurements of ^{127}[I^-], and MC-ICP-MS measurements of I^- $^{129}I/^{127}I$ ratios and IO_3^- $^{129}I/^{127}I$ ratios were used to first calculate

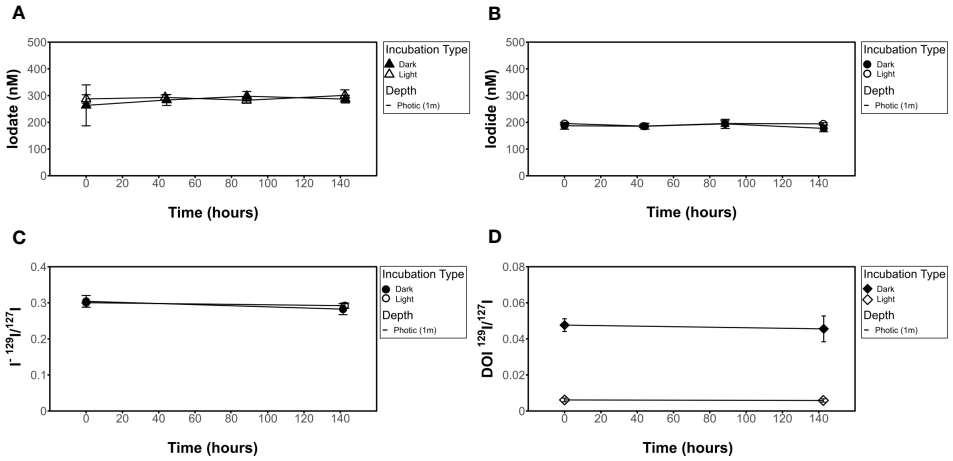

FIGURE 4
Influence of light on filtered seawater for $[IO_3^-]$, $[I^-]$, I^- $^{129}I/^{127}I$ ratios, and DOI $^{129}I/^{127}I$ ratios. No change seen in **(A)** $[IO_3^-]$, **(B)** $[I^-]$, **(C)** $^{129}I/^{127}I$ I^- isotope ratio, or **(D)** $^{129}I/^{127}I$ DOI isotope ratio results in light (incubation 6) vs dark (incubation 8) experiments.

the total IO_3^- created from I^- oxidation in incubations between t_0 to t_{140} (t_{final}). These calculations were then used to determine the rate (nM/day) of I^- oxidation to IO_3^-.

$$R_{iodide_t} = \frac{^{129}\Delta[iodide]_t}{^{127}\Delta[iodide]_t} \quad (1)$$

$$R_{iodate_t} = \frac{^{129}\Delta[iodide]_t}{^{127}[iodate]_i + ^{127}\Delta[iodide]_t} \quad (2)$$

$$\Delta[iodate] = {}^{129}\Delta[iodide]_t + {}^{127}\Delta[iodide]_t \quad (3)$$

The $^{127}[iodate]_i$ (initial $[IO_3^-]$ pre-spike addition) and the isotope ratios of I^- and IO_3^- at a given time t (R_{iodide_t} and R_{iodate_t}, respectively) are measured (Equations 1, 2). Since I^- oxidation to IO_3^- is the only quantifiable source of ^{129}I to R_{iodate_t} and negligibly fractionated, we can assume that changes in R_{iodate_t} from ^{129}I and ^{127}I are from I^- oxidation (i.e., $\Delta[iodate]$ in Equation 3) are contributed at an isotope

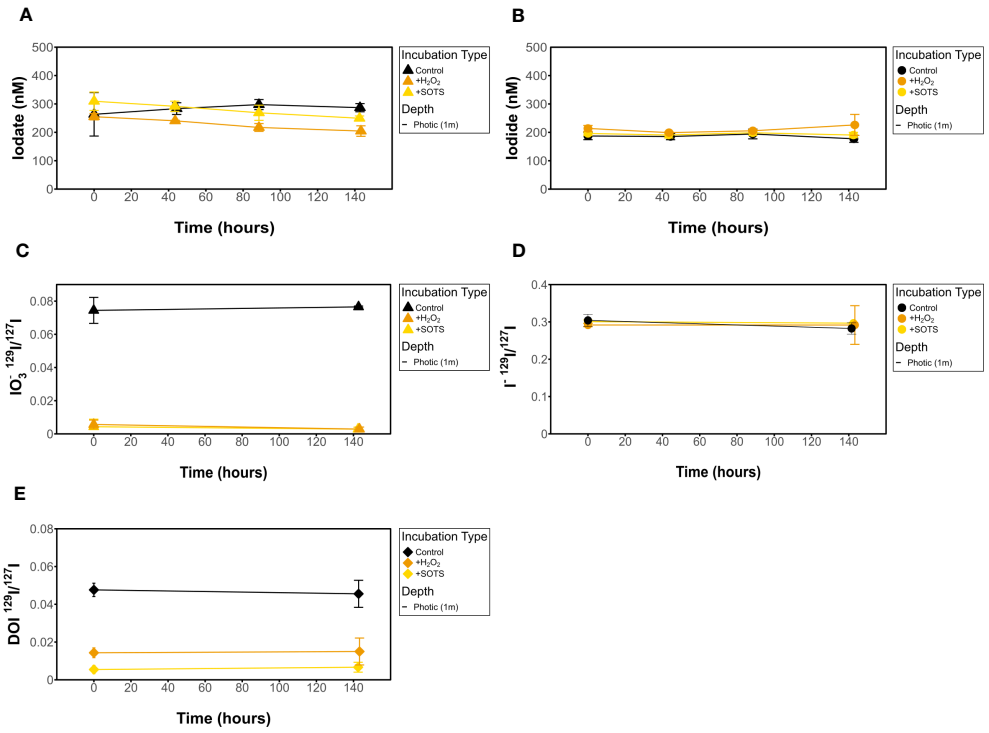

FIGURE 5
Influence of H_2O_2 and SOTS on filtered **(A)** $[IO_3^-]$, **(B)** $[I^-]$, **(C)** IO_3^- $^{129}I/^{127}I$ ratios, **(D)** I^- $^{129}I/^{127}I$ ratios, and **(E)** DOI $^{129}I/^{127}I$ ratios for dark incubations.

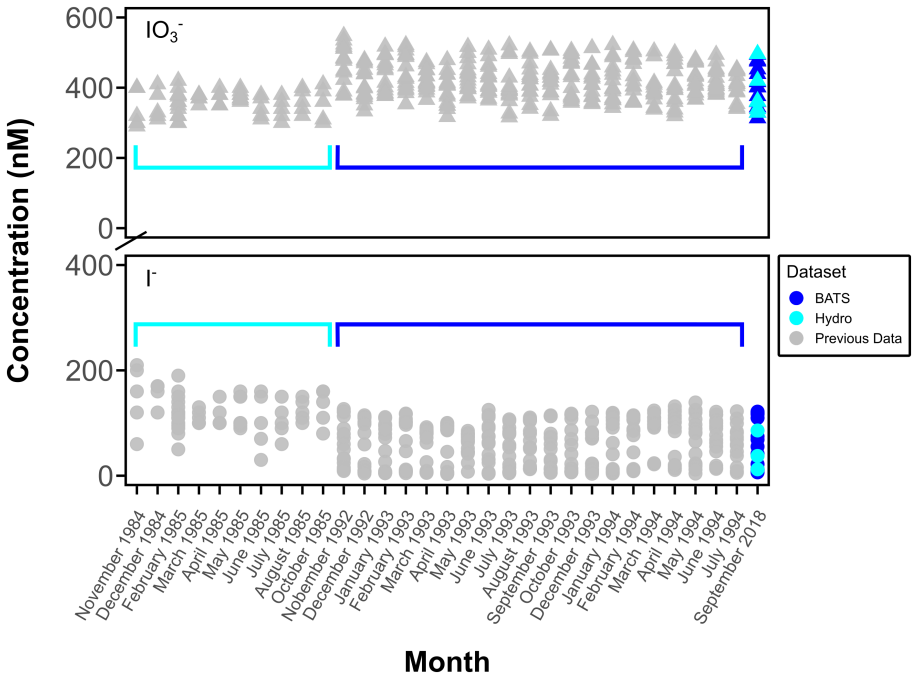

FIGURE 6
Comparison of previous BATS and Hydrostation S monthly concentration data of I^- (●) and IO_3^- (▲). Data from Campos et al., 1996 (BATS) and Jickells et al., 1988 (Hydrostation S) (gray symbols, surface to 200 m (Hydrostation S) and to 600 m (BATS)) and this study (blue and cyan symbols, surface to 600 m).

ratio equivalent to R_{iodide_t} (Equation 1). As such, Equation 1 can be rearranged to solve for $^{127}\Delta[iodide]_t$ which can be substituted into Equation 2 to solve for $^{129}\Delta[iodide]_t$. Plugging $^{129}\Delta[iodide]_t$ into Equation 1 then allows to solve for $^{127}\Delta[iodide]_t$ which then can be used in Equation 3 to solve for $\Delta[iodate]$. Based on the measured standard deviations of R_{iodide_t}, R_{iodate_t}, $^{127}[iodate]_i$ values and the hours of the incubation, we can then solve for the rate of I^- oxidation to IO_3^- taking place in the incubations in nM/day (Table 3).

4 Discussion

We measured the iodine speciation of shipboard incubations performed as part of the Bermuda Atlantic Time Series (BATS) in the Sargasso Sea in September of 2018, as well as depth profiles of $[IO_3^-]$ and $[I^-]$ from both BATS and Hydrostation S stations. Depth profiles repeat a typical trend for iodine redox species in surface waters, including increases in I^- at the sea surface and nearly complete IO_3^- below the euphotic zone (Figure 2). Incubation treatments described above (Table 1) tested the significance of the presence of the ROS $O_2^{\bullet-}$ (added as SOTS) and H_2O_2 on IO_3^- and I^- concentrations in natural seawater settings.

4.1 Temporal and methodological iodine comparison

This is the first report of $O_2^{\bullet-}$ at BATS, although iodine speciation at BATS and Hydrostation S has been previously reported through investigations of depth profiles of $[I^-]$ and $[IO_3^-]$ over time to a depth of up to 2500 m (Jickells et al., 1988; Campos et al., 1996) (Figure 2A, Figure 6). The similarities between measured iodine speciation profiles provide some constraints on the reproducibility of variable iodine speciation techniques used between labs. Our current measured data for depth profiles of IO_3^- and I^- at BATS generally agree with that of Campos et al. (1996) and demonstrate little change in iodine speciation with time. We also extended those investigations here to the bottom waters at 4500 m. While not the focus here, we note that our new bottom water data additionally show elevated I^-, consistent with other studies demonstrating likely benthic I^- fluxes in abyssal plains (Francois, 1987a; Francois, 1987b; Kennedy and Elderfield 1987a; Kennedy and Elderfield 1987b; Moriyasu et al., 2023).

Our data from Hydrostation S also generally overlaps with the range observed in Jickells et al. (1988); however, we note that our I^- data have a range that extends below that of these previous data. One explanation is that Jickells et al. (1988) measured I^- via difference between total iodine – determined via a UV-oxidation technique – and the spectrophotometrically measured IO_3^-, as was done here. Note that the opposite is true for Campos et al. (1996), who reduced IO_3^- to I^- and calculated IO_3^- via difference following voltametric analysis (Total I – I^-). For both cases, given that total iodine includes organic iodine, this implies the potential that DOI is contributing to either the I^- or IO_3^- pool, depending on the technique. While not thoroughly evaluated in this study, we note that DOI concentrations in measured incubations were up to 10% of the total iodine pool, so this could explain the difference between ours and earlier studies.

Alternatively, the difference is Hydrostation S data ranges between the two studies could reflect real changes in hydrography or primary production. For the seasonal study of Jickells et al. (1988), these previous seasonal IO_3^- lows and I^- high values were generally observed in the summer and interpreted to reflect more limited water mass exchange, which allows the combination of local Bermuda inshore inputs and primary productivity to limit IO_3^- availability. In the absence of a seasonal iodine context, it is difficult to explain the differences from our September 2018 data, but it is likely that increased water mass exchange – increasing the supply of high IO_3^- and low I^- from deeper waters and the Sargasso Sea generally – plays an important role. For example, the similarities in our 2018 BATS and Hydrostation S data suggest the potential for increased hydrographic exchange between these two sites. Further, the September 2018 sampling overlapped with the passage of Hurricane Florence 750 miles southeast of Bermuda on September 9th, 2018. While the mixed layer depth from September 2018 is like that of previous years, hurricanes have been documented to influence nutrient and other chemical parameters via increased mixing (Babin et al., 2004).

We note that while seasonal iodine variations may be driven by variations in primary productivity and mixed layer depth, other factors may contribute to longer-term evolution of iodine speciation. Specifically, Hughes et al. (2021) demonstrate that I^- oxidation to IO_3^- may be linked to nitrification, which is sensitive to a range of factors – e.g., light, O_2, temperature, pH, and photochemically produced ROS (Pajares and Ramos, 2019; Morris et al., 2022). Given the baseline iodine speciation conditions documented here and in previous studies, BATS may be an ideal location to track potential future changes in iodine speciation linked to predictions of evolving nitrification from global warming and ocean acidification (Bemen et al., 2012). To our knowledge, the only other locations with multiple iodine measurements are from the Black Sea (Wong and Brewer, 1977; Luther and Campbell, 1991; Truesdale et al., 2001a) and Baltic Sea (Hou et al., 2001; Truesdale et al., 2001b; Aldahan et al., 2007; Truesdale et al., 2013), but iodine speciation changes there will additionally be sensitive to the well-known presence of hypoxia and euxinia.

4.2 Limitations of experimental approach

Prior to interpretations, it is important to discuss the limitations of our experimental and analytical approaches. First, while isotope ratio variations (or lack thereof) form the basis of our interpretations, we note that variability in triplicate measurements in isotopes and concentrations measured via ICP-MS and spectrophotometry all contribute to the uncertainty of our rate calculations (Table 3). As previously mentioned, we acknowledge that the spectrophotometric method of measuring [IO_3^-] is prone to interferences and relatively low precision (Truesdale, 1978; Luther et al., 1988). For example, variation observed in the IO_3^- concentration but not in IO_3^- isotope ratios for the ROS-amended incubations (Figure 5) is likely attributed to interferences and not iodine species variations (see Supplementary Information). That said, beyond this example, there was general agreement between IO_3^- concentration and iodine isotope trends in this study and between ours and previously measured IO_3^- concentrations at Hydrostation S and BATS (Figures 2 and 6).

Another important limitation is the duration of the experiments, which likely induced bottle effects in unfiltered conditions. For example, a subset of our experiments was unfiltered in order to retain particles and native biological communities, but changes in community composition is well known within prolonged bottle experiments, even within 24 hours (Berg et al., 1999). Our experiments lasted ~140 hours (due to the known sluggish iodine oxidation kinetics) and the biological communities of unfiltered controls were not monitored. As there were no nutrient enrichments in our unfiltered incubations, it is likely that native cells underwent physiological changes that altered the balance between phytoplankton and bacteria. While not observed here, such a turnover could have shifted the balance between iodine oxidation and reduction, or commenced cell senescence, which favors I^- release (e.g., Bluhm et al., 2010). This places a limitation on our ability to interpret biologically induced iodine oxidation and reduction in unfiltered incubations; however, biological turnover is not a factor in our filtered controls testing additional oxidation-reduction pathways.

An additional limitation on our experiments is uncertainty regarding the superoxide concentrations and decay rate in the SOTS amended incubations. Specifically, the superoxide concentration and decay rate were not quantified directly in these incubations. That said, SOTS was added at a concentration estimated to produce an excess superoxide (25-55 nM instantaneous superoxide) relative to the natural waters of BATS (Figure 2). The instantaneous superoxide concentration can be estimated from temperature-dependent decay constants – 4.3-9.9x10^{-5} s^{-1} at 28.2-29.2°C (Heller and Croot, 2010) – and the observed superoxide decay constant from analogous oligotrophic waters (0.01 s^{-1}; (Roe et al., 2016)). While experiments were conducted in a shipdeck chamber continuously refilled with local surface water, the temperature was not directly monitored; however, we note that the biggest uncertainty in k_{SOTS} comes from uncertainty in the values at a given temperature and not

TABLE 3 Constrained rate measurements of I^- oxidation to IO_3^- in control incubations (incubations 3 and 8) and those with addition of SOTS (incubation 11) and H_2O_2 (incubation 12).

Incubation	Incubation Parameters	Maximum Rate from averages of first and final timepoints
3	Photic, dark, unfiltered	0.94 nM/day ± 0.30
8	Photic, dark, filtered	2.99 nM/day ± 0.53
11	Photic, dark, filtered, +SOTS	0.45 nM/day ± 0.28
12	Photic, dark, filtered, +H_2O_2	0.92 nM/day ± 0.24

*Rates could only be calculated for incubations that included all parameters necessary for Equations 1–3.

from the temperature range. Regardless, the conservative estimate of 25 nM superoxide is still in excess of that measured in water column profiles from this study (Figure 2).

4.3 Rates of I^- oxidation

Understanding the rates of I^- oxidation to IO_3^- is essential for already applied marine iodine cycling models (Lu et al., 2018; Wadley et al., 2020), but direct constraints are limited. In this study, all incubations showed no discernable change in [IO_3^-], [I^-], or the $^{129}I/^{127}I$ of IO_3^- beyond uncertainties over the timeframe of the incubations (~140 hours) (Figures 3–5).

While direct observations of IO_3^- production from I^- remains an important goal, our use of a radiotracer still allows us to place novel constraints on the maximum rates of I^- oxidation to IO_3^- based on the limitations of our analytical uncertainties (Table 3). Specifically, a lack of change seen over time in these incubations in both concentration and $^{129}I/^{127}I$ ratios are used to constrain a rate of <2.99 nM/day ± 0.53 nM/day. Previously calculated values of I^- oxidation have been reported from BATS from mass balance studies to be between 0.74 and 18 nM/day (Table 4). The value calculated for our incubation studies fits well in this range (Table 2), supporting previous claims that oxidation of I^- to IO_3^- is slow in natural seawaters (Hardisty et al., 2020; Carpenter et al., 2021).

Further, we observe non-negligible ^{129}I in the initial post-spike sample for both the IO_3^- and DOI incubation pools. Hardisty et al. (2020) made a similar observation and provided some evidence that the iodine-129 spike, while overwhelmingly I^-, contains some oxidized iodine. An alternative explanation is that the IO_3^- or iodine intermediates rapidly form upon addition to seawater or other solutions. This observation implies the potential for near instantaneous formation of $^{129}IO_3^-$ or DOI upon addition of spike to samples. Since the increase in $^{129}I/^{127}I$ was not ongoing, this would require rapid quenching of an existing oxidant in seawater, thus inhibiting further oxidation.

4.4 Role of reactive oxygen species in I^- oxidation to IO_3^- in natural seawater

We provide here the most detailed and direct constraints to date of the potential for the ROS $O_2^{\bullet-}$ (added as the chemical source SOTS) and H_2O_2 to oxidize I^- to IO_3^- in natural seawater. To the point, in our incubations with added $O_2^{\bullet-}$ and H_2O_2, no oxidation of I^- to IO_3^- was observed in BATS seawater, as shown in $^{129}I/^{127}I$ ratios of IO_3^- (Figure 5). We emphasize that this does not completely rule out the role of ROS in I^- oxidation broadly. Below we consider the implications of these results in coordination with previous studies evaluating the role, if any, of ROS on iodine cycling.

First, it is possible that ROS is preferentially reacting with dissolved organic matter or another component of seawater (e.g., Mn, NOx) (Wuttig et al., 2013; Li et al., 2014; Sutherland et al., 2021). We did not constrain alternative electron acceptors here but given the oligotrophic nature of BATS and known low dissolved Mn (Wu et al., 2014), this would imply that preferential extracellular $O_2^{\bullet-}$ scavenging relative to I^- is common throughout most of the ocean, and intracellular ROS have been shown to be a significant oxygen sink (Sutherland et al., 2021), hence diminishing the likely role of $O_2^{\bullet-}$ in marine I^- oxidation more broadly. Some evidence for preferential reaction of ROS with other redox-active species may come from the interference observed for our spectrophotometric measurements of IO_3^-. Second, thermodynamic calculations predict that $O_2^{\bullet-}$ alone forms iodine intermediates and cannot fully oxidize I^- to IO_3^-, so it is likely that iodine intermediates such as I_2, HOI, or DOI, instead of IO_3^-, in samples with excess H_2O_2 or SOTS added, are forming. This implies a potential role of ROS in iodine redox species cycling but contrasts previous findings. As discussed in detail in Luther (2023), reactions with $O_2^{\bullet-}$ and I^- forms I_2 and subsequently I_2^- (Bielski et al., 1985; Schwarz and Bielski, 1986). I_2 reacts quickly with organic matter to form DOI, which may act as a bottleneck in some environments to titrate I_2 and prevent subsequent oxidation (e.g., Hardisty et al., 2020). Since the $^{129}I/^{127}I$ ratio of DOI did not change in experiments (Figure 5E), it implies relatively little, if any, oxidation to intermediates forming DOI. Beyond this, $O_2^{\bullet-}$ is not favorable to subsequently oxidize I_2/I_2^- to form IO_3^-. Instead, •OH or O_3 are required for subsequent HOI formation, and OH, O_3, and H_2O_2 can then oxidize to IO_2^-, and then subsequently to IO_3^-. O_3 is not prevalent beyond the marine micro-layer and thus is unlikely responsible for I^- oxidation elsewhere in seawater.

Ultimately, these thermodynamic considerations imply that combinations of $O_2^{\bullet-}$ and H_2O_2, and perhaps OH radicals produced during their reduction, are necessary for complete oxidation from I^- to IO_3^- via ROS. Therefore, ROS most likely play a minor, if any, role in IO_3^- formation given the combination of: slow predicted kinetics (e.g., Wong and Zhang, 2008), limited ROS in seawater relative to iodine, the up to four step oxidation sequence each consuming ROS (I^- ➔ I_2 ➔ HOI ➔ IO_2^- ➔ IO_3^-),

TABLE 4 Previously reported daily I^- oxidation rates.

Location	Rate	Method	Source
Bermuda Atlantic Time Series	<0.44-2.99 nM/day	^{129}I doped seawater incubations	This study
Bermuda Atlantic Time Series	0.74 nM/day	Seasonal mass balance	Campos et al., 1996
Bermuda Atlantic Time Series	<4-18 nM/day*	Predicted from measured nitrification rates	Newell et al., 2013; Hughes et al., 2021
Martha's Vineyard Sound	0.32-0.52 nM/day	^{129}I doped seawater incubations	Hardisty et al., 2020
Pacific Gyre	1.53 nM/day	Seasonal mass balance	Campos et al., 1996
Eastern Tropical Pacific	5.3 ± 0.5 × 10^{-4} nM/day	1-Dimensional iodide oxidation model	Moriyasu et al., 2023

*Calculated based on BATS nitrification rates (Newell et al., 2013) and IO_3^- production rate 2-9 times that of nitrification (Hughes et al., 2021).

abundance of DOM and other preferred electron acceptors/donor – such as Br and Mn – for ROS, titration of HOI with DOM, and the likelihood of back reactions of iodine intermediates to I^-.

4.5 Constraints on other redox pathways

The lack of change in [IO_3^-], [I^-] or $^{129}I/^{127}I$ isotope ratios over the incubation period (~140 hours) (Figure 4) for the incubations exposed to dark vs light conditions additionally provide constraints on the likelihood of iodine redox reaction pathways. First, interactions between light and organic matter represent an abiotic pathway for ROS production (Morris et al., 2022). If $^{129}IO_3^-$ formation had been observed in the light experiments, an abiotic ROS mechanism could have been inferred from a lack of $^{129}IO_3^-$ in both the dark and light +SOD controls. Second, natural light is also suggested to aid in photo-reduction of IO_3^- in seawater, although it is not known how important this reduction pathway may be for I^- accumulation in the surface ocean (Spokes and Liss, 1996; Chance et al., 2014). Conversion of IO_3^- to I^- observed in both isotopes and concentrations would provide evidence for such a pathway, but this was not observed in this study.

4.6 Implications for marine iodine redox cycling and distributions

Our results support mounting evidence that iodine cycling in some ocean regions, if not more broadly, may be considered semi-conservative. From this perspective, given the relatively oligotrophic conditions at BATS (Lipschultz et al., 2002), it is perhaps not surprising that IO_3^- production may be slow or isolated to specific depths or even seasons. For example, laboratory cultures have identified nitrification as a possible pathway of IO_3^- production, which occurs specifically at the nitrite maximum at BATS and other similar localities (Newell et al., 2013; Hughes et al., 2021). In addition, Luther (2023) provides thermodynamic constraints that OH is a powerful oxidant capable of producing IO_3^-. Oxygenated waters supporting dissolved Fe – such as hydrothermal plumes, some low oxygen zones, and the benthic boundary layer – produce elevated •OH via Fenton chemistry, which could oxidize I^- to IO_3^- (e.g., Shaw et al., 2021). Luther (2023) also suggests that O_3 and N_2O can form IO_3^-, indicating that marine microlayer (Carpenter et al., 2021) and the oxycline of oxygen deficient zones (Babbin et al., 2015) may be important for IO_3^- production, respectively. Lastly, IO_3^- reduction in surface waters is more clearly linked to phytoplankton, which show seasonal distributions at BATS (Michaels et al., 1994; Michaels and Knap, 1996; DuRand et al., 2001).

Ex situ mixing of source waters from "hotspots" of high primary productivity, oxygen deficient zones, and pore waters may initiate iodine speciation gradients in surface waters whose rates of change slow as water masses extend to the open ocean from coastal or productive settings. As a result, water mass mixing may have a more dramatic effect on the distribution of iodine species in the open surface ocean than previously known. For example, Chance et al. (2020) and Chance et al. (2010) provided some evidence that diffusion/advection of IO_3^- from below the mixed layer may be important for controlling surface ocean IO_3^- abundance. Even in oxygen deficient zones, Hardisty et al. (2021) provide evidence that below the oxycline that IO_3^- has the potential to reflect water mass mixing, as opposed to clear *in situ* IO_3^- reduction.

5 Conclusions

We performed shipboard incubation experiments of seawater at the Bermuda Atlantic Time Series in the Sargasso Sea. These included natural concentrations of iodine and the reactive oxygen species $O_2^{\bullet-}$ and H_2O_2 to better understand the mechanisms of oxidation of I^- to IO_3^- in surface seawaters and better constrain the rates at which oxidation of I^- to IO_3^- takes place in the open ocean. We provided evidence that rates of I^- oxidation are extremely slow, if anything, on a daily timescale. We explicitly tested the potential for iodine redox reaction with ROS, which did not oxidize I^- within the resolution of our analytical uncertainty.

Based on the sluggish iodine oxidation rates, it is likely that *ex situ* sources of transportation, such as water mass mixing and vertical diffusion, are more important in the distribution of iodine redox species from "hotspots" of formation, such as areas of very high biogeochemical activity, ODZ's, and pore waters (Hardisty et al., 2021). This study and similar continuing work will help to inform atmospheric models of O_3 destruction and paleoredox models of IO_3^- incorporation with carbonates for measurement of I/Ca values.

Data availability statement

The original contributions presented in the study are included in the article/Supplementary Material, further inquiries can be directed to the corresponding author.

Author contributions

AS: Writing – original draft, Writing – review & editing, Formal analysis. DH: Writing – review & editing, Conceptualization, Funding acquisition, Supervision, Writing – original draft. KS: Writing – review & editing, Formal analysis. CH: Writing – review & editing, Methodology, Resources.

Funding

The author(s) declare financial support was received for the research, authorship, and/or publication of this article. NSF grant (#1829406) funded the entirety of this work.

Acknowledgments

AS and DH would like to thank Jurek Blusztajn for assistance at the WHOI Plasma Facility. We thank the Chief Scientist (Rod

Johnson) and Captain and Crew of the R/V *Atlantic Explorer* for making sampling for this dataset possible.

Conflict of interest

The reviewer, RC, is currently organizing a Research Topic with the author, DH.

The remaining authors declare that the research was conducted in the absence of any commercial or financial relationships that could be construed as a potential conflict of interest.

The author(s) declared that they were an editorial board member of Frontiers, at the time of submission. This had no impact on the peer review process and the final decision.

Publisher's note

All claims expressed in this article are solely those of the authors and do not necessarily represent those of their affiliated organizations, or those of the publisher, the editors and the reviewers. Any product that may be evaluated in this article, or claim that may be made by its manufacturer, is not guaranteed or endorsed by the publisher.

Supplementary material

The Supplementary Material for this article can be found online at: https://www.frontiersin.org/articles/10.3389/fmars.2023.1272870/full#supplementary-material

References

Aldahan, A., Possnert, G., Alfimov, V., Cato, I., and Kekli, A. (2007). Anthropogenic 129I in the Baltic Sea. *Nucl. Instruments Methods Phys. Research Section B: Beam Interact. Materials Atoms* 259 (1), 491–495. doi: 10.1016/j.nimb.2007.01.242

Babbin, A. R., Bianchi, D., Jayakumar, A., and Ward, B. B. (2015). Rapid nitrous oxide cycling in the suboxic ocean. *Science* 348 (6239), 1127–1129. doi: 10.1126/SCIENCE.AAA8380/SUPPL_FILE/BABBIN-SM.PDF

Babin, S. M., Carton, J. A., Dickey, T. D., and Wiggert, J. D. (2004). Satellite evidence of hurricane-induced phytoplankton blooms in an oceanic desert. *J. Geophys. Res.-Oceans* 109, Artn c03043. doi: 10.1029/2003JC001938

Beman, M. J., Popp, B. N., and Alford, S. E. (2012). Quantification of ammonia oxidation rates and ammonia-oxidizing archaea and bacteria at high resolution in the Gulf of California and eastern tropical North Pacific Ocean. *Limnology Oceanography* 57 (3), 711–726. doi: 10.4319/lo.2012.57.3.0711

Berg, G. M., Glibert, P. M., and Chen, C. C. (1999). Dimension effects of enclosures on ecological processes in pelagic systems. *Limnol. Oceanogr.* 44, 1331–1340. doi: 10.4319/lo.1999.44.5.1331

Bielski, B. H. J., Cabelli, D. E., Arudi, R. L., and Ross, A. B. (1985). Reactivity of HO2/O–2 radicals in aqueous solution. *J. Phys. Chem. Reference Data* 14 (4), 1041. doi: 10.1063/1.555739

Bluhm, K., Croot, P., Wuttig, K., and Lochte, K. (2010). Transformation of iodate to iodide in marine phytoplankton driven by cell senescence. *Aquat. Biol.* 11, 1–15. doi: 10.3354/ab00284

Bond, R. J., Hansel, C. M., and Voelker, B. M. (2020). Heterotrophic bacteria exhibit a wide range of rates of extracellular production and decay of hydrogen peroxide. *Front. Mar. Sci.* 7. doi: 10.3389/FMARS.2020.00072/BIBTEX

Campos, M. L. A. M. (1997). New approach to evaluating dissolved iodine speciation in natural waters using cathodic stripping voltammetry and a storage study for preserving iodine species. *Mar. Chem.* 57, 107–117. doi: 10.1016/S0304-4203(96)00093-X

Campos, M. L. A. M., Farrenkopf, A. M., Jickells, T. D., and Luther, G. W. (1996). A comparison of dissolved iodine cycling at the Bermuda Atlantic Time-series Station and Hawaii Ocean Time-series Station. *Deep Sea Res. Part II: Topical Stud. Oceanography*. 43, 455–466. doi: 10.1016/0967-0645(95)00100-x

Carpenter, L. J., Chance, R. J., Sherwen, T., Adams, T. J., Ball, S. M., Evans, M. J., et al. (2021). Marine iodine emissions in a changing world. *Proc. R. Soc. A* 477 (2247), 20200824. doi: 10.1098/RSPA.2020.0824

Carpenter, L. J., MacDonald, S. M., Shaw, M. D., Kumar, R., Saunders, R. W., Parthipan, R., et al. (2013). Atmospheric iodine levels influenced by sea surface emissions of inorganic iodine. *Nat. Geosci.* 6, 108–111. doi: 10.1038/ngeo1687

Chance, R., Baker, A. R., Carpenter, L., and Jickells, T. D. (2014). "The distribution of iodide at the sea surface," in *Environmental Sciences: Processes and Impacts*. (Piccadilly, London: Royal Society of Chemistry) 118, 171–181. doi: 10.1039/c4em00139g

Chance, R., Tinel, L., Sarkar, A., Sinha, A. K., Mahajan, A. S., Chacko, R., et al. (2020). Surface inorganic iodine speciation in the Indian and southern oceans from 12°N to 70°S. *Front. Mar. Sci.* 7. doi: 10.3389/FMARS.2020.00621/BIBTEX

Chance, R., Weston, K., Baker, A. R., Hughes, C., Malin, G., Carpenter, L., et al. (2010). Seasonal and interannual variation of dissolved iodine speciation at a coastal Antarctic site. *Mar. Chem.* doi: 10.1016/j.marchem.2009.11.009

Diaz, J. M., Hansel, C. M., Voelker, B. M., Mendes, C. M., Andeer, P. F., and Zhang, T. (2013). Widespread production of extracellular superoxide by heterotrophic bacteria. *Science* 340 (6137), 1223–1226. doi: 10.1126/science.1237331

DuRand, M. D., Olson, R. J., and Chisholm, S. W. (2001). Phytoplankton population dynamics at the Bermuda Atlantic Time-series station in the Sargasso Sea. *Deep Sea Res. Part II: Topical Stud. Oceanography* 48 (8–9), 1983–2003. doi: 10.1016/S0967-0645(00)00166-1

Edwards, A., and Truesdale, V. W. (1997). Regeneration of inorganic iodine species in Loch Etive, a natural leaky incubator. *Estuarine Coast. Shelf Sci.* 45 (3), 357–366. doi: 10.1006/ECSS.1996.0185

Elderfield, H., and Truesdale, V. W. (1980). On the biophilic nature of iodine in seawater. *Earth Planetary Sci. Lett.* 50, 105–114. doi: 10.1016/0012-821X(80)90122-3

Farrenkopf, A. M., Dollhopf, M. E., Chadhain, S. N., Luther, G. W., and Nealson, K. H. (1997). Reduction of iodate in seawater during Arabian Sea shipboard incubations and in laboratory cultures of the marine bacterium Shewanella putrefaciens strain MR-4. *Mar. Chem.* 57, 347–354. doi: 10.1016/S0304-4203(97)00039-X

Francois, R. (1987a). The influence of humic substances on the geochemistry of iodine in nearshore and hemipelagic marine-sediments. *Geochimica Et Cosmochimica Acta* 51, 2417–2427. doi: 10.1016/0016-7037(87)90294-8

Francois, R. (1987b). Iodine in marine sedimentary humic substances. *Sci. Total Environ.* 62, 341–342. doi: 10.1016/0048-9697(87)90519-5

Hansard, S. P., Vermilyea, A. W., and Voelker, B. M. (2010). Measurements of superoxide radical concentration and decay kinetics in the Gulf of Alaska. *Deep-Sea Res. I* 57, 1111–1119. doi: 10.1016/j.dsr.2010.05.007

Hansel, C. M., and Diaz, J. M. (2021). Production of extracellular reactive oxygen species by marine biota. *Annu. Rev. Mar. Sci.* 2021 (13), 177–200. doi: 10.1146/annurev-marine-041320

Hansel, C. M., Diaz, J. M., and Plummer, S. (2019). Tight regulation of extracellular superoxide points to its vital role in the physiology of the globally relevant roseobacter clade. *MBio* 10 (2), e02668-18. doi: 10.1128/MBIO.02668-18/SUPPL_FILE/MBIO.02668-18-ST003.PDF

Hardisty, D. S., Horner, T. J., Evans, N., Moriyasu, R., Babbin, A. R., Wankel, S. D., et al. (2021). Limited iodate reduction in shipboard seawater incubations from the Eastern Tropical North Pacific oxygen deficient zone. *Earth Planetary Sci. Lett.* 554, 116676. doi: 10.1016/j.epsl.2020.116676

Hardisty, D. S., Horner, T. J., Wankel, S. D., Blusztajn, J., and Nielsen, S. G. (2020). Experimental observations of marine iodide oxidation using a novel sparge-interface MC-ICP-MS technique. *Chem. Geology*. 532, 119360. doi: 10.1016/j.chemgeo.2019.119360

He, P., Hou, X., Aldahan, A., Possnert, G., and Yi, P. (2013). Iodine isotopes species fingerprinting environmental conditions in surface water along the northeastern Atlantic Ocean. *Sci. Rep.* 3 (1), 1–8. doi: 10.1038/srep02685

Heller, M. I., and Croot, P. L. (2010). Application of a superoxide (O 2 –) thermal source (SOTS-1) for the determination and calibration of O 2 – fluxes in seawater. *Analytica Chimica Acta* 667, 1–13. doi: 10.1016/j.aca.2010.03.054

Hepach, H., Hughes, C., Hogg, K., Collings, S., and Chance, R. (2020). Senescence as the main driver of iodide release from a diverse range of marine phytoplankton. *Biogeosciences*. 17, 2453–2471. doi: 10.5194/bg-17-2453-2020

Hou, X., Aldahan, A., Nielsen, S. P., and Possnert, G. (2009). Time series of 129I and 127I speciation in precipitation from Denmark. *Environ. Sci. Technol.* 43 (17), 6522–6528. doi: 10.1021/ES9012678

Hou, X., Aldahan, A., Nielsen, S. P., Possnert, G., Nies, H., and Hedfors, J. (2007). Speciation of 129I and 127I in seawater and implications for sources and transport

pathways in the North Sea. *Environ. Sci. Technol.* 41, 5993–5999. doi: 10.1021/es070575x

Hou, X., Dahlgaard, H., and Nielsen, S. P. (2001). Chemical speciation analysis of 129I in seawater and a preliminary investigation to use it as a tracer for geochemical cycle study of stable iodine. *Mar. Chem.* 74, 145–155. doi: 10.1016/S0304-4203(01)00010-X

Hou, X., Dahlgaard, H., Rietz, B., Jacobsen, U., Nielsen, S. P., and Aarkrog, A. (1999). Determination of chemical species of iodine in seawater by radiochemical neutron activation analysis combined with ion-exchange preseparation. *Analytical Chem.* 71 (14), 2745–2750. doi: 10.1021/AC9813639

Hughes, C., Barton, E., Hepach, H., Chance, R., Pickering, M. D., Hogg, K., et al. (2021). Oxidation of iodide to iodate by cultures of marine ammonia-oxidising bacteria. *Mar. Chem.* 234, 104000. doi: 10.1016/J.MARCHEM.2021.104000

Ingold, K. U., Paul, T., Young, M. J., and Doiron, L. (1997). Invention of the first azo compound to serve as a superoxide thermal source under physiological conditions: Concept, synthesis, and chemical properties. *J. Of Am. Chem. Soc.* 119, 12364–12365. doi: 10.1021/ja972886l

Jickells, T. D., Boyd, S. S., and Knap, A. H. (1988). Iodine cycling in the Sargasso Sea and the Bermuda inshore waters. *Mar. Chem.* 24, 61–82. doi: 10.1016/0304-4203(88)90006-0

Jones, M. R., Chance, R., Dadic, R., Hannula, H. R., May, R., Ward, M., et al. (2023). Environmental iodine speciation quantification in seawater and snow using ion exchange chromatography and UV spectrophotometric detection. *Anal. Chim. Acta*, 1239. doi: 10.1016/j.aca.2022.340700

Kennedy, H. A., and Elderfield, H. (1987a). Iodine diagenesis in non-pelagic deep-sea sediments. *Geochimica et Cosmochimica Acta* 51, 2505–2514. doi: 10.1016/0016-7037(87)90301-2

Kennedy, H. A., and Elderfield, H. (1987b). Iodine diagenesis in pelagic deep-sea sediments. *Geochimica Et Cosmochimica Acta* 51, 2489–2504. doi: 10.1016/0016-7037(87)90300-0

Konya, K. G., Paul, T., Lin, S., Lusztyk, J., and Ingold, K. U. (2000). Laser flash photolysis studies on the first superoxide thermal source. First direct measurements of the rates of solvent-assisted 1,2- hydrogen atom shifts and a proposed new mechanism for this unusual rearrangement1. *J. Am. Chem. Soc.* 122, 7518–7527. doi: 10.1021/ja993570b

Li, H. P., Daniel, B., Creeley, D., Grandbois, R., Zhang, S., Xu, C., et al. (2014). Superoxide production by a manganese-oxidizing bacterium facilitates iodide oxidation. *Appl. Environ. Microbiol.* 80, 2693–2699. doi: 10.1128/AEM.00400-14

Li, H. P., Yeager, C. M., Brinkmeyer, R., Zhang, S., Ho, Y. F., Xu, C., et al. (2012). Bacterial production of organic acids enhances H2O 2-dependent iodide oxidation. *Environ. Sci. Technol.* 46, 4837–4844. doi: 10.1021/es203683v

Lipschultz, F., Bates, N. R., Carlson, C. A., and Hansell, D. A. (2002). New production in the Sargasso Sea: History and current status. *Global Biogeochemical Cycles* 16 (1), 1–1. doi: 10.1029/2000GB001319

Lu, W., Ridgwell, A., Thomas, E., Hardisty, D. S., Luo, G., Algeo, T. J., et al. (2018). Late inception of a resiliently oxygenated upper ocean. *Science.* 361, 174–177. doi: 10.1126/science.aar5372

Luhar, A. K., Galbally, I. E., Woodhouse, M. T., and Thatcher, M. (2017). An improved parameterisation of ozone dry deposition to the ocean and its impact in a global climate-chemistry model. *Atmospheric Chem. Phys.* 17, 3749–3767. doi: 10.5194/acp-17-3749-2017

Luther, G. W. I. (2023). Review on the physical chemistry of iodine transformations in the oceans. *Front. Mar. Sci.* 10, 1721–1724. doi: 10.3389/FMARS.2023.1085618

Luther, G. W., and Campbell, T. (1991). Iodine speciation in the water column of the Black Sea. *Deep Sea Research Part A. Oceanographic Res. Papers.* 38, S875–S882. doi: 10.1016/s0198-0149(10)80014-7

Luther, G. W., Swartz, C. B., and Ullman, W. J. (1988). Direct determination of iodide in seawater by Cathodic stripping square wave voltammetry. *Analytical Chem.* 60 (17). doi: 10.1021/ac00168a017

Luther, G. W., Wu, J., and Cullen, J. B. (1995). *Redox Chemistry of Iodine in Seawater*. (Washington, D.C.: American Chemical Society), 135–155. doi: 10.1021/BA-1995-0244.CH006

Michaels, A. F., and Knap, A. H. (1996). Overview of the U.S. JGOFS Bermuda Atlantic Time-series study and the hydrostation S program. *Deep-Sea Res. Part II: Topical Stud. Oceanography* 43 (2–3), 157–198. doi: 10.1016/0967-0645(96)00004-5

Michaels, A. F., Knap, A. H., Dow, R. L., Gundersen, K., Johnson, R. J., Sorensen, J., et al. (1994). Seasonal patterns of ocean biogeochemistry at the U.S. JGOFS Bermuda Atlantic time-series study site. *Deep-Sea Res. Part I.* 41, 1013–1038. doi: 10.1016/0967-0637(94)90016-7

Moriyasu, R., Evans, N., Bolster, K. M., Hardisty, D. S., and Moffett, J. W. (2020). The Distribution and Redox Speciation of Iodine in the Eastern Tropical North Pacific Ocean. *Global Biogeochem Cycles* 34 (2). doi: 10.1029/2019GB006302

Moriyasu, R., Bolster, K. M., Hardisty, D. S., Kadko, D. C., Stephens, M. P., and Moffett, J. W. (2023). Meridional survey of the central pacific reveals iodide accumulation in equatorial surface waters and benthic sources in the abyssal plain. *Global Biogeochem. Cycles* 37 (3), e2021GB007300. doi: 10.1029/2021GB007300

Morris, J. J., Rose, A. L., and Lu, Z. (2022). Reactive oxygen species in the world ocean and their impacts on marine ecosystems. *Redox Biol.* 52, 102285. doi: 10.1016/j.redox.2022.102285

Newell, S. E., Fawcett, S. E., and Ward, B. B. (2013). Depth distribution of ammonia oxidation rates and ammonia-oxidizer community composition in the Sargasso Sea. *Limnology Oceanography* 58 (4), 1491–1500. doi: 10.4319/LO.2013.58.4.1491

Pajares, S., and Ramos, R. (2019). Processes and microorganisms involved in the marine nitrogen cycle: knowledge and gaps. *Front. Mar. Sci.* 6. doi: 10.3389/fmars.2019.00739

Reifenhäuser, C., and Heumann, K. G. (1990). Development of a definitive method for iodine speciation in aquatic systems. *Fresenius J. Anal. Chem.* 336 (7), 559–563. doi: 10.1007/BF00331416/METRICS

Roe, K. L., Schneider, R. J., Hansel, C. M., and Voelker, B. M. (2016). Measurement of dark, particle-generated superoxide and hydrogen peroxide production and decay in the subtropical and temperate North Pacific Ocean. *Deep-Sea Res. I* 107, 59–69. doi: 10.1016/j.dsr.2015.10.012

Rose, A. L., Webb, E. A., Waite, T. D., and Moffett, J. W. (2008). Measurement and implications of nonphotochemically generated superoxide in the equatorial pacific ocean. *Environ. Sci. Technol.* 42 (7), 2387–2393. doi: 10.1021/ES7024609/SUPPL_FILE/ES7024609-FILE003.PDF

Rusak, S. A., Peake, B. M., Richard, E., Nodder, S. D., and Cooper, W. J. (2011). Distributions of hydrogen peroxide and superoxide in seawater east of New Zealand. *Mar. Chem.* 127, 155–169. doi: 10.1016/j.marchem.2011.08.005

Schwarz, H. A., and Bielski, B. H. J. (1986). Reactions of HO2 and O2- with iodine and bromine and the I2- and I atom reduction potentials. *J. Phys. Chem.* 90 (7), 1445–1448. doi: 10.1021/J100398A045/ASSET/J100398A045.FP.PNG_V03

Shaw, T. J., Luther, G. W., Rosas, R., Oldham, V. E., Coffey, N. R., Ferry, J. L., et al. (2021). Fe-catalyzed sulfide oxidation in hydrothermal plumes is a source of reactive oxygen species to the ocean. *Proc. Natl. Acad. Sci. United States America* 118 (40), e2026654118. doi: 10.1073/PNAS.2026654118/SUPPL_FILE/PNAS.2026654118.SAPP.PDF

Spokes, L. J., and Liss, P. S. (1996). Photochemically induced redox reactions in seawater, II. Nitrogen and iodine. *Mar. Chem.* 54, 1–10. doi: 10.1016/0304-4203(96)00033-3

Sutherland, K. M., Grabb, K. C., Karolewski, J. S., Plummer, S., Farfan, G. A., Wankel, S. D., et al. (2020). Spatial heterogeneity in particle-associated, light-independent superoxide production within productive coastal waters. *J. Geophys. Res. Oceans* 125, e2020JC016747. doi: 10.1029/2020JC016747

Sutherland, K. M., Grabb, K. C., Karolewski, J. S., Taenzer, L., Hansel, C. M., and Wankel, S. D. (2021). The redox fate of hydrogen peroxide in the marine water column. *Limnology Oceanography* 66 (10), 3828–3841. doi: 10.1002/LNO.11922

Sutherland, K. M., Wankel, S. D., and Hansel, C. M. (2020). Dark biological superoxide production as a significant flux and sink of marine dissolved oxygen. *Proc. Natl. Acad. Sci. United States America*. doi: 10.1073/pnas.1912313117

Truesdale, V. W. (1978). The automatic determination of iodate- and total-iodine in seawater. *Mar. Chem.* 6 (3), 253–273. doi: 10.1016/0304-4203(78)90034-8

Truesdale, V. W., Nausch, G., and Baker, A. (2001a). The distribution of iodine in the Baltic Sea during summer. *Mar. Chem.* 74, 87–98. doi: 10.1016/S0304-4203(00)00115-8

Truesdale, V. W., Nausch, G., and Waite, T. J. (2013). The effects of the 2001 Barotropic intrusion of bottom-water upon the vertical distribution of inorganic iodine in the Gotland Deep. *Continental Shelf Res.* 55, 155–167. doi: 10.1016/j.csr.2013.01.005

Truesdale, V. W., Watts, S. F., and Rendell, A. R. (2001b). On the possibility of iodide oxidation in the near-surface of the Black Sea and its implications to iodine in the general ocean. *Deep Sea Res. Part I: Oceanographic Res. Papers* 48 (11), 2397–2412. doi: 10.1016/S0967-0637(01)00021-8

Wadley, M. R., Stevens, D. P., Jickells, T. D., Hughes, C., Chance, R., Hepach, H., et al. (2020). A global model for iodine speciation in the upper ocean. *Global Biogeochemical Cycles* 34 (9), e2019GB006467. doi: 10.1029/2019GB006467

Wong, G. T. F., and Brewer, P. G. (1977). The marine chemistry of iodine in anoxic basins. *Geochimica Cosmochimica Acta.* 41, 151–159. doi: 10.1016/0016-7037(77)90195-8

Wong, G. T. F., and Cheng, X. H. (1998). Dissolved organic iodine in marine waters: Determination, occurrence and analytical implications. *Mar. Chem.* 59, 271–281. doi: 10.1016/S0304-4203(97)00078-9

Wong, G. T. F., and Zhang, L. S. (2008). The kinetics of the reactions between iodide and hydrogen peroxide in seawater. *Mar. Chem.* 111, 22–29. doi: 10.1016/j.marchem.2007.04.007

Wu, J., Roshan, S., and Chen, G. (2014). The distribution of dissolved manganese in the tropical–subtropical North Atlantic during US GEOTRACES 2010 and 2011 cruises. *Mar. Chem.* 166, 9–24. doi: 10.1016/J.MARCHEM.2014.08.007

Wuttig, K., Heller, M. I., Croot, P. L., and Biogeochemistry, M. (2013). *Pathways of Superoxide (O 2 −) Decay in the Eastern Tropical North Atlantic*. (Washington, D. C.: American Chemical Society). doi: 10.1021/es401658t

Žic, V., and Branica, M. (2006). The distributions of iodate and iodide in Rogoznica Lake (East Adriatic Coast). *Estuarine Coast. Shelf Sci.* 66 (1–2), 55–66. doi: 10.1016/J.ECSS.2005.07.022

frontiers | Frontiers in Marine Science

TYPE Original Research
PUBLISHED 21 February 2024
DOI 10.3389/fmars.2024.1277595

Check for updates

OPEN ACCESS

EDITED BY
Shigeki Wada,
University of Tsukuba, Japan

REVIEWED BY
Yuhi Satoh,
Japan Agency for Marine-Earth Science and Technology, Japan
Atsushi Ooki,
Hokkaido University, Japan

*CORRESPONDENCE
Matthew R. Jones
matthew_r_jones@rocketmail.com
Lucy J. Carpenter
lucy.carpenter@york.ac.uk

†PRESENT ADDRESSES
Oban Jones,
Bermuda Institute for Ocean Sciences (BIOS), St. George's, Bermuda
Rebecca May,
Bermuda Institute for Ocean Sciences (BIOS), St. George's, Bermuda
Liselotte Tinel,
Institut Mines-Télécom (IMT) Nord Europe, Université of Lille, Centre for Energy and Environment, Lille, France
Katherine Weddell,
Fera Science Ltd, Biotech Campus, York, United Kingdom

RECEIVED 14 August 2023
ACCEPTED 29 January 2024
PUBLISHED 21 February 2024

CITATION
Jones MR, Chance R, Bell T, Jones O, Loades DC, May R, Tinel L, Weddell K, Widdicombe C and Carpenter LJ (2024) Iodide, iodate & dissolved organic iodine in the temperate coastal ocean.
Front. Mar. Sci. 11:1277595.
doi: 10.3389/fmars.2024.1277595

COPYRIGHT
© 2024 Jones, Chance, Bell, Jones, Loades, May, Tinel, Weddell, Widdicombe and Carpenter. This is an open-access article distributed under the terms of the Creative Commons Attribution License (CC BY). The use, distribution or reproduction in other forums is permitted, provided the original author(s) and the copyright owner(s) are credited and that the original publication in this journal is cited, in accordance with accepted academic practice. No use, distribution or reproduction is permitted which does not comply with these terms.

Iodide, iodate & dissolved organic iodine in the temperate coastal ocean

Matthew R. Jones[1*], Rosie Chance[1], Thomas Bell[2], Oban Jones[2†], David C. Loades[1], Rebecca May[2†], Liselotte Tinel[1†], Katherine Weddell[1†], Claire Widdicombe[2] and Lucy J. Carpenter[1*]

[1]Wolfson Atmospheric Chemistry Laboratory, University of York, York, United Kingdom, [2]Plymouth Marine Laboratory, Prospect Place, Plymouth, United Kingdom

The surface ocean is the main source of iodine to the atmosphere, where it plays a crucial role including in the catalytic removal of tropospheric ozone. The availability of surface oceanic iodine is governed by its biogeochemical cycling, the controls of which are poorly constrained. Here we show a near two-year time series of the primary iodine species, iodide, iodate and dissolved organic iodine (DOI) in inner shelf marine surface waters of the Western English Channel (UK). The median ± standard deviation concentrations between November 2019 and September 2021 (n=76) were: iodide 88 ± 17 nM (range 61-149 nM), iodate 293 ± 28 nM (198-382 nM), DOI 16 ± 16 nM (<0.12-75 nM) and total dissolved iodine (dI_T) 399 ± 30 nM (314-477 nM). Though lower than inorganic iodine ion concentrations, DOI was a persistent and non-negligible component of dI_T, which is consistent with previous studies in coastal waters. Over the time series, dI_T was not conserved and the missing pool of iodine accounted for ~6% of the observed concentration suggesting complex mechanisms governing dI_T removal and renewal. The contribution of excess iodine (*I**) sourced from the coastal margin towards dI_T was generally low (3 ± 29 nM) but exceptional events influenced dI_T concentrations by up to ±100 nM. The seasonal variability in iodine speciation was asynchronous with the observed phytoplankton primary productivity. Nevertheless, iodate reduction began as light levels and then biomass increased in spring and iodide attained its peak concentration in mid to late autumn during post-bloom conditions. Dissolved organic iodine was present, but variable, throughout the year. During winter, iodate concentrations increased due to the advection of North Atlantic surface waters. The timing of changes in iodine speciation and the magnitude of *I** subsumed by seawater processes supports the paradigm that transformations between iodine species are biologically mediated, though not directly linked.

KEYWORDS

iodine speciation, biogeochemistry, marine systems, seasonal time series, iodide, iodate

1 Introduction

Elemental iodine transformations are an important global biogeochemical cycle that influences our environment (Tsunogai and Sase, 1969; Carpenter et al., 2021). Iodine in seawater impacts climate (He et al., 2021; Cuevas et al., 2022) and global health because it contributes to the removal of harmful ozone from the atmospheric boundary layer directly *via* the reaction of ozone with iodide at the sea surface (Garland et al., 1980) and indirectly *via* release of iodine in gaseous form to the atmosphere (Carpenter et al., 2013; Carpenter et al., 2021). Photochemical transformations of iodine gases can lead to new particle formation that may act as cloud condensation nuclei (He et al., 2023), thus influencing atmospheric radiative properties (Saiz-Lopez et al., 2012; Gómez Martín et al., 2022). Iodine emissions from seawater are in the form of organic compounds (Lovelock, 1975; Carpenter et al., 2003) and inorganic molecules (Carpenter et al., 2013; MacDonald et al., 2014; Tinel et al., 2020; Carpenter et al., 2021), the latter are most important in terms of emissions (Carpenter et al., 2021). Iodine in the terrestrial environment is predominantly sourced by emissions from coastal seawater (Fuge, 1989; Fuge and Johnson, 2015). These emissions improve regional air quality by removing ground level ozone (Carpenter et al., 2013; Carpenter et al., 2021) and are the main source of iodine – an essential micronutrient (WHO) – to soils and subsequently the food chain (Fuge and Johnson, 2015).

In oceanic seawater, iodine is classified as a biophilic element (Goldschmidt, 1954) and is primarily in the forms of thermodynamically stable iodate (IO_3^-), iodide (I^-; ~25% of the total dissolved iodine (dI_T) in surface waters) and iodine associated with dissolved organic material (typically representing ~5% of dI_T; Elderfield and Truesdale, 1980; Wong, 1980; Luther et al., 1991; Wong, 1991; Chance et al., 2014; Fuge and Johnson, 2015; Luther, 2023). The central tenet of iodine marine biogeochemistry is that transformations between soluble chemical species are biologically mediated (Tsunogai and Sase, 1969; Amachi et al., 2007), though chemical processes cannot be ruled out (Schnur et al., 2024). This tenet derives from observations of temporal changes in iodine speciation in ocean waters concluding that from spring through to autumn iodide accumulates and iodate is removed, and over winter the reverse occurs (Truesdale, 1978; Jickells et al., 1988; Campos et al., 1996; Tian et al., 1996; Truesdale and Jones, 2000; Truesdale and Upstill-Goddard, 2003; Waite et al., 2006; Chance et al., 2010; Satoh et al., 2019a; Shi et al., 2023). These observations support the observed global ocean iodide-nitrate anticorrelation and the supposition that iodate is either assimilated during primary production and iodide is released, or iodate is enzymatically reduced, possibly by nitrate reductase enzymes (Tsunogai and Sase, 1969; Wong and Zhang, 1992; Campos et al., 1999; Amachi et al., 2005; Amachi et al., 2007).

Microbially forced changes to iodine species have been observed in experimental systems. Iodate reduction occurred during phytoplankton growth (Waite and Truesdale, 2003; Hung et al., 2005; Amachi et al., 2007) and senescence, the latter concurrently with increasing bacterial biomass (Bluhm et al., 2010; Carrano et al., 2020; Hepach et al., 2020). Both, laboratory and field observations indicate a significant lag time between iodate loss and iodide formation (Chance et al., 2007; Bluhm et al., 2010; Chance et al., 2010; Carrano et al., 2020; Hepach et al., 2020). Iodide oxidation may also occur directly by bacteria (iodide oxidation rate, ~75 mM d^{-1}) or be an indirect artefact of bacterial processes [*e.g.*, ammonia oxidation (~2.5 µM d^{-1}), organic acid-mediated hydrogen peroxide production (~14.4 mM d^{-1}) or manganese oxide catalysed superoxide production (Amachi et al., 2005; Li et al., 2012; Li et al., 2014; Hughes et al., 2021)].

Relative to open ocean and outer shelf waters, the concentration of dissolved iodine in coastal inner shelf waters is lower (Truesdale, 1978; Truesdale, 1994; Truesdale and Upstill-Goddard, 2003; Satoh et al., 2019a; Satoh et al., 2023; Shi et al., 2023). The reason for this is not well known (Chance et al., 2014), though a chemical transformation to a particulate fraction may account for the apparent depreciated soluble iodine concentrations (Truesdale, 1994; Truesdale and Upstill-Goddard, 2003; Satoh et al., 2019a; Satoh et al., 2023). Processes directly influencing the iodine cycle in wider coastal environments include interaction with dissolved organic material during its remineralization and sorption to particulate material (Truesdale, 1978; Tian et al., 1996; Satoh et al., 2019a; Shi et al., 2023), the mixing of deeper low oxygen high iodide waters to the surface (Shi et al., 2023), and significant changes in dissolved organic iodine (DOI) concentration (ΔDOI up to 100 nM; Satoh et al., 2019a). In coastal systems, the iodine cycle may also be influenced by higher life forms including macroalgae and invertebrates (*e.g.*, jellyfish) that use organic and inorganic iodine species as antioxidants and signaling molecules (Silverstone et al., 1977; Küpper et al., 1998; Prieto et al., 2010; Cross et al., 2015; Gonzales et al., 2017; Tymon et al., 2017; Carrano et al., 2020; Carrano et al., 2021). Furthermore, inner shelf waters have a greater opportunity for interactions with sediments, which can influence water column iodine speciation (*e.g.*, Ullman and Aller, 1980; Francois, 1987; Farrenkopf and Luther, 2002). When abiotic processes are combined with microbial processes they should meet the observed net rates of coastal *in situ* iodide oxidation of 0.33-0.52 nM d^{-1} (Hardisty et al., 2020).

The presence of elevated levels of organic material and nutrients from terrestrial sources is a significant difference between inner shelf and open ocean marine systems (Mendoza and Zika, 2014; Barrón and Duarte, 2015; Carr et al., 2019). The presence of organic material influences DOI formation and iodine geochemistry because DOI can account for up to 40% of dI_T in estuarine and coastal environments (Luther et al., 1991; Abdel-Moati, 1999; Cook et al., 2000; Wong and Cheng, 2001a; Satoh et al., 2019a). Though DOI consists of many varied compounds (Schulz et al., 1974; Harvey, 1980; Wong, 1982; Luther et al., 1991; Cook et al., 2000; Moulay, 2013) some may be hypervalent organic iodine (Francois, 1987) while a fraction (pico-molar) is covalently bonded volatile iodine (Lovelock, 1975; Schall and Heumann, 1993; Dembitsky, 2006).

In this paper, we present a near two-year time series detailing the major iodine species in temperate inner shelf marine surface waters of the Western English Channel. These coastal waters extend from the shoreline and outer limit of estuaries to depths of ~30 m, and have near to oceanic salinities. The time series provides insight

into the factors controlling iodine speciation at the sea surface and therefore its impacts on the magnitude of ozone deposition, sea-to-air iodine flux, availability of iodine as a nutrient to terrestrial environments and air quality (Fuge, 1989; Carpenter et al., 2013; Fuge and Johnson, 2015; Carpenter et al., 2021). To evaluate the controlling factors, the inner shelf iodine species were compared to those on the outer shelf at the Western Channel Observatory (Station L4). All observations were part of a larger project aiming to constrain the role of the sea-surface microlayer in controlling ozone flux. The data will be used to inform those observations and subsequent research. The novelty of these data is the inclusion of DOI and a quantification of the fraction of excess iodine due to the interaction of the terrestrial marine system. These data also provide vital inner shelf iodine species concentrations to constrain modelling studies, *i.e.*, Sherwen et al. (2019); Wadley et al. (2020) and Pound et al. (2023).

2 Methods

2.1 Location and sampling

From November 2019 through to September 2021 seawater was collected from inner and outer shelf locations in the Western English Channel (Figure 1) by the crew of the Plymouth Marine Laboratory's (UK) research vessel *Plymouth Quest*. The samples were taken from the vessel's clean underway system (inlet depth 3 m). The inner shelf location was ~0.5 km offshore of Rame Head, Cornwall, and in the vicinity of the Penlee Point Atmospheric Observatory, the water column depth was 20-25 m. The inner shelf site was further split into two; an east site (50° 19' 12" N, 4° 10' 12" W) and a west site (50° 18' 32.4" N, 4° 11' 27.6" W) because sampling was always conducted upwind of the Penlee Point Atmospheric Observatory. The samples were collected approximately weekly (weather permitting), sampling was more intensive in 2021 than in 2020. A total of 76 weeks of samples were collected from these locations. The outer shelf location was the Western Channel Observatory (Station L4; 50°15′ N, 4°13′ W; 52 m depth) situated ~6 km offshore from which 14 samples were collected at monthly intervals during the springs, summers and autumns of 2020 and 2021. Following collection, all seawater was filtered through Whatman fine glass fibre membranes (GF/F; nominal pore size 0.7 µm). Filtered seawater was stored at -20°C in acid-washed plastic containers to preserve iodine speciation (Campos, 1997). Before analysis, samples were thawed overnight at 4°C and in the dark.

2.2 Analytical

2.2.1 Iodine species

Iodide was determined spectrophotometrically following an ion chromatography (IC) separation of a 400 µL sample (Jones et al., 2023). Separation and determination were conducted on an Agilent

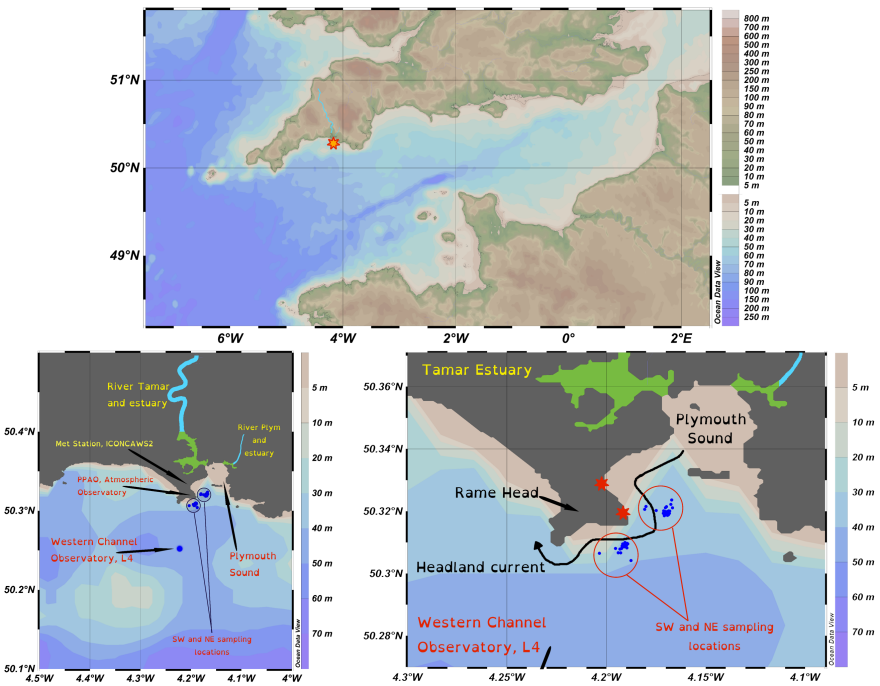

FIGURE 1
Location map of sampling site(s). Top, English Channel with the UK to the north and France to the south, the Tamar River is highlighted in light blue and the sampling locations by the star. Bottom left, annotated map showing inner and outer shelf sampling locations (SW, NE and L4), and major rivers (light blue) and their estuaries (green) running into Plymouth Sound. Bottom right, inner shelf sampling stations relative to Rame Head, the meteorological stations (red stars), and the path of the Rame Head Current. Map produced in Ocean Data View, Schlitzer, R., Ocean Data View, https://odv.awi.de, 2018.

1100 HPLC with a 1260 series detector. The UV detector monitored absorbance at 226 nm over a 60 mm path length. The IC isocratic mobile phase (0.4 M NaCl) ran at 0.64 mL min^{-1}. The IC guard and analytical columns were Dionex IonPac AS-23 4×50 mm and 4×250 mm, respectively. Once injected, the chromatogram was collected for 16.1 minutes, iodide eluted at *c.*11 minutes. Gravimetrically prepared stock solutions of potassium iodide (KI; Fisher >99.0%) in 18.1 MΩ deionized water were used to prepare analytical standards. Iodate and DOI were quantified as iodide following chemical amendments before the chromatography (Jones et al., 2023). Hydroxylamine hydrochloride (NH_2OH-HCl; Sigma-Aldrich Reagent Plus, 99%) was added to a final concentration of 7 mM to reduce iodate to iodide and enable the measurement of the inorganic iodine fraction (I_{inorg} = iodide + iodate) and quantification, by difference, of iodate. A second chemical manipulation enabled measurement of the total dissolved iodine fraction ($dI_T = I_{inorg}$ + DOI) and hence quantification, by difference, of DOI (Lister and Rosenblum, 1963; Takayanagi and Wong, 1986; Abdel-Moati, 1999; Jones et al., 2023). For DOI determination, the chemical amendment to the sample was an addition of hypochlorite, in the form of calcium hypochlorite ($Ca(ClO)_2$; Sigma-Aldrich Technical Grade), to a final concentration of 189 µM. After 1 h, the hypochlorite was neutralized through addition of sodium sulfite (Na_2SO_3; Sigma-Aldrich, min. 98%) to a concentration of 380 µM and then NH_2OH-HCl was added to a final concentration of 7 mM. There may be an underestimation of the DOI concentration as the analytical method may not capture all iodine within DOI (Luther and Cole, 1988; Wong and Cheng, 1998; Wong and Cheng, 2001b). The methods were found to yield iodate and DOI measurements in excellent agreement with values obtained using the established methods of spectrophotometry (116 ± 9%, n=103) and UV-degradation (98 ± 4%, n=98) (Jones et al., 2023). All samples, treated and untreated, were measured in triplicate and the standard deviation of those determinations was used to calculate the analytical error. The relative standard deviation for each analysis was typically <2%. Sample concentrations were blank corrected using values derived from the additions of the amendments to deionized H_2O. All samples were quantified as iodide, which had a detection limit of 0.12 nM, calculated as the equivalent concentration of 3× the standard deviation of ten repeated 1 nM standards.

2.2.2 Nutrient, physicochemical, dissolved organic carbon and meteorological measurements

Except for the soluble iodine species and dissolved organic carbon, all analytes [nutrients (Supporting Information (SI), Supplementary Figure SI.1) and physicochemical parameters (Supplementary Figure SI.2)] were determined by the Plymouth Marine Laboratory (UK). Nutrient analysis was conducted on a 5-channel segmented flow system (Bran+Luebbe) with quality control procedures implemented. Phosphate was determined as phosphor-molybdenum blue (analytical Λ = 710 nm) (Zhang and Chi, 2002) and silicate as silico-molybdenum blue (Kirkwood, 1989). Nitrate and nitrite ions were determined using the Greiss method; nitrate was reduced on a copper cadmium column in an ammonium chloride solution (Brewer and Riley, 1965; Grasshoff, 1976). Ammonia was determined as indophenol blue (analytical Λ = 650 nm) (Mantoura and Woodward, 1983). Due to it being subject to storage and contamination problems, the ammonium data should be viewed more as trends rather than highly accurate concentrations. Chlorophyll-α (chl-α; mg L^{-1}) concentrations were determined fluorometrically from acetone extractions of the particulate phase captured on GF/F filters and normalized for filtrate volume (Yentsch and Menzel, 1963). An array of electronic sensors (Supplementary Table SI.1), referred to as the CTD, were deployed from the research vessel beginning in January 2020. The calibrated sensors measured seawater conductivity (salinity), temperature, pressure, turbidity, *in situ* photosynthetically active radiation (PAR), oxygen and fluorescence (a proxy for chl-α). Phytoplankton biomass (mg carbon (C) L^{-1}) on the outer shelf location was taken from the British Oceanographic Data Centre (BODC; Widdicombe and Harbour, 2021). The biomass on the inner shelf was calculated by applying the ratio of the CTD-measured fluorescence from the inner to outer shelf sites as a multiplicative factor to the outer shelf biomass. Dissolved organic carbon (DOC) was calibrated using a total organic carbon standard (TOC standard 50 mg L^{-1}, Sigma-Aldrich). Samples, standards and blanks for DOC analysis were diluted in 18.1 MΩ deionized water, placed in 12 mL vials and covered with tin foil. These samples were acidified with small volumes of 1.2 M HCl and then the DOC content was determined using an Elementar Vario TOC cube. Supporting meteorological data was retrieved from the WeatherUnderground station (ICONCAWS2, Cawsands Bay). The met station was situated ~1 km from the inner shelf sampling locations (Figure 1).

2.2.3 Rationalisation and excess iodine (*I**)

The established practice that accounts for the dilution of seawater by freshwater is to normalize analyte concentrations to a salinity of 35 (termed 'rationalization', see Equation 1; Truesdale, 1994), this approach assumes that the freshwater end member has a zero iodine concentration. Rationalisation (*R*) does not provide knowledge of a species/elements behavior in the environment, just a relative abundance to all dissolved salts (Truesdale, 1995).

$$R[X] = [X]_{sample} \times \frac{[S_P]_{sample}}{35} \quad (1)$$

To evaluate contributions to dI_T from estuarine and submarine groundwater discharge, we examined how observed dI_T concentrations deviated from a conservative mixing curve (linear model). This model was chosen because most observations suggest that dI_T behaves conservatively in estuarine systems (Luther et al., 1991; Abdel-Moati, 1999; Cook et al., 2000; Truesdale et al., 2001; Lin, 2023). Mixing curve end members were defined using the outer shelf average dI_T (406.5 ± 15.0, n=6) of the six highest salinity samples (S_P = 34.93 ± 0.08, n=6), and an assumed freshwater dI_T concentration of 25 nM (Fuge, 1989) and salinity of zero. The freshwater endmember is the average of southern UK surface ($\bar{x}$=23 nM, n=9) and well waters ($\bar{x}$=26 nM,

n=6). Excess iodine (I^*) was calculated as the difference in determined and predicted dI_T.

2.2.4 Statistical analysis

Concentrations of all chemical species may exhibit short-term variability, i.e. concentration changes driven by variability on a scale shorter than the approximately weekly sampling resolution. This variability may reflect relatively rapid diel natural processes that may not have been fully captured such as tidal fluctuation, precipitation, photosynthesis and photochemistry or multi-day processes such as phytoplankton bloom progression. To focus on longer-term seasonal changes, the subsequent comparisons of chemical species concentrations, unless explicitly stated, are from a LOESS regression model with a 12-point spline (R-package(s) ggplot2/predictdf or Tidyverse/geom_smooth). The model fitted a localized quadratic curve with a 12-point spline that effectively smoothed short-period natural variability while succinctly capturing mid to longer-period changes. A consequence of comparing LOESS model values is that the relative concentration changes between chemical species are more conservative than were measured. Pearson correlation coefficients were used to assess potential relationships between all biological, physiochemical and iodine species, both rationalized and unrationalised (Data Table 01).

3 Results

Here we focus on the 76 samples collected from the inner shelf waters. The (14) outer shelf samples are used as a comparison to inform the discussion of the inner shelf samples. The similarities, within a 12-point spline 95% confidence limit, and difference of the inner and outer shelf samples are observable in Figure 2; Supplementary Figures SI.1, SI.2.

3.1 Water column characteristics

Within the inner shelf waters, the homogenous temperature distribution with depth indicates that the summer waters were generally well-mixed, *i.e.*, there was no significant temperature step change between the surface and deepest measuring point (Figure 3; Supplementary Figure SI.3). However, there were small differences in salinity, during the 2020-2021 autumn-winter and winter-spring transitions because of a winter pycnocline (δS_P ~1) at ~8 m (Figure 3; Supplementary Figure SI.3). Also, in summer 2020 there was higher salinity (S_P >35.5) in the near surface waters (<2 m) (Figure 3; Supplementary Figure SI.3). The salinity profiles indicated a small seasonality in the waters to a depth of ~10 m (Figure 3; Supplementary Figure SI.3). Winter salinity generally ranged between 33.2 and 34.5 (two early samples were measured at S_P = 32.9) while summer salinity ranged between 34.5 to 35.5 (Figure 3). Lower winter salinities are likely because of higher flows of terrestrially sourced water (river and groundwater) due to greater precipitation (Supplementary Figure SI.4).

3.2 Dissolved iodine species

3.2.1 Inner shelf total dissolved iodine

Total dissolved iodine (dI_T) exhibited a bi-modal seasonal maximum with maxima in the winter/spring and summer/autumn transitions (Table 1; Figures 2A, 4E) – referred to as the early and late season maxima. These maxima were more evident in 2020 than in 2021. The 2020 early season maxima were due to an accumulation over the four months beginning December 2019 where dI_T increased by 54 nM up to 440 nM. That increase was entirely removed by July 2020 leaving only 369 nM of dI_T. The late season maxima (Table 1), was due to dI_T increasing by ~60 nM up to 426 nM from July to late August. High dI_T concentrations (>415 nM) remained for 2 months during autumn. A subsequent loss of ~50 nM down to 375 nM dI_T occurred between November 2019 and the December 2020 winter minimum. The changes in dI_T during 2021 follow a broadly similar pattern to those during 2020, but the maximum concentrations were lower. The 2020 early and late season maxima, 406 and 419 nM, were in early April and mid-September, respectively, with new iodine contributing 21 and 34 nM. Also, the early summer (June) of both years exhibited a small (relative to early and late season maxima) increase in dI_T. This early summer maximum in 2020 was incorporated within the spring maximum.

3.2.2 Inner shelf iodide

Iodide ranged from 61 to 149 nM (average 88 ± 17 nM), with a seasonality characterized by high concentrations in the summer/autumn transition and low concentrations in the autumn/winter transition (Table 1), albeit with significant temporal differences between years (Figure 2A). In 2020, iodide was represented by a bi-modal distribution model (maxima in May and August) and in 2021 a single maximum (September). During winter 2019/2020 until early March iodide concentrations were relatively invariant at 68 ± 3 nM. Iodide increased at a rate of 1.1 nM d^{-1} through to the first maximum of 109 nM in late May. The summer iodide minimum (81 nM) in July was followed by a late summer maximum in August (98 nM), this maximum concentration plateaued for ~6 weeks. The year 2020 ended with iodide decreasing to 77 nM (end of November). In contrast, and following the winter minimum of 2021, iodide concentrations gradually increased at ~0.1 nM d^{-1} between mid-March and July, then more rapidly by ~1 nM d^{-1} over August. For both years, the lowest iodide concentrations were found in February, 65 nM in 2020 and 71 nM in 2021.

3.2.3 Inner shelf dissolved organic iodine

Dissolved organic iodine represented 5 ± 4% of dI_T and had an average concentration of 19 ± 16 nM. In 2020, temporal changes in DOI were broadly similar to those of iodide with bi-modal maxima over spring-summer, while in 2021 changes were more nuanced (Figure 2A). Both years began with decreasing concentrations through to March. Over the first winter, DOI concentrations decreased from 30 to 7 nM, from December 2019 to February 2020. Coincidently, the relative decrease in DOI from January 2021 (20 nM) through to March 2021 (2 nM) was similar to the previous

10.3389/fmars.2024.1277595

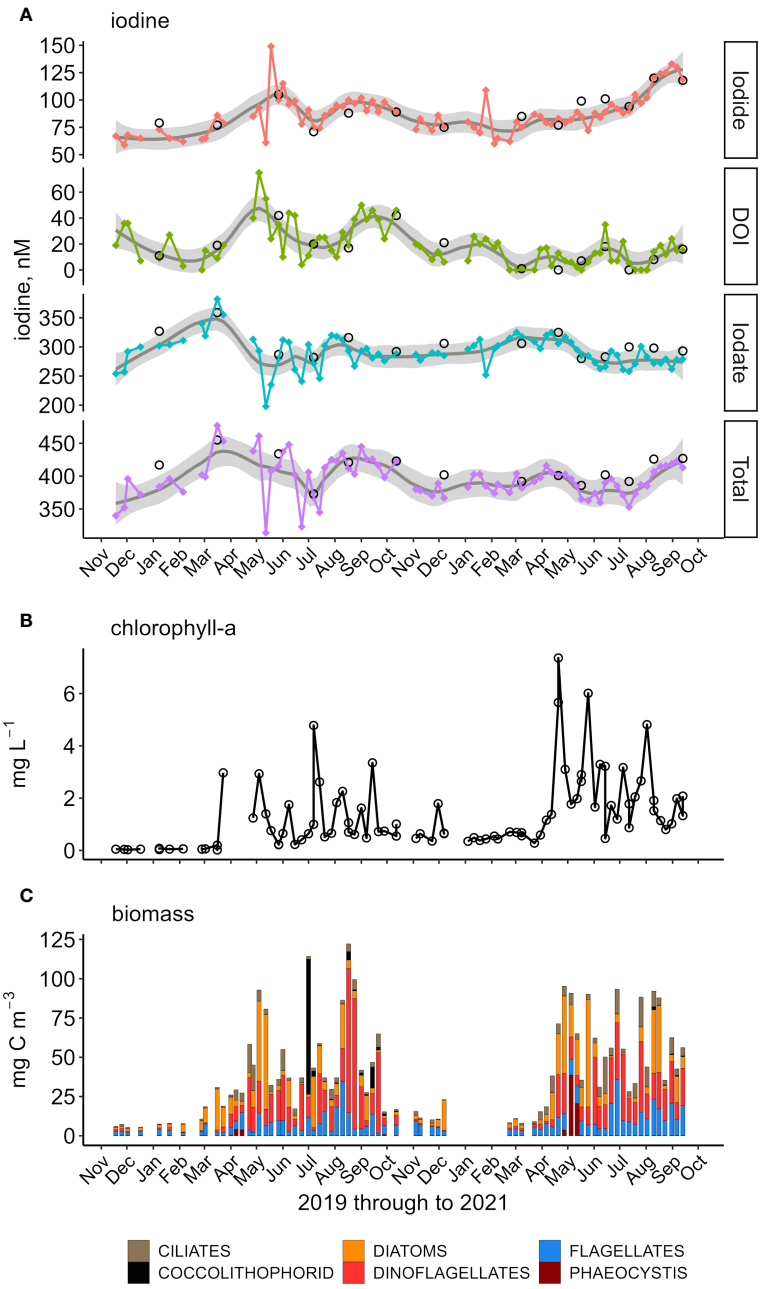

FIGURE 2
(A) Temporal change of iodine species and the total dissolved iodine in inner shelf waters; DOI, dissolved organic iodine. The grey envelope represents the 95% confidence range over a 12-point LOESS moving average. Large circles, outer shelf. Breaks in the time series data are because no samples were collected for a period of >16 d. **(B)** Inner shelf chlorophyll-α concentrations and **(C)** Outer shelf phytoplankton biomass broken down by dominant group.

year. The bimodal 2020 DOI profile showed early and late maxima occurring in May and September with >40 nM DOI. From late summer, the DOI concentrations decreased through to December by >30 nM. This was followed by a mid-winter maximum of 20 nM DOI (January 2021). In both 2020 and 2021, DOI concentrations decreased at the beginning of each year as iodate increased.

3.2.4 Inner shelf iodate

Iodate contributed 74 ± 5% of dI_T and had an average concentration of 293 ± 27 nM (Table 2). Though a significant contributor of dI_T, iodate showed only a single seasonal maximum which occurred in the winter/spring transition (Table 1; Figure 2A) and followed a gradual increase over autumn and winter. In March 2020, iodate peaked at 351 nM following a 64 nM increase (LOESS regression model, actual increase of 95 nM) from November 2019. In March 2021, the iodate maximum of 316 nM followed a smaller increase of 34 nM over the seven months from September 2020. There were inter-annual differences in the changes of iodate concentration following its seasonal maximum (Figure 2A). In the spring of 2020, iodate decreased by 85 nM from 351 to 269 nM

10.3389/fmars.2024.1277595

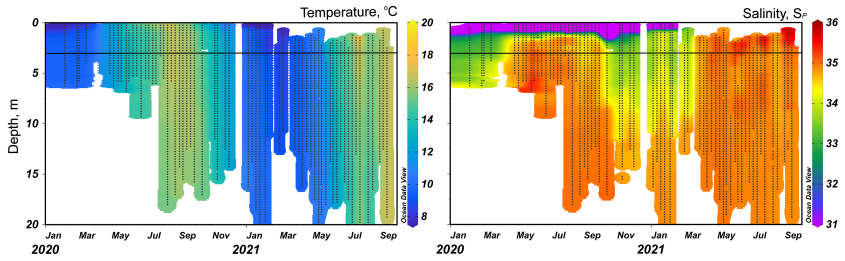

FIGURE 3
Temperature and salinity profiles of the inner shelf waters, the water column depth is variable but was no more than 20-25 m. The horizontal black line represents the sampling depth. #1.) During winter to summer of 2020 water column measurements were curtailed at ~6 m and full profiles are unavailable. #2.) 2020 abnormally low salinities in waters shallower than 2.5 m is a sampling artefact. #3.) 2021 near surface water values are not available as sampling was not conducted. Profiles produced in Ocean Data View, Schlitzer, R., Ocean Data View, https://odv.awi.de, 2018.

according to the LOESS model. These model values do not capture the significantly larger measured decrease of 184 nM observed between the only two iodate outliers (> ± 3σ) of 382 nM on 16/03/2020 and 198 nM on 12/05/2020, representing a rate of iodate decrease of 3.3 nM d^{-1} between early and late spring. In comparison, the rate of observed iodate decrease in spring 2021 was less rapid at only 1.2 nM d^{-1}; in this year the early spring (March–April) iodate concentrations were reasonably stable (314 ± 1 nM) rather than spiking to >380 nM. In the summer of 2020, iodate increased up to 305 nM in August whereas in the summer of 2021 concentrations remained low (275 ± 2 nM LOESS model *vs* 275 ± 12 nM measured, n=16).

3.3 Chlorophyll-α, biomass, phytoplankton assemblage and nutrients

Chlorophyll-α is an indicator of phytoplankton biomass and reflects the level of primary production. In general, chl-α was low in winter (2019: 0.05 mg L^{-1}; 2020: 0.4 mg L^{-1}) and higher in summer, spiking to >3 mg L^{-1} (2020) and >5 mg L^{-1} in 2020 (Figure 2B). Both years saw the first rise in chl-α in late March whereafter concentrations varied by up to 3 mg L^{-1} as phytoplankton blooms progressed through the summer. Nevertheless, in the summer of 2020 chl-α minimum concentrations were maintained at the relatively low winter 2020 concentrations whereas in 2021 summer chl-α was generally (except June 2002) maintained at >1.5 mg L^{-1}. In the outer shelf waters, four primary phytoplankton groups were present: diatoms, dinoflagellates, flagellates and to some lesser extent ciliates (Figure 2C). During the 2019/2020 winter, the biomass (mg carbon (C) m^{-3}) was approximately half of that during winter 2020/2021. Following the first winter, an early spring (March) diatom bloom preceded the subsequent gradual build-up of biomass through April. The main spring bloom was in May 2020 (>50% diatoms by biomass). In contrast, the May 2021 spring bloom appeared more suddenly, from April onwards. Following the spring bloom, there were differences between years in the progression of phytoplankton and how biomass was maintained within the water column. In 2020, and with one exception, the summer biomass was ~40 mg C m^{-3} until the late summer bloom (>100 mg C m^{-3} with >80% dinoflagellates). The exception was a 1-week period where coccolithophores were present in mid-summer (July) and the biomass increased to 114 mg C m^{-3} (75% coccolithophores). This coccolithophore bloom was present over a large area (Supplementary Figures SI.6, SI.7). In contrast, following the 2021 spring bloom, there was an approximately 5-week periodicity in the arrival of mixed assemblage phytoplankton blooms. This cycling ensured that the median biomass during the summer of 2021 remained higher than that of the summer of 2020, 56 ± 25 *vs* 42 ± 29 mg C m^{-3}, respectively. In general, concentrations of the major (nitrate, phosphate, silicate) and minor (ammonia, nitrate) nutrients were greater on the inner shelf than on the outer shelf (Supplementary Figure SI.1, compare the position of discrete open circles (outer shelf) relative to connected filled circles (inner shelf)). Nitrate showed a strong winter-to-summer seasonality; winter concentrations were between 15 and 20 µM (outer shelf >5 µM) and summer concentrations were typically <2 µM (outer shelf <0.5 µM). The seasonal cycles for phosphate and silicate were similar to nitrate. The minor nutrients, nitrite and ammonia,

TABLE 1 Comparison of iodine species concentrations during transitions between the classical season categories.

transition	months	Total I			Iodide			Iodate			DOI		
winter/spring	FMA	406	±	19	75	±	10	323	±	8	10	±	9
spring/summer	MJJ	390	±	7	92	±	4	279	±	4	19	±	6
summer/autumn	ASO	420	±	5	101	±	10	288	±	2	31	±	13
autumn/winter	NDJ	385	±	14	73	±	3	295	±	16	17	±	1

Months: FMA, February, March and April; MJJ, May, June and July; ASO, August, September and October; NDJ, November, December and January. Total dissolved iodine, dI_T, and dissolved organic iodine, DOI.

behaved similarly within the inner shelf waters, these species exhibited a bi-modal model with high concentrations in February and October (~1.0 µM NH_3 and >0.3 µM NO_2^-). The corresponding minima were in spring early/summer (<0.4 µM NH_3 and <0.1 µM NO_2^-) and mid-winter.

4 Discussion

4.1 Nature of the sampling site

The North Atlantic Ocean is the source water for the Western English Channel (French and British territorial and exclusive economic zone waters). Prevailing winds force Atlantic waters into the Western English Channel and these progress eastwards, water column mixing on the shelf is controlled by tides and weather (Cooper, 1960; Huthnance, 2010). Outer shelf waters develop a thermocline with a typical depth of ~20 m (Supplementary Figure SI.5), this stratification begins in March and ends in October, though severe wind events induce mixing with deep waters (Cooper, 1960; Huthnance, 2010). Seasonal stratification is known to impact the vertical distribution of iodine species, in that development of a thermocline facilitates the accumulation of iodide in the surface layer in association with biological activity, while overturning will dilute this by mixing with deeper, higher iodate/lower iodide waters (Chance et al., 2014; Wadley et al., 2020). These processes will impact the seasonally stratified outer shelf site which supplies the inner shelf, but will not take place at the inner shelf site as it is fully mixed year-round.

The water column at the inner shelf location was within the Rame Head current [Figure 1 and Uncles et al. (2015)]. Even in summer, the inner shelf sampling site does not undergo seasonal thermal stratification as observed on the outer shelf (Uncles et al., 2015). Moreover, the seawater dynamics of Plymouth Sound and within the Rame Head current mean that turbulent mixing processes including seabed friction, tide-, wind- and density-driven flows and the Coriolis Force limit stratification of waters between 0.5 and ~30 m deep on periods longer than a diel cycle (Wright, 1993; Upstill-Goddard, 2006; Bosboom and Stive, 2021). The temperature of the generally well mixed inner shelf water column (Figure 3; Supplementary Figure SI.3) was between 8 and 11°C during winter, 12 to 13°C during spring and autumn, and >16°C during summer.

Relative to the estimated global deep ocean dI_T concentration of ~450-480 nM (Tsunogai and Sase, 1969; Barker and Zeitlin, 1972; Elderfield and Truesdale, 1980; Jickells et al., 1988; Nakayama et al., 1989; McTaggart et al., 1994; Campos et al., 1996; Tian et al., 1996; Farrenkopf et al., 1997; Moriyasu et al., 2020; Moriyasu et al., 2023; Schnur et al., 2024) inner shelf waters were depleted ($\bar{x}$=400 ± 30 nM, range 314-477 nM; Table 2). Nevertheless, the average dI_T concentration of both inner and outer shelf seawater was within the range of reported Atlantic surface waters dI_T concentrations (≈435 nM, Elderfield and Truesdale (1980) and Truesdale et al. (2000); 390 ± 20 nM, He et al. (2013)). The inner shelf dI_T concentration showed a bi-modal seasonal maximum (Figures 2A, 4E). The first maximum was likely caused by winter advection of Atlantic surface waters across the shelf as the spring dI_T concentrations (>400 nM) were more similar to surface Atlantic source waters (Elderfield and Truesdale, 1980; Truesdale et al., 2000; He et al., 2013).

Advection and tidal forcing of Western English Channel shelf sea waters into Plymouth Sound results in those waters exiting via a broad headland current that first flows into Cawsand Bay and then around Rame Head (Siddorn et al., 2003; Uncles et al., 2015). The residence time of seawater in Plymouth Sound prior to arriving at the sampling site is ~2.5 days (Uncles et al., 2015). During this period, freshwaters, (*e.g.*, submarine groundwater discharge and estuarine waters – River Plym (minor contribution) and River Tamar (major contribution)) will influence seawater composition. Additions of terrestrial and anthropogenic material within freshwaters entering Plymouth Sound coupled with the residence time are the likely cause of the higher inner shelf nutrient concentrations (Section 3.3; Supplementary Figures SI.1, SI.4) with higher nutrients driving higher primary productivity (Lotze et al., 2006; Canfield et al., 2010).

4.2 Iodine dynamics in a terrestrially influenced inner shelf seawater

4.2.1 Influence of freshwater

Seawater at the outer shelf site is primarily ocean sourced with only episodic summer inputs from the Tamar River (Rees et al., 2009; Supplementary Figure SI.5) while inner shelf waters are continuously modified by terrestrially derived fresh water. In freshwater, the primary iodine species are iodide or DOI (Schwehr and Santschi, 2003; Tang et al., 2013; Zhang et al., 2013). Freshwater chemical species entering the marine system because of submarine groundwater discharge (Tait et al., 2023) or from estuaries may first undergo chemical changes and removal and resuspension cycles due to ion exchange and precipitation, though whether dI_T behavior is conservative is under debate (Smith and Butler, 1979; Ullman and Aller, 1980; Takayanagi and Cossa, 1985; Francois, 1987; Luther and Cole, 1988; Abdel-Moati, 1999; Cook et al., 2000; Jones and Tebo, 2021; Lin, 2023). In the case of iodine, estuarine processes may even entirely remove any freshwater iodine such that the only effect of freshwater is expected to be dilution of the seawater concentration, *i.e.*, it can be described by Equation 1 (Takayanagi and Cossa, 1985). However, with no measurement of iodine concentrations in Plymouth Sound's freshwater sources (two major estuaries plus ground water submarine discharge), we cannot definitively state this.

Calculation of excess iodine (I^*) provides a means to estimate additional sources of dI_T to the inner shelf, albeit with uncertainty arising from poorly constrained freshwater and marine endmember concentrations. From 73 samples, 34 had negative I^* and 39 (53%) had positive I^*, therefore there was both a sink and a source of dI_T. The average I^* contribution was 3 ± 29 nM (n=73) and 60 (82%) samples were within one standard deviation (29 nM) of equality ($I^* = 0$). There were nine samples with I^* >25 nM (range, 28-98 nM) and five with I^* ranging from -28 to -90 nM indicating that episodic process(es) that influence I^* could significantly alter dI_T by more than the assumed freshwater concentration (25 nM). Though I^* is higher in summer than winter when river flow is correspondingly low (Supplementary Figure SI.8A) there appears to be no relationship

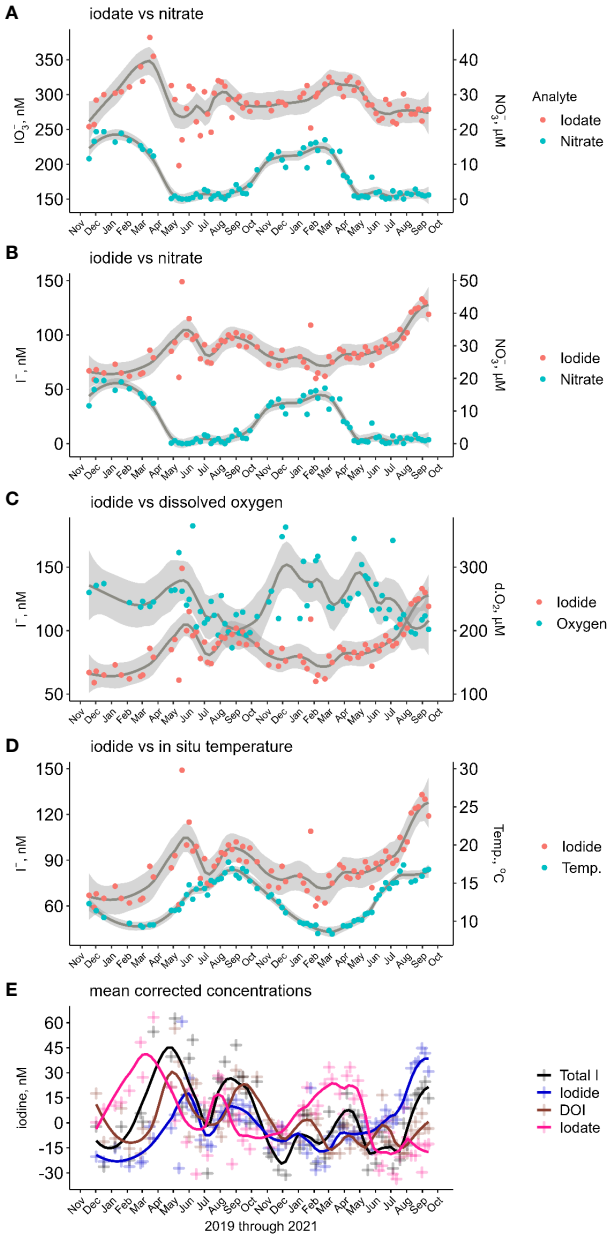

FIGURE 4
(A–D) Comparison of iodate and iodide to nitrate, dissolved oxygen and seawater temperature in the inner shelf waters. The grey envelopes represent the 95% confidence range over a 12-point LOESS moving average. **(E)** Temporal change from mean corrected total dissolved iodine and iodine species in inner shelf waters.

with river flow (Supplementary Figure SI.8B), nor is there a strong relationship in I^* with the fraction of freshwater in the sample (Supplementary Figure SI.8C) or tide height (Supplementary Figure SI.8D). Nevertheless, iodine concentrations in the water column of an estuary have previously been observed to increase as river flow decreases (Abdel-Moati, 1999). Lower estuarine flow rates result in longer residence times for estuarine waters, and hence, more estuarine processes/sediment pore water interactions. This is important because upper sediment pore water dI_T concentrations of the lower Tamar River estuary are generally between 2-5 µM (Upstill-Goddard and Elderfield, 1988) so at low river flow they may be a source of iodine as iodide but not iodate. Conversely, sediment entrapment to the water column that increases suspended load may decrease soluble iodine concentration (Truesdale, 1994; Truesdale and Upstill-Goddard, 2003; Satoh et al., 2019a; Satoh et al., 2023). The low relative mean contribution of I^* (3 nM) and the relative consistency of dI_T (399 ± 30 nM) indicates that seawater successfully subsumes seawater margin processed dI_T contributions.

Rationalized iodine (Section 2.2.3) supported the initial conclusion that dI_T was not conserved over seasonal and annual scales at the inner shelf sampling site (Figures 5B, C). This is consistent with the fact these waters show asynchronous cycling of iodate, iodide and DOI (Figures 2A, 4E). Over a year it was anticipated that the dI_T concentrations may be conserved because

TABLE 2 Statistical analysis of two years of measured iodine species concentrations (nM) broken down by inner or outer shelf sampling location.

Iodine	location	mean	median	sigma	range			δ(max – min)
dI_T	L4 and PPAO	400	399	30.3	314	–	477	163
	L4	411	410	22	373	–	455	82
	PPAO	397	396	31.5	314	–	477	163
Iodide, IO_3^-	L4 and PPAO	88.8	88	17.4	61	–	149	88
	L4	91.3	88.5	15.6	71	–	120	49
	PPAO	88.3	88	17.8	61	–	149	88
Iodate, I^-	L4 and PPAO	293	293	27.5	198	–	382	184
	L4	304	299	21.9	280	–	359	79
	PPAO	290	290	28.1	198	–	382	184
DOI	L4 and PPAO	18.8	16	15.9	<0.12	–	75	75
	L4	15.9	16.5	13.3	<0.12	–	42	42
	PPAO	19.4	15	16.4	<0.12	–	75	75

The analytical detection limit for the method is 0.12 nM. Total dissolved iodine, dI_T and DOI, dissolved organic iodine.

dI_T has previously shown conservative properties (Tian et al., 1996). A contributing factor towards the non-conservation of dI_T is that the variability in the spatial concentration of dI_T in North Atlantic surface waters is also high (390 ± 20 nM He et al., 2013 and outer shelf dI_T Figure 2A). In terms of concentration, and once normalized for salinity, the dI_T ($\bar{x}$=413 ± 31 nM) concentrations observed at the inner shelf are closer to the Truesdale et al. (2000) than the He et al. (2013) observations. Importantly, observed and normalized dI_T changes over time were similar (Figure 5B) indicating dilution of seawater by freshwater while in Plymouth Sound is not a significant driver of the concentration changes over the seasonal time series. This conclusion is also in agreement with Shi et al. (2023) who did not find a relationship between salinity and dI_T over a wider salinity range, S_P = 26-31 during a 4.5-year time series in a fjord.

4.2.2 Terrestrial influence on inner shelf seawater

In UK coastal waters, *in situ* processes have been found to dominate over estuarine inputs for influencing iodine concentrations (Smith and Butler, 1979; Truesdale and Upstill-Goddard, 2003). To test whether inner shelf processes were influencing iodine concentration and speciation we compared 14 paired inner and outer shelf samples, each pair collected within 30 minutes. A Student t-test of those paired samples (Table 3) indicated that outer and inner shelf iodide and DOI were statistically similar but dI_T and iodate were significantly lower. The monthly average difference of iodate (20 ± 5 nM or 7%) between the outer and inner shelf was consistent throughout the year except during the transition periods in May and October (Figure 6). Salinity rationalized iodate and dI_T are known to decrease towards the coast though a cause for this effect has not yet been identified (Truesdale, 1978; Wong and Zhang, 1992; Truesdale and Jones, 2000; Truesdale and Upstill-Goddard, 2003). Mesoscale processes on the inner shelf that can change as a function of water column depth and influence iodine speciation range from the physical (*e.g.*, mixing of the bottom boundary layer (deepest 10 m) of the water column by interaction with the seabed and wave refraction from the coasts) to chemical (*e.g.*, additions through submarine groundwater discharge, anthropogenic material from point and diffusive sources, natural terrestrial organic and inorganic material and elevated mineral surface areas or suspended load that catalyze reactions). Despite the statistical differences, the 95% confidence level of the inner shelf LOESS model tracks the outer shelf measured dI_T and iodine speciation concentrations (Figure 2A). We infer from these similar temporal changes that the inner and outer shelf concentrations were likely driven by the same suite of processes. Superimposed on these, we propose that there are additional process taking place closer to the shore that decreased inner shelf iodate by ~20 nM without increasing iodide or DOI concentrations. An iodate loss rate of ~8 nM d^{-1} was calculated from the residence time of seawater in Plymouth Sound (~2.5 days) and the 20 nM inner to outer shelf iodate concentration difference (Figure 6). This rate is similar to Truesdale's (1978) estimated rate of iodate removal, ~16 nM d^{-1}, in the Menai Strait (Wales, UK). In our study, the outer to inner shelf iodide concentration difference (-2 nM or ~2% of the iodide, Table 3) was not significant and therefore the inner shelf waters did not follow the previously observed behavior of iodide increasing shoreward (Truesdale, 1978; Wong and Zhang, 1992; Truesdale and Jones, 2000; Truesdale and Upstill-Goddard, 2003). The inner and outer shelf DOI concentrations of the present study were also very similar (Table 3), though the 1 nM higher inner shelf DOI is ~6% of the total DOI. The asynchronous seasonal concentration changes of iodine species (Figures 2A, 4E) and non-conservation of dI_T (Figures 2A, 6B) indicate that there was another pool of (undetected) iodine or an *ex situ* removal and renewal process that influenced the inner shelf waters.

4.3 The missing pool of iodine

4.3.1 Biological particulate iodine

Our study aimed to constrain iodine cycling within the soluble fraction but because dI_T was not conserved we must consider the

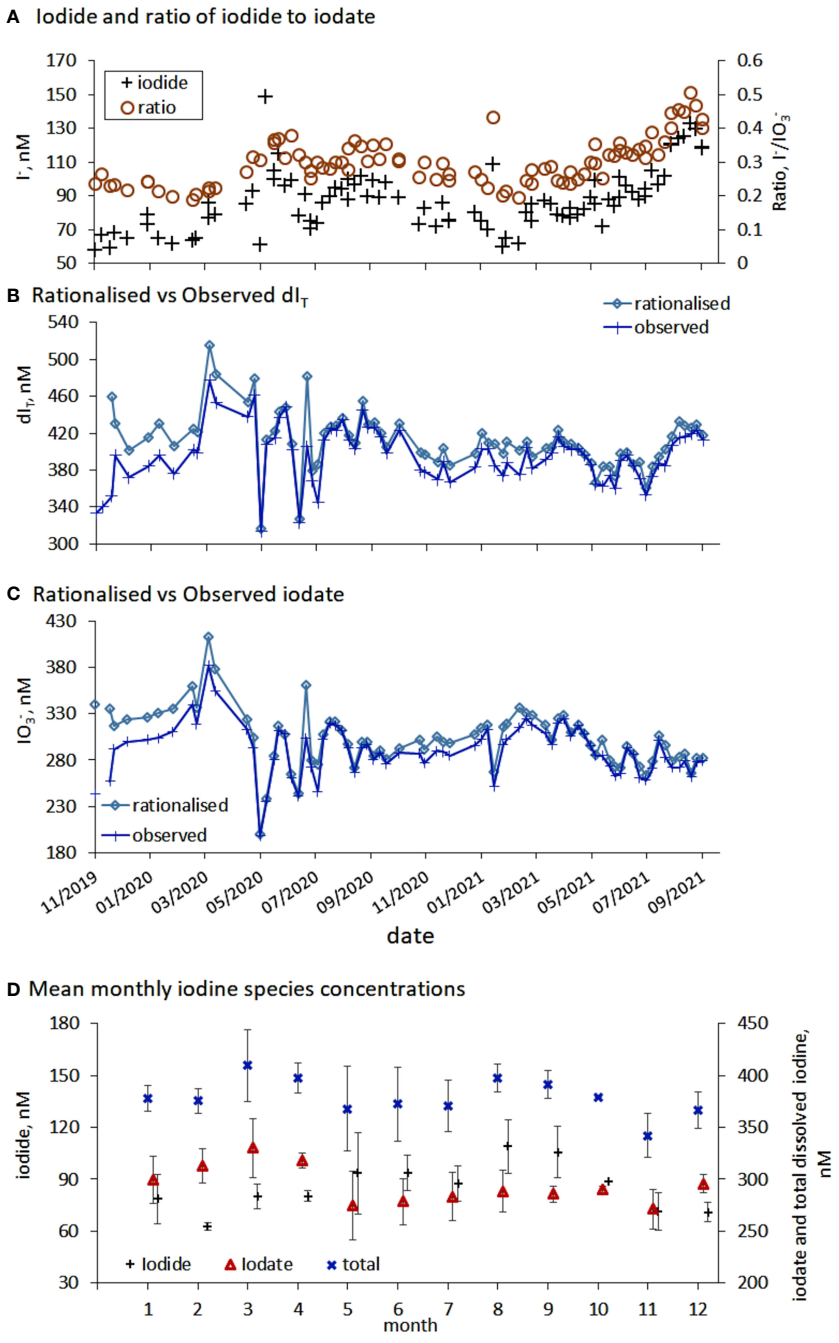

FIGURE 5
(A) Comparison between the inners shelf iodide concentration and the ratio of iodide to iodate. **(B–C)** Comparison between temporal changes in rationalised (normalised to a salinity of S_P=35) and observed total dissolved iodine (dI_T) and iodate. **(D)** Average calendar (2020 and 2021) iodine concentration for inorganic iodine species (iodide, iodate and total dissolved iodine) in the inner shelf waters, error bars represent the standard deviations of the measurements.

possibility that the missing iodine is in the particulate phase. The concentration of total particulate iodine (pI_T) in the coastal Pacific and open Atlantic Ocean surface seawaters is ~1 nM (Wong et al., 1976; Satoh et al., 2023). The low pI_T concentration suggests that pI_T cannot account for the tens of nanomolar dI_T inner shelf missing pool of iodine. Though pI_T was not measured we can estimate the biological contribution towards pI_T. Particulate iodine is split into three pools, biological [pI_{Bio}, incorporated within organisms, primarily phytoplankton as the largest biomass in the water column (Sigman and Hain, 2012)], organic (*i.e.*, large amorphous colloids, aggregates and detrital matter) and inorganic (*e.g.*, calcite or ferromanganese particles). The iodine content of the plankton biomass can be estimated from the carbon to iodine ratio of $1{:}1{\times}10^{-4}$ (Elderfield and Truesdale, 1980) and the inner shelf biomass (mg C m^{-3}, Section 2.2.2). Our estimate of pI_{Bio} ranged from 0.004 to 0.096 nM, this is 1000× lower than dI_T and 10× lower

TABLE 3 Average (± standard deviation), correlation co-efficient (R^2) and results of one tail student t-Test for the 14 paired samples that were collected on the same days at the inner and outer shelf location.

Fraction/species	R^2	t-Test	P	PPAO, nM	L4, nM	result
				($\bar{x} \pm \sigma$)	($\bar{x} \pm \sigma$)	
dI_T	0.529	4.46	0.0003	391 ± 22	411 ± 22	Accept
I^-	0.793	1.33	0.103	89 ± 17	91 ± 16	Reject
IO_3^-	0.533	4.06	0.0007	287 ± 19	304 ± 22	Accept
DOI	0.666	-0.36	0.363	17 ± 14	16 ± 13	Reject
rationalised dI_T	0.627	3.00	0.005	402 ± 22	414 ± 24	Accept
rationalised IO_3^-	0.625	2.76	0.008	295 ± 22	306 ± 23	Accept

Hypothesis tests if the mean and variance are dissimilar. For 14 paired samples there are 13 degrees of freedom and a t Critical value of 1.77. Total dissolved iodine, dI_T, and dissolved organic iodine, DOI. Rationalised concentrations are salinity normalised to $S_P = 35$.

than the expected pI_T (Wong et al., 1976; Satoh et al., 2023). Therefore, pI_{Bio} is only a small portion of pI_T and unlikely to be the missing pool of iodine.

4.3.2 Dissolved/particulate organic iodine

The significant concentration of DOI observed (19 nM, Table 2) is evidence that iodine was present in soluble organic structures. There exist a large variety of possible iodinated low molecular weight organic material (Bichsel and von Gunten, 1999; Wong and Cheng, 2001a; Sherrill et al., 2004; Du et al., 2023). One reason for elevated DOI is that there are higher organic material concentrations in inner shelf waters relative to outer shelf water. This organic material has a different structure and composition strongly influenced by terrestrially derived material (Muller, 2018 and references therein). Inner shelf organic material availability is also influenced seasonally because increased seasonal precipitation flushes material from the terrestrial to the marine environment. However, on the inner shelf, the temporal variation in dissolved organic carbon (DOC) was low and its concentration did not exhibit a strong seasonality (data not shown). A steady-state DOC system has the potential for continuous DOI formation. As well as bacterial processes in estuarine systems that convert DOI to inorganic iodine (Luther et al., 1991) the decomposition of DOI *via* photochemistry or ozonation produces iodide and iodate (Wong and Cheng, 2001b; Sherrill et al., 2004). Photochemical breakdown of DOI is of the order of hours and ozonation of DOI is of the order of minutes (Wong and Cheng, 2001b; Sherrill et al., 2004). With lower winter solar irradiation and therefore levels of photochemistry this may allow winter DOI to accumulate as observed (Figures 2A, 4E). Organic material is generally also required for the photochemical formation of reactive intermediate species that influence iodine cycling (Liebhafsky, 1934; Hughes et al., 1971; Rush and Bielski, 1985; Neta et al., 1988; Lymar et al., 2000; Wong and Zhang, 2008; Sharpless and Blough, 2014; Hardisty et al., 2020; Luther, 2023).

The iodine species hypoiodous acid and molecular iodine, which oxidize organic carbon, are also the most likely to undertake nucleophilic substitution reactions to form DOI. Hypoiodous acid, though thermodynamically stable at pH = 8 (pK = 10.6; Truesdale and Luther, 1995), forms molecular iodine following its comproportionation with iodide (Luther et al., 1995; Truesdale and Luther, 1995; Bichsel and von Gunten, 1999; Li et al.,

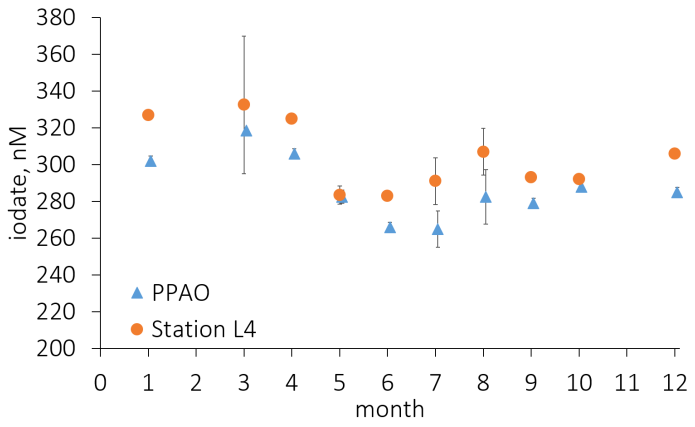

FIGURE 6
Average collated inner and outer shelf monthly observed coincident mean iodate (IO_3^-) concentrations. Mean iodate difference, excluding the transition months of May and October, is ~20 nM. Error bars represent the standard deviation of all observations for those calendar months.

2020; Du et al., 2023). Iodate is also an iodinating agent for organic material (Baer et al., 2011; Zhdankin and Muñiz, 2017) and may be significant as a precursor ion for DOI. Iodate sequestration into organic material which then precipitates to sediments because of increasing ionic strength has been suggested as the mechanism for iodate removal in estuarine systems (Cook et al., 2000; Wong and Zhang, 2003). In soils, estuaries and marine systems an organoiodate has been found to form concurrently with the removal of inorganic iodate (Francois, 1987; Luther et al., 1991). When considering whether there is iodide or iodate within organic structures it has been found that iodate forms the more reactive form of DOI in both *ex situ* seawaters amended with humic acid and porewaters fluxing from sediments (Francois, 1987; Bowley et al., 2016; Satoh and Imai, 2021). In laboratory experiments that had no external forcing, *i.e.*, no advanced oxidation processes such as photochemistry or ozonation, organoiodate had a half-life of *circa* 10 *d* (Bowley et al., 2016). As DOI is present, iodine may also be retained in particulate organic carbon and may contribute to the missing pool of iodine.

Alternatively, we must also acknowledge that there may be a portion of the DOI that is not recoverable by the analytical method (Jones et al., 2023). However, a comparison of the concentration recoveries of the chemical digestion method versus a UV digestion showed the chemical digestion method was high (98 ± 4%, n=92; Jones et al. (2023)). Furthermore, the agreement between the measured DOI and the ratio of DOI to inorganic iodine found here and that found by other authors using different digestion techniques suggests that this undetected pool of dissolved iodine may not be significant (Truesdale, 1975; Luther et al., 1991; Wong and Cheng, 1998; Truesdale et al., 2001; Schwehr and Santschi, 2003; Takeda et al., 2016). Any unrecovered organic iodine in the dissolved fraction is likely to be small and not account for the missing pool of iodine.

4.3.3 Sediment-water interactions

As well as a 'missing iodine' pool in the water column, we consider mechanisms that might remove (and subsequently renew) dissolved iodine on the inner shelf over seasonal scales. Once iodine species are adsorbed or absorbed by the water column's suspended load (organic or inorganic) they can be deposited onto the sediment-water interface. At the interface, iodate may be retained or chemically reduced (Francois, 1987; Anschutz et al., 2000). Sediment porosity controls the distance oxygen can travel into sediments and whether redox processes occur at the sediment-water interface or deeper. Plymouth Sound sediments are porous because they have a high percentage of sand (Franco et al., 2017; Johnson et al., 2022). In interstitial porewaters, the iodine species derive from organic material remineralization in oxygenated (Francois, 1987) or anoxic sediments (Ullman and Aller, 1980) or following iodate reduction in hypoxic or suboxic sediments (Chapman and Truesdale, 2011). Solution phase iodine species is scavenged at the oxic interface by ferro-manganese minerals or other reactions relating to soluble phase metal cycling and/or organic material cycling (Harvey, 1980; Ullman and Aller, 1985; Francois, 1987; Luther et al., 1997; Anschutz et al., 2000; Satoh and Imai, 2021). Nevertheless, oxygenated sediments can also be a source of iodide to overlying waters and iodide fluxes increase as oxygen concentrations decrease (Chapman and Truesdale, 2011; Satoh and Imai, 2021; Ooki et al., 2022).

To test if iodide was fluxing from sediments and increasing concentrations in inner shelf waters we considered excess nitrogen (N^*) because sediments are a known source of nitrogen. The N^* value provides the nitrogen deficit or excess relative to the canonical nitrogen to phosphate Redfield Ratio (RR) of 16 (Equation 2).

$$N^* = [N_{Total} = \sum NO_2^-, NO_3^-, NH_4^+] - [PO_4^{3-}] \times RR \quad (2)$$

If the concentration of seawater nitrogen is lower than that predicted there will be a negative N^*, whereas a positive N^* value indicates that the seawater is enriched with nitrogen. The N^* rationalization is typically used in open ocean settings though it has been used in shelf sea systems (Kim et al., 2011; Moon et al., 2021). The N^*-iodide relationship was negative (Supplementary Figure SI.9), so inner shelf waters had higher iodide when nitrogen was deficient. The N^*-iodate relationship was positive and this was likely forced by the winter advection of low primary productivity, high nutrient North Atlantic waters combining with excess freshwater bringing terrestrial runoff (Supplementary Figures SI.4, SI.9). Nevertheless, the iodate loss during spring and summer, the accumulation of iodide over summer and autumn and the non-conservation of dI_T may be accounted for by iodate deposition to and a slow flux of iodide from the sedimentary system.

4.4 Seasonal controls on dissolved iodine speciation

Within dI_T, the relative contribution of iodine species was: iodate 73 ± 6%; iodide 22 ± 4%; and DOI 5 ± 4%. The relative contributions are of a similar magnitude to those observed in northeast Atlantic surface waters, 89% iodate and 12% iodide (He et al., 2013). The late autumn dI_T maxima was caused by the gradual build-up of iodide through the warmer summer months, a process observed in the Mediterranean Sea and North Atlantic Fjords (Tian et al., 1996; Shi et al., 2023). The seasonal iodine speciation changes at the inner shelf, which were also observed at the outer shelf (Figure 2), are the first to be reported for UK coastal waters (Truesdale and Upstill-Goddard, 2003) though seasonal changes in iodine speciation have been reported in other locations (Jickells et al., 1988; Campos et al., 1996; Tian et al., 1996; Chance et al., 2010; Shi et al., 2023). Changes in iodine species and dI_T mean that the iodide to iodate ratio was not conserved but the iodide/iodate ratio (0.3 ± 0.07 ($\bar{x}\pm\sigma$), range 0.19-0.51) did follow the same temporal pattern as the change in iodide (Results Section 3.1.2 and Figure 5A).

4.4.1 Biological control

The timing of certain changes in iodine speciation (Figures 2, 4) supports the paradigm that transformations between iodine species are biologically mediated. However, the near coincident relationship between seasonal changes in inorganic iodine species

and nitrate (Figures 4A, B), a key nutrient for marine biological systems, and inorganic iodine and dissolved oxygen (Figure 4C), the product of photosynthesis, were not statistically significant. Oxygen is an oxidant of iodide, although not thought to be significant in oxygenated systems (Luther et al., 1995), thus the relationship between dissolved oxygen and iodine speciation was likely not causal. In terms of phytoplankton, which are the main controllers of nutrient concentration, laboratory culture experiments have shown iodide production as phytoplankton cultures collapse and bacterial numbers increase (Chance et al., 2007; Bluhm et al., 2010; Hepach et al., 2020). For discrete phytoplankton blooms, a time lag of 60 days between iodate reduction and iodide production was observed in Antarctic coastal waters (Chance et al., 2010) and in culturing studies (Chance et al., 2007; Bluhm et al., 2010; Hepach et al., 2020). A time lag of 60 days was successfully used to constrain an ocean iodine model (Wadley et al., 2020). The lag times from the 2020 iodate LOESS maximum (358 nM, March 2020) and iodide and DOI maxima were 65 and 42 days, respectively (Figures 2A, 4E). However, for 2021, and because iodide concentrations were still increasing in September 2021, the lag between the iodate (314 nM, March) and iodide maxima was a minimum of 190 days. The different phytoplankton succession sequences of summer 2020 and 2021 may explain the different lag phases of the iodine species. In 2020, the outer shelf had an early and late bloom (Figure 2C) with a transient coccolithophore presence in mid-summer (Supplementary Figures SI.6I, SI.7G). In 2021, the bloom cycle occurred at approximately 5-week intervals. With just two discrete blooms in 2020, we propose that a senescence phase evolved between those blooms that allowed for heterotrophic organisms to take advantage of the conditions resulting in a time lag of 60 d, whereas in 2021, the heterotrophic organisms could not establish themselves as the bloom successions cycled too quickly so the time lag, 190 d, arrived towards the end of the growing season.

If dI_T is conserved (Tian et al., 1996; Waite et al., 2006) and iodine speciation changes were due to *in situ* biological conversion between iodide to iodate and *vice versa* and pI_{Bio} was low, then a correlation could be expected between soluble iodine species. Moreover, as DOI may form because of the iodination of organic material (Dunford and Ralston, 1983) a relationship may also exist between DOI and an inorganic iodine species. The linear correlation coefficient between iodate and iodide was R^2_{iodide} = 0.05 and between iodate and DOI, R^2_{DOI} = 0.07. Adjusting the temporal changes in iodine species concentrations to synchronize based on time lags did not improve correlations; after applying the 2020 time lag of 65 days the correlation coefficients were R^2_{iodide} = 0.01 and R^2_{DOI} = 0.03. Other than for iodate, there was no observed iodine speciation seasonality with concentration changes related to major nutrient changes (nitrate, phosphate and silicate). That iodine did not follow a nutrient-like profile supports Truesdale and Jones's (2000) proposal that iodine does not show nutrient-like behavior. Therefore, the pattern of iodine speciation change on the inner and outer shelf of the Western English Chanel is not consistent with a simple biological uptake or a direct iodate to iodide reduction coupled with phytoplankton growth (Waite and Truesdale, 2003; Hung et al., 2005; Amachi et al., 2007). As decreasing concentrations of dI_T are not concurrent with increasing biomass then other processes must also be involved in iodine speciation changes and iodine storage.

As well as phytoplankton, higher life forms and the habitats in which they live may influence iodine speciation. The multi-stage growth cycle of jellyfish depends on the availability of iodide and a specific DOI (Silverstone et al., 1977; Prieto et al., 2010). On the inner shelf, elevated DOI is somewhat coincident with elevated iodide (Figure 2A). High DOI concentrations can kinetically protect organo-iodine signaling compounds used by mature jellyfish to induce strobilation in benthic populations (Silverstone et al., 1977; Prieto et al., 2010). Also, cnidarian (jellyfish) control iodine speciation to help relieve oxidative stress (Berking et al., 2005). On the outer shelf, zooplankton pre-empts the winter/spring transition primary production bloom (Smyth et al., 2010) but during initial bloom conditions, zooplankton concentrations are kept low by a significant population of gelatinous planula larvae (jellyfish; Cross et al., 2015). Macroalgae (kelp) also interact with the iodine cycle for the benefit of relieving oxidative stress (Küpper et al., 2008). The Rame Head current flows through Cawsand Bay (Siddorn et al., 2003; Uncles et al., 2015), which is a warm, shallow, lateral bay and a habitat for *Laminaria* kelp (Teagle and Smale, 2018). Though used to relieve chemical stress the effect of iodine species cycling in this role is highly localized, within 0.1-1.0 m distance, from the kelp (Küpper et al., 1998; Carrano et al., 2021). If Cawsand Bay kelp beds were a strong influence on iodine speciation we would expect similar seasonal cycles yet cycles between 2020 and 2021 were different (Figure 2). Finally, seagrass can produce halocarbons including iodomethane (Weinberg et al., 2013) and the iodine content within the flesh of seagrass fluctuates on a seasonal cycle (Satoh et al., 2019b; Satoh et al., 2020), so it is possible that they may locally influence iodine speciation. However, even though seagrass is present in Plymouth Sound and Cawsand Bay (Howard-Williams, 2022) there is insufficient evidence to assess its effect here.

5 Conclusions

A range of biologically mediated processes coupled with potential sediment interactions and seawater margin processed aqueous iodine may influence the cycling of iodine in the temperate coastal marine environment. Nearly two years of observations of iodine species on the inner and outer shelf of temperate coastal surface waters showed the following; 1.) winter iodate concentrations increased because of renewal through advection/mixing of source waters, 2.) dissolved organic iodine increased during winter, 3.) iodate reduction began as light levels and biomass increased, 4.) there was a significant time lag between iodate reduction and iodide and DOI accumulation, 5.) iodide and DOI accumulated during warmer periods within a well-mixed water column, 6.) the asynchronous progression of iodine species resulted in dI_T not being conserved, 7.) the near coincident seasonal concentration changes for iodate and nitrate were not statistically significant, 8.) seawater margin processed aqueous iodine may sometimes be significant but concentrations are subsumed by seawater and 9.) a significant pool of iodine remains unaccounted for and is required to conserve the concentration of dI_T in the water column.

There are many processes and systems, which range in scale from the mesoscale to the molecular, that influence iodine species formation

and cycling. We were unable to identify a definitive suite of coupled processes that cause iodine species transformations. However, the combination of processes that influenced iodine speciation on a seasonal scale commenced in late spring and ran through to autumn, so were likely biological in origin. The processes driving the iodine cycle may be due to the relationship between phytoplankton and bacterial or archaeal populations or due to seasonal changes in organic material composition. Autochthonous and allochthonous (terrestrial input) DOC are also photochemically labile and this characteristic influences the formation of reactive intermediate species and their subsequent interaction with iodine and the function of organoiodate. This work has shown that our understanding of iodine's marine biogeochemistry is still insufficient for the requirement to understand the processes controlling oceanic surface iodine speciation and thus how it influences iodine's role in the chemistry of the atmosphere.

Data availability statement

The raw data supporting the conclusions of this article will be made available by the authors, without undue reservation.

Author contributions

MJ: Data curation, Formal analysis, Investigation, Methodology, Writing – original draft, Writing – review & editing. RC: Conceptualization, Data curation, Formal analysis, Investigation, Writing – review & editing. TB: Methodology, Writing – review & editing. OJ: Investigation, Writing – review & editing. DL: Investigation, Writing – review & editing. RM: Investigation, Writing – review & editing. LT: Conceptualization, Formal analysis, Investigation, Writing – review & editing. KW: Formal analysis, Investigation, Writing – review & editing. CW: Formal analysis, Funding acquisition, Methodology, Writing – review & editing. LC: Conceptualization, Funding acquisition, Writing – review & editing.

Funding

The author(s) declare financial support was received for the research, authorship, and/or publication of this article. This work was funded by a European Research Council (ERC) (project O3-SML; grant agreement no. 833290) grant under the European Union's Horizon 2020 programme to LC. This work was also supported by the UK Natural Environment Research Council's National Capability Long-term Single Centre Science Programme, Climate Linked Atlantic Sector Science, grant number NE/R015953/1, and is a contribution to Theme 1.3 - Biological Dynamics.

Acknowledgments

This paper also contributes to the science plan of the Surface Ocean-Lower Atmosphere Study (SOLAS), which is partially supported by the U.S. National Science Foundation (Grant OCE-1840868) via the Scientific Committee on Oceanic Research (SCOR). We are especially grateful to Plymouth Marine Laboratory and the crew of the RV *Plymouth Quest*, for collecting and filtering seawater samples. We thank the reviewers for their time, insights and comments that helped improve this paper.

Conflict of interest

Author KW is employed by Fidra, though at the time of research, she was with the University of York.

The remaining authors declare that the research was conducted in the absence of any commercial or financial relationships that could be construed as a potential conflict of interest.

Publisher's note

All claims expressed in this article are solely those of the authors and do not necessarily represent those of their affiliated organizations, or those of the publisher, the editors and the reviewers. Any product that may be evaluated in this article, or claim that may be made by its manufacturer, is not guaranteed or endorsed by the publisher.

Supplementary material

The Supplementary Material for this article can be found online at: https://www.frontiersin.org/articles/10.3389/fmars.2024.1277595/full#supplementary-material

References

Abdel-Moati, M. A. R. (1999). Iodine speciation in the Nile River estuary. *Mar. Chem.* 65, 211–225. doi: 10.1016/S0304-4203(99)00003-1

Amachi, S., Kawaguchi, N., Muramatsu, Y., Tsuchiya, S., Watanabe, Y., Shinoyama, H., et al. (2007). Dissimilatory iodate reduction by marine Pseudomonas sp. strain SCT. *Appl. Environ. Microbiol.* 73, 5725–5730. doi: 10.1128/AEM.00241-07

Amachi, S., Muramatsu, Y., Akiyama, Y., Miyazaki, K., Yoshiki, S., Hanada, S., et al. (2005). Isolation of iodide-oxidizing bacteria from iodide-rich natural gas brines and seawaters. *Microb. Ecol.* 49, 547–557. doi: 10.1007/s00248-004-0056-0

Anschutz, P., Sundby, B., Lefrançois, L., Luther, G. W., and Mucci, A. (2000). Interactions between metal oxides and species of nitrogen and iodine in bioturbated marine sediments. *Geochimica Cosmochimica Acta* 64, 2751–2763. doi: 10.1016/S0016-7037(00)00400-2

Baer, M. D., Pham, V.-T., Fulton, J. L., Schenter, G. K., Balasubramanian, M., and Mundy, C. J. (2011). Is iodate a strongly hydrated cation? *J. Phys. Chem. Lett.* 2, 2650–2654. doi: 10.1021/jz2011435

Barker, D. R., and Zeitlin, H. (1972). Metal-ion concentrations in sea-surface microlayer and size-separated atmospheric aerosol samples in Hawaii. *J. Geophysical Res.* 77, 5076–5086. doi: 10.1029/JC077i027p05076

Barrón, C., and Duarte, C. M. (2015). Dissolved organic carbon pools and export from the coastal ocean. *Global Biogeochemical Cycles* 29, 1725–1738. doi: 10.1002/2014GB005056

Berking, S., Czech, N., Gerharz, M., Herrmann, K., Hoffmann, U., Raifer, H., et al. (2005). A newly discovered oxidant defence system and its involvement in the development of *Aurelia aurita* (Scyphozoa, Cnidaria): reactive oxygen species and elemental iodine control medusa formation. *Int. J. Dev. Biol.* 49, 969–976. doi: 10.1387/ijdb.052024sb

Bichsel, Y., and von Gunten, U. (1999). Determination of iodide and iodate by ion chromatography with postcolumn reaction and UV/Visible detection. *Anal. Chem.* 71, 34–38. doi: 10.1021/ac980658j

Bluhm, K., Croot, P., Wuttig, K., and Lochte, K. (2010). Transformation of iodate to iodide in marine phytoplankton driven by cell senescence. *Aquat. Biol.* 11, 1–15. doi: 10.3354/ab00284

Bosboom, J., and Stive, M. (2021) *Coastal dynamics* (LibreTexts). Available at: https://geo.libretexts.org/Bookshelves/Oceanography/Coastal_Dynamics_(Bosboom_and_Stive (Accessed November 10, 2023).

Bowley, H. E., Young, S. D., Ander, E. L., Crout, N. M. J., Watts, M. J., and Bailey, E. H. (2016). Iodine binding to humic acid. *Chemosphere* 157, 208–214. doi: 10.1016/j.chemosphere.2016.05.028

Brewer, P. G., and Riley, J. P. (1965). The automatic determination of nitrate in sea water. *Deep Sea Res. Oceanographic Abstracts* 12, 765–772. doi: 10.1016/0011-7471(65)90797-7

Campos, M. L. A. M. (1997). New approach to evaluating dissolved iodine speciation in natural waters using cathodic stripping voltammetry and a storage study for preserving iodine species. *Mar. Chem.* 57, 107–117. doi: 10.1016/S0304-4203(96)00093-X

Campos, M., Farrenkopf, A. M., Jickells, T. D., and Luther, G. W. (1996). A comparison of dissolved iodine cycling at the Bermuda Atlantic Time-Series station and Hawaii Ocean Time-Series station. *Deep-Sea Res. Part II-Topical Stud. Oceanography* 43, 455–466. doi: 10.1016/0967-0645(95)00100-X

Campos, M., Sanders, R., and Jickells, T. (1999). The dissolved iodate and iodide distribution in the South Atlantic from the Weddell Sea to Brazil. *Mar. Chem.* 65, 167–175. doi: 10.1016/S0304-4203(98)00094-2

Canfield, D. E., Glazer, A. N., and Falkowski, P. G. (2010). The evolution and future of earth's nitrogen cycle. *Science* 330, 192–196. doi: 10.1126/science.1186120

Carpenter, L. J., Chance, R. J., Sherwen, T., Adams, T. J., Ball, S. M., Evans, M. J., et al. (2021). Marine iodine emissions in a changing world. *Proc. R. Soc. A: Mathematical Phys. Eng. Sci.* 477, 20200824. doi: 10.1098/rspa.2020.0824

Carpenter, L. J., Liss, P. S., and Penkett, S. A. (2003). Marine organohalogens in the atmosphere over the Atlantic and Southern Oceans. *J. Geophysical Research: Atmospheres* 108. doi: 10.1029/2002JD002769

Carpenter, L. J., MacDonald, S. M., Shaw, M. D., Kumar, R., Saunders, R. W., Parthipan, R., et al. (2013). Atmospheric iodine levels influenced by sea surface emissions of inorganic iodine. *Nat. Geosci* 6, 108–111. doi: 10.1038/ngeo1687

Carr, N., Davis, C. E., Blackbird, S., Daniels, L. R., Preece, C., Woodward, M., et al. (2019). Seasonal and spatial variability in the optical characteristics of DOM in a temperate shelf sea. *Prog. Oceanography* 177, 101929. doi: 10.1016/j.pocean.2018.02.025

Carrano, M. W., Carrano, C. J., Edwards, M. S., Al-Adilah, H., Fontana, Y., Sayer, M. D. J., et al. (2021). Laminaria kelps impact iodine speciation chemistry in coastal seawater. *Estuarine Coast. Shelf Sci.* 262, 107531. doi: 10.1016/j.ecss.2021.107531

Carrano, M. W., Yarimizu, K., Gonzales, J. L., Cruz-López, R., Edwards, M. S., Tymon, T. M., et al. (2020). The influence of marine algae on iodine speciation in the coastal ocean. *Algae* 35, 167–176. doi: 10.4490/algae.2020.35.5.25

Chance, R., Baker, A. R., Carpenter, L., and Jickells, T. D. (2014). The distribution of iodide at the sea surface. *Environ. Sci.: Processes Impacts* 16, 1841–1859. doi: 10.1039/C4EM00139G

Chance, R., Malin, G., Jickells, T., and Baker, A. R. (2007). Reduction of iodate to iodide by cold water diatom cultures. *Mar. Chem.* 105, 169–180. doi: 10.1016/j.marchem.2006.06.008

Chance, R., Weston, K., Baker, A. R., Hughes, C., Malin, G., Carpenter, L., et al. (2010). Seasonal and interannual variation of dissolved iodine speciation at a coastal Antarctic site. *Mar. Chem.* 118, 171–181. doi: 10.1016/j.marchem.2009.11.009

Chapman, P., and Truesdale, V. W. (2011). Preliminary evidence for iodate reduction in bottom waters of the Gulf of Mexico during an hypoxic event. *Aquat Geochem* 17, 671–695. doi: 10.1007/s10498-011-9123-6

Cook, P. L. M., Carpenter, P. D., and Butler, E. C. V. (2000). Speciation of dissolved iodine in the waters of a humic-rich estuary. *Mar. Chem.* 69, 179–192. doi: 10.1016/S0304-4203(99)00104-8

Cooper, L. H. N. (1960). The water flow into the English Channel from the south-west. *J. Mar. Biol. Assoc. United Kingdom* 39, 173–208. doi: 10.1017/S0025315400013242

Cross, J., Nimmo-Smith, W. A. M., Hosegood, P. J., and Torres, R. (2015). The role of advection in the distribution of plankton populations at a moored 1-D coastal observatory. *Prog. Oceanography* 137, 342–359. doi: 10.1016/j.pocean.2015.04.016

Cuevas, C. A., Fernandez, R. P., Kinnison, D. E., Li, Q., Lamarque, J.-F., Trabelsi, T., et al. (2022). The influence of iodine on the Antarctic stratospheric ozone hole. *Proc. Natl. Acad. Sci.* 119, e2110864119. doi: 10.1073/pnas.2110864119

Dembitsky, V. M. (2006). Biogenic iodine and iodine-containing metabolites. *Natural Product Commun.* 1, 139–175. doi: 10.1177/1934578X0600100210

Du, J., Kim, K., Son, S., Pan, D., Kim, S., and Choi, W. (2023). MnO_2-induced oxidation of iodide in frozen solution. *Environ. Sci. Technol.* 57, 5317–5326. doi: 10.1021/acs.est.3c00604

Dunford, H. B., and Ralston, I. M. (1983). On the mechanism of iodination of tyrosine. *Biochem. Biophys. Res. Commun.* 116, 639–643. doi: 10.1016/0006-291X(83)90572-7

Elderfield, H., and Truesdale, V. W. (1980). On the biophilic nature of iodine in seawater. *Earth Planetary Sci. Lett.* 50, 105–114. doi: 10.1016/0012-821X(80)90122-3

Farrenkopf, A. M., and Luther, III, G. W. (2002). Iodine chemistry reflects productivity and denitrification in the Arabian Sea: Evidence for flux of dissolved species from sediments of western India into the OMZ. *Deep Sea Res. Part II: Topical Stud. Oceanography* 49, 2303–2318. doi: 10.1016/S0967-0645(02)00038-3

Farrenkopf, A. M., Luther, G. W., Truesdale, V. W., and van der Weijden, C. H. (1997). Sub-surface iodide maxima: evidence for biologically catalyzed redox cycling in Arabian Sea OMZ during the SW intermonsoon. *Deep Sea Res. Part II: Topical Stud. Oceanography* 44, 1391–1409. doi: 10.1016/S0967-0645(97)00013-1

Franco, A., Mazik, K., and Roberts, L. (2017). Whitsand and Looe Bay MCZ and surround subtidal sediment data analysis and reporting. The University of Hull.

Francois, R. (1987). The influence of humic substances on the geochemistry of iodine in nearshore and hemipelagic marine sediments. *Geochimica Cosmochimica Acta* 51, 2417–2427. doi: 10.1016/0016-7037(87)90294-8

Fuge, R. (1989). Iodine in waters: possible links with endemic goitre. *Appl. Geochemistry* 4, 203–208. doi: 10.1016/0883-2927(89)90051-6

Fuge, R., and Johnson, C. C. (2015). Iodine and human health, the role of environmental geochemistry and diet, a review. *Appl. Geochemistry* 63, 282–302. doi: 10.1016/j.apgeochem.2015.09.013

Garland, J. A., Elzerman, A. W., and Penkett, S. A. (1980). The mechanism for dry deposition of ozone to seawater surfaces. *J. Geophys. Res.-Oceans Atmos.* 85, 7488–7492.

Goldschmidt, V. M. (1954). *Geochemistry* (London: Oxford U.P).

Gómez Martín, J. C., Saiz-Lopez, A., Cuevas, C. A., Baker, A. R., and Fernández, R. P. (2022). On the speciation of iodine in marine aerosol. *J. Geophysical Research: Atmospheres* 127, e2021JD036081. doi: 10.1029/2021JD036081

Gonzales, J., Tymon, T., Küpper, F. C., Edwards, M. S., and Carrano, C. J. (2017). The potential role of kelp forests on iodine speciation in coastal seawater. *PloS One* 12, e0180755. doi: 10.1371/journal.pone.0180755

Grasshoff, K. (1976). *Methods of Seawater Analysis* (New York: Verlag Chemie).

Hardisty, D. S., Horner, T. J., Wankel, S. D., Blusztajn, J., and Nielsen, S. G. (2020). Experimental observations of marine iodide oxidation using a novel sparge-interface MC-ICP-MS technique. *Chem. Geology* 532, 119360. doi: 10.1016/j.chemgeo.2019.119360

Harvey, G. R. (1980). A study of the chemistry of iodine and bromine in marine sediments. *Mar. Chem.* 8, 327–332. doi: 10.1016/0304-4203(80)90021-3

He, P., Hou, X., Aldahan, A., Possnert, G., and Yi, P. (2013). Iodine isotopes species fingerprinting environmental conditions in surface water along the northeastern Atlantic Ocean. *Sci. Rep.* 3, 2685. doi: 10.1038/srep02685

He, X.-C., Simon, M., Iyer, S., Xie, H.-B., Rörup, B., Shen, J., et al. (2023). Iodine oxoacids enhance nucleation of sulfuric acid particles in the atmosphere. *Science* 382, 1308–1314. doi: 10.1126/science.adh2526

He, X.-C., Tham, Y. J., Dada, L., Wang, M., Finkenzeller, H., Stolzenburg, D., et al. (2021). Role of iodine oxoacids in atmospheric aerosol nucleation. *Science* 371, 589–595. doi: 10.1126/science.abe0298

Hepach, H., Hughes, C., Hogg, K., Collings, S., and Chance, R. (2020). Senescence as the main driver of iodide release from a diverse range of marine phytoplankton. *Biogeosciences* 17, 2453–2471. doi: 10.5194/bg-17-2453-2020

Howard-Williams, E. (2022). Seagrass Natural Capital Assessment: The Plymouth Sound and Estuaries SAC. NECR420. Second edition (UK: Natural England).

Hughes, C., Barton, E., Hepach, H., Chance, R., Pickering, M. D., Hogg, K., et al. (2021). Oxidation of iodide to iodate by cultures of marine ammonia-oxidising bacteria. *Mar. Chem.* 234, 104000. doi: 10.1016/j.marchem.2021.104000

Hughes, M. N., Nicklin, H. G., and Sackrule, W. (1971). The chemistry of peroxonitrites. Part III. The reaction of peroxonitrite with nucleophiles in alkali, and other nitrite producing reactions. *J. Chem. Soc A*, 3722–3725. doi: 10.1039/J19710003722

Hung, C.-C., Wong, G. T. F., and Dunstan, W. M. (2005). Iodate reduction activity in nitrate reductase extracts from marine phytoplankton. *Bull. Mar. Sci.* 76, 61–72.

Huthnance, J. (2010). *Temperature and salinity* Vol. 39–106. Eds. P. Buckley, D. Connor, D. Cook, M. Cox, T. Dale, S. Dye, et al (London: DEFRA on behalf of the United Kingdom Marine Monitoring and Assessment Strategy (UKMMAS) Community).

ICONCAWS2 (-) *WeatherUnderground station ICONCAWS2*. Available at: https://www.wunderground.com/dashboard/pws/ICONCAWS2 (Accessed December 12, 2021).

Jickells, T. D., Boyd, S. S., and Knap, A. H. (1988). Iodine cycling in the Sargasso Sea and the Bermuda inshore waters. *Mar. Chem.* 24, 61–82. doi: 10.1016/0304-4203(88)90006-0

Johnson, G., Burrows, F., Crabtree, R., and Warner, I. (2022). *Plymouth Sound & Estuaries SAC Subtidal Sediment Data Analysis Report 2017*. (UK: Natural England).

Jones, M. R., Chance, R., Dadic, R., Hannula, H.-R., May, R., Ward, M., et al. (2023). Environmental iodine speciation quantification in seawater and snow using ion exchange chromatography and UV spectrophotometric detection. *Analytica Chimica Acta* 1239, 340700. doi: 10.1016/j.aca.2022.340700

Jones, M. R., and Tebo, B. M. (2021). Novel manganese cycling at very low ionic strengths in the Columbia River Estuary. *Water Res.* 207, 117801. doi: 10.1016/j.watres.2021.117801

Kim, T.-W., Lee, K., Najjar, R. G., Jeong, H.-D., and Jeong, H. J. (2011). Increasing N abundance in the Northwestern Pacific Ocean due to atmospheric nitrogen deposition. *Science* 334, 505–509. doi: 10.1126/science.1206583

Kirkwood, D. S. (1989). Simultaneous determination of selected nutrients in seawater. *Int. Council Explor. Sea (ICES)*. Annual Report, 29.

Küpper, F. C., Carpenter, L. J., McFiggans, G. B., Palmer, C. J., Waite, T. J., Boneberg, E.-M., et al. (2008). Iodide accumulation provides kelp with an inorganic antioxidant impacting atmospheric chemistry. *PNAS* 105, 6954–6958. doi: 10.1073/pnas.0709959105

Küpper, F. C., Schweigert, N., Ar Gall, E., Legendre, J.-M., Vilter, H., and Kloareg, B. (1998). Iodine uptake in *Laminariales* involves extracellular, haloperoxidase-mediated oxidation of iodide. *Planta* 207, 163–171. doi: 10.1007/s004250050469

Li, H.-P., Daniel, B., Creeley, D., Grandbois, R., Zhang, S., Xu, C., et al. (2014). Superoxide production by a manganese-oxidizing bacterium facilitates iodide oxidation. *Appl. Environ. Microbiol.* 80, 2693–2699. doi: 10.1128/AEM.00400-14

Li, H.-P., Yeager, C. M., Brinkmeyer, R., Zhang, S., Ho, Y.-F., Xu, C., et al. (2012). Bacterial production of organic acids enhances H_2O_2-dependent iodide oxidation. *Environ. Sci. Technol.* 46, 4837–4844. doi: 10.1021/es203683v

Li, J., Jiang, J., Pang, S., Cao, Y., Zhou, Y., and Guan, C. (2020). Oxidation of iodide and hypoiodous acid by non-chlorinated water treatment oxidants and formation of iodinated organic compounds: A review. *Chem. Eng. J.* 386, 123822. doi: 10.1016/j.cej.2019.123822

Liebhafsky, H. A. (1934). The catalytic decomposition of hydrogen peroxide by the iodine—iodide couple. IV. The approach to the steady state. *J. Am. Chem. Soc* 56, 2369–2372. doi: 10.1021/ja01326a043

Lin, J. (2023). Dissolved iodine in the changjiang river estuary, China. *Water Sci. Technol.* 88, 1269–1279. doi: 10.2166/wst.2023.263

Lister, M. W., and Rosenblum, P. (1963). Rates of reaction of hypochlorite ions with sulphite and iodide ions. *Can. J. Chem.* 41, 3013–3020. doi: 10.1139/v63-442

Lotze, H. K., Lenihan, H. S., Bourque, B. J., Bradbury, R. H., Cooke, R. G., Kay, M. C., et al. (2006). Depletion, degradation, and recovery potential of estuaries and coastal seas. *Science* 312, 1806–1809. doi: 10.1126/science.1128035

Lovelock, J. E. (1975). Natural halocarbons in the air and in the sea. *Nature* 256, 193–194. doi: 10.1038/256193a0

Luther, G. W. (2023). Review on the physical chemistry of iodine transformations in the oceans. *Front. Mar. Sci.* 10. doi: 10.3389/fmars.2023.1085618

Luther, G. W., and Cole, H. (1988). Iodine speciation in Chesapeake Bay waters. *Mar. Chem.* 24, 315–325. doi: 10.1016/0304-4203(88)90039-4

Luther, G. W., Ferdelman, T., Culberson, C. H., Kostka, J., and Wu, J. (1991). Iodine chemistry in the water column of the Chesapeake Bay: Evidence for organic iodine forms. *Estuarine Coast. Shelf Sci.* 32, 267–279. doi: 10.1016/0272-7714(91)90020-C

Luther, G. W., Sundby, B., Lewis, B. L., Brendel, P. J., and Silverberg, N. (1997). Interactions of manganese with the nitrogen cycle: Alternative pathways to dinitrogen. *Geochimica Cosmochimica Acta* 61, 4043–4052. doi: 10.1016/S0016-7037(97)00239-1

Luther, G. W., Wu, J., and Cullen, J. B. (1995). "Redox chemistry of iodine in seawater," in *Aquatic Chemistry Advances in Chemistry* (American Chemical Society), 135–155. doi: 10.1021/ba-1995-0244.ch006

Lymar, S. V., Schwarz, H. A., and Czapski, G. (2000). Medium effects on reactions of the carbonate radical with thiocyanate, iodide, and ferrocyanide ions. *Radiat. Phys. Chem.* 59, 387–392. doi: 10.1016/S0969-806X(00)00277-2

MacDonald, S. M., Gómez Martín, J. C., Chance, R., Warriner, S., Saiz-Lopez, A., Carpenter, L. J., et al. (2014). A laboratory characterisation of inorganic iodine emissions from the sea surface: dependence on oceanic variables and parameterisation for global modelling. *Atmospheric Chem. Phys.* 14, 5841–5852. doi: 10.5194/acp-14-5841-2014

Mantoura, R. F. C., and Woodward, E. M. S. (1983). Optimization of the indophenol blue method for the automated determination of ammonia in estuarine waters. *Estuarine Coast. Shelf Sci.* 17, 219–224. doi: 10.1016/0272-7714(83)90067-7

McTaggart, A. R., Butler, E. C. V., Haddad, P. R., and Middleton, J. H. (1994). Iodide and iodate concentrations in eastern Australian subtropical waters, with iodide by ion chromatography. *Mar. Chem.* 47, 159–172. doi: 10.1016/0304-4203(94)90106-6

Mendoza, W. G., and Zika, R. G. (2014). On the temporal variation of DOM fluorescence on the southwest Florida continental shelf. *Prog. Oceanography* 120, 189–204. doi: 10.1016/j.pocean.2013.08.010

Moon, J.-Y., Lee, K., Lim, W.-A., Lee, E., Dai, M., Choi, Y.-H., et al. (2021). Anthropogenic nitrogen is changing the East China and Yellow seas from being N deficient to being P deficient. *Limnology Oceanography* 66, 914–924. doi: 10.1002/lno.11651

Moriyasu, R., Bolster, K. M., Hardisty, D. S., Kadko, D. C., Stephens, M. P., and Moffett, J. W. (2023). Meridional survey of the central pacific reveals iodide accumulation in equatorial surface waters and benthic sources in the abyssal plain. *Global Biogeochemical Cycles* 37, e2021GB007300. doi: 10.1029/2021GB007300

Moriyasu, R., Evans, N., Bolster, K. M., Hardisty, D. S., and Moffett, J. W. (2020). The distribution and redox speciation of iodine in the eastern tropical North Pacific Ocean. *Global Biogeochemical Cycles* 34, e2019GB006302. doi: 10.1029/2019GB006302

Moulay, S. (2013). Molecular iodine/polymer complexes. *J. Polymer Eng.* 33, 389–443. doi: 10.1515/polyeng-2012-0122

Muller, F. L. L. (2018). Exploring the potential role of terrestrially derived humic substances in the marine biogeochemistry of iron. *Front. Earth Sci.* 6. doi: 10.3389/feart.2018.00159

Nakayama, E., Kimoto, T., Isshiki, K., Sohrin, Y., and Okazaki, S. (1989). Determination and distribution of iodide- and total-iodine in the North Pacific Ocean - by using a new automated electrochemical method. *Mar. Chem.* 27, 105–116. doi: 10.1016/0304-4203(89)90030-3

Neta, P., Huie, R. E., and Ross, A. B. (1988). Rate constants for reactions of inorganic radicals in aqueous solution. *J. Phys. Chem. Reference Data* 17, 1027–1284. doi: 10.1063/1.555808

Ooki, A., Minamikawa, K., Meng, F., Miyashita, N., Hirawake, T., Ueno, H., et al. (2022). Marine sediment as a likely source of methyl and ethyl iodides in subpolar and polar seas. *Commun. Earth Environ.* 3, 1–7. doi: 10.1038/s43247-022-00513-7

Pound, R. J., Brown, L. V., Evans, M. J., and Carpenter, L. J. (2023). An improved estimate of inorganic iodine emissions from the ocean using a coupled surface microlayer box model. *EGUsphere* 1–40. doi: 10.5194/egusphere-2023-2447

Prieto, L., Astorga, D., Navarro, G., and Ruiz, J. (2010). Environmental control of phase transition and polyp survival of a massive-outbreaker jellyfish. *PloS One* 5, e13793. doi: 10.1371/journal.pone.0013793

Rees, A. P., Hope, S. B., Widdicombe, C. E., Dixon, J. L., Woodward, E. M. S., and Fitzsimons, M. F. (2009). Alkaline phosphatase activity in the western English Channel: Elevations induced by high summertime rainfall. *Estuarine Coast. Shelf Sci.* 81, 569–574. doi: 10.1016/j.ecss.2008.12.005

Rush, J. D., and Bielski, B. H. J. (1985). Pulse radiolytic studies of the reactions of HO_2/O_2^- with Fe(II)/Fe(III) ions - the reactivity of HO_2/O_2^- with ferric ions and its implication on the occurrence of the Haber-Weiss reaction. *J. Phys. Chem.* 89, 5062–5066. doi: 10.1021/j100269a035

Saiz-Lopez, A., Plane, J. M. C., Baker, A. R., Carpenter, L. J., von Glasow, R., Gómez Martín, J. C., et al. (2012). Atmospheric chemistry of iodine. *Chem. Rev.* 112, 1773–1804. doi: 10.1021/cr200029u

Satoh, Y., and Imai, S. (2021). Flux and pathway of iodine dissolution from brackish lake sediment in the northeast of Japan. *Sci. Total Environ.* 789, 147942. doi: 10.1016/j.scitotenv.2021.147942

Satoh, Y., Otosaka, S., Suzuki, T., and Nakanishi, T. (2023). Factors regulating the concentration of particulate iodine in coastal seawater. *Limnol. Oceanogr.* 68, 1580–1594. doi: 10.1002/lno.12369

Satoh, Y., Wada, S., and Hama, T. (2019a). Vertical and seasonal variations of dissolved iodine concentration in coastal seawater on the northwestern Pacific coast of central Japan. *Continental Shelf Res.* 188, 103966. doi: 10.1016/j.csr.2019.103966

Satoh, Y., Wada, S., and Hisamatsu, S. (2019b). Seasonal variations in iodine concentrations in a brown alga (*Ecklonia cava* Kjellman) and a seagrass (*Zostera marina* L.) in the northwestern Pacific coast of central Japan. *J. Oceanogr* 75, 111–117. doi: 10.1007/s10872-018-0479-8

Satoh, Y., Wada, S., and Hisamatsu, S. (2020). Relationship between iodine and carbohydrate contents in the seagrass *Zostera marina* on the northwestern Pacific coast of central Japan. *Botanica Marina* 63, 273–281. doi: 10.1515/bot-2020-0004

Schall, C., and Heumann, K. G. (1993). GC determination of volatile organoiodine and organobromine compounds in Arctic seawater and air samples. *Fresenius J. Anal. Chem.* 346, 717–722. doi: 10.1007/BF00321279

Schnur, A. A., Sutherland, K. M., Hansel, C. M., and Hardisty, D. S. (2024). Rates and pathways of iodine speciation transformations at the Bermuda Atlantic Time Series. *Front. Mar. Sci.* 10. doi: 10.3389/fmars.2023.1272870

Schulz, R. C., Fleischer, D., Henglein, A., Bössler, H. M., Trisnadi, J., and Tanaka, H. (1974). Addition compounds and complexes with polymers and models. *Pure Appl. Chem.* 38, 227–247. doi: 10.1351/pac197438010227

Schwehr, K. A., and Santschi, P. H. (2003). Sensitive determination of iodine species, including organo-iodine, for freshwater and seawater samples using high performance liquid chromatography and spectrophotometric detection. *Analytica Chimica Acta* 482, 59–71. doi: 10.1016/S0003-2670(03)00197-1

Sharpless, C. M., and Blough, N. V. (2014). The importance of charge-transfer interactions in determining chromophoric dissolved organic matter (CDOM) optical and photochemical properties. *Environ. Sci.: Processes Impacts* 16, 654–671. doi: 10.1039/C3EM00573A

Sherrill, J., Whitaker, B. R., and Wong, G. T. F. (2004). Effects of ozonation on the speciation of dissolved iodine in artificial seawater. *J. Zoo Wildlife Med.* 35, 347–355. doi: 10.1638/03-025

Sherwen, T., Chance, R. J., Tinel, L., Ellis, D., Evans, M. J., and Carpenter, L. J. (2019). A machine-learning-based global sea-surface iodide distribution. *Earth System Sci. Data* 11, 1239–1262. doi: 10.5194/essd-11-1239-2019

Shi, Q., Kim, J. S., and Wallace, D. W. (2023). Speciation of dissolved inorganic iodine in a coastal fjord: a time-series study from Bedford Basin, Nova Scotia, Canada. *Front. Mar. Sci.* 10. doi: 10.3389/fmars.2023.1171999

Siddorn, J. R., Allen, J. I., and Uncles, R. J. (2003). Heat, salt and tracer transport in the Plymouth Sound coastal region: a 3-D modelling study. *J. Mar. Biol. Assoc. United Kingdom* 83, 673–682. doi: 10.1017/S002531540300763Xh

Sigman, D. M., and Hain, M. P. (2012). The biological productivity of the ocean | Learn science at scitable. *Nat. Educ. Knowledge* 10, 21.

Silverstone, M., Tosteson, T. R., and Cutress, C. E. (1977). The effect of iodide and various iodocompounds on initiation of strobilation in *Aurelia*. *Gen. Comp. Endocrinol.* 32, 108–113. doi: 10.1016/0016-6480(77)90087-9

Smith, J. D., and Butler, E. C. V. (1979). Speciation of dissolved iodine in estuarine waters. *Nature* 277, 468–469. doi: 10.1038/277468a0

Smyth, T. J., Fishwick, J. R., AL-Moosawi, L., Cummings, D. G., Harris, C., Kitidis, V., et al. (2010). A broad spatio-temporal view of the Western English Channel observatory. *J. Plankton Res.* 32, 585–601. doi: 10.1093/plankt/fbp128

Tait, D. R., Santos, I. R., Lamontagne, S., Sippo, J. Z., McMahon, A., Jeffrey, L. C., et al. (2023). Submarine groundwater discharge exceeds river inputs as a source of nutrients to the Great Barrier Reef. *Environ. Sci. Technol.* 57, 15627–15634. doi: 10.1021/acs.est.3c03725

Takayanagi, K., and Cossa, D. (1985). Behaviour of dissolved iodine in the upper St. Lawrence Estuary. *Can. J. Earth Sci.* 22, 644–646. doi: 10.1139/e85-067

Takayanagi, K., and Wong, G. T. F. (1986). The oxidation of iodide to iodate for the polarographic determination of total iodine in natural waters. *Talanta* 33, 451–454. doi: 10.1016/0039-9140(86)80115-1

Takeda, A., Tsukada, H., Takaku, Y., Satta, N., Baba, M., Shibata, T., et al. (2016). Determination of iodide, iodate and total iodine in natural water samples by HPLC with amperometric and spectrophotometric detection, and off-line uv irradiation. *Analytical Sci.* 32, 839–845. doi: 10.2116/analsci.32.839

Tang, Q., Xu, Q., Zhang, F., Huang, Y., Liu, J., Wang, X., et al. (2013). Geochemistry of iodine-rich groundwater in the Taiyuan Basin of central Shanxi Province, North China. *J. Geochemical Explor.* 135, 117–123. doi: 10.1016/j.gexplo.2012.08.019

Teagle, H., and Smale, D. A. (2018). Climate-driven substitution of habitat-forming species leads to reduced biodiversity within a temperate marine community. *Diversity Distributions* 24, 1367–1380. doi: 10.1111/ddi.12775

Tian, R. C., Marty, J. C., Nicolas, E., Chiavérini, J., Ruiz-Ping, D., and Pizay, M. D. (1996). Iodine speciation: a potential indicator to evaluate new production versus regenerated production. *Deep Sea Res. Part I: Oceanographic Res. Papers* 43, 723–738. doi: 10.1016/0967-0637(96)00023-4

Tinel, L., Adams, T. J., Hollis, L. D. J., Bridger, A. J. M., Chance, R. J., Ward, M. W., et al. (2020). Influence of the sea surface microlayer on oceanic iodine emissions. *Environ. Sci. Technol.* 54, 13228–13237. doi: 10.1021/acs.est.0c02736

Truesdale, V. W. (1975). 'Reactive' and 'unreactive' iodine in seawater — A possible indication of an organically bound iodine fraction. *Mar. Chem.* 3, 111–119. doi: 10.1016/0304-4203(75)90018-3

Truesdale, V. W. (1978). Iodine in inshore and off-shore marine waters. *Mar. Chem.* 6, 1–13. doi: 10.1016/0304-4203(78)90002-6

Truesdale, V. W. (1994). Distribution of dissolved iodine in the Irish Sea, a temperate shelf sea. *Estuarine Coast. Shelf Sci.* 38, 435–446. doi: 10.1006/ecss.1994.1030

Truesdale, V. W. (1995). The distribution of dissolved iodine in hebridean waters during mid-winter. *Mar. Environ. Res.* 40, 277–288. doi: 10.1016/0141-1136(94)00147-H

Truesdale, V. W., Bale, A. J., and Woodward, E. M. S. (2000). The meridional distribution of dissolved iodine in near-surface waters of the Atlantic Ocean. *Prog. Oceanography* 45, 387–400. doi: 10.1016/S0079-6611(00)00009-4

Truesdale, V. W., and Jones, K. (2000). Steady-state mixing of iodine in shelf seas off the British Isles. *Continental Shelf Res.* 20, 1889–1905. doi: 10.1016/S0278-4343(00)00050-9

Truesdale, V. W., and Luther, G. W. (1995). Molecular iodine reduction by natural and model organic substances in seawater. *Aquat Geochem* 1, 89–104. doi: 10.1007/BF01025232

Truesdale, V. W., Nausch, G., and Baker, A. (2001). The distribution of iodine in the Baltic Sea during summer. *Mar. Chem.* 74, 87–98. doi: 10.1016/S0304-4203(00)00115-8

Truesdale, V. W., and Upstill-Goddard, R. (2003). Dissolved iodate and total iodine along the British east coast. *Estuarine Coast. Shelf Sci.* 56, 261–270. doi: 10.1016/S0272-7714(02)00161-0

Tsunogai, S., and Sase, T. (1969). Formation of iodide-iodine in the ocean. *Deep Sea Res. Oceanographic Abstracts* 16, 489–496. doi: 10.1016/0011-7471(69)90037-0

Tymon, T. M., Miller, E. P., Gonzales, J. L., Raab, A., Küpper, F. C., and Carrano, C. J. (2017). Some aspects of the iodine metabolism of the giant kelp *Macrocystis pyrifera* (*phaeophyceae*). *J. Inorganic Biochem.* 177, 82–88. doi: 10.1016/j.jinorgbio.2017.09.003

Ullman, W. J., and Aller, R. C. (1980). Dissolved iodine flux from estuarine sediments and implications for the enrichment of iodine at the sediment water interface. *Geochimica Cosmochimica Acta* 44, 1177–1184. doi: 10.1016/0016-7037(80)90071-X

Ullman, W. J., and Aller, R. C. (1985). The geochemistry of iodine in near-shore carbonate sediments. *Geochimica Cosmochimica Acta* 49, 967–978. doi: 10.1016/0016-7037(85)90311-4

Uncles, R. J., Stephens, J. A., and Harris, C. (2015). Physical processes in a coupled bay–estuary coastal system: Whitsand Bay and Plymouth Sound. *Prog. Oceanography* 137, 360–384. doi: 10.1016/j.pocean.2015.04.019

Upstill-Goddard, R. C. (2006). Air–sea gas exchange in the coastal zone. *Estuarine Coast. Shelf Sci.* 70, 388–404. doi: 10.1016/j.ecss.2006.05.043

Upstill-Goddard, R. C., and Elderfield, H. (1988). The role of diagenesis in the estuarine budgets of iodine and bromine. *Continental Shelf Res.* 8, 405–430. doi: 10.1016/0278-4343(88)90012-X

Wadley, M. R., Stevens, D. P., Jickells, T. D., Hughes, C., Chance, R., Hepach, H., et al. (2020). A global model for iodine speciation in the upper ocean. *Global Biogeochemical Cycles* 34, e2019GB006467. doi: 10.1029/2019GB006467

Waite, T. J., and Truesdale, V. W. (2003). Iodate reduction by *Isochrysis galbana* is relatively insensitive to de-activation of nitrate reductase activity—are phytoplankton really responsible for iodate reduction in seawater? *Mar. Chem.* 81, 137–148. doi: 10.1016/S0304-4203(03)00013-6

Waite, T. J., Truesdale, V. W., and Olafsson, J. (2006). The distribution of dissolved inorganic iodine in the seas around Iceland. *Mar. Chem.* 101, 54–67. doi: 10.1016/j.marchem.2006.01.003

Weinberg, I., Bahlmann, E., Michaelis, W., and Seifert, R. (2013). Determination of fluxes and isotopic composition of halocarbons from seagrass meadows using a dynamic flux chamber. *Atmospheric Environ.* 73, 34–40. doi: 10.1016/j.atmosenv.2013.03.006

WHO. Available at: https://www.who.int/health-topics/micronutrients (Accessed January 11, 2024).

Widdicombe, C. E., and Harbour, D. (2021). Phytoplankton taxonomic abundance and biomass time-series at Plymouth Station L4 in the Western English Channel 1992-2020. *English Channel Publisher: NERC EDS Br. Oceanographic Data Centre NOC.* doi: 10.5285/c9386b5c-b459-782f-e053-6c86abc0d129

Wong, G. T. F. (1980). The stability of dissolved inorganic species of iodine in seawater. *Mar. Chem.* 9, 13–24. doi: 10.1016/0304-4203(80)90003-1

Wong, G. T. F. (1982). The stability of molecular iodine in seawater. *Mar. Chem.* 11, 91–95. doi: 10.1016/0304-4203(82)90051-2

Wong, G. (1991). The marine geochemistry of iodine. *Rev. In Aquat. Sci.* 4, 45–73.

Wong, G. T. F., Brewer, P. G., and Spencer, D. W. (1976). The distribution of particulate iodine in the Atlantic Ocean. *Earth Planetary Sci. Lett.* 32, 441–450. doi: 10.1016/0012-821X(76)90084-4

Wong, G. T. F., and Cheng, X.-H. (1998). Dissolved organic iodine in marine waters: Determination, occurrence and analytical implications. *Mar. Chem.* 59, 271–281. doi: 10.1016/S0304-4203(97)00078-9

Wong, G. T. F., and Cheng, X.-H. (2001a). Dissolved organic iodine in marine waters: role in the estuarine geochemistry of iodine. *J. Environ. Monit.* 3, 257–263. doi: 10.1039/B007229J

Wong, G. T. F., and Cheng, X.-H. (2001b). The formation of iodide in inshore waters from the photochemical decomposition of dissolved organic iodine. *Mar. Chem.* 74, 53–64. doi: 10.1016/S0304-4203(00)00095-5

Wong, G. T. F., and Zhang, L. (1992). Changes in iodine speciation across coastal hydrographic fronts in southeastern United States continental shelf waters. *Continental Shelf Res.* 12, 717–733. doi: 10.1016/0278-4343(92)90027-H

Wong, G. T. F., and Zhang, L.-S. (2003). Seasonal variations in the speciation of dissolved iodine in the Chesapeake Bay. *Estuarine Coast. Shelf Sci.* 56, 1093–1106. doi: 10.1016/S0272-7714(02)00310-4

Wong, G. T. F., and Zhang, L.-S. (2008). The kinetics of the reactions between iodide and hydrogen peroxide in seawater. *Mar. Chem.* 111, 22–29. doi: 10.1016/j.marchem.2007.04.007

Wright, L. D. (1993). Micromorphodynamics of the inner continental shelf: A middle atlantic bight case study. *J. Coast. Res.*, 93–124.

Yentsch, C. S., and Menzel, D. W. (1963). A method for the determination of phytoplankton chlorophyll and phaeophytin by fluorescence. *Deep-Sea Res.* 10, 221–231. doi: 10.1016/0011-7471(63)90358-9

Zhang, J.-Z., and Chi, J. (2002). Automated analysis of nanomolar concentrations of phosphate in natural waters with liquid waveguide. *Environ. Sci. Technol.* 36, 1048–1053. doi: 10.1021/es011094v

Zhang, E., Wang, Y., Qian, Y., Ma, T., Zhang, D., Zhan, H., et al. (2013). Iodine in groundwater of the North China Plain: Spatial patterns and hydrogeochemical processes of enrichment. *J. Geochemical Explor.* 135, 40–53. doi: 10.1016/j.gexplo.2012.11.016

Zhdankin, V. V., and Muñiz, K. (2017). Editorial for the special issue on hypervalent iodine reagents. *J. Org. Chem.* 82, 11667–11668. doi: 10.1021/acs.joc.7b02531

Frontiers in Marine Science

Explores ocean-based solutions for emerging global challenges

The third most-cited marine and freshwater biology journal, advancing our understanding of marine systems and addressing global challenges including overfishing, pollution, and climate change.

Discover the latest Research Topics

See more →

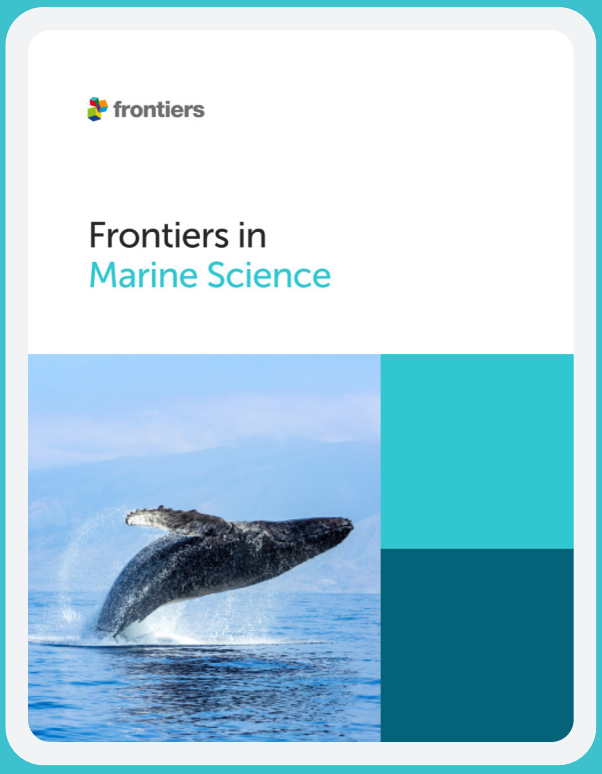

Frontiers

Avenue du Tribunal-Fédéral 34
1005 Lausanne, Switzerland
frontiersin.org

Contact us

+41 (0)21 510 17 00
frontiersin.org/about/contact